

Forsmark site investigation

Anisotropy of thermal properties in metagranite at Forsmark

Comparison between large-scale field measurements, small-scale field measurements and laboratory measurements

Jan Sundberg, John Wrafter,
Fredrik Mossmark, Anders Sundberg
Geo Innova AB

September 2007

Svensk Kärnbränslehantering AB

Swedish Nuclear Fuel
and Waste Management Co
Box 250, SE-101 24 Stockholm
Tel +46 8 459 84 00



Forsmark site investigation

Anisotropy of thermal properties in metagranite at Forsmark

Comparison between large-scale field measurements, small-scale field measurements and laboratory measurements

Jan Sundberg, John Wrafter,
Fredrik Mossmark, Anders Sundberg
Geo Innova AB

September 2007

Keywords: AP PF 400-05-071, Thermal properties, Thermal conductivity, Anisotropy, Field measurement.

This report concerns a study which was conducted for SKB. The conclusions and viewpoints presented in the report are those of the authors and do not necessarily coincide with those of the client.

Data in SKB's database can be changed for different reasons. Minor changes in SKB's database will not necessarily result in a revised report. Data revisions may also be presented as supplements, available at www.skb.se.

A pdf version of this document can be downloaded from www.skb.se.

Preface

The work has been conducted by a project group comprising Jan Sundberg (Geo Innova AB) – responsible for the design of the project, and scientific support; Jarmo Mäkinen (Drillcon Core AB) – drilling of boreholes; Thomas Karlsson (PLU-teknik) and Anders Eng (ACUO Engineering) – large-scale field tests: instrumentation and implementation; Gerry Johansson (Geocon AB) – position determination of the boreholes; Fredrik Mossmark (Geo Innova AB) – multi-probe field tests: operation and evaluation of data; Anders Sundberg (Geo Innova AB) – mathematical calculations of large-scale field-test data; Johan Claesson (CTH) – support for mathematical modelling work; Christin Dóse (Geosigma AB) – Boremap mapping of the cored boreholes; and Flavio Lanaro and Ulrika Lindberg (Berg Bygg consult AB) – 3D modelling of the rock volume using RVS. SKB's Forsmark on-site personnel included Göran Nilsson – responsible for core drilling activities; Assen Simenov – support regarding geology; Folke Eriksson – logistical support; and Lars-Åke Claesson – procurement of hand drilling services. John Wrafter (Geo Innova AB) was the project leader and the editor of this report.

Abstract

This report presents the results of an investigation of anisotropy of thermal properties in the dominant metagranitic rock, an activity performed in connection with the site investigation at Forsmark. The investigation comprised the measurement of thermal properties at three different scales using different methods appropriate for each scale, two in situ and one laboratory. The metagranite in the investigation area is distinctly foliated.

Anisotropy of thermal properties in the rock mass may impact on the design of a deep repository. The purpose of the investigations presented here is to verify the existence of, as well as to quantify, the directional dependence on thermal properties within deformed granite at the Forsmark site investigation area.

Anisotropy of thermal transport properties has been determined for different scales. A large-scale test involved heating a centrally positioned borehole, c. 18 m long, and measuring temperature at different points in four surrounding boreholes. Throughout both the heating and cooling periods (1.5 months in total) temperatures were recorded at regular intervals. Based on the thermal response, the thermal conductivity parallel both to the foliation and perpendicular to the foliation was evaluated. Smaller-scale field tests, performed by the so-called multi-probe method, were carried out at six locations. In addition, laboratory measurements using the transient plane source method (TPS) were performed on core samples taken from one of the boreholes drilled for the large-scale tests. In all methods, thermal conductivity, both parallel to the foliation and perpendicular to the foliation, were determined.

For the large-scale experiment, evaluation of temperature curves for various sensor combinations for different periods of the heating-cooling cycle give unrealistic anisotropy factors and thermal conductivities, which indicates that measurements are influenced by convection, in spite of the boreholes being grouted and filled with bentonite. This convection was probably induced primarily by high temperature gradients but also by hydraulic head differences. These disturbances are most pronounced during the heating period. The best results are therefore obtained some time after the heating has ended, when the large temperature gradients are lowered and the thermal process is “calming down”. The latter two-thirds of the cooling period are considered to be the most reliable period as regards evaluation of the anisotropy factor.

To reduce sensitivity to errors in the distance between the heater and the sensors, data from several sensors were used in the same calculation, to obtain averaged values which are not as dependent on deficiencies in measurement data for individual sensor positions. The best approximation of the anisotropy factor from the large-scale experiment is judged to be 1.15, based on the final 2/3 of the cooling curve for the centrally placed sensors.

Laboratory measurements indicate an average anisotropy factor of 1.4 for the centimetre scale. The multiprobe method which measures larger volumes of rock have yielded a mean anisotropy factor of 1.15, similar to the result of the large-scale experiment, both of which are considerably lower than for the small-scale laboratory measurements. A scale dependence on anisotropy factor is indicated.

The effective thermal conductivity without regard to any particular direction is given by the geometric means of thermal conductivity in the two principal directions. For laboratory measurements the mean effective thermal conductivity is 3.45 W/(m·K), which is similar to the value of 3.42 W/(m·K) obtained from the multiprobe measurements. The evaluated thermal conductivity from the large-scale experiment is judged to be overestimated by approximately 10 to 20 percent due to a convective component.

The laboratory measured heat capacities with the calorimetric method seem to be somewhat higher than the heat capacity calculated from the diffusivity measurements with the multiprobe method.

Sammanfattning

I denna rapport presenteras resultat från undersökningar av anisotropi för termiska egenskaper i den dominerande bergarten metagranit. Undersökningarna utfördes som en del av platsundersökningar i Forsmark. Undersökningarna omfattade mätning av termiska egenskaper i tre olika skalor. Tre olika mätmetoder, anpassade för de olika skalorna, användes. Två typer av mätningar utfördes in situ och en på laboratorium. Metagraniten i undersökningsområdet är tydligt folierad.

Anisotropi för termiska egenskaper i bergmassan kan påverka utformningen av ett djupförvar. Syftet med undersökningarna är dels att verifiera förekomsten av, och dels att kvantifiera riktning beroende för, termiska egenskaper i deformerad graniten i undersökningsområdet i Forsmark.

Anisotropi för termiska transportegenskaper undersöktes i olika skalor. Storskaligt försök utfördes genom att ett centralt borrhål, ca 18 m långt, värmdes och temperaturen mättes på olika punkter i fyra omgivande borrhål. Både under uppvärmning och avsvälning (totalt 1,5 månader) registrerades temperaturen med regelbundna intervall. Utifrån uppmätta temperaturvariationer beräknades termisk konduktivitet parallellt med, och vinkelrätt mot, foliationen. Fältförsök i mindre skala utfördes på sex platser enligt den så kallade flersondsmetoden. Dessutom utfördes laboratorieförsök enligt TPS-metoden (Transient Plane Source). För dessa försök användes kärnprover från ett av de borrhål som borrades för det storskaliga försöket. Termisk konduktivitet beräknades både parallellt med, och vinkelrätt mot, foliationen för samtliga mätmetoder.

För det storskaliga försöket gav utvärdering av temperaturkurvor för olika sensorkombinationer under olika perioder av uppvärmnings-/avsvälningssyckeln realistiska anisotropifaktorer och termiska konduktiviteter. Detta indikerar att mätningarna påverkades av konvektion trots att borrhålen injekterades med cement och fylldes med bentonit. Denna konvektion var troligen i första hand beroende på stora temperaturgradienter, men också på skillnader i hydrauliskt tryck. Dessa störningar är tydligast under uppvärmningsperioden. Därför erhöles bäst resultat en tid efter att värmningen avslutats, då de höga temperaturgradienterna sänkts och de termiska processerna avtagit. De senare två tredjedelarna av avsvälningsperioden anses vara mest tillförlitliga för utvärdering av anisotropifaktor.

För att minska känsligheten för fel i avståndet mellan värmaren och sensorerna, användes data från flera sensorer i samma beräkning. Detta för att erhålla medelvärden som inte är beroende av brister i mätning av position för enskilda sensorer. Den bästa uppskattningen av anisotropifaktor, från storskaliga försök, bedöms vara 1,15, baserat på de sista 2/3 av avsvälningssyckeln för de centralt placerade sensorerna.

Laboratorieundersökningar indikerade en anisotropifaktor på 1,4 i centimeterskalan (medelvärde). Flersondsmetoden, som mäter på stora bergsvolymer, gav en anisotropifaktor på 1,15 (medelvärde). Detta stämmer väl överens med resultatet av de storskaliga mätningarna, men båda in situ-metoderna gav märkbart lägre resultat än de småskaliga laboratorieundersökningarna. Detta indikerar att anisotropifaktorn är skalberoende.

Den effektiva termiska konduktiviteten, utan hänsyn till riktning, ges av det geometriska medelvärdet för termisk konduktivitet i de två principiella riktningarna. För laboratorieundersökningarna är medel av den effektiva termiska konduktiviteten 3,45 W/(m·K), vilket överensstämmer väl med värdet 3,42 W/(m·K), som erhålls från mätningarna enligt flersondsmetoden. Termisk konduktivitet beräknad från de storskaliga försöken bedöms vara överskattad med ungefär 10–20 %, på grund av den konvektiva komponenten.

Laboratiemätningar av värmekapacitet enligt kalorimetrisk metod gav något högre resultat än vid beräkning av värmekapacitet från diffusivitetmätningar enligt flersondsmetoden.

Contents

1	Introduction	9
2	Objective and scope	11
3	Equipment and methods	13
3.1	Large-scale experiment	13
3.1.1	General description of method and equipment	13
3.1.2	Preparatory field work	13
3.1.3	Installation of instrumentation and measurement	16
3.1.4	Data handling and analysis	19
3.1.5	Nonconformities	23
3.2	Multi-probe measurements	24
3.2.1	General description of method and equipment	24
3.2.2	Execution of field work	25
3.2.3	Data handling and analysis	25
3.2.4	Nonconformities	26
3.3	Laboratory measurements	26
4	Results	27
4.1	Geology	27
4.2	Large-scale measurements	30
4.3	Multi-probe measurements	33
4.4	Laboratory measurements	34
5	Summary and discussions	35
5.1	Discussion/evaluation	35
5.2	Uncertainties	36
5.3	Conclusions	37
	References	39
Appendix 1	Large-scale field measurement of anisotropic thermal properties at Forsmark	41
	Appendices attached on CD	
Appendix 1.1	Results and coordinates	
Appendix 1.2	Borehole data	
Appendix 1.3	Various temperature and power graphs	
Appendix 1.4	Borehole temperature curves	
Appendix 1.5	Sketches of the boreholes	
Appendix 1.6	Temperature fitting curves	
Appendix 1.7	Uncertainty calculations regarding heater and sensor positions	
Appendix 1.8	A formula for a continuous line heat source in anisotropic ground	
Appendix 2	Small-scale field measurements using the multi probe method: Assessment of anisotropy of thermal properties in granitic rock at Forsmark	
Appendix 3	Forsmark site investigation – Borehole KFM90B – An anisotropic analysis of thermal properties of rocks using a calorimetric method and TPS method	
Appendix 4	Forsmark site investigation – Borehole KFM90B – Determination of porosity by water saturation and density by buoyancy technique	
Appendix 5	Boremap mapping of KFM90B–KFM90F	
Appendix 6	RVS modelling of outcrop AFM001264 – Forsmark	
Appendix 7	Installation av givare och värmare för mätning av anisotropiska termiska egenskaper i stor skala i fält	

1 Introduction

SKB are performing investigations for the localisation of a deep repository for spent nuclear fuel at two sites, Forsmark /SKB 2006a/ and Oskarshamn /SKB 2006b/. Investigations of the thermal properties of the rock mass at Forsmark have been reported in /Sundberg et al. 2005/ and /SKB 2006a/. This report presents the results of measurements of anisotropy of thermal properties at different scales both in the field and in the laboratory, an activity performed within the site investigation at Forsmark. The work was carried out in accordance with activity plan AP PF 400-05-071. For the field activities relating to the methods of measurement, there are no method description documents. For this reason, a detailed description is presented in the activity plan. In Table 1-1, controlling documents for performing this activity are listed. Both activity plan and method descriptions are SKB's internal controlling documents.

The investigation comprised the measurement of thermal properties in the dominant granite rock at three different scales using different methods appropriate for each scale, two in situ and one laboratory. The rock investigated is located close to borehole KFM07A /Petersson et al. 2005/, see Figure 1-1. The granite in this area is distinctly foliated /SKB 2006a/, and for this reason was considered a suitable location for evaluating the anisotropy in thermal properties. The field measurements were conducted during the period October 2005 to March 2006. Laboratory measurements were carried out by the Swedish National Testing and Research Institute (SP) in May–June 2006. The thermal properties of the rock are of interest for a deep repository in that they set limits for how close waste fuel canisters can be placed to each other. The results from the different measurements reported in this report provide information concerning the anisotropy of thermal properties in the dominant granite, a factor which may have implications for the design of a deep repository.

Table 1-1. Controlling documents for the performance of the activity.

Activity plan	Number	Version
Mätning av anisotropa termiska egenskaper i stor skala i fält.	AP PF 400-05-071	1.0 (in Swedish)
KFM90B. Termiska laboratoriebestämningar.	AP PF 400-06-023	1.0 (in Swedish)
Method descriptions	Number	Version
Instruktion för inmätning och avvägning av objekt.	SKB MD 110.001	1.0 (in Swedish)
Metodbeskrivning för TV-loggning med BIPS.	SKB MD 222.006	1.0 (in Swedish)
Determining thermal conductivity and thermal capacity by the TPS method.	SKB MD 191.001	2.0
Determining density and porosity of intact rock.	SKB MD 160.002	2.0
Metodbeskrivning för Boremapkartering.	SKB MD 143.006	1.0 (in Swedish)
Mätsystembeskrivning för Boremap.	SKB MD 146.001	1.0 (in Swedish)
Instruktion: Regler för bergarters benämningar vid platsundersökningen i Forsmark.	SKB MD 132.005	1.0 (in Swedish)
Other method descriptions – see separate reports of laboratory results (Appendices 3 and 4) and Boremap mapping (Appendix 5).		
Multi-probe method.	/Sundberg 2003/	

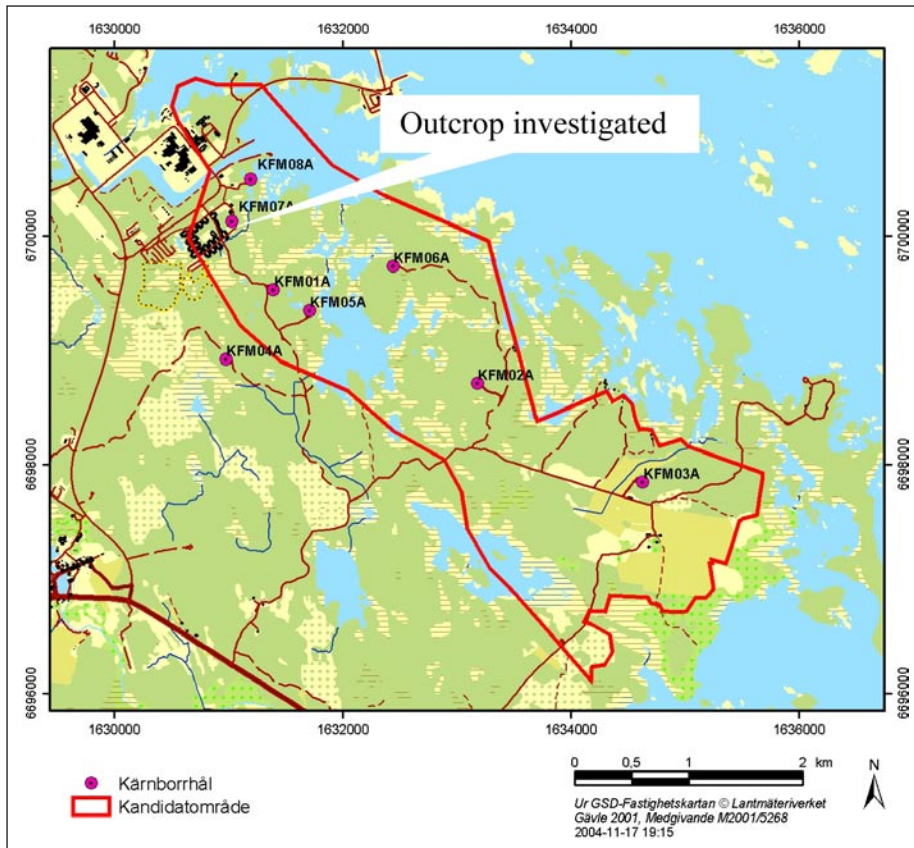


Figure 1-1. General overview of Forsmark site investigation area and location of field investigations.

The three different methods used for determining thermal properties are:

1. Large-scale field tests.
2. Small-scale field tests using the multi-probe method.
3. Laboratory measurements using the transient plane source method (TPS).

For the purpose of the large-scale tests six sub-vertical boreholes, KFM90A–F, were cored, all having a length of between 18 and 24 m.

All data in Sicada are traceable by the activity plan numbers given in Table 1-2.

Table 1-2. Data references

Subactivity	Database	Activity Plan number
Large-scale field tests	Sicada	AP PF 400-05-071
Multi-probe method	Sicada	AP PF 400-05-071
Laboratory measurements	Sicada	AP PF 400-06-023

2 Objective and scope

Anisotropy of thermal properties in the rock mass may impact on the design of a deep repository.

The rocks at Forsmark have been subjected to some degree of ductile deformation, both lineation and foliation. The preferred alignment of mineral grains produced by this deformation may produce anisotropy in thermal transport properties. The thermal conductivity is generally expected to be higher parallel with the mineral foliation and lower perpendicular to the foliation plane. There are two reasons for this. One is that conductive minerals will control the heat flow parallel to the foliation; the minerals extend longer in this plane and are not interrupted to the same extent by less conductive minerals. Perpendicular to the foliation there is a higher density of transitions between different minerals, resulting in less conductive minerals having greater influence. The second reason is that most minerals are thermally anisotropic showing large variation in thermal conductivity depending on direction. In a foliated rock, some minerals, e.g. biotite, will tend to be aligned with their highest conductivities in the plane of foliation.

Previous laboratory measurements of foliated granite at Forsmark /Dinges 2006/ have indicated the presence of anisotropy of thermal conductivity related to the foliation structure in the rock.

The objective of the investigations presented here are:

- To verify the existence of, as well as to quantify, the directional dependence on thermal properties within deformed granite at the Forsmark site investigation area.
- To investigate the scale dependence on anisotropy of thermal properties by performing measurements at centimetre scale up to metre scale.

Field tests, which measure a larger volume of rock, are performed in order to investigate if, and to what extent, thermal property anisotropy occurs at larger scales within the dominant granitic rock in the Forsmark area. Based on the results of the field measurements, it may be possible for laboratory results to be upscaled to a scale more relevant for heat transport away from the waste fuel canisters.

The investigations are confined to an area close to borehole KFM07A. Two uncovered outcrops, a pit (ID AFM001264) and a trench (ID AFM0012645), were chosen for the investigations. The area was chosen based on observations in the nearby borehole (KFM07A). The area, dominated by granite (rock code 101057), is considered by geologists to be representative of the candidate area, although the distinct foliation is somewhat more developed here than is normal for the rest of candidate area.

Anisotropy of thermal transport properties has been determined using different methods. A large-scale test was performed in the pit and involved drilling boreholes, installation of a heater and other instrumentation, a heating period followed by a cooling period (1.5 months in total) during which temperatures in a series of boreholes were recorded at regular intervals and stored using a logging device. Smaller-scale field tests, performed by the so-called multi-probe method, were carried out at six locations, three in the pit and three in the trench. Each small-scale measurement was completed in a matter of hours. Last but not least, laboratory measurements were performed on core samples taken from one of the boreholes drilled for the large-scale tests.

The parameters to be measured by each method are thermal conductivity (λ , W/(m·K)) and diffusivity (κ , m²/s), both parallel to the foliation and perpendicular to the foliation. Heat capacity (C , J/(m³·K)) can be calculated from $C=\lambda/\kappa$. Laboratory measurement requires a known value of heat capacity in order to evaluate the thermal conductivity in the different directions.

3 Equipment and methods

3.1 Large-scale experiment

3.1.1 General description of method and equipment

The principle of the large-scale tests is as follows. A 13 m long heater is placed in a centrally positioned borehole oriented parallel to the foliation in the direction of maximum dip, while temperature is measured by a series of sensors placed at different points in four surrounding boreholes at approximately 0.75 m or 1.5 m distance positioned parallel and perpendicular to the foliation. Based on the thermal response logged during both the heating and cooling period, the thermal conductivity parallel to the foliation and perpendicular to the foliation can be evaluated. The configuration of the large-scale test is illustrated schematically in Figure 3-1. The central borehole was approximately 18 m long whereas the surrounding boreholes were drilled to a length of about 20 m. A 24 m long reference borehole was also drilled to monitor natural temperature variation in the rock mass.

The work was carried out in accordance with activity plan AP PF 400-05-071 – Mätning av anisotropa termiska egenskaper i stor skala i fält (internal SKB document).

3.1.2 Preparatory field work

The implementation of the large-scale field experiment is briefly described below. For detailed descriptions, the reader is referred to the method descriptions referred to in Table 1-1, as well as Appendix 1 and 7.

The following steps were involved in the fieldwork for the large-scale experiment:

1. The overburden was removed at two locations close to drill site KFM07. The uncovered outcrops in the pit (ID AFM001264) and trench (ID AFM0012645) were geologically mapped (see Appendix 5). Original groundwater levels were above the bedrock-overburden contact. The sites were kept water-free by pumping.
2. With due consideration to lithology, fracturing and foliation, suitable positions for the large-scale experiment were proposed by the site geologist. The positions for drilling the reference borehole and the central heating borehole were marked out on the rock surface.
3. The strike and dip of the foliation were measured at several locations. The positions on the rock surface for the temperature monitoring holes were measured and marked out.
4. Instructions were given to the drilling team and the surveying engineer to drill the boreholes with an azimuth of 260° and an inclination of 82°, which is parallel to the dip direction of the foliation.
5. Six boreholes were core drilled. For each borehole, the drill rig was positioned and oriented with the help of the surveying engineer. The drilling operations were performed between October 10, 2005 and October 28, 2005. Drillcon Core AB, Nora, Sweden, carried out the drilling.
6. Core drilling of the boreholes was performed with two borehole dimensions. KFM90A and 90B were drilled with a borehole diameter of 76 mm, whereas KFM90C–90F were drilled with a diameter of 56 mm. KFM90A was drilled about 10 m away from the heater borehole for the purpose of collecting reference temperature measurements. The reference borehole was drilled first in order to verify that the foliation was oriented as expected. The drilled borehole lengths according to the drilling team are given in Table 3-2. This data was stored in the Sicada database.
7. The cores were placed in cases.

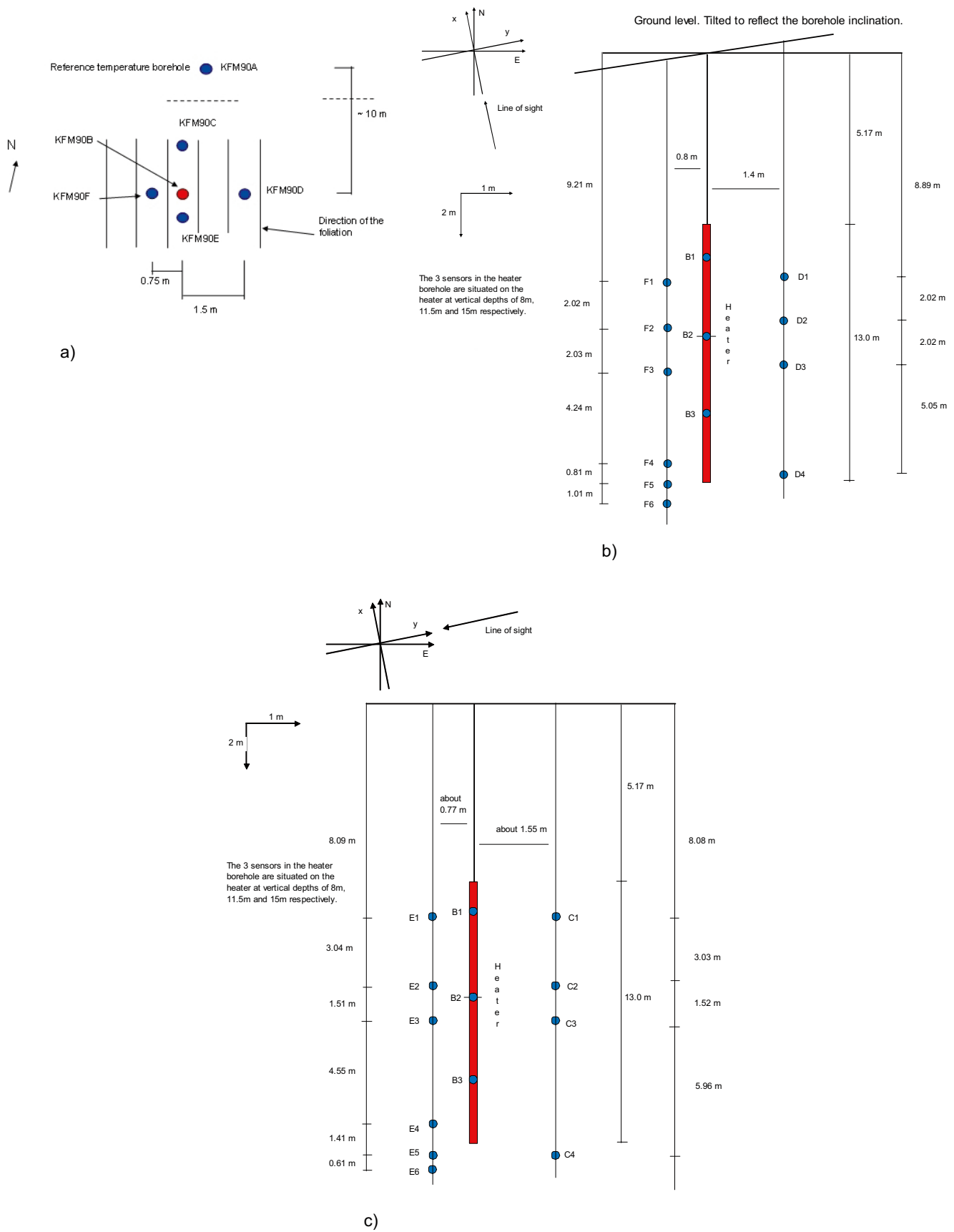


Figure 3-1. Schematic views of the set up of the thermal experiment. a) View from top, b) profile parallel to foliation and c) profile perpendicular to foliation. Note that the bedrock surface was covered with a layer of insulating material for the duration of the experiment.

8. Observations concerning lithology, orientation of foliation, fracture frequency were recorded. The foliation was judged to be generally parallel to the borehole core axes as was expected (Figure 3-3), although some local deviations from the parallel were noted. Two fracture zones were recorded in several boreholes, one at 5–8 m, the other between about 14 and 17 m. The rock was generally homogenous. Minor occurrences of amphibolite and pegmatite were noted. Based on these observations suitable positions for the temperature sensors were determined. It was considered undesirable for the temperature sensors to be positioned at the same levels as the occurrence of subordinate rock types.
9. The positions (x, y, z coordinates) of the boreholes at the rock surface were measured according to method description SKB MD 110.001. Data was delivered to Sicada.
10. The orientations (azimuth and inclination) of the boreholes were measured by the surveying engineer (Table 3-1). Coordinates at 3 m regular intervals along the borehole were calculated. Data was delivered to Sicada.



Figure 3-2. Drilling at location for large-scale experiment.



Figure 3-3. Drill cores with core axis parallel to foliation.

Table 3-1. Position of each borehole (measured from surface) according to original surveying. This data has been stored in Sicada. Both these and the coordinates from the second surveying (Appendix 1.2) were used in evaluation of results.

Borehole	Elevation m.a.s.l. (position at ground surface)	Inclination (degrees) at upper end of borehole	Bearing (degrees) at upper end of borehole
KFM90A	0.343	-82.34	278.34
KFM90B	-0.553	-81.85	261.66
KFM90C	-0.784	-81.82	262.52
KFM90D	-0.364	-81.74	260.02
KFM90E	-0.426	-81.77	259.71
KFM90F	-0.624	-81.73	261.42

11. Boreholes KFM90B, 90C and 90F were pressure grouted with Lafarge cement, which was allowed to set. After setting the boreholes were redrilled. The purpose of grouting was to seal fractures and prevent water movement during the testing period. Flushing of these boreholes indicated that the grouting had effectively sealed the holes. Grouting of boreholes KFM90D and 90E was not considered necessary since no loss of water was observed on filling the holes with water.
12. The boreholes were image logged using the BIPS system according to method description SKB MD 222.006.
13. Boremap mapping of the boreholes were performed between the 2nd and 9th of November in 2005 according to method descriptions SKB MD 143.006 and SKB MD 146.001. Results are presented in Appendix 5 and are stored in Sicada.
14. The holes were plugged until the instrumentation was inserted.
15. On 19 June 2006, after the completion of the experiment, the positions and orientations of the boreholes were surveyed once more for verification purposes (Appendix 1.2). The coordinates from this survey were not delivered to Sicada. However, both these and the original set of coordinates were used in the evaluation described below. It was considered important to check the accuracy of the coordinates, since the results are heavily dependent on the coordinates from the borehole measurement. The difference between the measurements gives an indication of the uncertainty.

3.1.3 Installation of instrumentation and measurement

Instrumentation for the tests was installed in the boreholes in accordance with the activity plan and Figure 3-1 above. For a more detailed description see Appendix 7. The heat source was positioned in the central borehole (KFM90B), whereas the four surrounding boreholes (KFM90C–KFM90F) and the reference borehole (KFM90A) were equipped with thermal sensors.

The installation team were given the desired positions along the boreholes (measured from the top of the boreholes) at which the sensors were to be installed. Knowing the inclination of the boreholes, the lengths along the boreholes (measured from top of the borehole) that corresponded to a certain vertical depth could be determined. The sensors for each borehole were then secured on certain places along a pole, which then was inserted into the borehole. It should be noted, however, that when securing the sensors on the poles the team chose to use the depths to the bottom of the boreholes as reference points. The lengths of the boreholes were determined by the installation team using a measuring tape and a lead-weight (Table 3-2). These lengths differed slightly from those recorded by the drilling team (Table 3-2). Since there is always some uncertainty regarding the exact depth of a borehole of this kind, the vertical positions of the sensors might be uncertain. For more information regarding this, see Appendix 1.2. Prior to installation, the boreholes were flushed clean in order to clean them from rock and grouting debris.

Table 3-2. Borehole lengths (measured from surface). Lengths measured by the installation team were used in the thermal anisotropy calculations.

Borehole	Length of boreholes according to installation team (m)	Length of boreholes according to drilling team (m). Data reported to Sicada.
KFM90B	18.17	18.2
KFM90C	20.03	20.0
KFM90D	20.47	20.4
KFM90E	20.35	20.3
KFM90F	20.09	20.1

Boreholes C and D were inserted with four temperature sensors each, six sensors were placed in each of boreholes E and F, while three sensors were inserted in borehole B. Three sensors were placed at different depths in boreholes A as references. The sensors were named according to the borehole they were inserted into and their vertical position relative to each other. For example, the uppermost sensor in borehole C was called C1, while the lowest one was called C4. For approximate locations of the sensors, see Appendix 1.5.

A heater was inserted into borehole B. Problems with the heater (electric earth faults) arose on two occasions due to water infiltration. After the first failure, another heater of the same type was installed. After a second failure, a new heater was installed. This new heater consisted of a 26 m long heating cable which was folded along the length of a 13 m long rod. The actual length of the heater was thereby 13 m, and it was placed on the bottom of borehole B.

The boreholes were filled with bentonite slurry to achieve uniform and controlled thermal contact between both heater and sensors, and the surrounding rock mass, as well as to further inhibit water movements. However, the installation team was not able to fix the position of the rods while pumping in the bentonite. Therefore, there is an uncertainty regarding the horizontal position of the heater and sensors. This uncertainty is based on the borehole radius and the dimensions of the inserted equipment and is about ± 27.5 mm for the heater and ± 25.5 mm for the sensors (see Appendix 1.7 for calculation details).

Soil was used to even out the surface irregularities in the immediate vicinity of the test area. The test area was also covered with a layer of insulating material for the duration of the experiment.

Temperatures were logged until stable conditions were reached. The experiment consisted of a heating period, during which the power was set to about 150 W/m, and a cooling period, where the heater was turned off to let the surroundings cool down. The heating period lasted for 20 days from 31 January 2006, 15:34:46 until 20 February 2006 12:14:46. The heater was then turned off, whereas measurements were continued for an additional 23 days until 15 March 2006, 16:24:46, when the experiment was ended. For the duration of the experiment, the sensors collected new temperature data every 10 minutes.

The temperature trends for borehole C are shown as an example in Figure 3-4 below. One notable observation is the trend of sensor C1, which first increases in temperature faster than the others and then decreases in temperature faster during the cooling period. Temperature graphs for all boreholes can be found in Appendix 1.3.

The power was set to about 150 W/m, but the curve varies slightly over time, see Figure 3-5. After an initial period of disturbance, the power fluctuated around 150 W/m during the rest of the heating period. This initial disturbance was caused by adjustments towards the set value. The average power output after the initial adjustments (29.5 hours) was calculated to be 149.2 W/m.

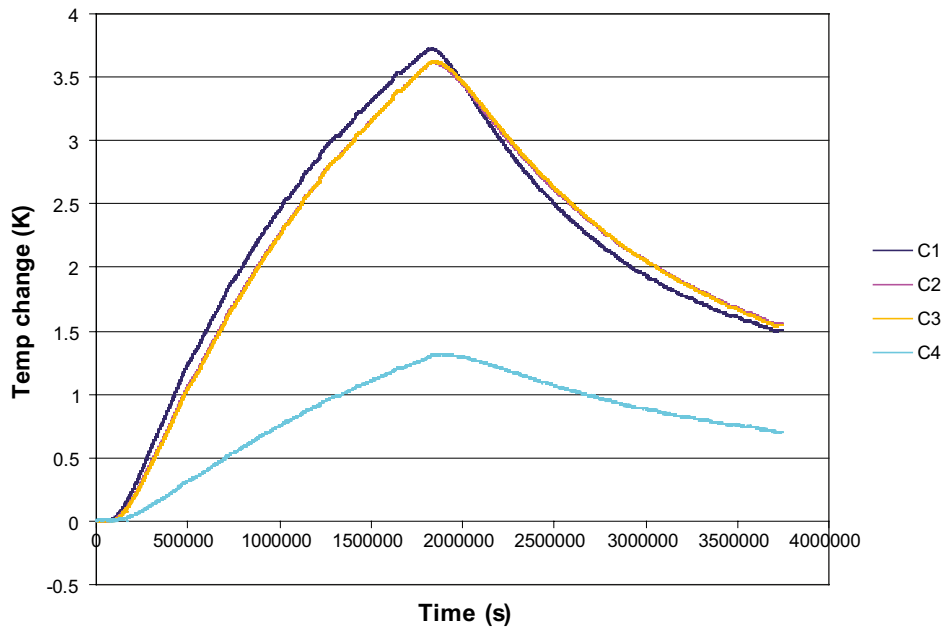


Figure 3-4. Example of the heating and cooling trends for the different sensors in borehole C.

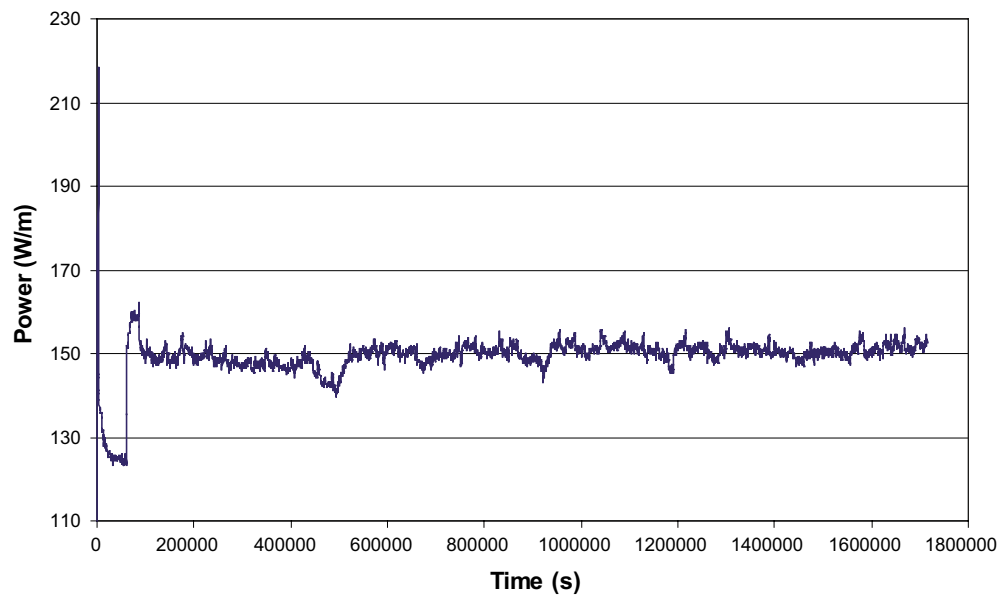


Figure 3-5. Power output from heater during the heating period.

3.1.4 Data handling and analysis

The temperature data was processed in MathCAD in order to calculate the thermal conductivity and heat capacity in different areas of the site. To do this required transforming the positions of the heater and the temperature sensors into a new coordinate system with its z axis along borehole KFM90B. In addition, the temperature data was corrected for natural temperature changes as indicated by sensors in the reference borehole, KFM90A.

Calculation of sensor coordinates

Creating the new x-y-z coordinate system

The original coordinate system that was used for the positioning and measurement of the boreholes was a system with Northing, Easting and Z axis. Each borehole had been measured, resulting in coordinates at regular intervals down along the boreholes. The coordinates included values of Northing, Easting, elevation above sea level, vertical depth with respect to ground level and length along the borehole. It also included the inclination and bearing in degrees at the same points along the borehole. Borehole coordinates are listed in Appendix 1.2. Figure 3-6 shows the surface position of the boreholes, and Table 3-3 the distances between borehole KFM90B and the surrounding boreholes. The orientations of the boreholes seen from above are shown in Figure 3-7.

Table 3-3. Distance to borehole B (measured at surface; coordinates from original measurement).

Borehole	Distance to borehole KFM90B, (m)
KFM90C	1.508
KFM90D	1.515
KFM90E	0.733
KFM90F	0.829

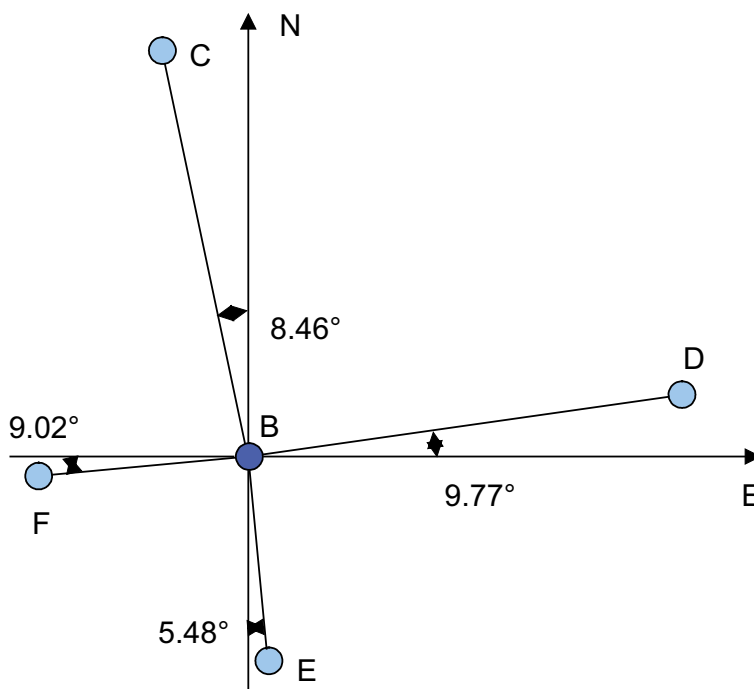


Figure 3-6. Position of the boreholes with respect to Northing and Easting axes.

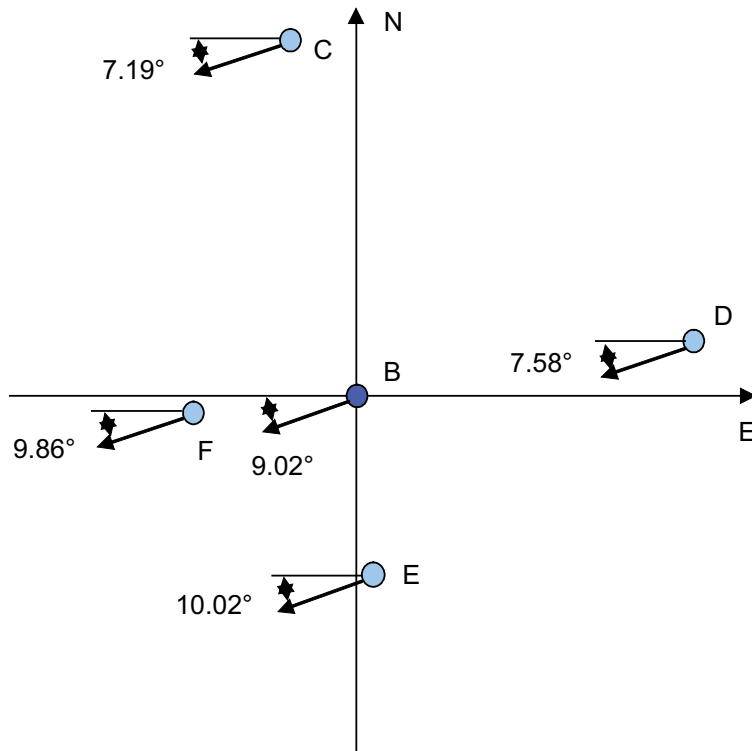


Figure 3-7. Directions (angles) of the boreholes seen from above. The arrows are only intended as angle markers. They do not show the actual lengths of the boreholes, nor are they representative for the angles. (Coordinates from original measurement)

The coordinate system required for the thermal anisotropy calculations has its origin at the middle of the heater, almost 12 m below the ground surface. Its z axis stretches along the central borehole, KFM90B, with the positive direction downwards. Since borehole B is not directed vertically downwards, but has an inclination of about 82°, the z axis is tilted in space. The x axis is directed parallel to a vector extending from the top of borehole B and the top of borehole C, which has then been mirrored onto the plane which has the z axis as normal (see Figure 3-8.). The y axis is simply directed perpendicular to x and z in the north-east direction.

To create the axes of this coordinate system the z vector was calculated. This vector was approximated from the start to the end of the heater and directed downwards. Then the vector between the top of boreholes B and C was calculated. Another vector perpendicular to the first vector in the surface plane (N-E plane) was created. Both these vectors were assumed to lie in a horizontal surface plane and thus had no Z component. After that these two vectors were mirrored onto the tilted plane (see Figure 3-8), which has borehole B as a normal vector. This gave the x and y vector. Finally, the x, y and z vectors were normalized (divided by the vector length). The theory behind these calculations are described by /Sparr 1994/.

Transforming the N-E-Z coordinates into x-y-z coordinates

The N-E and Z coordinates for the sensors were found by interpolating along the length of the boreholes. Both the information about the N-E-Z coordinates for different lengths along the boreholes and the borehole lengths for the position of the sensors (see Appendix 1.2) were used in these calculations. The N-E coordinates were then transformed into X1-Y1 coordinates, an intermediate step in the transformation of the N-E-Z coordinates into the tilted x-y-z coordinates that were required. The X1-Y1 coordinate system had its origin on the top of borehole B (i.e. same coordinate axis vectors as the N-E system, but with a movement of the origin).

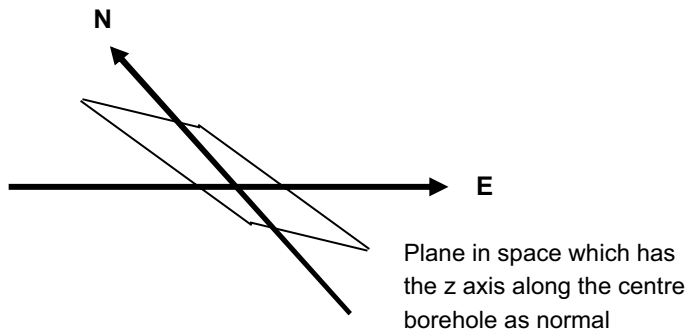


Figure 3-8. Descriptive picture of the plane with the z axis along the centre borehole as normal. The x and y axis's are mirrored onto this plane from the N-E plane.

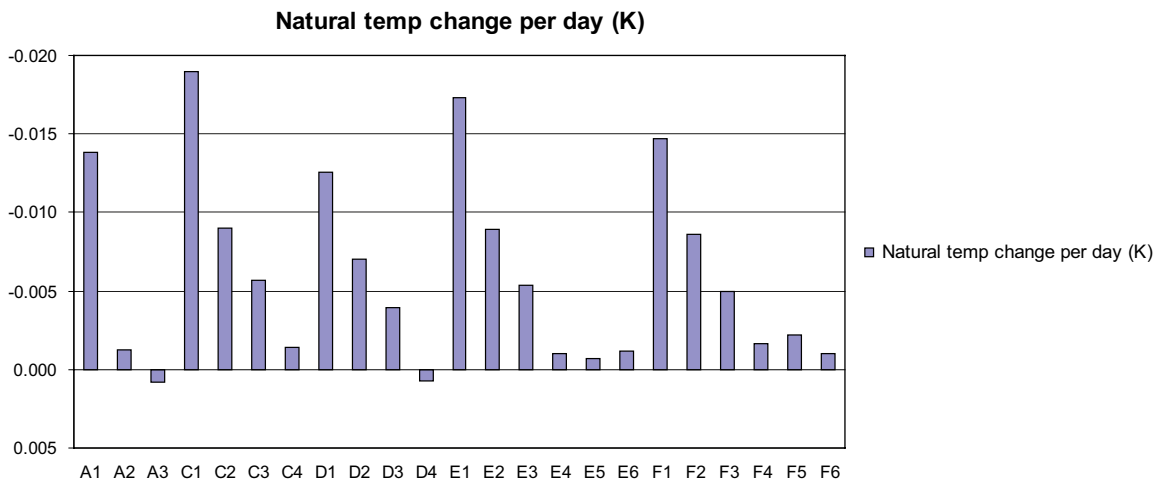


Figure 3-9. Summary of the natural temperature drift per day (over 15 days just before the experiment started) for the different sensors. Temperature drifts for sensor B1, B2 and B3 are not available due to reinstallation of the heater.

A transformation matrix was created from the x-y-z axes which had already been calculated. This matrix was then used to transform the sensor coordinates in the X1-Y1-Z system to coordinates in the new x-y-x system. The origin was also moved downwards to the middle of the heater. More about the theory behind this calculation can be found in /Sparr 1994/. The resulting coordinates of the sensors in the new x-y-z system can be found in Appendix 1.2.

Temperature data adjustments

During the experiment, the natural temperature in the bedrock changed not only because of the heater, but also because of an induced temperature disturbance from the ground surface due to changes in air temperature. It is necessary to correct the measured temperatures during the experiment for these natural temperature changes, called temperature drift.

Temperature measurement data was collected not only for the period of the experiment, but also for a period before the experiment was started (Table 3-9). In the latter data set, the only parameter that affected the temperature was changes in air temperature. By looking at the last 15 days before the experiment, the average temperature drift could be calculated for each borehole. The temperature drift was then subtracted from the temperature values to give the correct temperature data.

However, because of unusable data (due to re-installations of heater) from sensor B1, B2 and B3, the temperature drift data from boreholes KFM90E and KFM90F was used instead. The temperature drift for B1 was approximated as the mean of the temperature drifts from sensor E1 and F1. Data from sensor E2 and F2 were used for B2 and data from E3 and F3 were used for B3.

Description of the MathCAD algorithm

Conceptually, the problem of evaluating the thermal conductivity parallel and perpendicular to the foliation can be considered in terms of a subhorizontal cylinder having its axis perpendicular (y direction) to the foliation plane. The circular cross-section of the cylinder is parallel to the plane of foliation and contains the mutually perpendicular x and z directions, where the latter is defined by the trace of the central borehole. The thermal conductivity in the x-direction is assumed to be the same as in the z-direction, but different from the y-direction.

MathCAD was used to process the temperature data and calculate the thermal conductivity in the two principle directions and heat capacity for different combination of sensors. The algorithm uses parameters such as temperature trends, distance from heater to sensor, and average heater power output to derive the results. The theoretical basis for evaluation is expressed by the equation below, derived in Appendix 1 /Claesson 2006/. It is valid in 3D and evaluates thermal conductivity in the x- and y-directions. Heat is produced in the interval $-H$ to H . The origin is at the half length of the heater.

$$T(x, y, z, t, \lambda_x, \lambda_y, C) = \frac{q}{4\pi \cdot \sqrt{\lambda_x \cdot \lambda_y}} \cdot \int_{H \cdot \sqrt{\frac{C}{4 \cdot \lambda_x \cdot t}}}^{\infty} e^{-\left(x^2 + \frac{\lambda_x}{\lambda_y} \cdot y^2\right) \cdot \left(\frac{s}{H}\right)^2} \cdot \frac{1}{s} \cdot F(s, z) ds$$

$$F(s, z) = \operatorname{erf}\left[\left(1 - \frac{z}{H}\right) \cdot s\right] + \operatorname{erf}\left[\left(1 + \frac{z}{H}\right) \cdot s\right]$$

T = temperature

x, y, z = sensor coordinates in the x, y, z system

λ_x, λ_y = thermal conductivity in the x and y direction

C = heat capacity

q = power output per unit of length

H = half the heater length (6.5m) T = time

erf() = error function

s = integration variable

The calculation begins with arbitrary starting values for the yet unknown thermal conductivity and heat capacity. Together with coordinates for all sensors and the average power output, the MathCAD algorithm makes a straight forward calculation using the above formula to generate a resulting temperature curve for those parameters. This curve is then compared with the measured temperature curve for that particular sensor, and is then optimized step by step by changing the conductivity and capacity values, until the two curves are as similar as possible. This is a Least Square operation using the Conjugate Gradient method.

Since the algorithm calculates the thermal conductivity in both x and y directions, it cannot achieve this by treating only a single sensor at a time. It needs data from at least two sensors, located approximately perpendicular to each other with respect to the central heater. For example, c1d1 represents the first level pair of sensors in boreholes C and D.

When the cooling curve is used, the evaluation is made in a slightly different way. The MathCAD algorithm comprises two steps. First the temperatures are calculated under the assumption that the heating is continuing. In the second step, the algorithm is used with a negative power output ($t=0$ when the heating stops). These two solutions are superimposed and the resulting temperature is then compared with the measured temperature in the same way as described above.

Data reduction

Computing the complex calculations is very time consuming and a lot of time could be saved by reducing the amount of temperature data. The original temperature file includes temperatures measured every 10 minutes for several weeks. The whole experiment produced 6,197 rows of temperature data (one row per temperature update). When the amount of data was reduced to only 62 rows (temperature data update every 60,000 s only), the processing time decreased considerably. A comparison of the results from the calculations with 62 rows with those using 6,197 rows showed only small differences ($\pm 0.2\%$ at the most). Thus, all calculations were done with only 62 rows. Row 0–28 contained data from the heating period, while row 29–61 contained data from the cooling period. The temperature data was imported to MathCAD from an excel sheet matrix with one row for each measurement update and one column for each sensor.

3.1.5 Nonconformities

Table 3-4 lists the nonconformities relative to the activity plan.

Table 3-4. Deviations from plan of activities for thermal property anisotropy measurements according to AP-PF-400-05-071.

Activity/subactivity	According to AP-PF-400-05-071	Execution
Heat source	The heaters to be used are two 7 m long rods with an active length of 6.5 m, which when attached end to end give a total active heating length of 13 m.	Because of earth fault problems with the heaters originally installed, a heating cable 26 m long folded in two about a wooden rod was used instead.
Diameter of boreholes	Boreholes other than the heater borehole are drilled with a diameter of 56 mm.	The reference borehole has a diameter of 76 mm, which is the same as the heater borehole.
Grouting of boreholes	Grouting of heater borehole to seal conductive fractures planned.	Grouting was performed in two additional boreholes involved in thermal experiment.
BIPS logging of boreholes	The project leader decides if BIPS logging of the reference hole is necessary.	BIPS logging of the reference hole was not performed, since detailed mapping was considered unnecessary for this borehole.
Heater power output	The linear heater source has a power output of 100 W/m.	The output was set at 150 W/m to pronounce the temperature response.
Horizontal position of heater cable and temperature sensors	The exact position of the temperature sensors and heater cable, both horizontally and vertically, is critical for evaluation.	The horizontal position of the instrumentation in the borehole could not be fixed when pumping in the bentonite slurry, which means that the exact position of the sensors and heater is uncertain.
Vertical position of heater cable and temperature sensors	The exact position of the temperature sensors and heater cable, both horizontally and vertically, is critical for evaluation.	The levels at which the instruments were positioned were measured in relation to the bottom of the boreholes. These measurements were then used to calculate the distance from sensor positions to the ground surface. However, borehole length measurements made by the installation team differ slightly to those obtained by the drilling team. Moreover, the bottom of a borehole may be irregular and sludge may have collected, making it difficult to measure accurately. Therefore, it is difficult to determine the exact levels, relative to the reference plane at the surface, at which the sensors were positioned.

3.2 Multi-probe measurements

3.2.1 General description of method and equipment

Measurement of thermal conductivity in different directions was carried out at six locations using the multi-probe method. The multi-probe method can be considered to be a downscaled version of the large-scale experiment described in section 3.1. Three short boreholes are drilled so that in a plan view they create an angle parallel and perpendicular to the foliation; see Figure 3-10. The method is conducted by heating the rock with a probe installed in one borehole and monitoring changes in temperature in observation boreholes at a known distance from the probe; see Figure 3-11. The multi-probe method has previously been described in /Sundberg 1988/, but has been modified here for application to the measurement of anisotropic thermal properties.

The heater probe, c. 1.2 m long, consisted of a resistor with an even heat output along its length, supplied electrically from a device with a constant electrical current and voltage output (Delta Elektronika ES030-5). Temperature was monitored with thermistors of type YSI 44033 that have a tolerance of $\pm 0.1^\circ\text{C}$. Data measurements were logged with a data logger (Datataker 500).

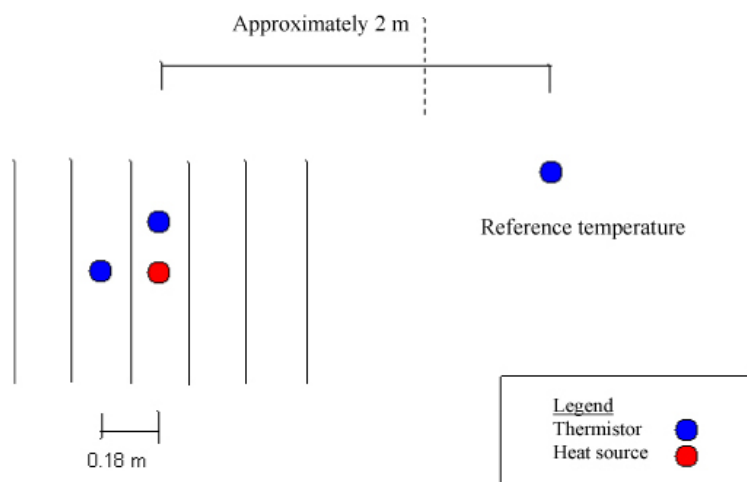


Figure 3-10. Schematic layout of an installation of heat probe, observation and reference thermistors for the multi-probe method.



Figure 3-11. Multi-probe measurements in progress.

3.2.2 Execution of field work

The following main steps were involved in the fieldwork for the multi-probe measurements:

1. Six locations were chosen for the multi-probe measurements, three in the pit (Site A, outcrop ID AFM001264) and three in the trench (Site B, outcrop ID AFM0012645). Site B is the same site as for the large-scale experiment. A reference location for background temperature measurement at each site was also chosen. All measuring locations were marked out as shown in Figure 3-12. Based on observations of the outcrop surface, all locations were considered to be comprised of homogenous foliated granitic rock, without any prominent fractures or joints.
2. The holes were drilled using a Hilti hand-held drill. They comprised three vertical holes, 18 mm in diameter, at each of the six measurement locations in addition to a reference hole at both sites. At each measuring position, the holes were drilled parallel to each other, and roughly parallel to the sub-vertical foliation plane, as shown in Figure 3-10. The central heater hole was drilled to a depth of about 1.15 m while the temperature measurement holes were drilled to 0.6 m.
3. The positions (x, y, z coordinates) of the boreholes at the rock surface were measured according to method description SKB MD 110.001. Data was delivered to Sicada.
4. The orientations (azimuth and inclination) of the boreholes were measured. Coordinates at decimetre intervals along the boreholes were calculated. Data was delivered to Sicada.
5. The holes were plugged until the measurements were performed.
6. A bentonite clay/water mixture (slurry) was poured into the boreholes to fill the space between the rock and the installed equipment.
7. Measurements were carried out as described in detail in Appendix 2. Reference is also made to Appendix 2 for photographs and diagrams illustrating the method.

3.2.3 Data handling and analysis

As with the large-scale experiment, MathCAD was used to process the temperature data and calculate the thermal conductivity and heat capacity for the rock mass at each location; see Appendix 2 for details.

The theoretical basis for evaluation of the data is identical to that used for the large-scale experiment as described in section 3.1.4.



Figure 3-12. Rock surface before drilling at HFM97, one of the locations for the multi-probe measurements. Note orientation of foliation from top to bottom of picture.

3.2.4 Nonconformities

Table 3-5. Deviations from programme for thermal property anisotropy measurements according to AP PF 400-05-071.

Activity/subactivity	According to AP PF 400-05-071	Execution
Drilling of shallow holes for multi-probe method.	These boreholes are to have a diameter of 16 mm.	A 18 mm diameter drill was used instead, since suitable 16 mm drills were not available.

3.3 Laboratory measurements

Six representative samples of foliated granite to granodiorite (101057) were chosen from the core from borehole KFM90B for laboratory measurement of thermal properties. The relationship between foliation and the core axis was noted for each sample, see Table 3-6. After consultations with laboratory personnel at the Swedish National Testing and Research Institute (SP), the samples were appropriately marked and dispatched to SP for analysis. The analytical work was carried out in accordance with activity plan AP PF 400-06-023 (internal SKB document).

Thermal properties of the six specimens were measured at ambient temperature (20°C). The determination of the thermal properties is based on a direct measurement method, the so called “Transient Plane Source Method” (TPS). Thermal properties are determined under the assumption that the specimens are anisotropic. The sensor is placed on the foliation plane and thermal conductivity in this plane and perpendicular to foliation plane is determined, see Figure 3-13. For anisotropic analysis with the TPS method, specific heat is needed as input. The specific heat capacity was measured by the calorimetric method.

For detailed descriptions of the preparation and measurement procedures used, see Appendices 3 and 4.

Table 3-6. Core samples for laboratory measurement.

ID no.	Secup (m)	Seclow (m)	Comment
KFM90B-294-90V	8.19	8.26	Dip direction of foliation parallel to drill core axis.
KFM90B-295-90V	8.93	9.00	Foliation plane diverges slightly from drill core axis (sample cut parallel to foliation).
KFM90B-296-90V	10.15	10.22	Foliation not clearly defined – (sample cut parallel to drill core axis).
KFM90B-297-90V	14.68	14.75	Dip direction of foliation parallel to drill core axis.
KFM90B-298-90V	17.44	17.51	Dip direction of foliation parallel to drill core axis.
KFM90B-299-90V	17.99	18.06	Dip direction of foliation parallel to drill core axis.

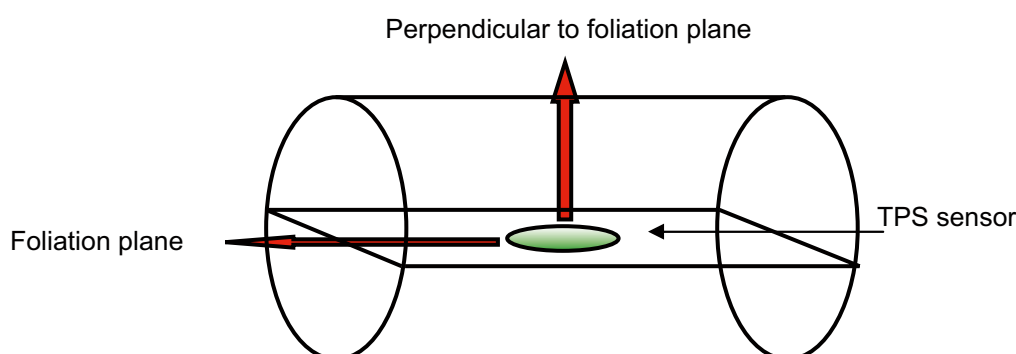


Figure 3-13. The position of the TPS sensor in relation to the foliation plane of the drill core sample.

4 Results

4.1 Geology

The candidate volume at Forsmark is situated within a tectonic lens dominated by a homogenous metagranite. Inside the lens, the bedrock is characterised by less intense ductile deformation than outside the tectonic lens. In the internal parts of the lens, the rocks are more lineated than foliated, whereas, as the margins of the lens are approached, the tectonic foliation in the metagranite increases in intensity /SKB 2006b/. On a larger scale, the lens consists of a large synform fold plunging to the south-east and SSE. On a smaller scale, the orientations of the planar ductile fabrics (foliation) are dictated by the large-scale folding. Along the foliated, south-western marginal part of the tectonic lens (e.g. drill site 7), the foliation dips steeply to the south-west. It is in this area, close to drill site 7, that the thermal anisotropy measurements were performed.

Based on observations from both the surface and the boreholes, the geology of the location for the large-scale experiment can be summarised as follows. The metagranite to granodiorite (rock code 101057) is the dominant lithology, making up more than 90% of the rock volume. Important subordinate rock types are amphibolite (rock code 102017; Figure 4-1) and pegmatite (rock code 101061), both occurring as dykes, irregular bodies, and veins. The metagranite to granodiorite displays a well-developed foliation generally striking approximately N-S and dipping steeply (c. 80°) to the west; see Figure 4-2. The amphibolite and pegmatite are generally aligned parallel to the foliation. The foliation locally deviates from the dominant orientation, this being most common at levels 8.5–13 m and 17–19 m below the surface. These deviating foliations, which generally dip 20–30° less steeply than normal, are often associated with the occurrence of dykes and veins.

Sub-horizontal fractures were observed in several boreholes at two distinct levels, one at 5–8 m, the other between about 14 and 17 m; see Figure 4-3. Two gently-dipping fracture zones have tentatively been proposed for the upper level at 5–8 m (Appendix 6). Less frequent sub-vertical fractures have been recorded, mainly from the lower parts of the boreholes. A narrow steeply-dipping fracture zone striking 158° has been mapped on the eastern part of the outcrop. At the surface, the nearest borehole, KFM90D, lies about 1 m west of the zone. The zone has been modelled as a planar structure intersecting borehole KFM90D at approximately 5 m depth (Appendix 6).



Figure 4-1. Photograph showing typical occurrence of amphibolite dykes in metagranite to granodiorite.

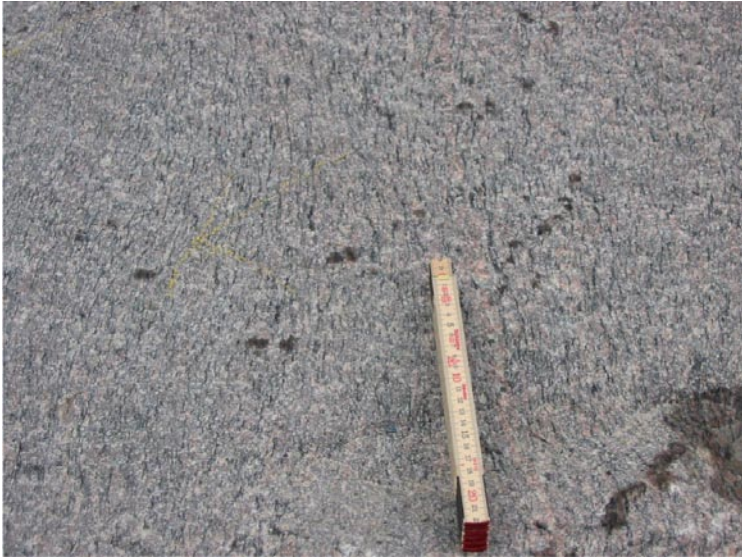


Figure 4-2. Foliation in metagranite to granodiorite.

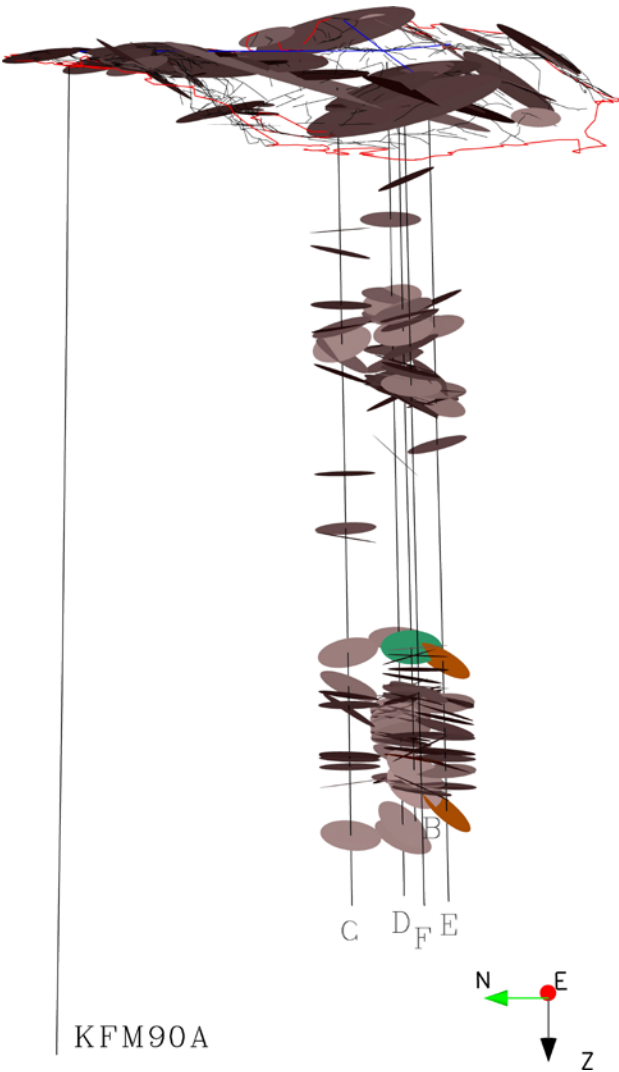


Figure 4-3. Visualisation of sub-horizontal fractures from outcrop mapping and borehole logging.

The upper set of temperature sensors (8–13 m) in boreholes C to F are positioned between the two sub-horizontal fracture zones. The lower set of sensors (17–19 m) in the same boreholes lie immediately below the lower fracture zone. However, the lower 2–3 m of the heater, which reaches a depth of c. 18 m (borehole length) and from which the lower set of sensors receives their heat, is positioned within the lower fracture zone.

Modelling of minor lithologies within the volume enclosed by the five boreholes shows that dykes or bodies of amphibolite and pegmatite (of significant thickness and/or extent) are generally absent between the heater borehole and the measurement boreholes, see Figure 4-4. One exception is a steeply-dipping minor amphibolite dyke at c. 10 m depth in borehole KFM90C, which if it has the same orientation as observed in the borehole would occur as a sheet between sensor C1 in borehole KFM90C and the heater in KFM90B. Given the relatively large amount of data available from a limited volume of rock, it is considered highly unlikely that any larger amphibolite dyke or body is present between the boreholes.

The Boremap mapping of boreholes KFM90B–F is stored in Sicada. For a fuller description of the geology of the boreholes, see Appendix 5. Well Cad-presentations of borehole KFM90B–F are also shown in Appendix 5. For results of the 3-dimensional modelling of the investigated rock volume using the Rock Visualisation System (RVS) see Appendix 6.

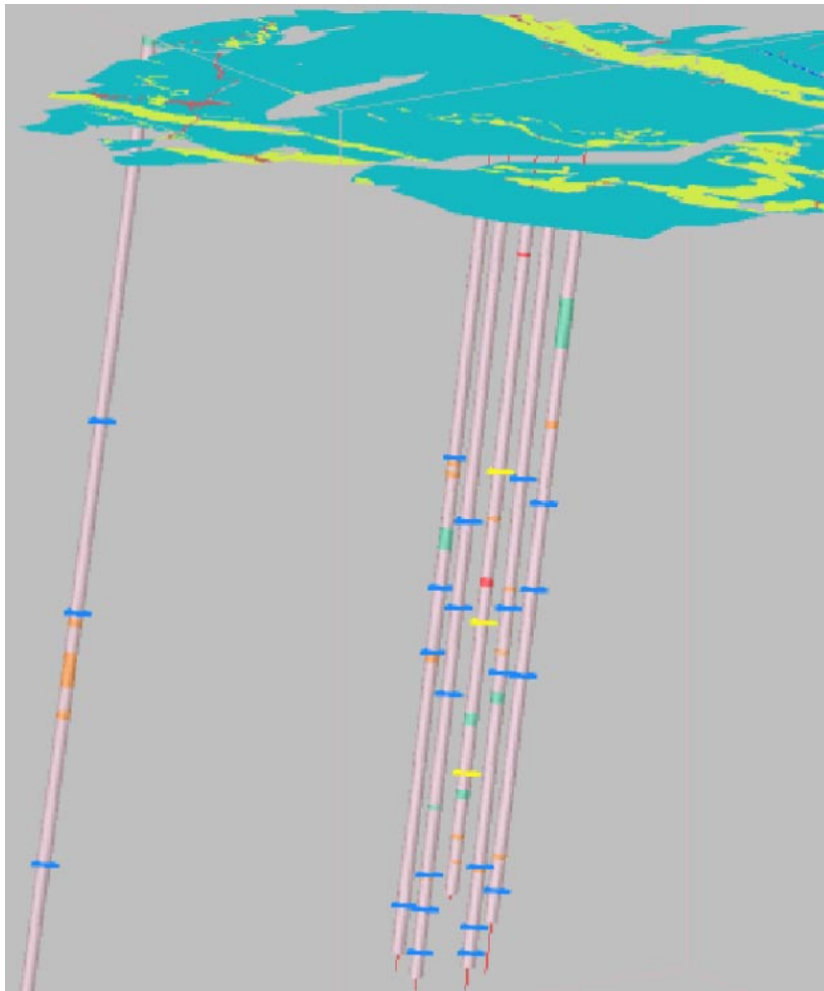


Figure 4-4. Visualisation in a west (left) to east (right) direction of the temperature sensors in relation to the lithologies in the boreholes. Low accuracy sensors are yellow, whereas the blue markings indicate the position of the high accuracy sensors. In the boreholes, amphibolite is indicated by green, pegmatite by orange, and granite by red. The dominant rock type, metagranite to granodiorite, is represented by the pale colour. From left to right the identification codes of the boreholes are KFM90A, KFM90C, KFM90F, KFM90B, KFM90E and KFM90D. The bright green colour at the surface represents amphibolite dykes.

4.2 Large-scale measurements

In order to evaluate the thermal conductivity parallel (x direction) and perpendicular (y direction) to a foliation plane, at least two temperature sensors are needed in the two principle directions. The anisotropy factor is calculated as the thermal conductivity in the x direction divided by the conductivity in the y direction. The conductivity in the x direction is expected to be higher than in the y direction because of the structural anisotropy in the rock.

Figure 4-5 shows the results of calculations of the anisotropy factor of thermal conductivity based on pairs of temperature sensors. A sensor pair refers to two sensors on the same horizontal level in different boreholes, one borehole aligned in the same plane of foliation as the heater borehole, the other in a plane perpendicular to the plane of foliation. For example, c1d1 refers to results from sensors on level 1 in boreholes C and D; see Figure 3-1. Various time periods are displayed: 0–28 refers to the heating period, 29–61 to the cooling period and 0–61 to the entire period. For levels 1 and 2, the estimated anisotropy factor varies from just below 1 to approximately 1.25. For level 3, the estimated anisotropy factor is less than 1 for all evaluated time periods. Levels 4–6, which lie below the lower end of the heater, have yielded anisotropy factors considerably lower than 1. Furthermore, there is a tendency towards higher anisotropy factors during the cooling period compared to the heating period for levels 1 to 3, whereas the opposite is the case for levels 4 to 6.

The geometric mean of thermal conductivity of the two principal directions gives a 2D approximation of the effective thermal conductivity. Results for different sensor pairs and different periods are presented in Figure 4-6. Considering the cooling period only, it can be seen that the geometric mean for most sensor pairs varies between 3.8 and 4.0 W/(m·K). The values are notably higher for the heating period for most sensor pairs.

A range of assumptions were made to investigate the sensitivity of the results to the identified uncertainties. The results presented above apply to calculations using the borehole lengths measured by the installation team, and not those reported by the drilling team, and the coordinates determined from the original position (x,y) based on the first bearing and inclination measurements. In Appendix 1, the results of different sensitivity analyses are presented. Determinations of the anisotropy factor is generally only influenced slightly by using the borehole lengths reported by the drilling team, or by using the revised coordinates from the second borehole position measurement. Sensitivity of the results to changes in the temperature drift is also small. Analysis of moving the horizontal position of the heater and temperature sensors within the limits of the cross-sectional area of the boreholes shows that the anisotropy factor is rather sensitive to varying the distance between the sensors and the heater (see Appendix 1.7 for theoretical background).

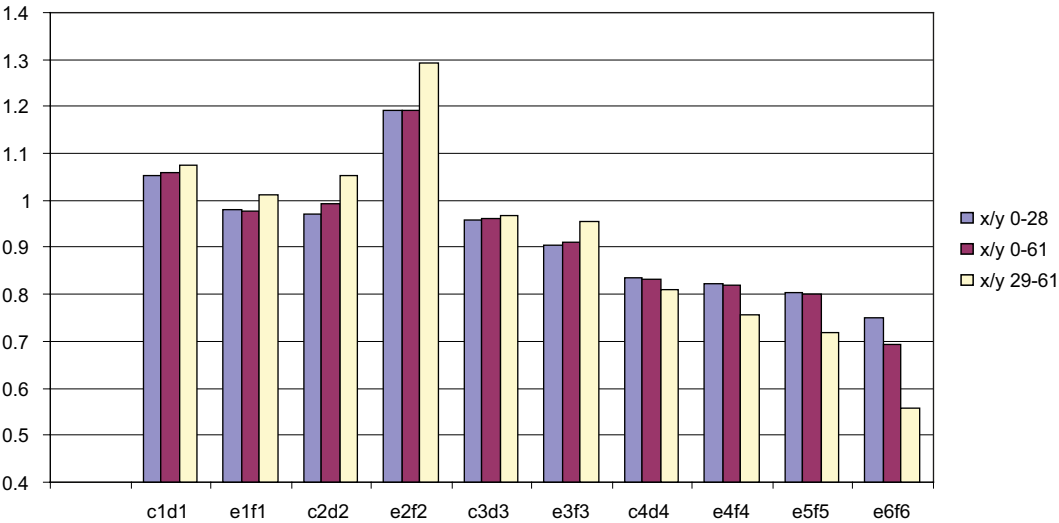


Figure 4-5. Anisotropy factors (thermal conductivity) for different periods and sensor pairs. For position of the temperature sensors, see Figure 3-1.

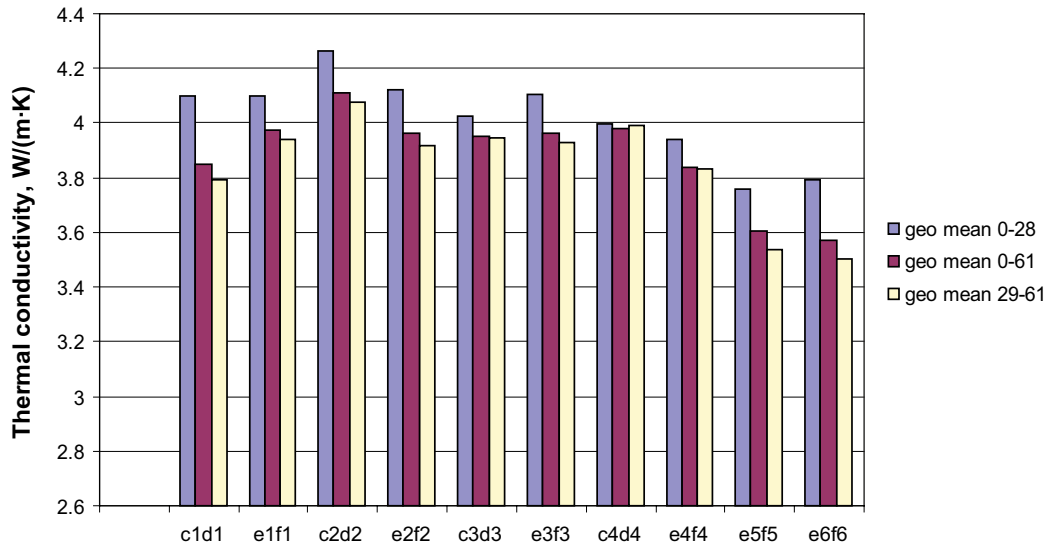


Figure 4-6. Geometric mean of thermal conductivity for different periods and sensor pairs. For position of the temperature sensors, see Figure 3-1.

So as to reduce the influence of errors in the relative horizontal positions of the sensors in the boreholes, the fitting procedure was also performed for various combinations of sensors. Consequently, thermal conductivities for the x and y directions respectively, as well as heat capacity, have been calculated by fitting to a large number of time-temperature curves. By using data from several sensors (e.g. all sensors at approximately the same level, c2d2e2f2) in the same calculation, averaged values are obtained which are not as dependent on deficiencies in measurement data for individual sensor positions. Calculations using data from various combinations of sensors, for different time periods are presented in Figure 4-7. Here, a fourth period (40–61), corresponding to the latter two-thirds of the cooling period, is included. The reason for including this period is that the goodness of fit between the simulated and measured temperature curves is a lot better (see Appendix 1) for this period compared to the other evaluated periods, at least for the combined sensor calculations. In the calculations involving several temperature sensors, only the coordinates from the second surveying were used (see Appendix 1.2).

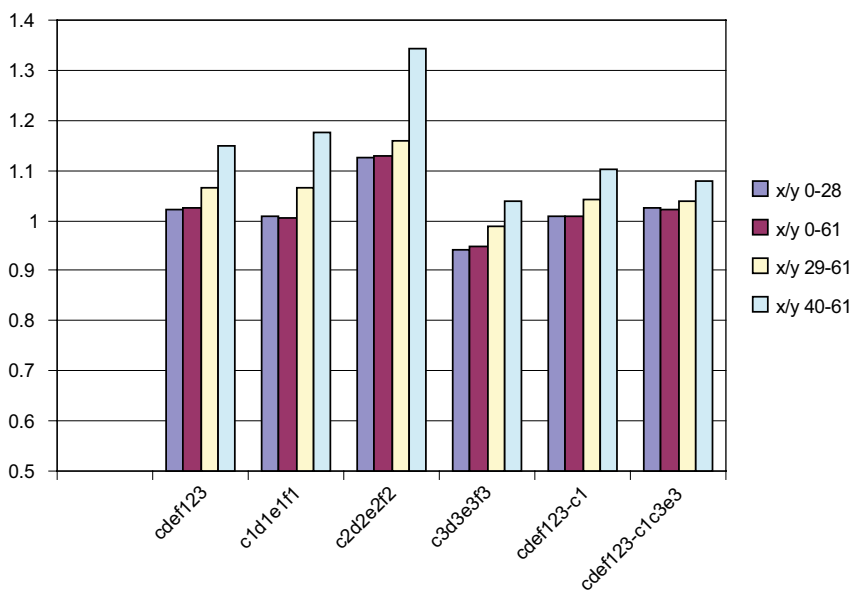


Figure 4-7. Anisotropy factors for different combinations of temperature sensors for different parts of the evaluation period; heating period (0–28), whole period (0–61), cooling period (29–61) and end of cooling period (40–61). For example, cdef123 stands for sensors at levels 1, 2, and 3 in boreholes c to f.

From left to right in Figure 4-7, the first group focuses on all sensors from levels 1–3. The second, third and fourth groups respectively examine levels 1, 2 and 3 separately. The last two groups represent levels 1–3 with sensors c1 and c1c3e3 excluded respectively. They were excluded because of some uncertainties in the results due to possible secondary rocks. Similar to that seen for the sensor pairs, the highest anisotropic factors are obtained for the cooling period, but in particular for time interval 40–61. There is a clear trend towards higher calculated anisotropies as the evaluation shifts from the heating period to the latter part of the cooling period. The opposite trend is noted for the geometric mean thermal conductivity for the rock mass; Figure 4-8. Furthermore, with the exception of one investigated case, the heat capacity is higher for the cooling period, and particularly so for the latter part of the cooling period; see Figure 4-9. These observations indicate that conditions have not been stable for the entire period during which temperatures were measured.

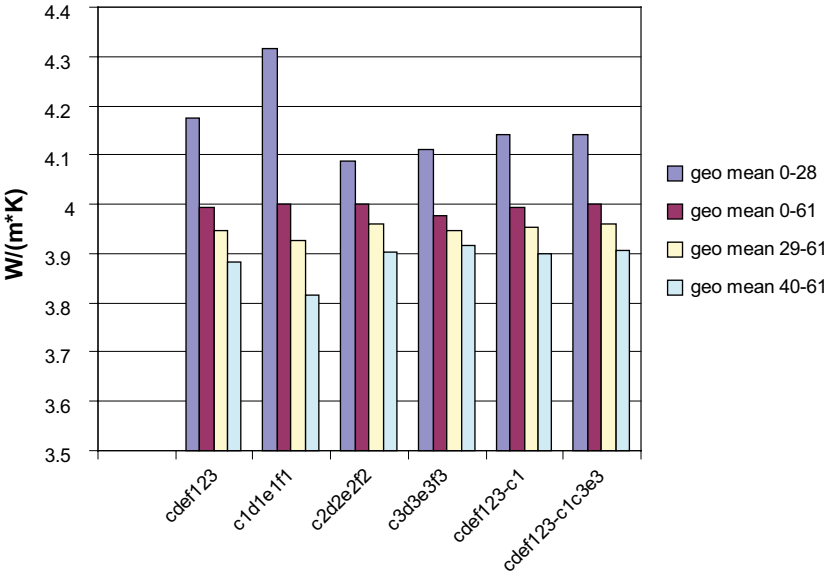


Figure 4-8. Geometric mean of the thermal conductivity parallel and perpendicular to the foliation based on different combinations of temperature sensors and different parts of the evaluation period; heating period (0–28), whole period (0–61), cooling period (29–61) and end of cooling period (40–61).

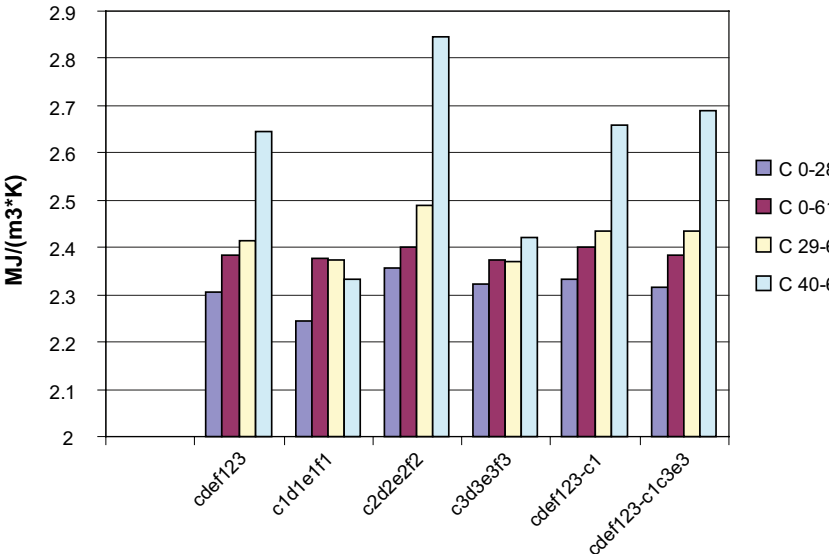


Figure 4-9. Heat capacity results from several calculations with different combinations of sensors for different periods.

4.3 Multi-probe measurements

The data from the multi-probe measurements are assessed through iterative fitting between a calculated and a measured temperature curve. The data sets used for fitting included data captured after 2,500 seconds of heating but after compensation with data from temperature drift measurements from the reference thermistor. The exclusion of data for $t < 2,500$ s was made to avoid interference from noise during the initial unaffected period and from transition resistance caused by the bentonite clay surrounding the heat probe.

The fitting procedure involves minimising the deviation between the measured temperature and the simulated temperature development. The deviation for fitting with data where the initial period has been excluded was found to be smaller than for all data.

In Table 4-1, thermal property results from the preferred fitting procedure are presented for the six measurement locations, three at site A (trench) and three at site B (pit). The large-scale experiment was also carried out at site B. For a more detailed presentation of the results see Appendix 2.

By comparing thermal conductivity results for the direction parallel to the foliation to those for the perpendicular direction, the degree of anisotropy can be expressed. In Figure 4-10, $\lambda_{\text{parallel}}$ is divided by $\lambda_{\text{perpendicular}}$ for each location. The variation in degree of anisotropy for thermal conductivity between the different locations is large, with the parallel conductivity varying from 0% to 40% higher than the perpendicular. On average 13 percent higher conductivity was found for $\lambda_{\text{parallel}}$ than for $\lambda_{\text{perpendicular}}$. An effective thermal conductivity for each location was approximated by calculating the geometric mean of the parallel and perpendicular values; see Table 4-1. A mean effective thermal conductivity of 3.43 W/(m·K) was derived for the six locations.

Based on this rather limited data set, no differences between the two sites, A (trench) and B (pit) as regards thermal properties or their degree of anisotropy can be discerned. Site A includes HFM91–93, while site B includes HFM95–97.

Table 4-1. Thermal conductivity and heat capacity results from multi-probe measurements. Fitting with data where the initial experimental period ($t < 2,500$ s) has been excluded. Site A (trench) includes HFM91–93, while site B (pit) includes HFM95–97.

Location	Thermal conductivity		Factor of anisotropy	Effective thermal conductivity	Heat capacity, C (J/(m ³ ·K))
	$\lambda_{\text{parallel}}$ (W/(m·K))	$\lambda_{\text{perpendicular}}$ (W/(m·K))	$\lambda_{\text{parallel}}/\lambda_{\text{perpendicular}}$	Geometric mean (W/(m·K))	
HFM91	3.64	3.19	1.14	3.41	1.99·10 ⁶
HFM92	3.86	3.27	1.18	3.55	1.97·10 ⁶
HFM93	3.41	3.36	1.02	3.38	2.02·10 ⁶
HFM95	3.44	3.45	1.0	3.44	1.93·10 ⁶
HFM96	4.02	2.88	1.40	3.40	2.05·10 ⁶
HFM97	3.55	3.26	1.09	3.40	2.07·10 ⁶
Mean	3.65	3.24	1.14	3.43	2.00·10⁶
Mean site A; HFM91-93	3.64	3.27	1.11	3.45	1.99·10⁶
Mean site B; HFM95-97	3.67	3.20	1.16	3.42	2.01·10⁶

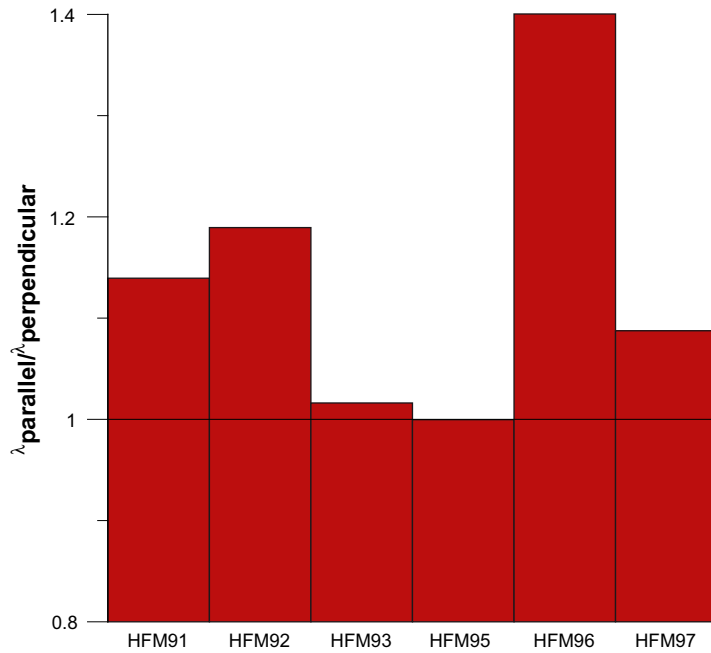


Figure 4-10. $\lambda_{parallel}/\lambda_{perpendicular}$ for results of thermal conductivity from fitting procedure with compensated temperature data where the initial 2,500 s of the experiment period has been excluded.

4.4 Laboratory measurements

The results of the laboratory measurements are summarised in Table 4-2. For a fuller description of the results see Appendices 3 and 4. The results of the measured heat capacity using the calorimetric method are converted to volumetric heat capacity [$J/m^3 \cdot K$] by using the measured wet density of the samples. These data are used as input for the anisotropic thermal conductivity calculations.

Measured thermal conductivity in the foliation plane (FP) and perpendicular to the foliation plane (PFP) are reported in Table 4-2. The relationship between thermal conductivity in the foliation plane (FP) and perpendicular to the foliation plane (PFP) is known as the anisotropy factor. The anisotropy factor varies from 1.06 to 1.73 and has a mean of 1.40. The anisotropy factor from laboratory measurements is very sensitive to errors in heat capacity.

Table 4-2. Thermal properties of samples of metagranite-granodiorite (101057) at 20°C. Thermal conductivity and diffusivity were determined by the TPS method and using calorimetrically measured heat capacity as input.

Sample identification	Thermal conductivity (W/(m·K))		Factor of anisotropy $\lambda_{parallel}/\lambda_{perpendicular}$	Effective thermal conductivity Geometric mean (W/(m·K))	Thermal diffusivity		Heat capacity (J/(m ³ ·K))
	$\lambda_{parallel}$ (W/(m·K))	$\lambda_{perpendicular}$ (W/(m·K))			κ_{pa} (m ² /s)	κ_{pe} (m ² /s)	
KFM90B-294-90V	4.04	2.97	1.36	3.46	1.89	1.39	2.14·10 ⁶
KFM90B-295-90V	3.72	3.51	1.06	3.61	1.69	1.59	2.20·10 ⁶
KFM90B-296-90V	4.01	3.10	1.29	3.53	1.84	1.43	2.17·10 ⁶
KFM90B-297-90V	4.13	2.78	1.49	3.39	1.88	1.26	2.19·10 ⁶
KFM90B-298-90V	4.25	2.85	1.49	3.48	1.97	1.32	2.15·10 ⁶
KFM90B-299-90V	4.26	2.47	1.73	3.24	1.99	1.16	2.13·10 ⁶
Mean	4.07	2.95	1.40	3.45	1.88	1.36	2.16·10⁶

5 Summary and discussions

5.1 Discussion/evaluation

In Table 5-1 results for the different methods are summarized. Unrealistic results have been excluded from the table. There is an obvious scale dependence on the anisotropy factor as indicated by a comparison of laboratory measurements (1.4) with the multiprobe method (1.16) and the large-scale measurements (ca 1.15), see Table 5-1. The differences in the results of the multiprobe method compared to the large-scale measurement seem to be rather small and the results range approximately within the same interval. The average of the geometric means for laboratory and multiprobe measurements are very similar. The laboratory measured heat capacities with the calorimetric method seem to be somewhat higher than the heat capacity determined from the diffusivity measurements with the multiprobe method.

For the large-scale experiment, the anisotropy factor obtained from several calculations of individual pairs of sensors gives unrealistic results, particularly for those sensors located at deeper levels, below the lower end of the heater. Moreover, the geometric mean of the two directions of thermal conductivity is often unrealistically high (by a factor of 10–20%) and the evaluated thermal conductivity varies between different time periods of the heating and cooling cycle. The most plausible explanation for this is that the large-scale measurements are influenced by convection, in spite of grouting and bentonite filling. This convection was probably induced primarily by high temperature gradients but also by hydraulic head differences. These disturbances are most pronounced during the heating period. The best results are therefore obtained some time after the heating has ended, when the large temperature gradients are lowered and the thermal process is “calming down”. The latter two-thirds of the cooling period are considered to be the most reliable period. However, even the last part of the curve is judged to overestimate the true thermal conductivity. The geometric mean thermal conductivities derived from the large-scale experiment (Figure 4-8) are 12–15% higher than expected, as indicated by laboratory measurements and the multi-probe method. These results are therefore excluded from Table 5-1.

Table 5-1. Summary of results for the different methods. Excluded data are judged not to be reliable.

Method	Thermal conductivity			Geometric mean W/(m·K)	Heat capacity C (J/(m ² ·K))	Number of measurement	Comment
	$\lambda_{\text{parallel}}$ W/(m·K)	$\lambda_{\text{perpendicular}}$ W/(m·K)	Factor of anisotropy $\lambda_{\text{pa}}/\lambda_{\text{pe}}$ Mean and range				
Laboratory measurements	4.07	2.95	1.40 (1.06–1.73)	3.45	2.16·E6	6	
Multiprobe	3.67	3.20	1.16 (1.0–1.4)	3.42	2.01·E6	3	From “Site B” only; the same site as for the large-scale experiment.
Large scale, all sensors per level for the middle part of heater	–	–	1.19 (1.04–1.34)	–	–	3	Based on mean of evaluation of sensors at three different levels for the middle part of the heater probe, and last part of cooling curve.
Large scale, all sensors at all three levels for the middle part of the heater	–	–	1.15	–	–	1	Based on simultaneous evaluation of all sensors for the middle part of the heater probe, and last part of cooling curve.

The resulting anisotropy factor may have a higher degree of reliability. Results from temperature sensors in the principal directions are needed to estimate the thermal conductivity in the two principal directions in the large-scale and multiprobe measurements. The derived results are sensitive to errors in the distance between the heater and the sensors. For this reason, data from several sensors in the large scale experiment were used in the same calculation, to obtain averaged values which are not as dependent on deficiencies in measurement data for individual sensor positions. According to Figure 4-7 an anisotropy factor of 1.15 is obtained from sensor combination cdefl23, i.e. all sensors from levels 1, 2 and 3, when the final 2/3 of the cooling curve is used. These results are included in Table 5-1.

The lower set of sensors in the large scale experiment (levels 4 to 6), which produce particularly anomalous results, may have been more severely affected by the proposed convective component. This explanation is considered plausible, since the lower end of the heater, from which the deeper level sensors receive their heat, is located in a zone of high fracture frequency where conditions for water movement are particularly favourable.

5.2 Uncertainties

- The anisotropy factor in thermal conductivity from laboratory measurements is very sensitive to errors in heat capacity.
- The uncertainty in thermal conductivity (geometric mean) is judged to be relatively small for laboratory and multiprobe measurements.
- The evaluation of the large-scale and multiprobe experiment is sensitive to errors in the relative distance between heater and temperature sensors for the two directions. There is an uncertainty regarding the horizontal position of the heater and sensors, since these instruments could not be fixed in the borehole in the xy plane. Uncertainties are however limited to the radius of the borehole. Analysis has indicated that an error of 2.5% for each sensor can give up to 5% error in thermal conductivity for each of the x and y directions, which in turn can give an error of up to 10% in anisotropy factor. Two separate measurements of the borehole coordinates have been made, which give significant differences in the xy-coordinates for temperature sensors. This implies that there may be uncertainties in the distances between heater and sensors. However, comparison of the two measurements shows that the radial distance to the heater is only negligibly affected, which implies a minor influence on the evaluated results of the anisotropy factor between the two measurements.
- There may also be uncertainties in the position of the sensors and heater along the length of the boreholes. This is because the instrumentation was positioned in relation to the bottom of the boreholes, which are difficult to measure with a high degree of accuracy. Two different measurements were made, one by the drilling team, the other by the installation team. Determinations of the anisotropy factor for the centrally placed sensors are not influenced or only slightly influenced by choice of borehole lengths measurements. However, results from the lower level sensors (levels 4 to 6) are rather sensitive to the sensors vertical (z) position.
- A convective component is believed to be involved in the large-scale experiment in spite of grouting and filling with bentonite slurry. Support for this assertion are 1) a good fit between measured and calculated curves cannot not be achieved by assuming that conductivity was the only heat transport mechanism, 2) the derived effective thermal conductivity is higher than expected, and 3) both the estimated anisotropy factor and effective thermal conductivity vary for different time periods. Such a convective disturbance would be expected to be larger during the heating period than during the latter part of the cooling period.
- The results from the sensors at the lower end of the heater are excluded from the evaluation due to larger uncertainties in results, caused by greater sensitivity to convection and the vertical position of the sensors, as described above.
- The influence of the thermal properties of the bentonite material in the boreholes has not been considered. Since the heater and the sensors are not centred, the effect may vary in different directions.

- The effect of secondary rock types is judged to be low. Based on interpretation of the geological model, the upper sensor in borehole C (c1) is most likely to be affected by secondary rock types, in this case a thin amphibolite body. This point has only a limited influence on the results.
- The influence from the natural temperature drift in the rock mass on the evaluated thermal conductivity is judged to be small.
- The evaluation model assumes that the thermal conductivity in the x and z directions in the foliation plane, are equal. This assumption may be incorrect. Errors associated with this assumption would only have a small influence on the centrally positioned sensors.

The results presented above apply to calculations using the borehole lengths measured by the installation team, and not those reported by the drilling team. The coordinates determined from the original position (x, y), bearing and inclination measurements were used. In Appendix 1, the results of different sensitivity analyses are presented. Determinations of the anisotropy factor is generally only influenced slightly by using the borehole lengths reported by the drilling team, or by using the revised coordinates from the second borehole position measurement. Sensitivity of the results to changes in the temperature drift is also rather small. Analysis of moving the horizontal position of the heater and temperature sensors within the limits of the cross-sectional area of the boreholes shows that the anisotropy factor is rather sensitive to varying the distance between the sensors and the heater (see Appendix 1).

5.3 Conclusions

- There is good agreement between thermal conductivity (geometric mean) for laboratory and multiprobe measurements.
- Laboratory measurements indicate an average anisotropy factor of 1.4 for the centimetre scale. Field measurements which measure larger volumes of rock have yielded anisotropy factors of approximately 1.15, considerably lower than for the small-scale measurements. A distinct scale dependence on anisotropy factor is indicated. A plausible explanation for the scale dependence is that the foliation is more clearly defined at the cm scale but is more variable at the dm to m scale.
- The evaluation of the large-scale experiment is influenced by uncertainties in sensor locations and disturbances by convection, partly induced by heating. The grouting of the rock mass and bentonite slurry in the holes was not successful in preventing convection. The evaluated thermal conductivity from the large-scale experiment is judged to be overestimated due to this convective “contribution”.
- The best approximation of thermal conductivity and anisotropy factor from the large-scale experiment is judged to be based on the last part of the cooling curve (40–61) for the centrally placed sensors.
- Uncertainties due to errors in the xy-position of temperature sensors are reduced if evaluation is based on simultaneous calculation of all sensors on one or more levels.
- The conclusions of this investigation with regard to the scale dependence of anisotropy of thermal conductivity are summarised in Table 5-2.

Table 5-2. Conclusions of investigation with regard to the scale dependence of thermal conductivity.

Scale	Thermal conductivity	
	Mean factor of anisotropy $\lambda_{pa}/\lambda_{pe}$	Geometric mean $W/(m\cdot K)$
Centimetre scale	1.40	3.45
Decimetre to metre scale	1.15	3.42

References

Dinges C, 2006. Forsmark site investigation. Drill hole KFM04A. Thermal properties: Anisotropic thermal conductivity and thermal diffusivity determined using the Hot Disk thermal constants analyser (the TPS technique). SKB P-06-285, Svensk Kärnbränslehantering AB.

Petersson J, Skogsmo G, Wängnerud A, Berglund J, 2005. Forsmark site investigation. Boremap mapping of telescopic borehole KFM07A. SKB P-05-102, Svensk Kärnbränslehantering AB.

SKB, 2006a. Site descriptive modelling Forsmark stage 2.1. Feedback for completion of the site investigation including input from safety assessment and repository engineering. SKB R-06-38, Svensk Kärnbränslehantering AB.

SKB, 2006b. Preliminary site description Laxemar stage 2.1. Feedback for completion of the site investigation including input from safety assessment and repository engineering. SKB R-06-110, Svensk Kärnbränslehantering AB.

Sparr G, 1994. Linjär Algebra, Studentlitteratur, ISBN 91-44-19752-7.

Sundberg J, 1988. Thermal properties of soils and rocks, Publ. A 57 Dissertation. Department of Geology, Chalmers University of Technology and University of Göteborg, Sweden.

Sundberg J, 2003. A strategy for the model development during site investigations, version 1.0. SKB R-03-10, Svensk Kärnbränslehantering AB.

Sundberg J, Back P, Bengtsson A, Ländell M, 2005. Thermal modelling, Preliminary site description Forsmark area – version 1.2. SKB R-05-31, Svensk Kärnbränslehantering AB.

Large-scale field measurement of anisotropic thermal properties at Forsmark

Date: 2006-08-14

Project number: 05030

Author: Anders Sundberg och Jan Sundberg, Geo Innova AB

Contents

1	Introduction	43
2	Results	43
2.1	Sensor pair calculations	43
2.1.1	Original coordinates	43
2.1.2	Influence of small horizontal movement from original coordinates	45
2.1.3	Influence of power output assuming original coordinates	47
2.1.4	Influence of temperature drift assuming original coordinates	47
2.1.5	New coordinates from revised borehole measurement	48
2.1.6	New coordinates including revised assumption of borehole length	50
2.2	Combined sensor calculations – new coordinates	51
2.3	Heater borehole evaluation	53
3	References	54

1 Introduction

An experiment has been conducted to determine the anisotropy in the thermal conductivity of the dominant granite at one location in the Forsmark area. The objective of the measurement is to determine the anisotropy in the thermal conductivity of the dominant granite. This is to be done by measuring how thermal sensors around a heater in the rock react when the heater is turned on. The results of these measurements are compiled in this appendix.

2 Results

All the following cases assume that the borehole lengths are those measured at the time of sensor installation and given in Appendix 1.2 (Table 11), except for the case in section 5.1.6 which investigates the consequences from another borehole length assumption (drilled length) which also can be seen in Appendix 1.2 (Table 11).

2.1 Sensor pair calculations

All the results belonging to this chapter have been achieved by calculating the results for one sensor pair at a time. A sensor pair is always two sensors on the same level, in different boreholes. The two boreholes should be perpendicular to each other, for example c1d1 which refers to results with only input temperature data from sensor c1 and d1.

2.1.1 Original coordinates

Figure 1 shows the anisotropic conductivity factor results from the calculations where the coordinates from the original borehole measurement were used in the calculations. The factor is calculated as the conductivity in the x direction divided by the conductivity in the y direction. The conductivity in the x direction was expected to be higher than in the y direction because of the anisotropy, i.e. an anisotropic conductivity factor higher than 1. For results in written form, see Appendix 1.1.

The anisotropic factor for a number of pairs is lower than 1. Another striking trend is that the anisotropic factors are considerably higher for the cooling period than for the heating period for levels 1–3. For levels 4–6 however, the situation is completely reversed and the anisotropic factors from the cooling period are lower than for the heating period. The results are also significantly lower for levels 4–6.

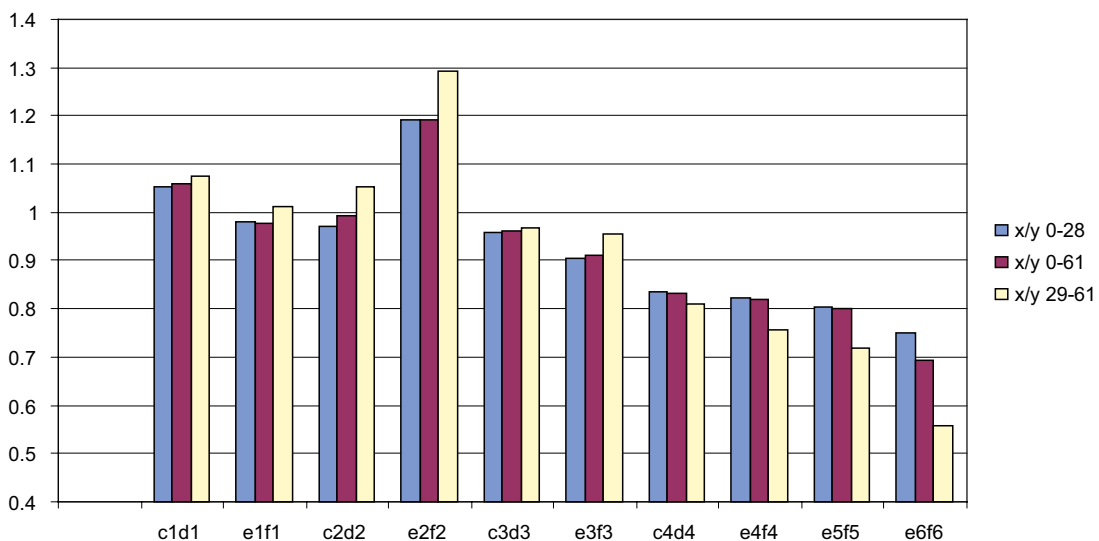


Figure 1. Anisotropic conductivity factors for different periods and sensor pairs.

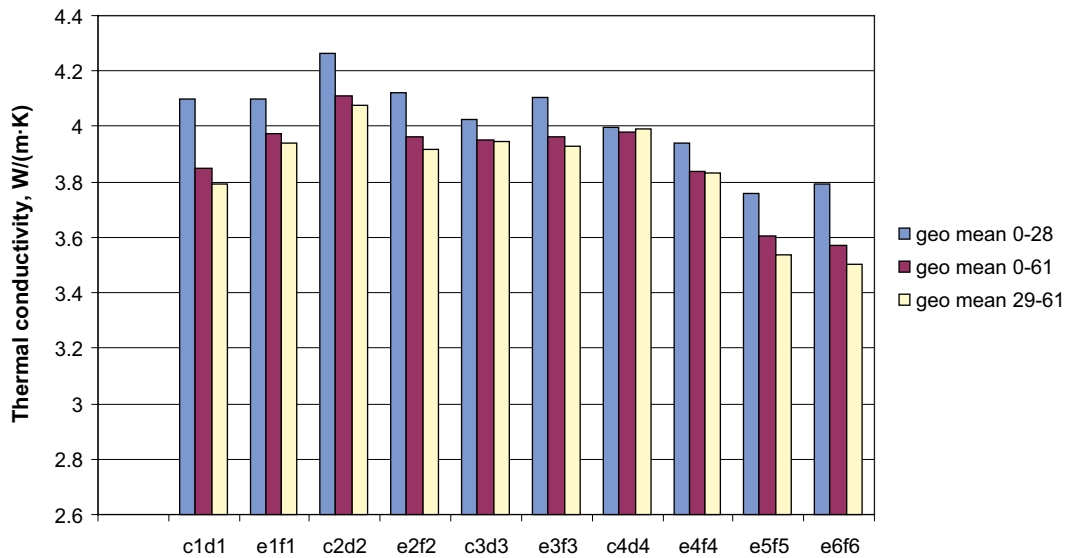


Figure 2. Geometrical mean of conductivity for different periods and sensor pairs.

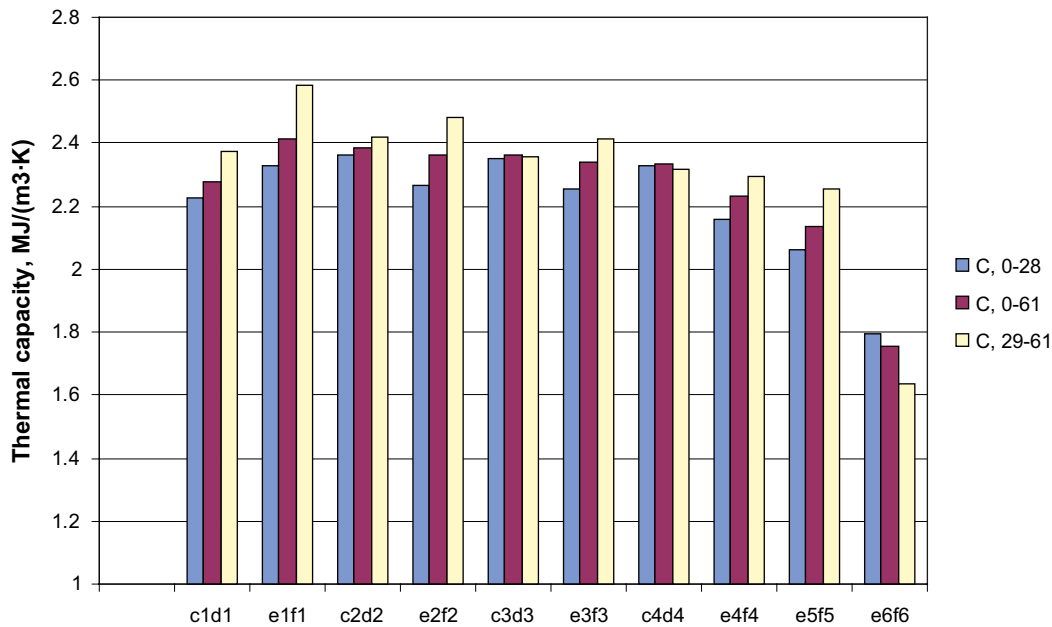


Figure 3. Heat capacity for different periods and sensor pairs.

The geometrical mean thermal conductivity for different sensor pairs for different periods is consistently notably higher for the heating period for all sensor pairs except c4d4, where the periods hardly differ at all. Since the expected geometric mean is expected to be around 3.5–3.7 W/(m, K), as indicated by previous laboratory measurements /SKB 2006b/ and the multi-probe method (this report), they are all a bit too high, except for levels 5–6.

Even though no clear trend can be seen, most sensor pairs have higher capacity for the cooling period than for then heating period. Since the expected heat capacity was about 2.2, the results are a little bit high, except for sensor e6f6 which is quite low.

Summarizing, it seems as if the cooling period gives notably more reasonable values than the heating period for the original coordinates. The exception is heat capacity.

2.1.2 Influence of small horizontal movement from original coordinates

A trial was made where the sensors and heater were moved in the xy plane as much as possible within the uncertainty interval of the borehole radius. The coordinates were changed in directions which seemed to give better conductivity results. For detailed description of this movement, see Table 1.

Figure 4 shows the anisotropic conductivity factor results from these coordinates. For results in written form, see Appendix 1.1.

The anisotropic conductivity factor average is notably higher than for the original coordinate case. This comes as no surprise, as the coordinates were intentionally moved in directions which were believed would increase the anisotropy.

The geometrical mean conductivity is slightly lower than the original coordinate case for all sensor pairs except c4d4, e5f5 and e6f6.

The only notable trend difference from the original coordinates is that the heat capacity values seem slightly lower for the ef pairs and slightly higher for the cd pairs for levels 1–4.

Table 1. The horizontal coordinate change (case 5.1.2). The table lists the numbers that have been added to the x and y coordinates for the sensors in each borehole.

Borehole	x	y
C	0.025	-0.025
D	0	-0.05
E	-0.025	-0.025
F	0	0

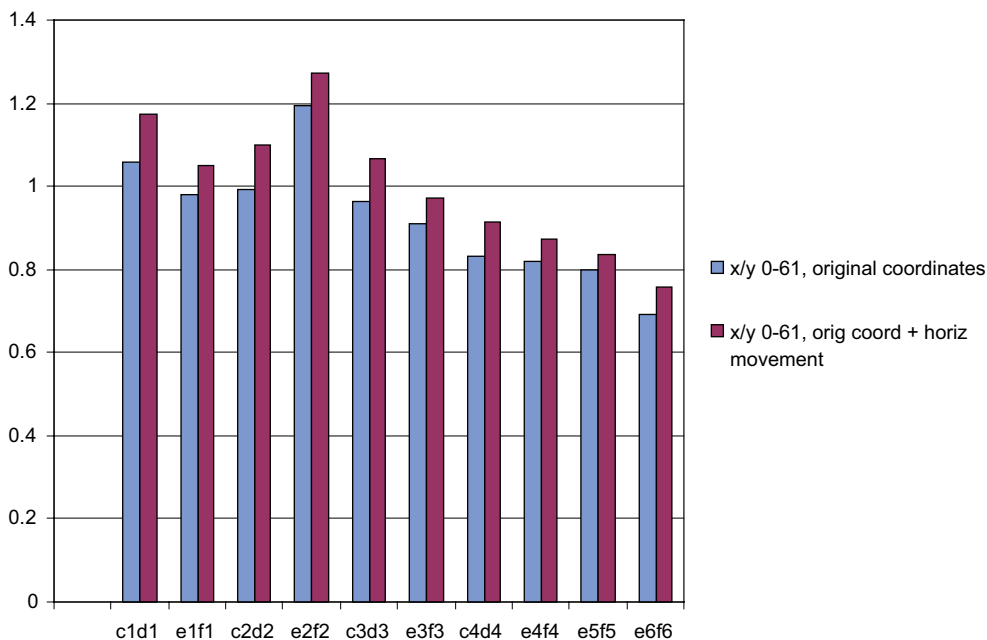


Figure 4. Anisotropic conductivity factors for different sensor pairs.

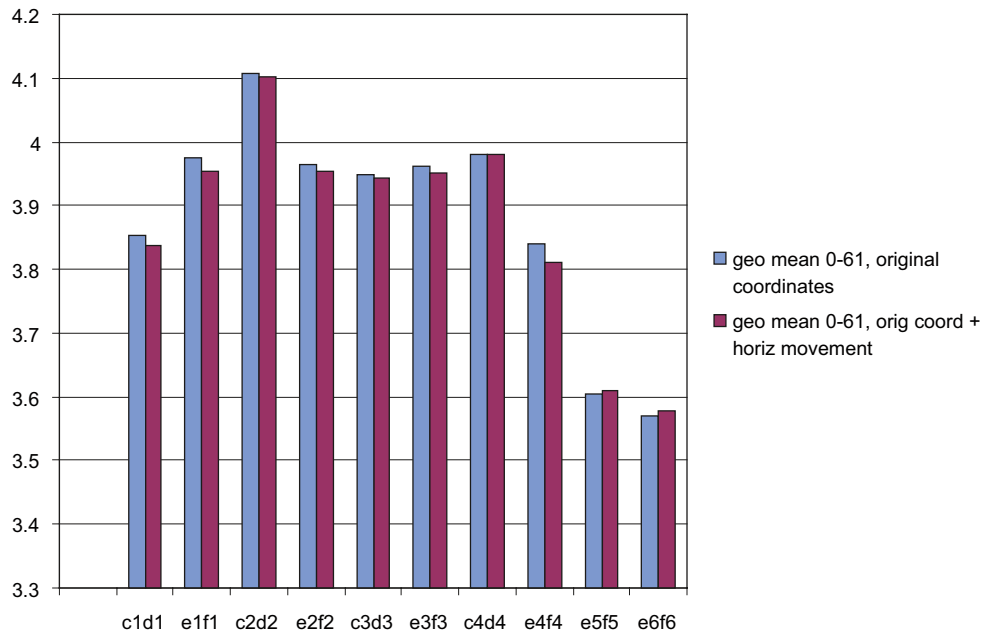


Figure 5. Geometrical mean of conductivity for different sensor pairs.

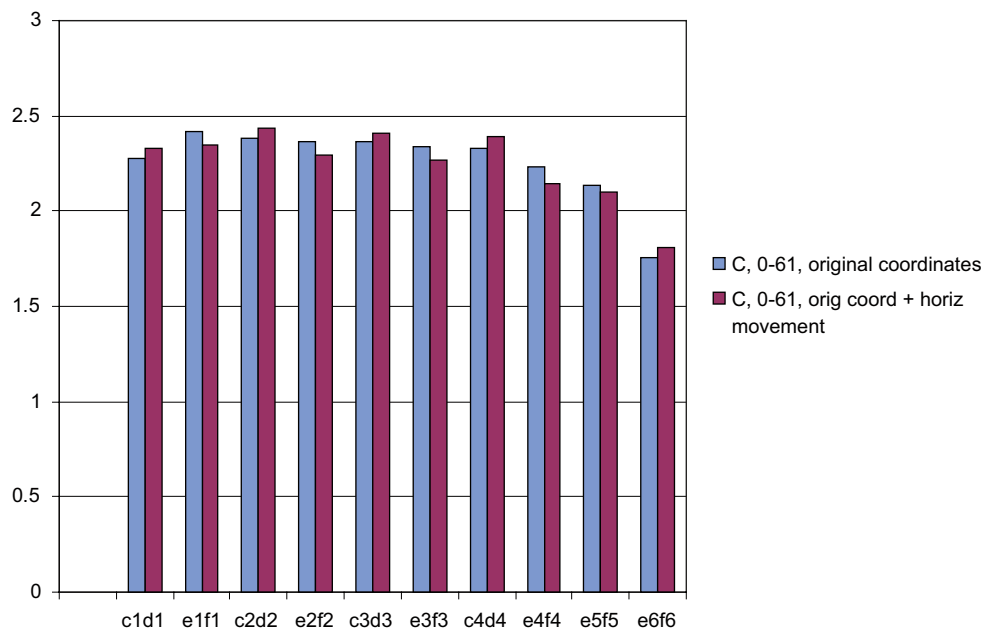


Figure 6. Heat capacity for different sensor pairs.

2.1.3 Influence of power output assuming original coordinates

A trial calculation was made where the stated average power output was decreased by 10% from 149.2 W/m to 134.3 W/m. Both the heating and cooling period were included. The reason for this was to confirm whether the geometrical mean of conductivity also would decrease by 10% as a consequence, which it did.

2.1.4 Influence of temperature drift assuming original coordinates

Another trial calculation was made where the influence of temperature drift was investigated. A cumulative temperature drift of $-0.003^{\circ}\text{C}/\text{day}$ was added to the temperature input data for the sensors in the x-direction (c1–c4 and e1–e6). Only results from the heating period are presented (Figure 7, 8 and 9). For results in written form, see Appendix 1.1.

A lesser temperature development in the x-direction would theoretically result in higher anisotropic factors. However, the results in this case are completely reversed. Moreover, all the sensors pairs are affected relatively little by the change, except e6f6 which is greatly affected.

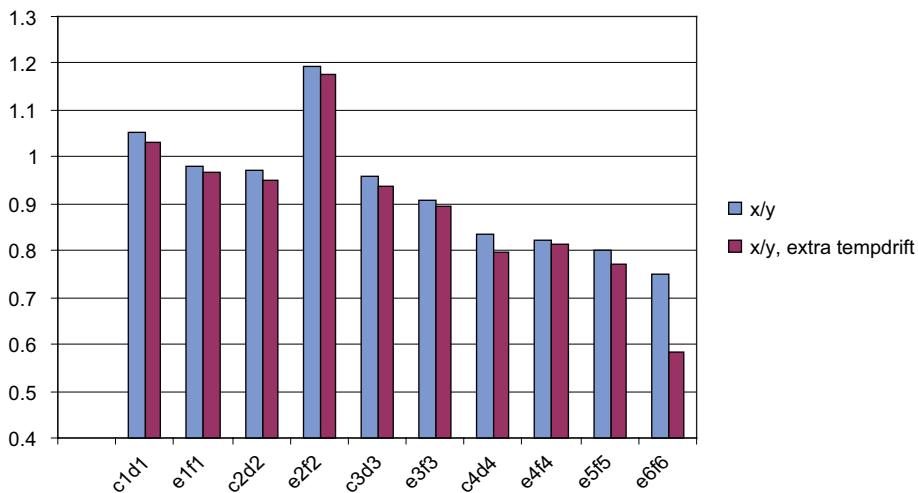


Figure 7. Anisotropic conductivity factors for different sensor pairs.

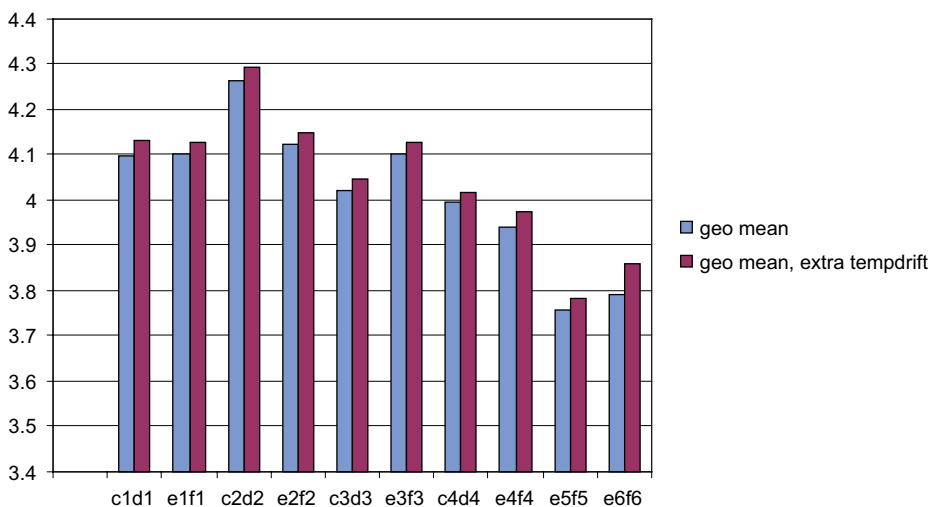


Figure 8. Geometrical mean of conductivity for different sensor pairs.

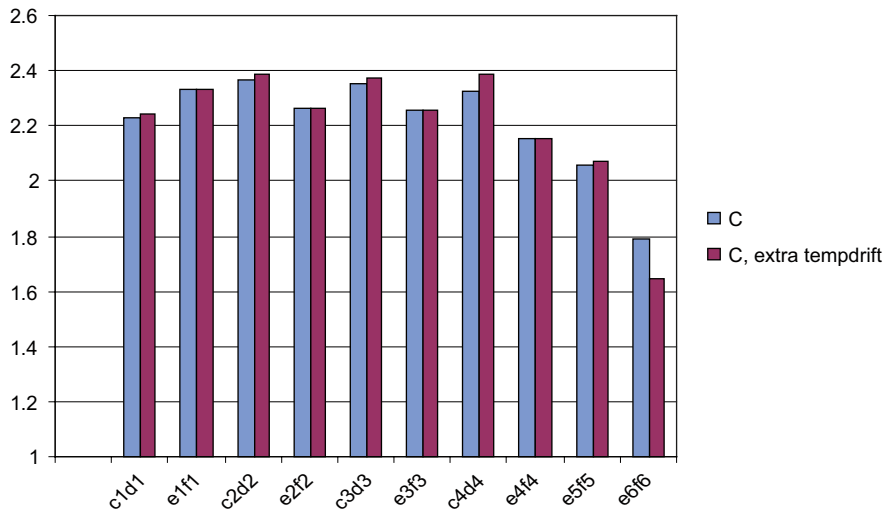


Figure 9. Heat capacity for different sensor pairs.

2.1.5 New coordinates from revised borehole measurement

A new borehole measurement took place a couple of months after the experiment ended (2006-06). These are the results using the new coordinates (Figure 10, 11 and 12).

As can be seen, these new anisotropic factors do not differ very much from the original coordinate case. There is no clear trend, although the new coordinates mostly gives slightly higher results.

Neither the geometrical mean of conductivity or the heat capacity seem affected very much by the new coordinates.

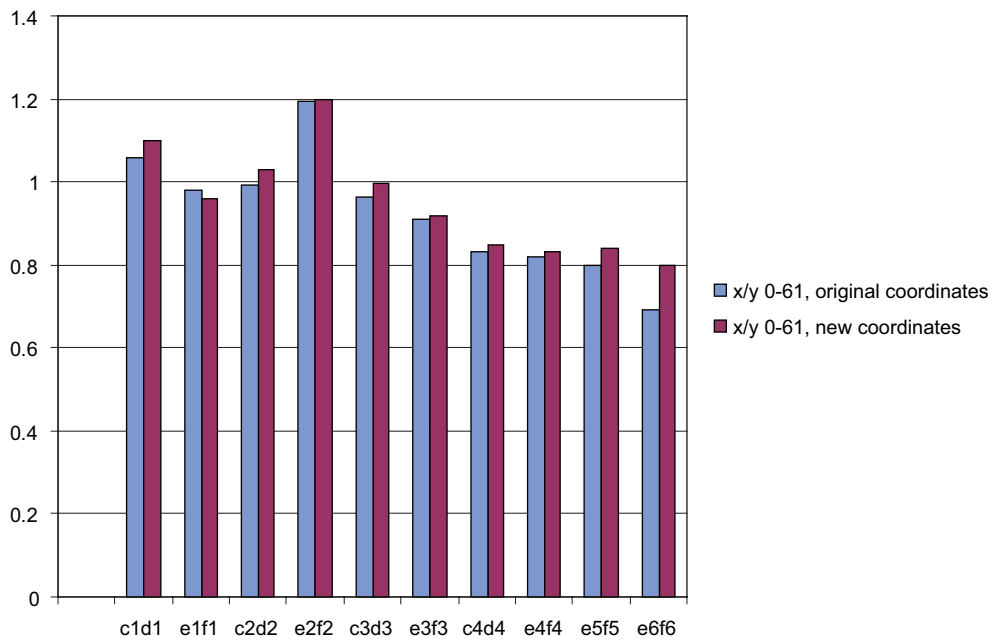


Figure 10. Anisotropic conductivity factors for different sensor pairs.

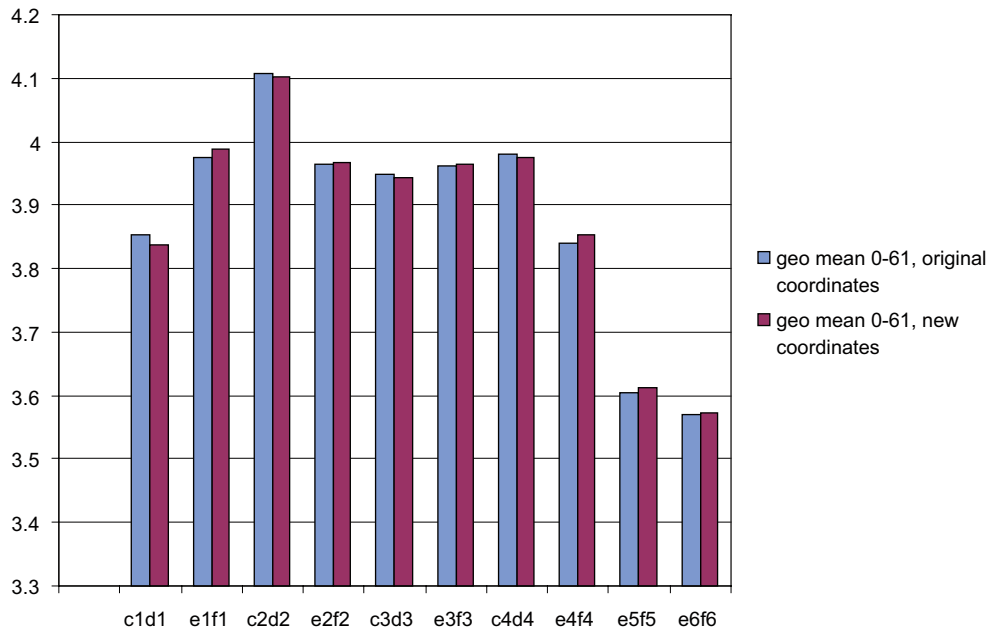


Figure 11. Geometrical mean of conductivity for different sensor pairs.

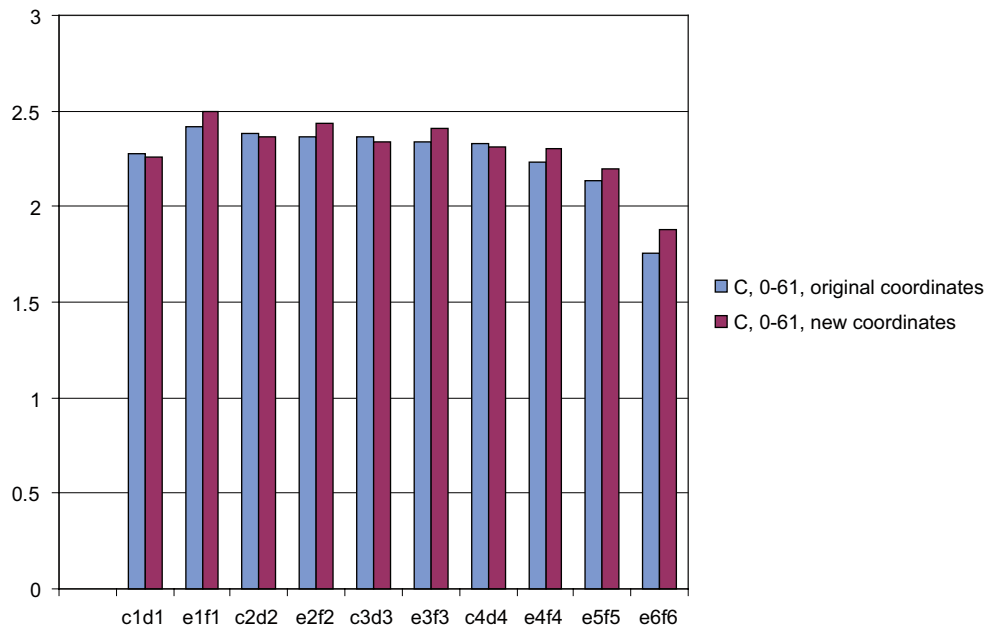


Figure 12. Heat capacity for different sensor pairs.

2.1.6 New coordinates including revised assumption of borehole length

Figure 13 shows a comparison of the anisotropic conductivity factors for the two different borehole lengths (drilled length and measured by installation team, see Appendix 1.2 for details about the two lengths). For results in written form, see Appendix 1.1. The whole experiment period, both heating and cooling (0–61) have been used when determining these values.

As expected, there is hardly any difference for levels 1–3 since they are situated near the middle of the heater and therefore are not affected when the borehole length is changed. However, for level 5–6 (which are situated below the heater) the case with the reported borehole length gives clearly lower anisotropic factors. It can therefore be assumed that the borehole length according to the installation team is a better estimation than the drilling team’s borehole length.

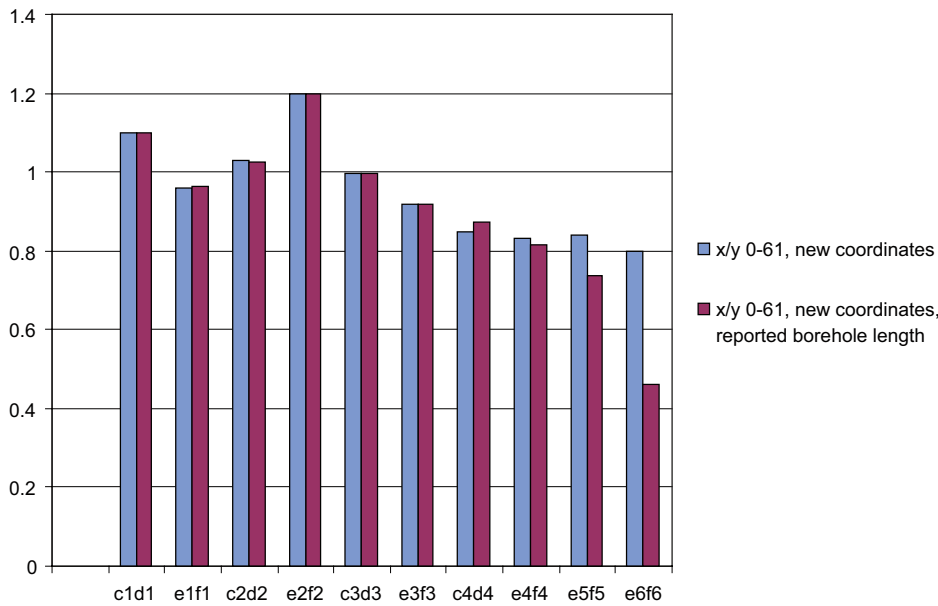


Figure 13. Anisotropic conductivity factors for different sensor pairs. “Reported borehole length” refers to measurements made by the drilling team.

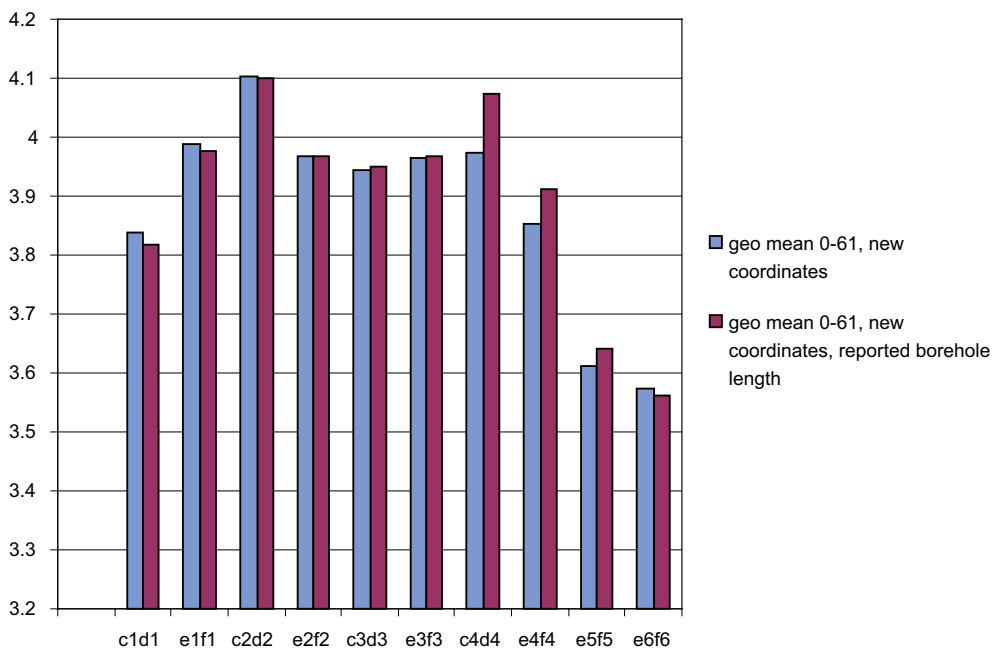


Figure 14. Geometrical mean of conductivity for different sensor pairs.

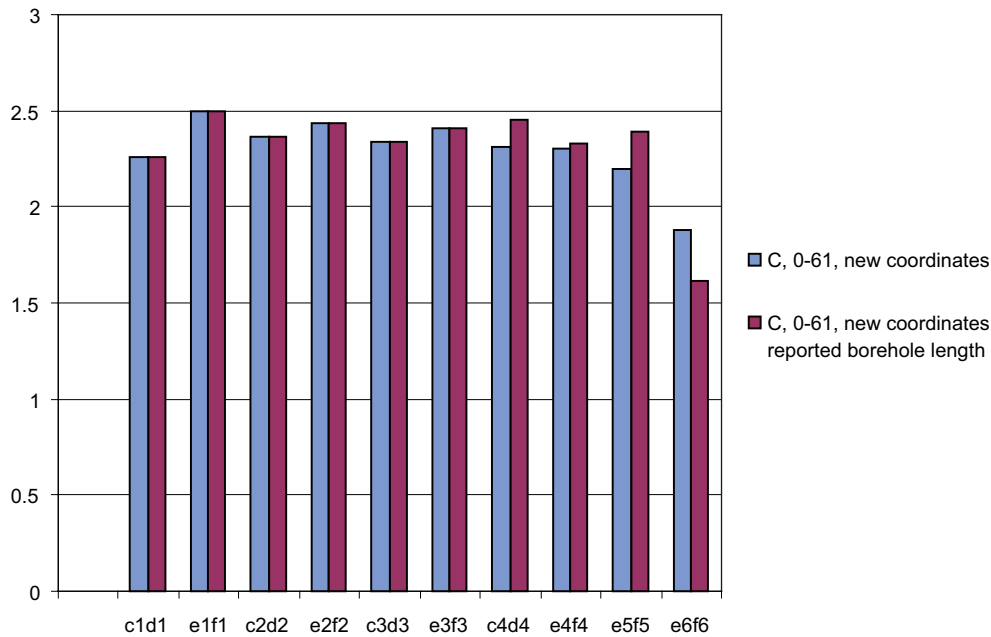


Figure 15. Heat capacity for different sensor pairs.

2.2 Combined sensor calculations – new coordinates

Until now, only a single sensor pair has been included as input data for each MathCAD calculation. However, it was also decided to do some calculations where several sensor pairs were included as input data. Only the new coordinates were used. Figure 16 presents the anisotropic conductivity factor results from several calculations with different combinations of sensors, over different periods. Here, a fourth period (40–61) is included. The reason for this fourth period is that the goodness of fit between the simulated and measured temperature curves are a lot better (see Appendix 1.6) for this period, at least for the combined sensor calculations. Period 40–61 refers to the latter two-thirds of the cooling period.

The first group of bars to the left is a result from calculations with data from all sensors included as input. The second group focuses on levels 1–3. The third and fourth groups represent levels 1–3 with sensor c1 and c1c3e3 excluded. They were excluded because of uncertainty of the result accuracy due to closely situated rock anomalies. Group 5–7 focuses on level 1, level 2 and level 3 respectively. Due to the conceivable inaccuracy of the results from sensor c1, c3 and e3, two more calculations were made of level 1 and 3 where these sensors were excluded and replaced by sensors on level 2 from the same borehole. Group 8–9 represent these two cases.

The anisotropic factors are still consistently higher for the cooling period, except for the last two groups where the anisotropic factors from the different periods are more or less equal. When one compares group 2 with group 4, the cooling period quotient decreases while the heating period quotient increases. These differences are only marginal though. Period 40–61 is usually markedly higher than the other periods, although there are some exceptions.

The geometrical mean of conductivity is consistently considerably higher for the heating period, except for the last group, where it differs much less.

The heat capacity is consistently higher for the cooling period except for c1d1e1f1.

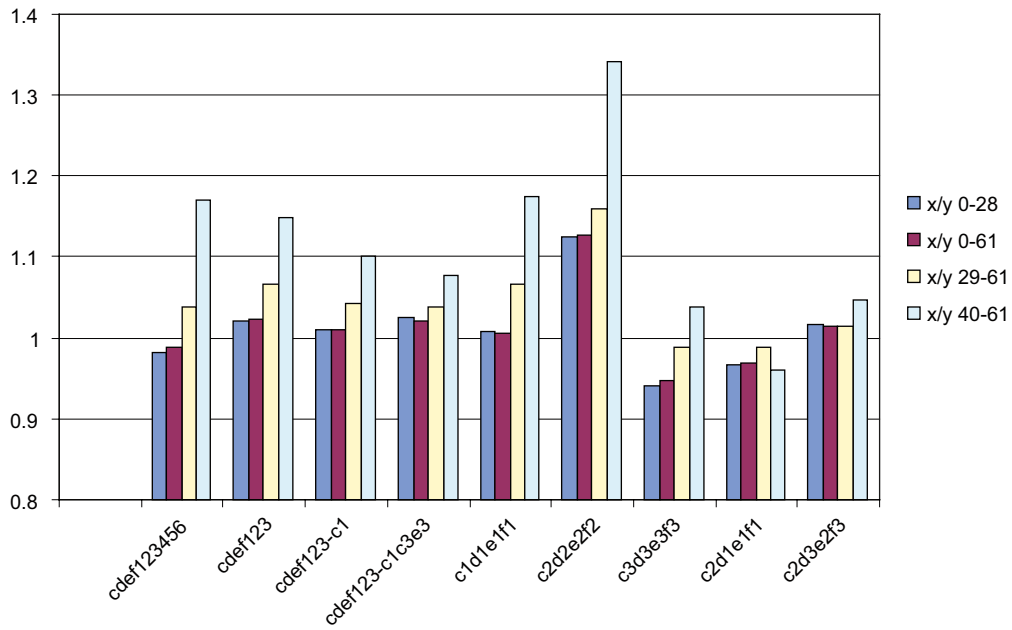


Figure 16. Anisotropic conductivity factors results from several calculations with different combinations of sensors, over different periods.

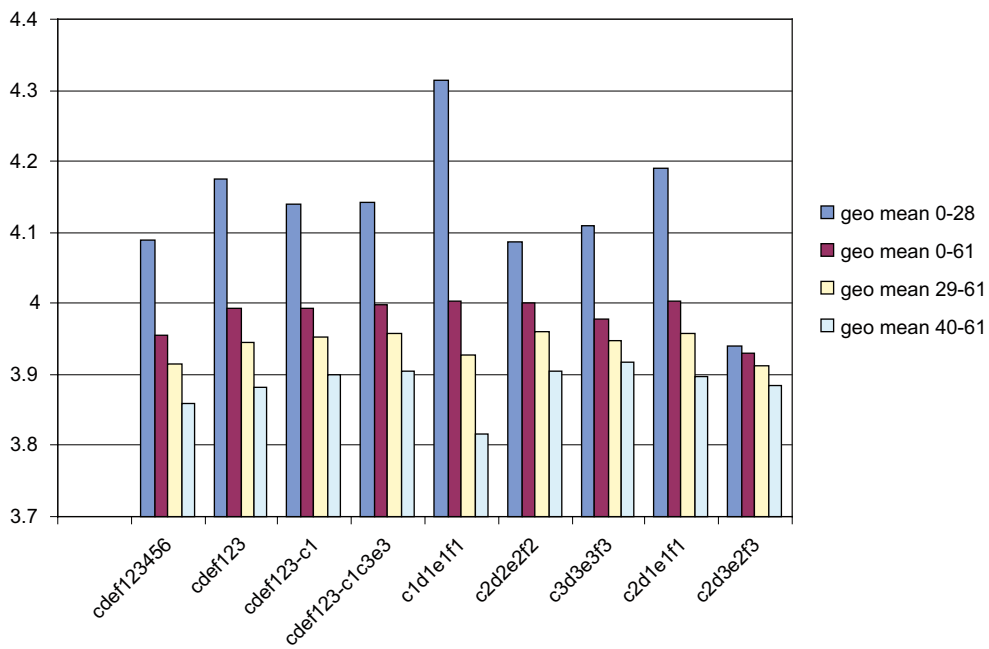


Figure 17. Geometrical mean of conductivity from several calculations with different combinations of sensors, over different periods.

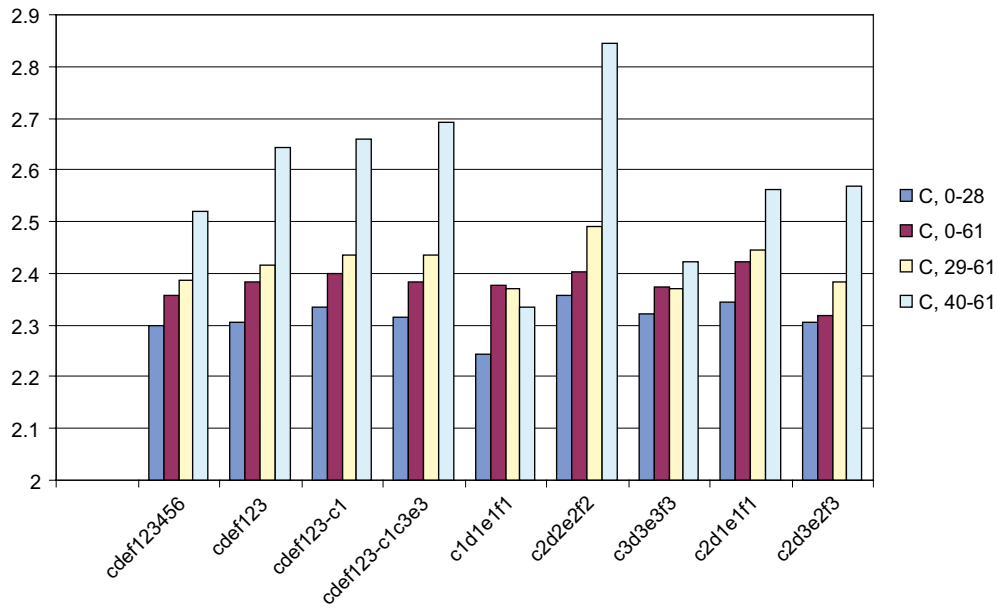


Figure 18. Heat capacity results from several calculations with different combinations of sensors, over different periods.

2.3 Heater borehole evaluation

An evaluation of the thermal conductivity around the heater was made. There were 3 thermal sensors at different locations along the heater. Sensor B1 was located at approximately 8 m below the ground, B2 at 11.5 m and B3 at 15 m.

The formula

$$T = q / (4\pi\lambda) \int_0^{\infty} (e^{-x}/x) dx$$

explains what the temperature T at the distance r at the time t will be for a continuous, infinitely thin and long, linear heat source /Carslaw and Jaeger 1959/, where:

T = temperature

q = power output per unit of length, W/m

$u = r^2 / (4\kappa t)$

λ = thermal conductivity, W/(m°C)

κ = thermal diffusivity, m²/s

r = radial distance between heater and sensor, m

t = time, s

If this equation is plotted in a logarithmic diagram it will after a certain time (when u is small) result in a straight line. The formula can then be simplified to

$$T = q / (4\pi\lambda) (\ln 4\kappa t / r^2 - \gamma)$$

where γ (Euler's constant) = 0.5772156649...

The thermal conductivity can be evaluated from the slope of the straight line.

The power output was approximated to 150 W/m. Only data after 518,400 seconds (6 days, one measurement every 600 seconds) was used in the evaluation. The temperature curves had notches on a few places and it was believed that they could influence the calculation of the average curve gradient. Therefore, the conductivity was also calculated using gradients of the curve periods between the notches, resulting in three periods. Table 2 presents the conductivity results. The heating curves are listed in Appendix 1.4.

Table 2. Thermal conductivity approximations of the area around sensor B1, B2 and B3. Results include data from the whole period and parts of the period.

	Thermal conductivity λ
B1 Whole period (518400-1714800)	4.044
B1 Period 1 (518400-928800)	3.683
B1 Period 2 (955200-1192800)	3.902
B1 Period 3 (1218000-1660800)	3.918
B2 Whole period (518400-1714800)	3.543
B2 Period 1 (518400-905400)	3.624
B2 Period 2 (976200-1161000)	2.787
B2 Period 3 (1231800-1458000)	3.286
B3 Whole period (518400-1714800)	4.360
B3 Period 1 (518400-868800)	4.218
B3 Period 2 (986400-1125600)	4.593
B3 Period 3 (1252200-1714800)	4.844

The different sensors give very different results although they are situated in the same borehole, only approximately 3.5 m apart from each other. The results also differ from period to period. This is especially true for sensor B2. The highest values are obtained from the deepest sensor.

3 References

Carlsaw H S, Jaeger J C, 1959. Conduction of heat in solids. Oxford, 2nd edition.

SKB, 2006. Site descriptive modelling – Forsmark stage 2.1. SKB R-06-38, Svensk Kärnbränslehantering AB.

APPENDIX 1.1 – Results and coordinates

Table 3 Results from original coordinates (case 5.1.1).

original coordinates, T-Is-aniso-fitting, interpol vert z, 060703 (A1)

1/100 of rows	cond x, 0-28	cond x, 0-61	cond x, 29-61	cond y, 0-28	cond y, 0-61	cond y, 29-61	geo mean 0-28	geo mean 0-61	geo mean 29-61	x/y 0-28	x/y 0-61	x/y 29-61	C, 0-28	C, 0-61	C, 29-61
c1d1	4.202	3.963	3.935	3.994	3.744	3.656	4.09668	3.851944	3.792936	1.052	1.0585	1.0763	2.229	2.28	2.375
e1f1	4.059	3.933	3.963	4.144	4.018	3.914	4.10128	3.975273	3.938424	0.979	0.9788	1.0125	2.329	2.415	2.584
c2d2	4.199	4.092	4.181	4.331	4.125	3.974	4.264489	4.108467	4.076186	0.97	0.992	1.0521	2.365	2.386	2.417
e2f2	4.503	4.329	4.457	3.777	3.63	3.447	4.124055	3.964123	3.919602	1.192	1.1926	1.293	2.266	2.363	2.483
c3d3	3.937	3.875	3.882	4.11	4.026	4.011	4.02257	3.949778	3.945973	0.958	0.9625	0.9678	2.353	2.361	2.359
e3f3	3.905	3.779	3.842	4.31	4.152	4.018	4.102505	3.961112	3.929015	0.906	0.9102	0.9562	2.256	2.34	2.414
c4d4	3.654	3.628	3.596	4.369	4.367	4.434	3.995538	3.980386	3.993077	0.836	0.8308	0.811	2.326	2.332	2.319
e4f4	3.579	3.479	3.332	4.343	4.237	4.412	3.942537	3.839339	3.83416	0.824	0.8211	0.7552	2.156	2.233	2.294
e5f5	3.366	3.224	2.995	4.192	4.029	4.176	3.756364	3.604094	3.536541	0.803	0.8002	0.7172	2.059	2.135	2.255
e6f6	3.285	2.971	2.614	4.377	4.289	4.696	3.791892	3.569681	3.503619	0.751	0.6927	0.5566	1.793	1.756	1.638

Table 4 Results from original coordinates + small horizontal change (case 5.1.2).

original coordinates, T-Is-aniso-fitting, MOVE 3, interpol vert z, 060703 (A2)

1/100 of rows	cond x, 0-28	cond x, 0-61	cond x, 29-61	cond y, 0-28	cond y, 0-61	cond y, 29-61	geo mean 0-28	geo mean 0-61	geo mean 29-61	x/y 0-28	x/y 0-61	x/y 29-61	C, 0-28	C, 0-61	C, 29-61
c1d1	4.415	4.16	4.132	3.78	3.539	3.454	4.085181	3.836957	3.777821	1.168	1.1755	1.1963	2.274	2.326	2.425
e1f1	4.189	4.051	4.088	3.986	3.858	3.749	4.08624	3.953322	3.914832	1.051	1.05	1.0904	2.255	2.343	2.518
c2d2	4.42	4.304	4.395	4.11	3.911	3.766	4.262183	4.102797	4.068362	1.075	1.1005	1.167	2.415	2.438	2.472
e2f2	4.653	4.464	4.59	3.651	3.504	3.327	4.121663	3.954979	3.907804	1.274	1.274	1.3796	2.192	2.292	2.419
c3d3	4.145	4.075	4.082	3.9	3.816	3.799	4.020634	3.943374	3.937959	1.063	1.0679	1.0745	2.404	2.413	2.414
e3f3	4.032	3.895	3.955	4.169	4.01	3.882	4.099928	3.952082	3.91833	0.967	0.9713	1.0188	2.185	2.27	2.351
c4d4	3.837	3.809	3.773	4.158	4.158	4.224	3.994277	3.979676	3.992136	0.923	0.9161	0.8932	2.384	2.39	2.377
e4f4	3.663	3.563	3.417	4.174	4.074	4.238	3.910161	3.809943	3.805423	0.878	0.8746	0.8063	2.074	2.146	2.199
e5f5	3.446	3.3	3.061	4.108	3.948	4.097	3.762468	3.609487	3.541316	0.839	0.8359	0.7471	2.024	2.1	2.22
e6f6	3.443	3.118	2.768	4.203	4.107	4.457	3.804067	3.578495	3.512403	0.819	0.7592	0.621	1.84	1.807	1.701

Table 5 The left table lists the original coordinates and the right table lists the coordinates of the case where the original coordinates have been changed horizontally (case 5.1.1 & 5.1.2).

Original coordinates, A Eng's depth (A1)	x	y	z
C1	1.528558	0.067482	-3.59499
C2	1.54214	0.083186	-0.56535
C3	1.55025	0.090257	0.954335
C4	1.588338	0.1133	6.914148
D1	0.054252	1.413941	-2.78138
D2	0.063008	1.40107	-0.76152
D3	0.07264	1.388328	1.258324
D4	0.099192	1.355773	6.308018
E1	-0.76263	-0.02894	-3.57907
E2	-0.76917	-0.015	-0.53888
E3	-0.77164	-0.00825	0.97099
E4	-0.77566	0.009524	5.520958
E5	-0.77687	0.013999	6.931208
E6	-0.77741	0.015774	7.541289
F1	-0.03356	-0.80494	-2.46238
F2	-0.03584	-0.80298	-0.44258
F3	-0.03762	-0.802	1.587373
F4	-0.04212	-0.80054	5.827349
F5	-0.04335	-0.79999	6.637307
F6	-0.04554	-0.79883	7.647187

Original coordinates + MOVE 3, A Eng's depth (A2)	x	y	z
C1	1.553558	0.042482	-3.59499
C2	1.56714	0.058186	-0.56535
C3	1.57525	0.065257	0.954335
C4	1.613338	0.0883	6.914148
D1	0.054252	1.363941	-2.78138
D2	0.063008	1.35107	-0.76152
D3	0.07264	1.338328	1.258324
D4	0.099192	1.305773	6.308018
E1	-0.78763	-0.05394	-3.57907
E2	-0.79417	-0.04	-0.53888
E3	-0.79664	-0.03325	0.97099
E4	-0.80066	-0.01548	5.520958
E5	-0.80187	-0.011	6.931208
E6	-0.80241	-0.00923	7.541289
F1	-0.03356	-0.80494	-2.46238
F2	-0.03584	-0.80298	-0.44258
F3	-0.03762	-0.802	1.587373
F4	-0.04212	-0.80054	5.827349
F5	-0.04335	-0.79999	6.637307
F6	-0.04554	-0.79883	7.647187

Appendix 1.1

Table 6 The horizontal coordinate change (case 5.1.2). The table lists the numbers that have been added to the x and y coordinates.

	x	y
C	0.025	-0.025
D	0	-0.05
E	-0.025	-0.025
F	0	0

Table 7 Results from the -10% power change calculation. The column to the far right confirms that the geometric mean of conductivity decreases by 10% when the power decreases by 10%. Original coordinates (case 5.1.3).

1/100 of rows	cond x	cond x, pow diff	cond y	cond y, pow diff	geo mean	geo mean, pow diff	x/y	x/y, pow diff	C	C, pow diff	geo mean pow diff / geo mean
c1d1	3.963	3.567	3.744	3.37	3.8519	3.4671011	1.058494	1.111	2.28	2.052	0.900091269
e1f1	3.933	3.54	4.018	3.617	3.9753	3.5782929	0.978845	1.11094	2.415	2.174	0.900137689
c2d2	4.092	3.683	4.125	3.713	4.1085	3.6979696	0.992	1.11101	2.386	2.148	0.900085043
e2f2	4.329	3.897	3.63	3.267	3.9641	3.5681226	1.192562	1.11098	2.363	2.127	0.900103944
c3d3	3.875	3.488	4.026	3.624	3.9498	3.5553498	0.962494	1.11094	2.361	2.125	0.900139032
e3f3	3.779	3.402	4.152	3.737	3.9611	3.5655678	0.910164	1.11093	2.34	2.106	0.900143159
c4d4	3.628	3.265	4.367	3.93	3.9804	3.5821013	0.830776	1.11119	2.332	2.099	0.899938088
e4f4	3.479	3.131	4.237	3.813	3.8393	3.4552139	0.8211	1.11117	2.233	2.091	0.899950225
e5f5	3.224	2.902	4.029	3.626	3.6041	3.2438637	0.800199	1.11105	2.135	1.922	0.900049622
e6f6	2.971	2.673	4.289	3.862	3.5697	3.2129622	0.692702	1.11102	1.756	1.58	0.900069955

Table 8 Results from the decreased temperature drift calculation (case 5.1.4). An additional temperature drift of -0.003°C per day was implemented on the sensors in hole C and E, and compared to the normal case. Original coordinates (case 5.1.4).

1/100 of rows	cond x	cond x, extra tempdrift	cond y	cond y, extra tempdrift	geo mean	geo mean, extra tempdrift	x/y	x/y, extra tempdrift	C	C, extra tempdrift
c1d1	4.202	4.198	3.994	4.067	4.0967	4.131980881	1.052078	1.03221047	2.229	2.246
e1f1	4.059	4.059	4.144	4.197	4.1013	4.127423288	0.979488	0.96711937	2.329	2.33
c2d2	4.199	4.186	4.331	4.406	4.2645	4.294591482	0.969522	0.95006809	2.365	2.384
e2f2	4.503	4.505	3.777	3.823	4.1241	4.150013855	1.192216	1.17839393	2.266	2.266
c3d3	3.937	3.922	4.11	4.176	4.0226	4.047007784	0.957908	0.93917625	2.353	2.372
e3f3	3.905	3.901	4.31	4.363	4.1025	4.125537904	0.906032	0.89410956	2.256	2.258
c4d4	3.654	3.588	4.369	4.497	3.9955	4.01686893	0.836347	0.79786524	2.326	2.386
e4f4	3.579	3.581	4.343	4.407	3.9425	3.972589458	0.824085	0.81257091	2.156	2.157
e5f5	3.366	3.324	4.192	4.308	3.7564	3.784150103	0.802958	0.77158774	2.059	2.073
e6f6	3.285	2.942	4.377	5.06	3.7919	3.858305327	0.750514	0.58142292	1.793	1.646

Table 9 Results from calculation with new coordinates (case 5.1.5).

New measure, T-Is-aniso-fitting, assuming A Eng's depth, 060629 (B1)

1/100 of rows	cond x, 0-28	cond x, 0-61	cond x, 29-61	cond y, 0-28	cond y, 0-61	cond y, 29-61	geo mean 0-28	geo mean 0-61	geo mean 29-61	x/y 0-28	x/y 0-61	x/y 29-61	C, 0-28	C, 0-61	C, 29-61
c1d1	4.267	4.022	3.995	3.911	3.663	3.574	4.085124	3.838305	3.778641	1.091	1.098	1.1178	2.208	2.259	2.355
e1f1	4.028	3.906	3.944	4.195	4.072	3.958	4.110652	3.988136	3.950994	0.96	0.9592	0.9965	2.408	2.494	2.665
c2d2	4.271	4.159	4.248	4.254	4.048	3.897	4.262492	4.103125	4.068717	1.004	1.0274	1.0901	2.342	2.364	2.397
e2f2	4.512	4.341	4.473	3.771	3.627	3.443	4.124894	3.967973	3.924352	1.196	1.1969	1.2992	2.337	2.436	2.554
c3d3	4.003	3.936	3.943	4.039	3.952	3.935	4.02096	3.943992	3.938998	0.991	0.996	1.002	2.33	2.338	2.338
e3f3	3.925	3.801	3.868	4.29	4.136	4	4.103444	3.964964	3.933446	0.915	0.919	0.967	2.327	2.41	2.484
c4d4	3.684	3.657	3.621	4.317	4.32	4.392	3.98796	3.9747	3.987911	0.853	0.8465	0.8245	2.31	2.316	2.304
e4f4	3.616	3.514	3.38	4.333	4.223	4.374	3.958299	3.852223	3.845012	0.835	0.8321	0.7727	2.221	2.303	2.369
e5f5	3.458	3.313	3.103	4.103	3.936	4.049	3.766719	3.61109	3.54458	0.843	0.8417	0.7664	2.116	2.196	2.323
e6f6	3.504	3.19	2.875	4.11	4.002	4.281	3.794923	3.573007	3.508258	0.853	0.7971	0.6716	1.911	1.883	1.795

Appendix 1.1

Table 10 Results from new coordinates with revised assumption of borehole length (case 5.1.6).

New measure, T-Is-aniso-fitting, assuming depth from hole measure, 060629 (B2)

1/100 of rows	cond x, 0-28	cond x, 0-61	cond x, 29-61	cond y, 0-28	cond y, 0-61	cond y, 29-61	geo mean 0-28	geo mean 0-61	geo mean 29-61	x/y 0- 28	x/y 0- 61	x/y 29- 61	C, 0-28	C, 0- 61	C, 29- 61
c1d1	4.251	4.002	3.974	3.892	3.64	3.551	4.067541	3.816711	3.756551	1.092	1.0995	1.1191	2.206	2.258	2.356
e1f1	4.024	3.9	3.937	4.179	4.053	3.939	4.100768	3.975764	3.938	0.963	0.9623	0.9995	2.411	2.499	2.674
c2d2	4.264	4.15	4.238	4.259	4.051	3.9	4.261499	4.100201	4.065489	1.001	1.0244	1.0867	2.342	2.364	2.398
e2f2	4.517	4.346	4.477	3.765	3.621	3.437	4.123894	3.966972	3.922684	1.2	1.2002	1.3026	2.34	2.439	2.559
c3d3	4.004	3.941	3.949	4.04	3.957	3.94	4.02196	3.948992	3.944497	0.991	0.996	1.0023	2.33	2.338	2.337
e3f3	3.925	3.803	3.869	4.291	4.138	4.003	4.103922	3.966965	3.93543	0.915	0.919	0.9665	2.326	2.41	2.481
c4d4	3.847	3.806	3.787	4.407	4.362	4.395	4.117491	4.074527	4.079689	0.873	0.8725	0.8617	2.448	2.455	2.448
e4f4	3.64	3.532	3.359	4.448	4.334	4.55	4.023769	3.912504	3.909405	0.818	0.815	0.7382	2.245	2.331	2.406
e5f5	3.271	3.126	2.897	4.421	4.242	4.397	3.802774	3.641496	3.569049	0.74	0.7369	0.6589	2.298	2.389	2.541
e6f6	2.743	2.42	1.991	5.218	5.245	6.14	3.783249	3.56271	3.49639	0.526	0.4614	0.3243	1.686	1.613	1.411

Table 11 The left table lists the new coordinates and the right table lists the coordinates of the case with revised assumption of borehole length (case 5.1.5 & 5.1.6).

New coordinates, A Eng's depth (B1)	x	y	z
C1	1.549184	0.071101	-3.60169
C2	1.562557	0.08596	-0.56748
C3	1.570962	0.091751	0.955461
C4	1.605719	0.112996	6.912415
D1	0.094115	1.405943	-2.7827
D2	0.108644	1.393127	-0.76089
D3	0.118786	1.379677	1.261026
D4	0.140236	1.345854	6.313933
E1	-0.74677	-0.01502	-3.57726
E2	-0.75784	-9.5E-05	-0.53175
E3	-0.76196	0.00612	0.979917
E4	-0.76582	0.017483	5.528359
E5	-0.76482	0.022523	6.937654
E6	-0.76347	0.025334	7.547257
F1	-0.03165	-0.79457	-2.47608
F2	-0.03336	-0.78953	-0.45677
F3	-0.03457	-0.78795	1.573033
F4	-0.03613	-0.79121	5.81355
F5	-0.03672	-0.79127	6.623569
F6	-0.03948	-0.78734	7.633027

New coordinates, depth from hole measure (B2)	x	y	z
C1	1.549088	0.071264	-3.66172
C2	1.562056	0.085883	-0.62757
C3	1.5708	0.09167	0.895472
C4	1.605516	0.112859	6.852434
D1	0.093623	1.40641	-2.88277
D2	0.108152	1.393594	-0.86096
D3	0.118525	1.380178	1.160954
D4	0.139646	1.346239	6.214232
E1	-0.74672	-0.01512	-3.65725
E2	-0.7576	-0.00036	-0.61188
E3	-0.7619	0.006018	0.89993
E4	-0.76577	0.017381	5.448372
E5	-0.76492	0.022316	6.857683
E6	-0.76357	0.025127	7.467286
F1	-0.03164	-0.79453	-2.49608
F2	-0.03336	-0.78948	-0.47678
F3	-0.03457	-0.78794	1.55303
F4	-0.03613	-0.79119	5.793547
F5	-0.03673	-0.79121	6.60356
F6	-0.0395	-0.78728	7.613018

Table 12 Results from calculation with combination of many sensors. New coordinates and period 40-61 included (case 5.2).

1/100 of rows	cond x, 0-28	cond x, 0-61	cond x, 29-61	cond x, 40-61	cond y, 0-28	cond y, 0-61	cond y, 29-61	cond y, 40-61	geo mean 0-28	geo mean 0-61	geo mean 29-61	geo mean 40-61	x/y 0-28	x/y 0-61	x/y 29-61	x/y 40-61	C, 0-28	C, 0-61	C, 29-61	C, 40-61
cdef123456	4.05	3.932	3.991	4.176	4.129	3.98	3.841	3.566	4.089309	3.955927	3.915282	3.858966	0.9809	0.988	1.0391	1.1711	2.299	2.358	2.388	2.519
cdef123	4.218	4.041	4.074	4.158	4.133	3.947	3.821	3.623	4.175284	3.993723	3.945473	3.881293	1.0206	1.024	1.0662	1.1477	2.306	2.383	2.416	2.644
cdef123-c1	4.16	4.014	4.037	4.093	4.121	3.974	3.872	3.714	4.140454	3.99395	3.953639	3.898898	1.0095	1.01	1.0426	1.102	2.334	2.4	2.436	2.659
cdef123-c1c3e3	4.194	4.04	4.034	4.053	4.089	3.958	3.885	3.762	4.141167	3.99879	3.958799	3.90479	1.0257	1.021	1.0384	1.0774	2.315	2.384	2.435	2.691
c1d1e1f1	4.33	4.012	4.057	4.137	4.3	3.992	3.802	3.519	4.314974	4.001988	3.927431	3.815508	1.007	1.005	1.0671	1.1756	2.243	2.377	2.372	2.334
c2d2e2f2	4.334	4.249	4.266	4.523	3.855	3.768	3.678	3.369	4.087489	4.001279	3.961104	3.903586	1.1243	1.128	1.1599	1.3425	2.358	2.402	2.489	2.844
c3d3e3f3	3.985	3.872	3.926	3.992	4.238	4.086	3.968	3.842	4.109554	3.977561	3.946944	3.916282	0.9403	0.948	0.9894	1.039	2.323	2.373	2.37	2.421
c2d1e1f1	4.121	3.94	3.937	3.817	4.259	4.07	3.979	3.978	4.189432	4.004472	3.957944	3.896669	0.9676	0.968	0.9894	0.9595	2.345	2.423	2.445	2.562
c2d3e2f3	3.972	3.959	3.941	3.975	3.909	3.9	3.885	3.798	3.940374	3.929389	3.9129	3.885492	1.0161	1.015	1.0144	1.0466	2.306	2.318	2.385	2.569

APPENDIX 1.2 – Borehole data

Table 13 The original coordinate borehole data. Both with length according to the installation team and the listed length from the drilling team.

Idcode	Northing (m)	Easting (m)	Elevation (m.a.s.l.) (m)	Drilled length (m)	Length installation team (m)	Vertical Depth (m)	Inclination (degrees)	Bearing (degrees)
KFM90A	6700073.679	1631004.14	0.343	0		0	-82.34	278.34
KFM90A	6700073.719	1631003.747	-2.631	3		2.97	-82.54	273.21
KFM90A	6700073.748	1631003.358	-5.605	6		5.95	-82.49	275.25
KFM90A	6700073.784	1631002.967	-8.58	9		8.92	-82.49	275.48
KFM90A	6700073.822	1631002.576	-11.554	12		11.9	-82.46	275.65
KFM90A	6700073.866	1631002.183	-14.528	15		14.87	-82.38	277.07
KFM90A	6700073.915	1631001.788	-17.501	18		17.84	-82.39	277
KFM90A	6700073.963	1631001.394	-20.475	21		20.82	-82.39	277.03
KFM90A	6700074.011	1631000.999	-23.448	24		23.79	-82.37	276.73
KFM90A	6700074.014	1631000.975	-23.627	24.18	24.18	23.97	-82.37	276.73
KFM90B	6700065.591	1631008.894	-0.553	0		0	-81.85	261.66
KFM90B	6700065.535	1631008.475	-3.523	3		2.97	-81.93	263.2
KFM90B	6700065.475	1631008.056	-6.493	6		5.94	-81.88	260.48
KFM90B	6700065.403	1631007.638	-9.463	9		8.91	-81.84	260.04
KFM90B	6700065.33	1631007.219	-12.433	12		11.88	-81.88	260.14
KFM90B	6700065.259	1631006.802	-15.403	15		14.85	-81.88	260.5
KFM90B	6700065.192	1631006.383	-18.372	18		17.82	-81.87	261.26
KFM90B	6700065.188	1631006.355	-18.57	18.2	18.17	18.02	-81.87	261.26
KFM90C	6700067.083	1631008.672	-0.784	0		0	-81.82	262.52
KFM90C	6700067.031	1631008.256	-3.755	3		2.97	-82.13	263.29
KFM90C	6700066.977	1631007.855	-6.727	6		5.94	-82.34	261.46
KFM90C	6700066.921	1631007.453	-9.7	9		8.92	-82.13	262.52
KFM90C	6700066.869	1631007.046	-12.671	12		11.89	-82.15	262.97
KFM90C	6700066.82	1631006.639	-15.643	15		14.86	-82.12	263.25
KFM90C	6700066.772	1631006.227	-18.614	18		17.83	-82.01	263.44
KFM90C	6700066.74	1631005.952	-20.595	20	20.03	19.81	-82.05	263.22
KFM90D	6700065.848	1631010.387	-0.364	0		0	-81.74	260.02
KFM90D	6700065.783	1631009.951	-3.331	3		2.97	-81.37	262.89
KFM90D	6700065.726	1631009.509	-6.298	6		5.93	-81.55	262.48
KFM90D	6700065.667	1631009.072	-9.266	9		8.9	-81.52	262.2
KFM90D	6700065.608	1631008.633	-12.233	12		11.87	-81.51	262.58
KFM90D	6700065.551	1631008.194	-15.2	15		14.84	-81.51	262.61
KFM90D	6700065.495	1631007.754	-18.167	18		17.8	-81.5	262.74
KFM90D	6700065.458	1631007.461	-20.145	20		19.78	-81.49	262.96
KFM90D	6700065.451	1631007.402	-20.54	20.4	20.47	20.18	-81.49	262.96
KFM90E	6700064.861	1631008.964	-0.426	0		0	-81.77	259.71
KFM90E	6700064.787	1631008.551	-3.396	3		2.97	-82.13	259.91
KFM90E	6700064.715	1631008.146	-6.368	6		5.94	-82.14	259.96
KFM90E	6700064.643	1631007.742	-9.34	9		8.91	-82.14	259.77
KFM90E	6700064.569	1631007.338	-12.312	12		11.89	-82.12	259.59
KFM90E	6700064.499	1631006.933	-15.283	15		14.86	-82.1	260.67
KFM90E	6700064.429	1631006.525	-18.255	18		17.83	-82.05	260.03
KFM90E	6700064.382	1631006.252	-20.236	20		19.81	-82.06	260.29
KFM90E	6700064.375	1631006.212	-20.533	20.3	20.35	20.11	-82.06	260.29
KFM90F	6700065.461	1631008.075	-0.624	0		0	-81.73	261.42
KFM90F	6700065.392	1631007.655	-3.594	3		2.97	-81.95	259.88
KFM90F	6700065.318	1631007.242	-6.564	6		5.94	-81.98	259.79
KFM90F	6700065.245	1631006.828	-9.535	9		8.91	-81.92	260.19
KFM90F	6700065.173	1631006.413	-12.505	12		11.88	-81.91	260.31
KFM90F	6700065.102	1631005.995	-15.475	15		14.85	-81.87	260.34
KFM90F	6700065.029	1631005.579	-18.445	18		17.82	-81.93	259.7
KFM90F	6700064.979	1631005.303	-20.425	20		19.8	-81.92	259.98
KFM90F	6700064.977	1631005.289	-20.524	20.1	20.09	19.9	-81.92	259.98

Appendix 1.2

Table 14 The new coordinate borehole data. The lowest measured point is not the bottom. Borehole length not specified.

Hole ID	Dip	Azimuth	Northing	Easting	Elevation
	Degrees	Degrees	Metres	Metres	Metres
KFM90A	-82.61	278.72	6700073.68	1631004.14	0.34
KFM90A	-82.54	273.21	6700073.74	1631003.76	-2.64
KFM90A	-82.49	275.25	6700073.77	1631003.37	-5.61
KFM90A	-82.49	275.48	6700073.81	1631002.98	-8.59
KFM90A	-82.46	275.65	6700073.84	1631002.59	-11.56
KFM90A	-82.38	277.07	6700073.89	1631002.2	-14.54
KFM90A	-82.39	277	6700073.94	1631001.8	-17.51
KFM90A	-82.39	277.03	6700073.98	1631001.41	-20.48
KFM90A	-82.37	276.73	6700074.03	1631001.01	-23.46
KFM90B	-81.891	260.289	6700065.586	1631008.894	-0.559
KFM90B	-81.930	263.200	6700065.510	1631008.480	-3.530
KFM90B	-81.880	260.480	6700065.450	1631008.060	-6.500
KFM90B	-81.840	260.040	6700065.380	1631007.640	-9.470
KFM90B	-81.880	260.140	6700065.310	1631007.220	-12.440
KFM90B	-81.880	260.500	6700065.230	1631006.810	-15.410
KFM90B	-81.870	261.260	6700065.170	1631006.390	-18.380
KFM90C	-82.040	263.414	6700067.078	1631008.676	-0.790
KFM90C	-82.130	263.290	6700067.030	1631008.260	-3.760
KFM90C	-82.340	261.460	6700066.980	1631007.860	-6.730
KFM90C	-82.130	262.520	6700066.920	1631007.460	-9.700
KFM90C	-82.150	262.970	6700066.870	1631007.050	-12.680
KFM90C	-82.120	263.250	6700066.820	1631006.640	-15.650
KFM90C	-82.010	263.440	6700066.770	1631006.230	-18.620
KFM90C	-82.050	263.220	6700066.740	1631005.960	-20.600
KFM90D	-81.40	263.60	6700065.85	1631010.39	-0.37
KFM90D	-81.37	262.89	6700065.8	1631009.94	-3.34
KFM90D	-81.55	262.48	6700065.74	1631009.5	-6.31
KFM90D	-81.52	262.2	6700065.68	1631009.06	-9.27
KFM90D	-81.51	262.58	6700065.63	1631008.62	-12.24
KFM90D	-81.51	262.61	6700065.57	1631008.18	-15.21
KFM90D	-81.5	262.74	6700065.51	1631007.74	-18.18
KFM90D	-81.49	262.96	6700065.48	1631007.45	-20.15
KFM90E	-81.98	258.88	6700064.86	1631008.97	-0.44
KFM90E	-82.13	259.91	6700064.78	1631008.56	-3.41
KFM90E	-82.14	259.96	6700064.71	1631008.16	-6.38
KFM90E	-82.14	259.77	6700064.64	1631007.75	-9.35
KFM90E	-82.12	259.59	6700064.56	1631007.35	-12.33
KFM90E	-82.1	260.67	6700064.49	1631006.94	-15.3
KFM90E	-82.05	260.03	6700064.42	1631006.53	-18.27
KFM90E	-82.06	260.29	6700064.38	1631006.26	-20.25
KFM90F	-81.94	259.01	6700065.46	1631008.08	-0.62
KFM90F	-81.95	259.88	6700065.38	1631007.67	-3.59
KFM90F	-81.98	259.79	6700065.31	1631007.26	-6.56
KFM90F	-81.92	260.19	6700065.23	1631006.84	-9.53
KFM90F	-81.91	260.31	6700065.16	1631006.43	-12.5
KFM90F	-81.87	260.34	6700065.09	1631006.01	-15.47
KFM90F	-81.93	259.7	6700065.02	1631005.59	-18.44
KFM90F	-81.92	259.98	6700064.97	1631005.32	-20.42

Table 15 Summary of the different hole lengths (length according to installation team and length from drilling team), sensor coordinates, and the reason for uncertainty.

Hole/sensor Id	Ground level with respect to s.l. (m)	Ground level over hole B's ground level (m)	Vertical depth relative to B's ground level	Vertical depth relative to ground level	inclination (at surface)	sinus inclination	Length coordinate along borehole from surface (X1)	Measured length of borehole according to installation team (X2)	Calculated distance between bottom and sensor (X3)	Length coordinate along borehole using hole length from drilling team (X4)	Borehole length from drilling team (X5)
KFM90A	0.343										
A1		0.90	8.00	8.90	82.34	0.991	8.98	24.18	15.20		24.18
A2		0.90	12.50	13.40	82.34	0.991	13.52	24.18	10.66		24.18
A3		0.90	18.40	19.30	82.34	0.991	19.47	24.18	4.71		24.18
KFM90B	-0.553										
B1		0.00	8.00	8.00	81.85	0.990	8.08	18.17	10.09		18.2
B2		0.00	11.50	11.50	81.85	0.990	11.62	18.17	6.55		18.2
B3		0.00	15.00	15.00	81.85	0.990	15.15	18.17	3.02		18.2
KFM90C	-0.784	-0.23	8.00	7.77	81.82	0.990	7.85	20.03	12.18	7.82	20
C2		-0.23	11.00	10.77	81.82	0.990	10.88	20.03	9.15	10.85	20
C3		-0.23	12.50	12.27	81.82	0.990	12.40	20.03	7.63	12.37	20
C4		-0.23	18.40	18.17	81.82	0.990	18.36	20.03	1.67	18.33	20
KFM90D	-0.364										
D1		0.19	9.00	9.19	81.74	0.990	9.29	20.47	11.18	9.22	20.4
D2		0.19	11.00	11.19	81.74	0.990	11.31	20.47	9.16	11.24	20.4
D3		0.19	13.00	13.19	81.74	0.990	13.33	20.47	7.14	13.26	20.4
D4		0.19	18.00	18.19	81.74	0.990	18.38	20.47	2.09	18.31	20.4
KFM90E	-0.426										
E1		0.13	8.00	8.13	81.77	0.990	8.21	20.35	12.14	8.16	20.3
E2		0.13	11.00	11.13	81.77	0.990	11.25	20.35	9.10	11.2	20.3
E3		0.13	12.50	12.63	81.77	0.990	12.76	20.35	7.59	12.71	20.3
E4		0.13	17.00	17.13	81.77	0.990	17.31	20.35	3.04	17.26	20.3
E5		0.13	18.40	18.53	81.77	0.990	18.72	20.35	1.63	18.67	20.3
E6		0.13	19.00	19.13	81.77	0.990	19.33	20.35	1.02	19.28	20.3
KFM90F	-0.624										
F1		-0.07	9.00	8.93	81.73	0.990	9.02	20.09	11.07	9.03	20.1
F2		-0.07	11.00	10.93	81.73	0.990	11.04	20.09	9.05	11.05	20.1
F3		-0.07	13.00	12.93	81.73	0.990	13.07	20.09	7.02	13.08	20.1
F4		-0.07	17.20	17.13	81.73	0.990	17.31	20.09	2.78	17.32	20.1
F5		-0.07	18.00	17.93	81.73	0.990	18.12	20.09	1.97	18.13	20.1
F6		-0.07	19.00	18.93	81.73	0.990	19.13	20.09	0.96	19.14	20.1

The installation team was given approximate vertical coordinates where the sensors should be situated. This was then re-calculated into length coordinates (X1) by using the surface inclination. The team then re-calculated the coordinates into coordinates measured from the bottom of the hole ($X3 = X2 - X1$) and used these values when placing the sensors on the sticks that was inserted into each sensor hole. Since the actual borehole length may differ from X2 (measured with measure tape) the sensors might not be situated on the X1 level. It is because of this that we also used the borehole length from the drilling team (X5) instead of the X2 length. By calculating $X4 = X5 - X3$ (earlier $X1 = X2 - X3$), you now get a different X1, thus a different sensor length coordinate (X4).

APPENDIX 1.3 – Various temperature and power graphs

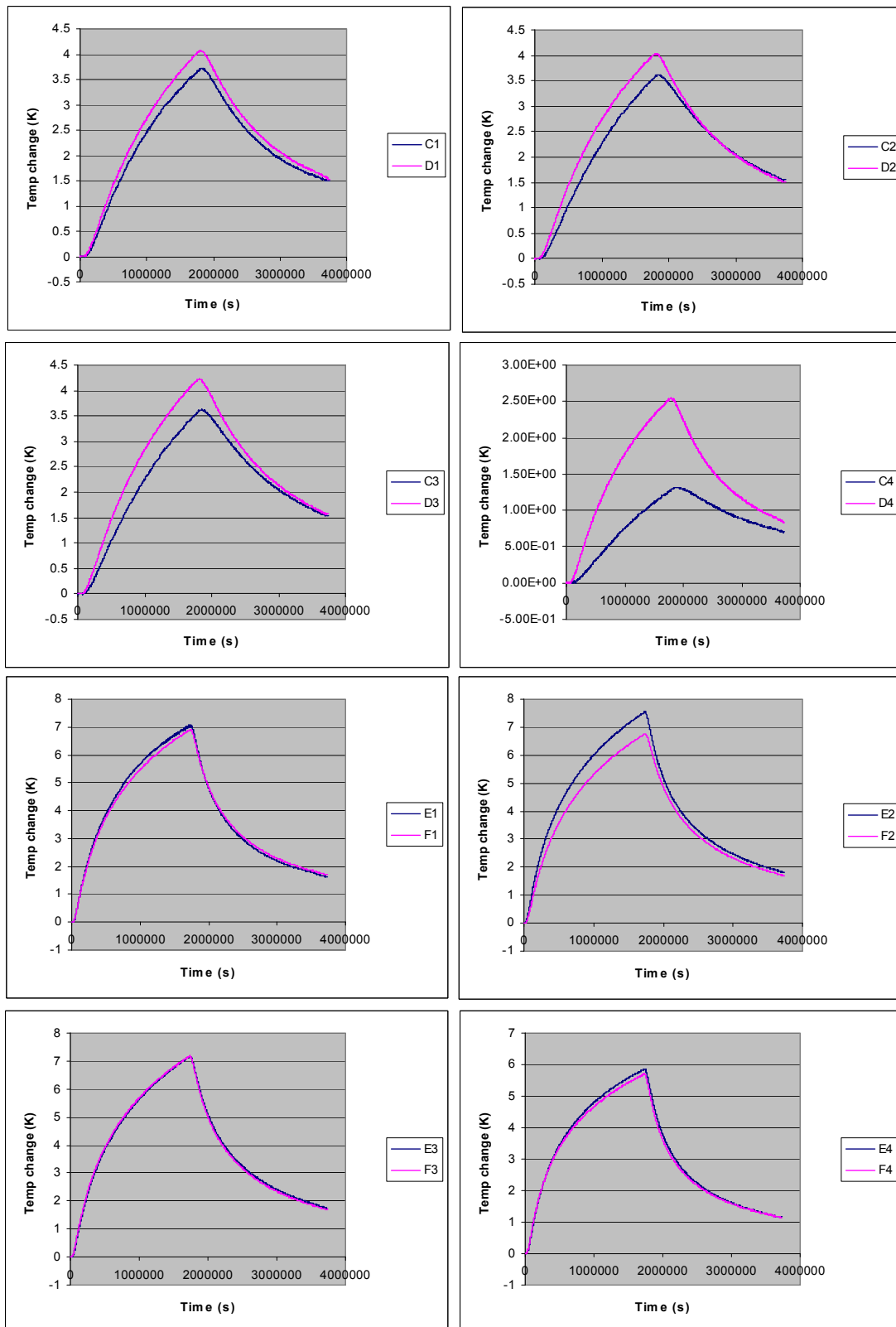


Figure 19 Measured temperature curves, heating and cooling for the different sensor pairs.

Appendix 1.3

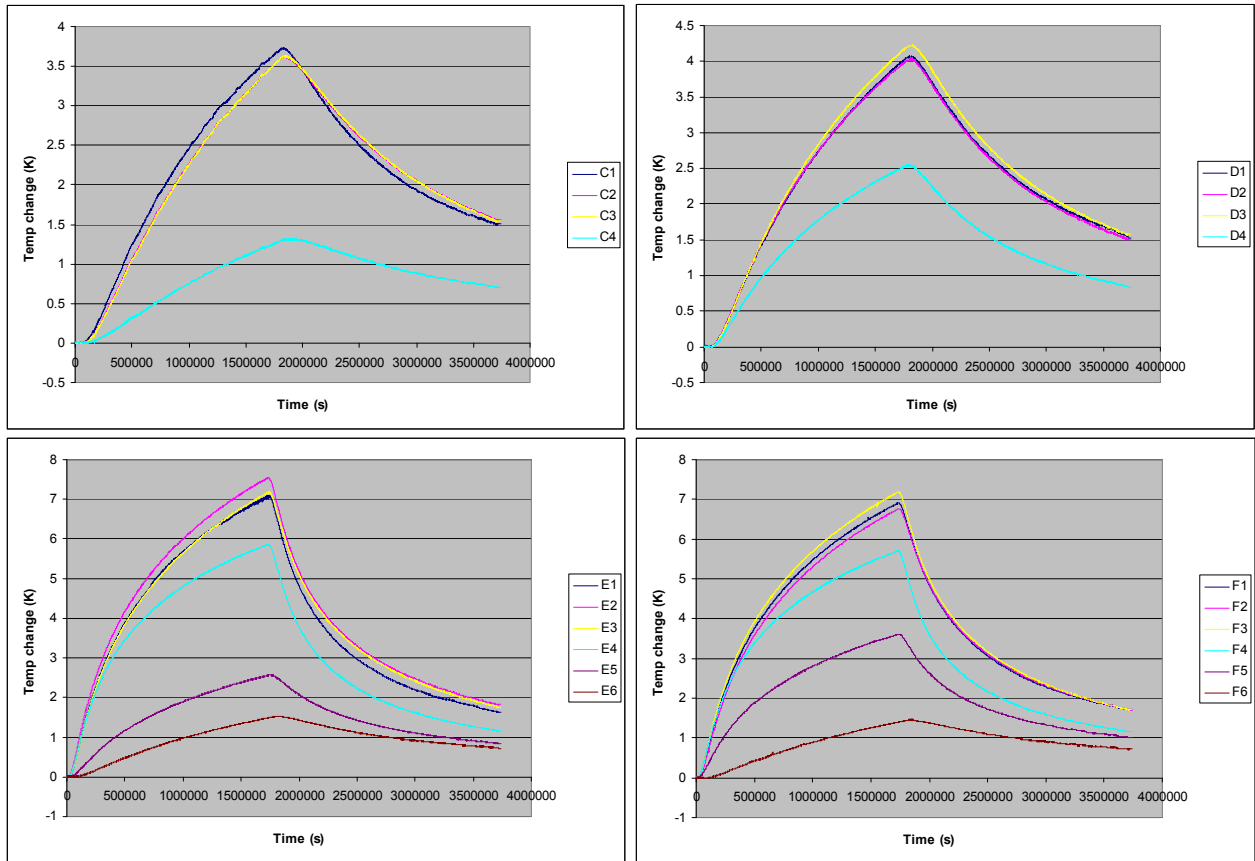


Figure 20 Measured temperature curves, heating and cooling, for the sensors in each borehole.

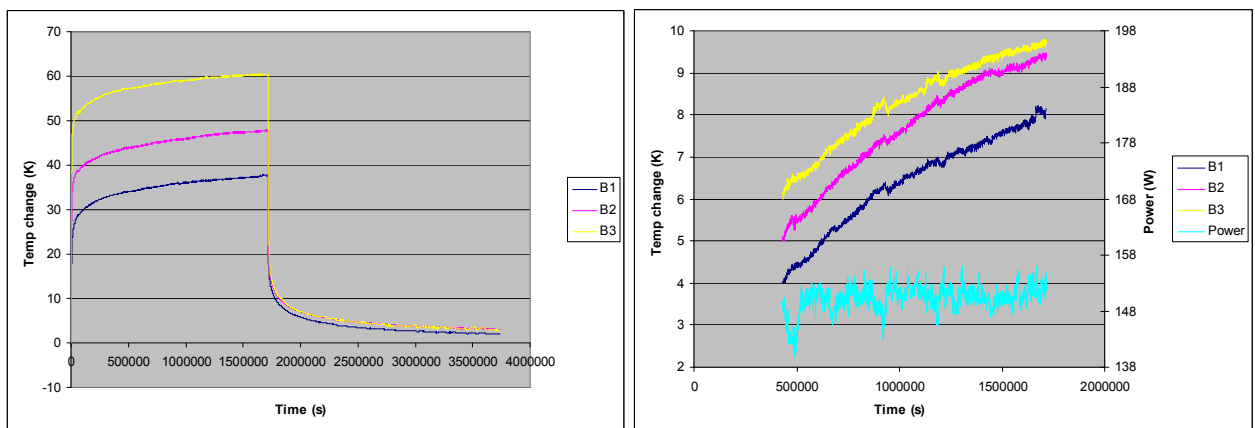


Figure 21 Sensor B1, B2 and B3. The left is both heating and cooling and the right is heating only, compared to the power output.

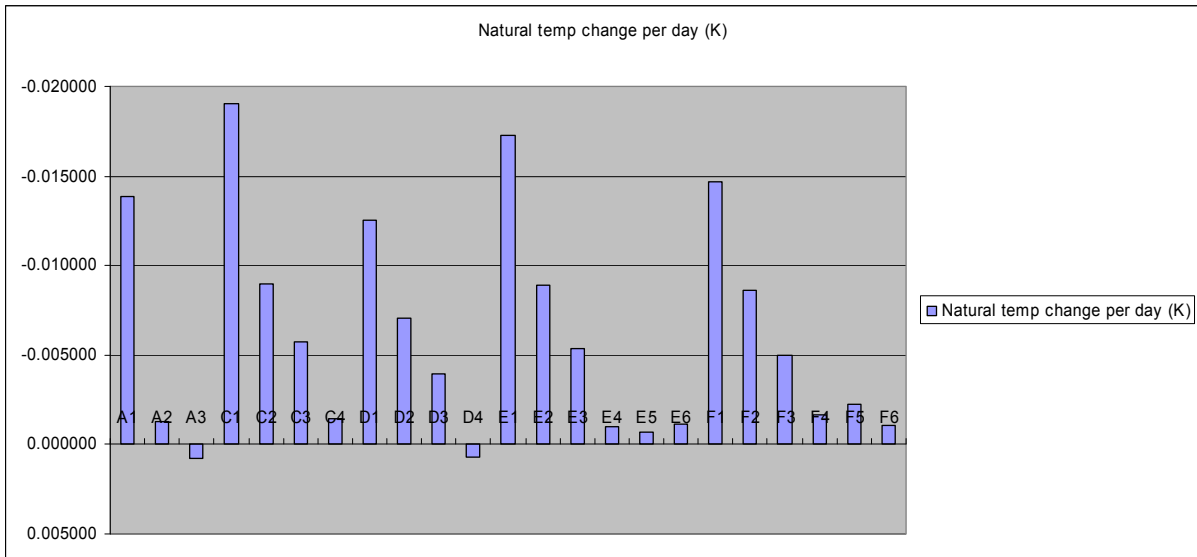


Figure 22 Summary of the natural temperature drift per day (over 15 days just before the experiment started) for the different sensors. Temperature drifts for sensor B1, B2 and B3 are not presented due to unusable values.

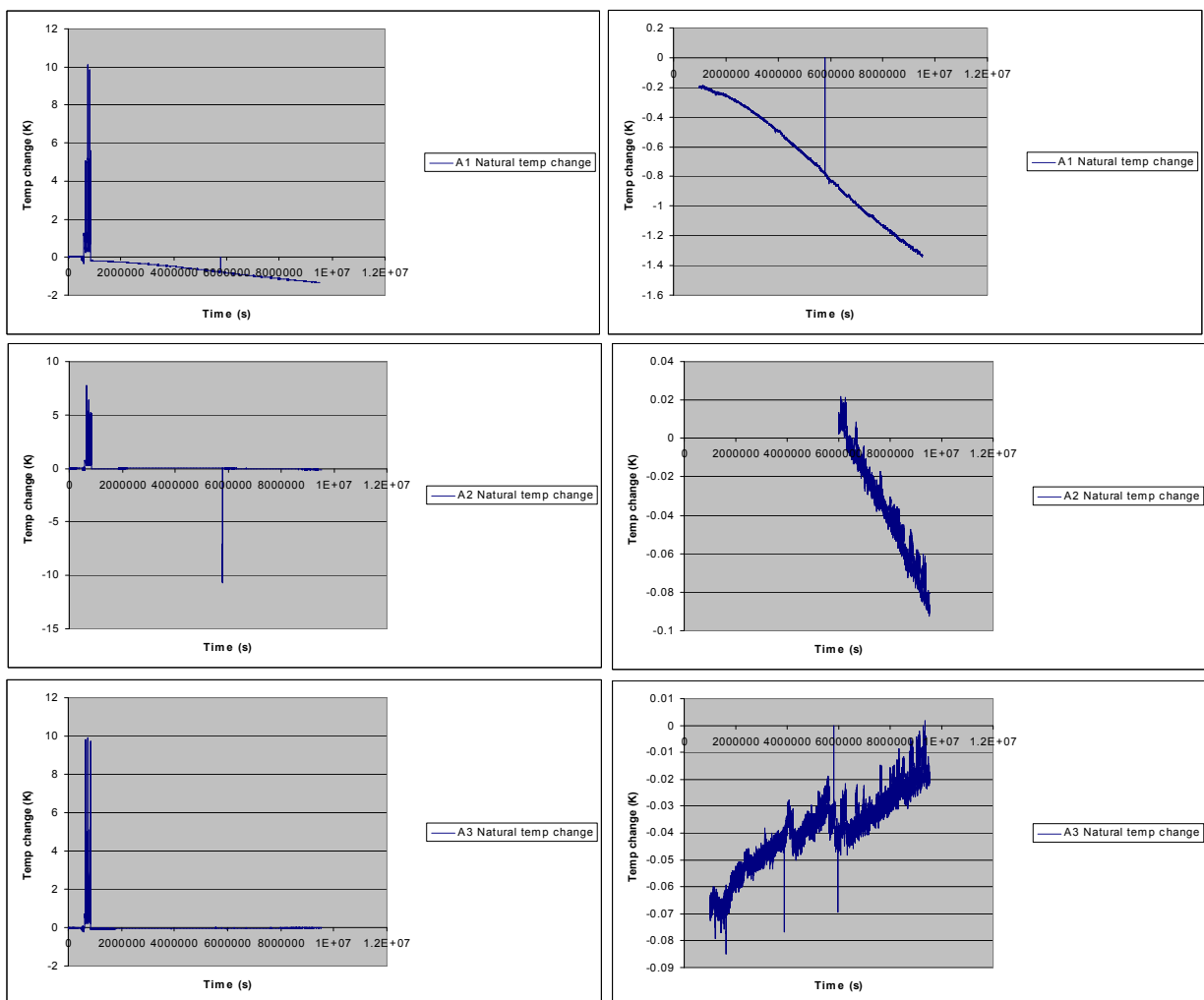


Figure 23 Natural temperature drifts of sensor A1-A3 before the experiment started. The left graphs are the original graphs. On the right graphs the disturbances seen on the left graphs have been excluded.

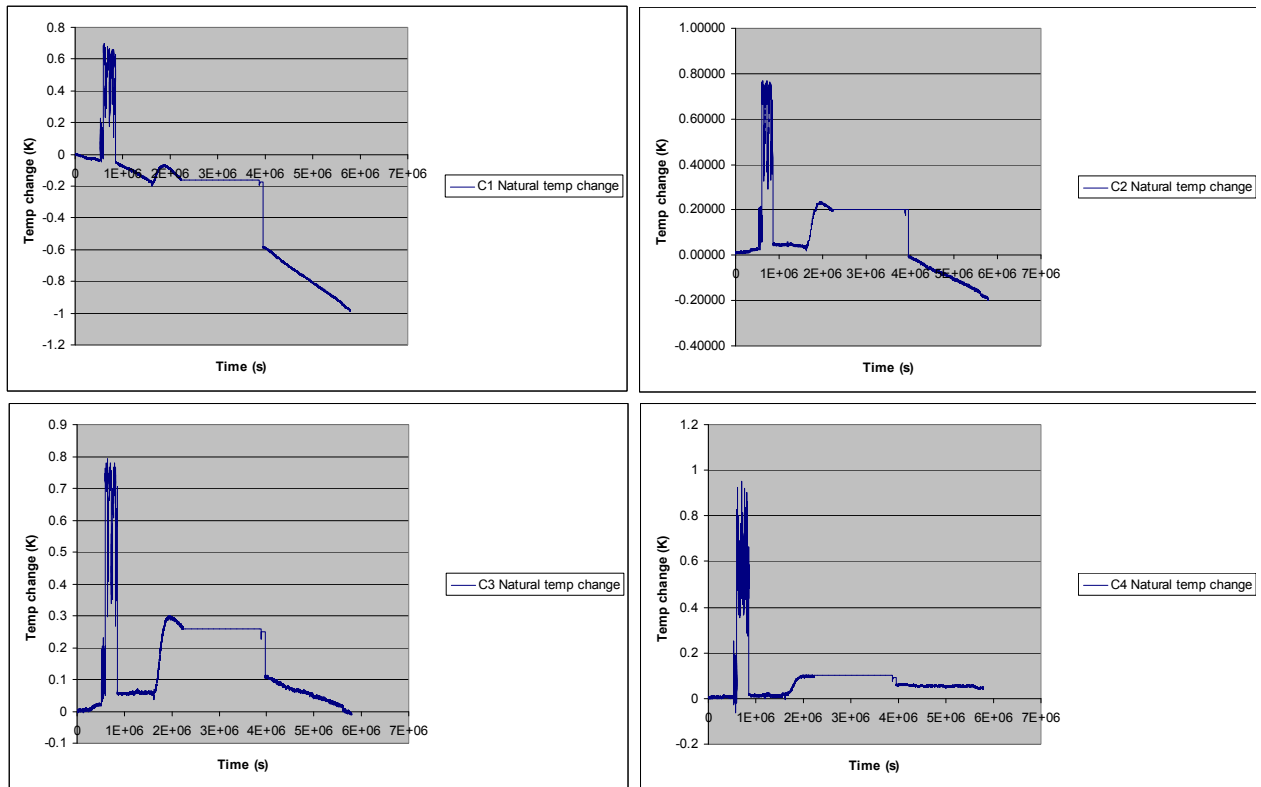


Figure 24 Natural temperature drift for sensor C1-C4 before the experiment started. Only the last 15 days used when calculating the temperature drift.

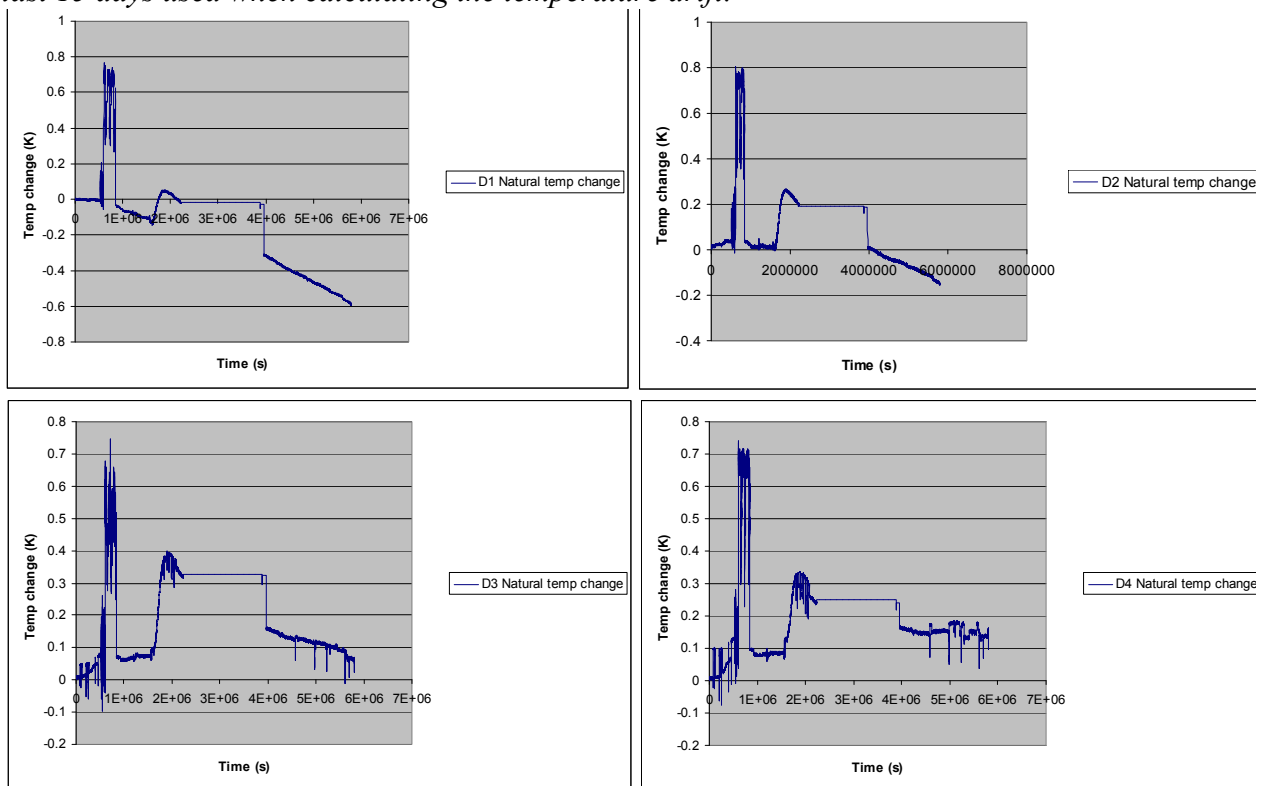


Figure 25 Natural temperature drift for sensor D1-D4 before the experiment started. Only the last 15 days used when calculating the temperature drift.

Appendix 1.3

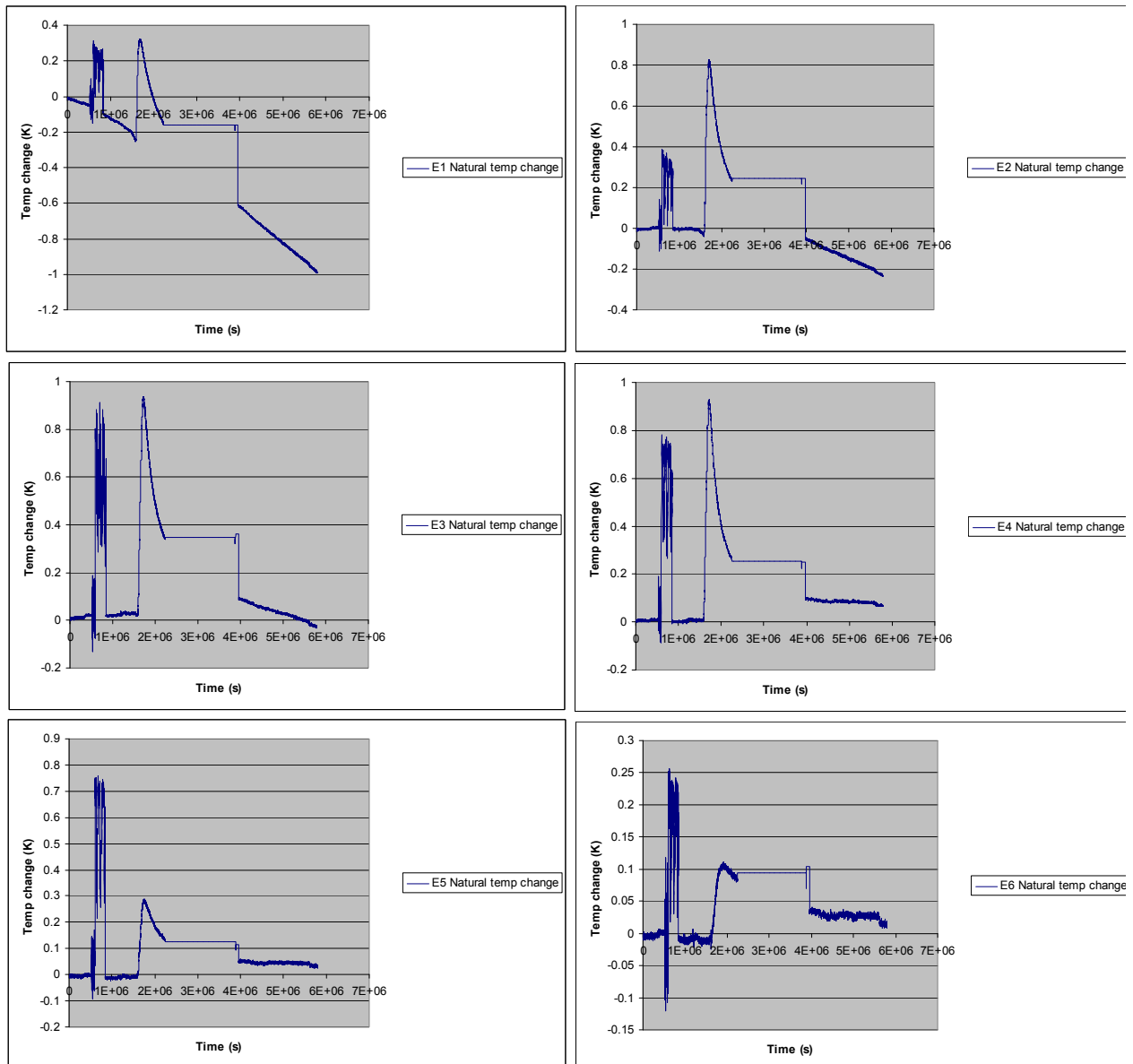


Figure 26 Natural temperature drift for sensor E1-E6 before the experiment started. Only the last 15 days used when calculating the temperature drift.

Appendix 1.3

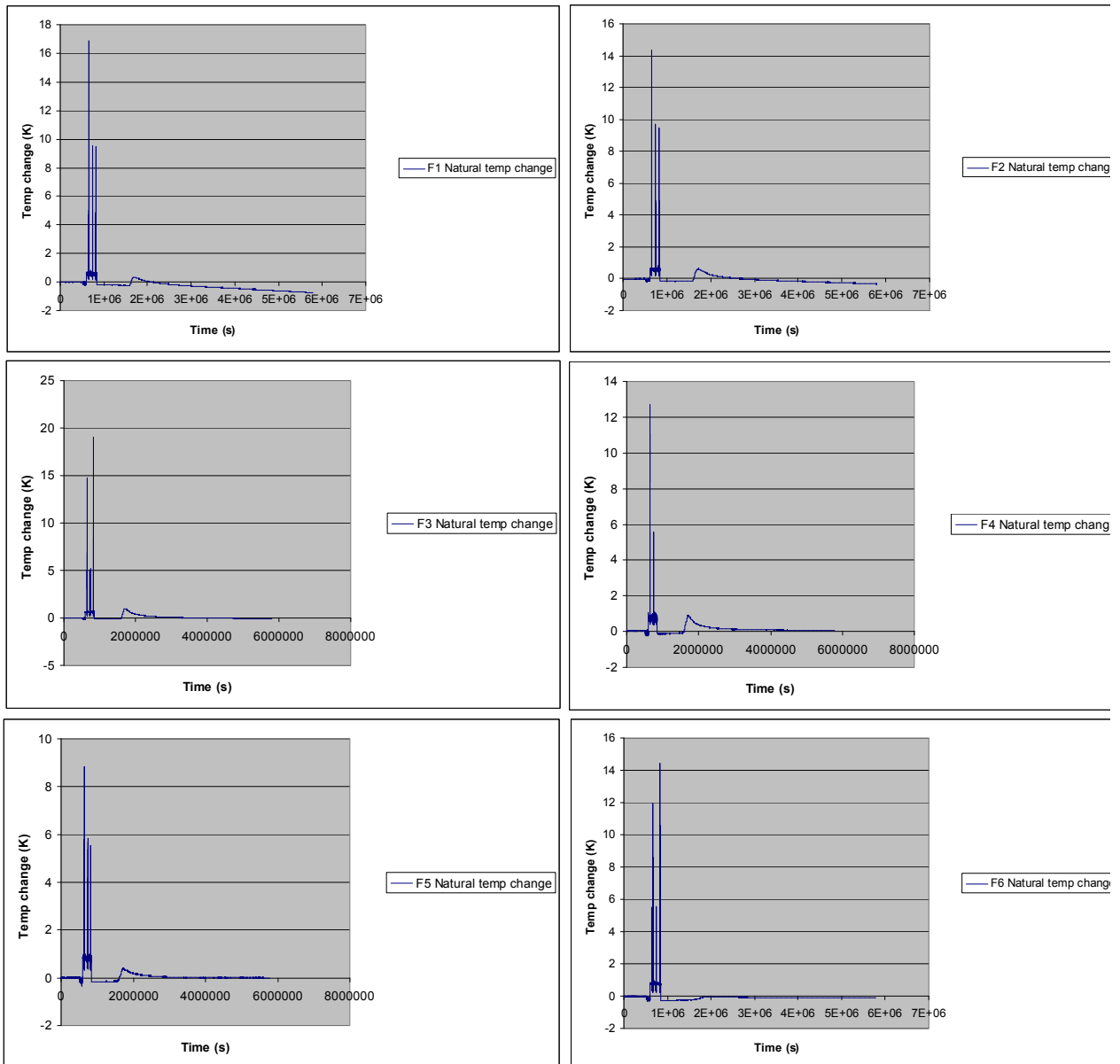


Figure 27 Natural temperature drift for sensor F1-F6 before the experiment started. Only the last 15 days used when calculating the temperature drift.

APPENDIX 1.4 – Borehole B temperature curves

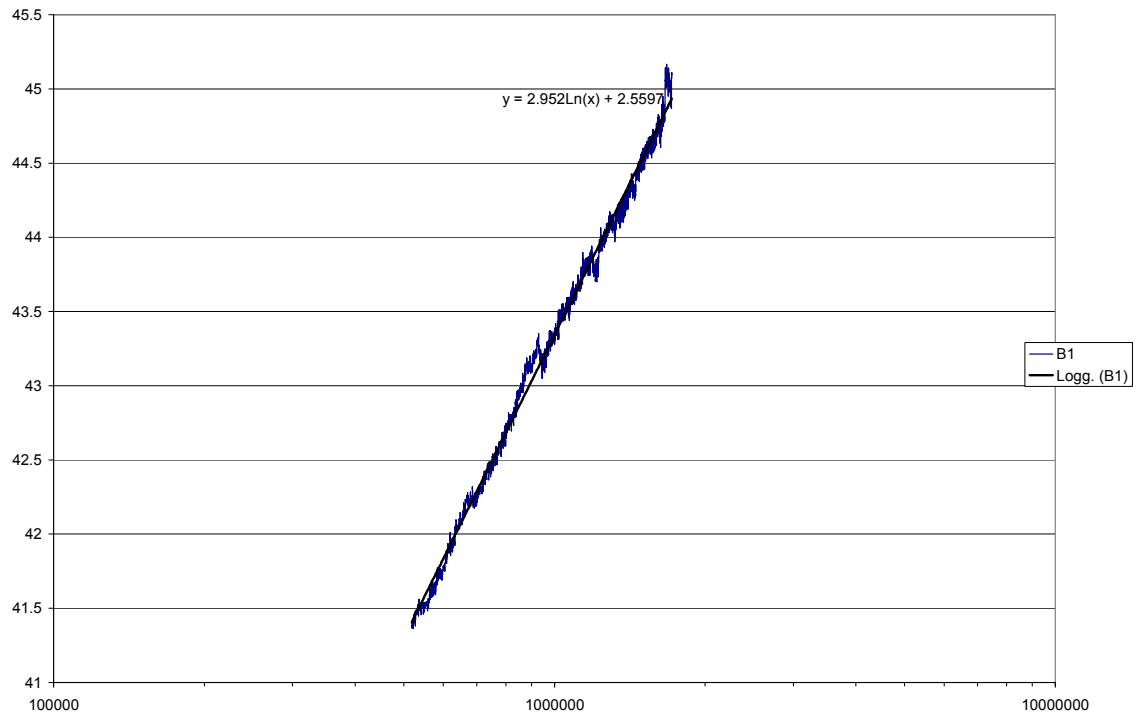


Figure 28 Temperature curve over sensor B1 with logarithmized time axis. Whole heating period except beginning.

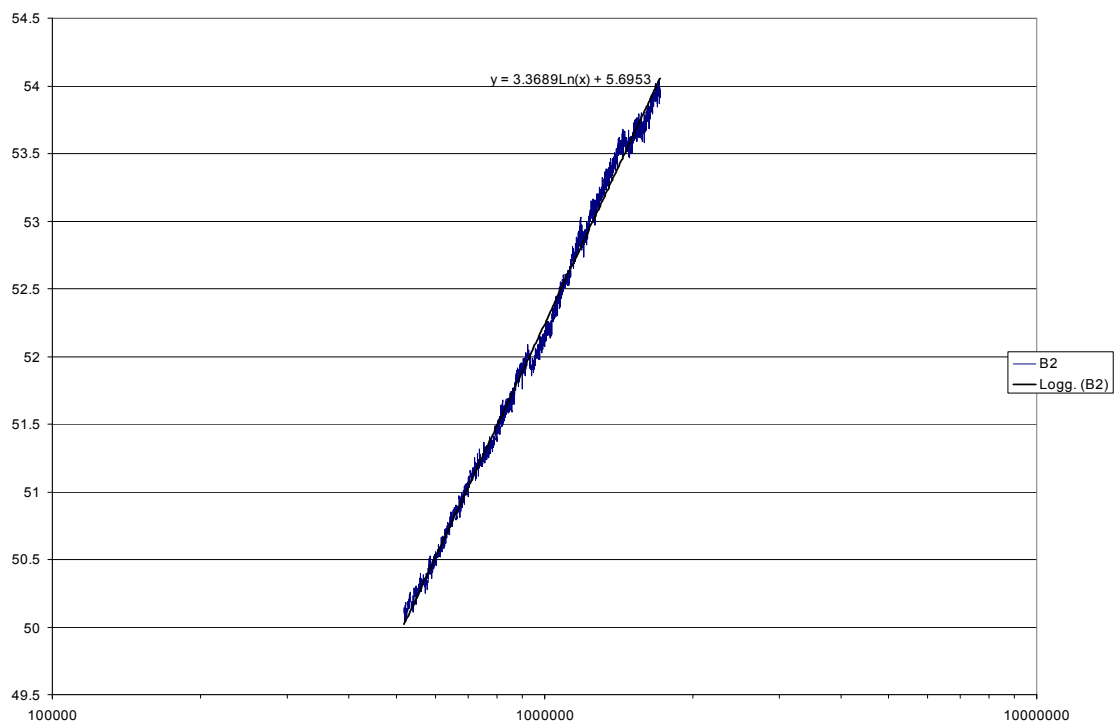


Figure 29 Temperature curve over sensor B2 with logarithmized time axis. Whole heating curve except beginning.

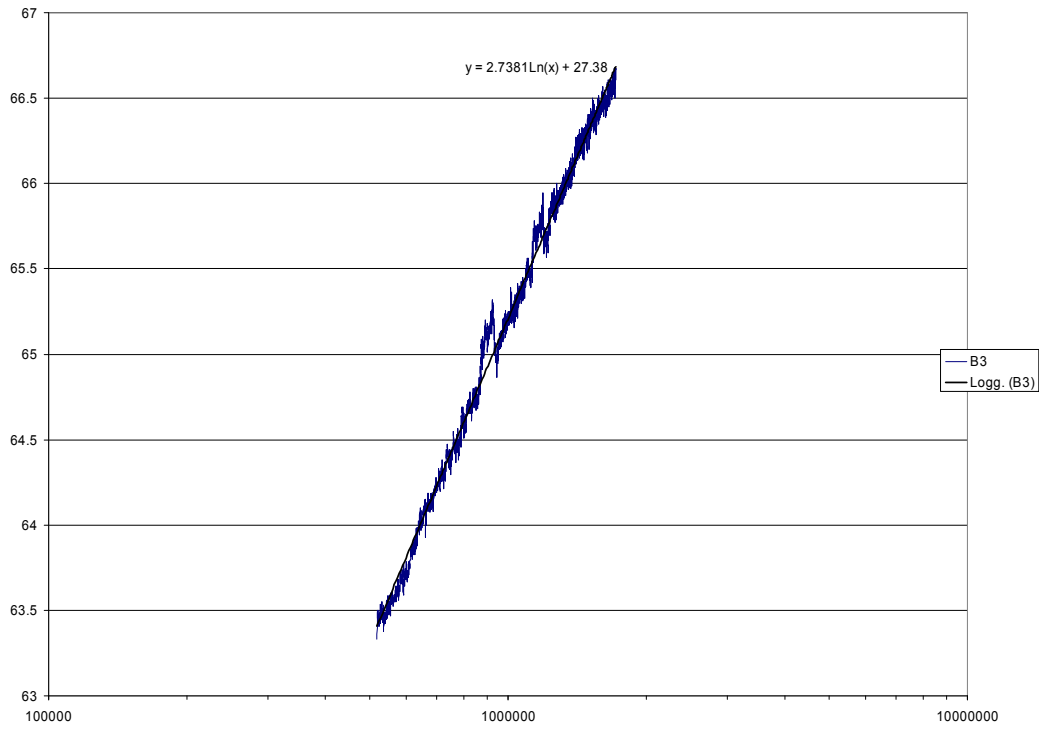


Figure 30 Temperature curve over sensor B3 with logarithmized time axis. Whole heating curve except beginning.

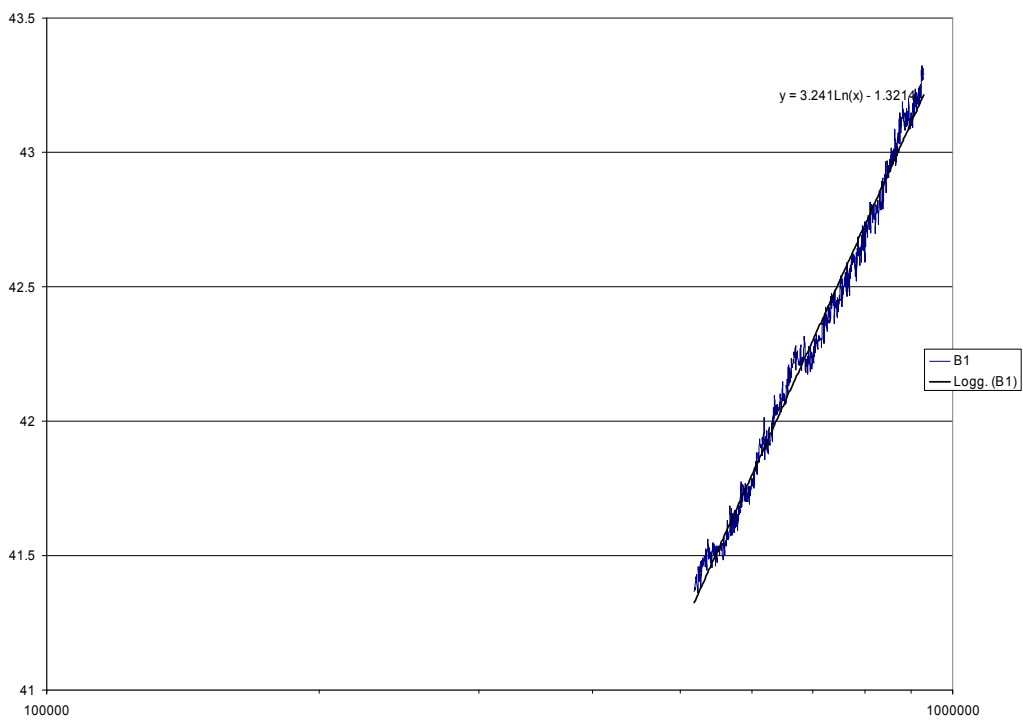


Figure 31 Temperature curve over sensor B1 with logarithmized time axis. Period 1 only.

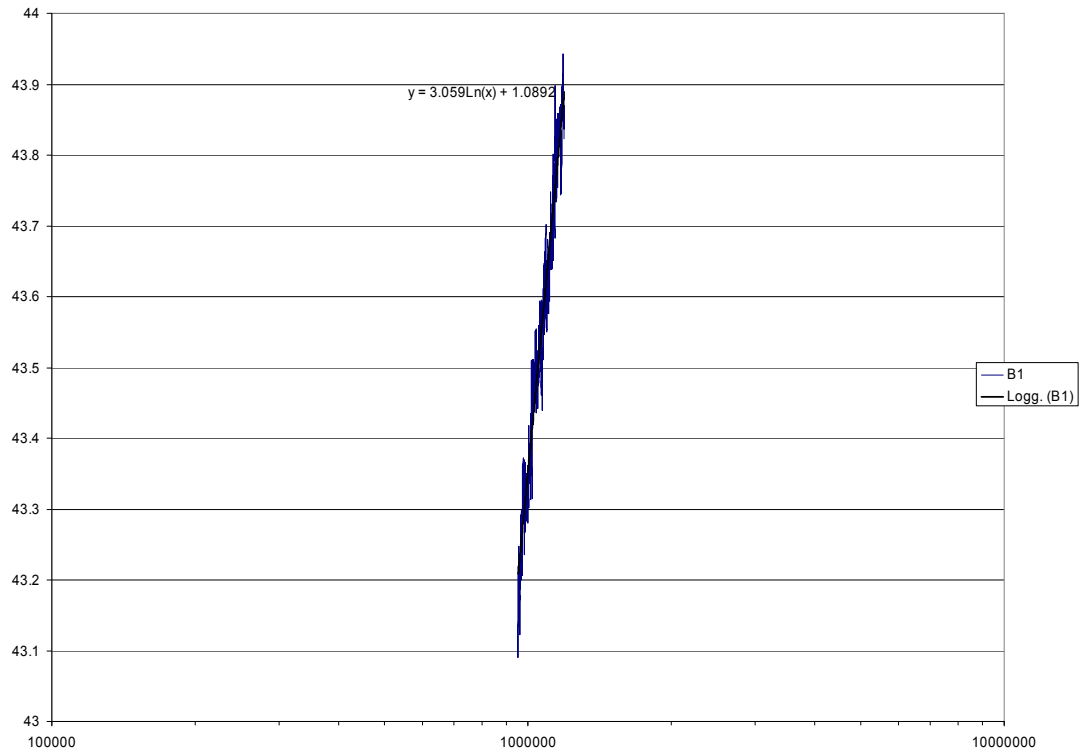


Figure 32 Temperature curve over sensor B1 with logarithmized time axis. Period 2 only.

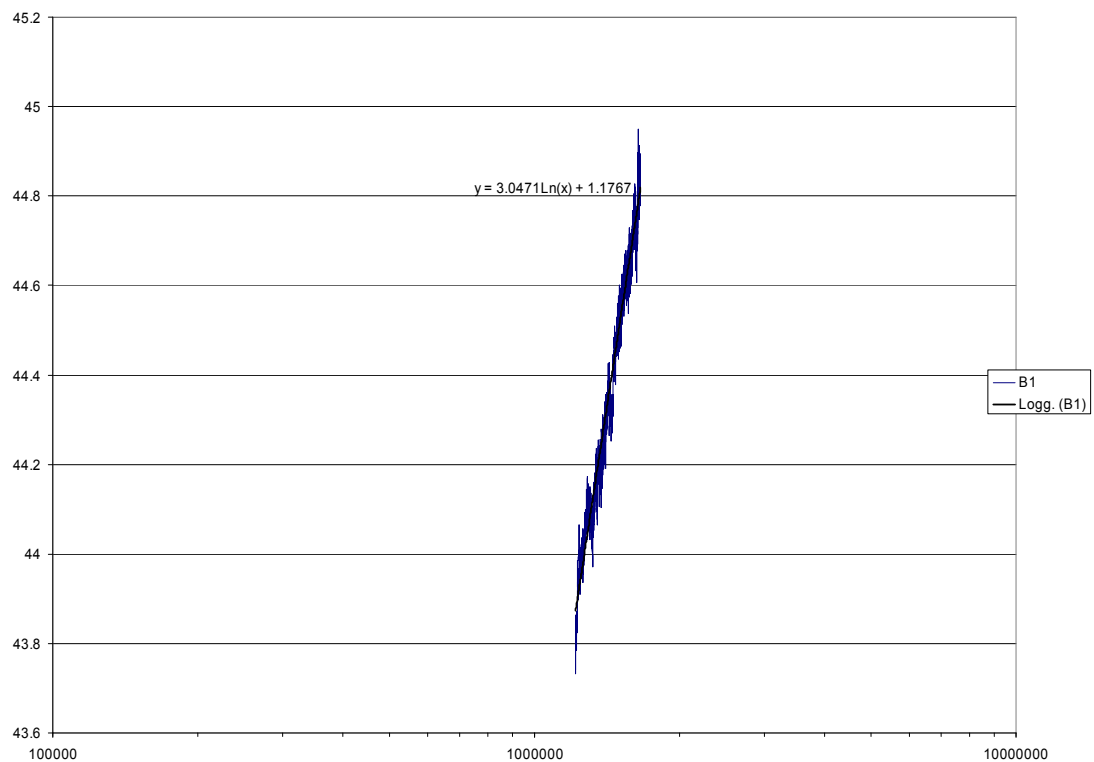


Figure 33 Temperature curve over sensor B1 with logarithmized time axis. Period 3 only.

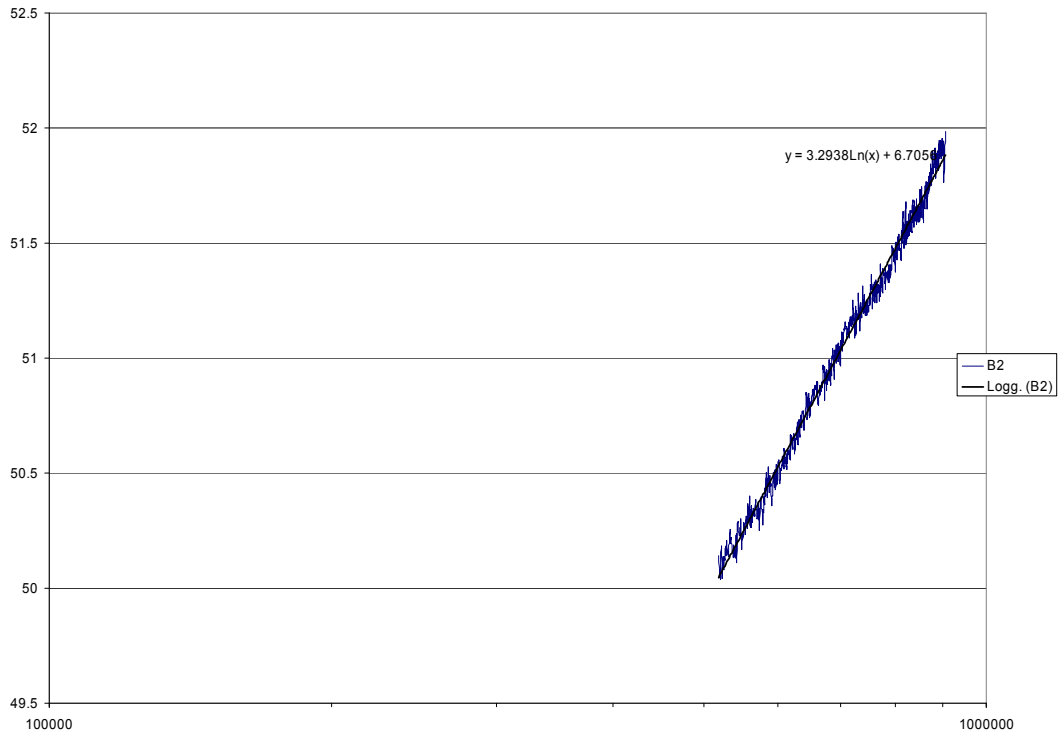


Figure 34 Temperature curve over sensor B2 with logarithmized time axis. Period 1 only.

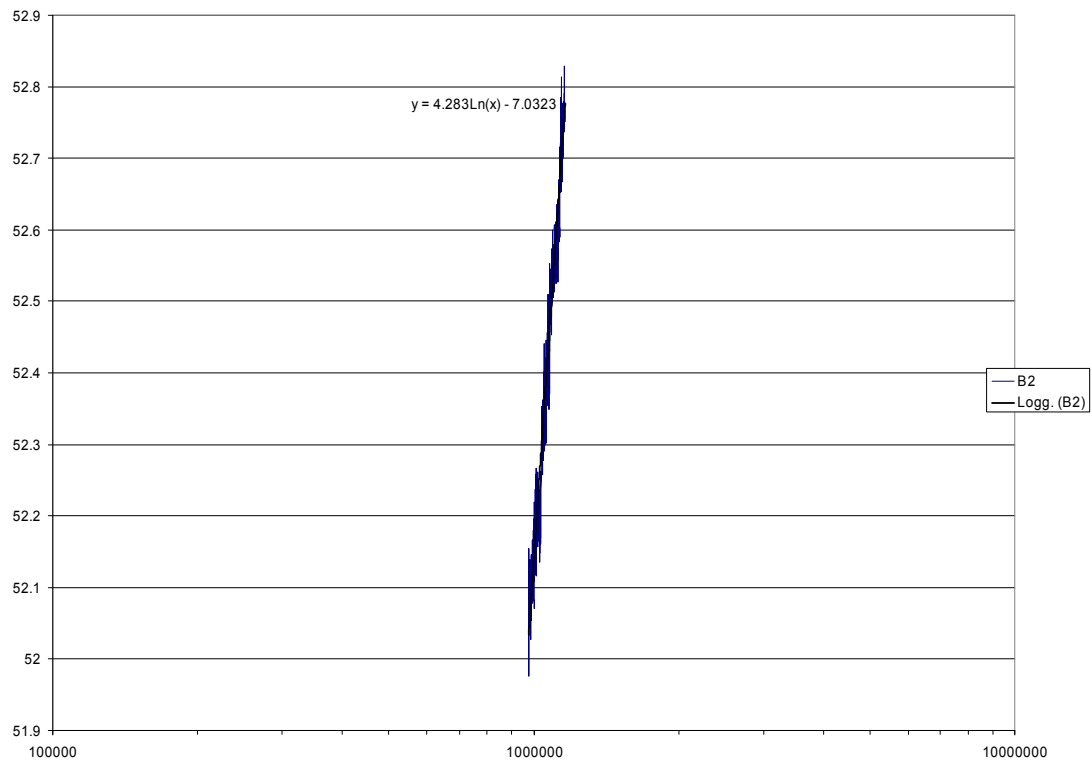


Figure 35 Temperature curve over sensor B2 with logarithmized time axis. Period 2 only.

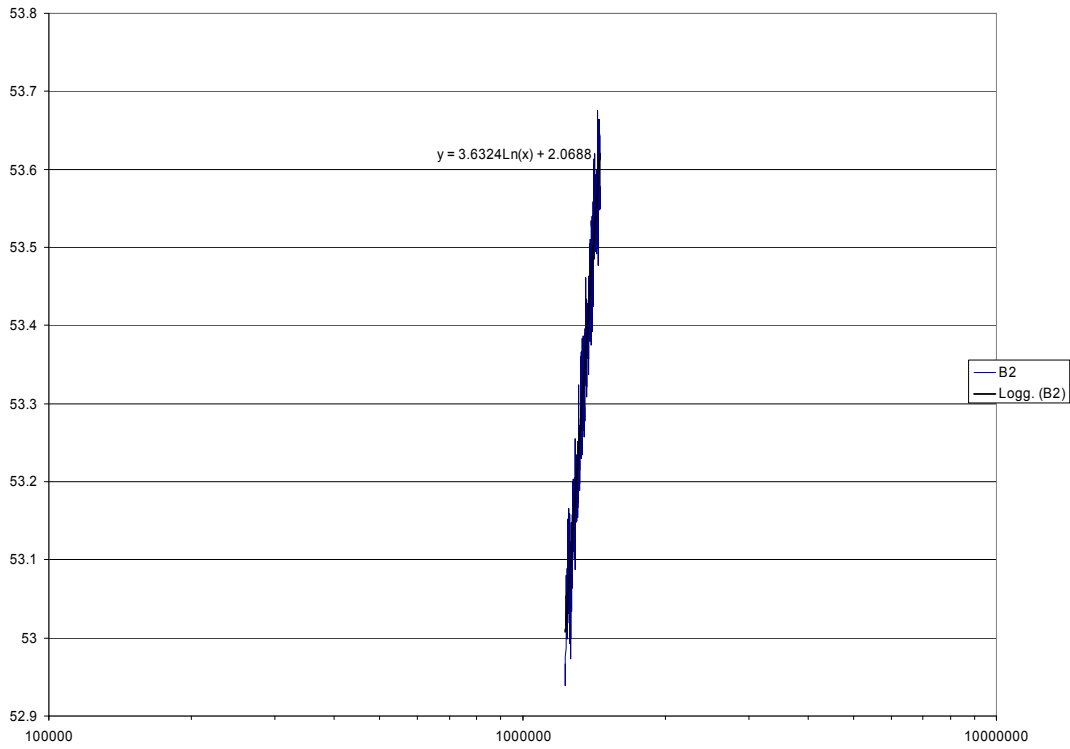


Figure 36 Temperature curve over sensor B2 with logarithmized time axis. Period 3 only.

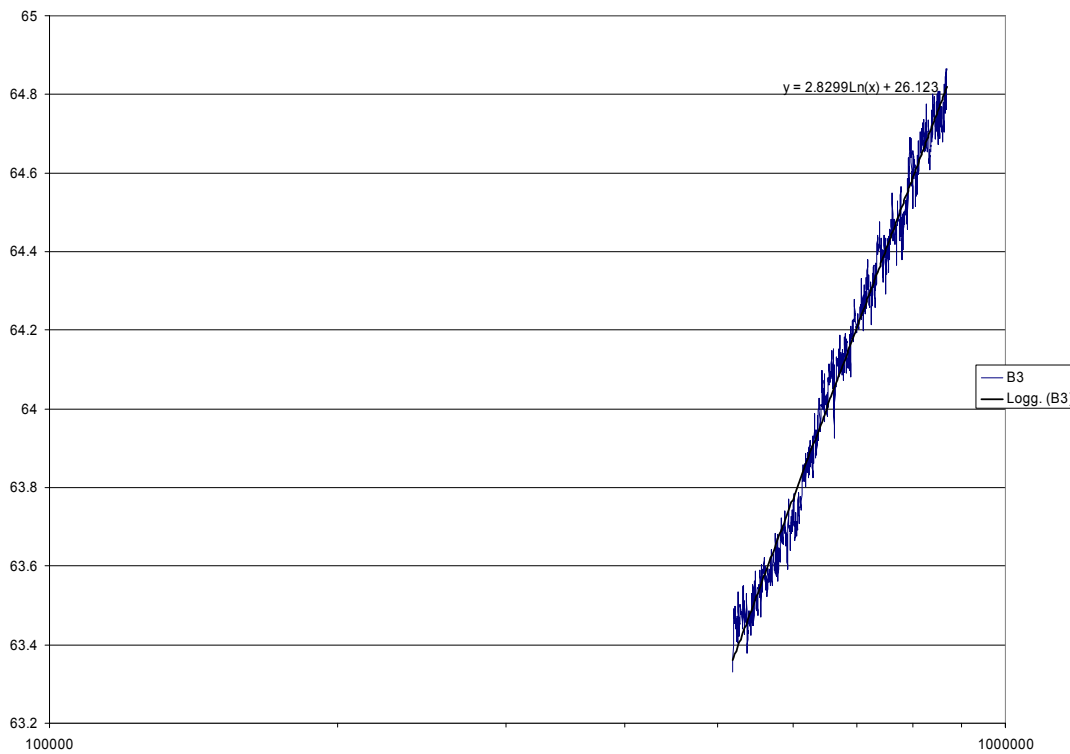


Figure 37 Temperature curve over sensor B3 with logarithmized time axis. Period 1 only.

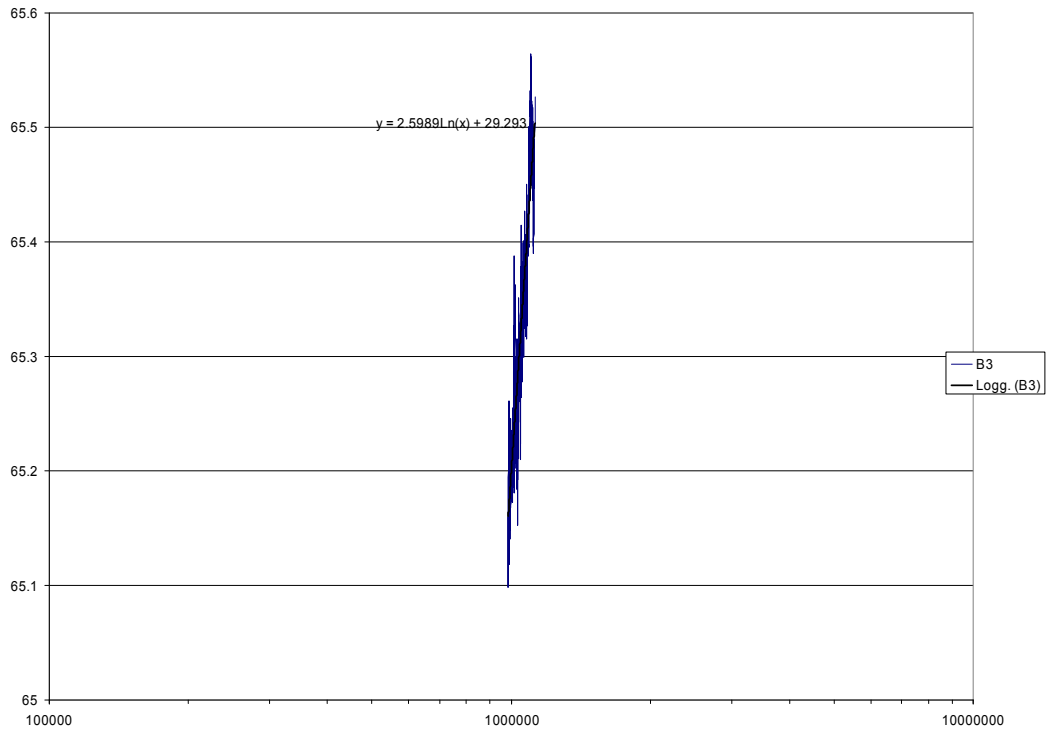


Figure 38 Temperature curve over sensor B3 with logarithmized time axis. Period 2 only.

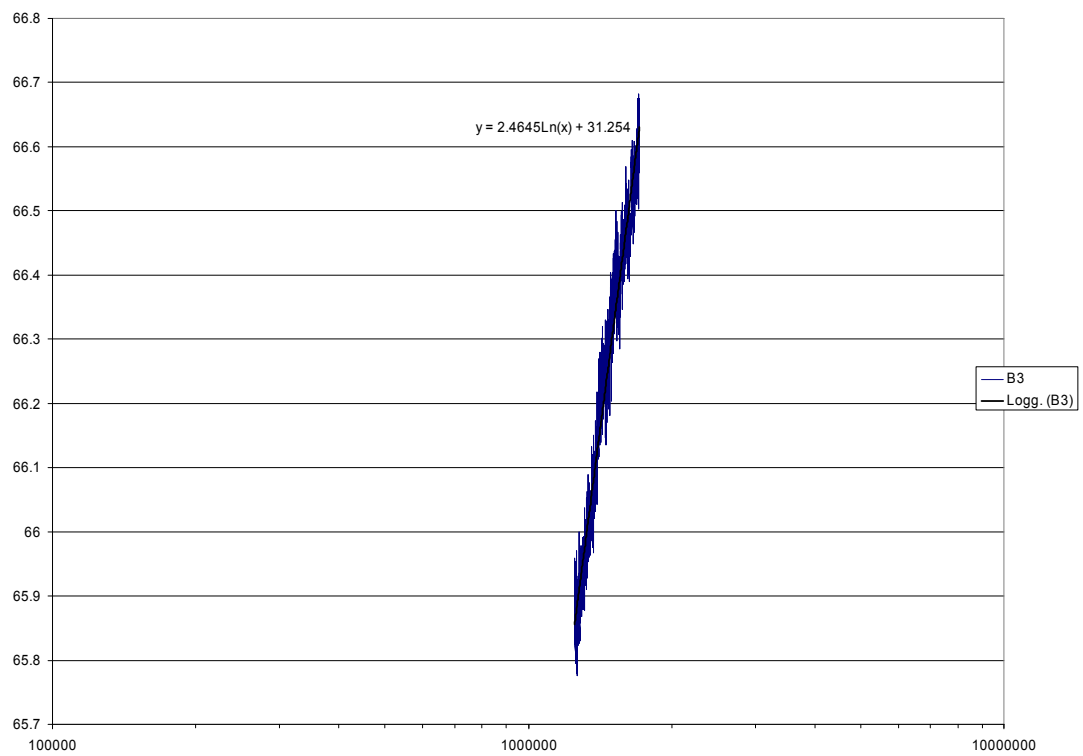


Figure 39 Temperature curve over sensor B3 with logarithmized time axis. Period 3 only.

APPENDIX 1.5 – Sketches of the boreholes

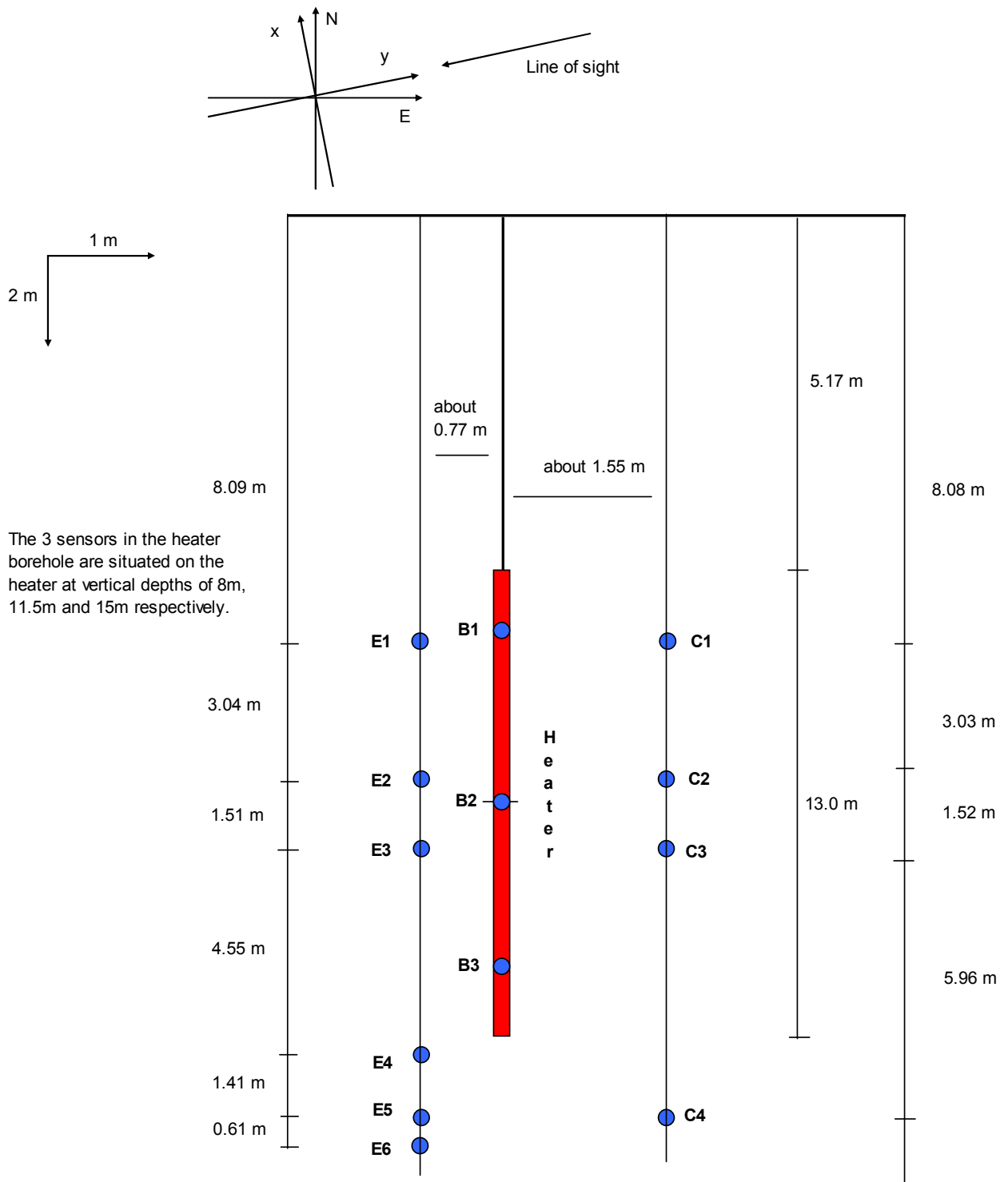


Figure 40 Schematic sketch of the boreholes. Intersection along x axis.

Appendix 1.5

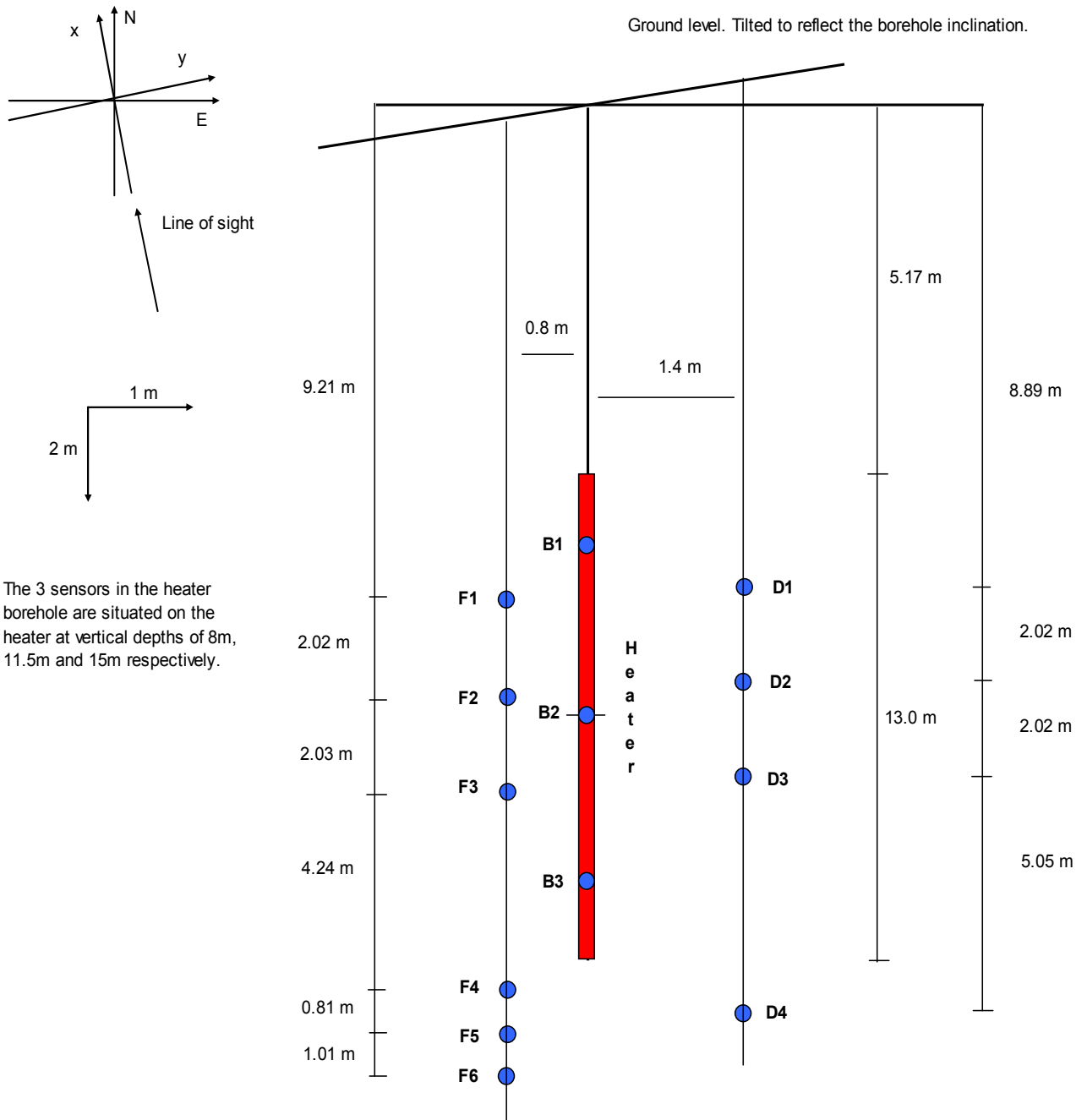


Figure 41 Schematic sketch of the boreholes. Intersection along y axis.

APPENDIX 1.6 – Temperature fitting curves

This document contains graphs with both the measured temperature (T_m) and the calculated temperature (T_d). The headings over the graphs show which sensors the graphs below represent, for example c1d1. They also show which time period that has been taken into consideration (Heating: 0-28, Cooling: 29-61, Whole: 0-61). Furthermore, at the top of each heading there is a sign in parenthesis, for example (A1). This sign represent a certain coordinate or sensor case. The different cases are presented below. All cases assume the borehole length from Installation PM (appendix 7) (that is, not the depth from the hole measure).

A1: Original coordinate measurements.

A2: Small horizontal movement from original coordinates.

B1: New coordinates.

C1: New coordinates, combination of all sensors.

C2: New coordinates, combination of sensors on level 1-3.

C3: New coordinates, combination of sensors on level 1-3 except c1.

C4: New coordinates, combination of sensors on level 1-3 except c1c3e3.

Each case will have at least two graphs; one where the measured temperature curve is compared to the calculated temperature curve, and one where the difference between the curves is shown. Case C will have several more graphs for each headline since each C headline contains much more sensors and all of them cannot fit in just one graph.

Each curve in the graphs is given a sign. The sign for case A and B is i1 or i2. i1 always represents the first sensor in the sensor pair and i2 the second. For example, for the graph over c1d1, i1 represents c1 and i2 represents d1.

For case C, each sensor is given a number as a sign:

C1 - 0

C2 - 1

C3 - 2

C4 - 3

D1 - 4

D2 - 5

D3 - 6

D4 - 7

E1 - 8

E2 - 9

E3 - 10

E4 - 11

E5 - 12

E6 - 13

F1 - 14

F2 - 15

F3 - 16

F4 - 17

F5 - 18

F6 - 19

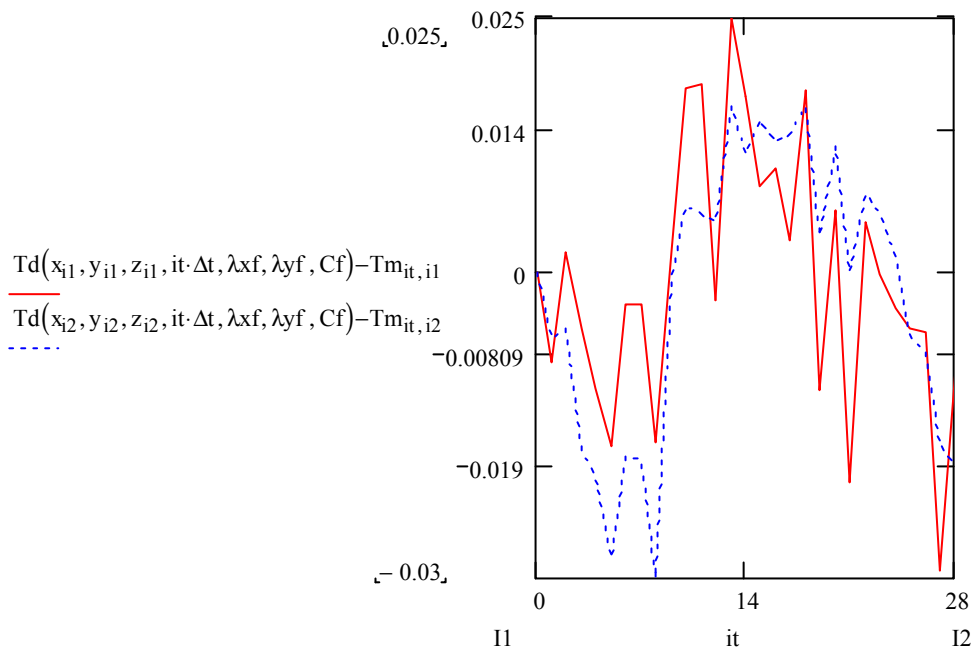
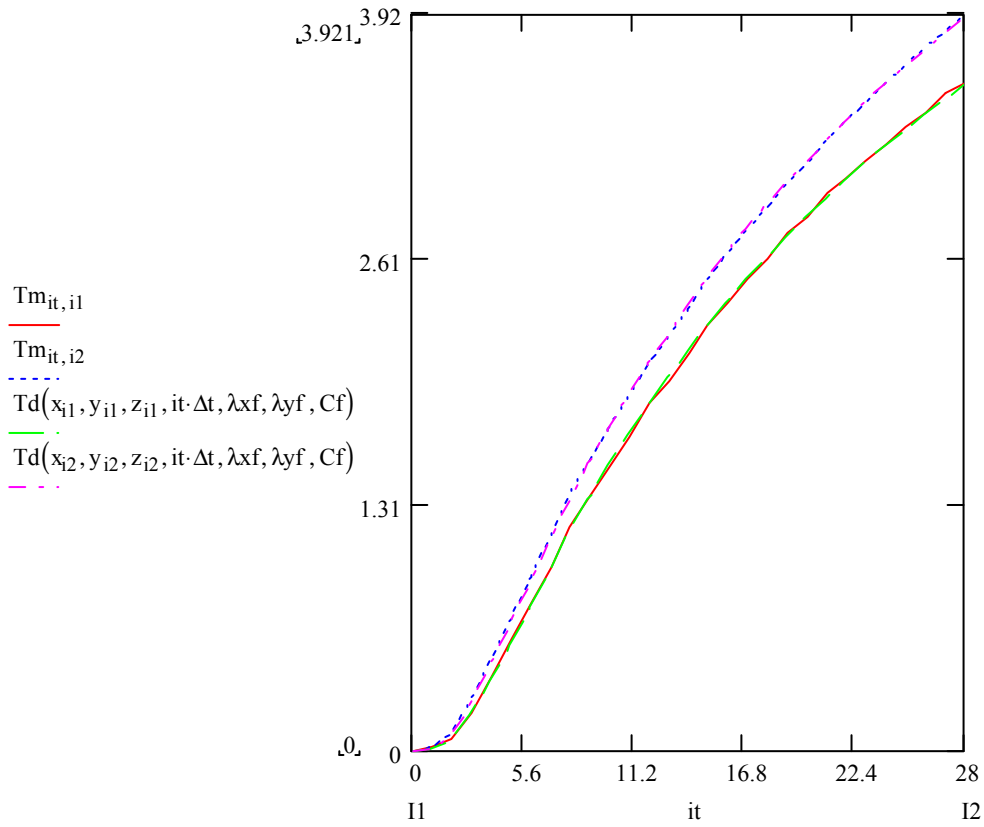
Appendix 1.6

The y axis represents the temperature change and the x axis represents the time, measured in no of temperature measurements.

Original coordinate measurements (A1)

0-28

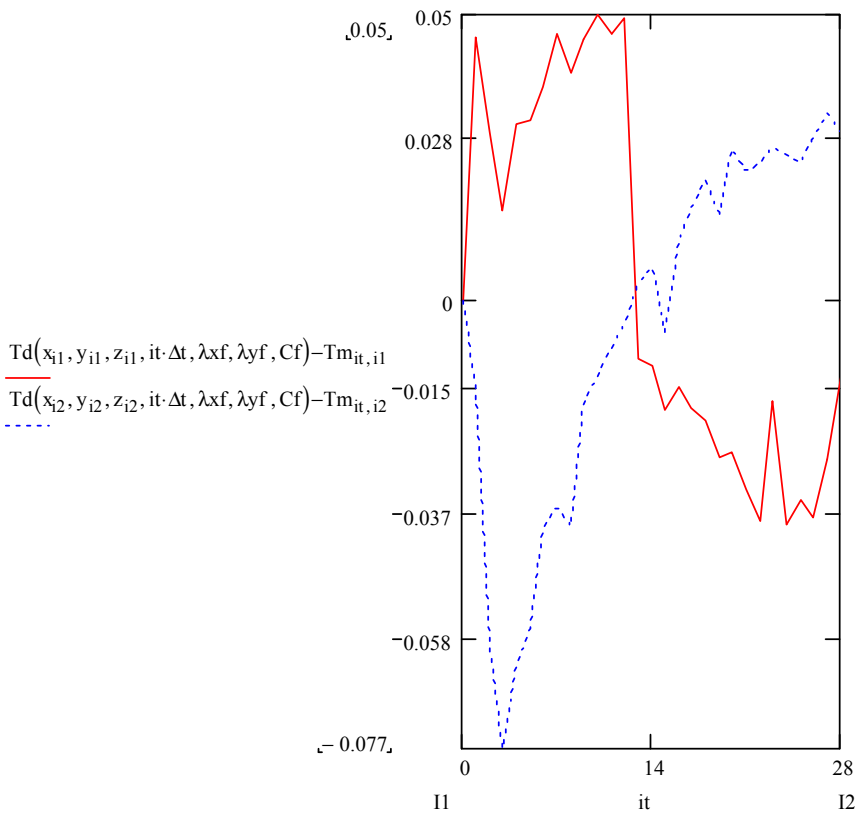
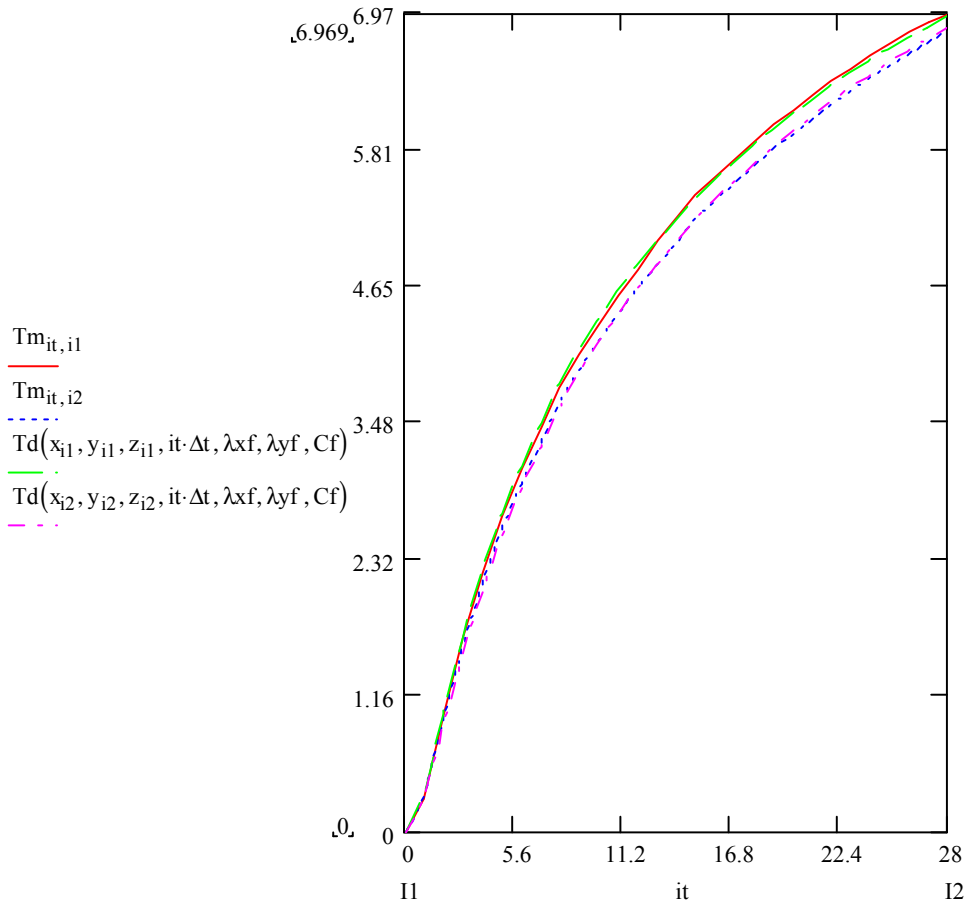
C1d1



Original coordinate measurements (A1)

0-28

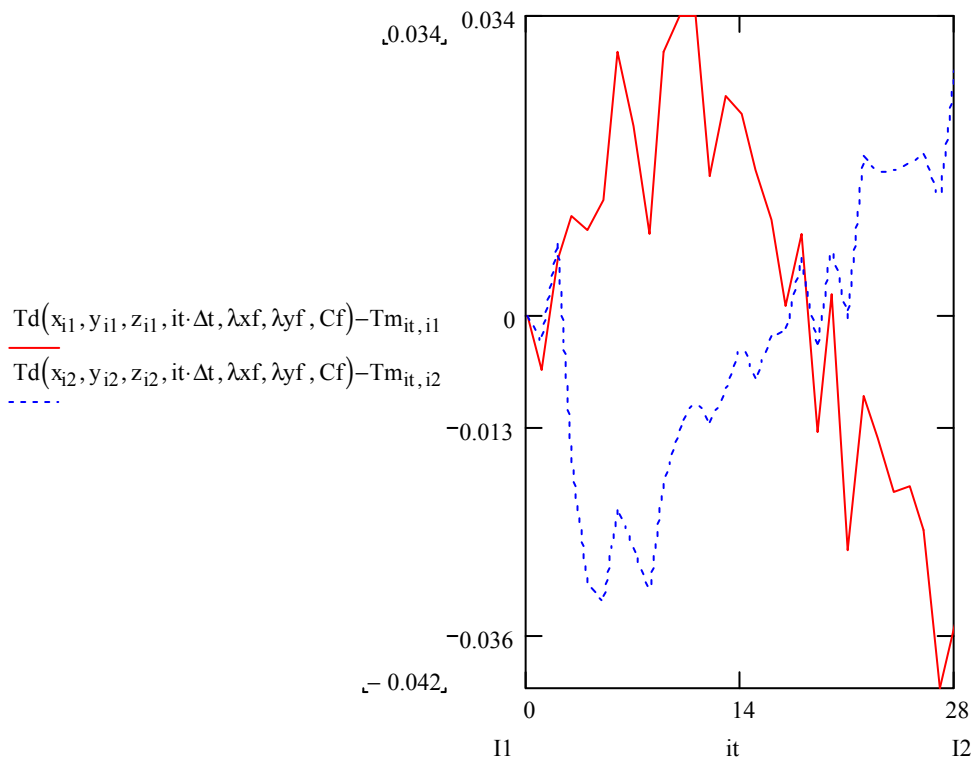
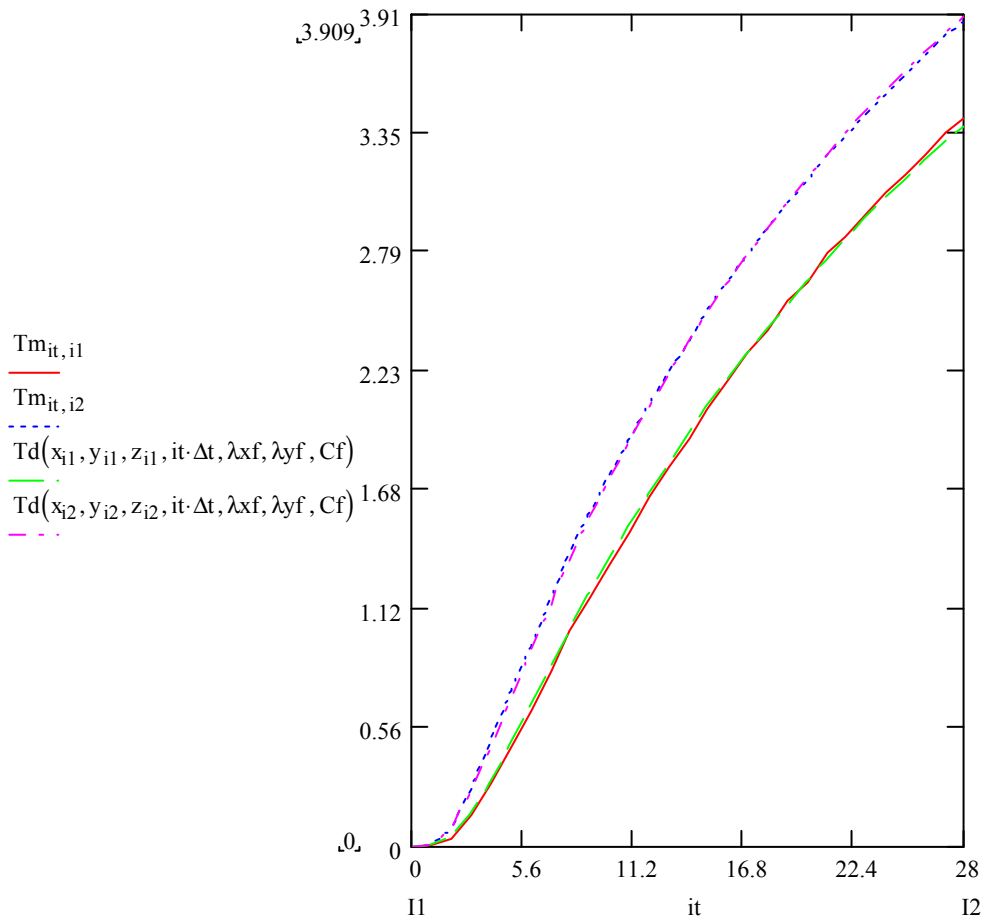
E1f1



Original coordinate measurements (A1)

0-28

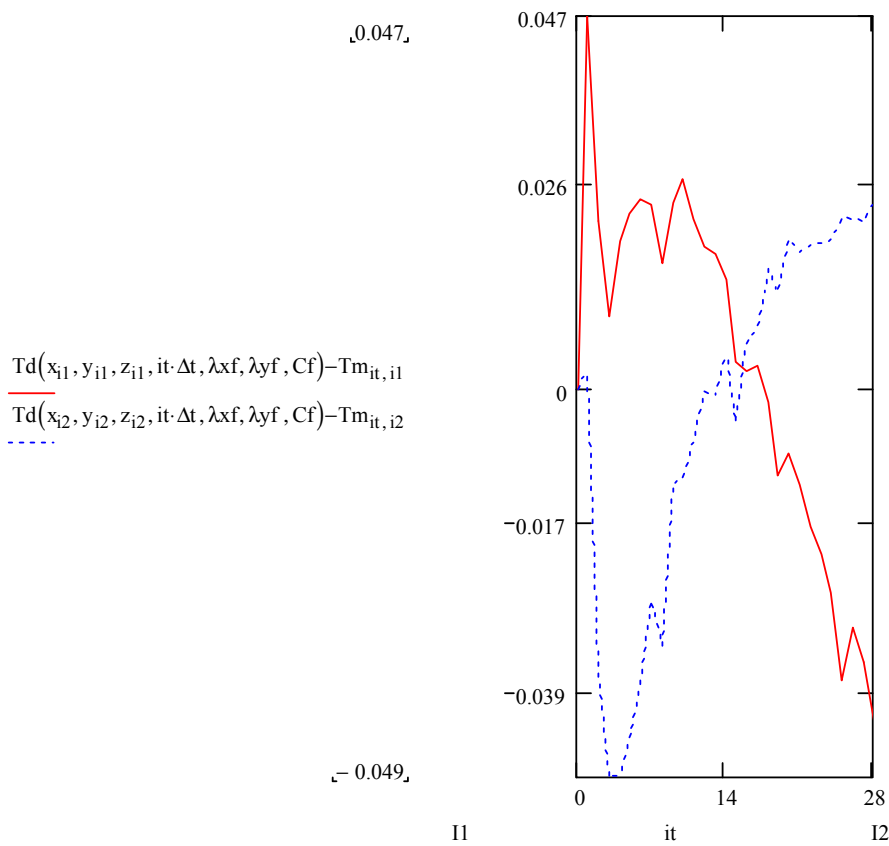
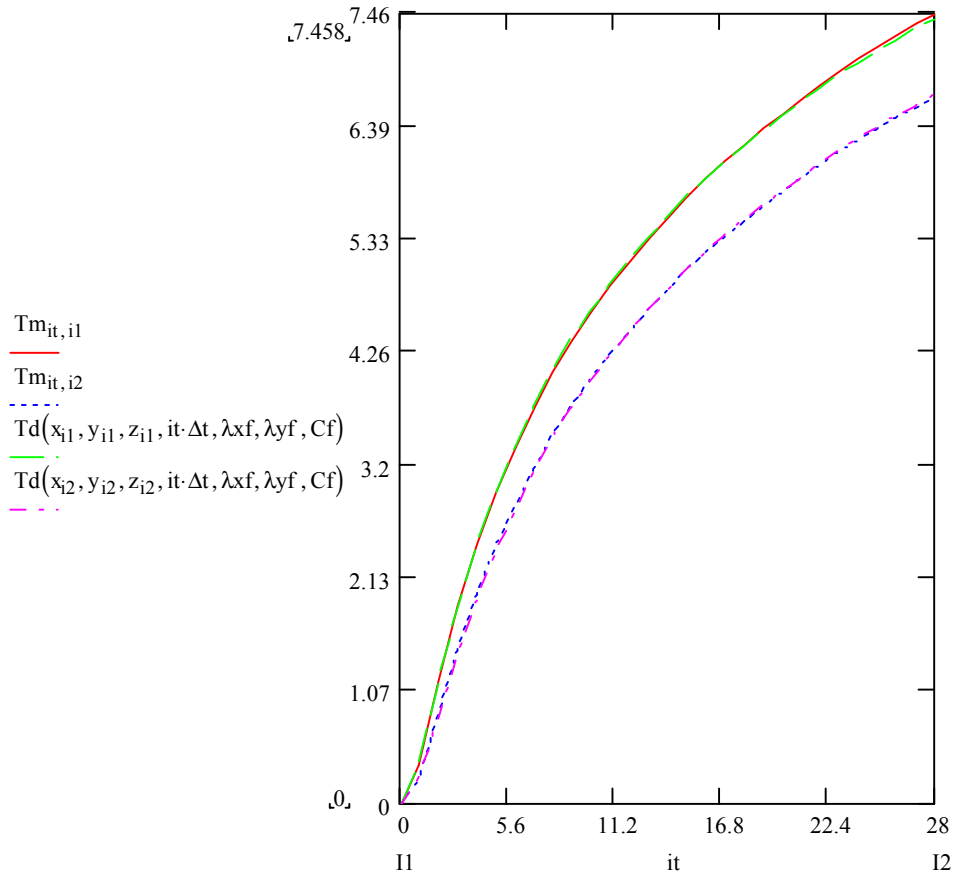
C2d2



Original measure (A1)

0-28

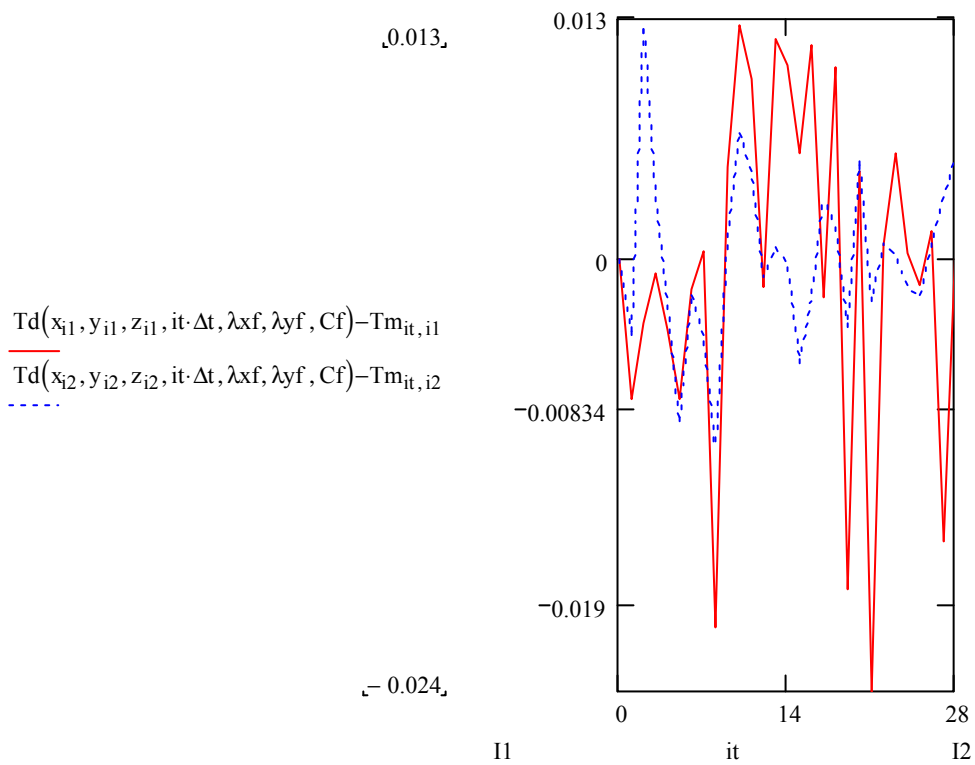
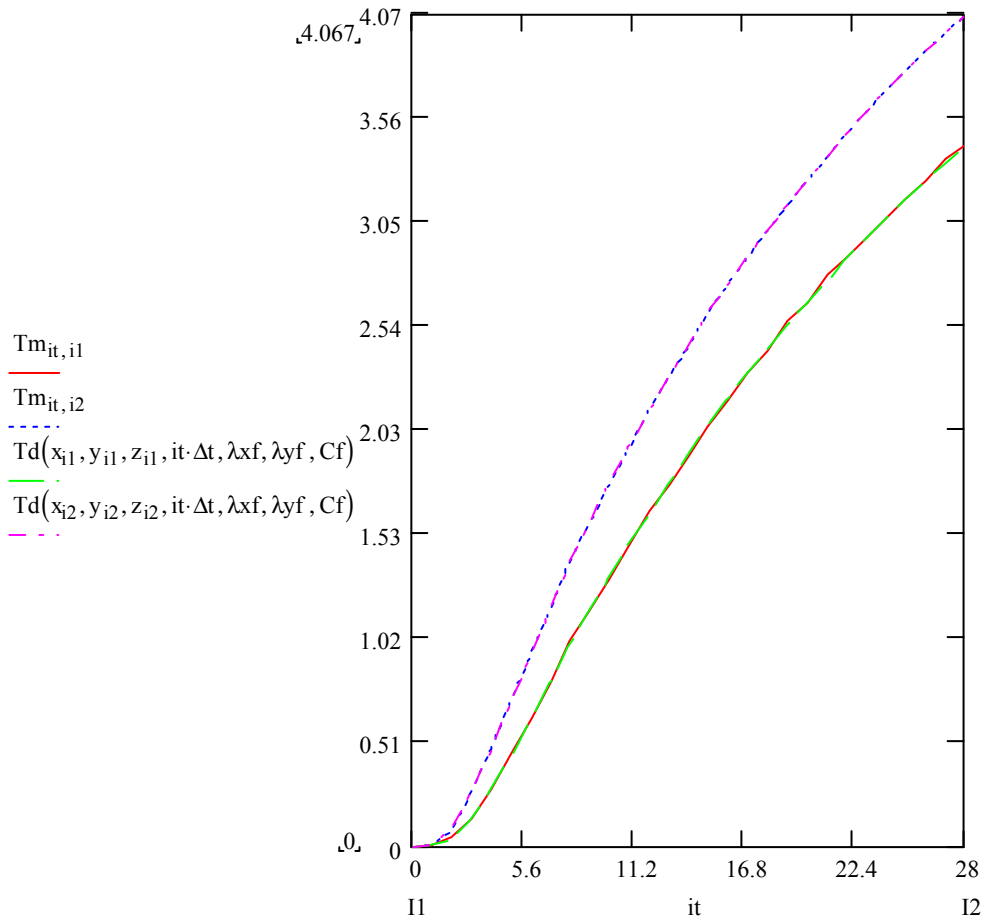
E2f2



Original coordinate measurements (A1)

0-28

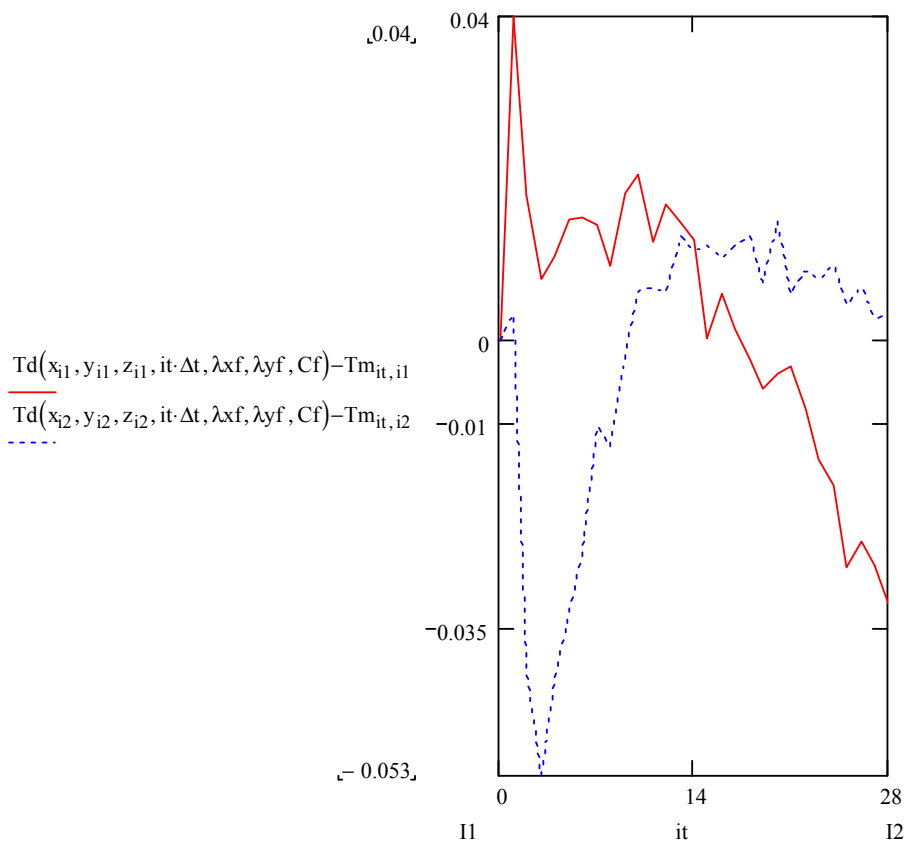
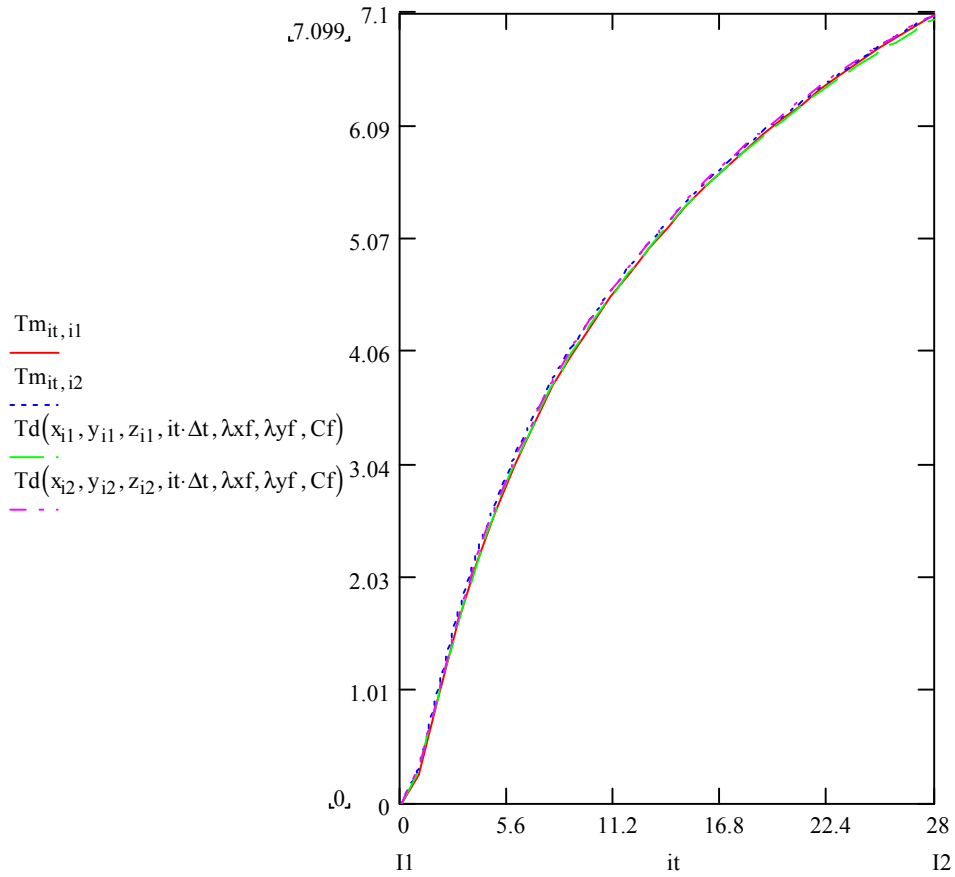
C3d3



Original measure (A1)

0-28

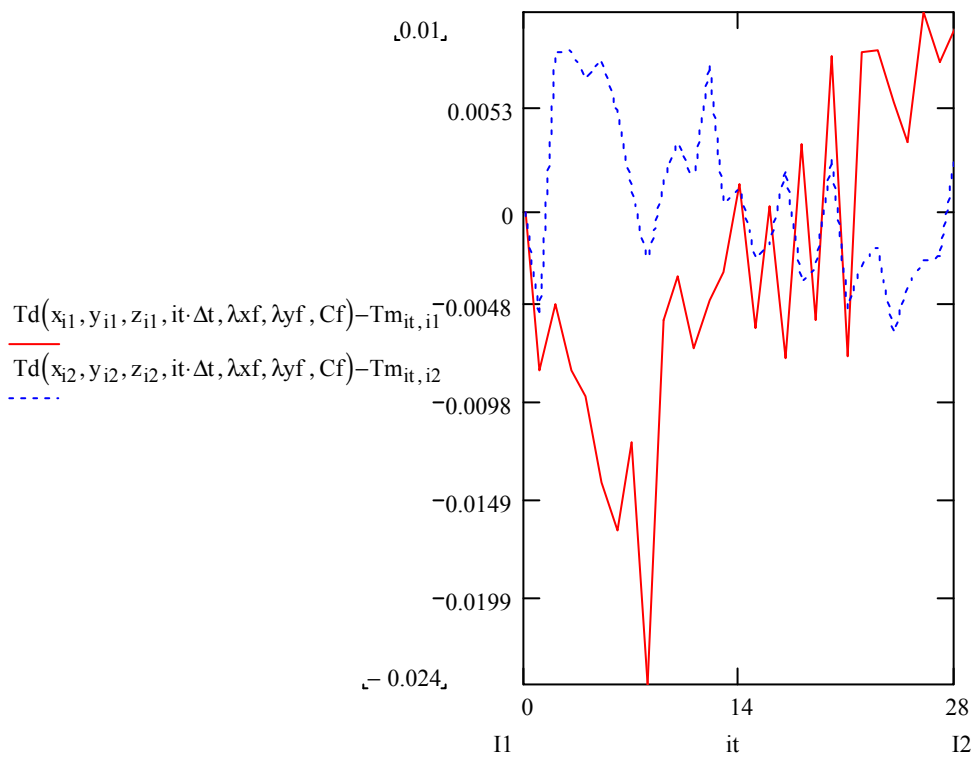
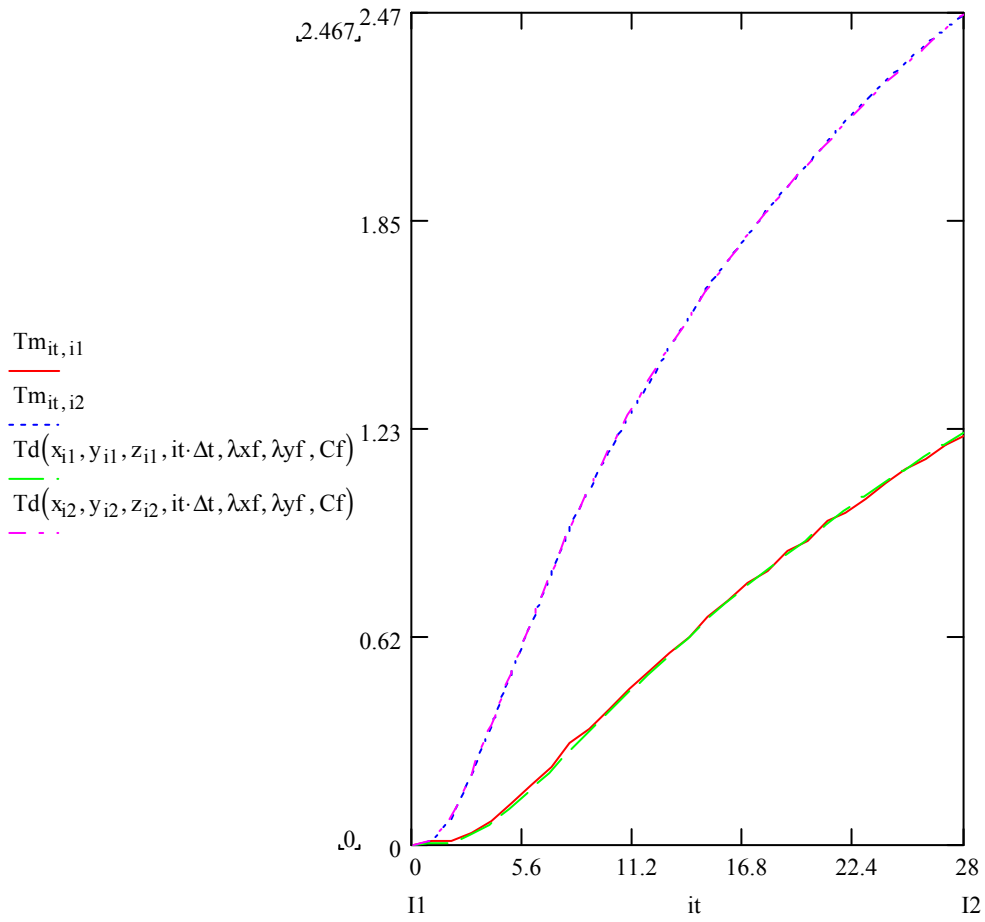
E3f3



Original coordinate measurements (A1)

0-28

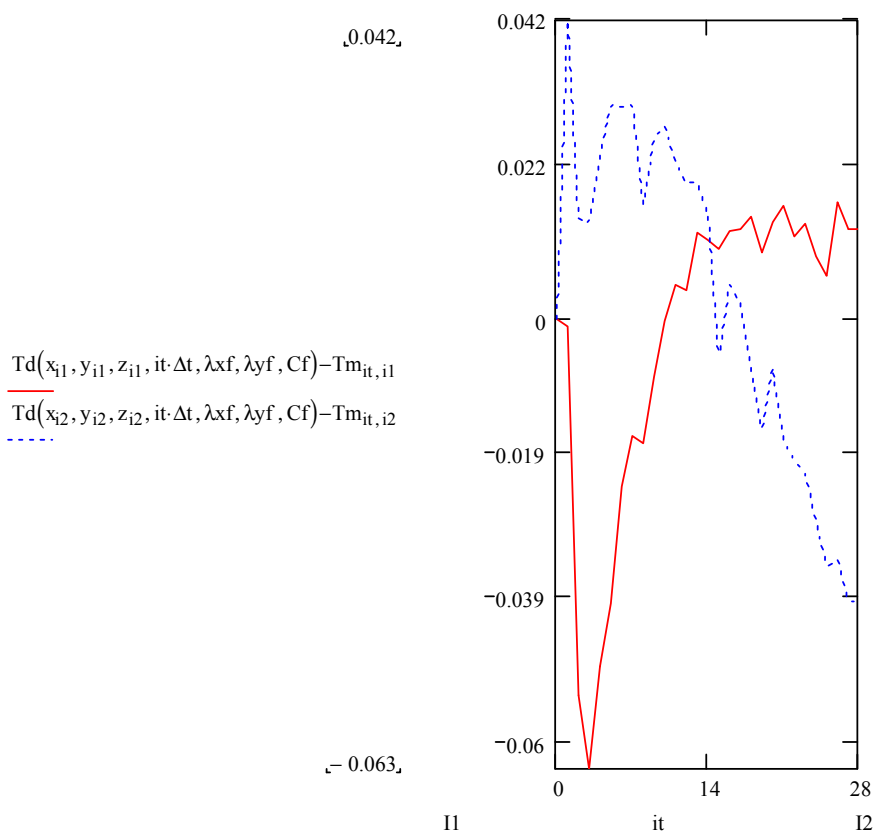
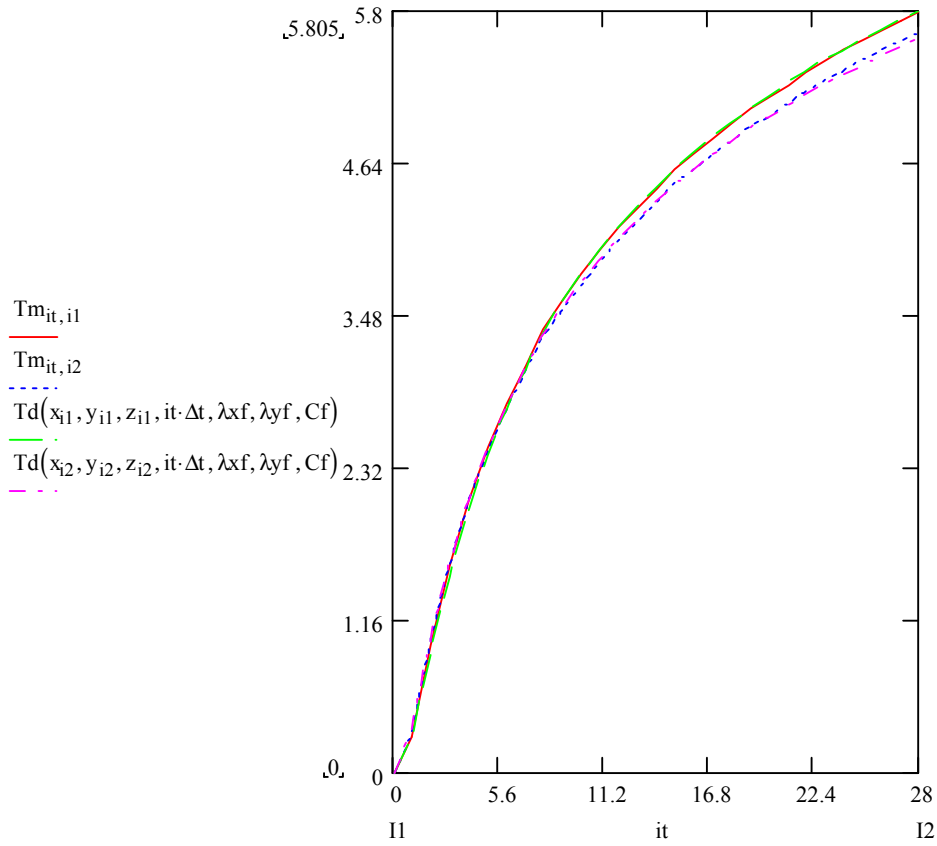
C4d4



Original coordinate measurements (A1)

0-28

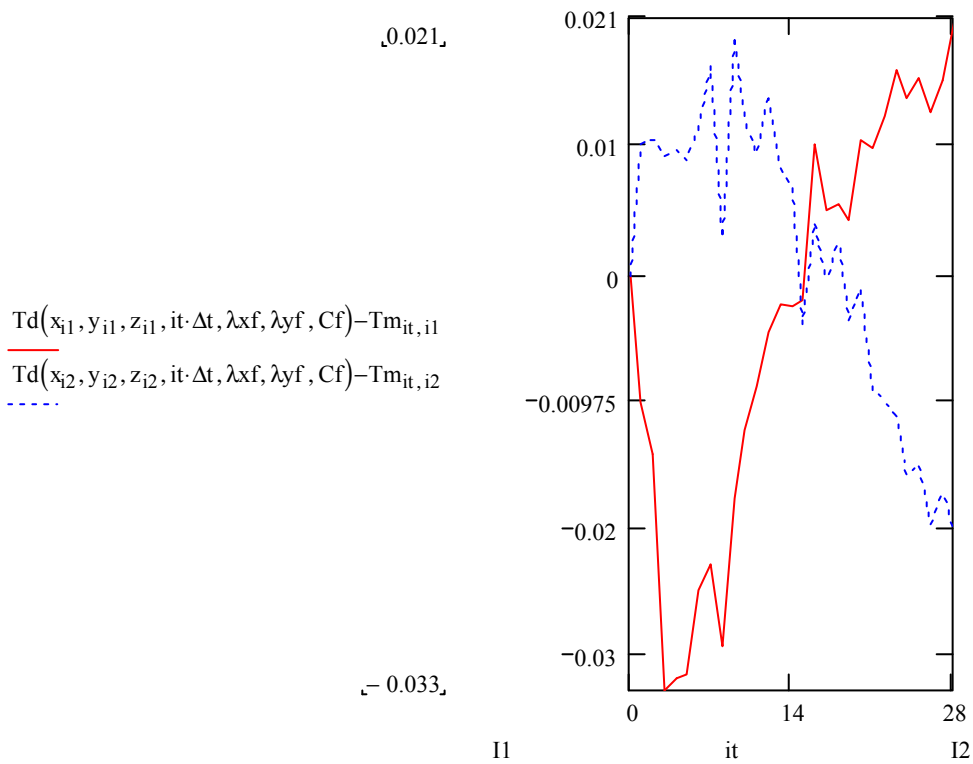
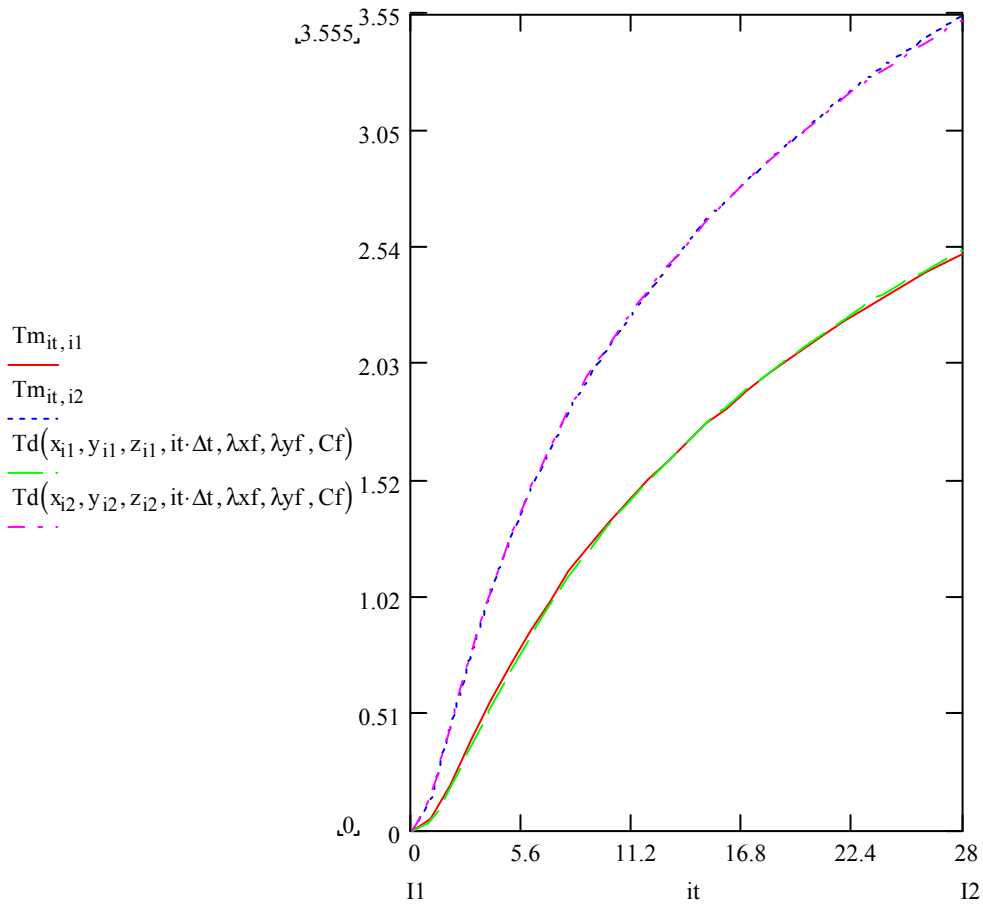
E4f4



Original coordinate measurements (A1)

0-28

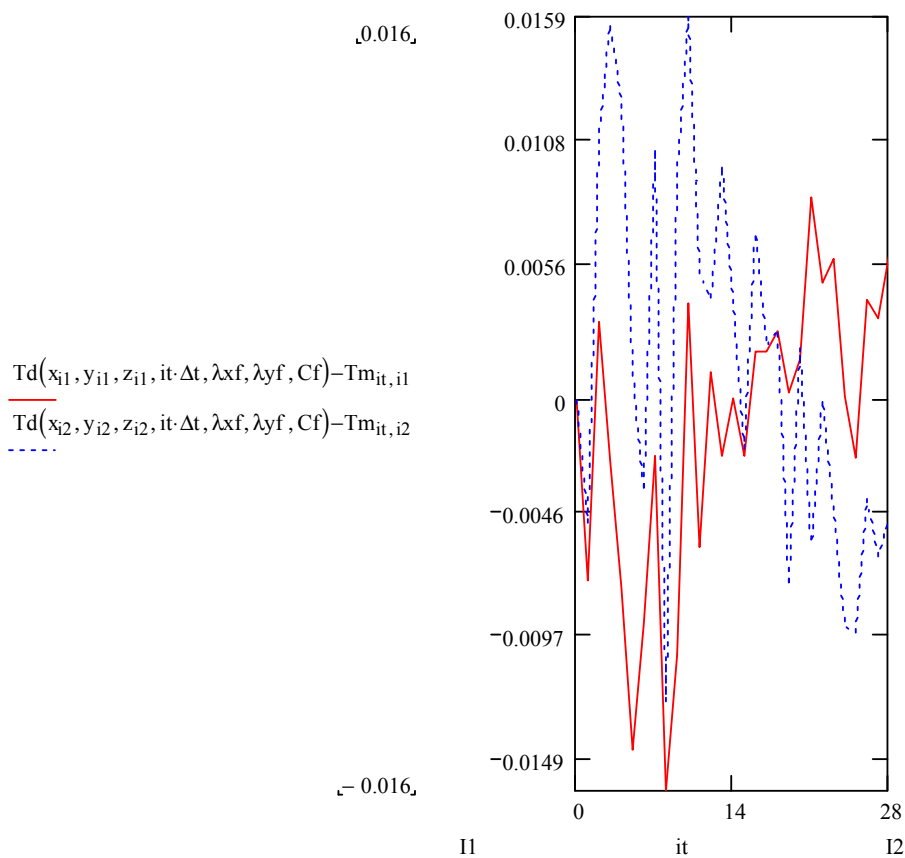
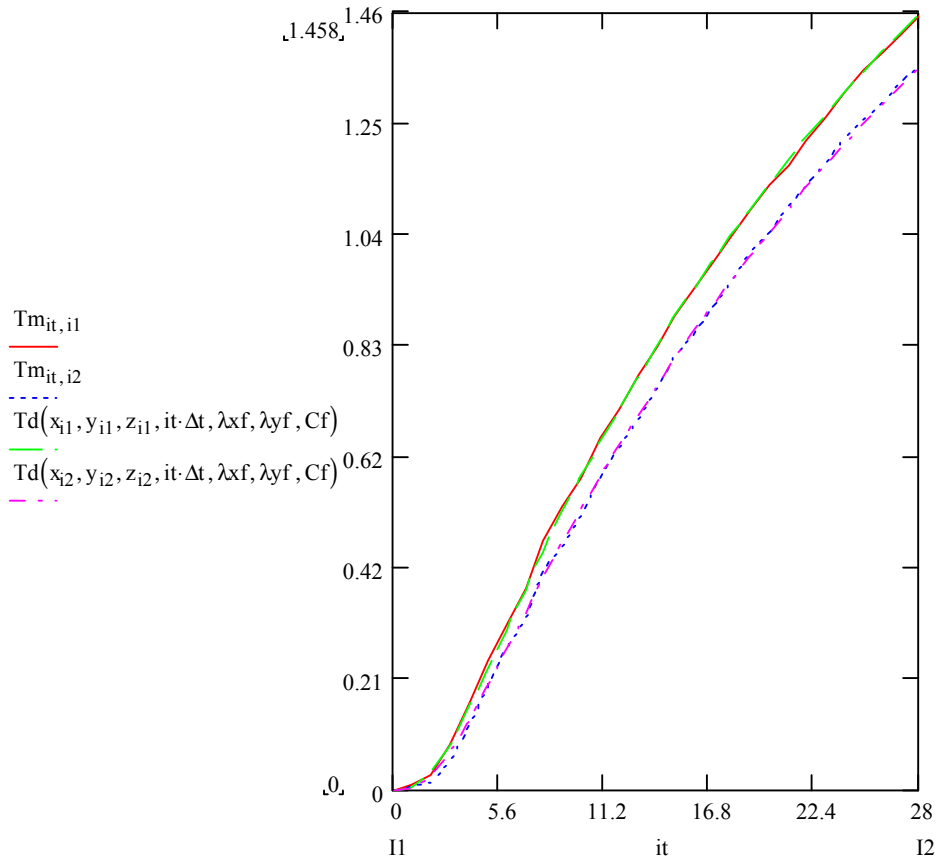
E5f5



Original coordinate measurements (A1)

0-28

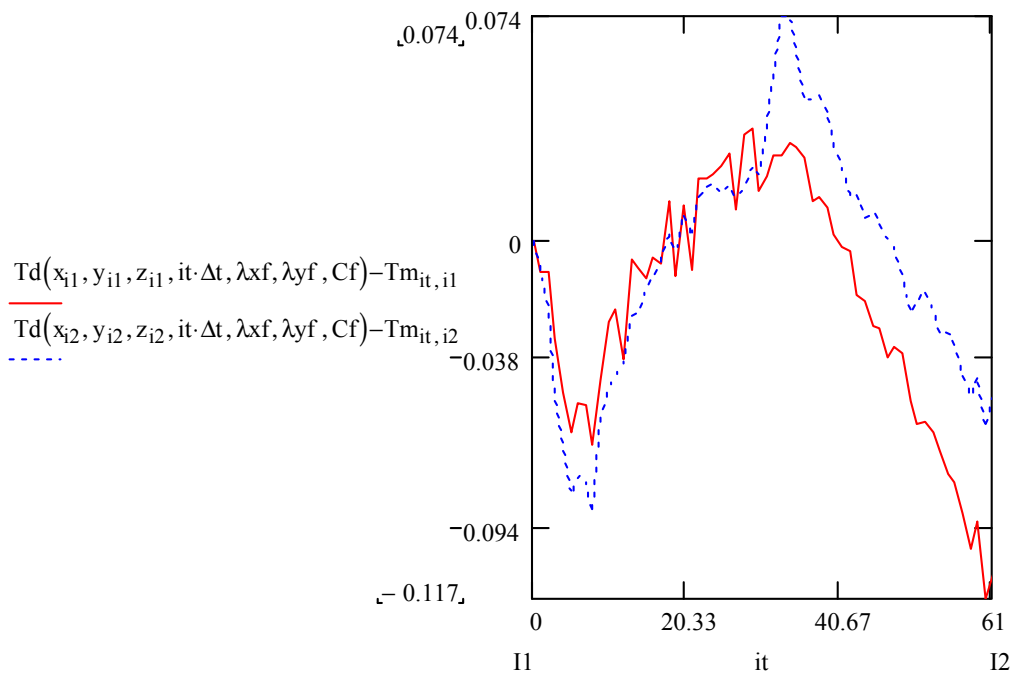
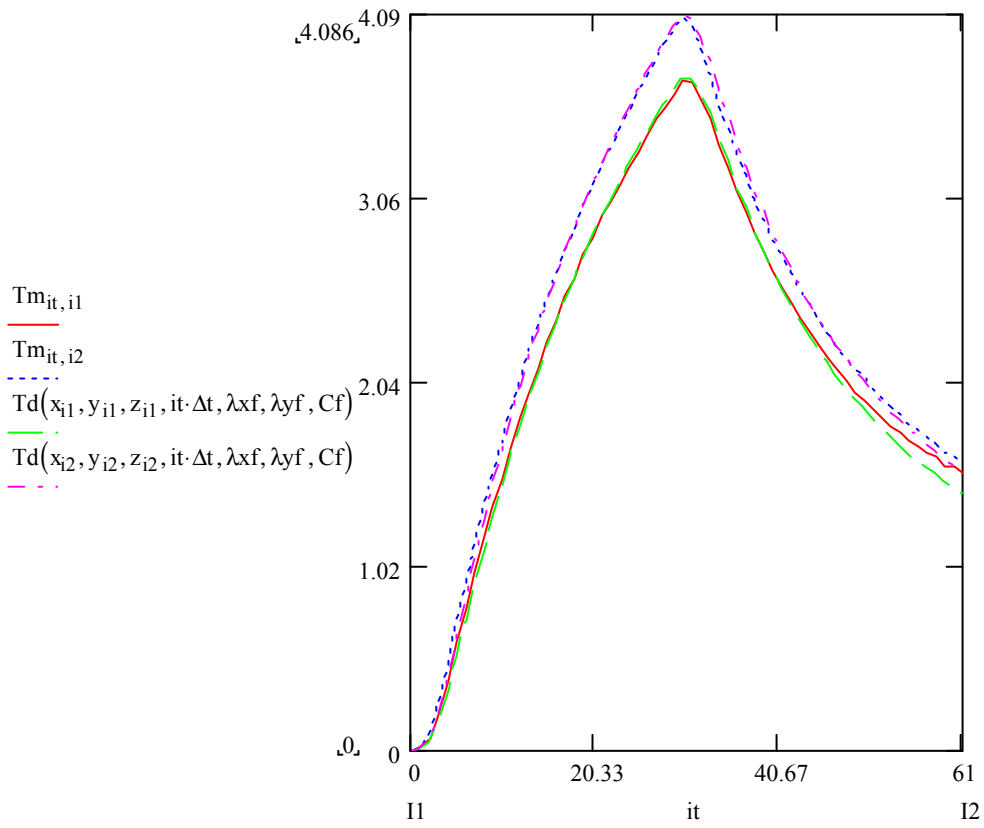
E6f6



Original coordinate measurements (A1)

0-61

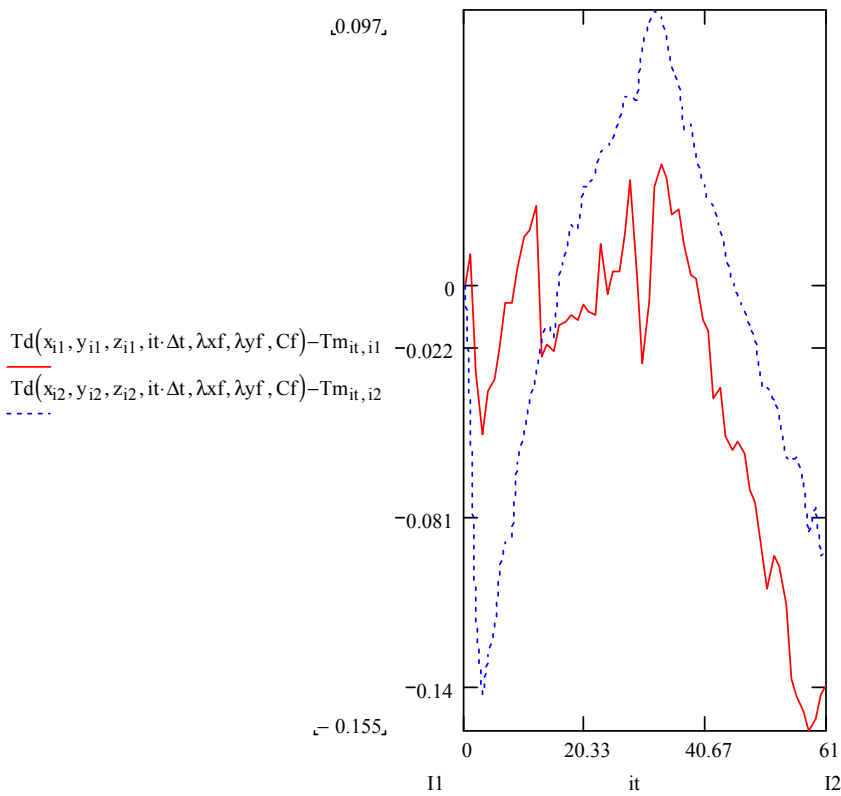
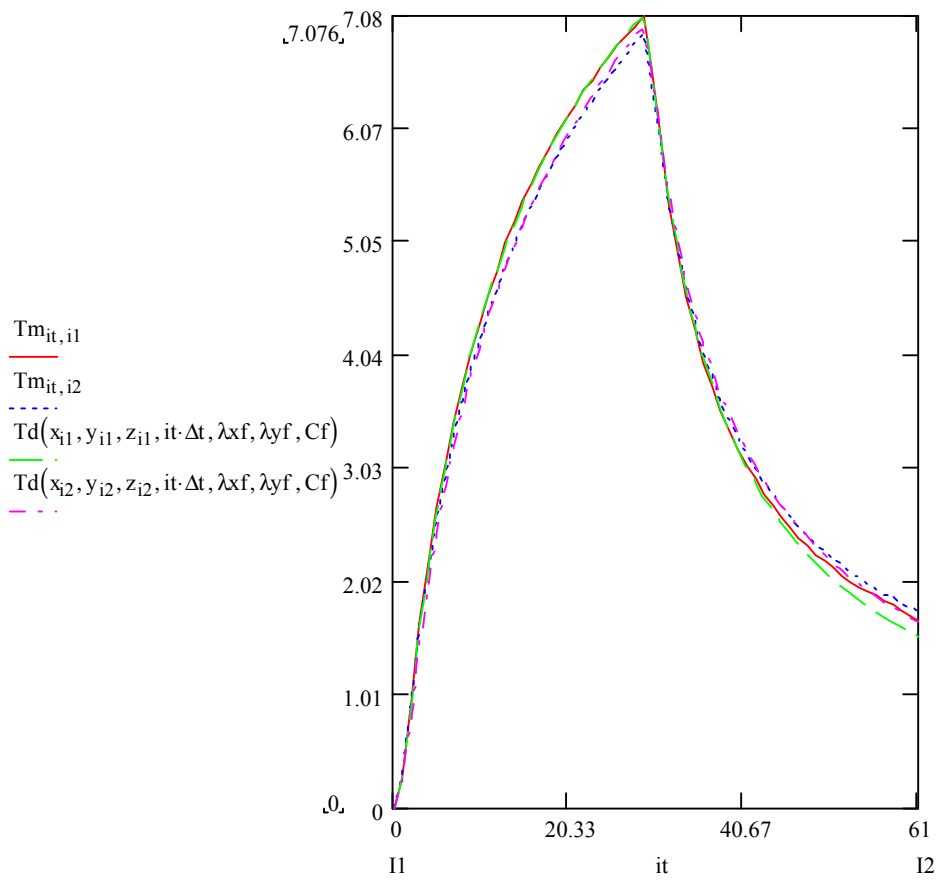
C1d1



Original coordinate measurements (A1)

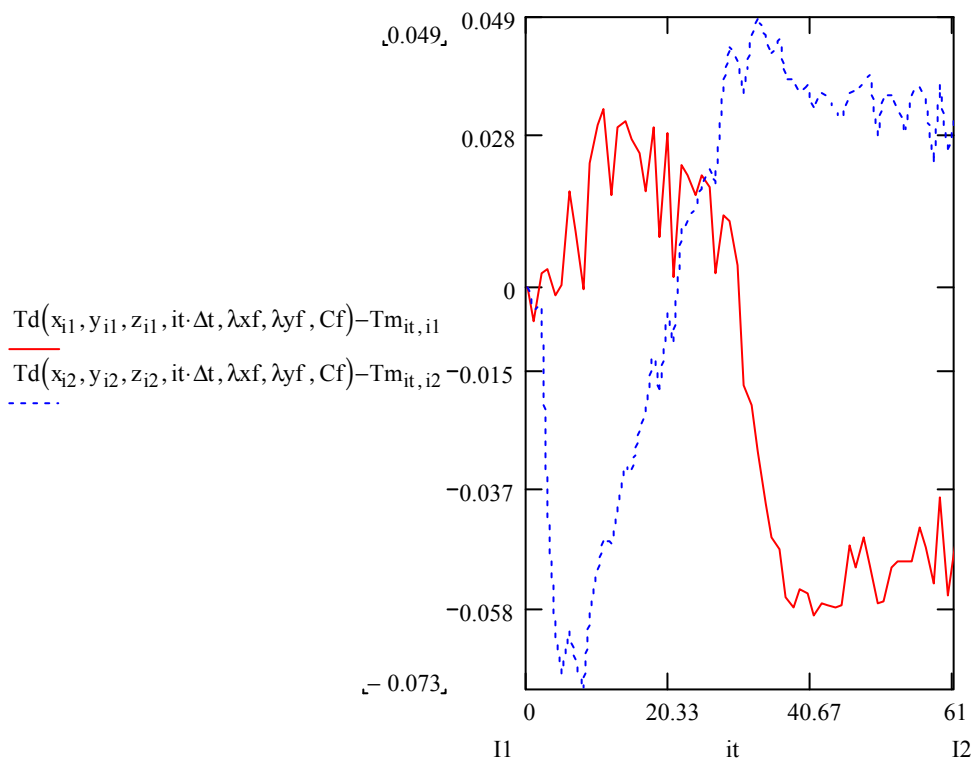
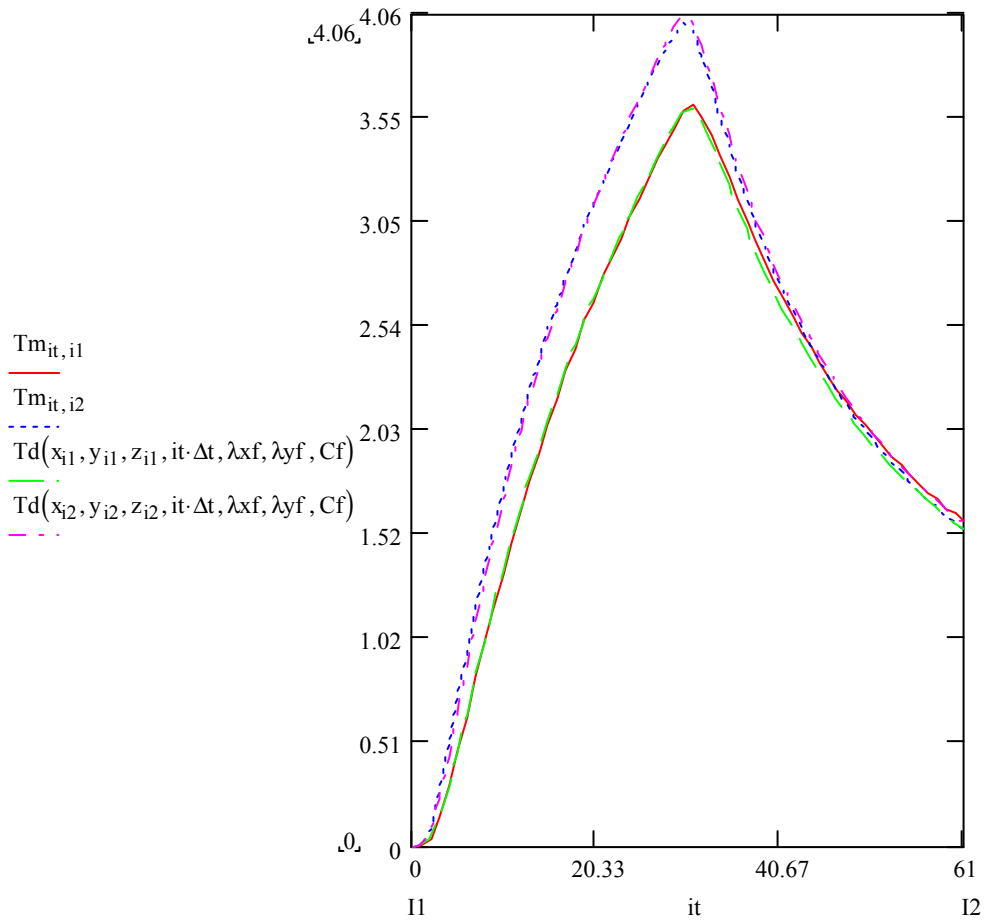
0-61

E1f1



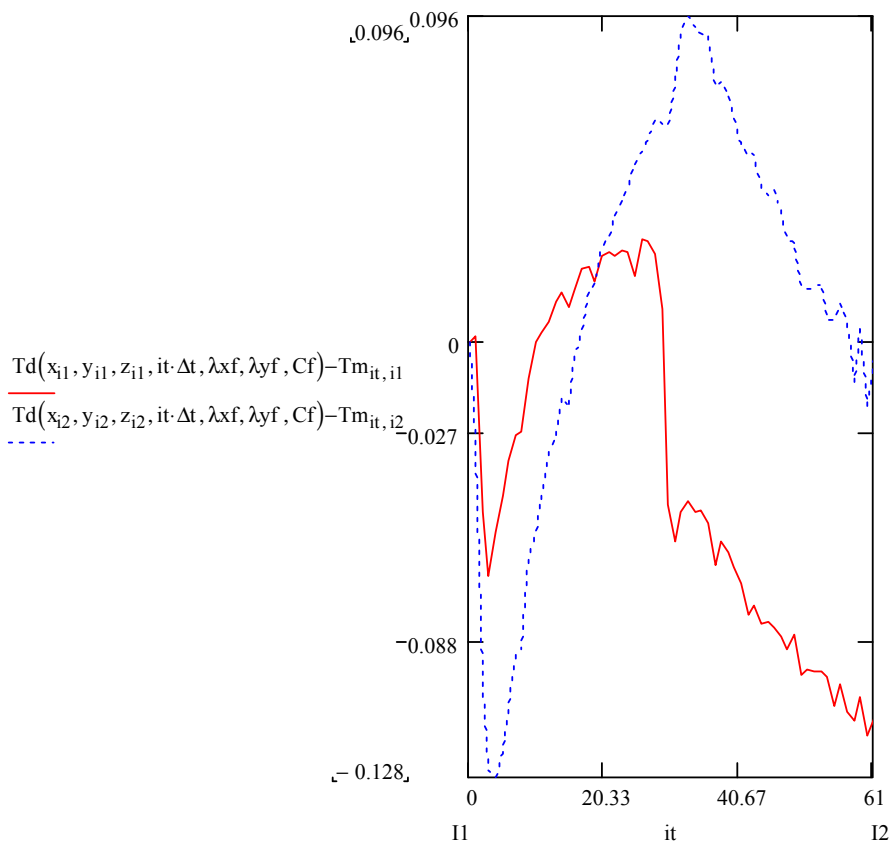
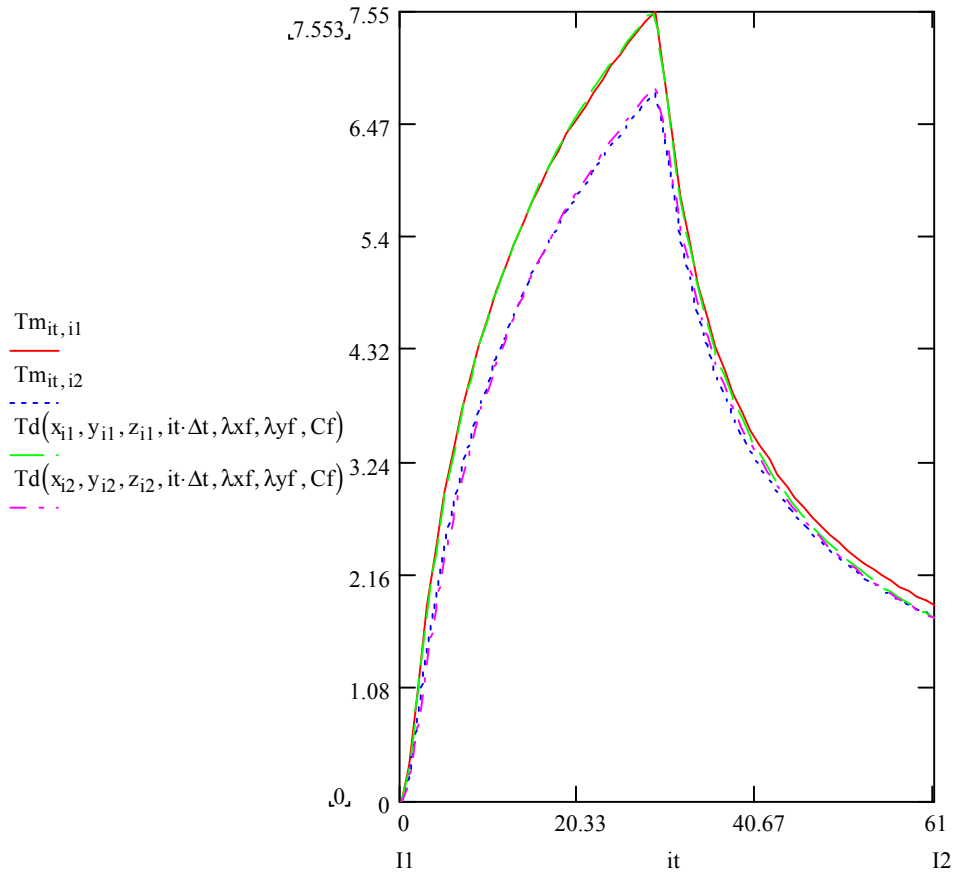
Original coordinate measurements (A1)

0-61
C2d2



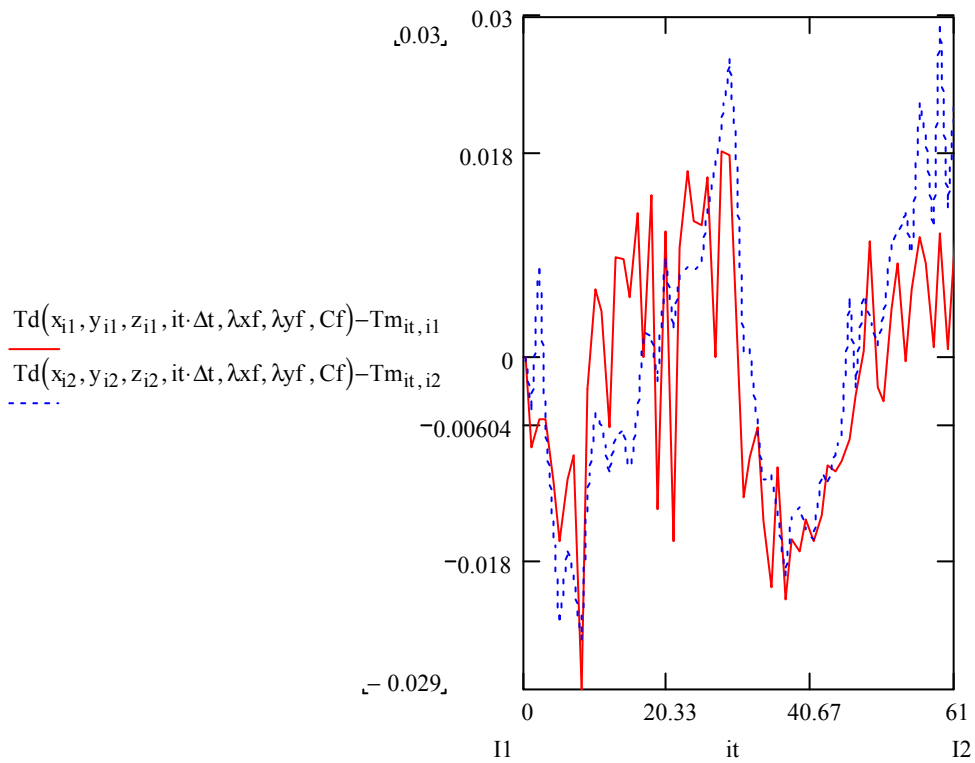
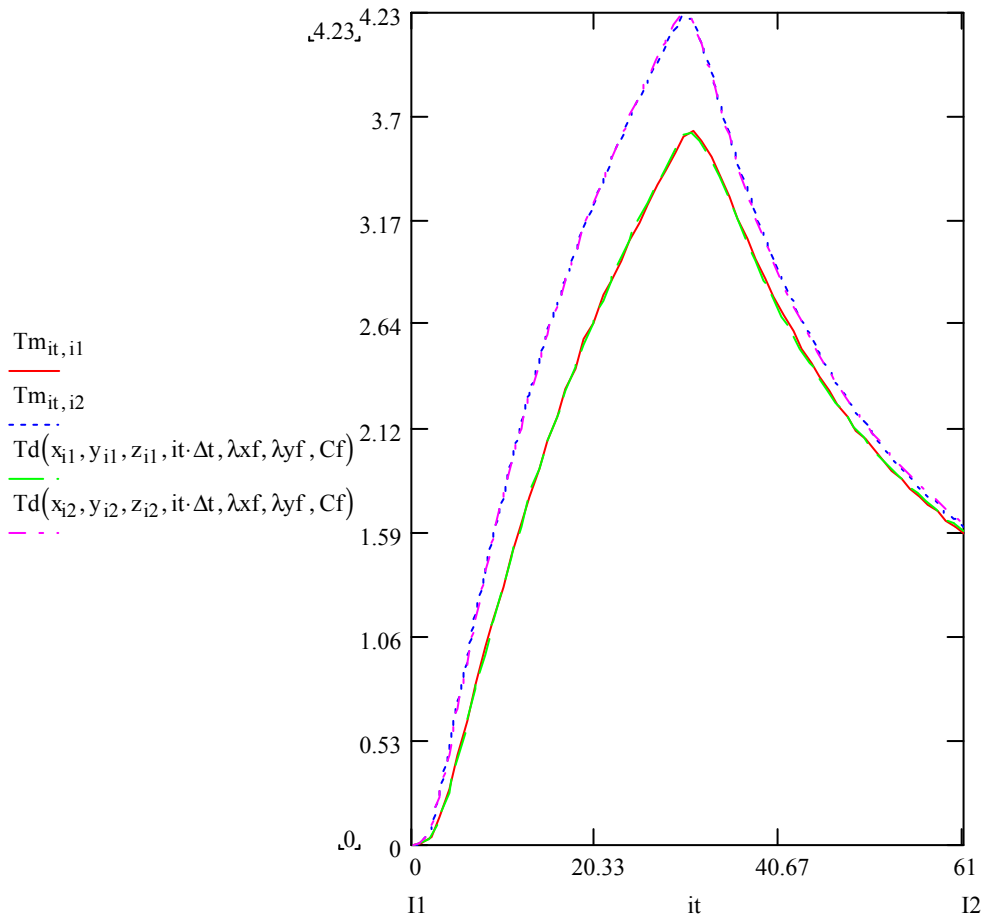
Original coordinate measurements (A1)

0-61
E2f2



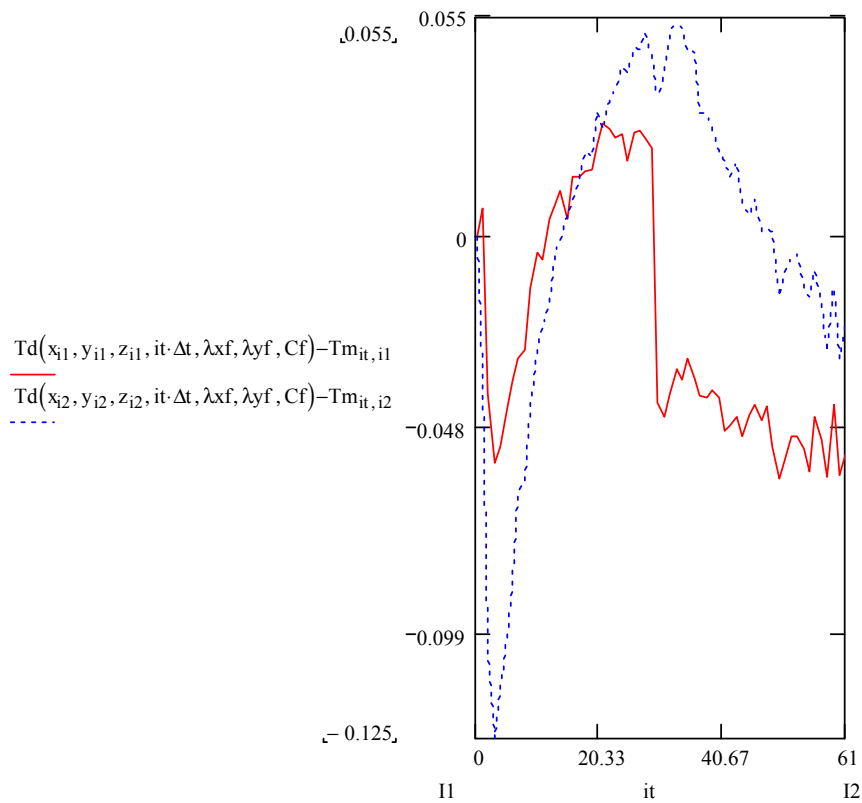
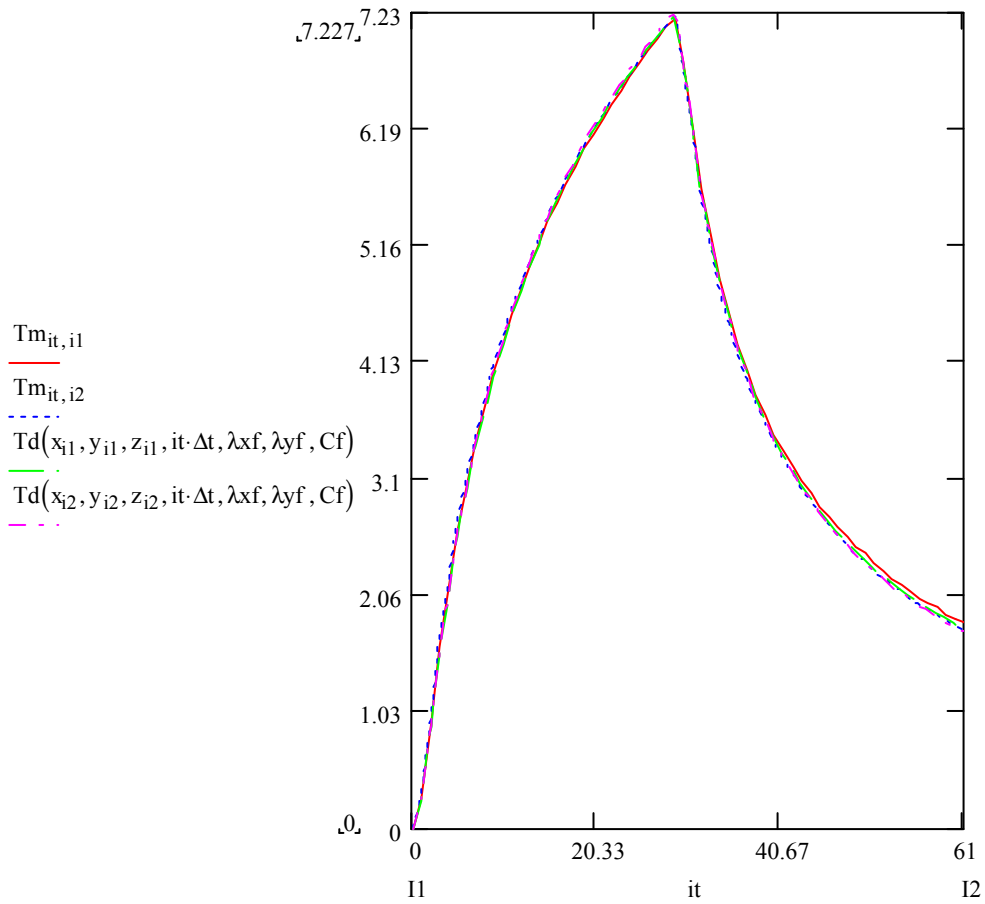
Original coordinate measurements (A1)

0-61
C3d3



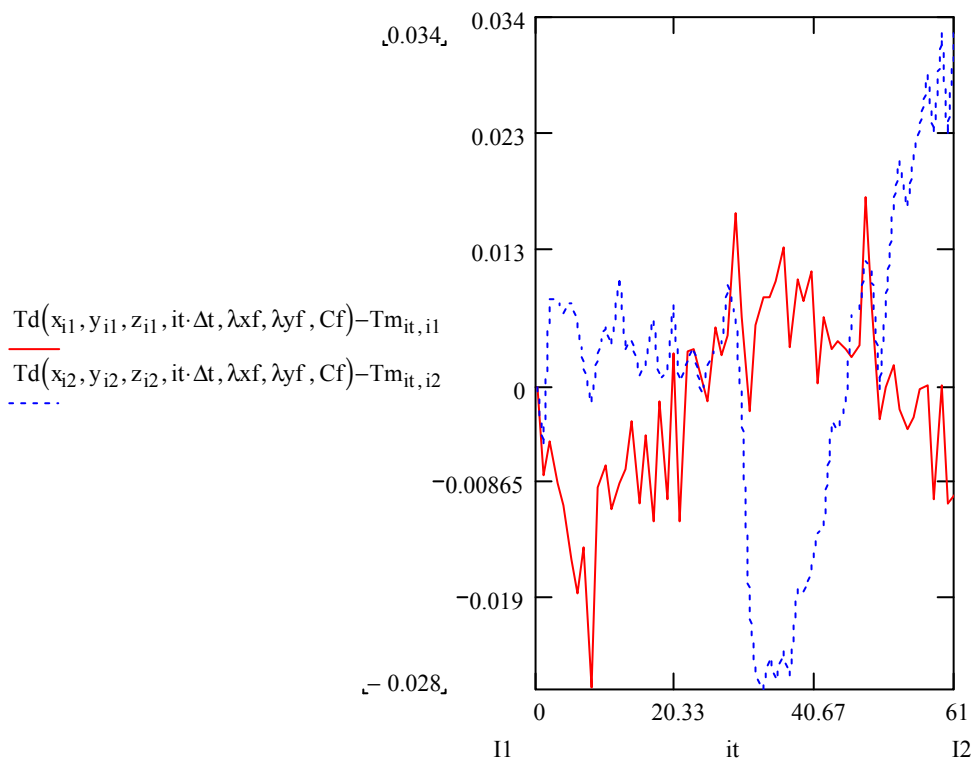
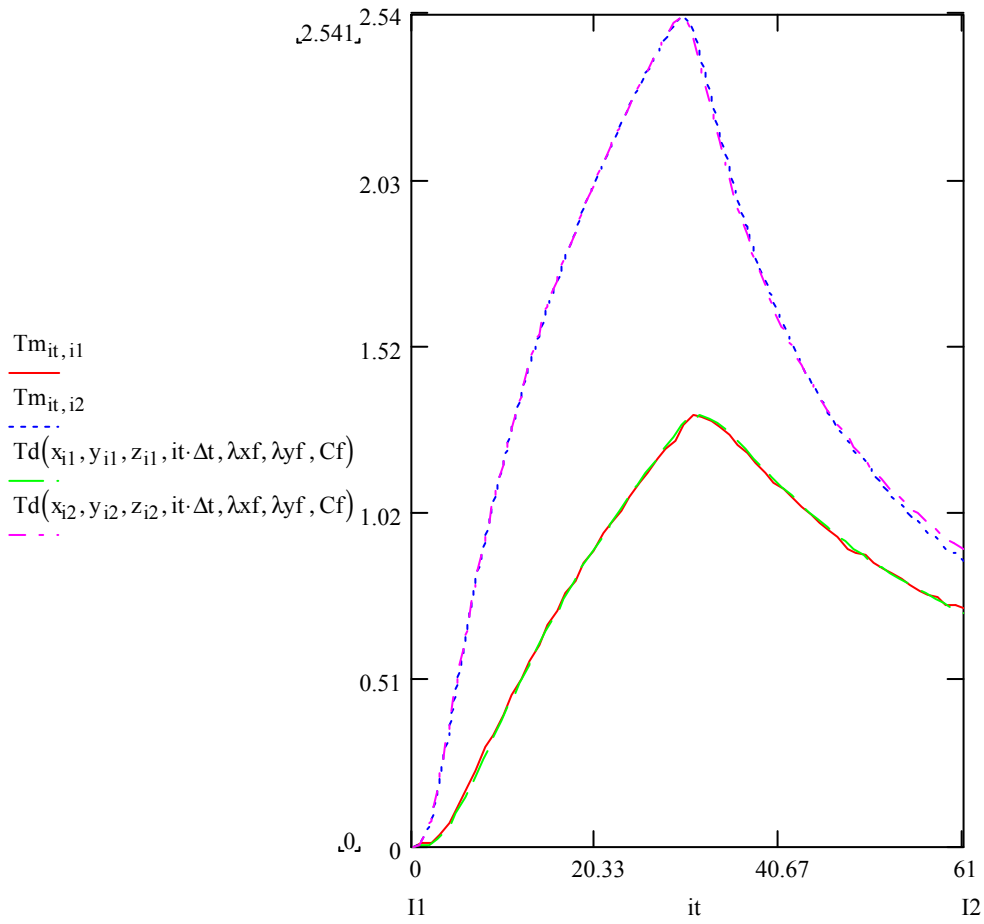
Original coordinate measurements (A1)

0-61
E3f3



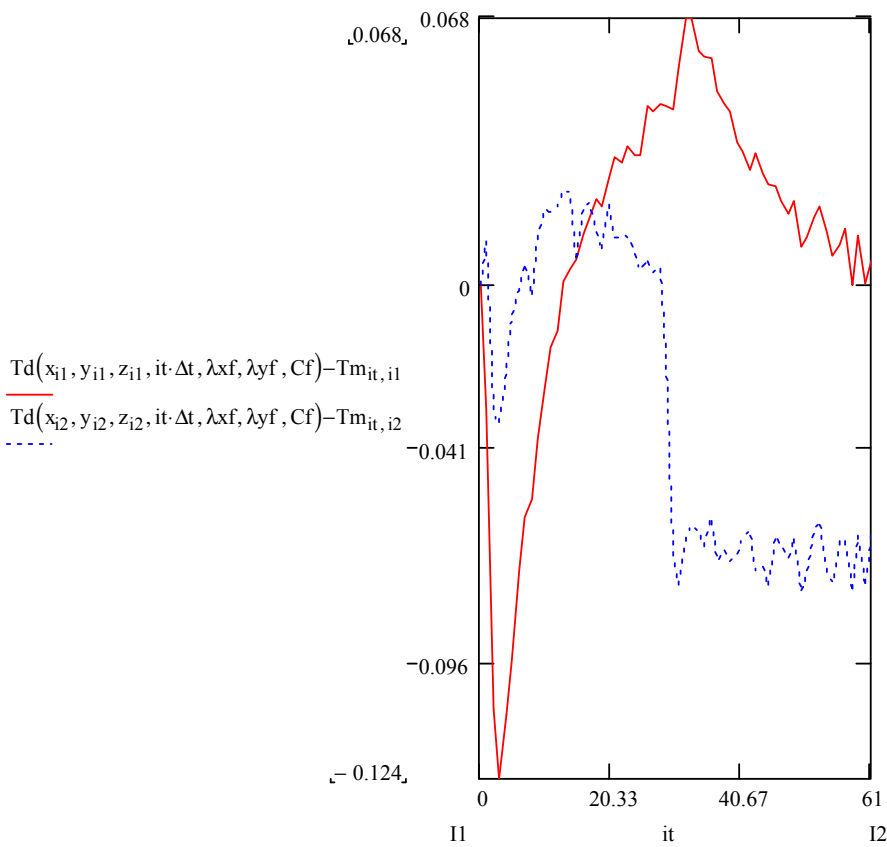
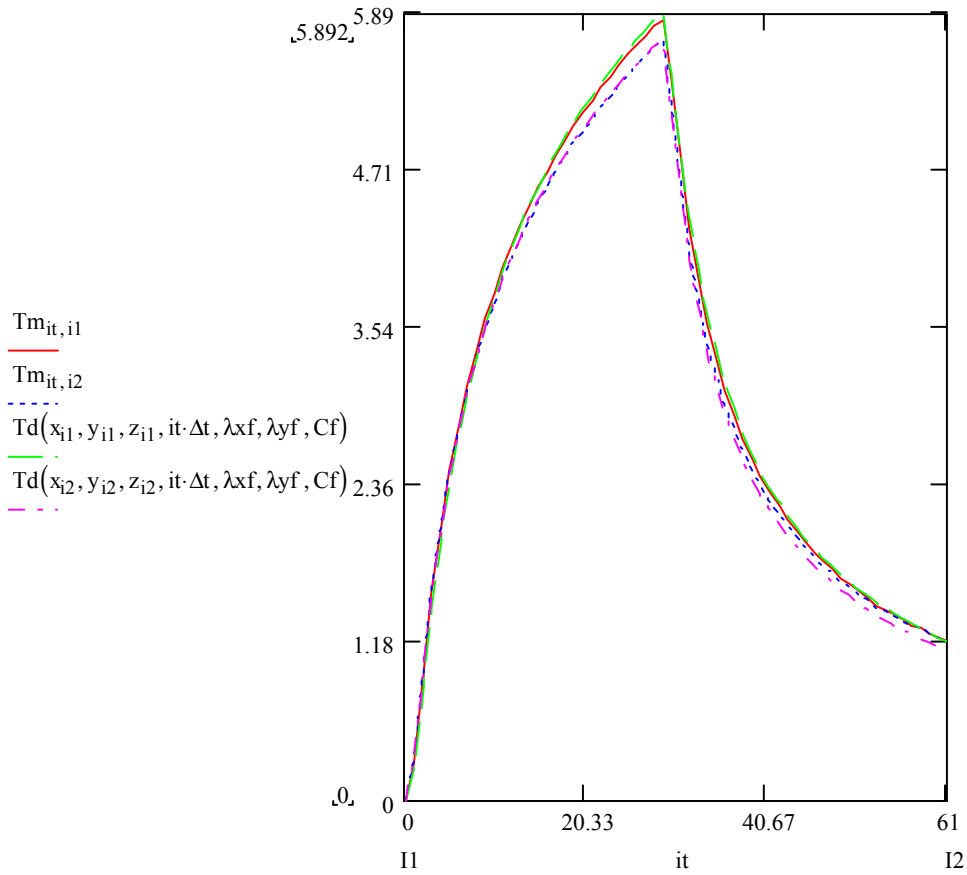
Original coordinate measurements (A1)

0-61
C4d4



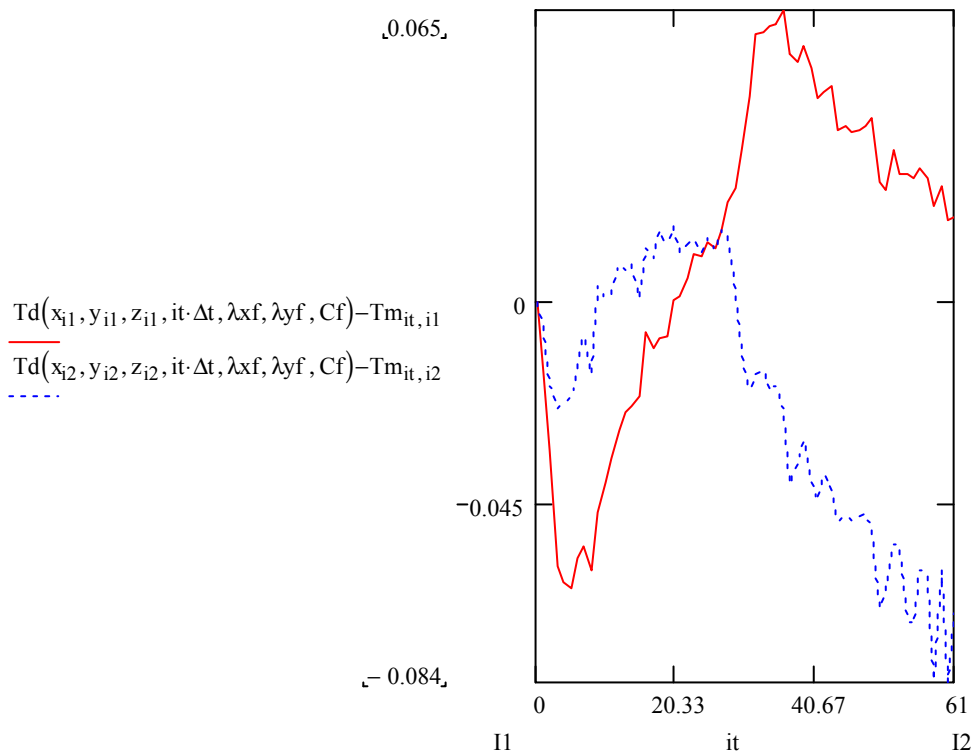
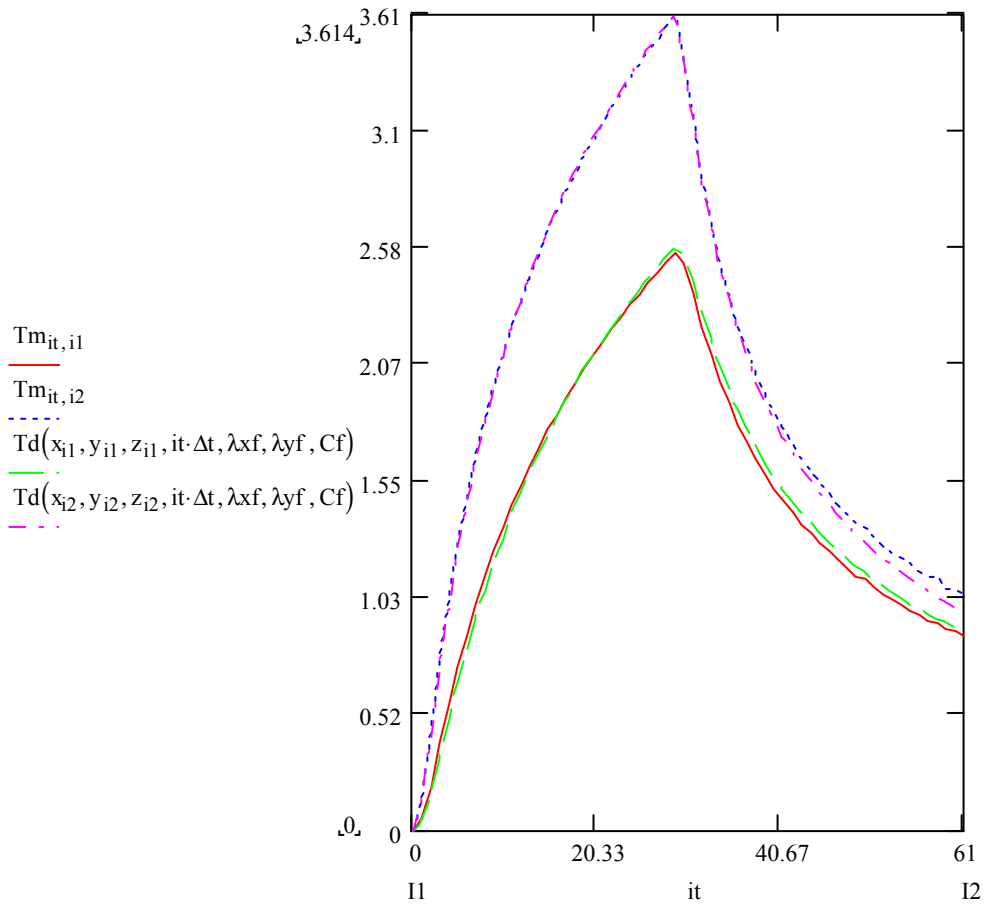
Original coordinate measurements (A1)

0-61
E4f4



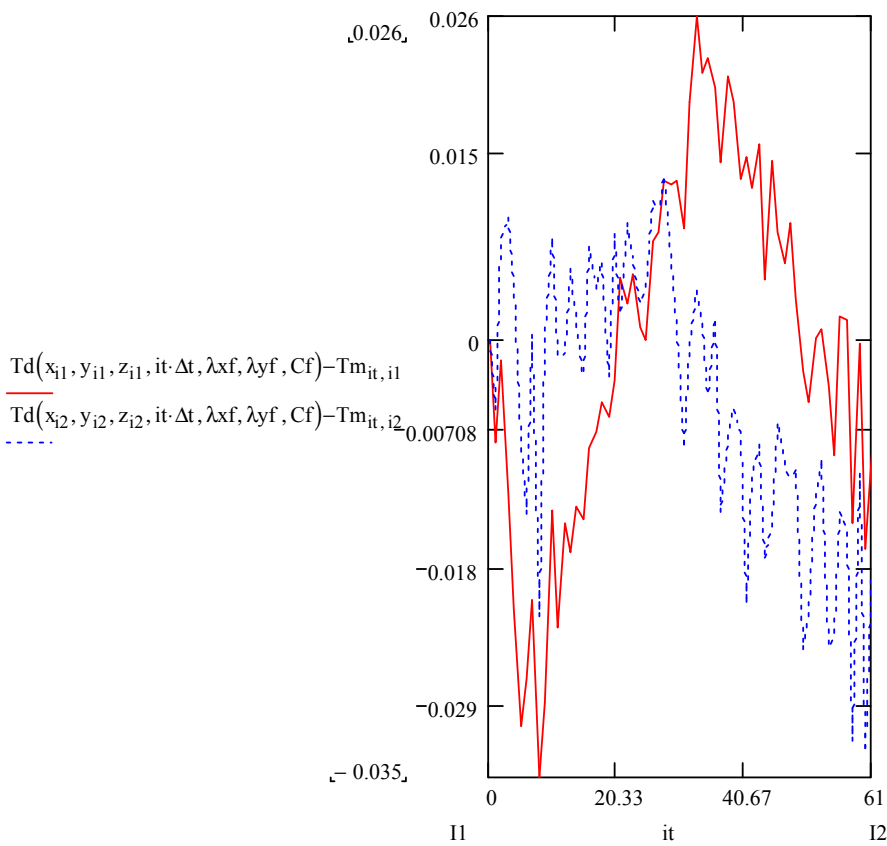
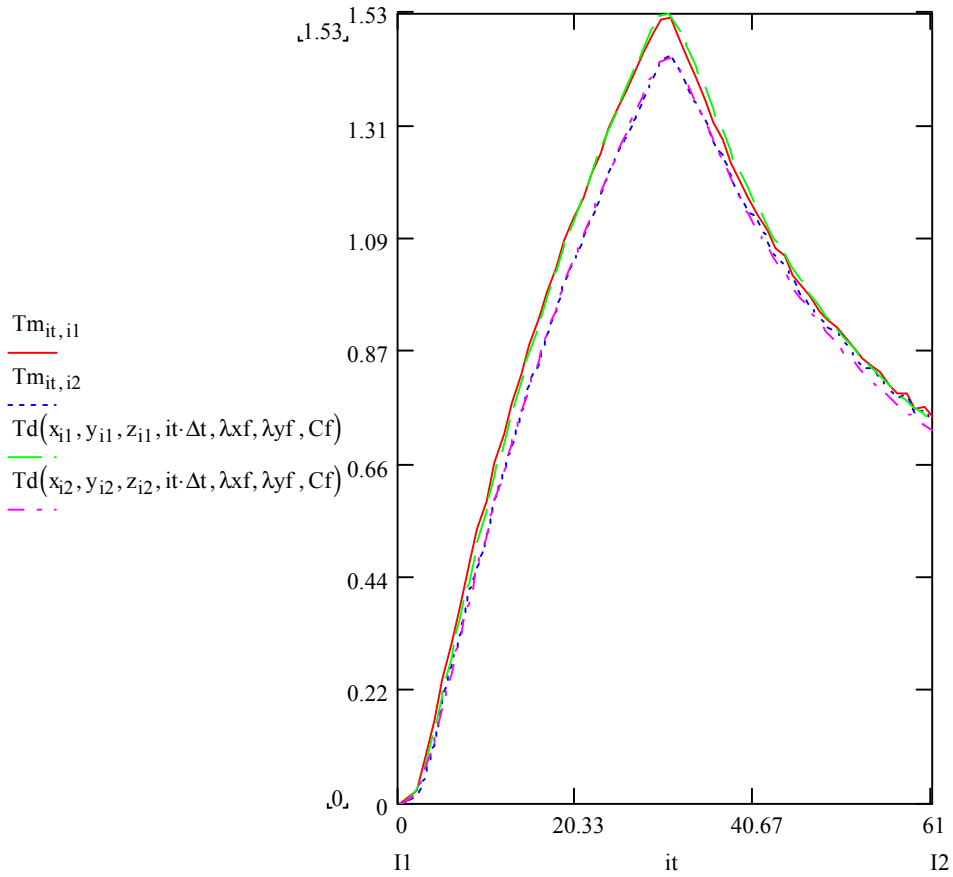
Original coordinate measurements (A1)

0-61
E5f5

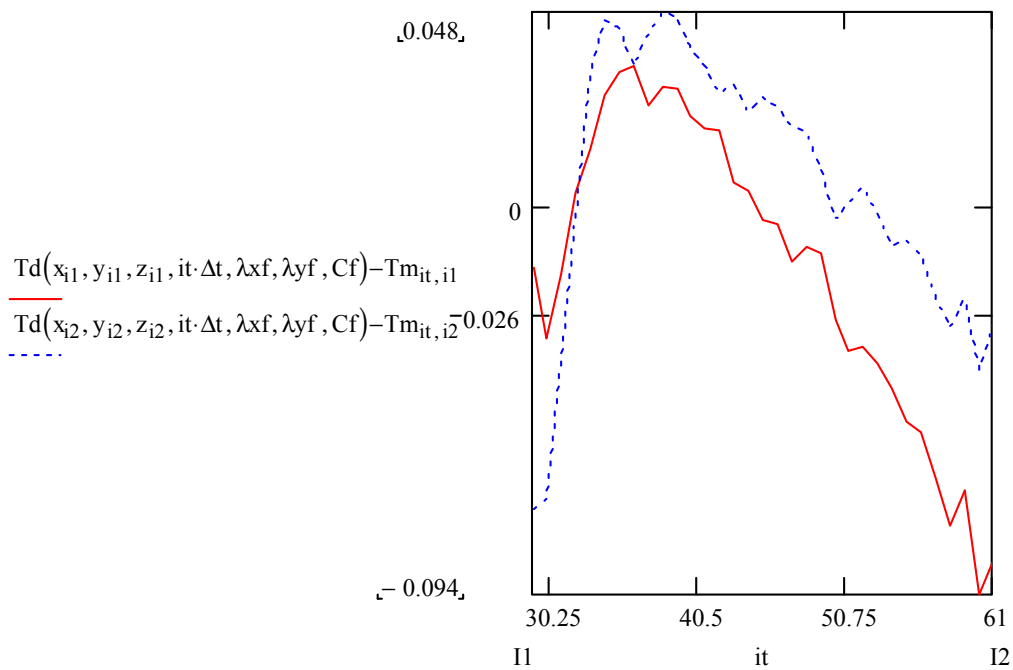
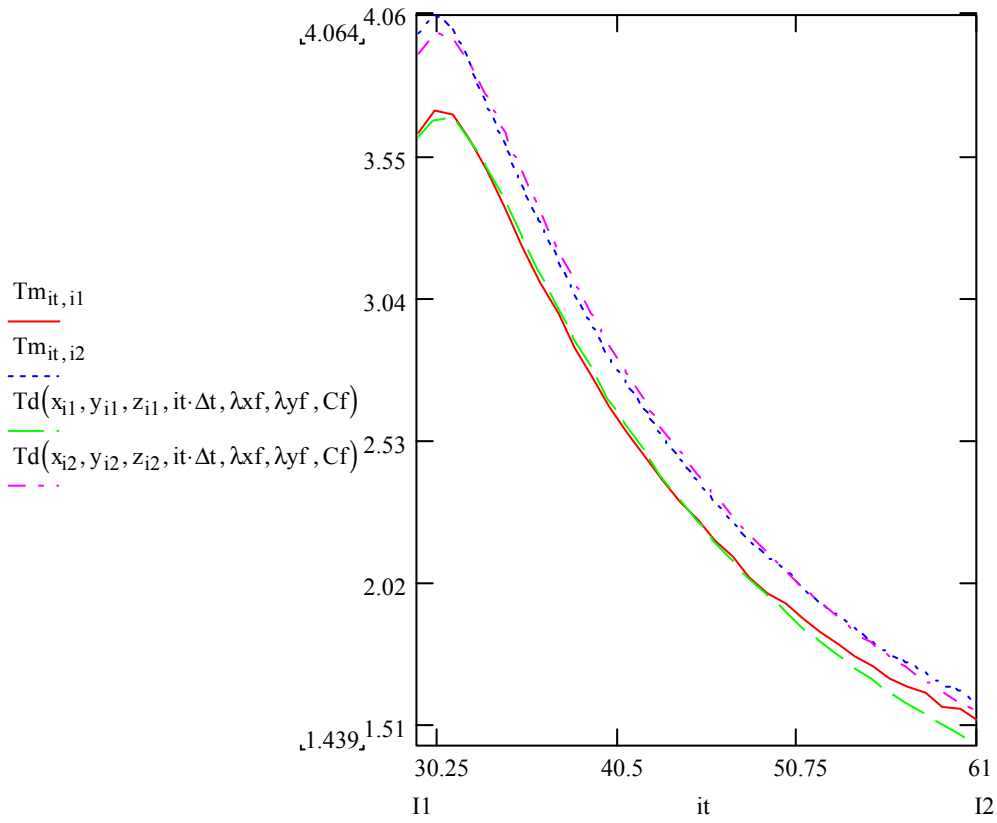


Original coordinate measurements (A1)

0-61
E6f6



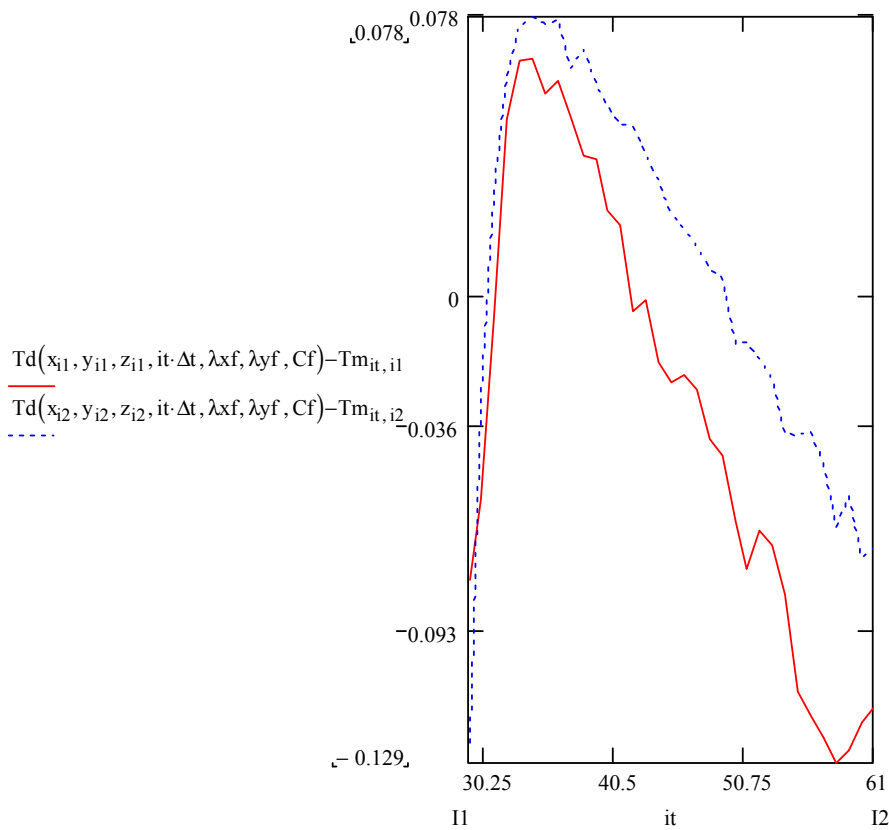
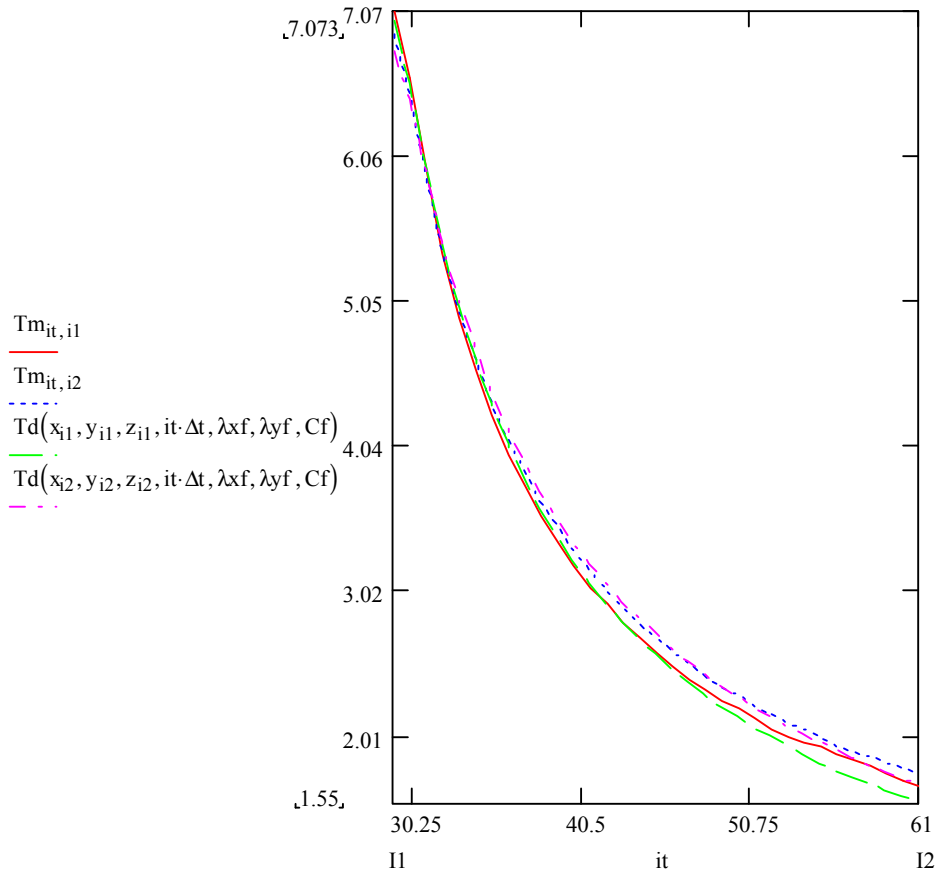
Original coordinate measurements (A1)
 29-61
 C1d1



Original coordinate measurements (A1)

29-61

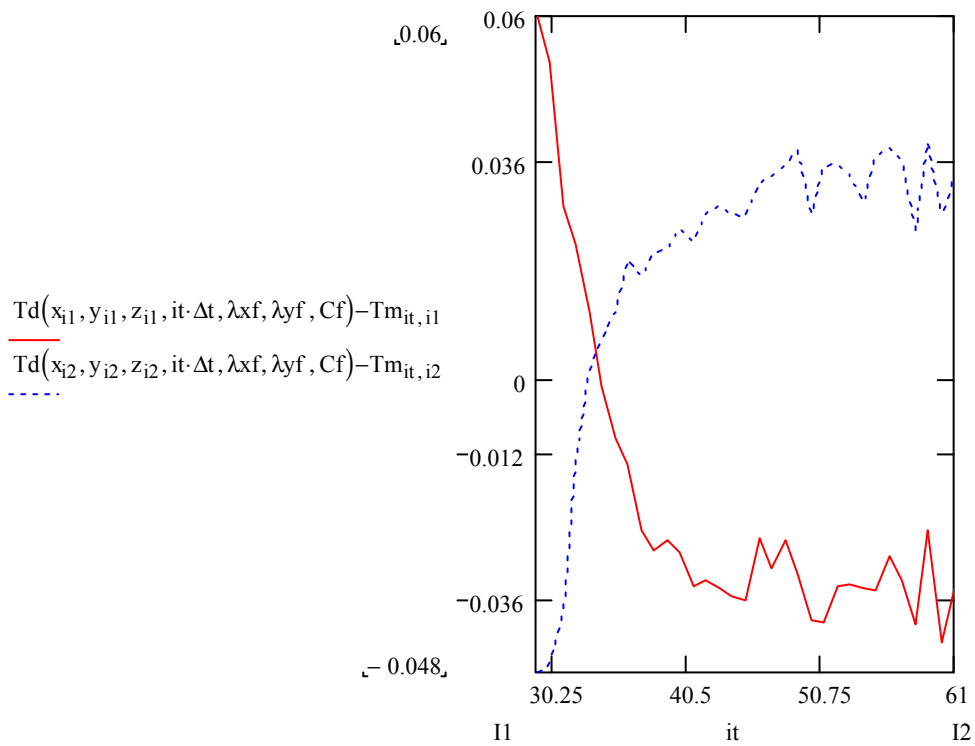
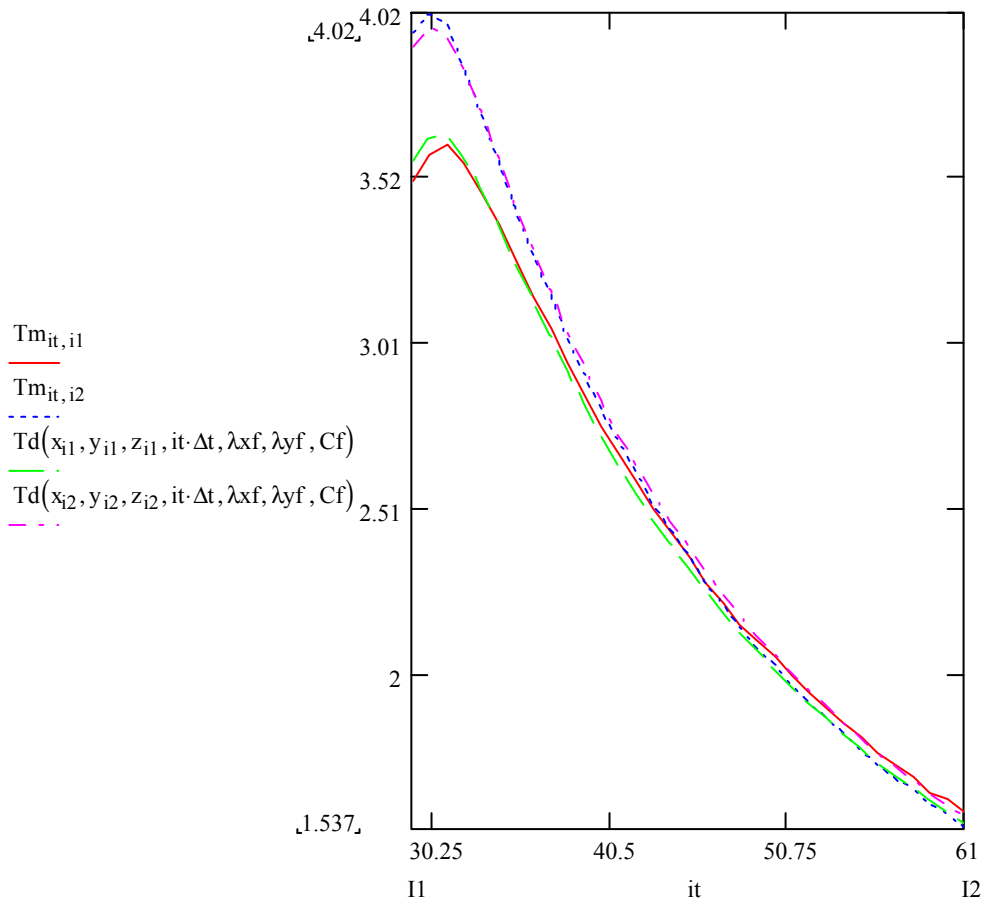
E1f1



Original coordinate measurements (A1)

29-61

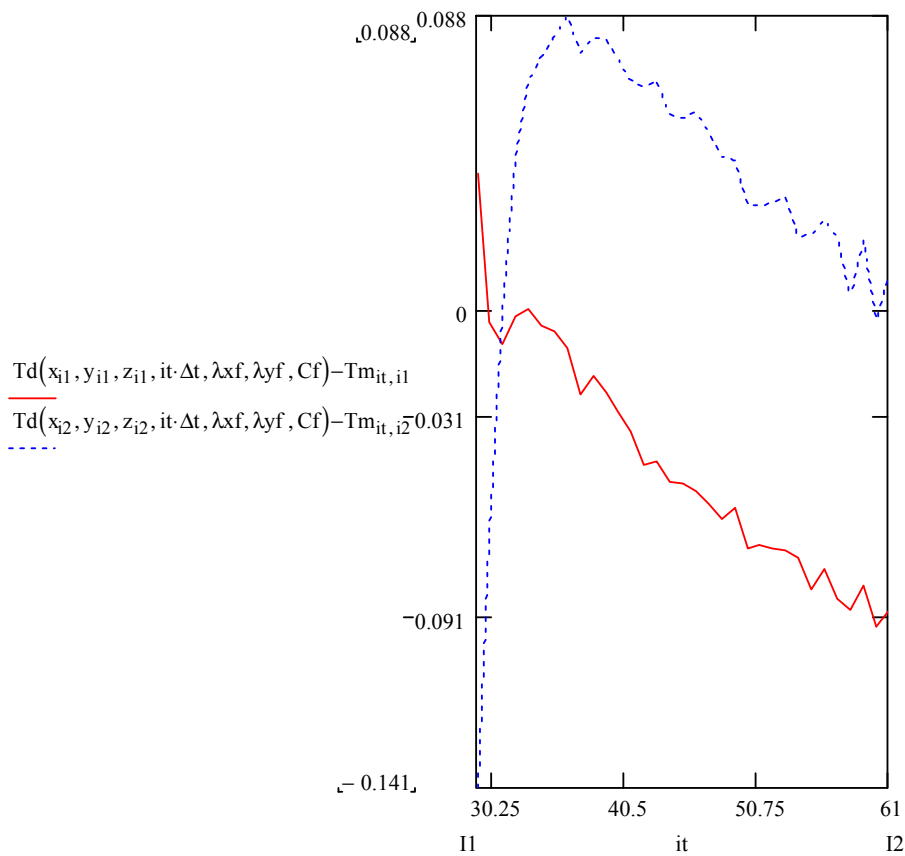
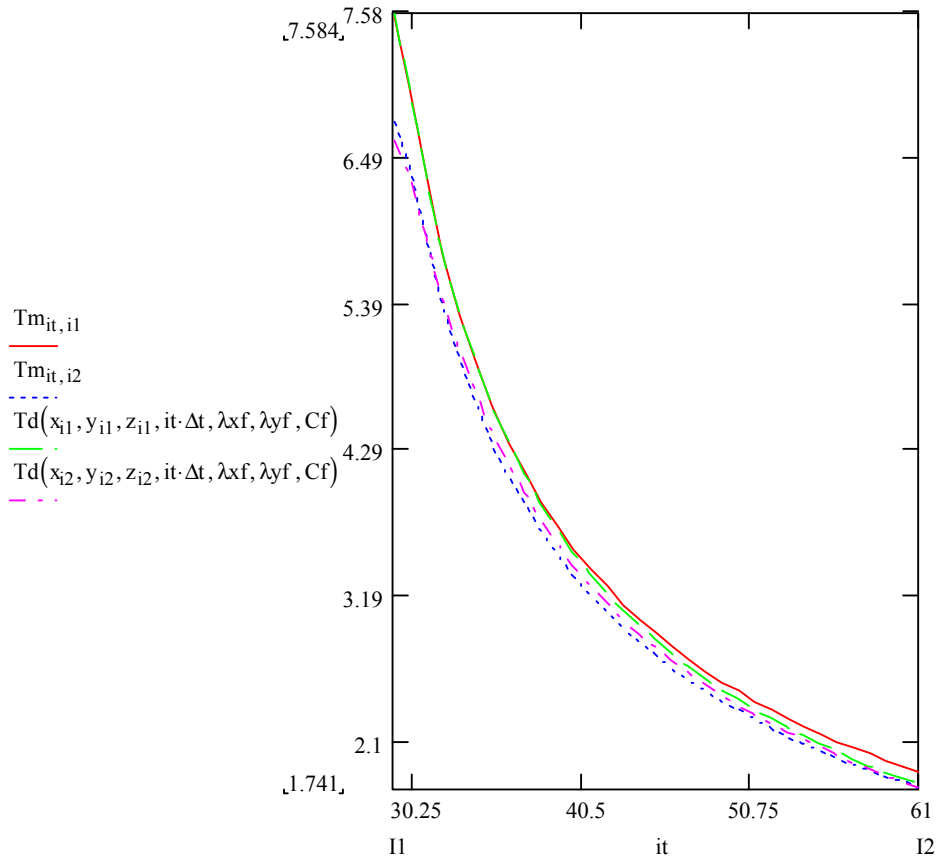
C2d2



Original coordinate measurements (A1)

29-61

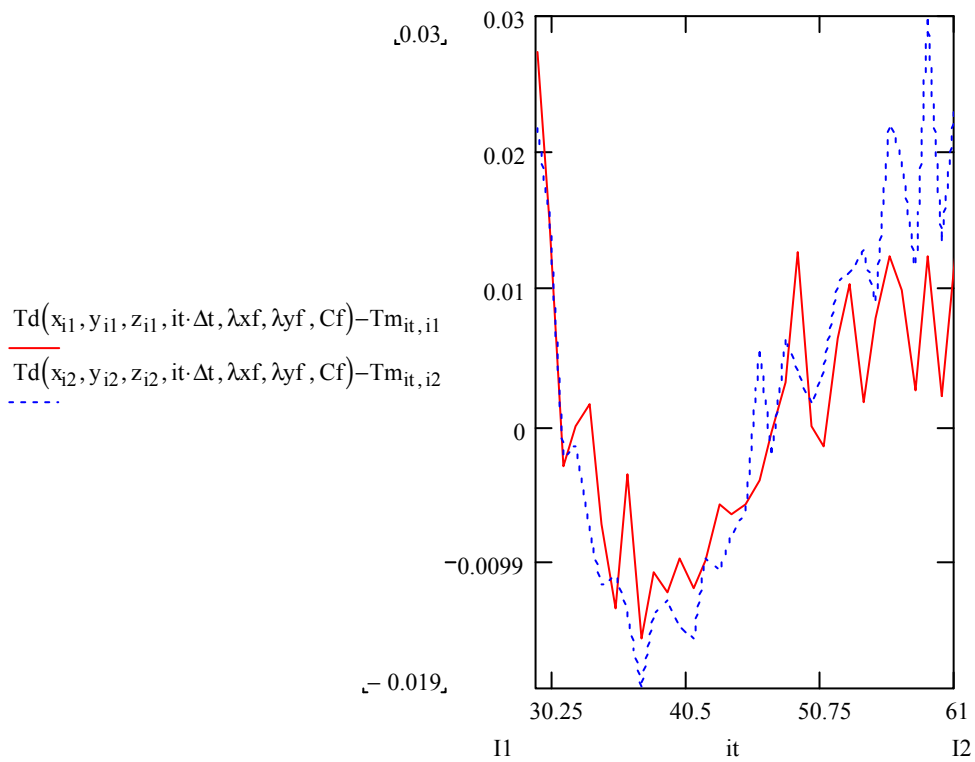
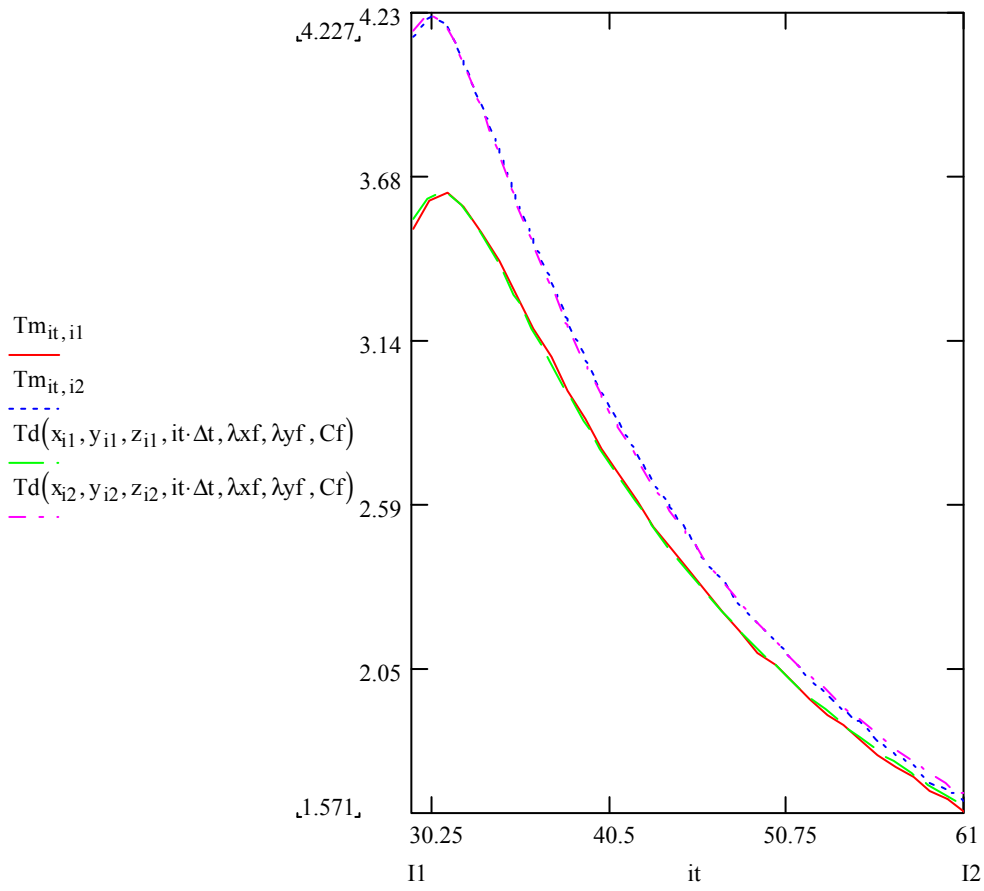
E2f2



Original coordinate measurements (A1)

29-61

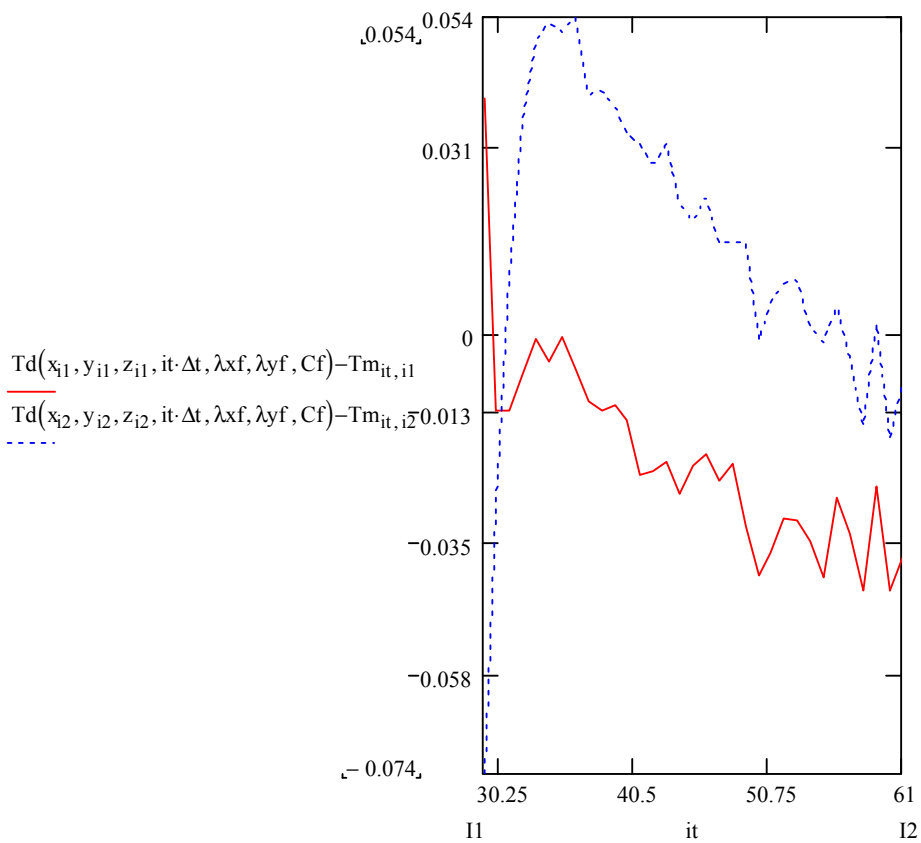
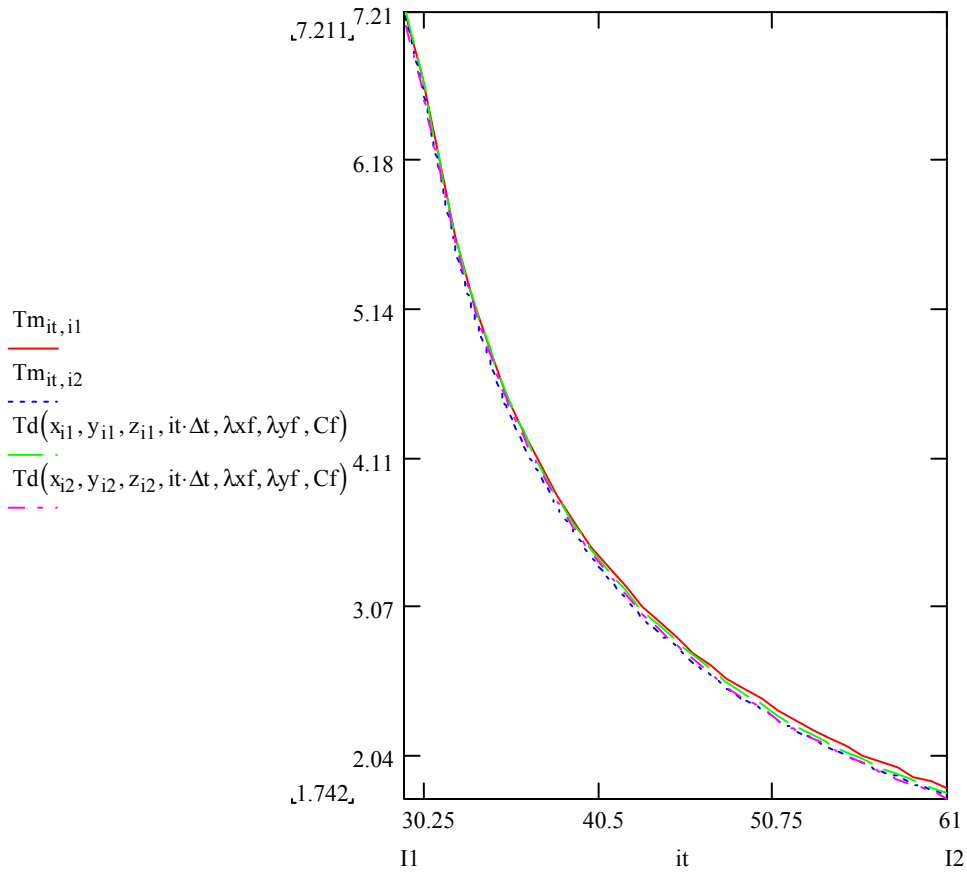
C3d3



Original coordinate measurements (A1)

29-61

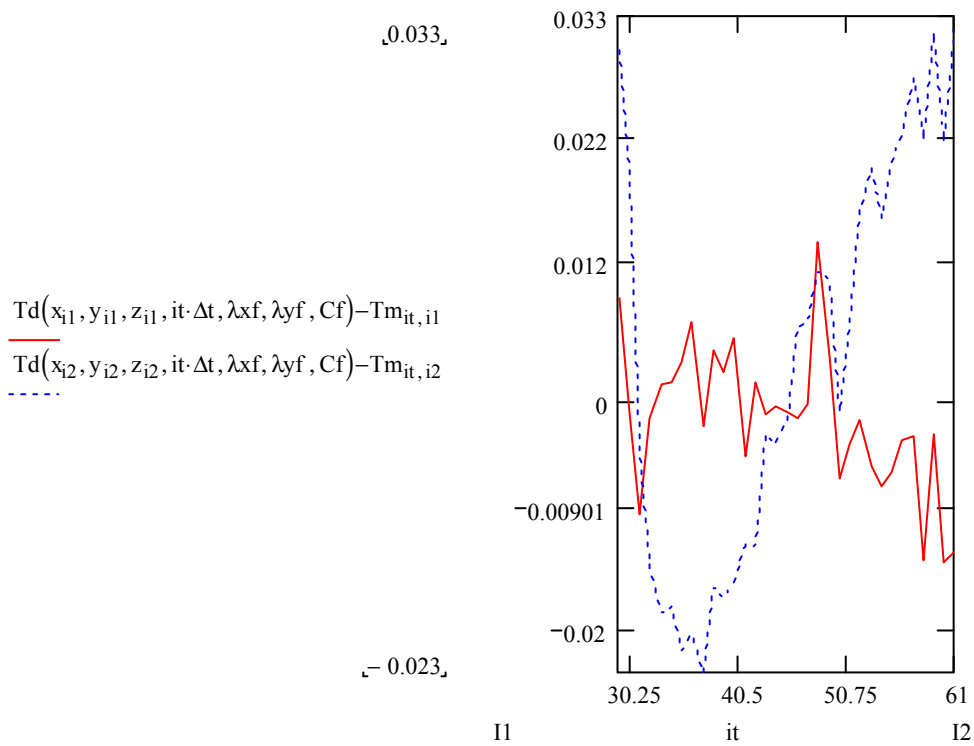
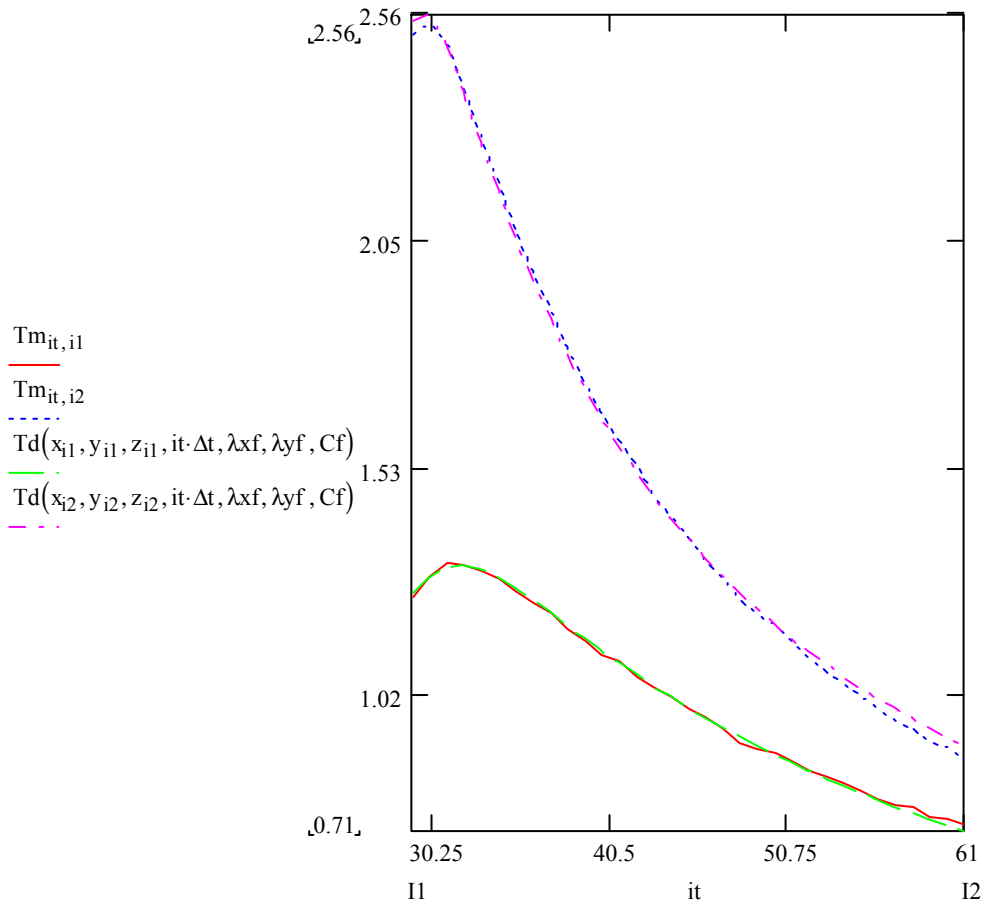
E3f3



Original coordinate measurements (A1)

29-61

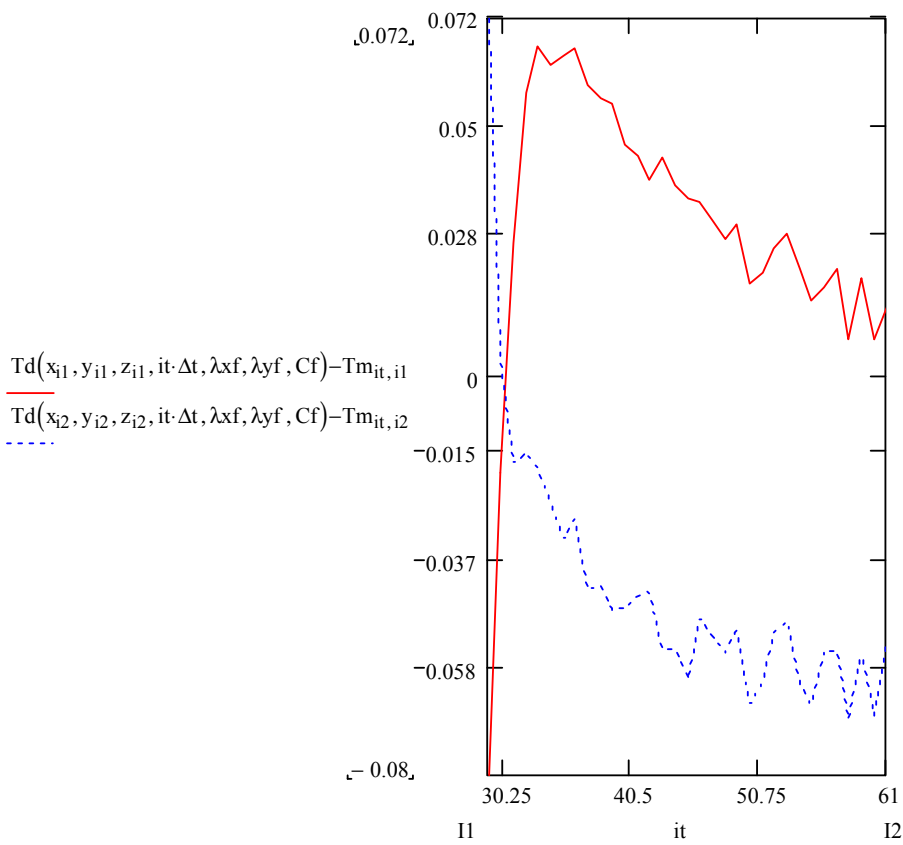
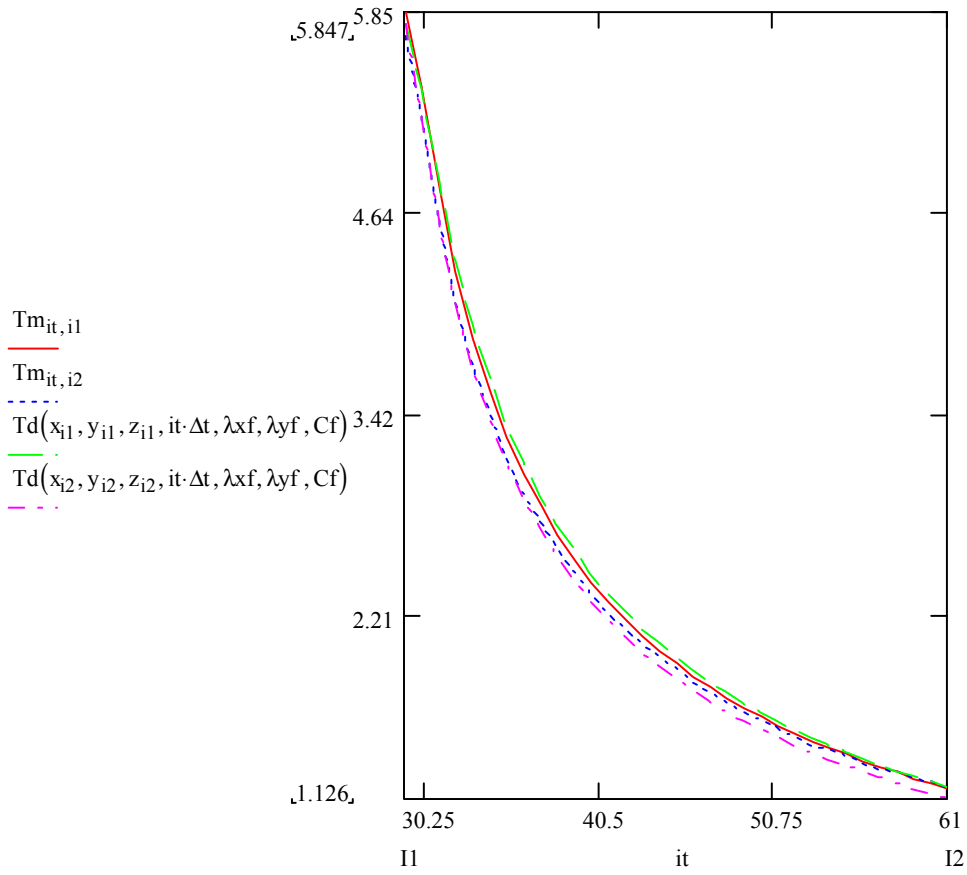
C4d4



Original coordinate measurements (A1)

29-61

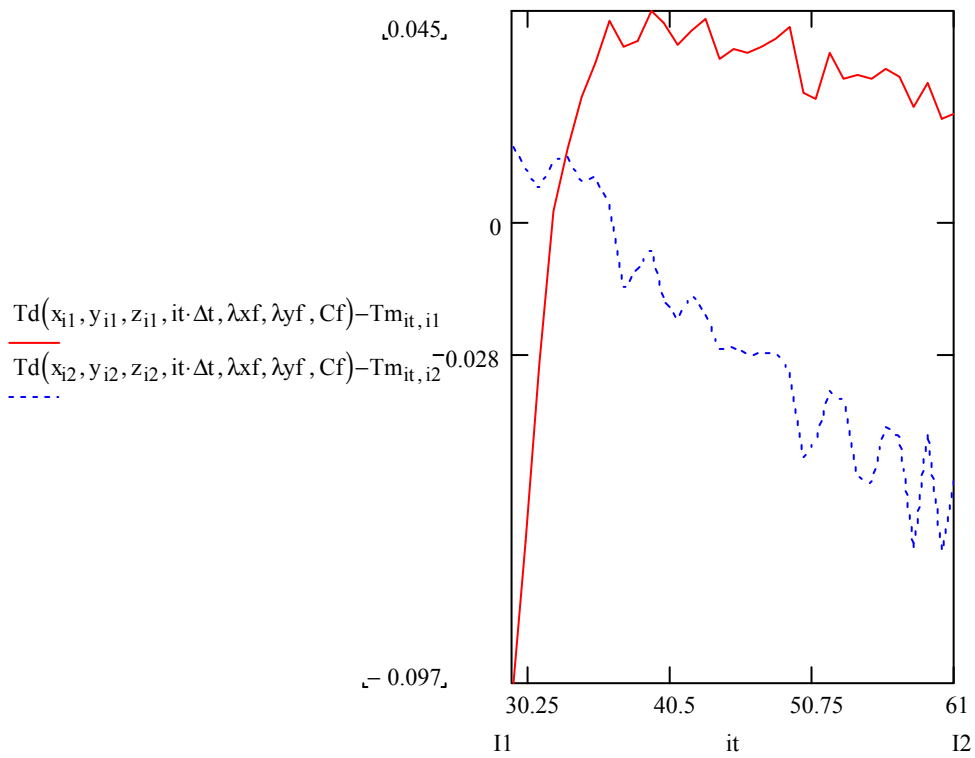
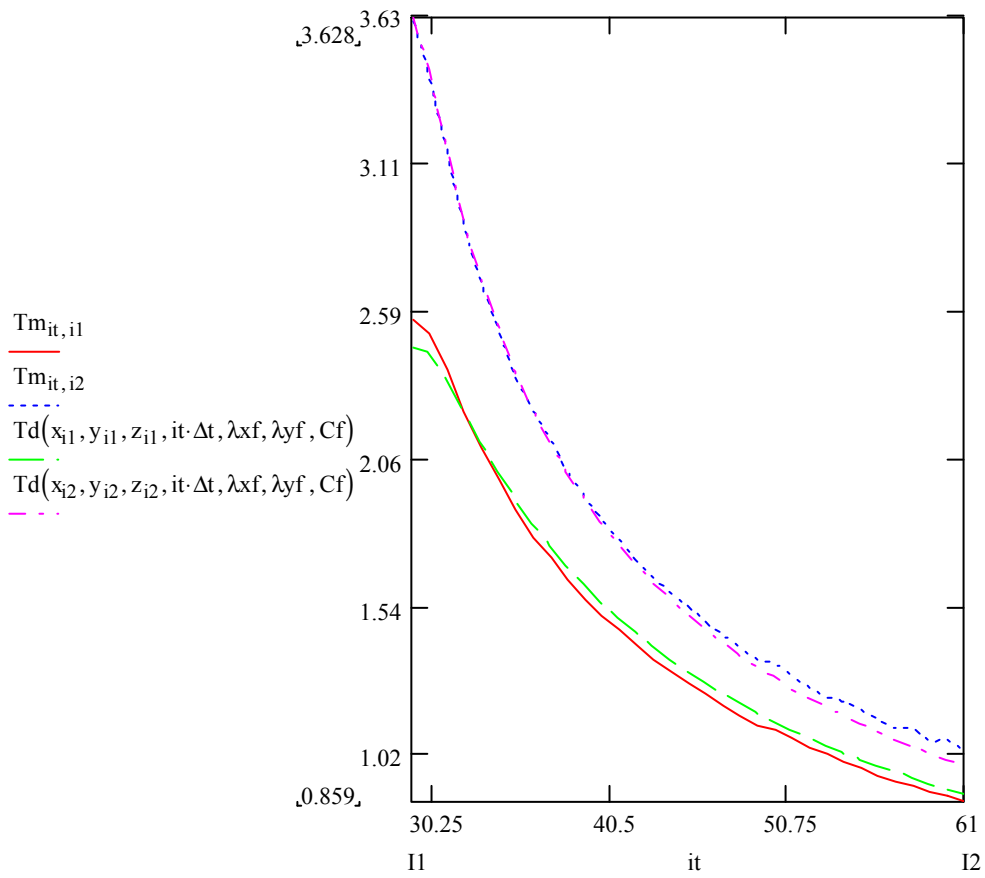
E4f4



Original coordinate measurements (A1)

29-61

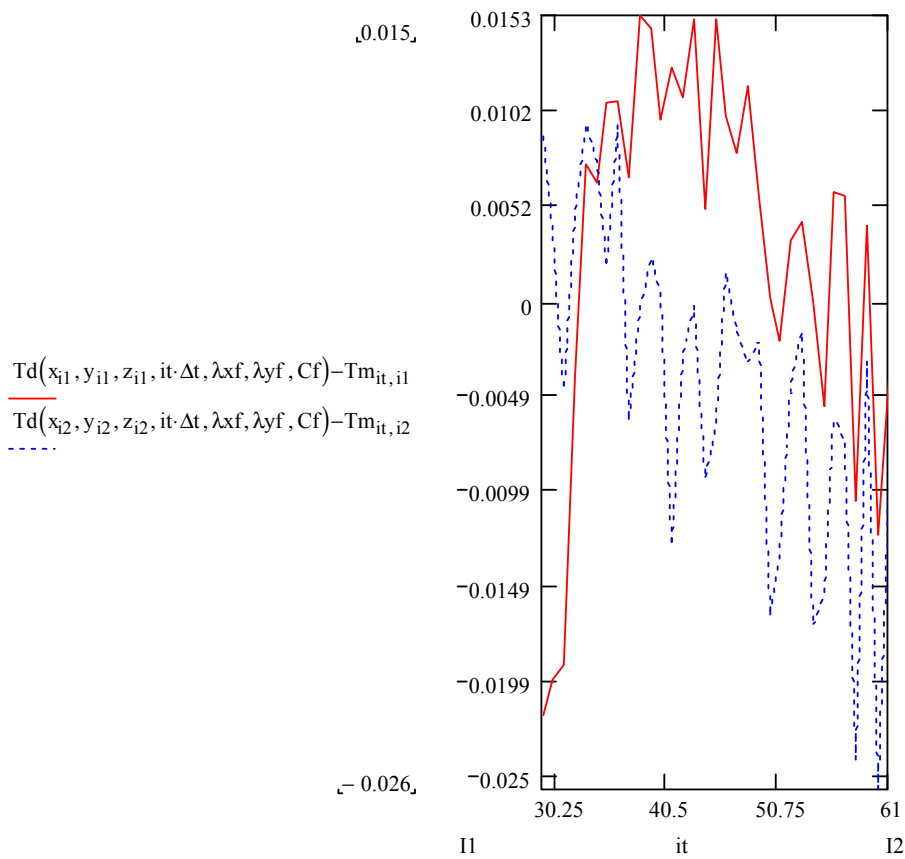
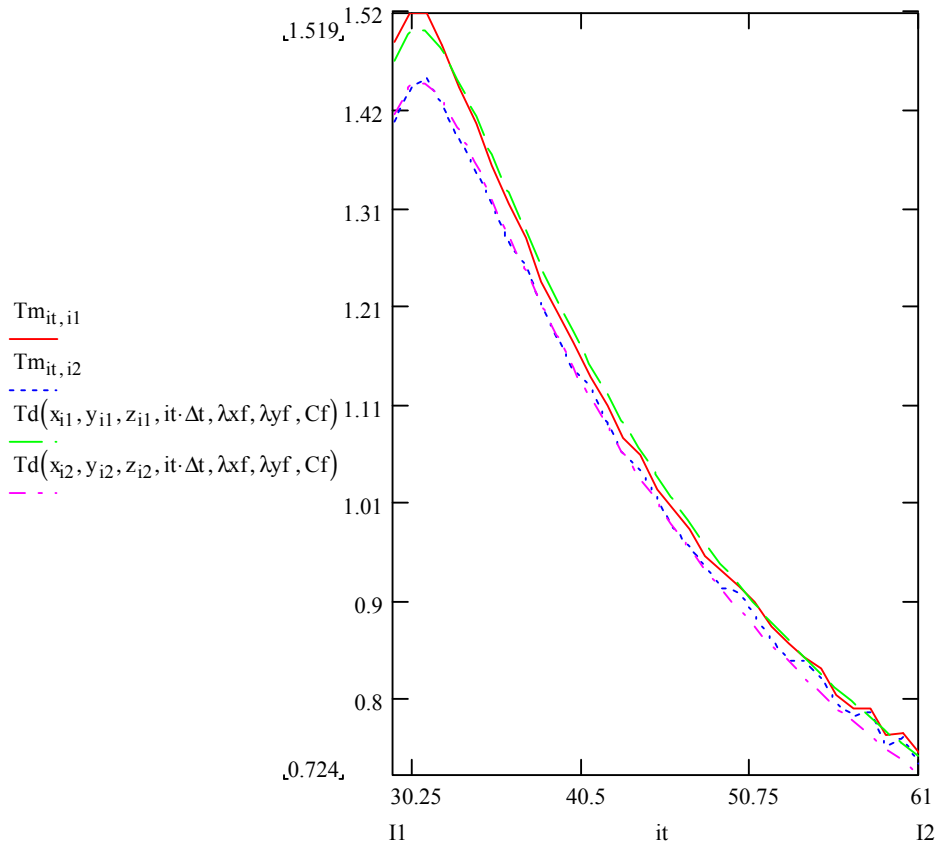
E5f5



Original coordinate measurements (A1)

29-61

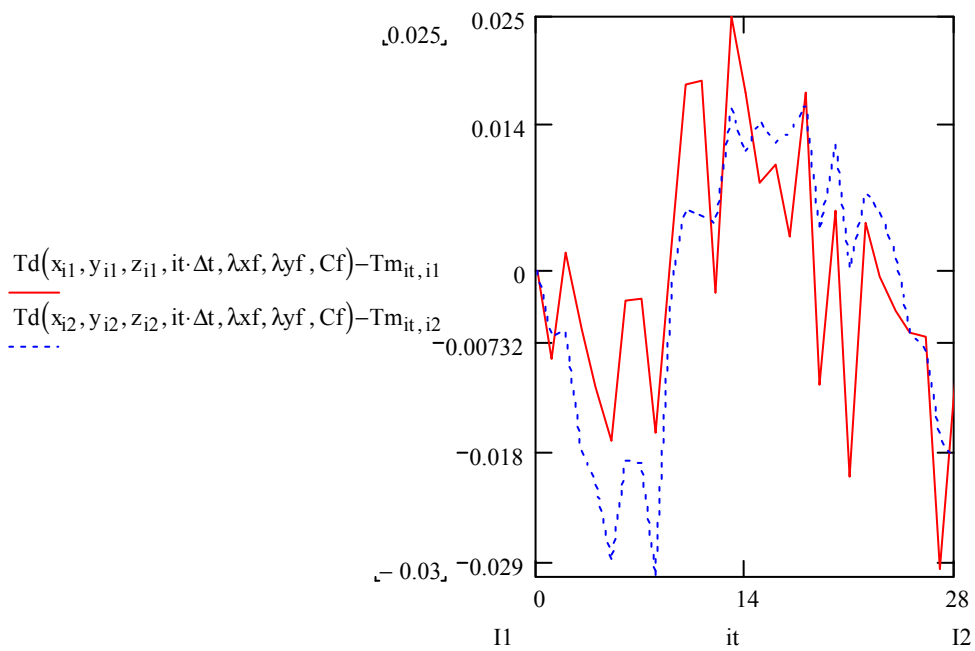
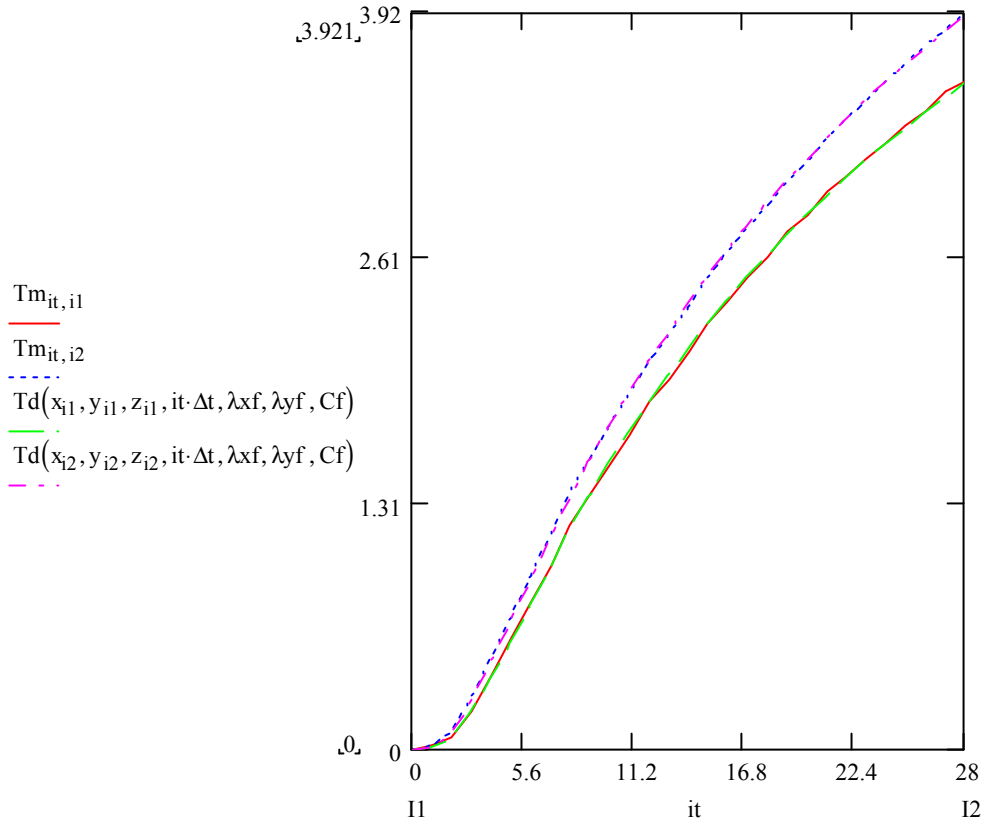
E6f6



Original coordinate measurements + MOVE 3 (A2)

0-28

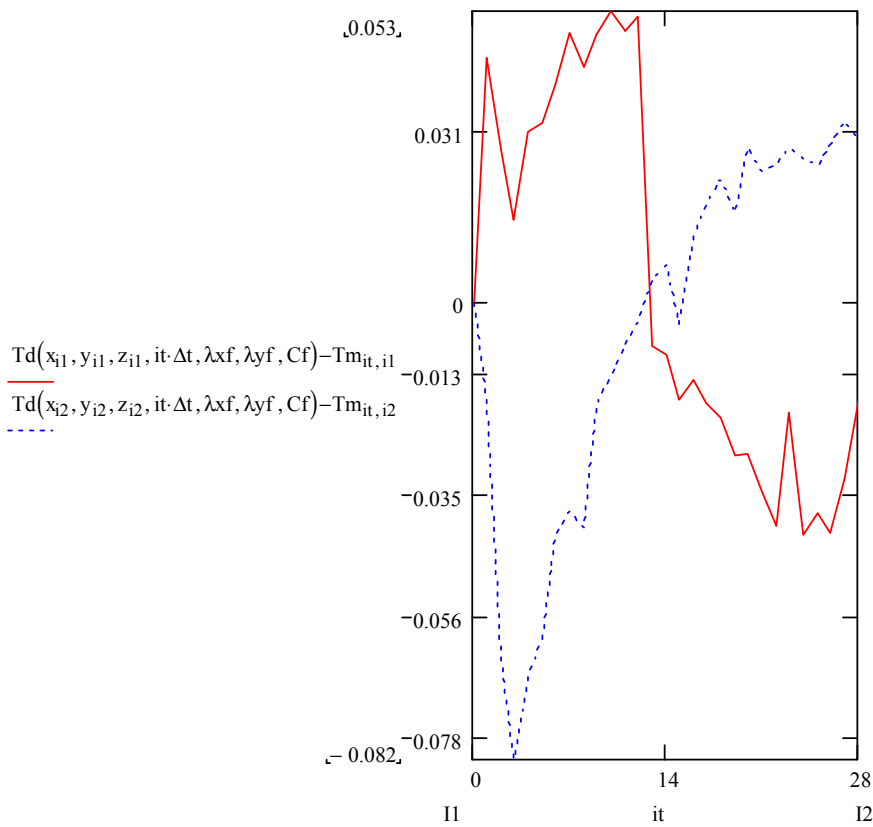
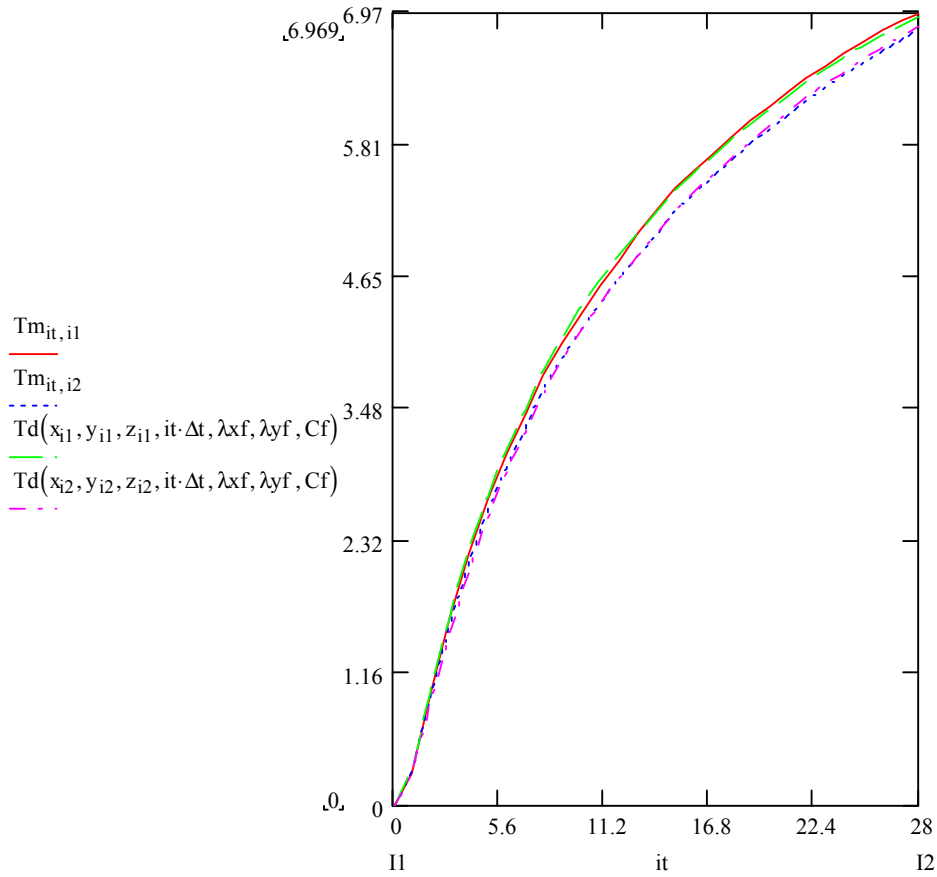
C1d1



Original coordinate measurements + MOVE 3 (A2)

0-28

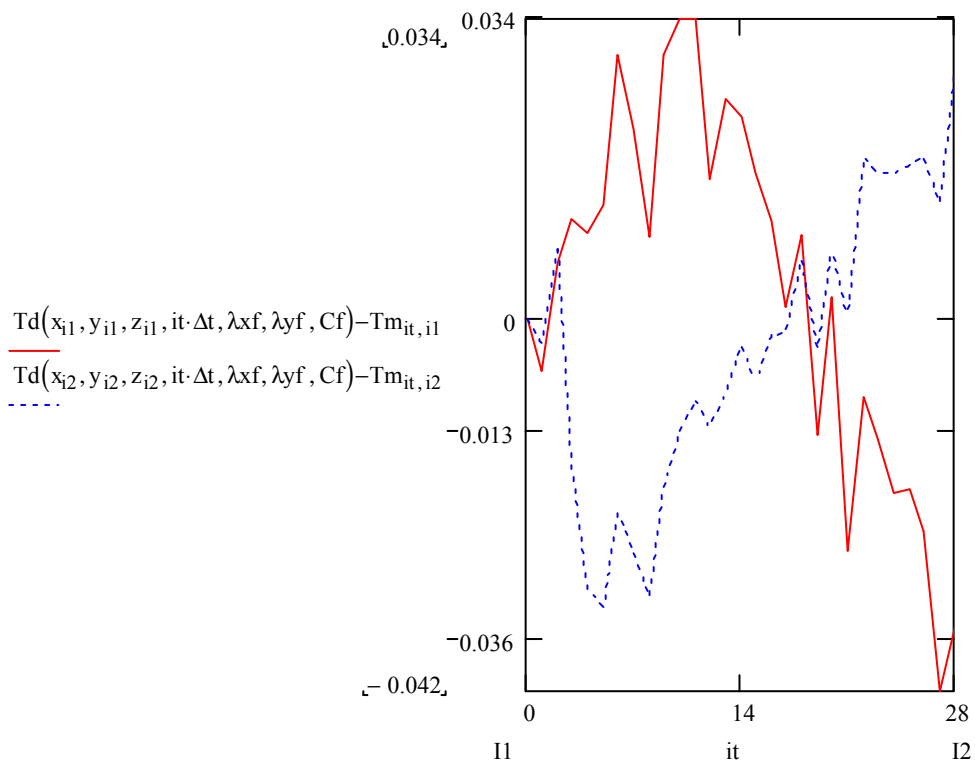
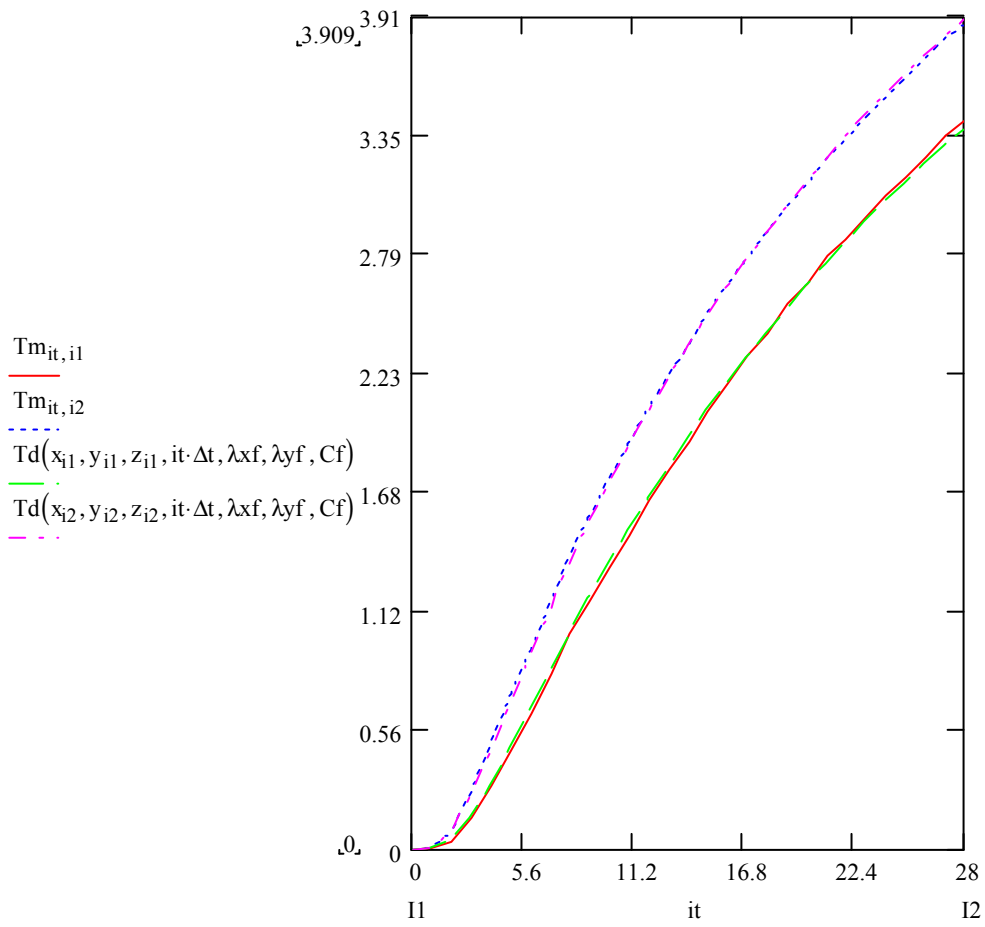
E1f1



Original coordinate measurements + MOVE 3 (A2)

0-28

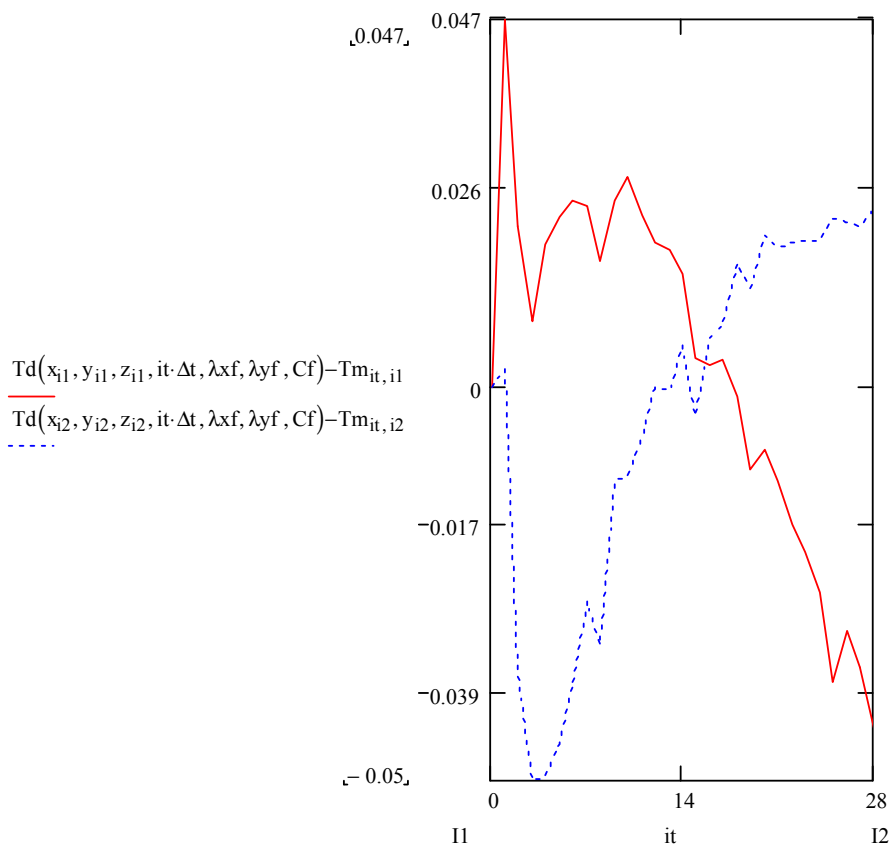
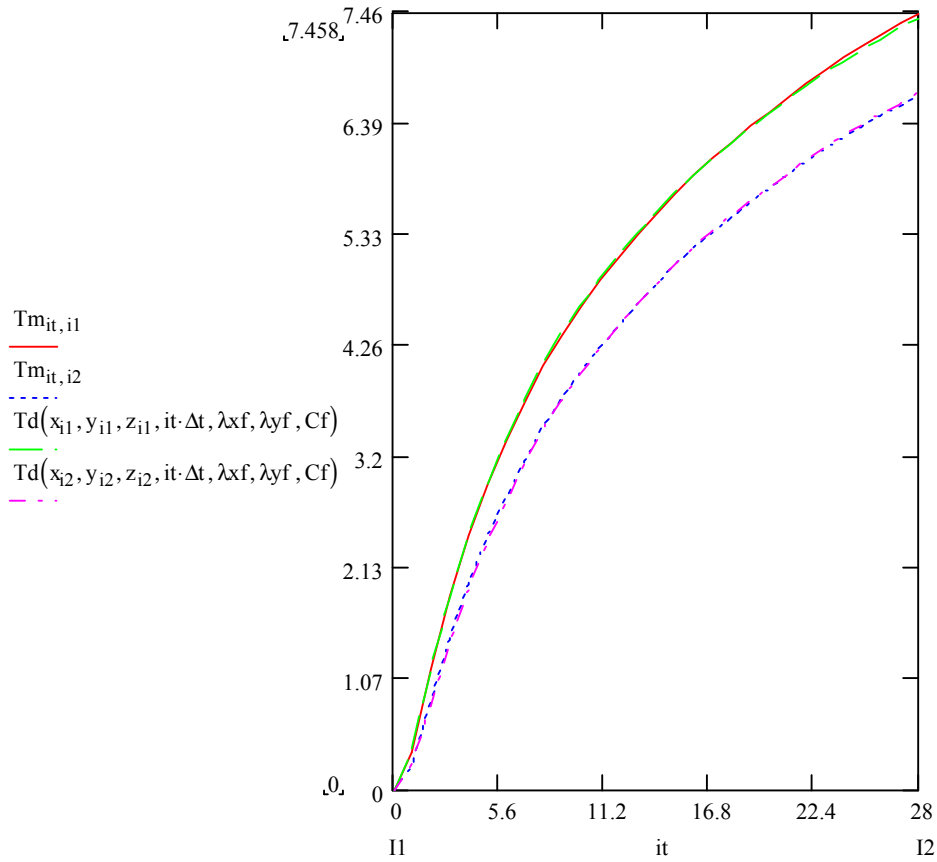
C2d2



Original coordinate measurements + MOVE 3 (A2)

0-28

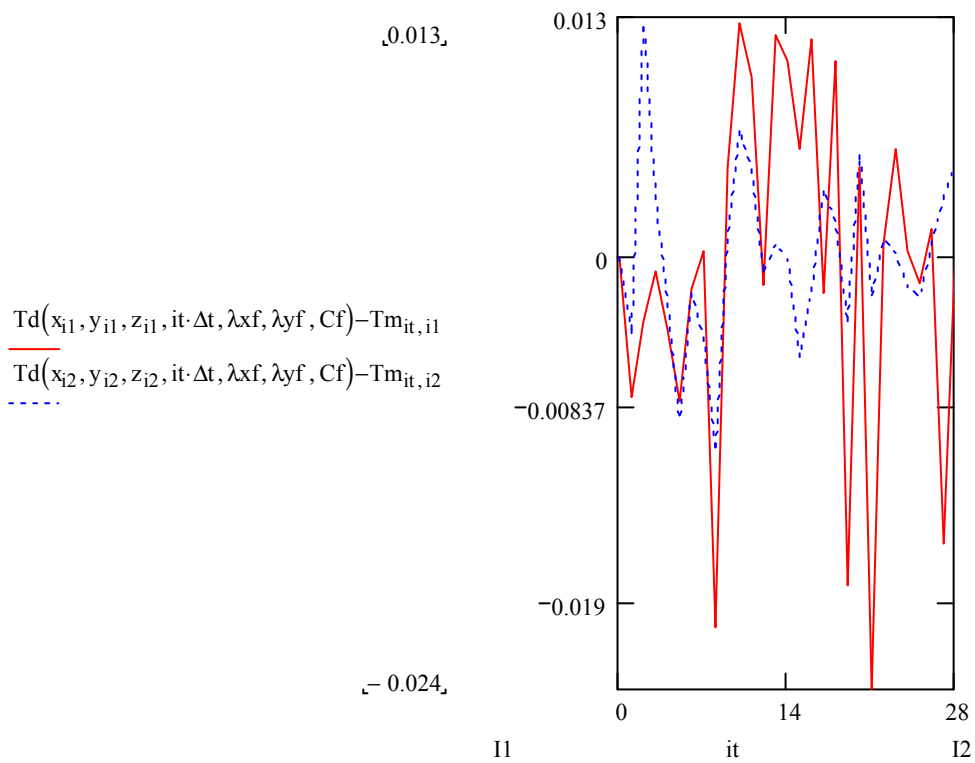
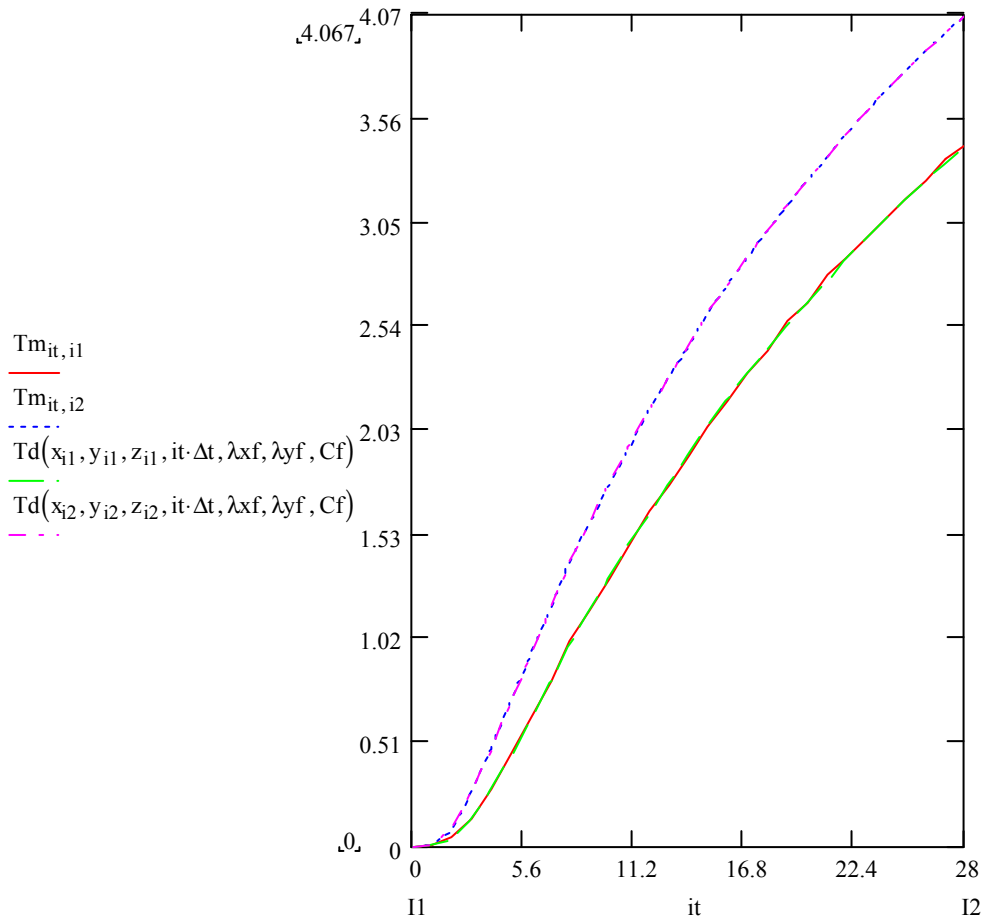
E2f2



Original coordinate measurements + MOVE 3 (A2)

0-28

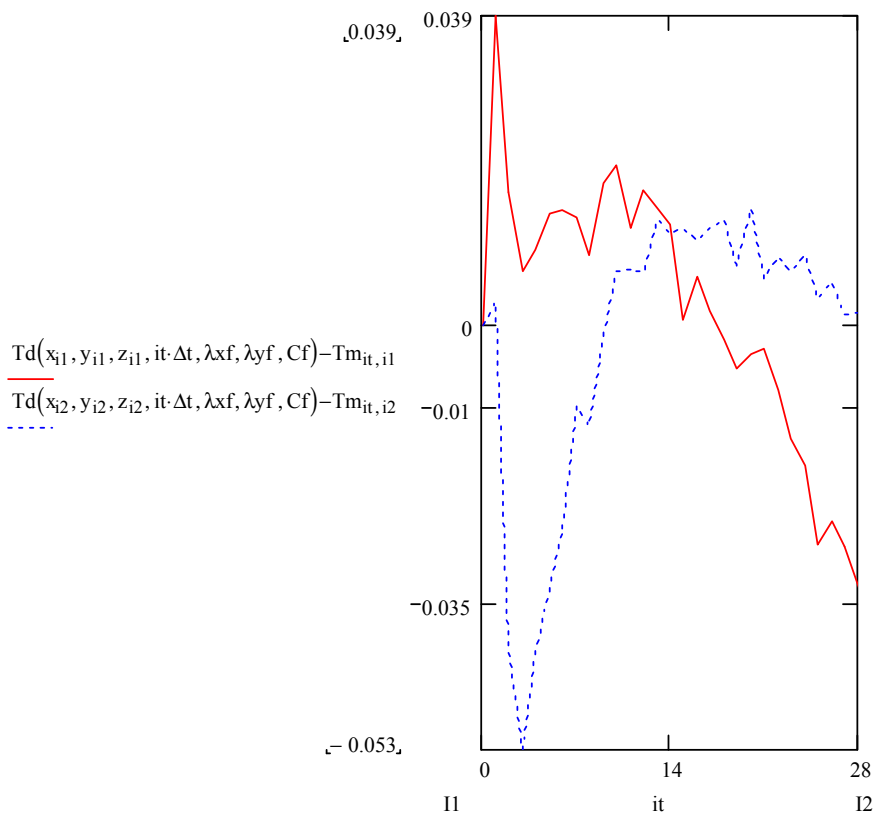
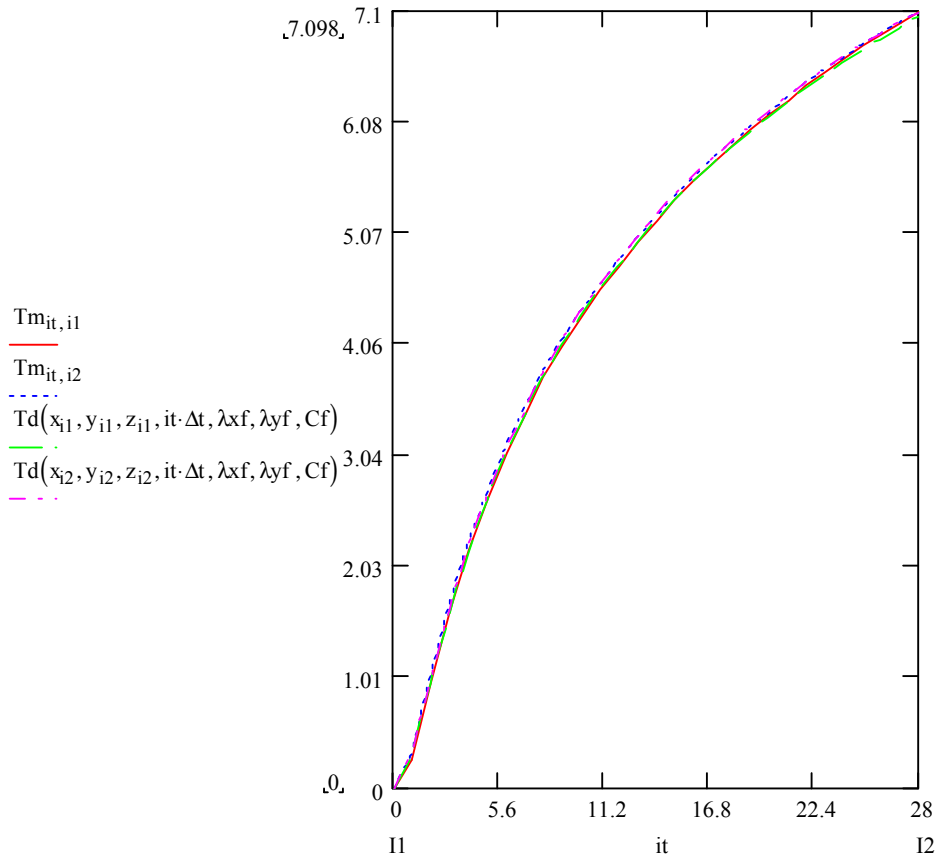
C3d3



Original coordinate measurements + MOVE 3 (A2)

0-28

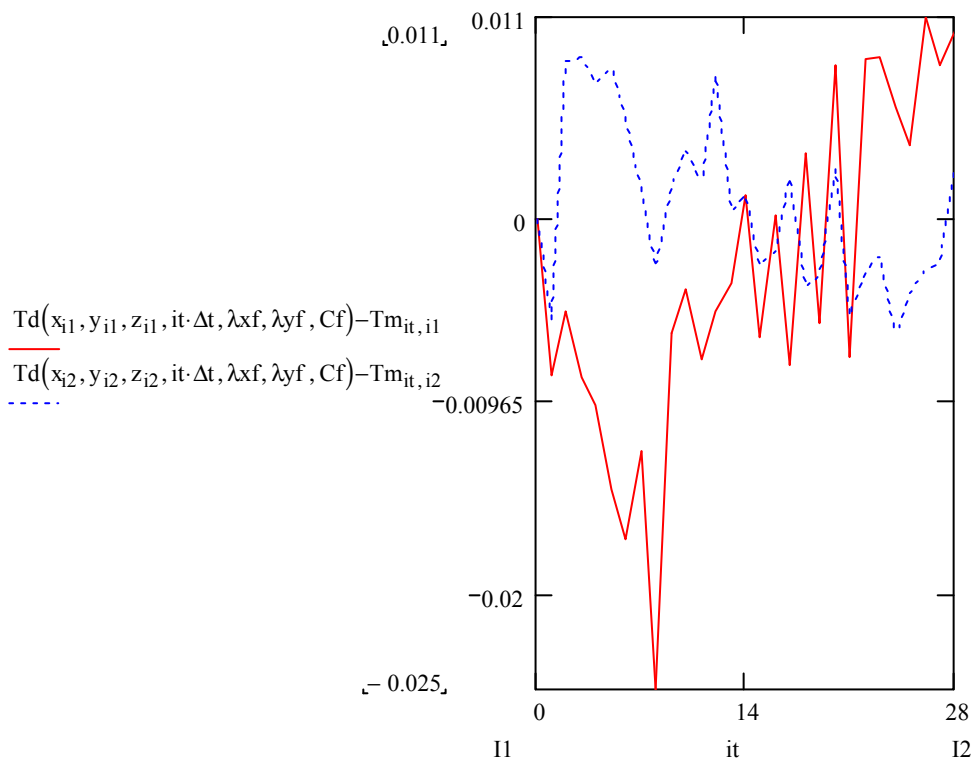
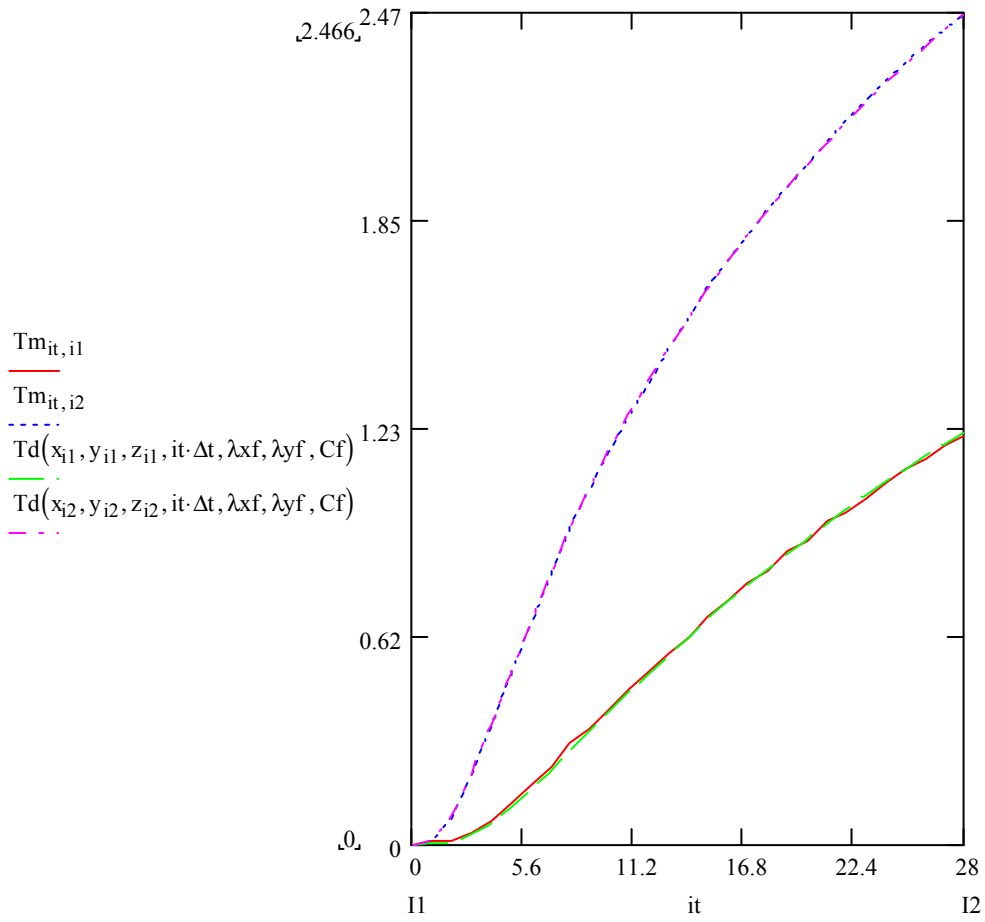
E3f3



Original coordinate measurements + MOVE 3 (A2)

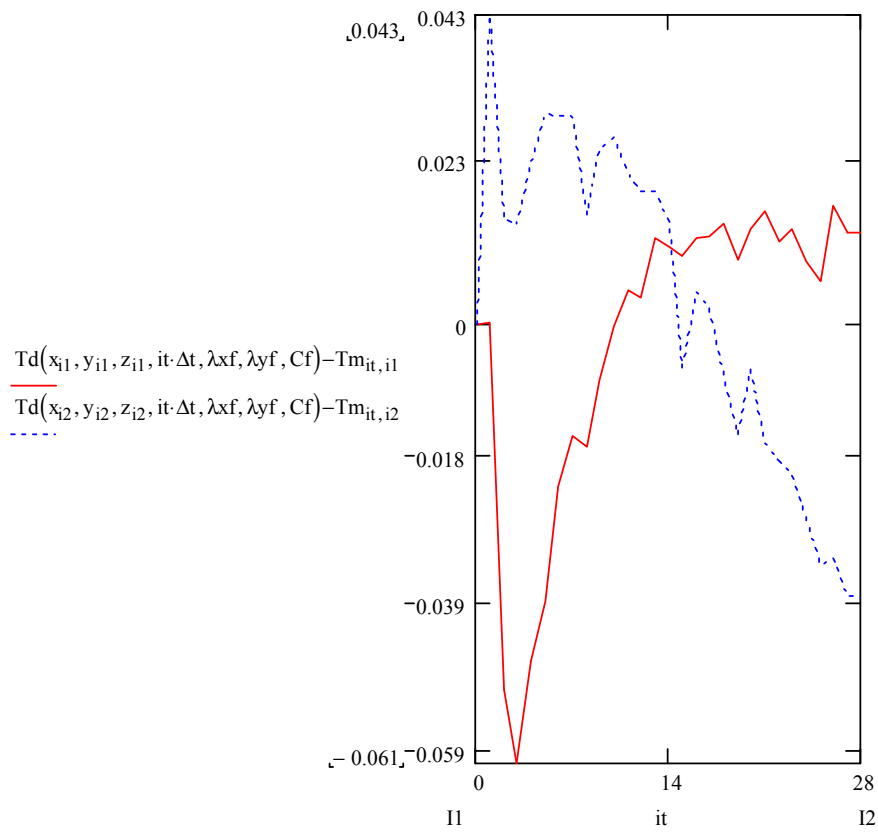
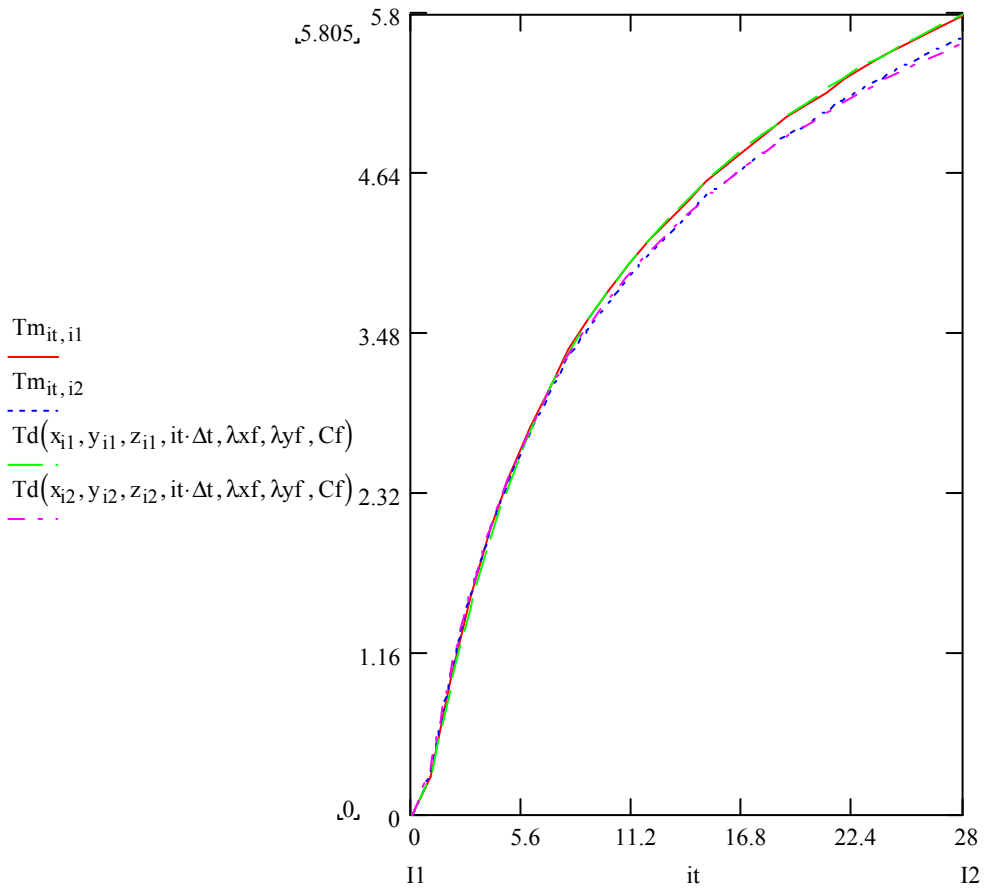
0-28

C4d4



Original coordinate measurements + MOVE 3 (A2)

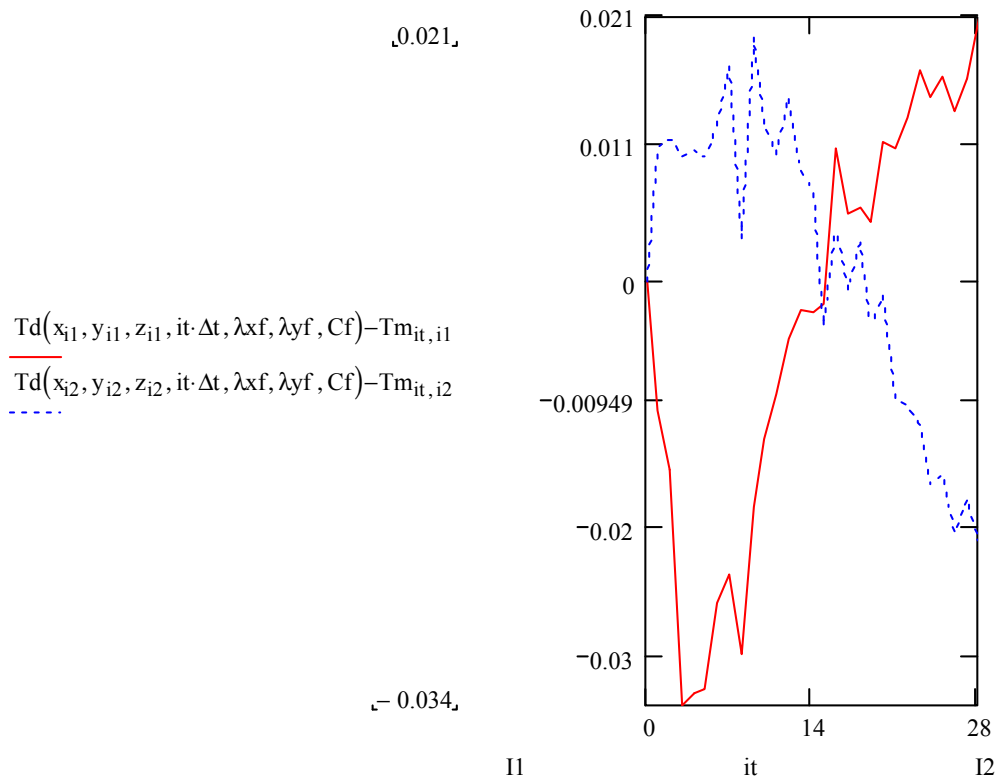
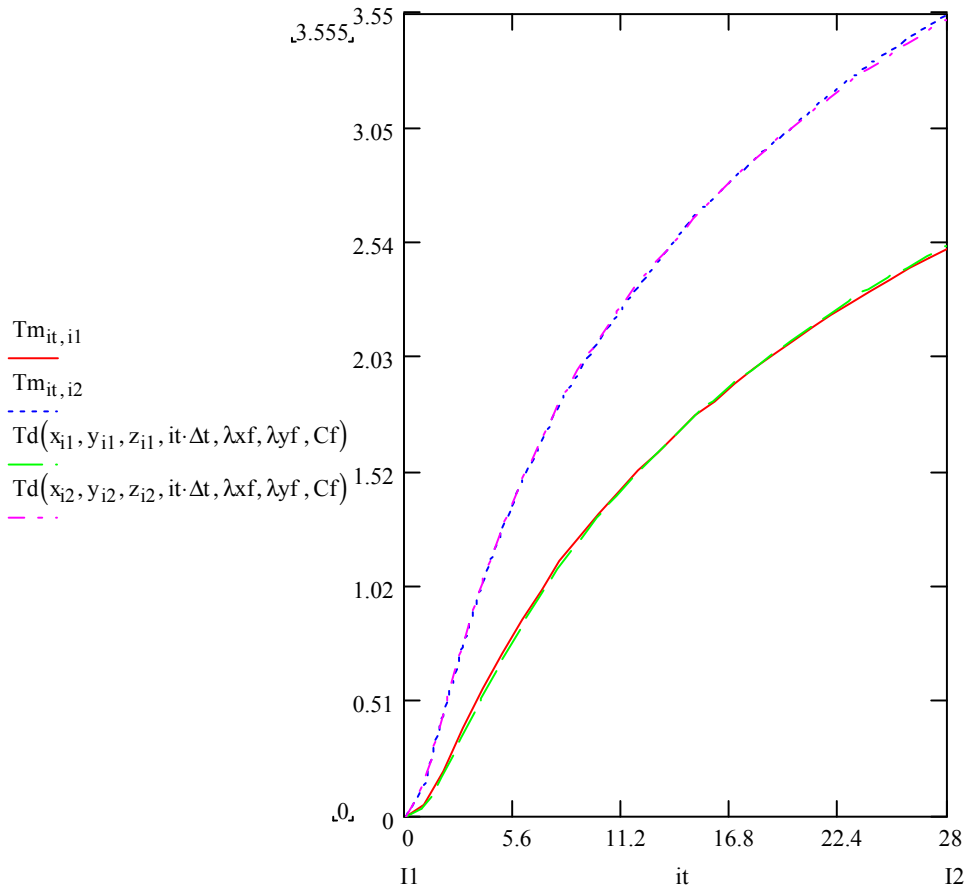
0-28
E4f4



Original coordinate measurements + MOVE 3 (A2)

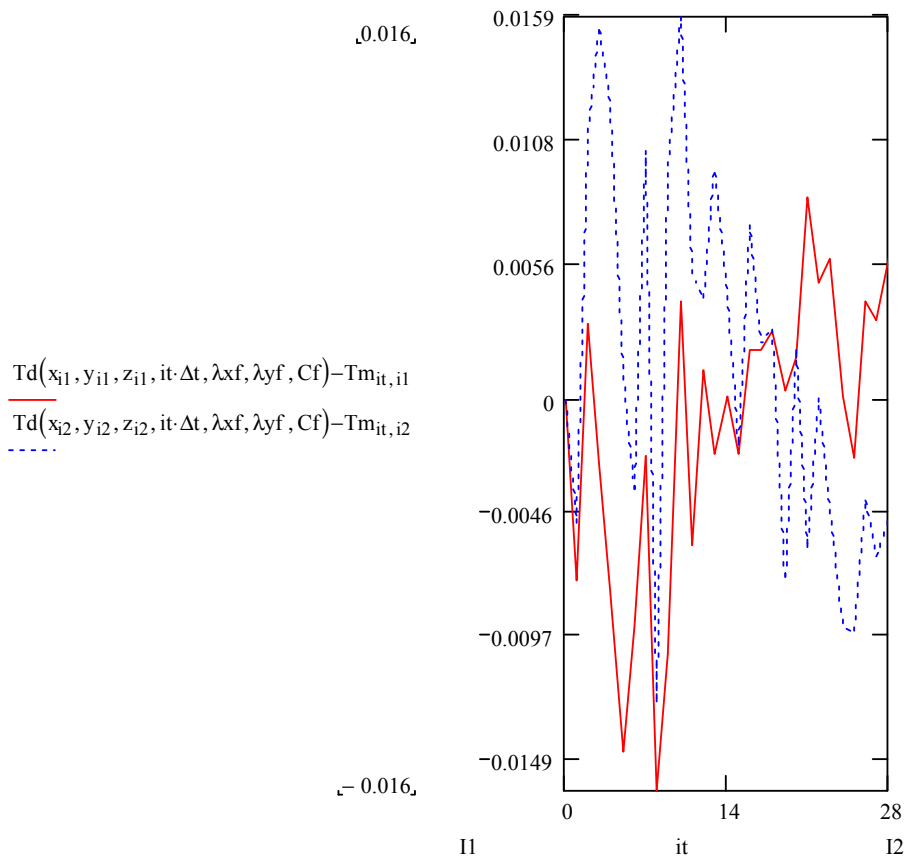
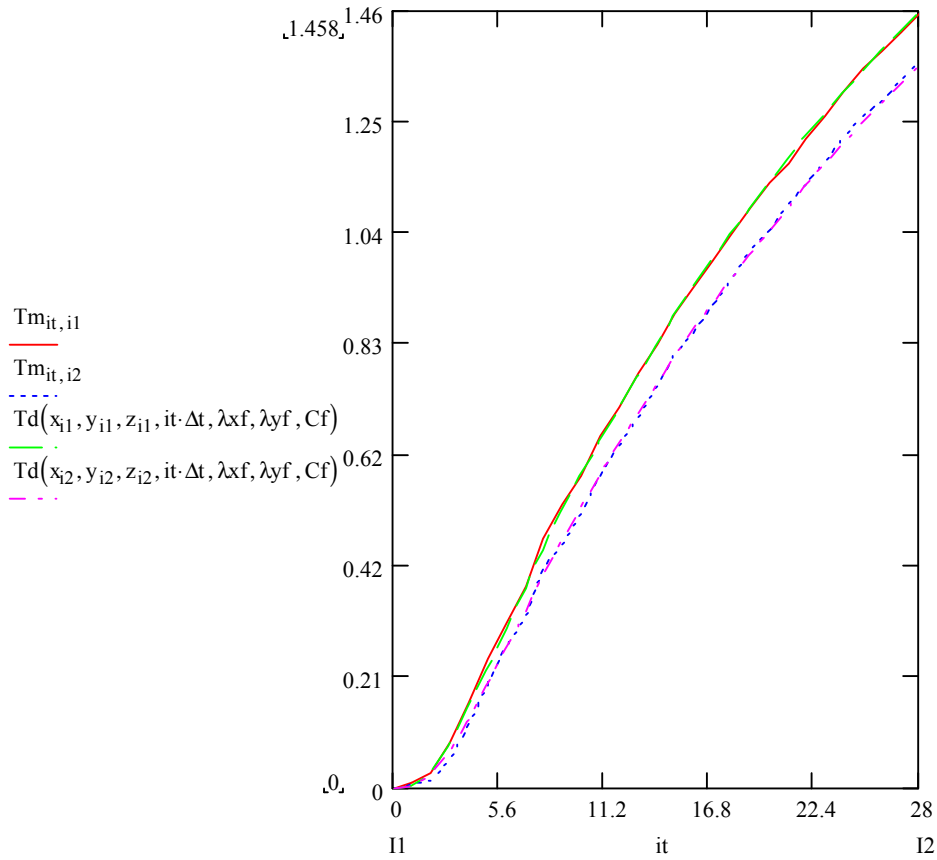
0-28

E5f5



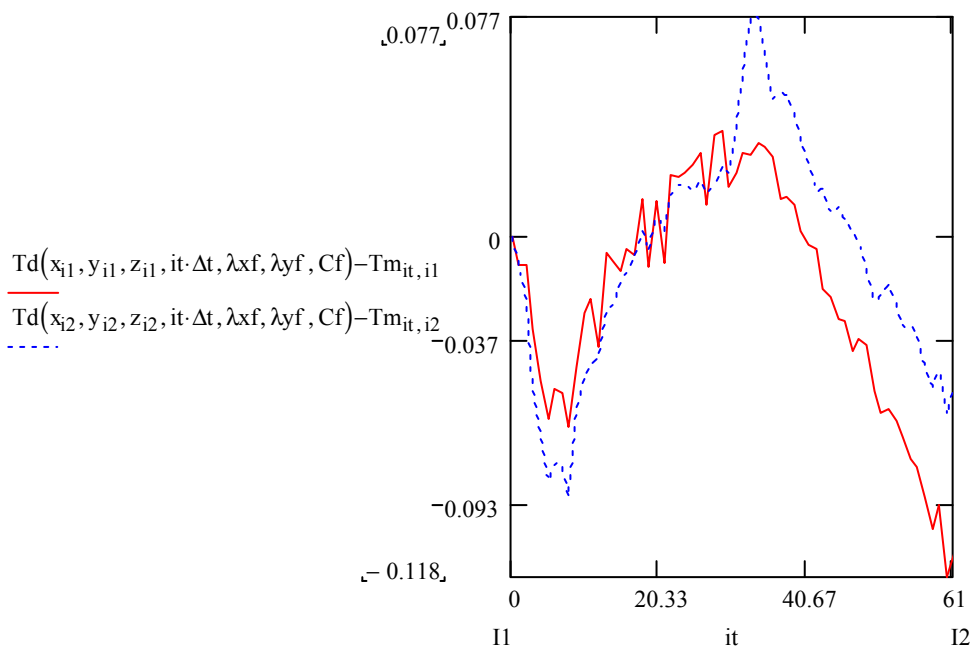
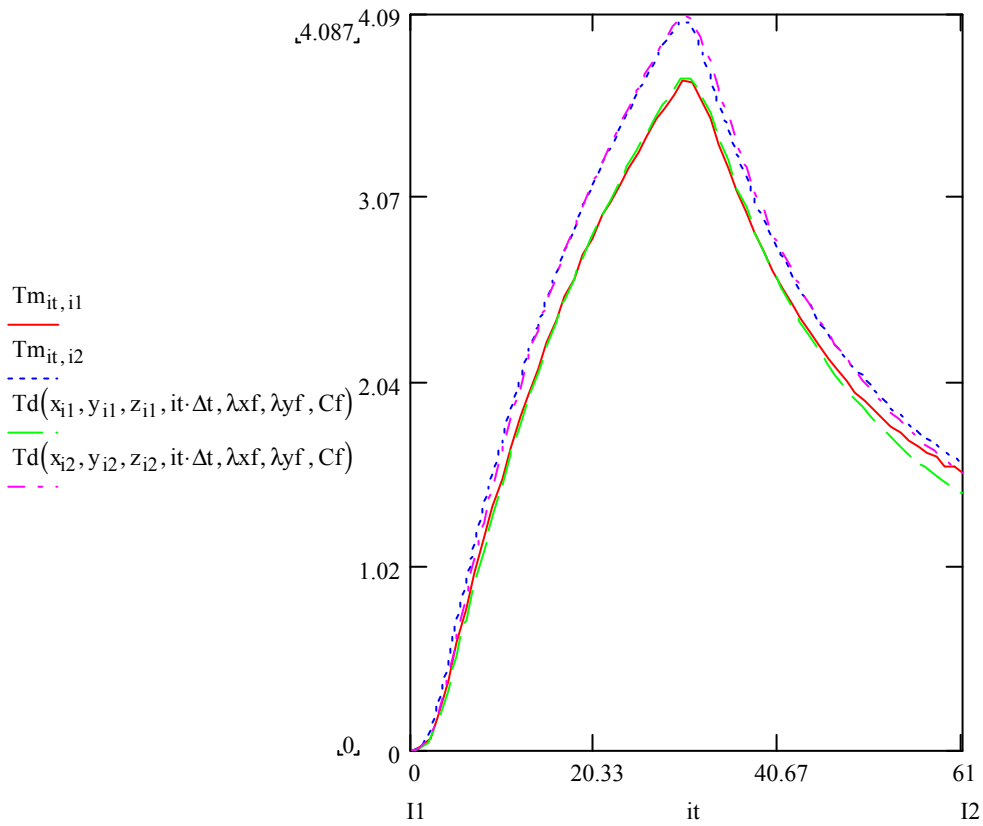
Original coordinate measurements + MOVE 3 (A2)

0-28
E6f6



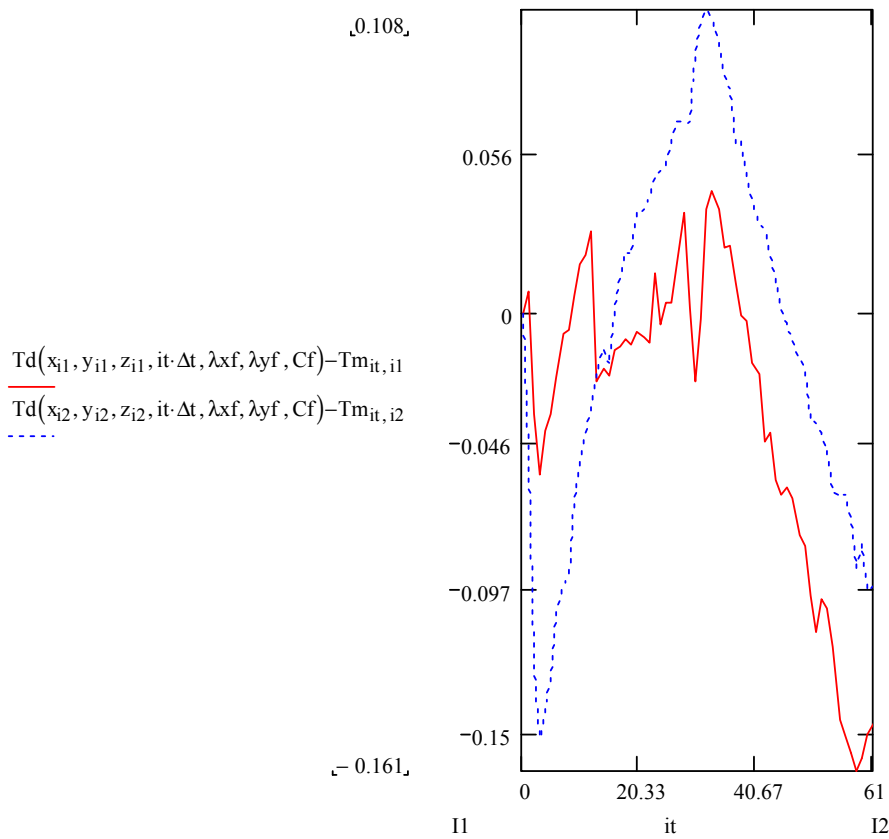
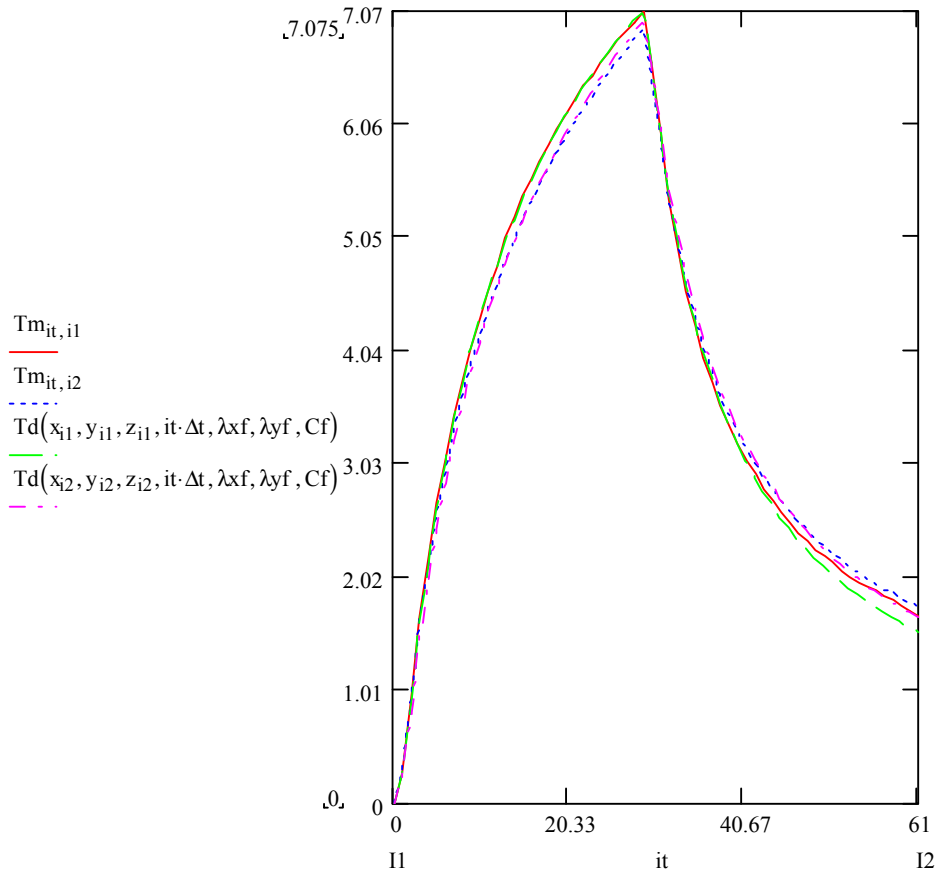
Original coordinate measurements + MOVE 3 (A2)

0-61
C1d1



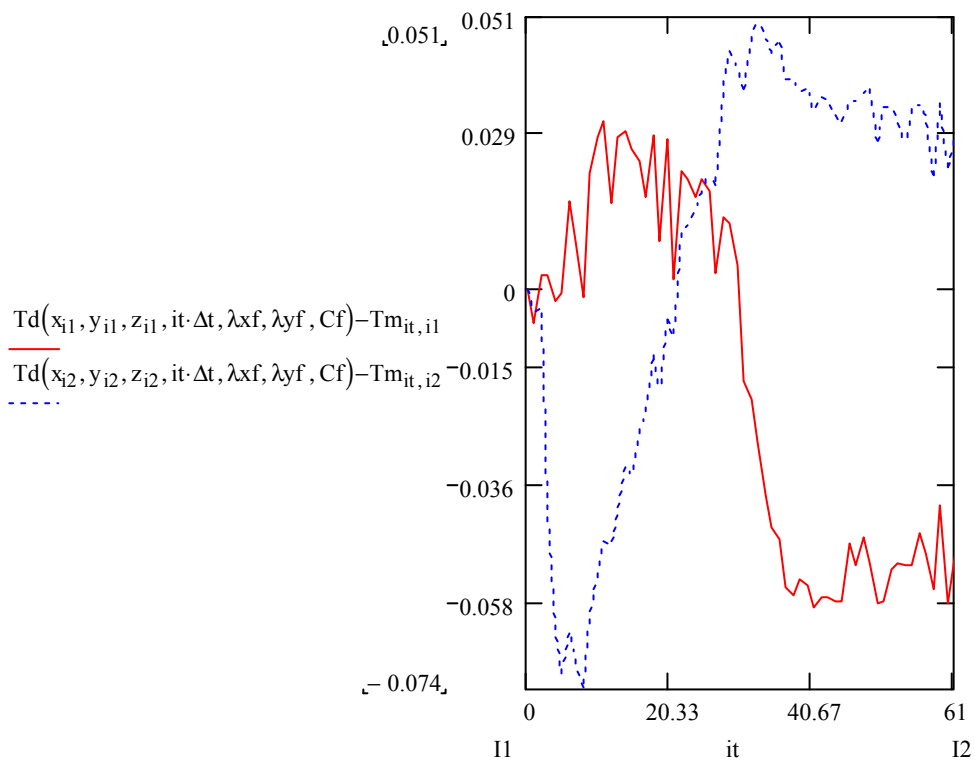
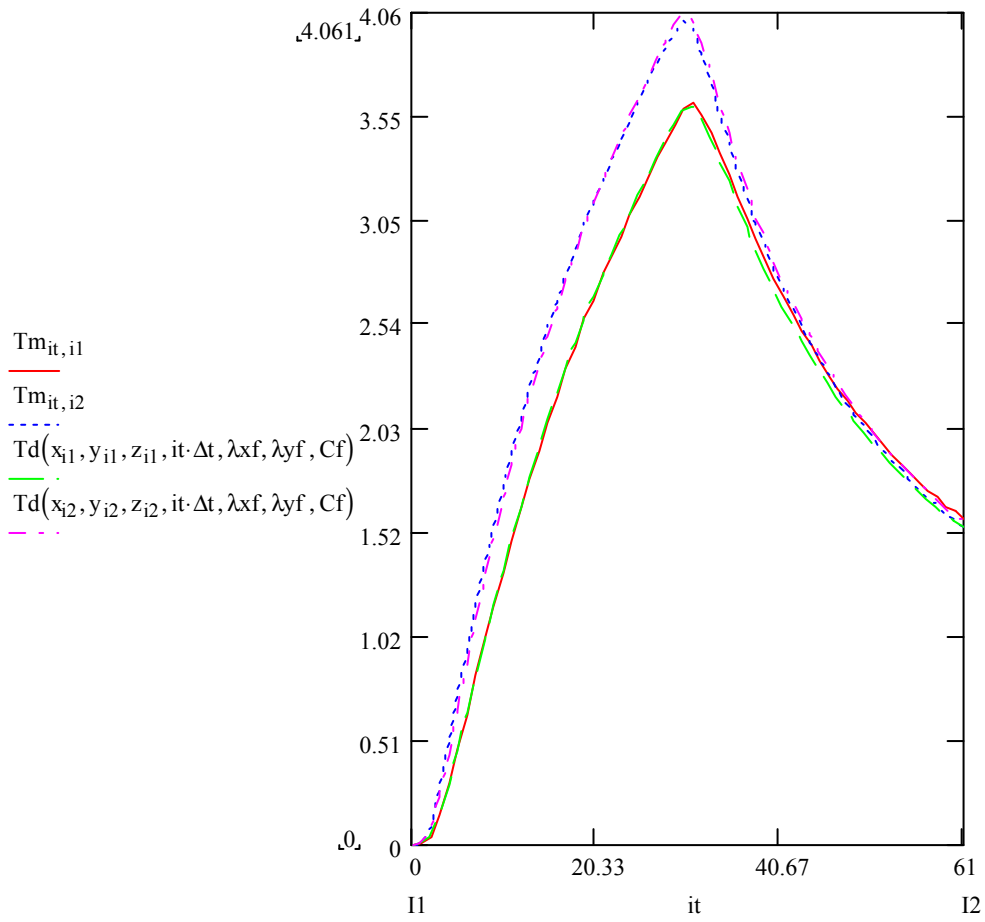
Original coordinate measurements + MOVE 3 (A2)

0-61
E1f1



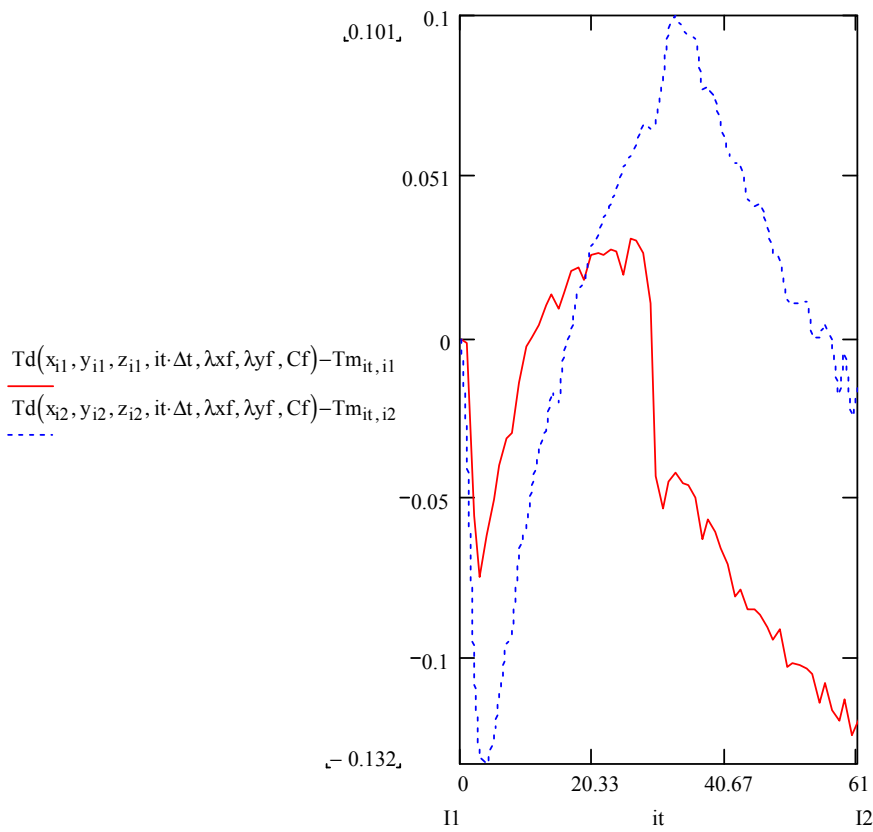
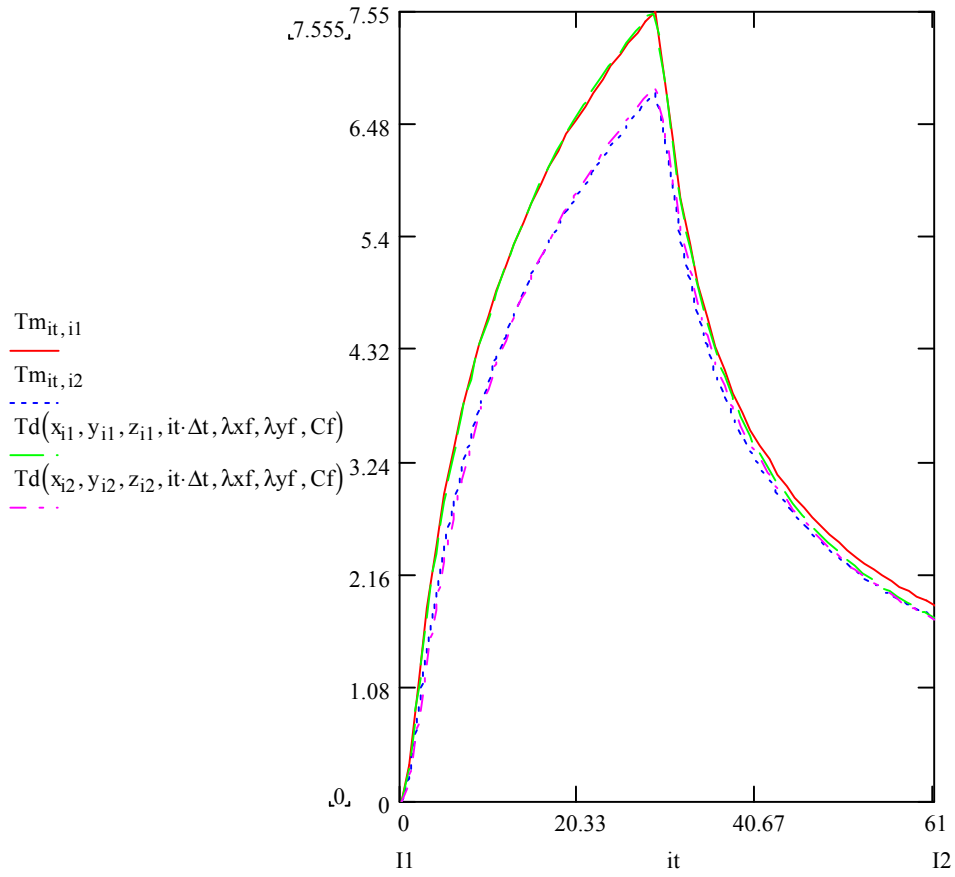
Original coordinate measurements + MOVE 3 (A2)

0-61
C2d2



Original coordinate measurements + MOVE 3 (A2)

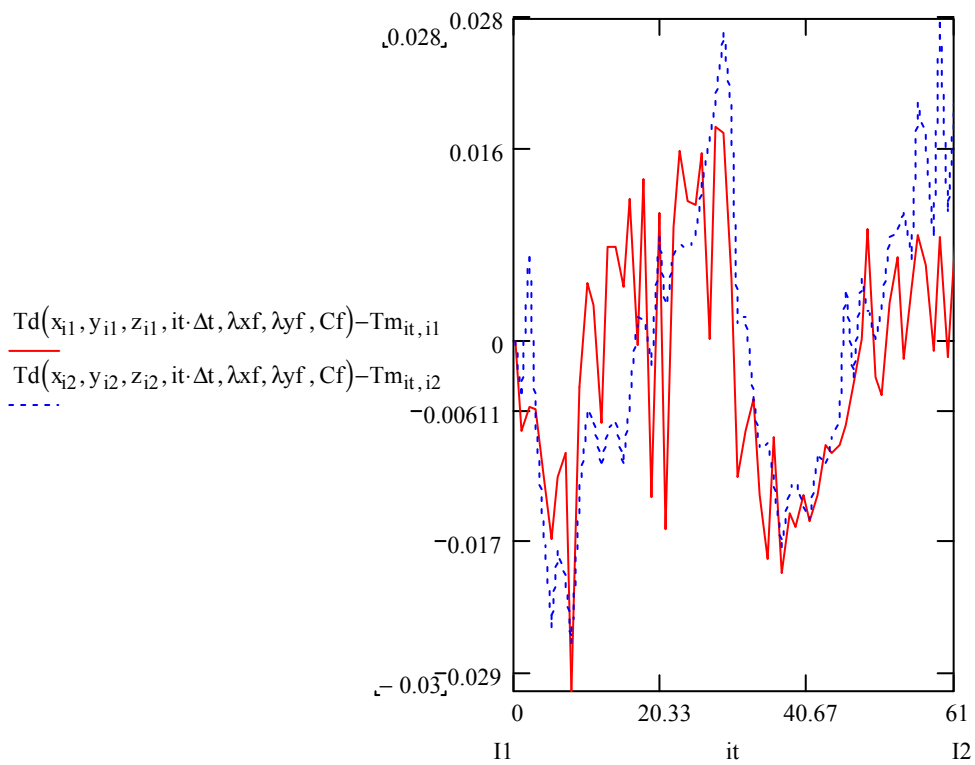
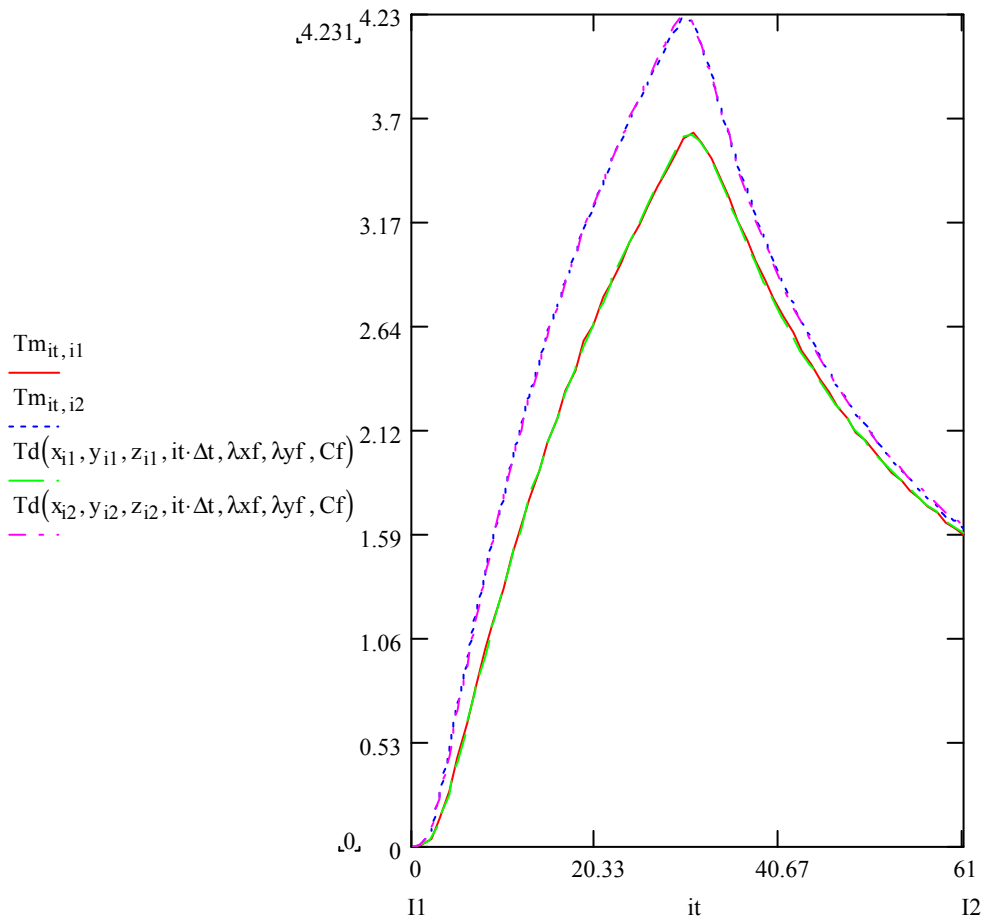
0-61
E2f2



Original coordinate measurements + MOVE 3 (A2)

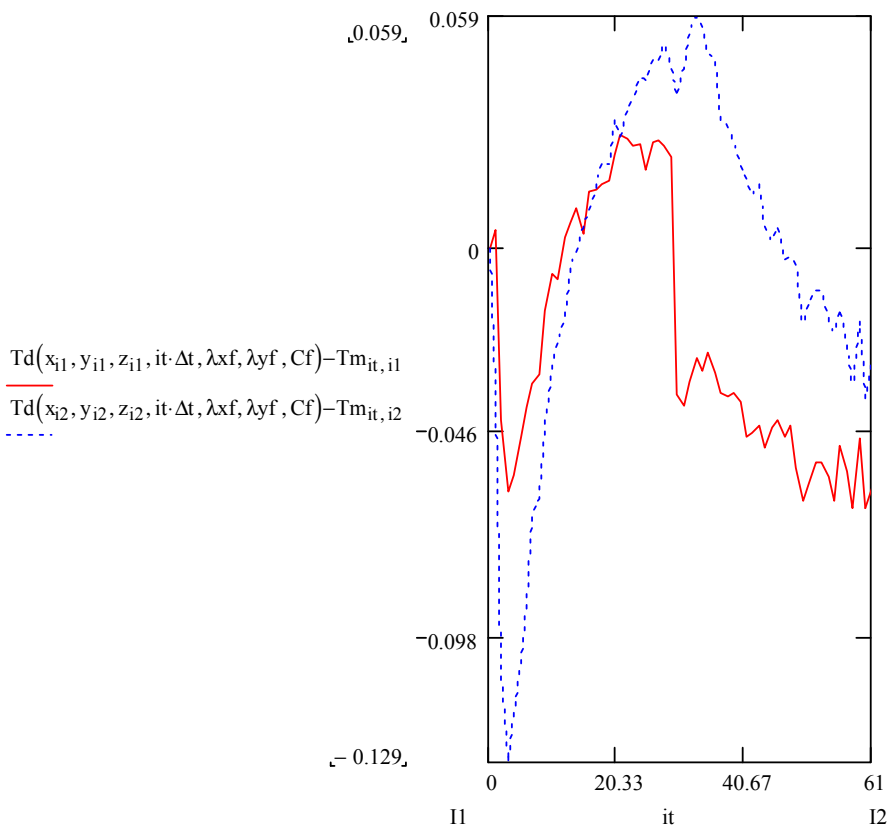
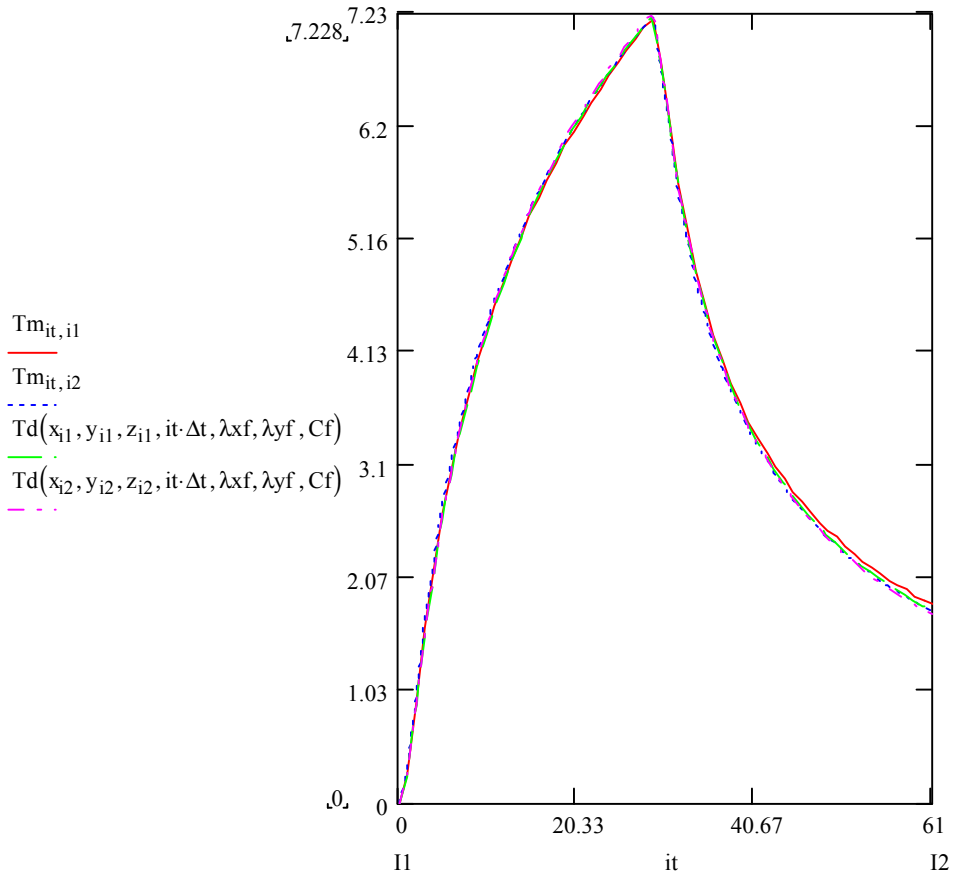
0-61

C3d3



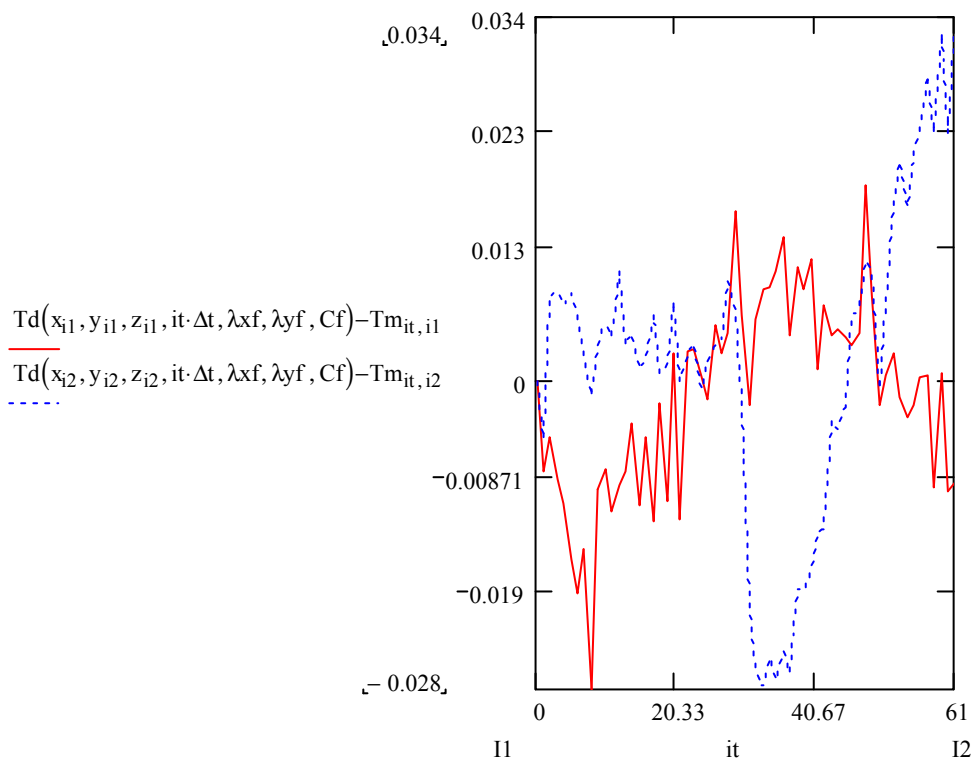
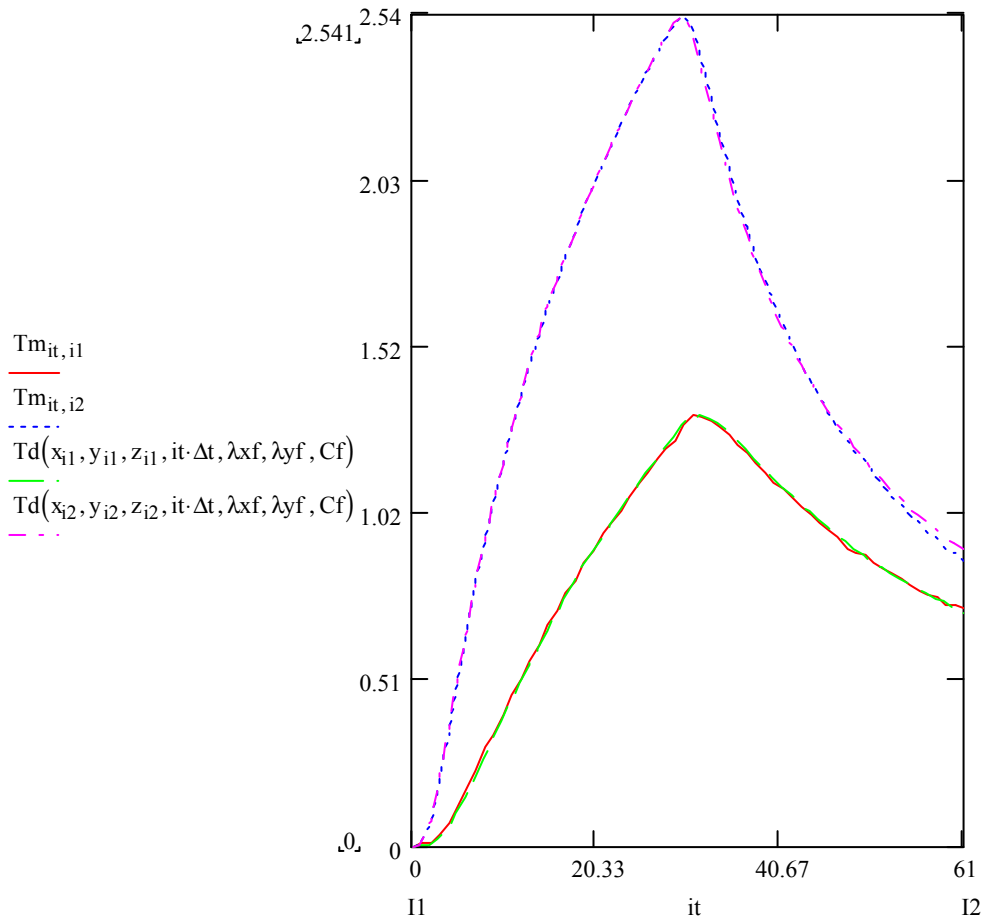
Original coordinate measurements + MOVE 3 (A2)

0-61
E3f3



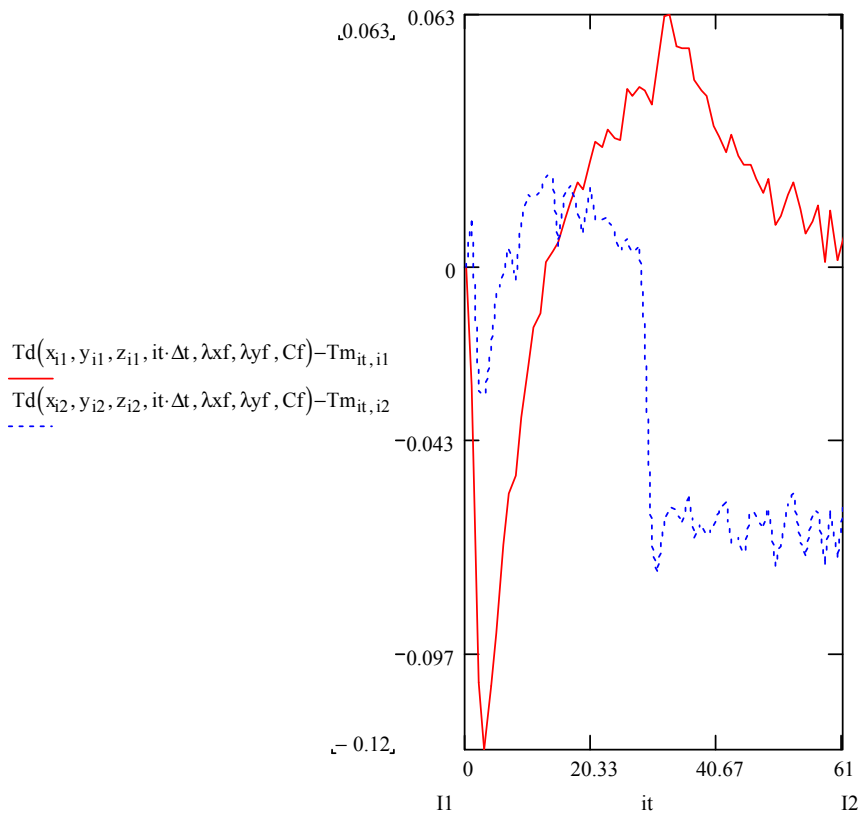
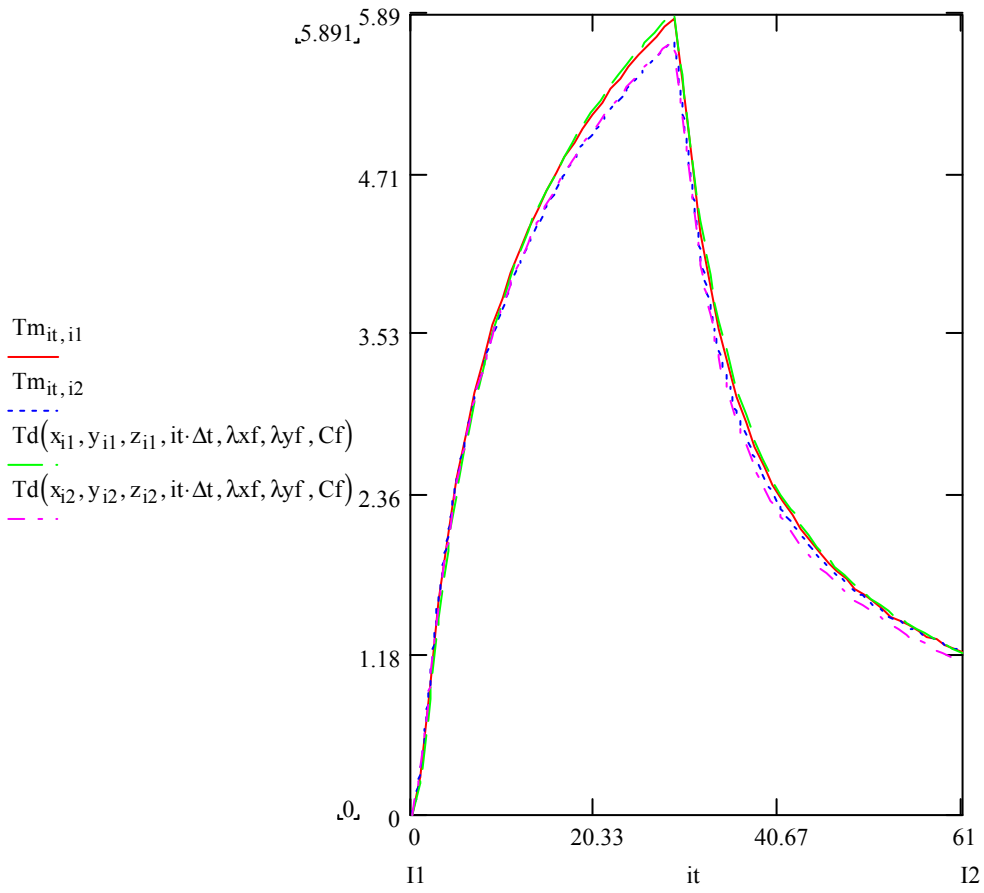
Original coordinate measurements + MOVE 3 (A2)

0-61
C4d4



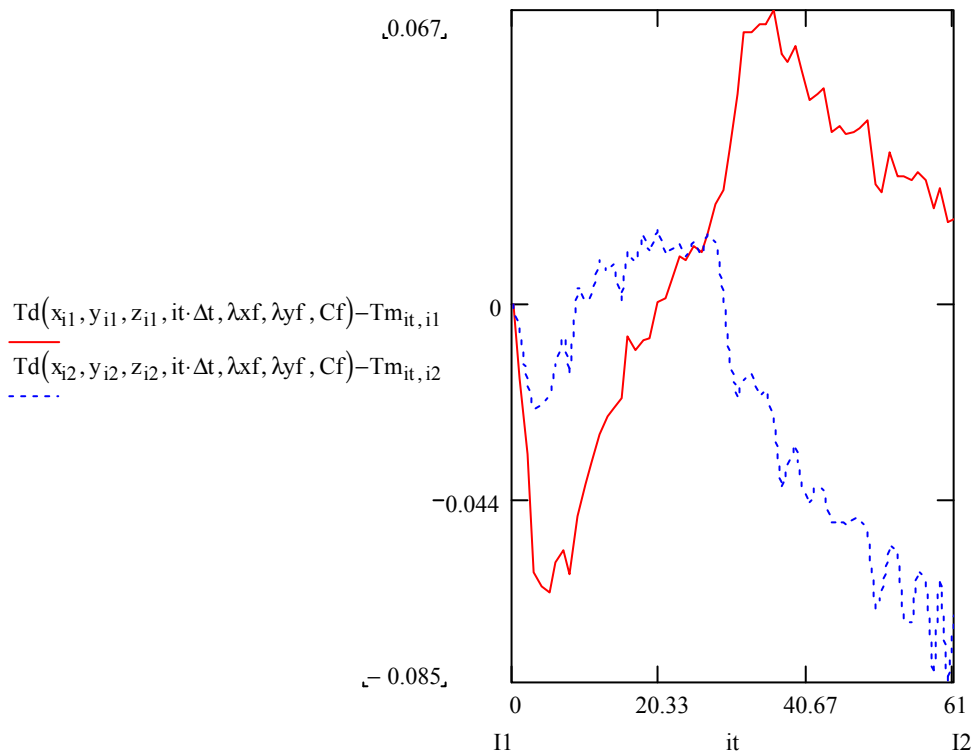
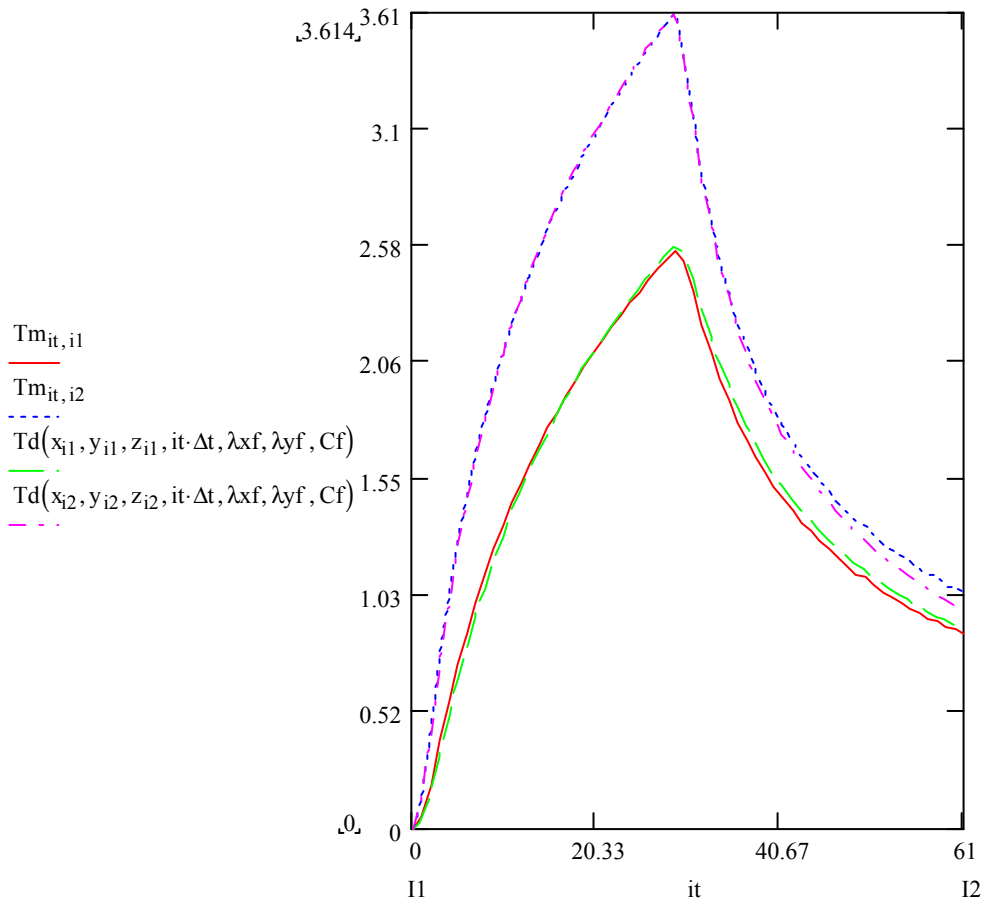
Original coordinate measurements + MOVE 3 (A2)

0-61
E4f4



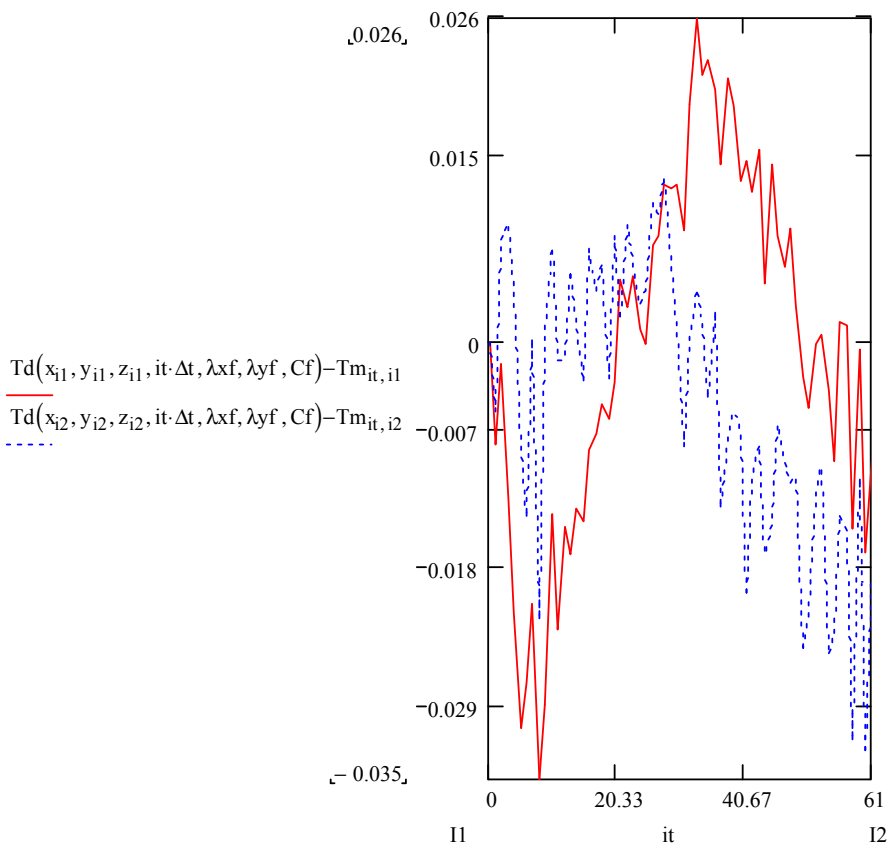
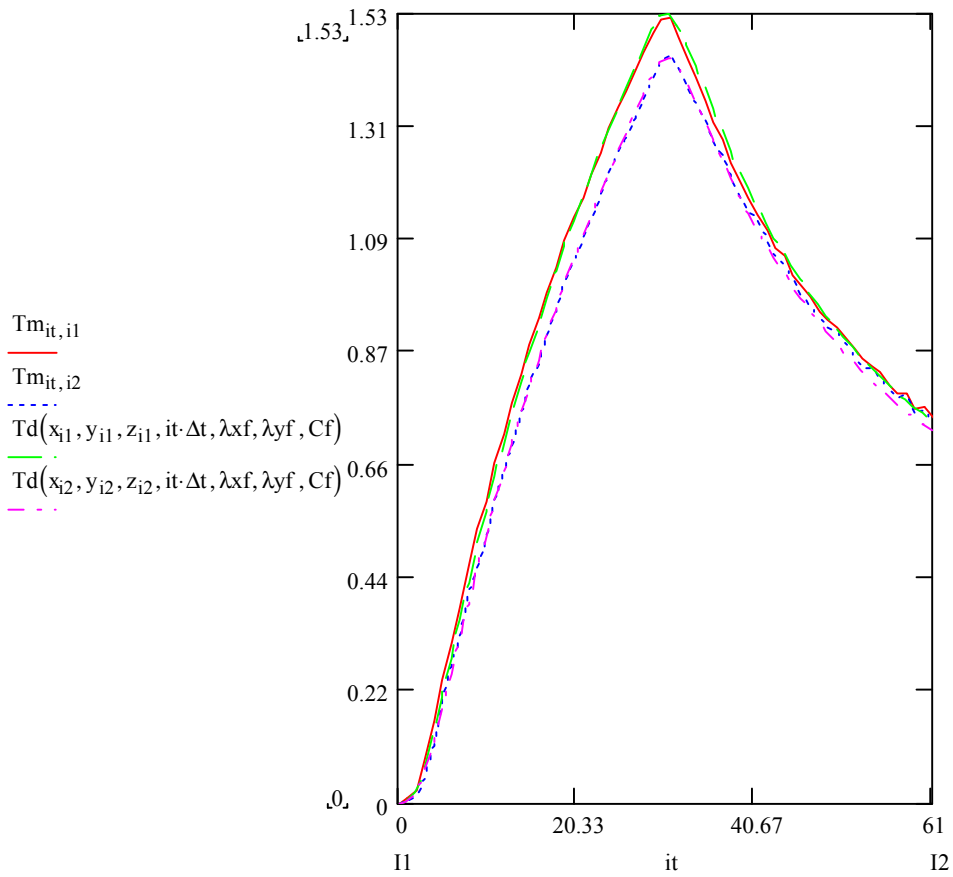
Original coordinate measurements + MOVE 3 (A2)

0-61
E5f5

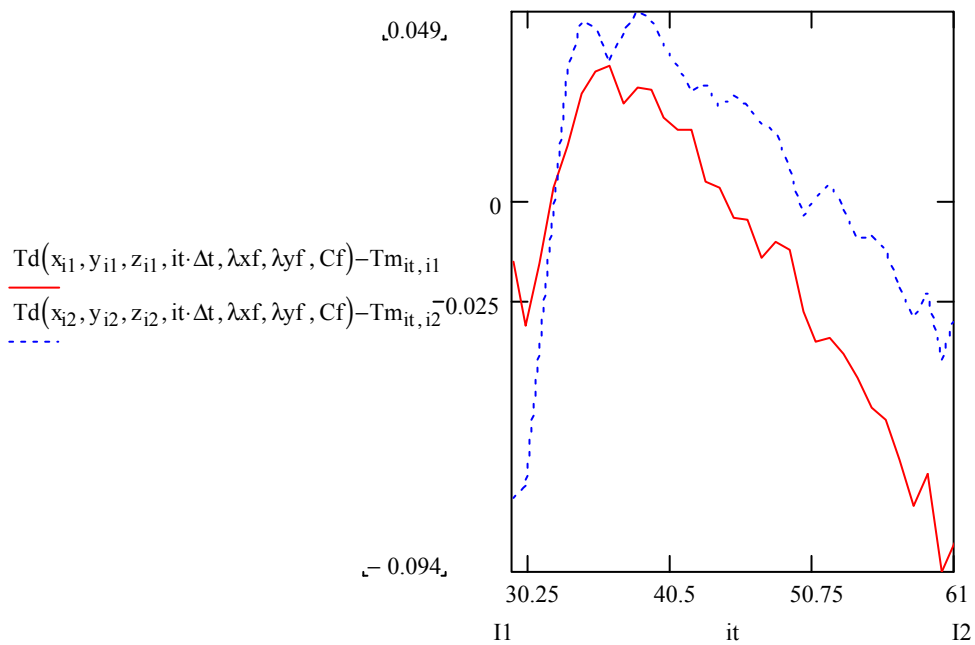
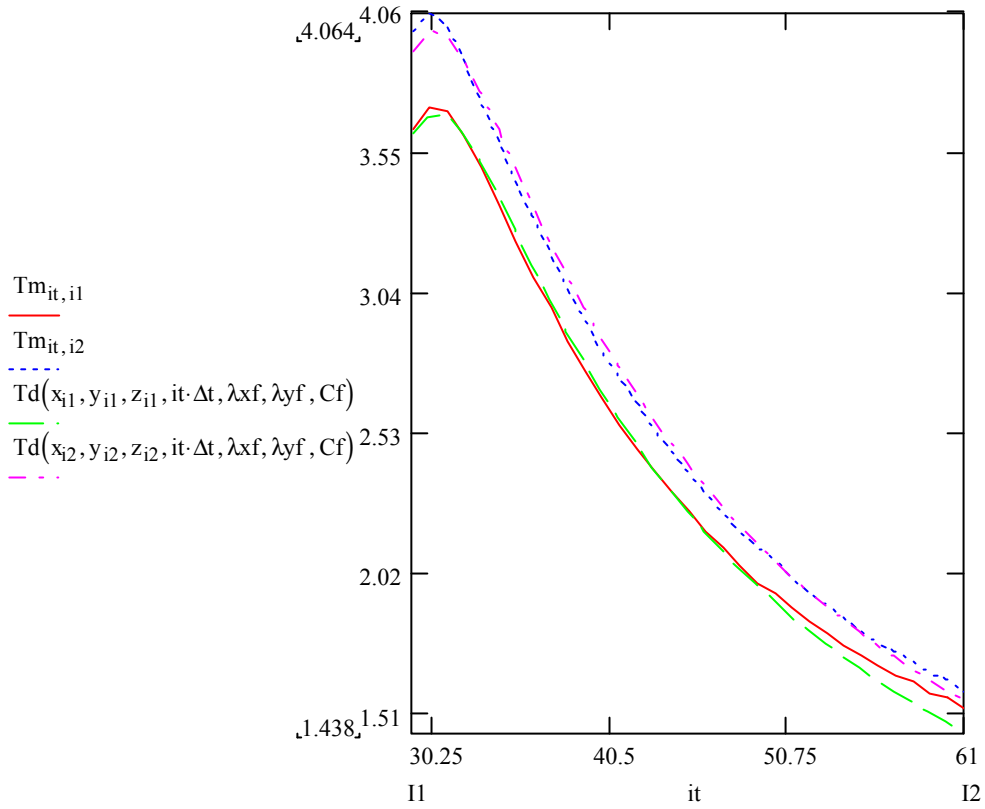


Original coordinate measurements + MOVE 3 (A2)

0-61
E6f6



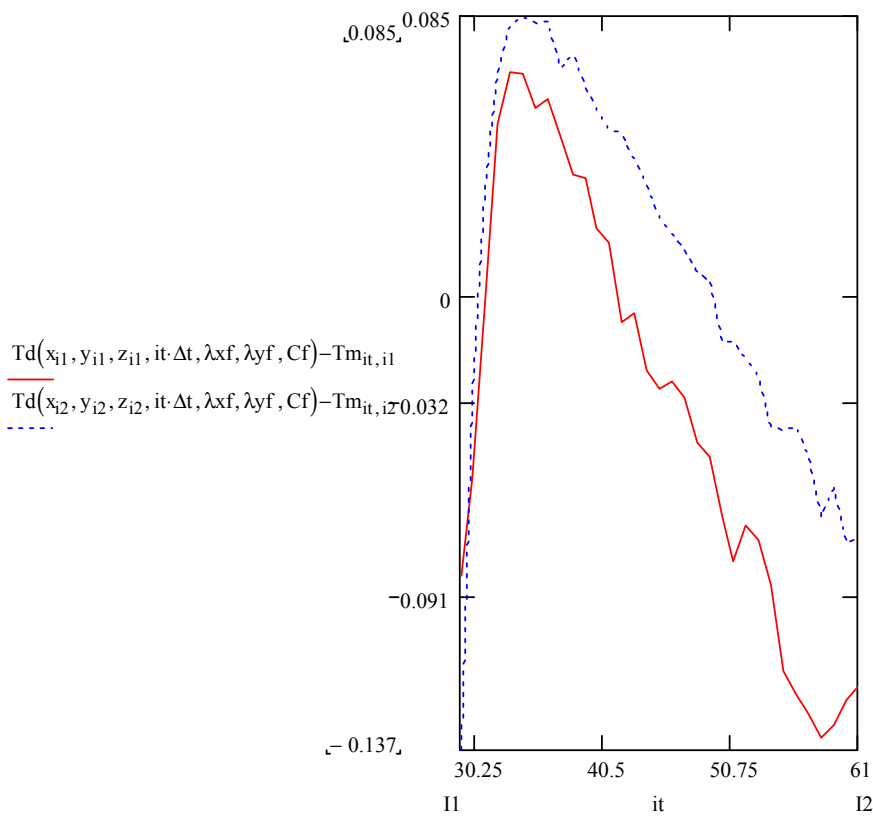
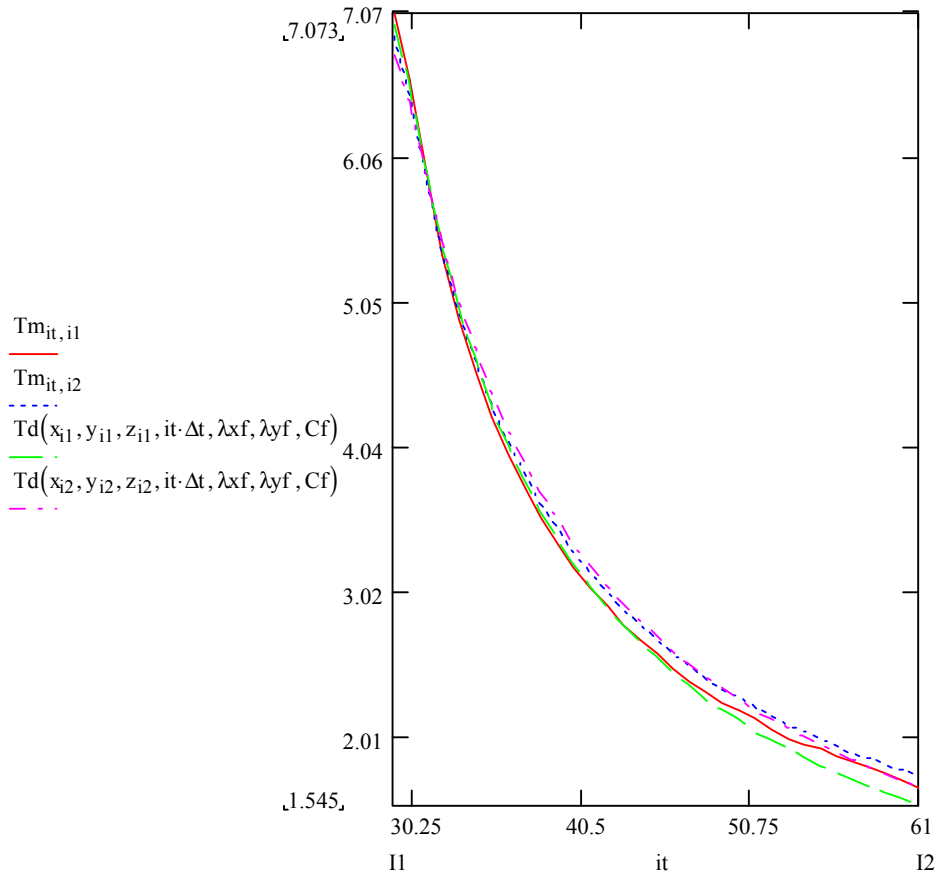
Original coordinate measurements + MOVE 3 (A2)
 29-61
 C1d1



Original coordinate measurements + MOVE 3 (A2)

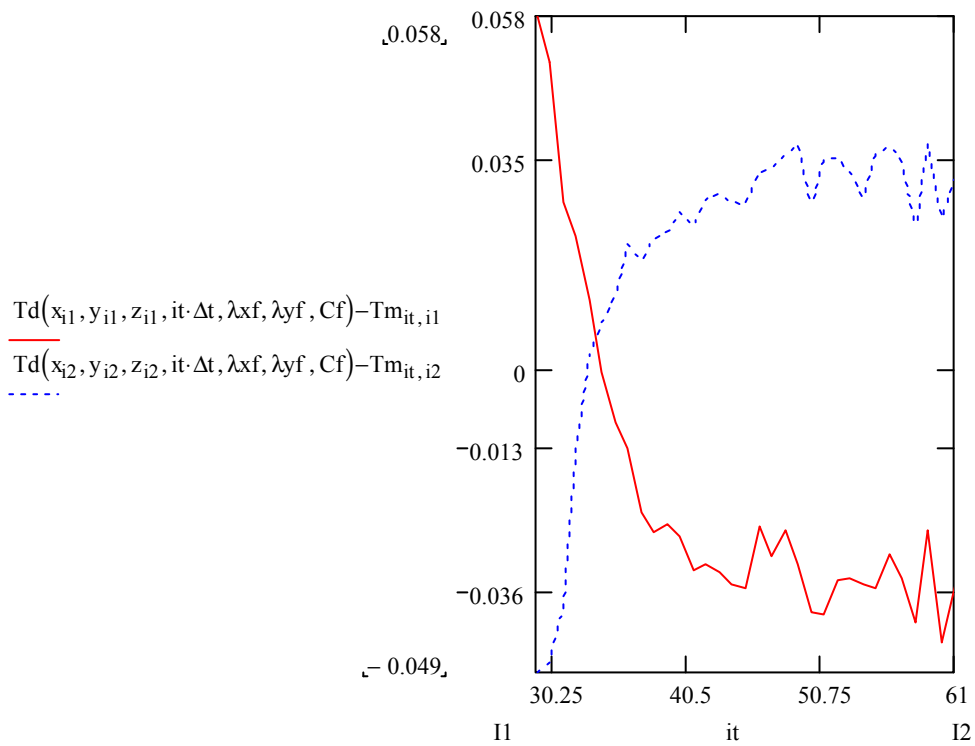
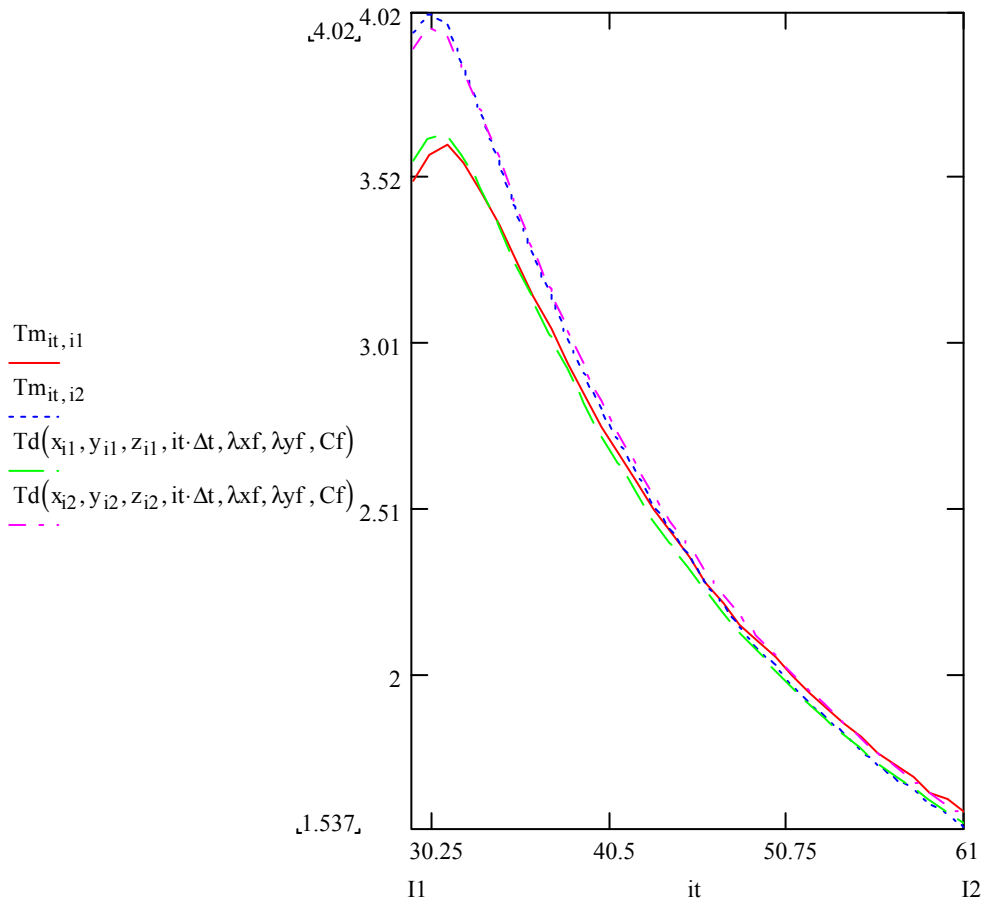
29-61

E1f1



Original coordinate measurements + MOVE 3 (A2)

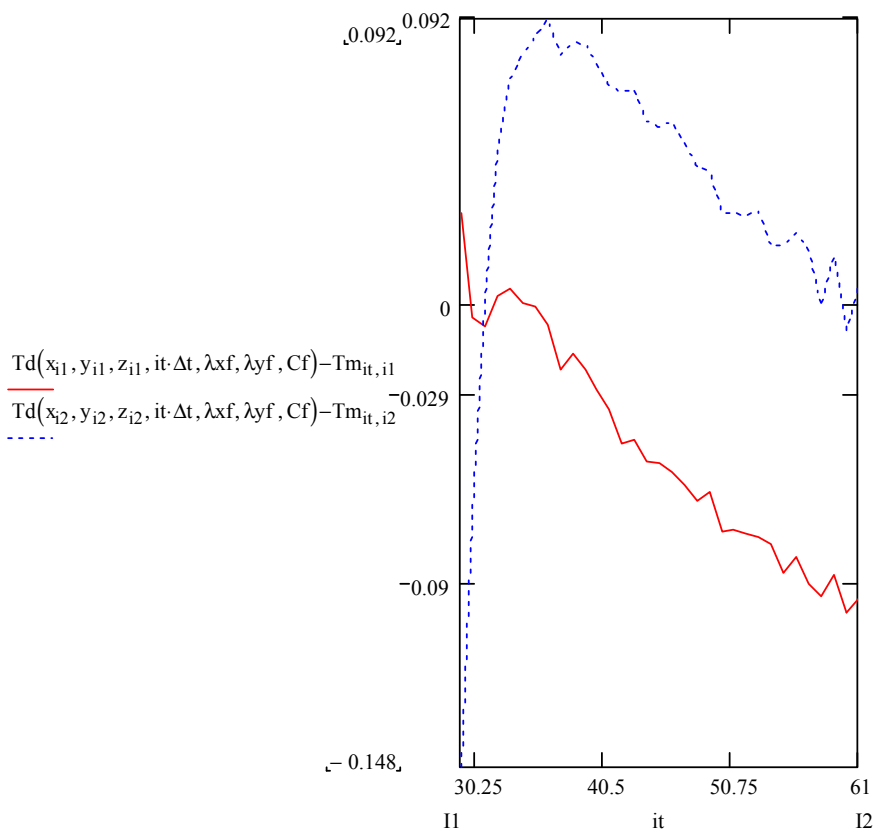
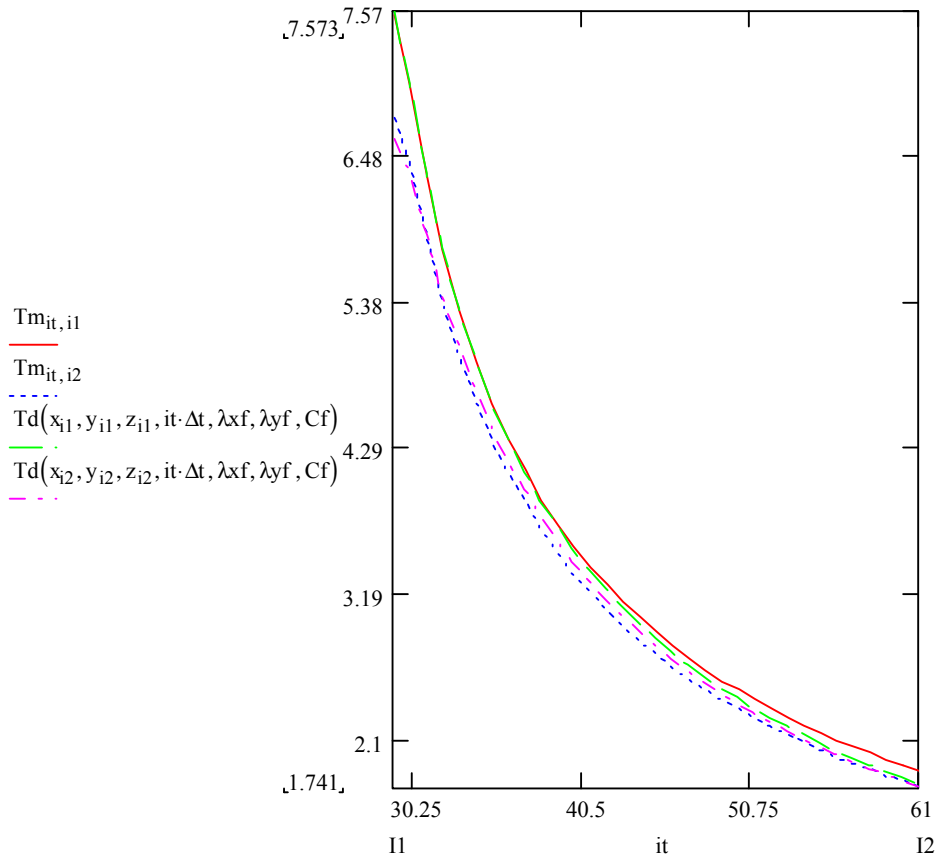
29-61
C2d2



Original coordinate measurements + MOVE 3 (A2)

29-61

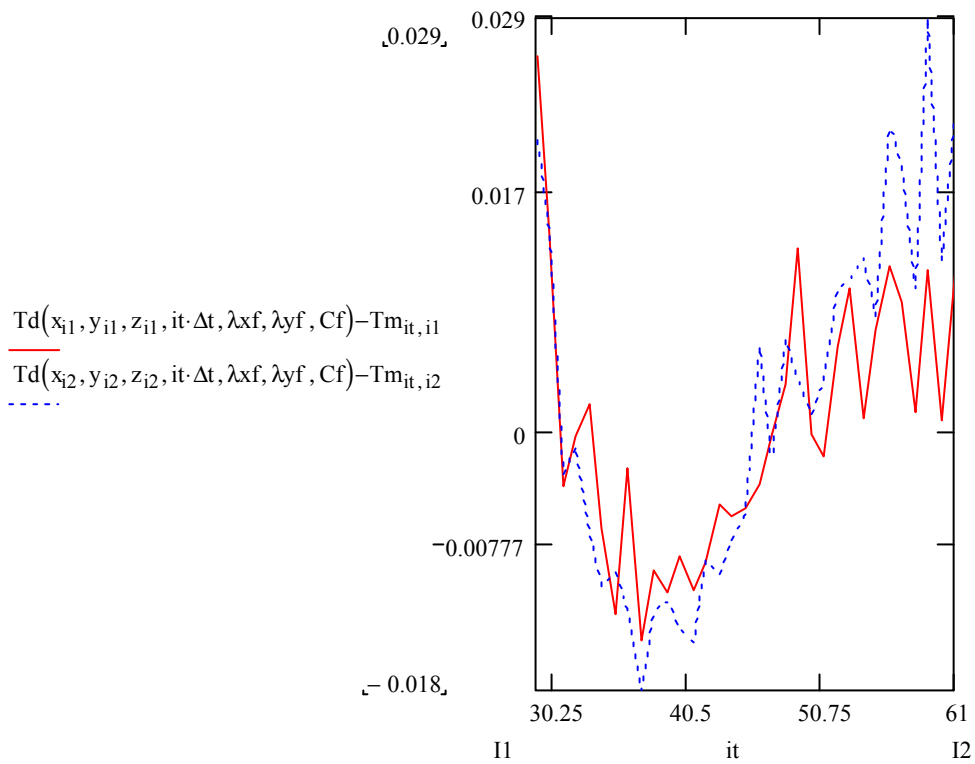
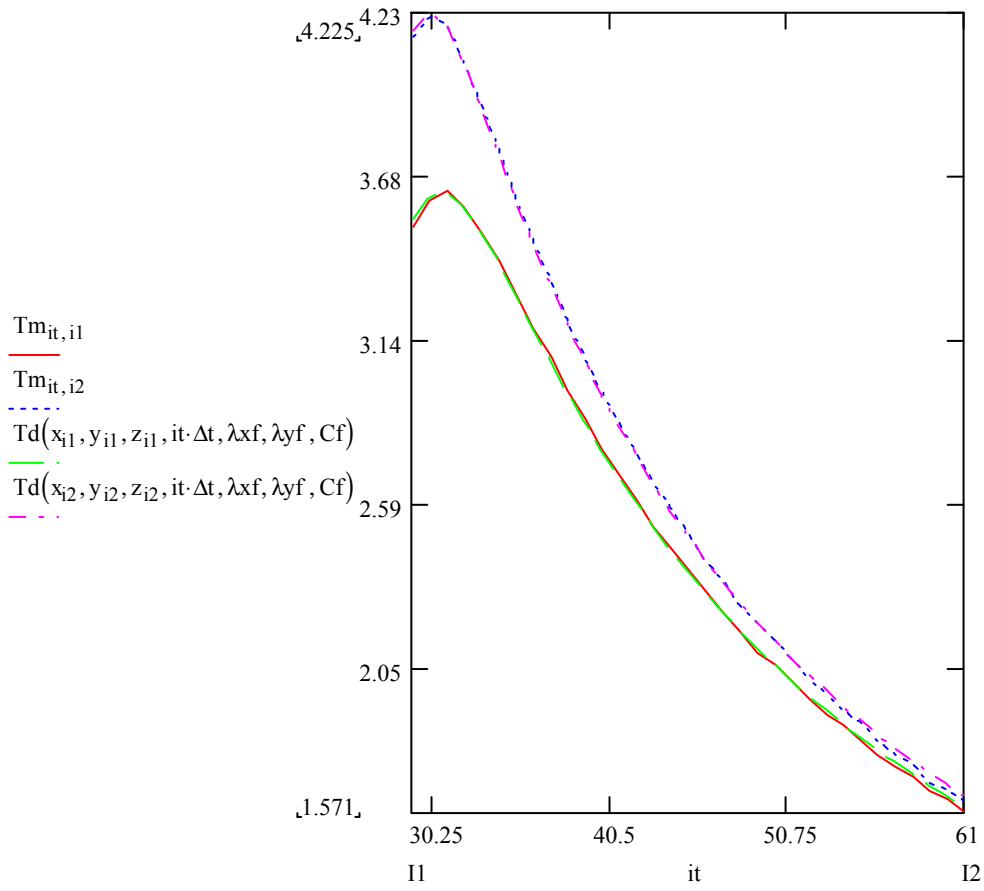
E2f2



Original coordinate measurements + MOVE 3 (A2)

29-61

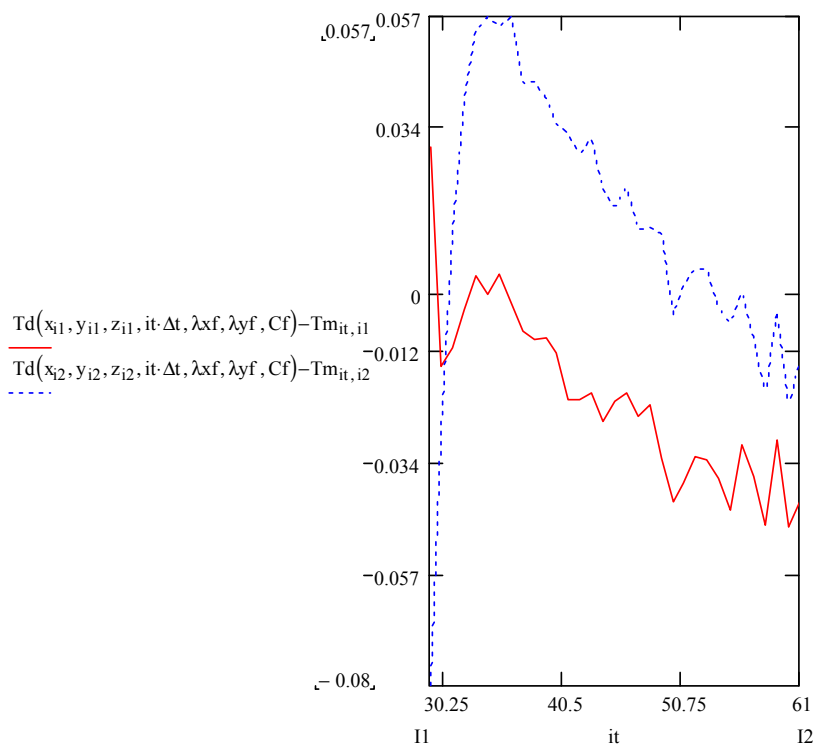
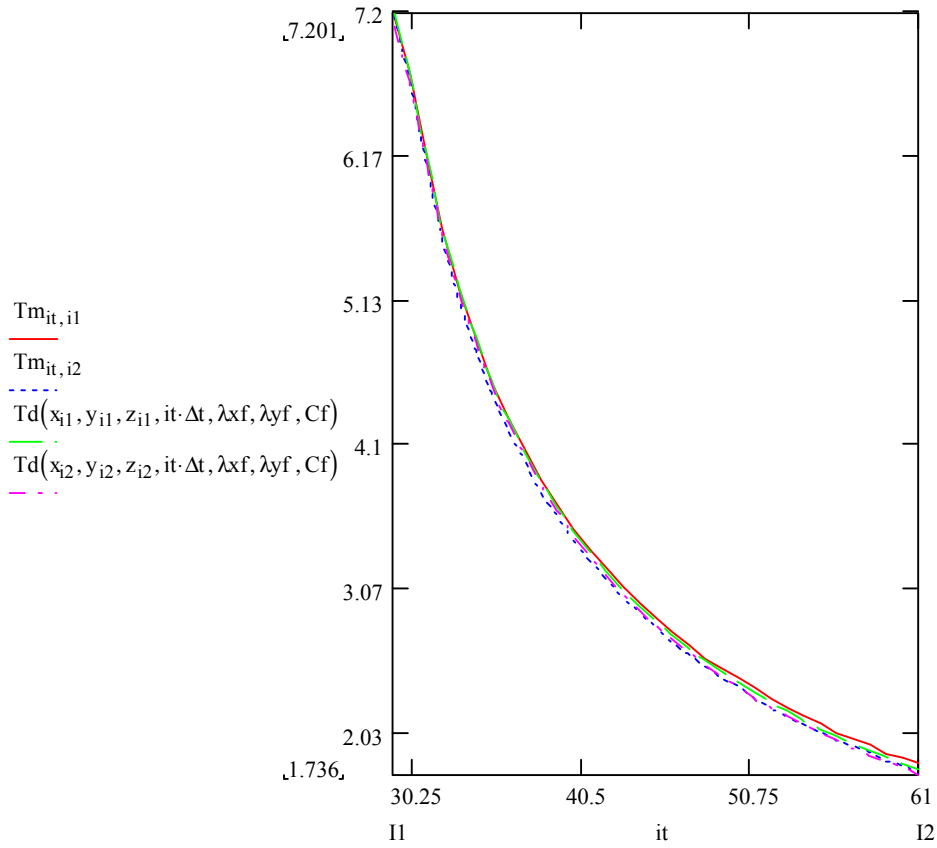
C3d3



Original coordinate measurements + MOVE 3 (A2)

29-61

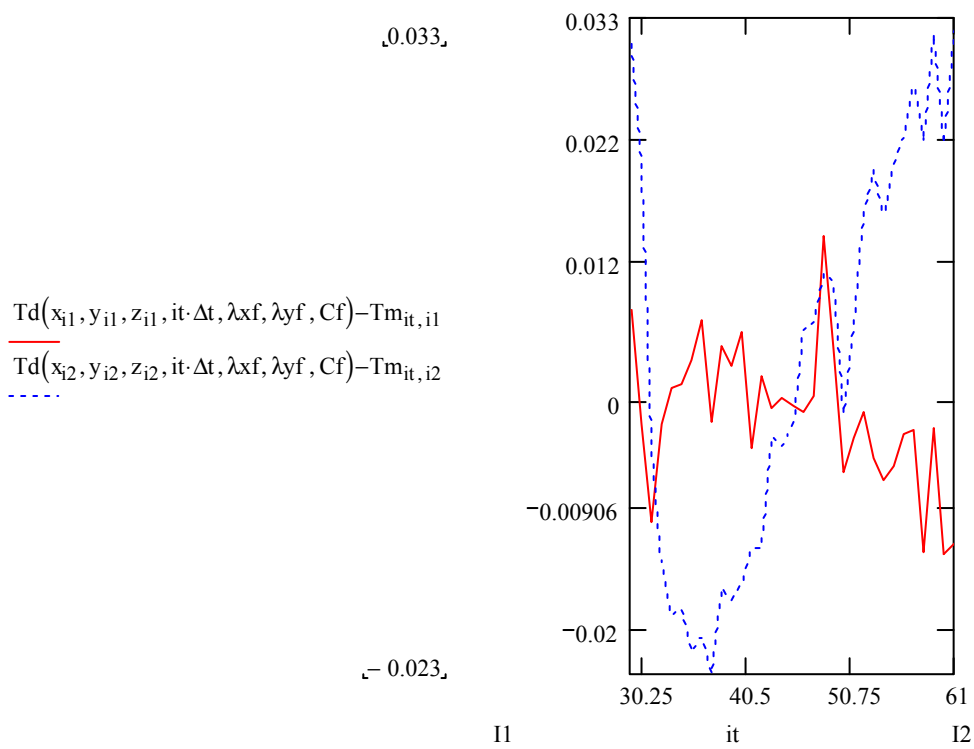
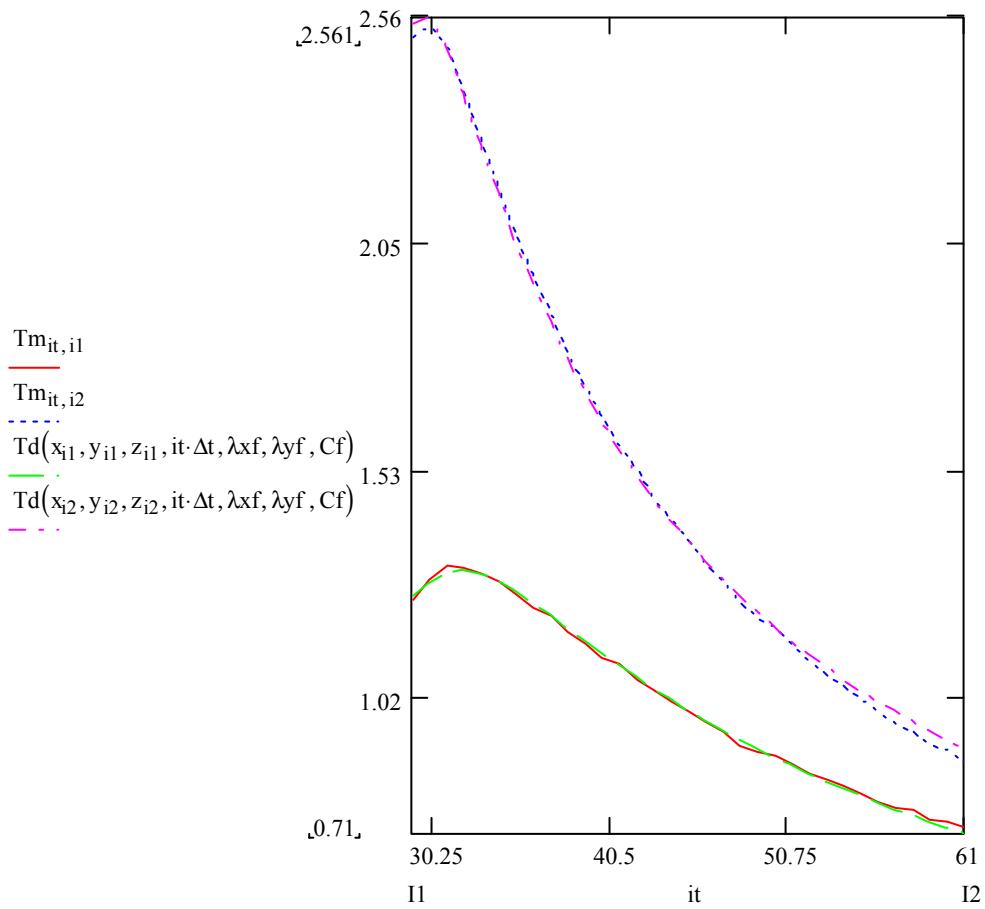
E3f3



Original coordinate measurements + MOVE 3 (A2)

29-61

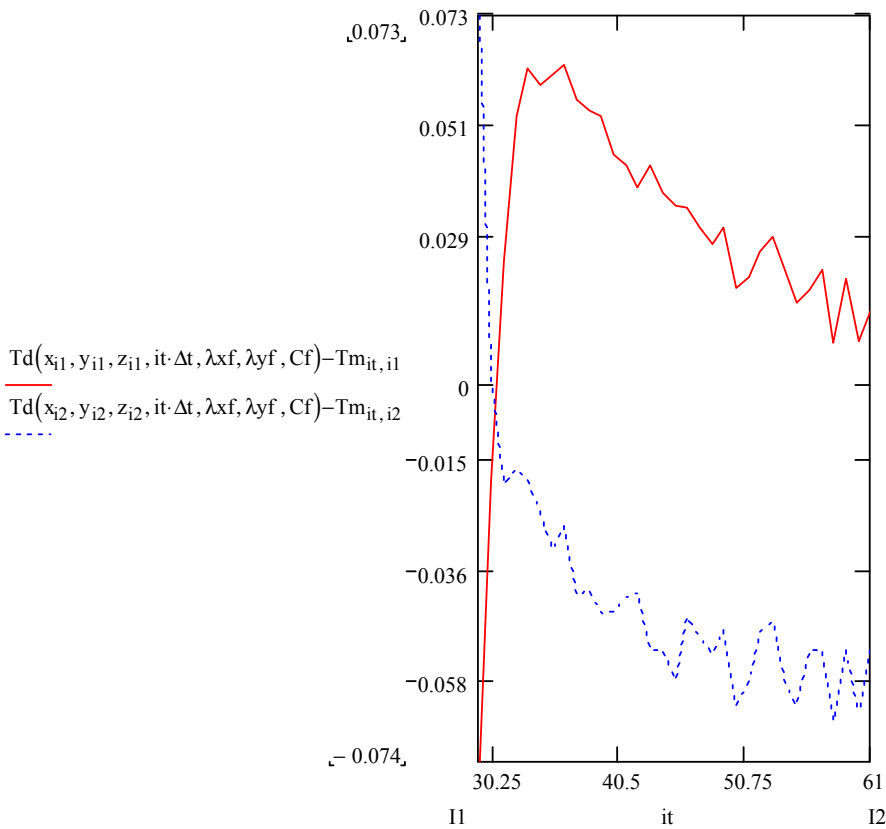
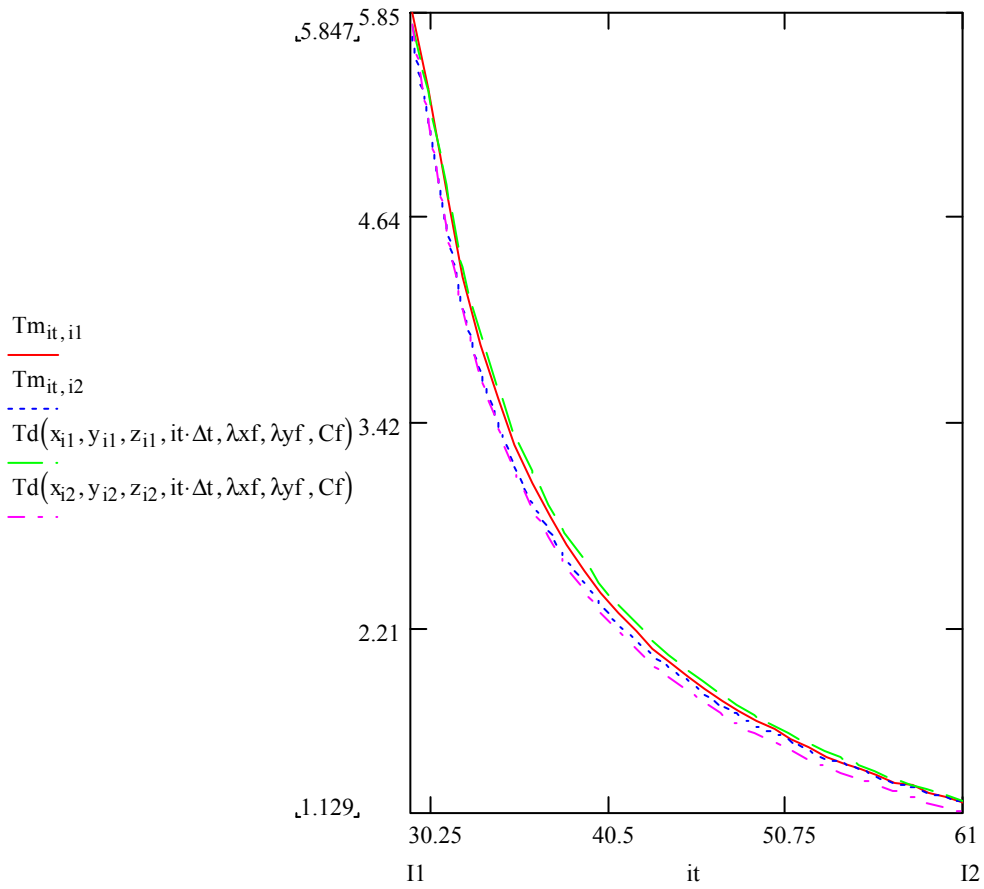
C4d4



Original coordinate measurements + MOVE 3 (A2)

29-61

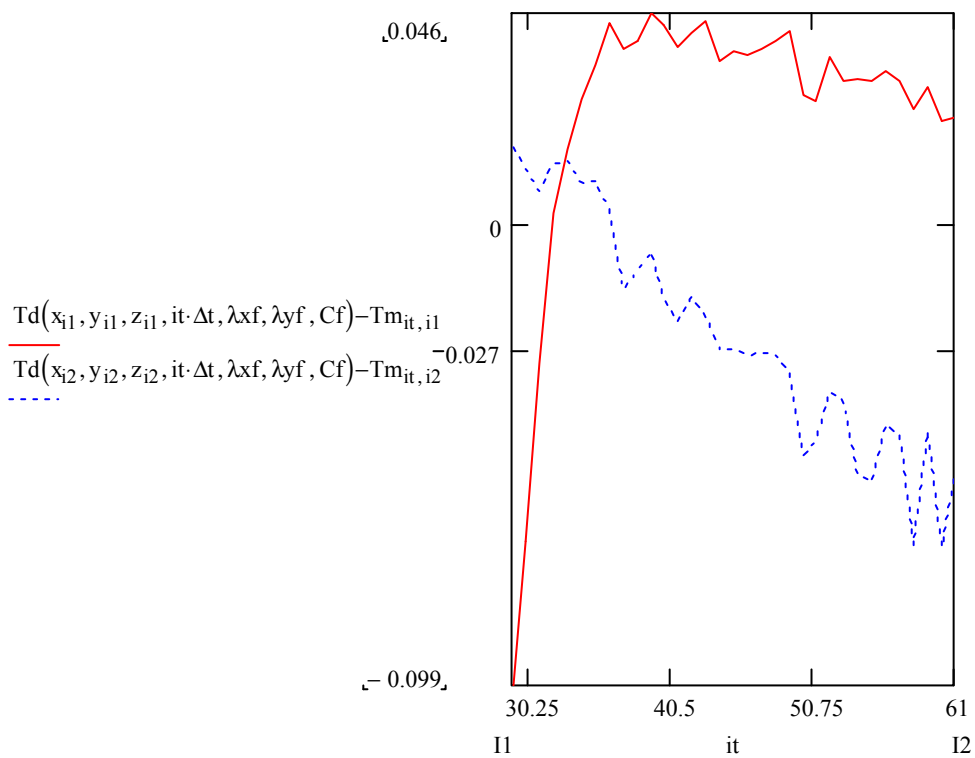
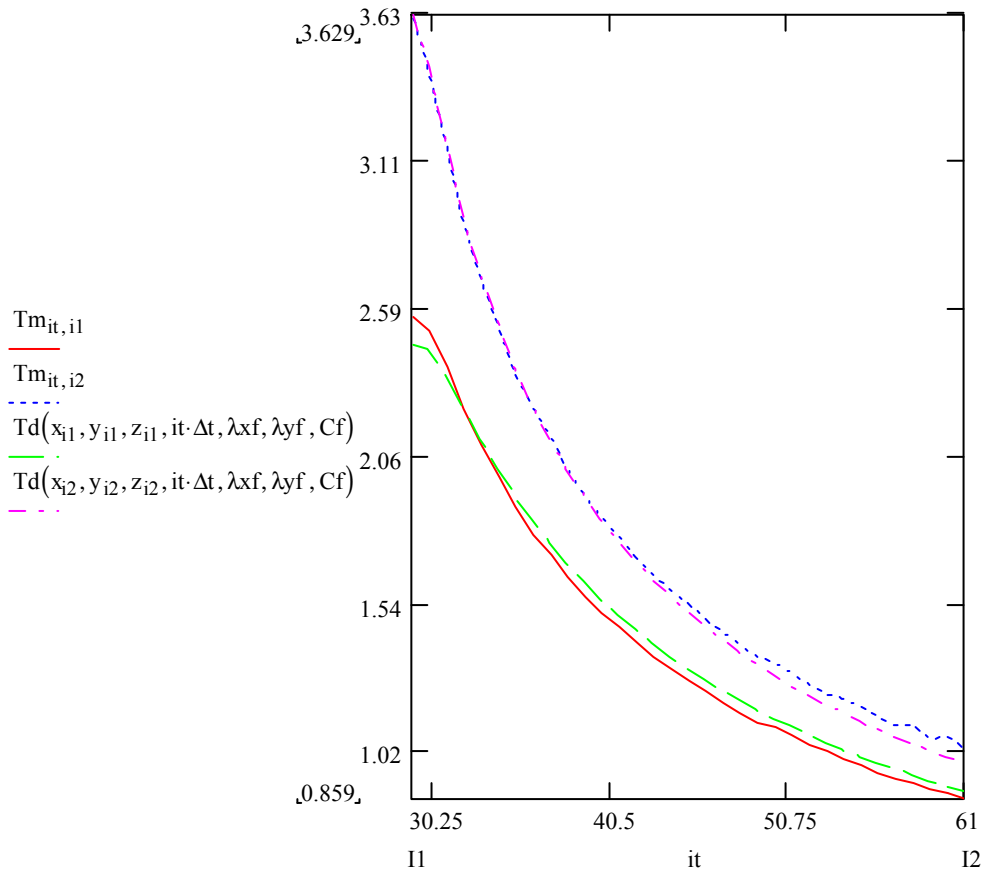
E4f4



Original coordinate measurements + MOVE 3 (A2)

29-61

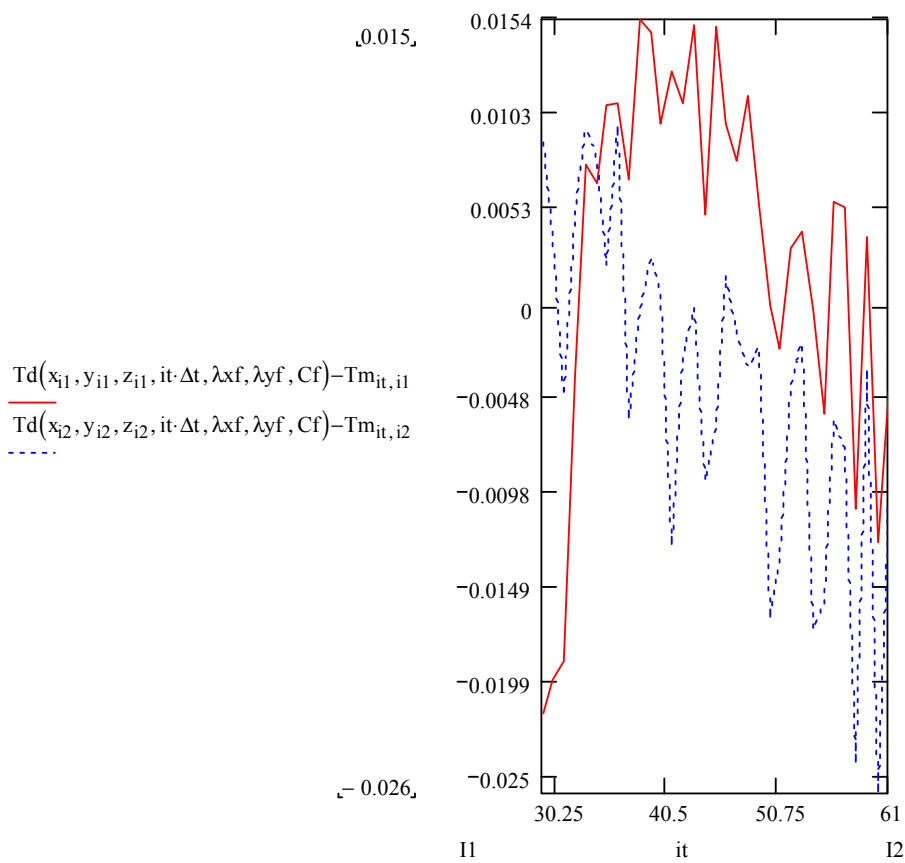
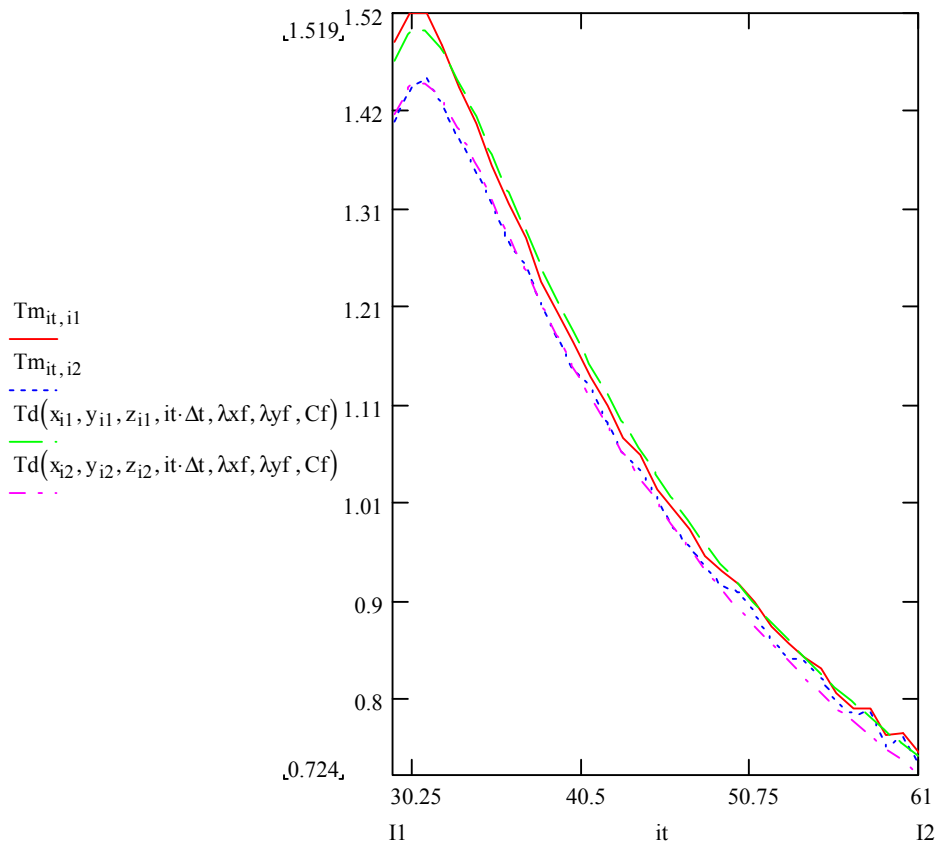
E5f5



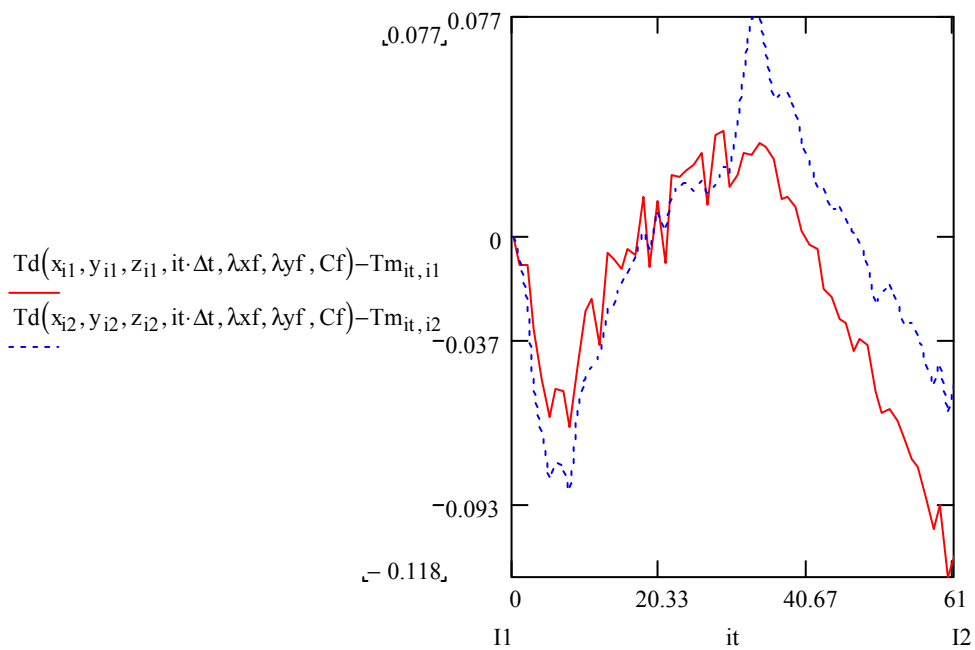
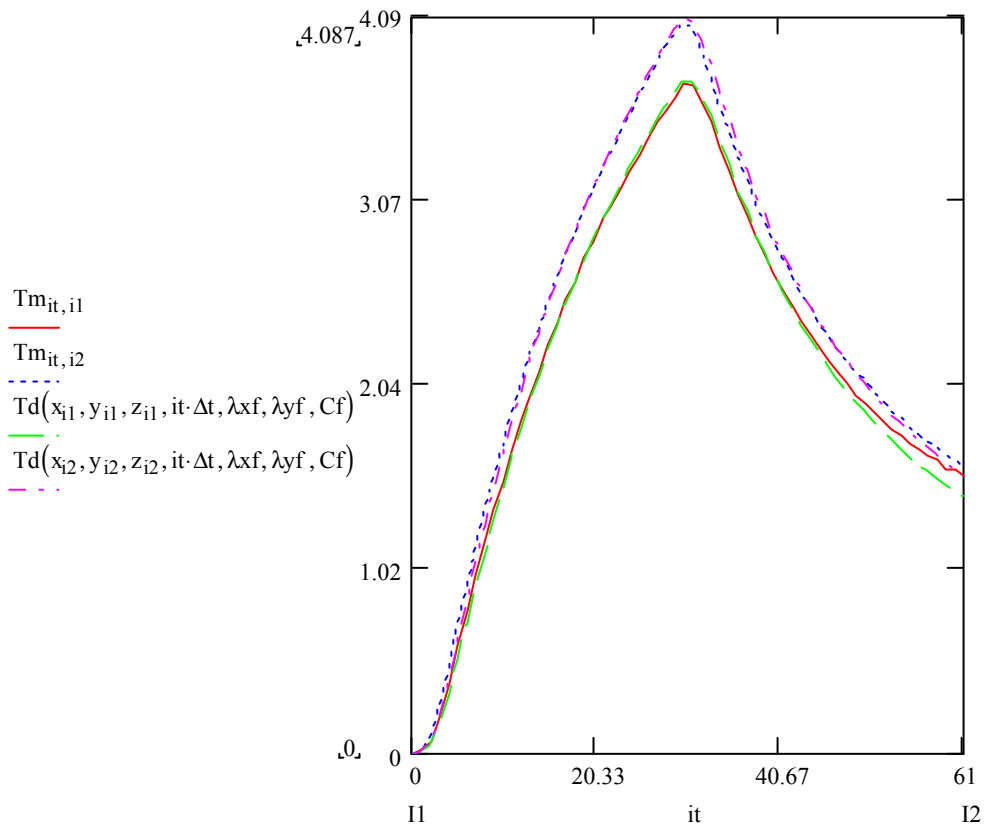
Original coordinate measurements + MOVE 3 (A2)

29-61

E6f6



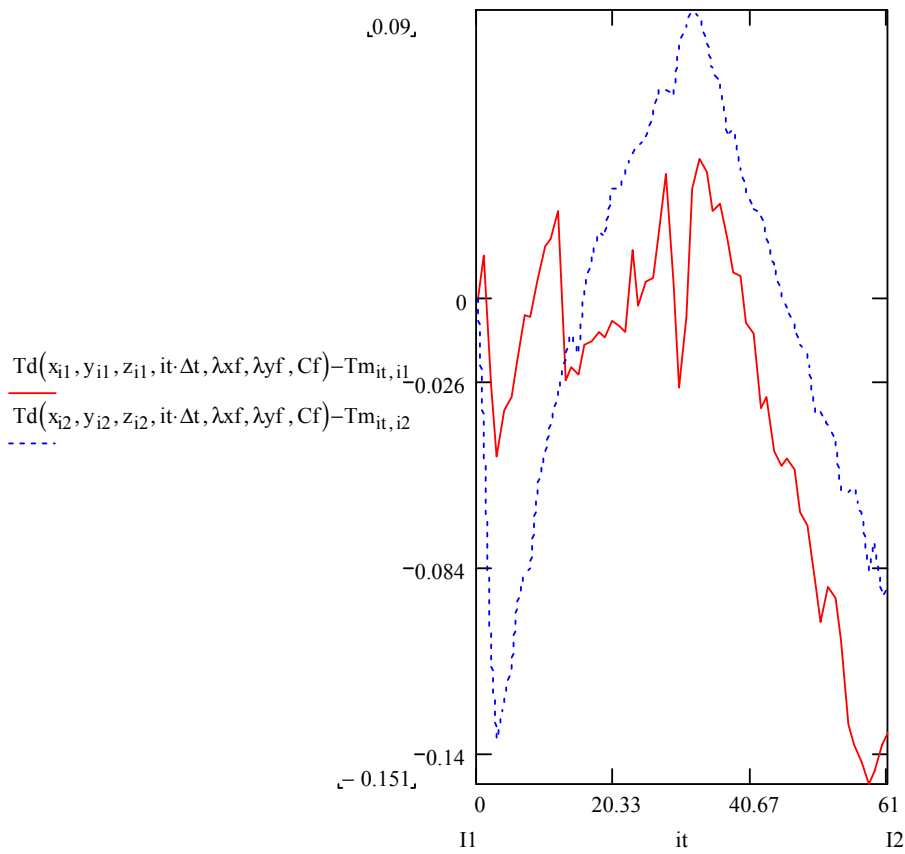
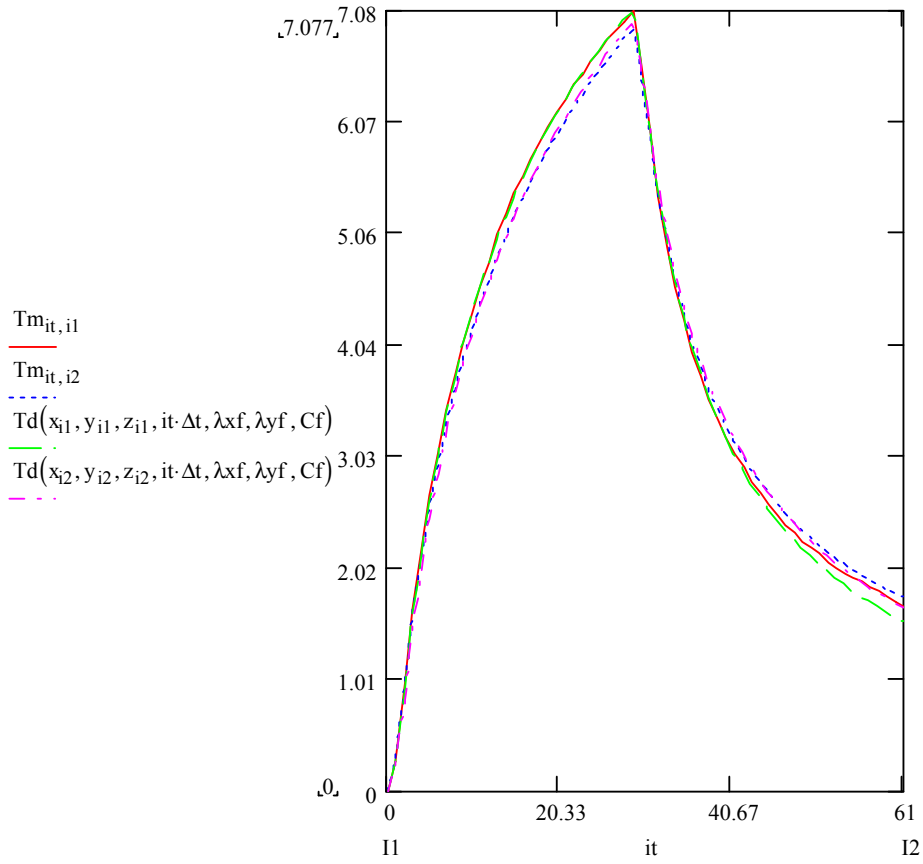
New measure, (B1)
 0-61
 C1d1



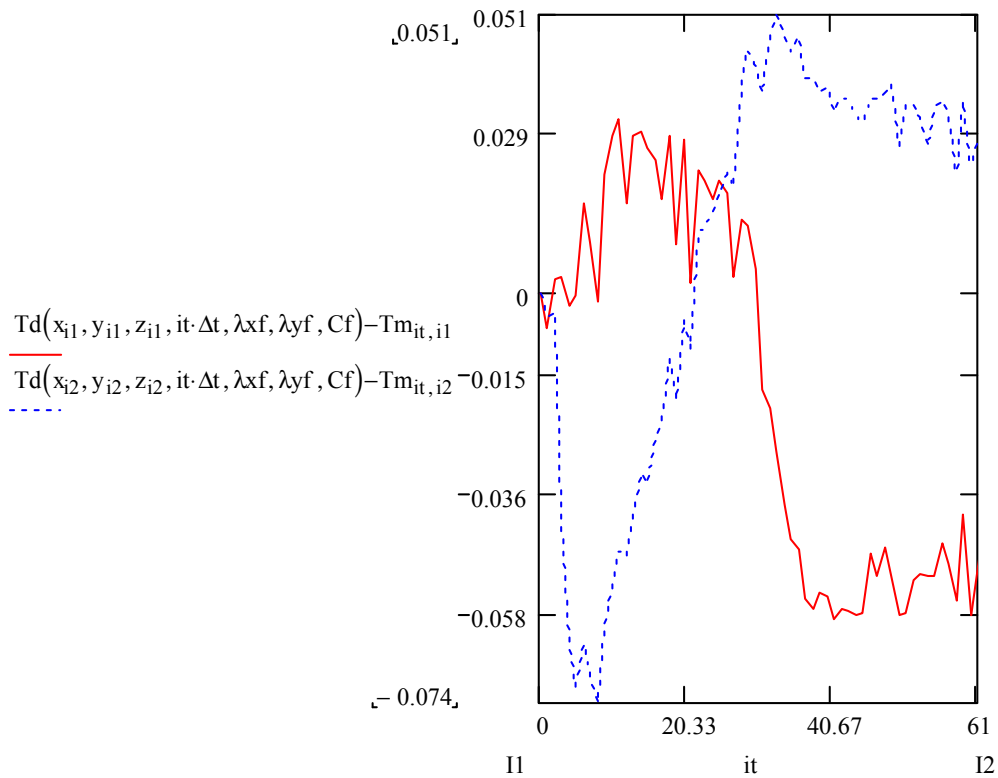
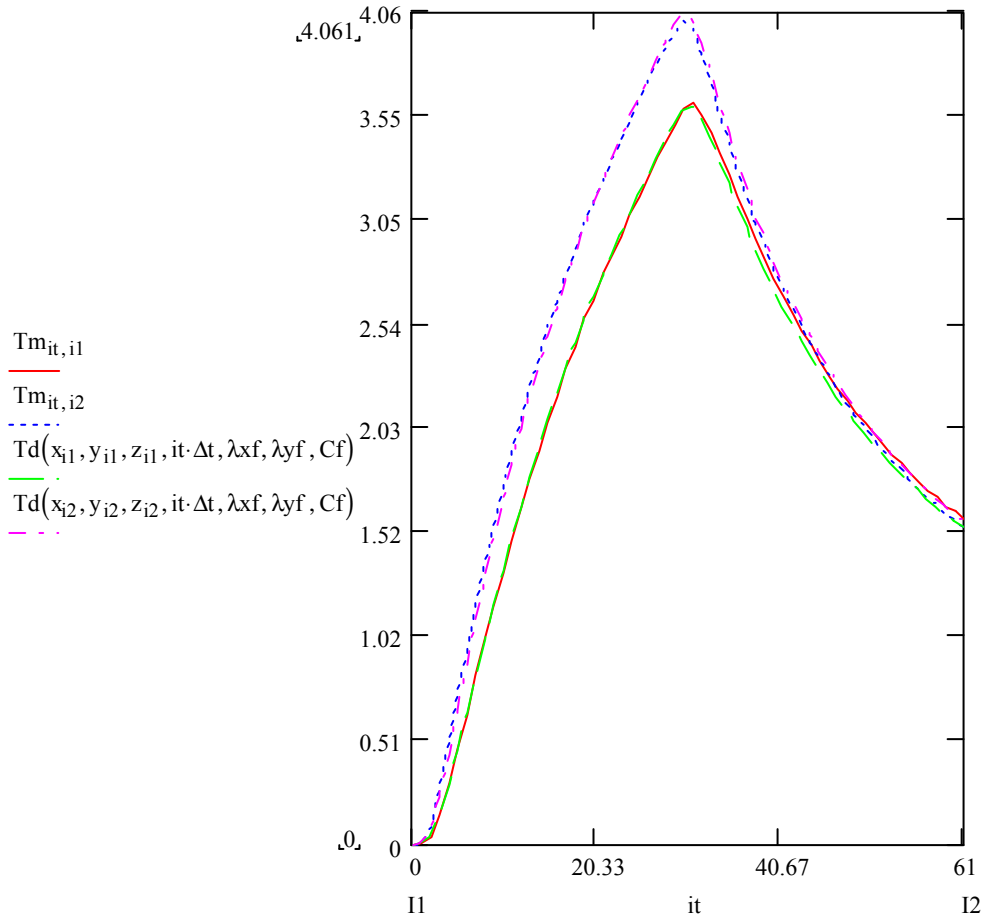
New measure, (B1)

0-61

E1f1



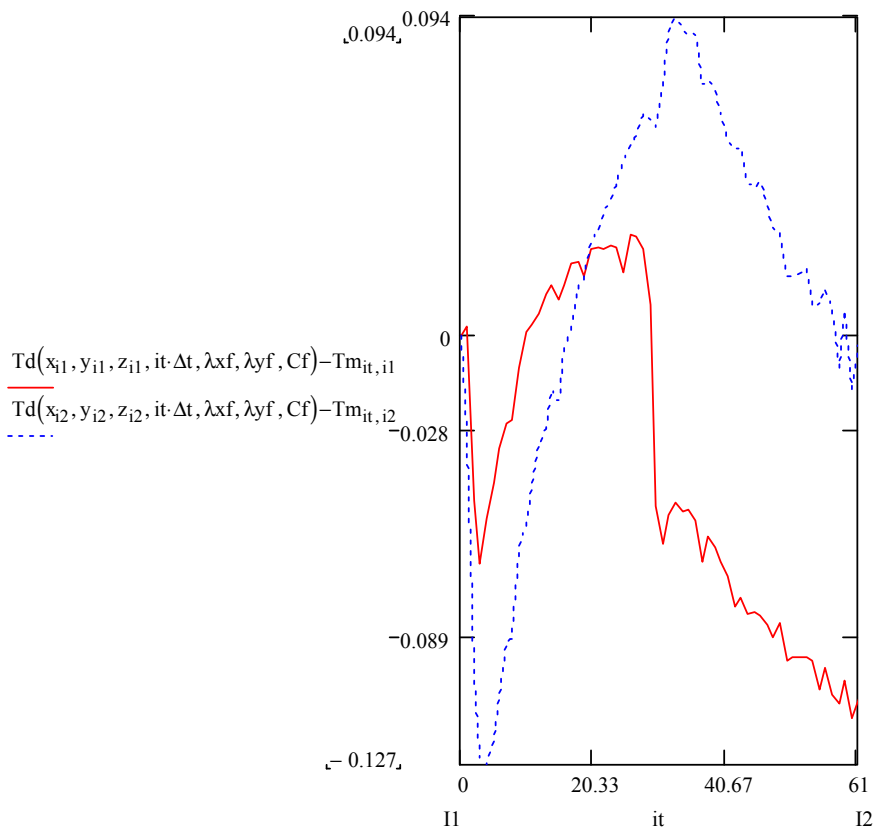
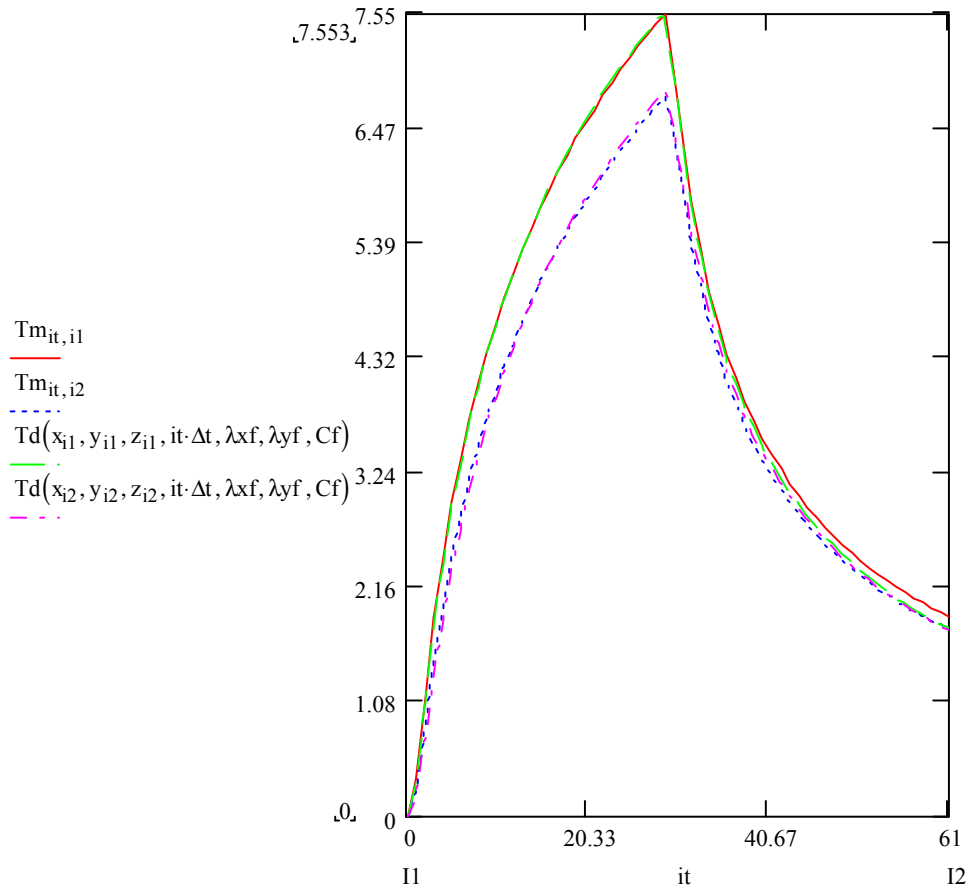
New measure, (B1)
 0-61
 C2d2



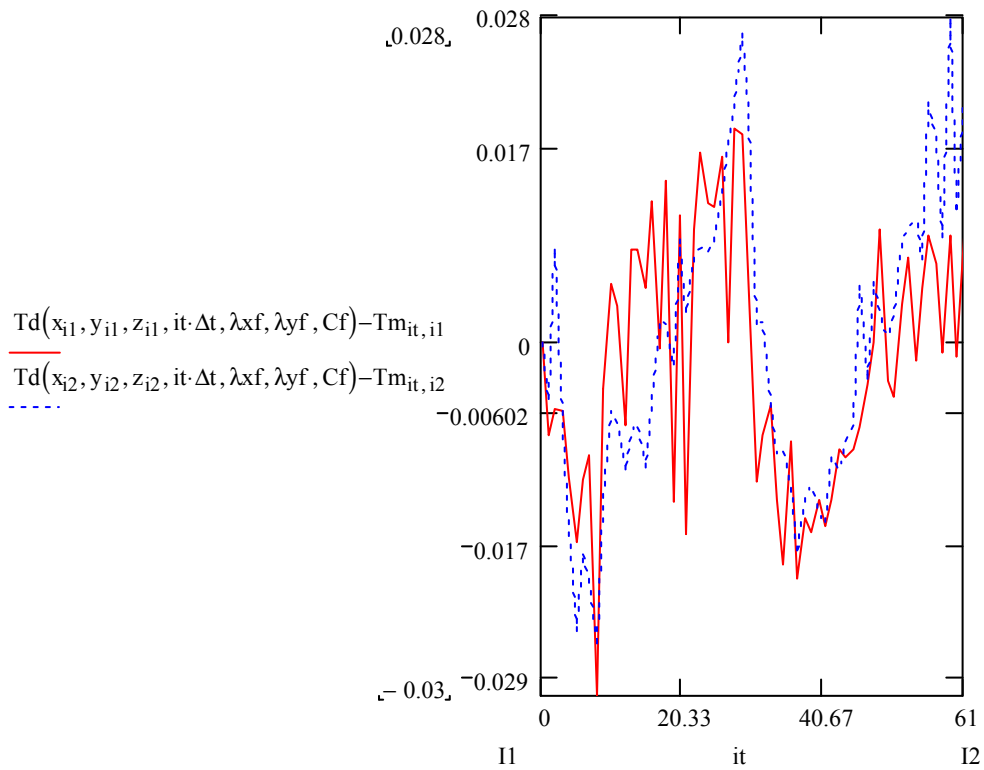
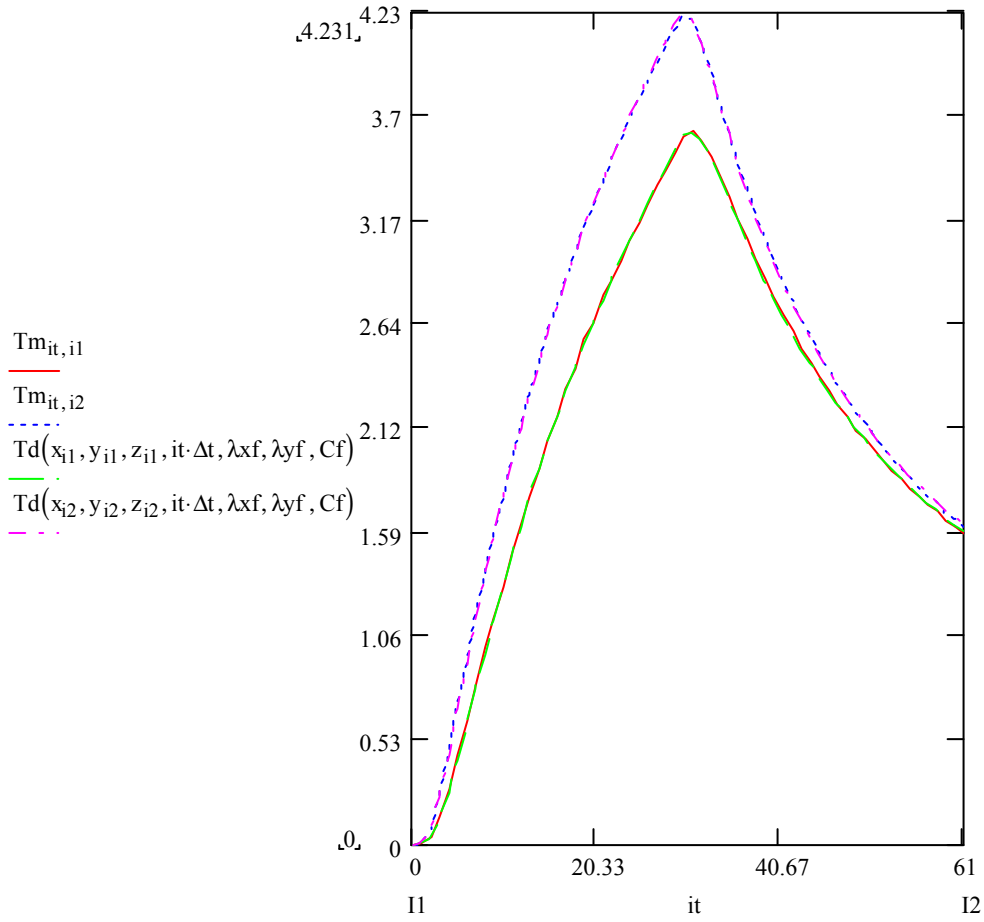
New measure, (B1)

0-61

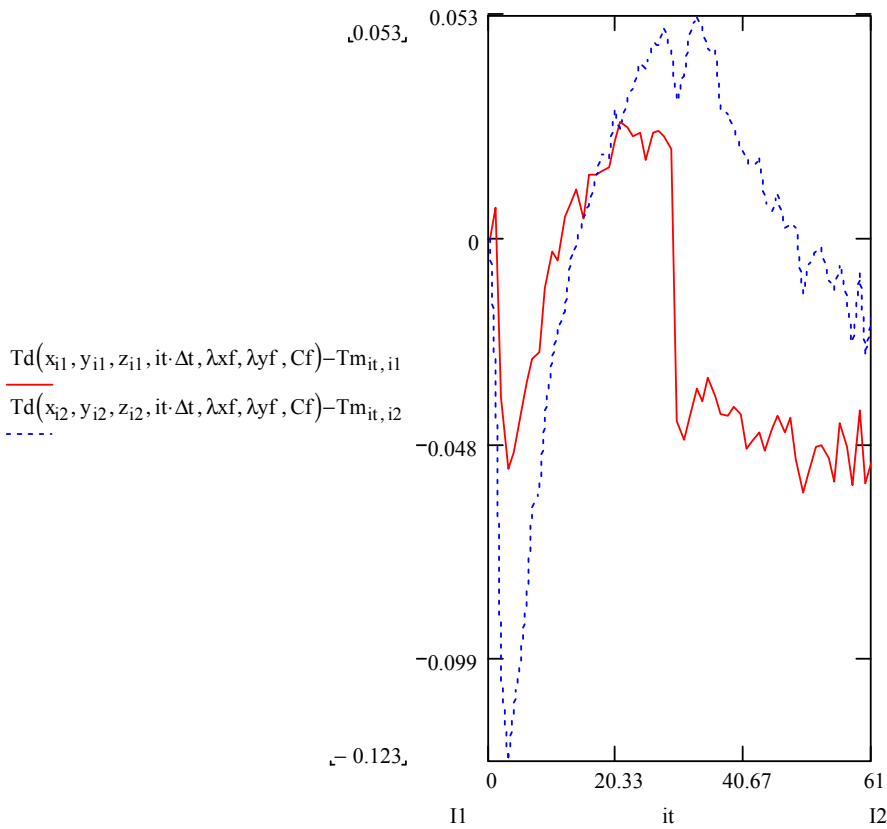
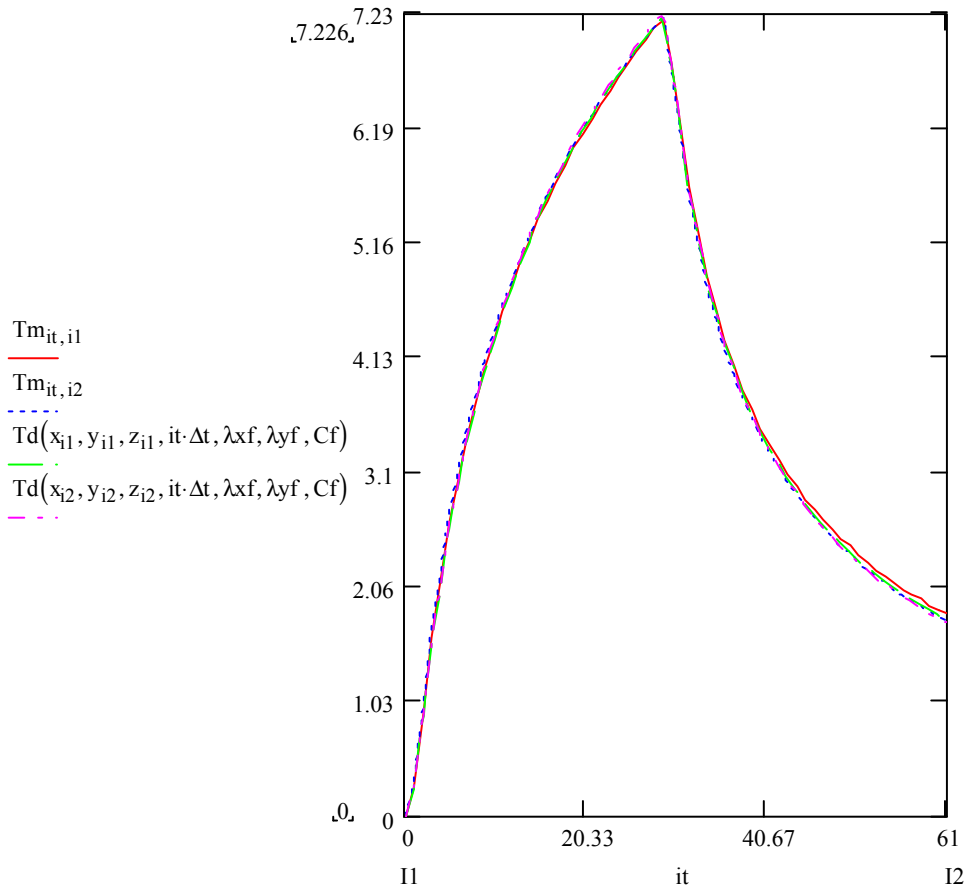
E2f2



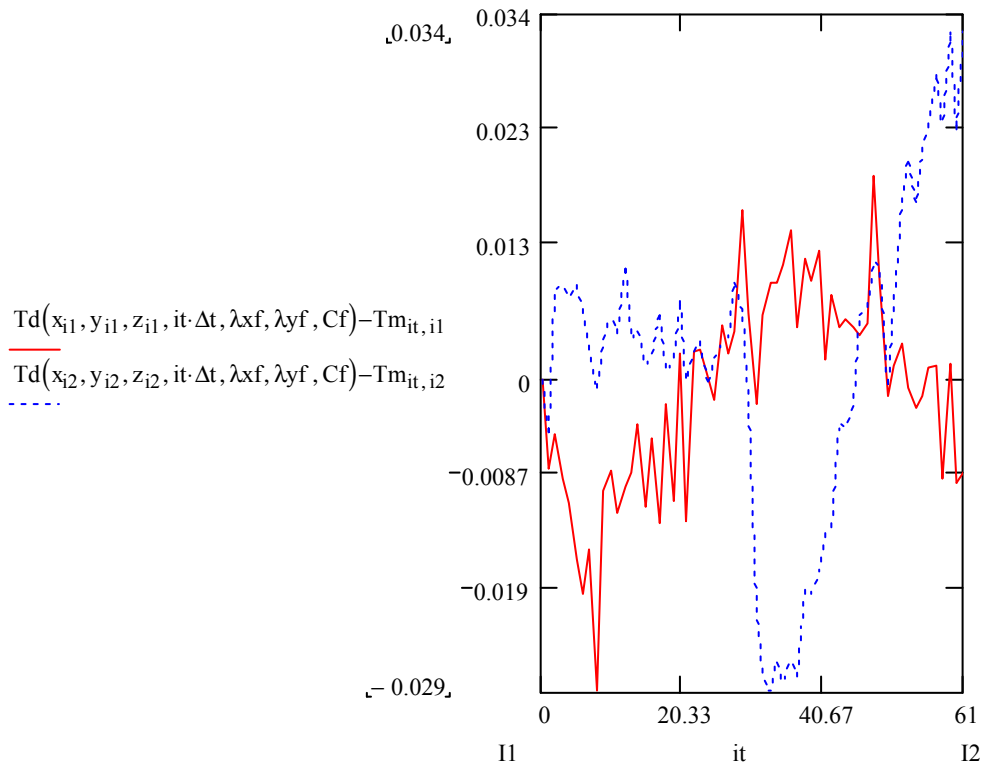
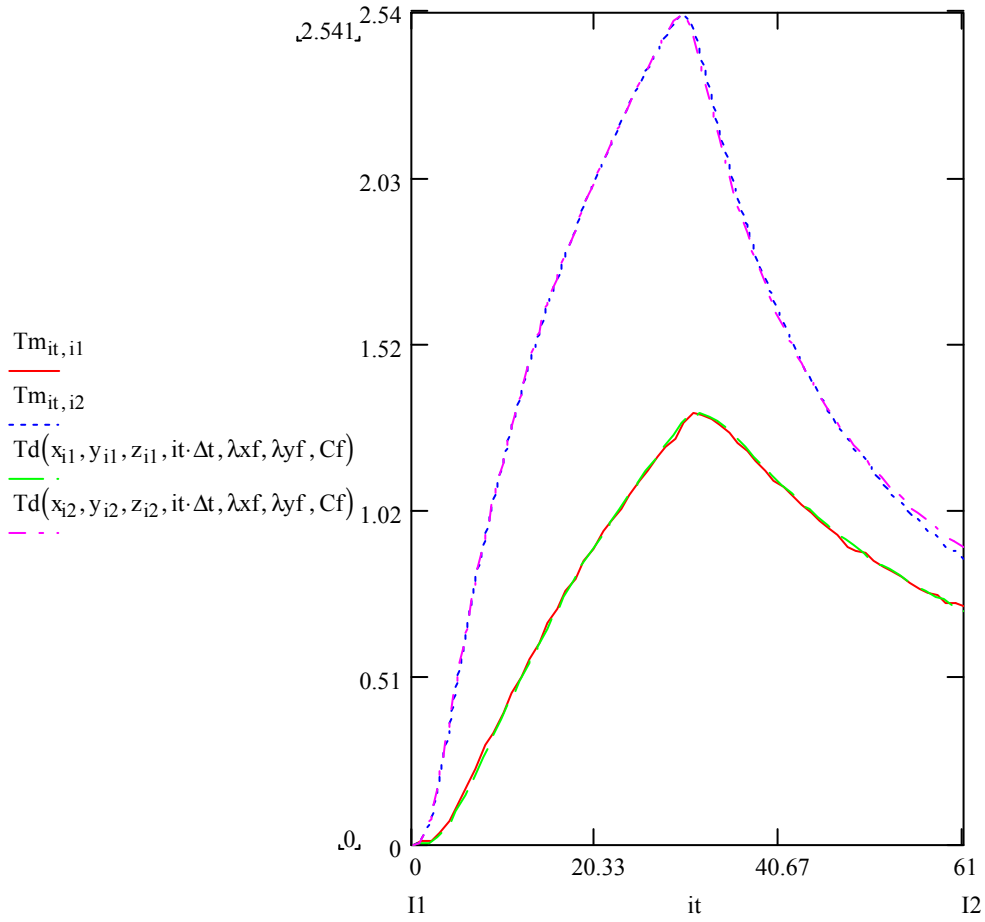
New measure, (B1)
 0-61
 C3d3



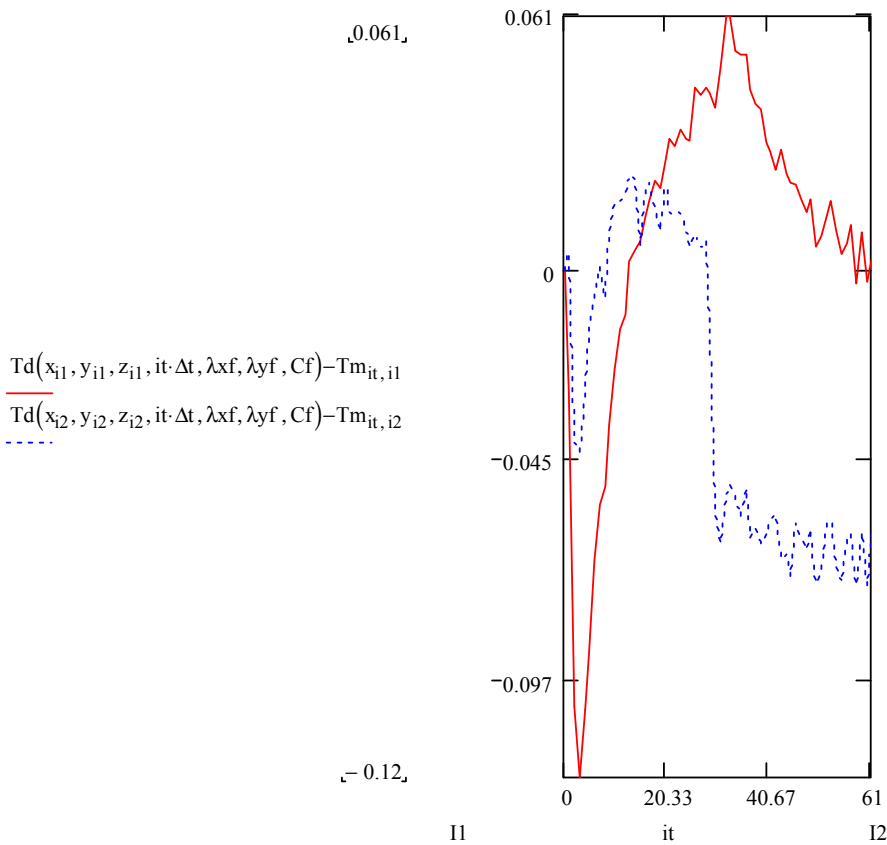
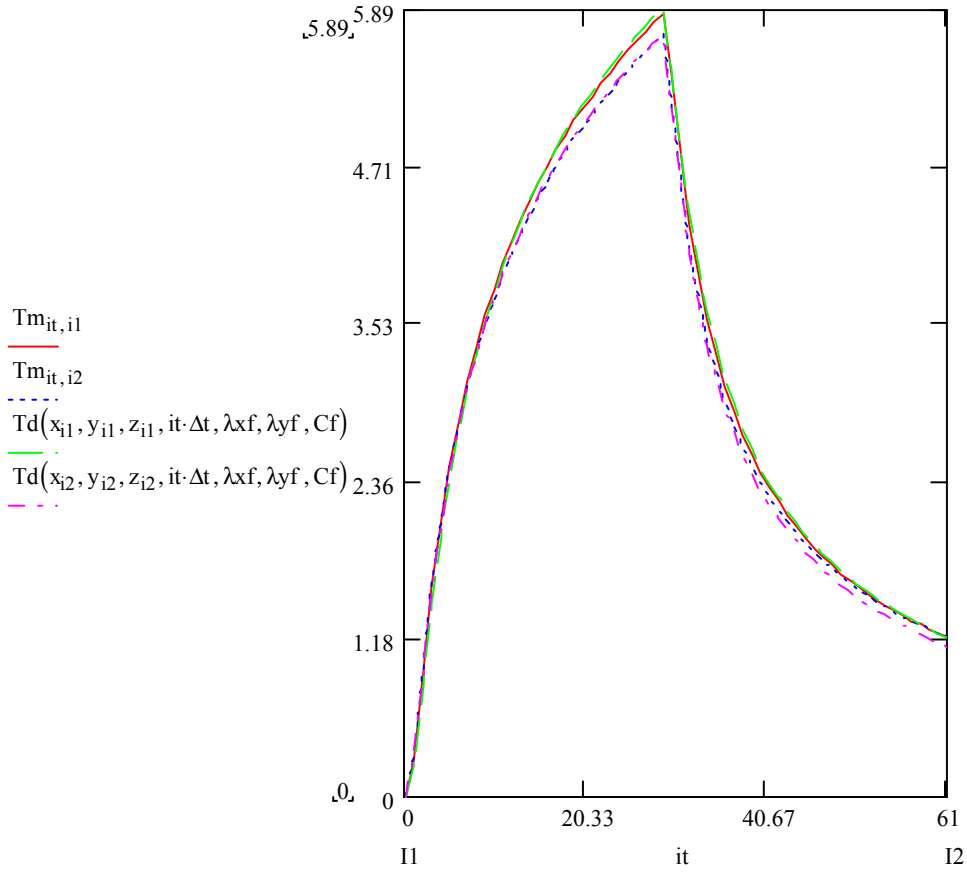
New measure, (B1)
 0-61
 E3f3



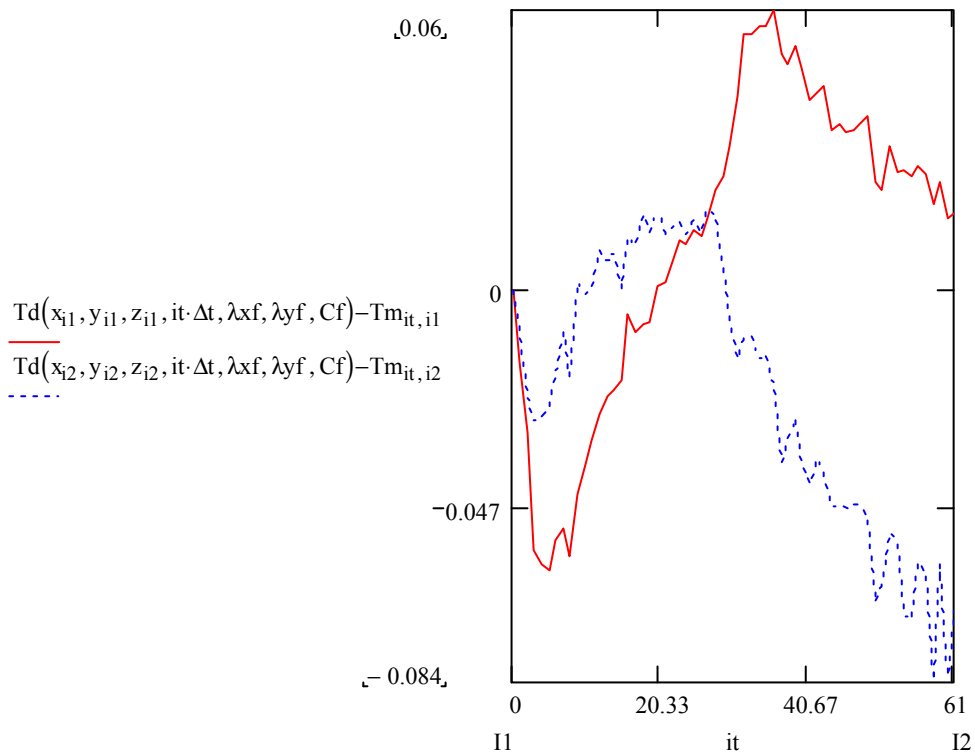
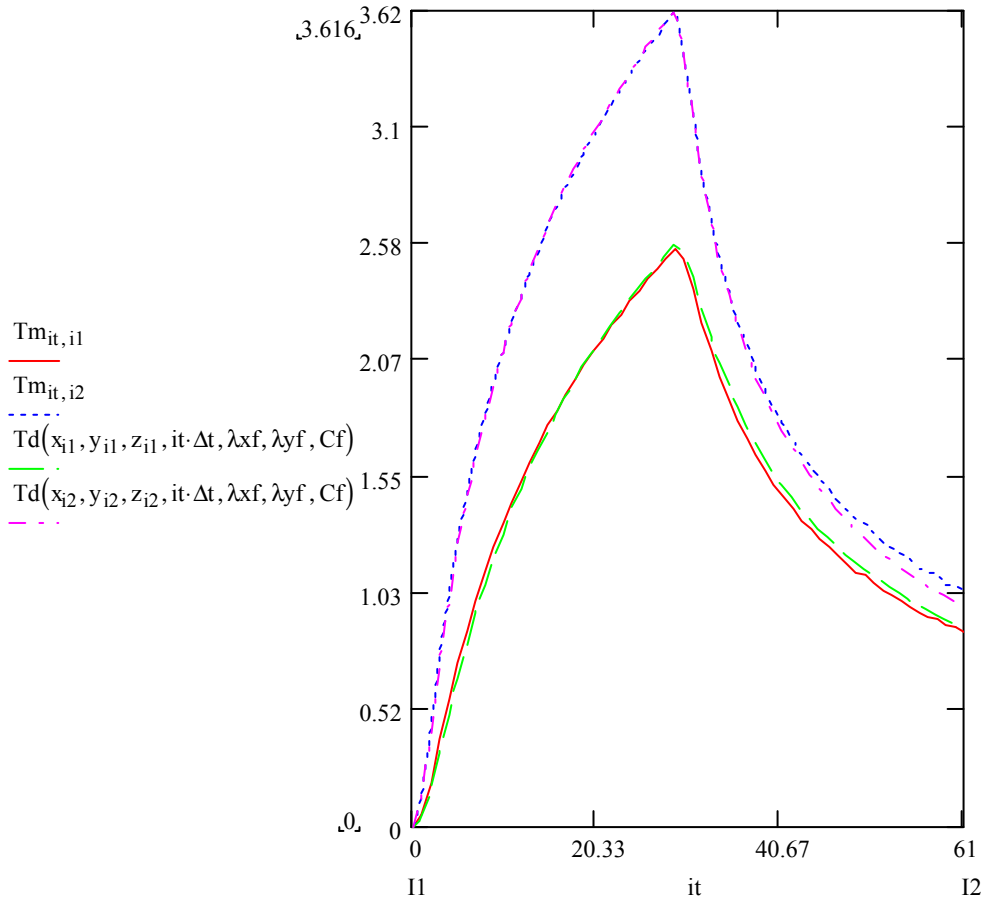
New measure, (B1)
 0-61
 C4d4



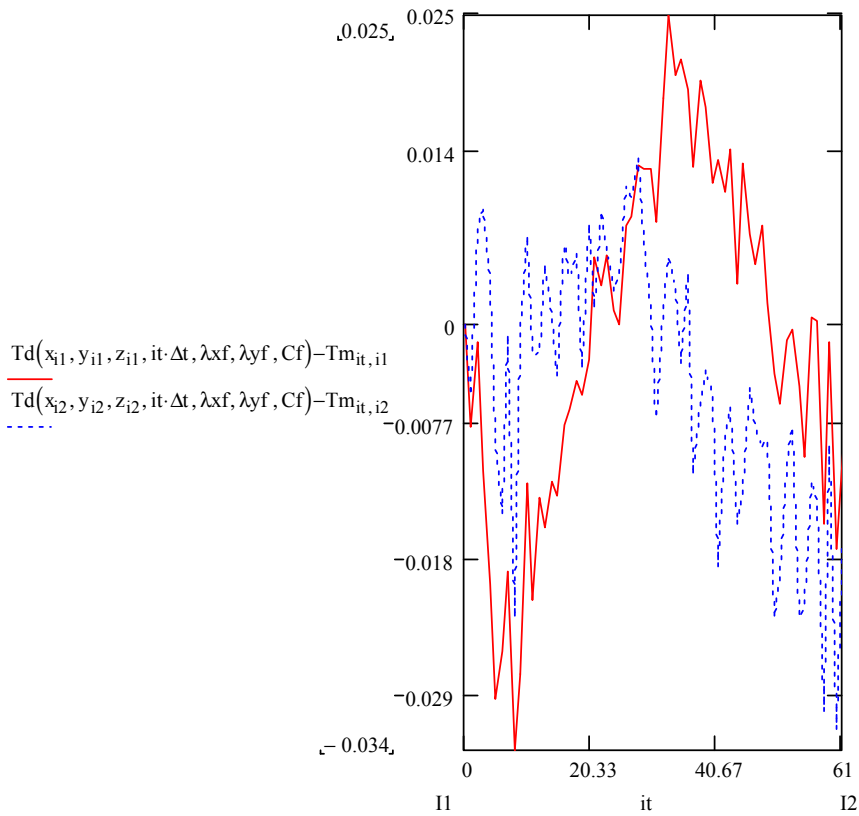
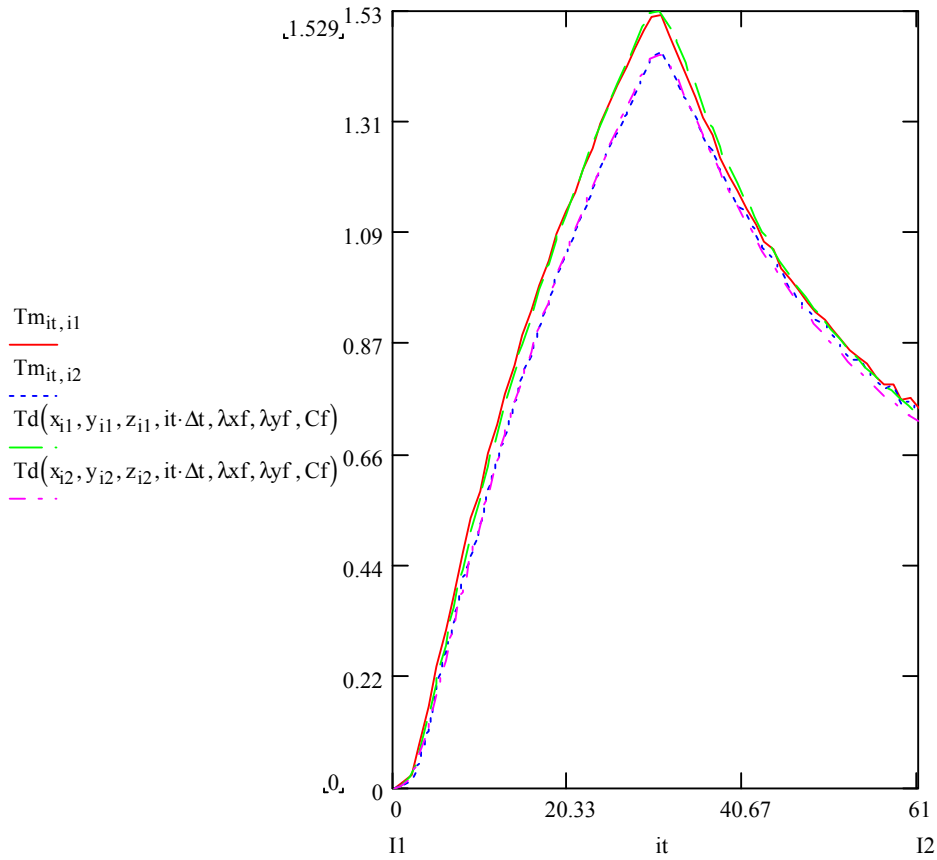
New measure, (B1)
 0-61
 E4f4



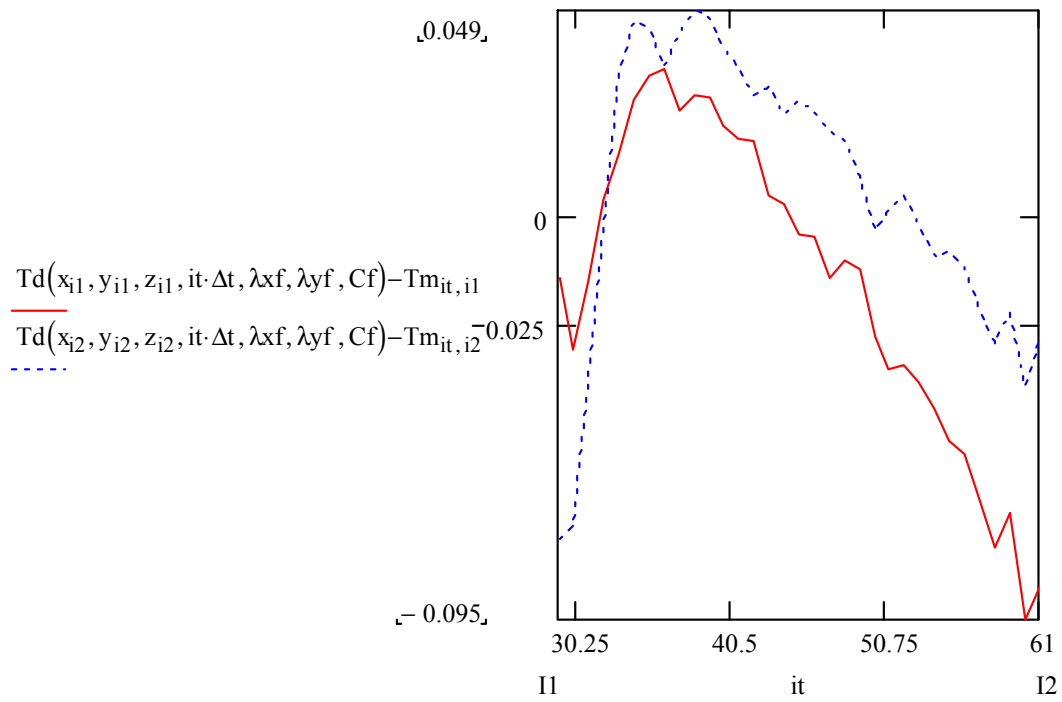
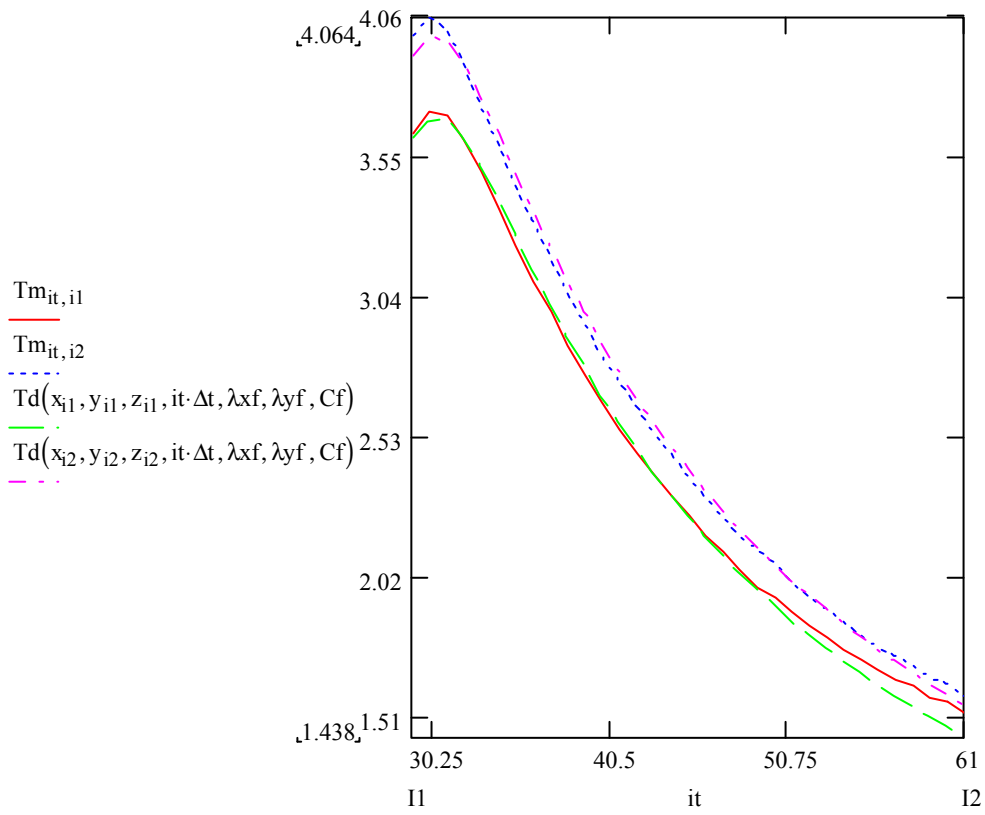
New measure, (B1)
 0-61
 E5f5



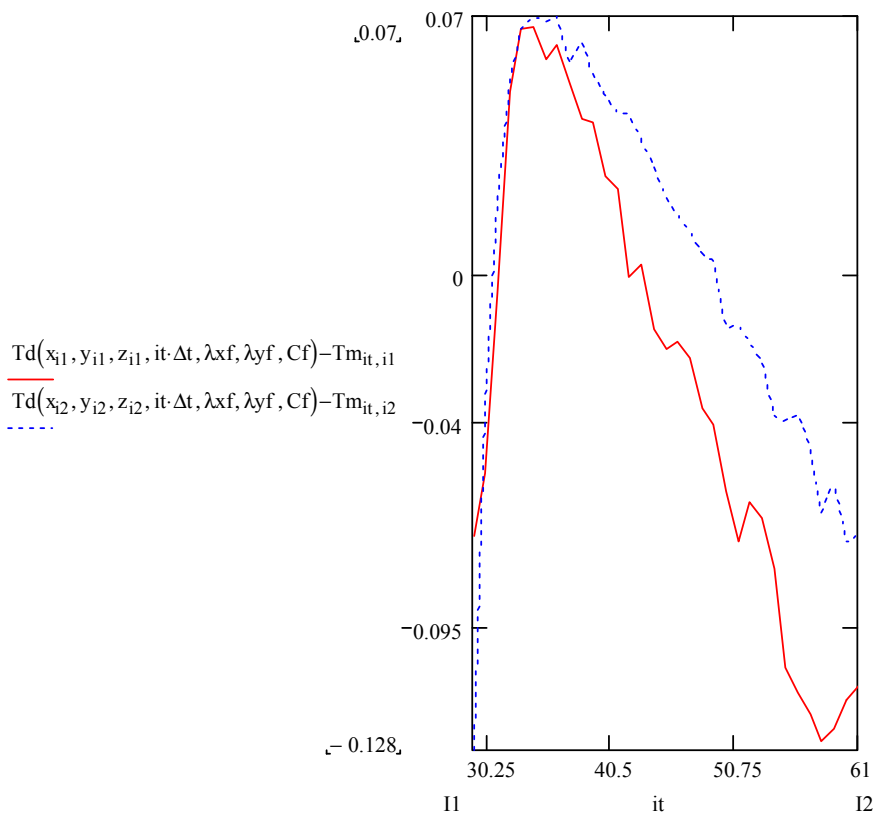
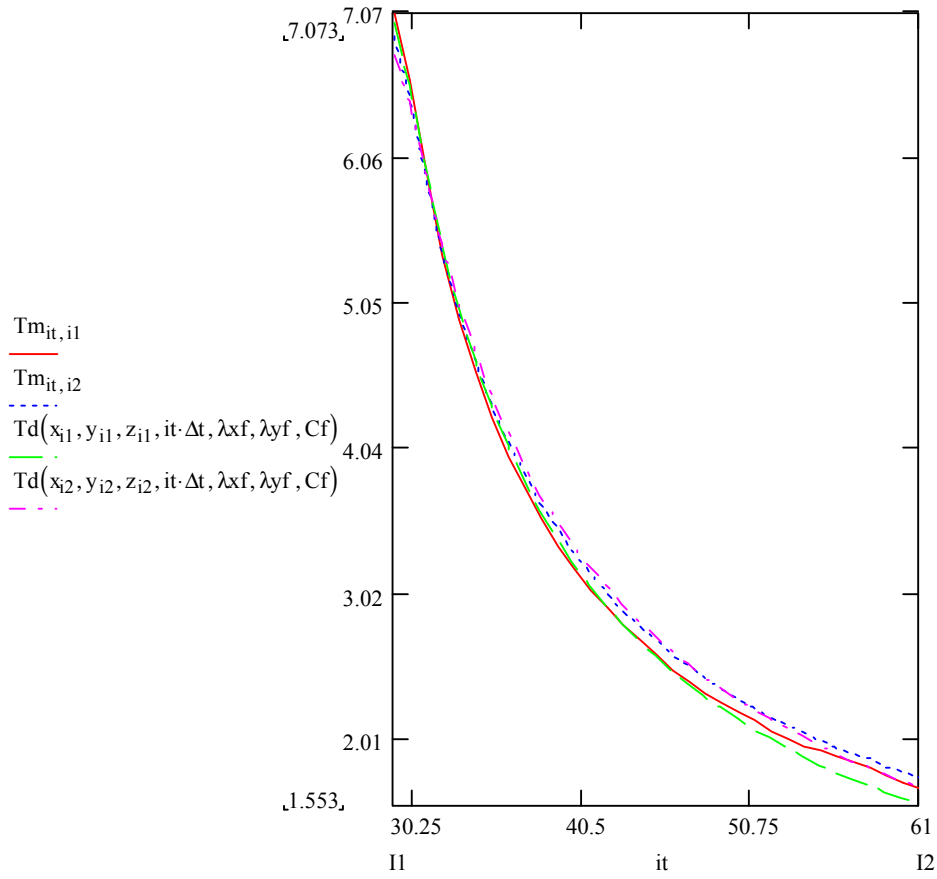
New measure, (B1)
 0-61
 E6f6



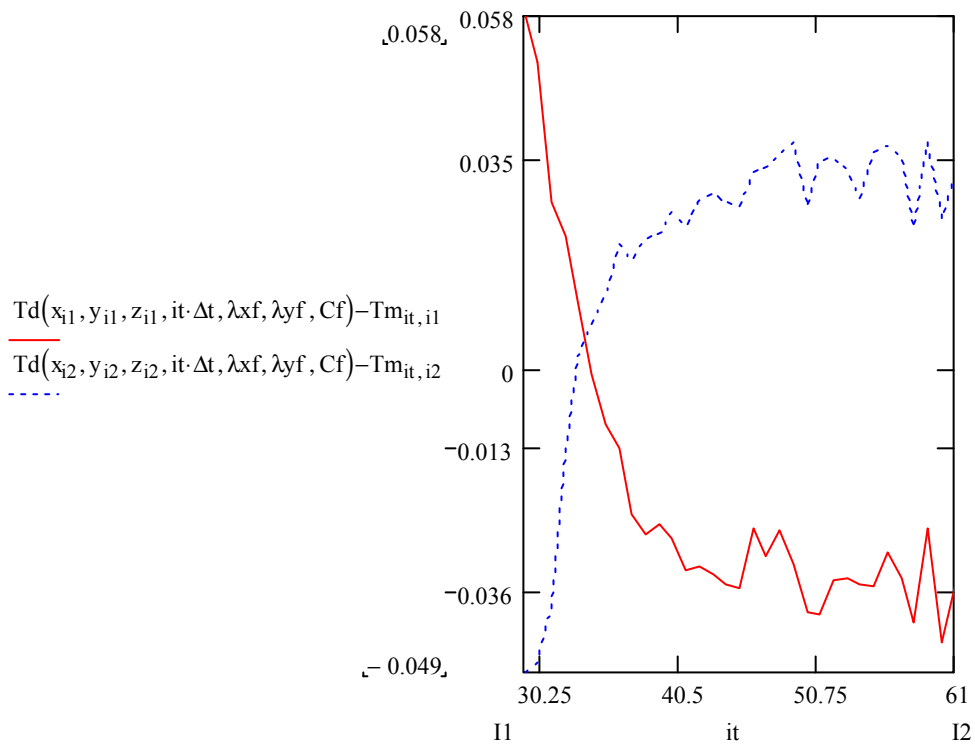
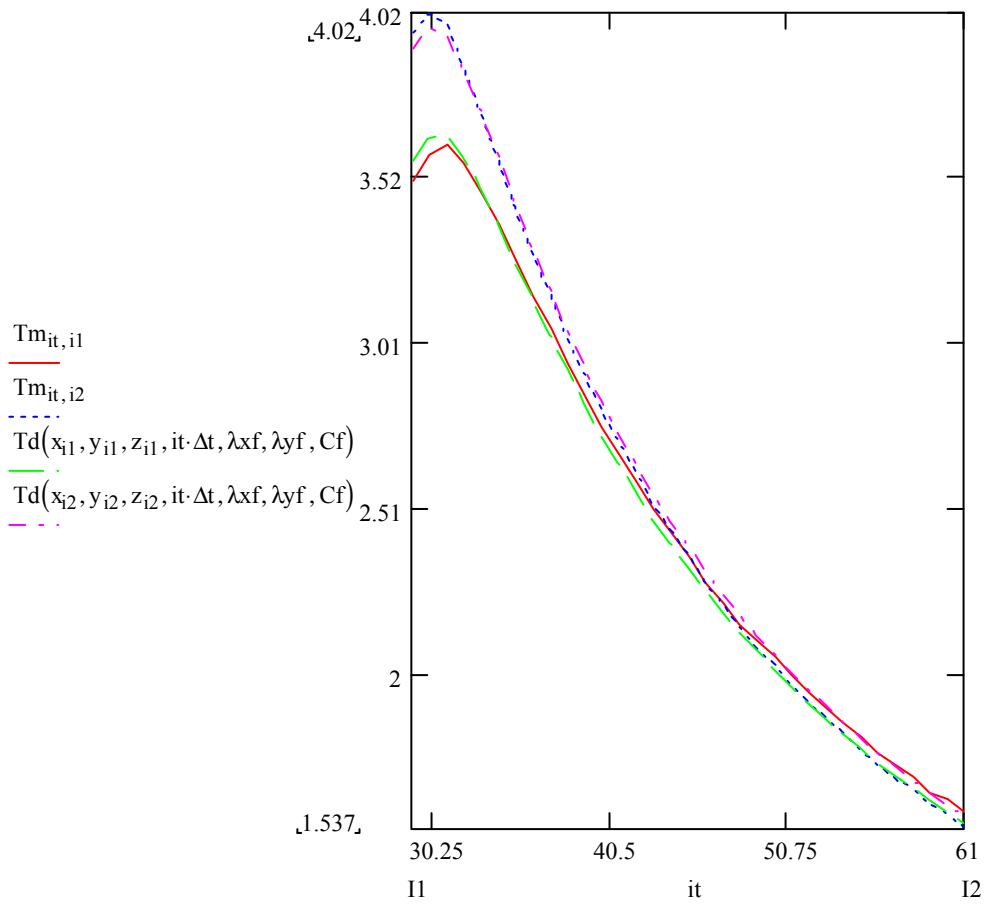
New measure, (B1)
 29-61
 C1d1



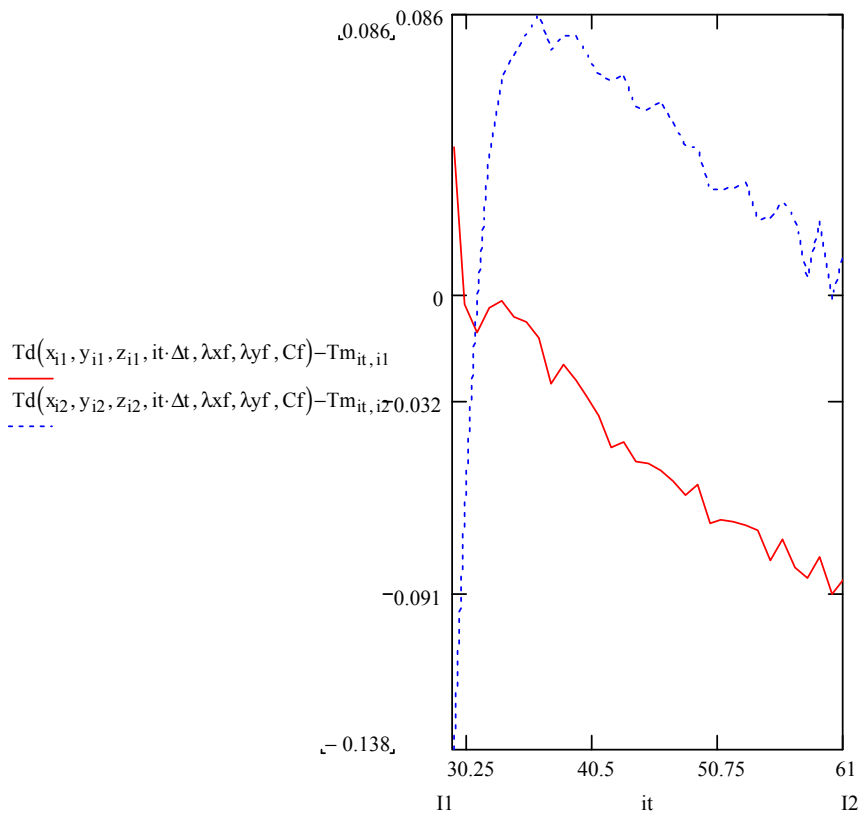
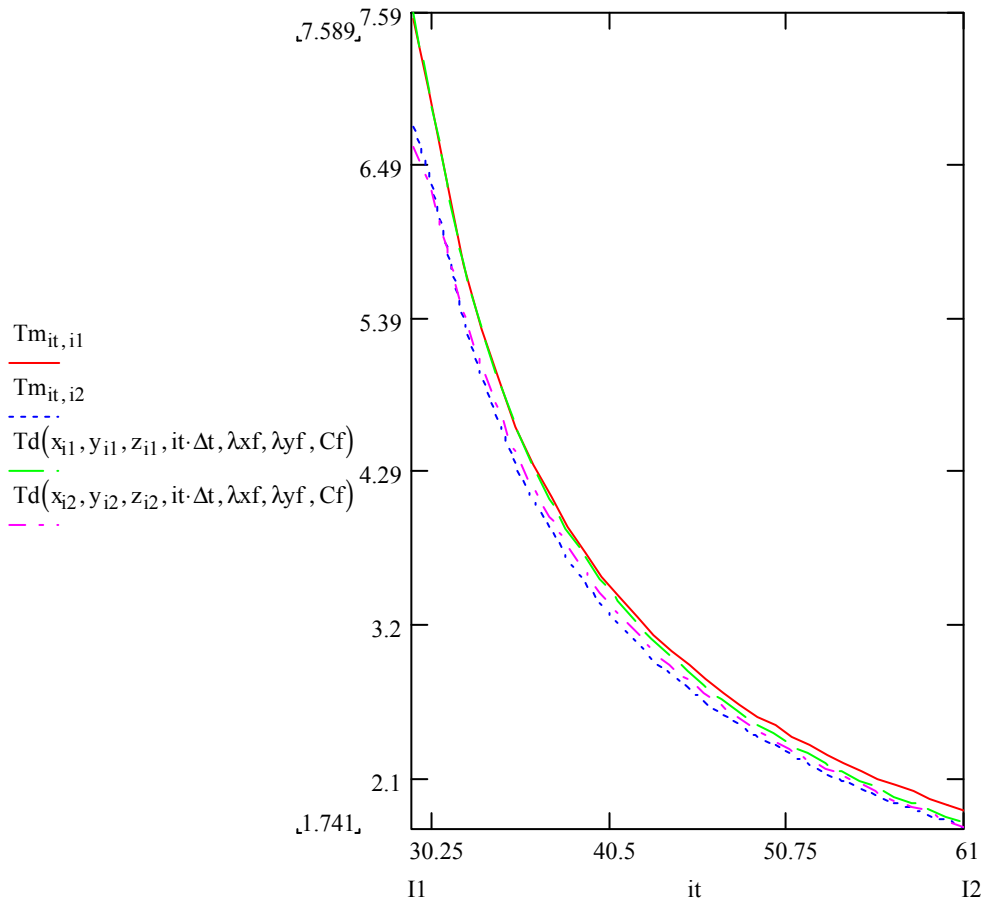
New measure, (B1)
 29-61
 E1f1



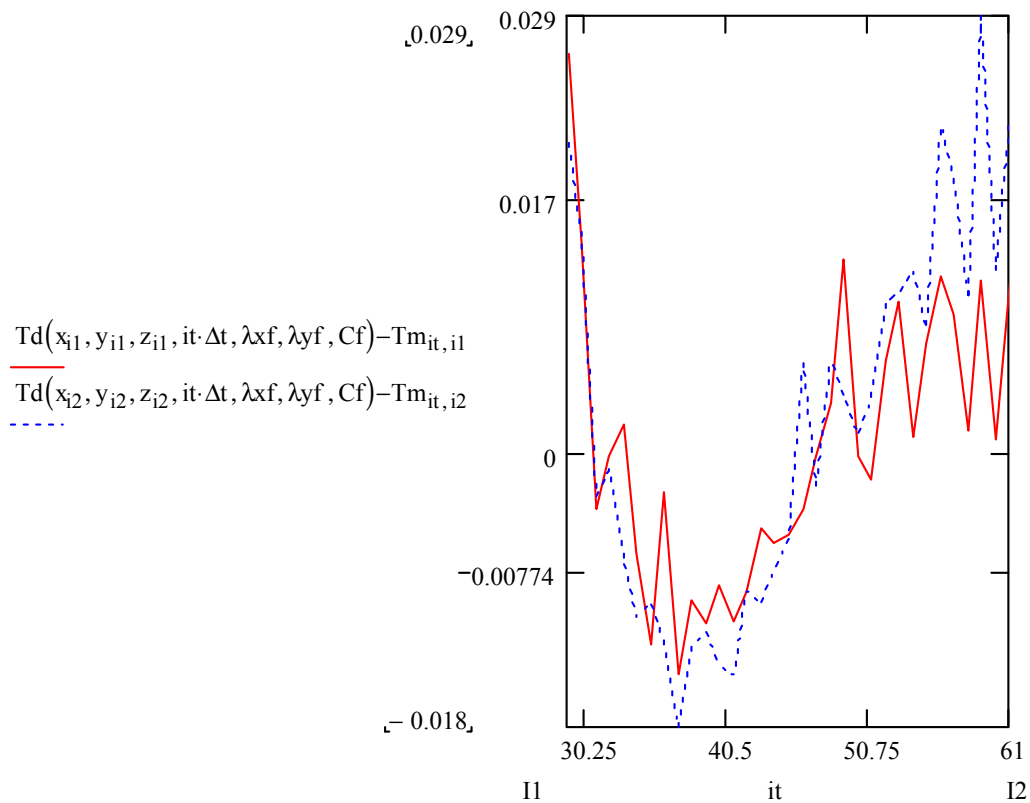
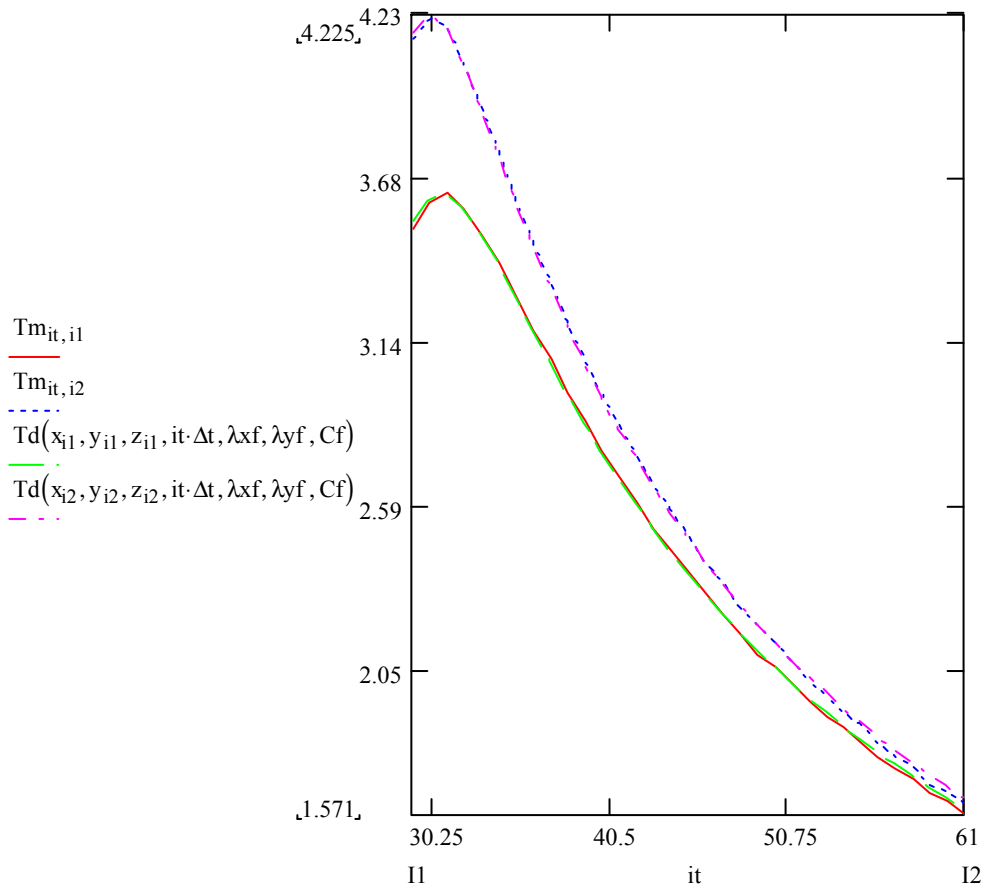
New measure, (B1)
 29-61
 C2d2



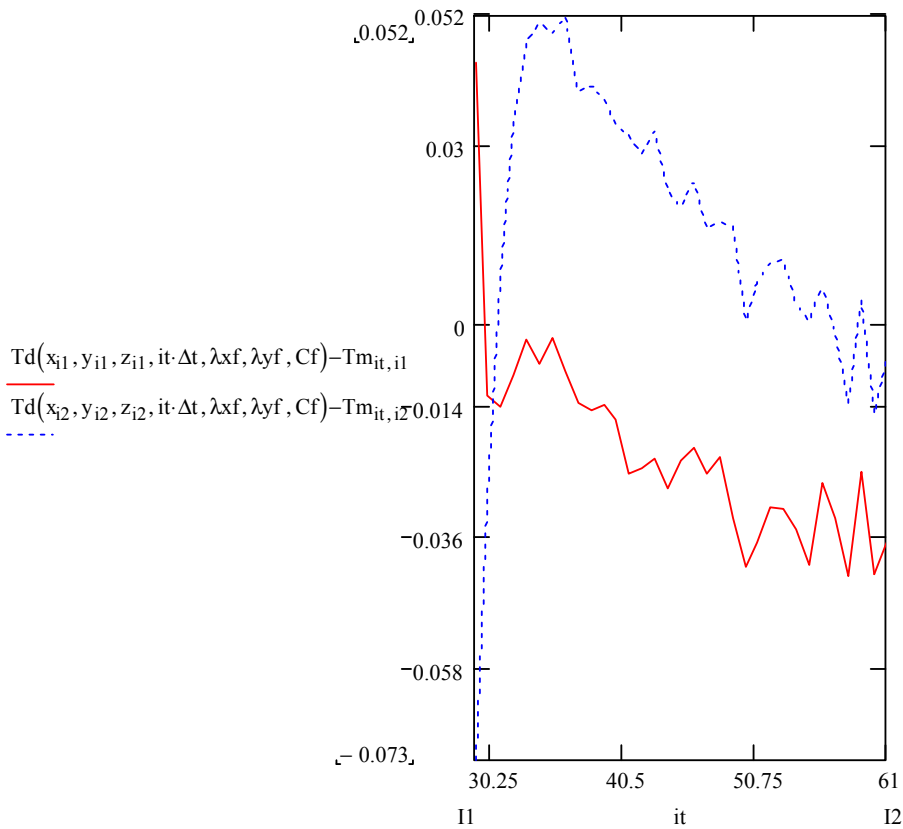
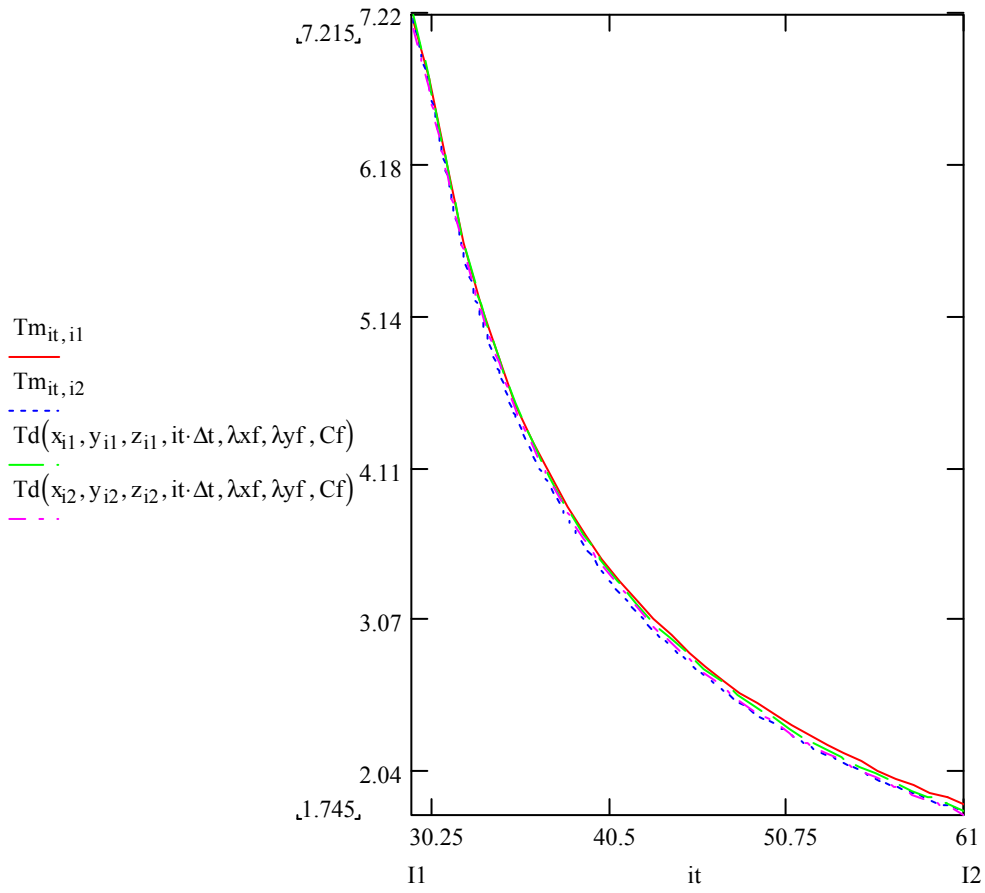
New measure, (B1)
 29-61
 E2f2



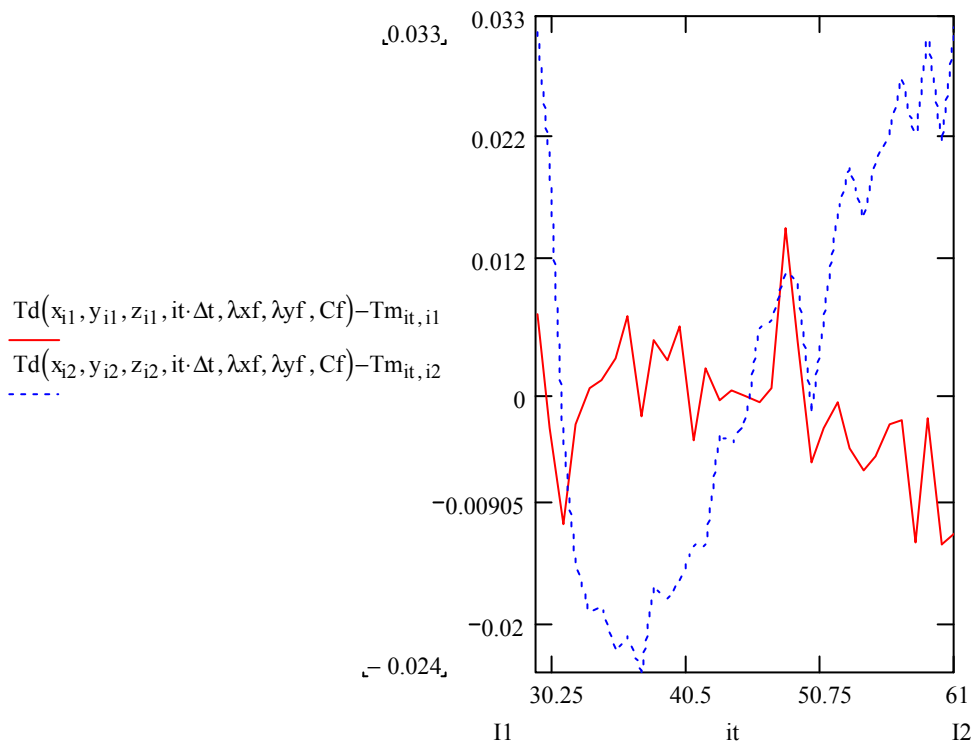
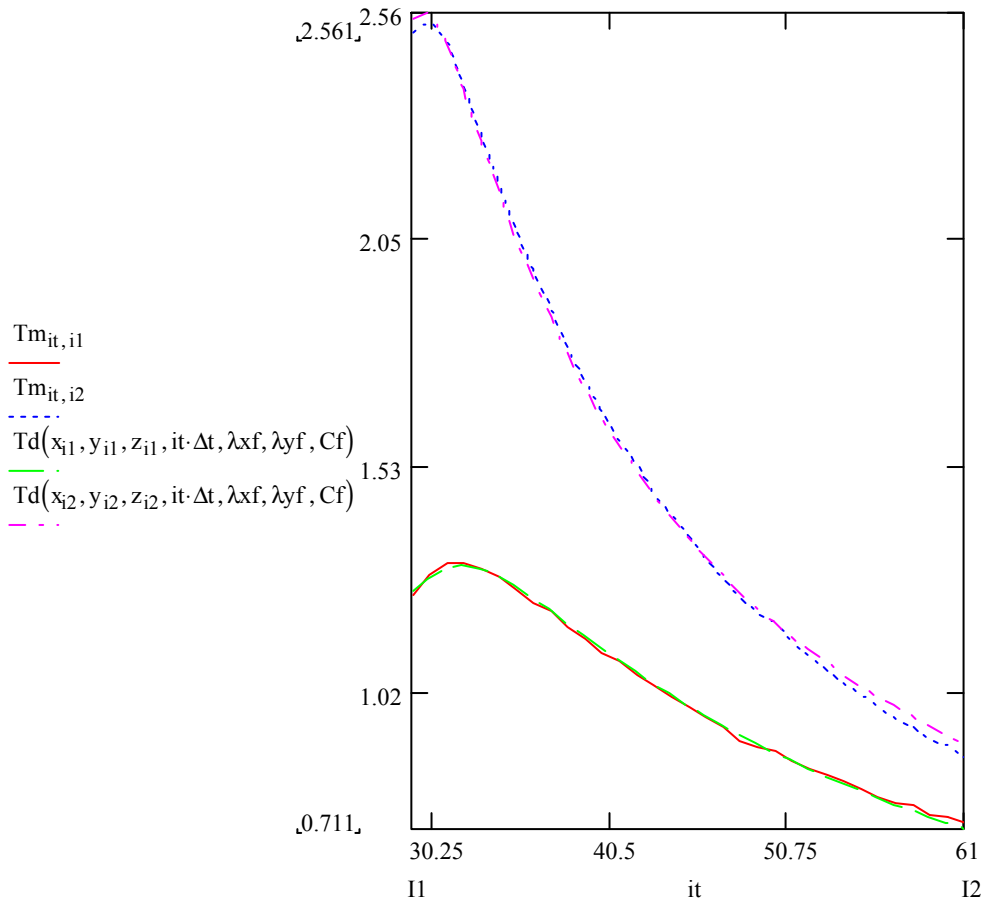
New measure, (B1)
 29-61
 C3d3



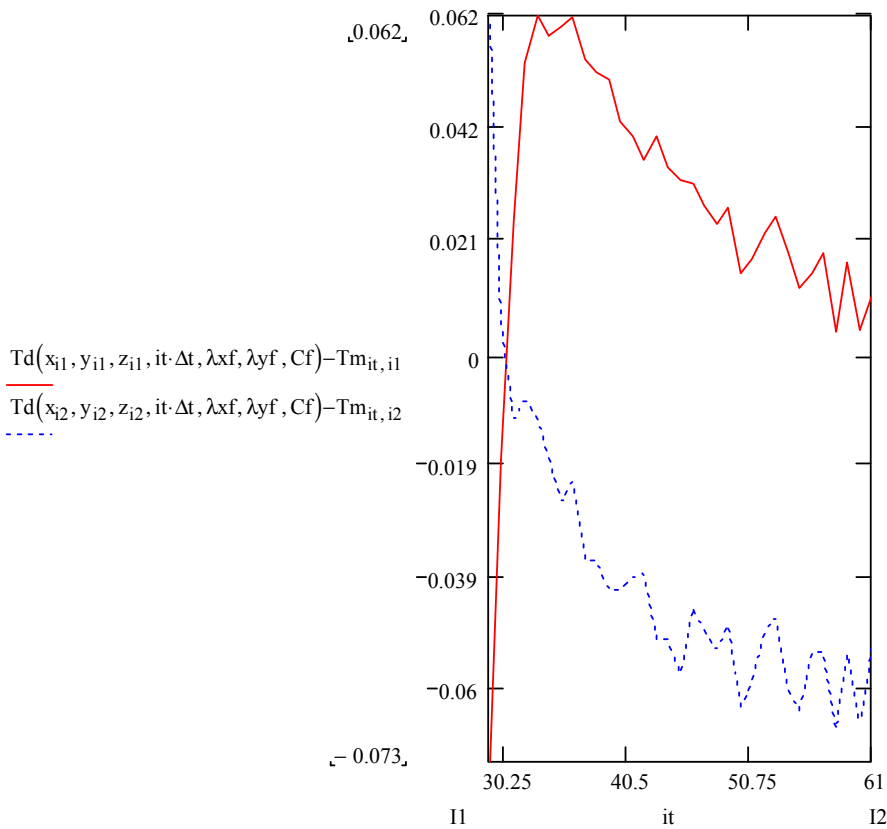
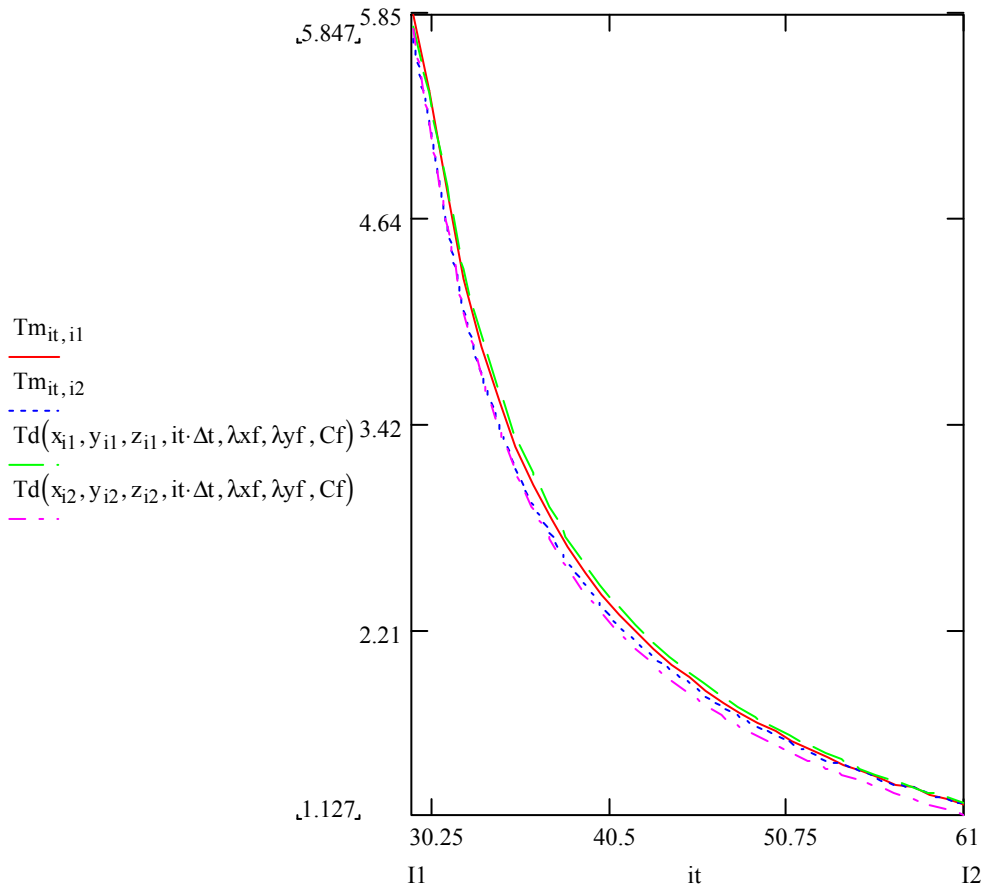
New measure, (B1)
 29-61
 E3f3



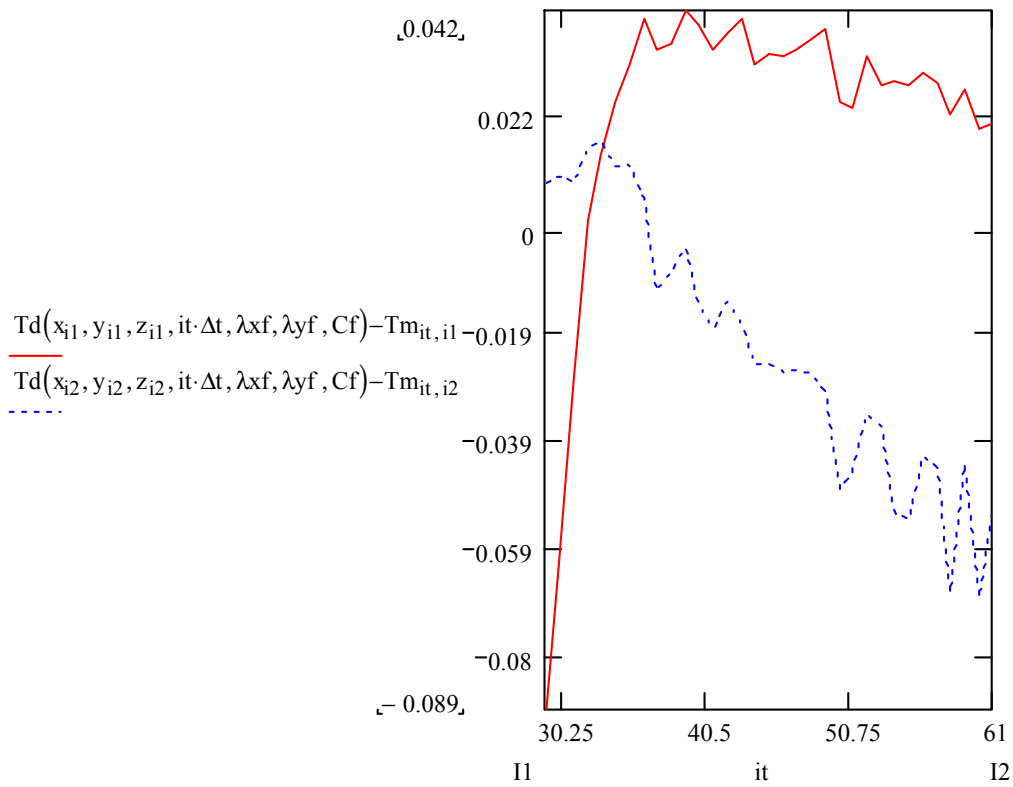
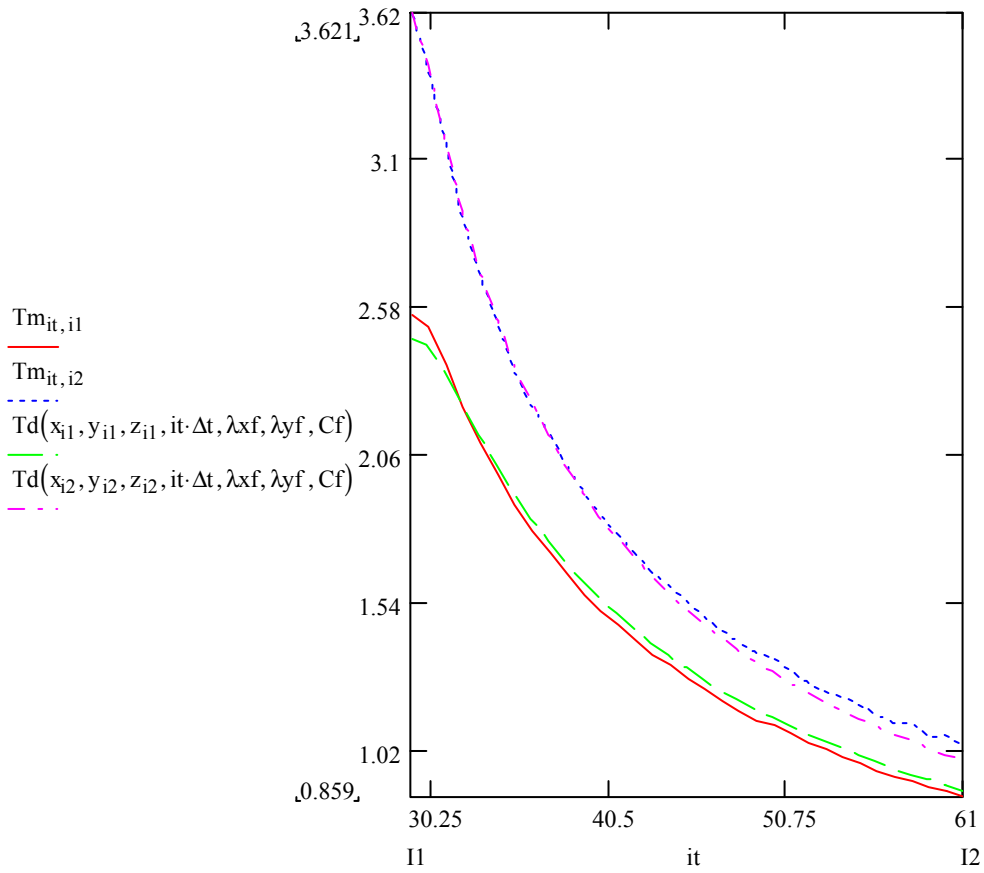
New measure, (B1)
 29-61
 C4d4



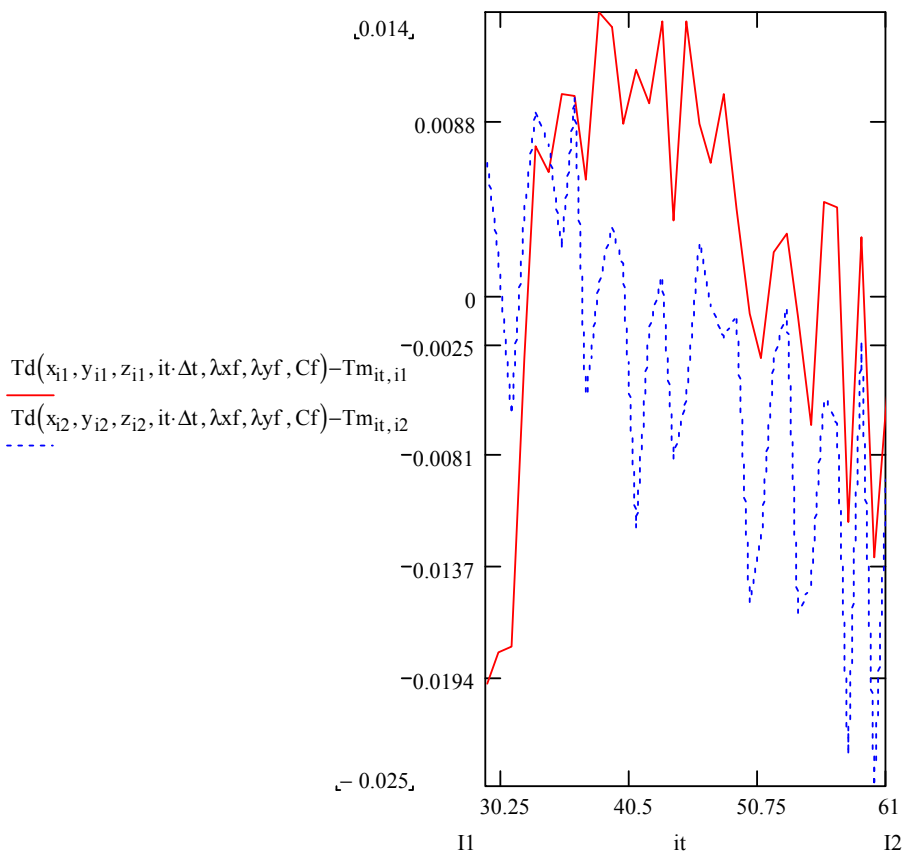
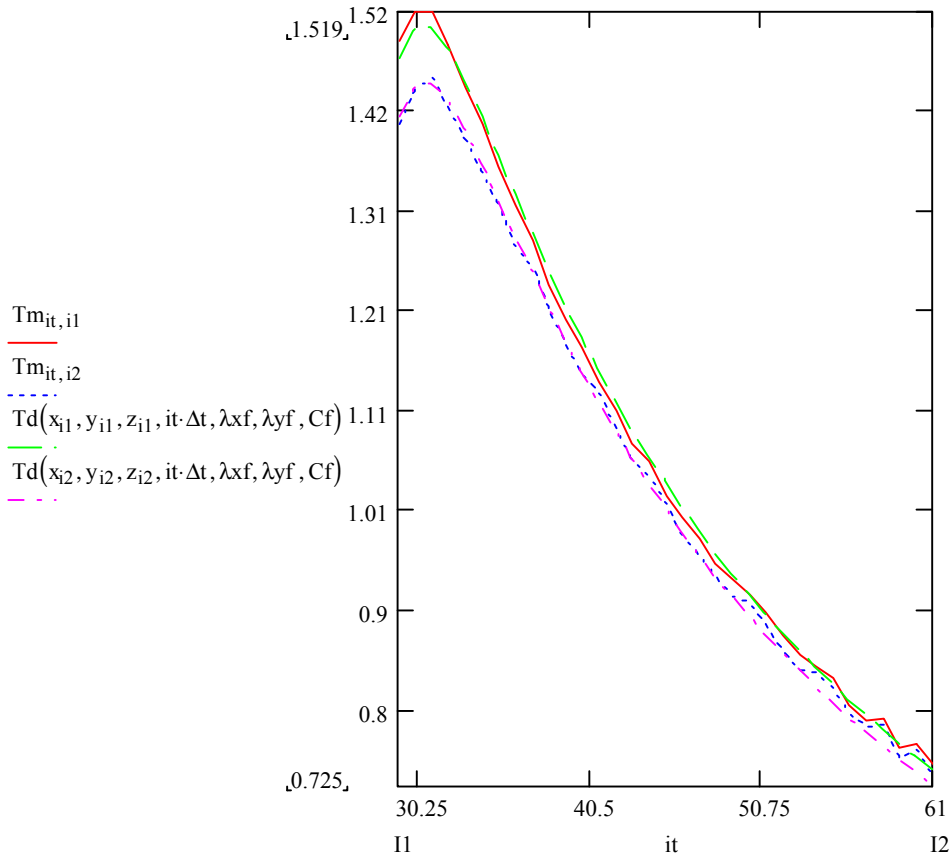
New measure, (B1)
 29-61
 E4f4



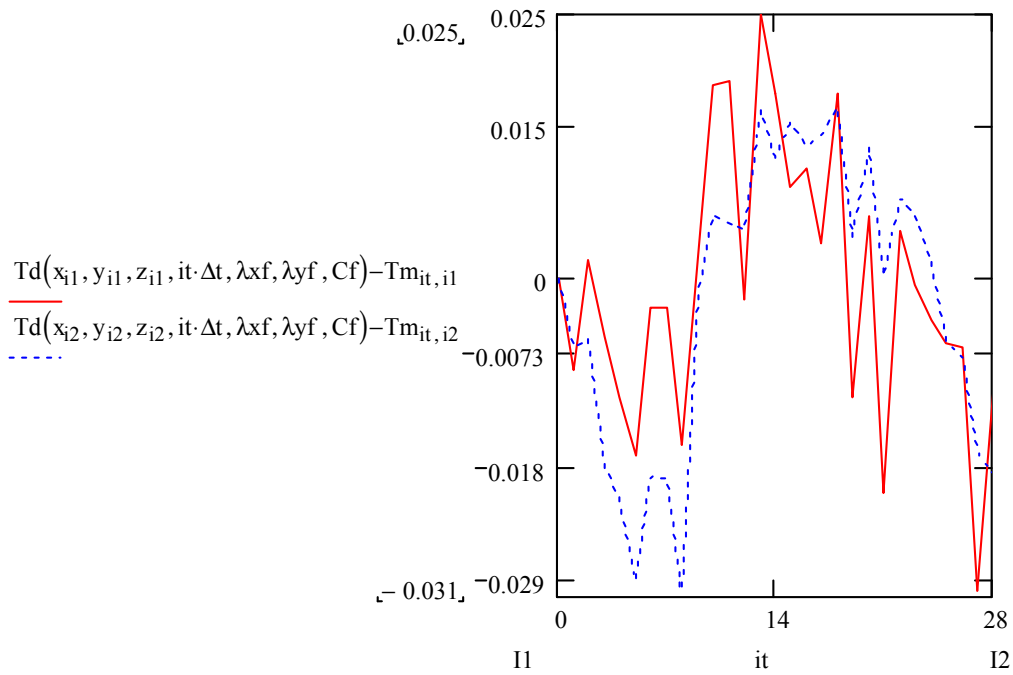
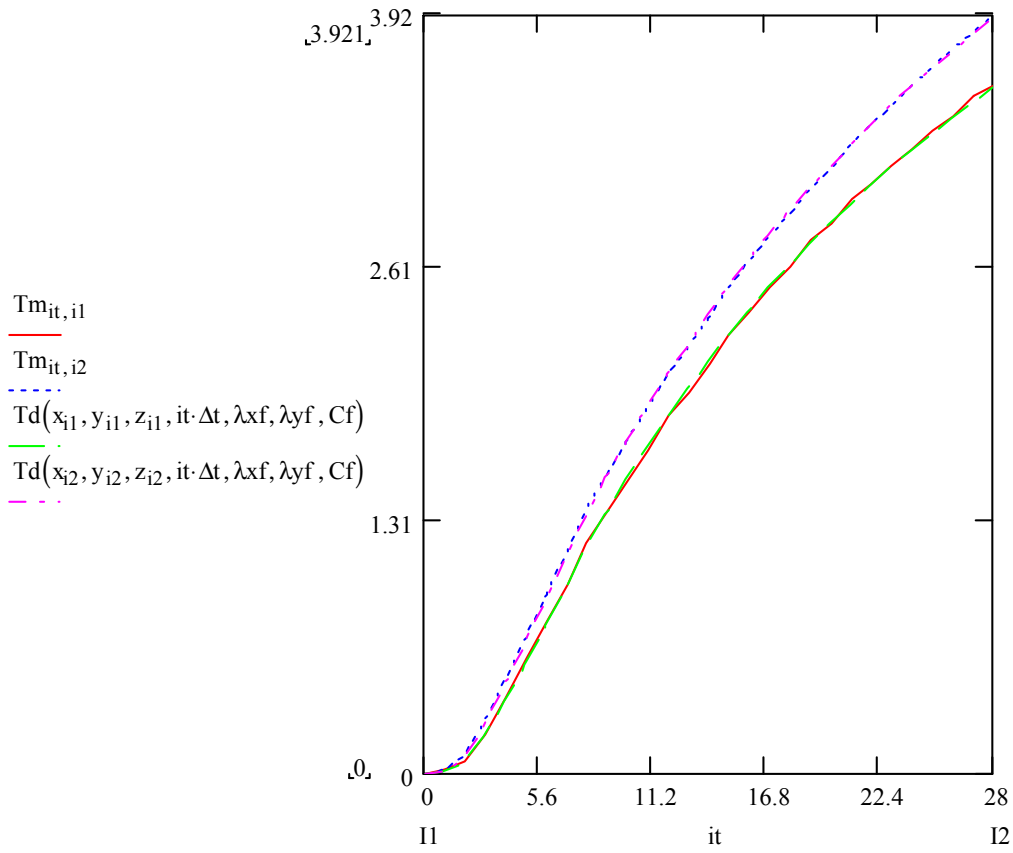
New measure, (B1)
 29-61
 E5f5



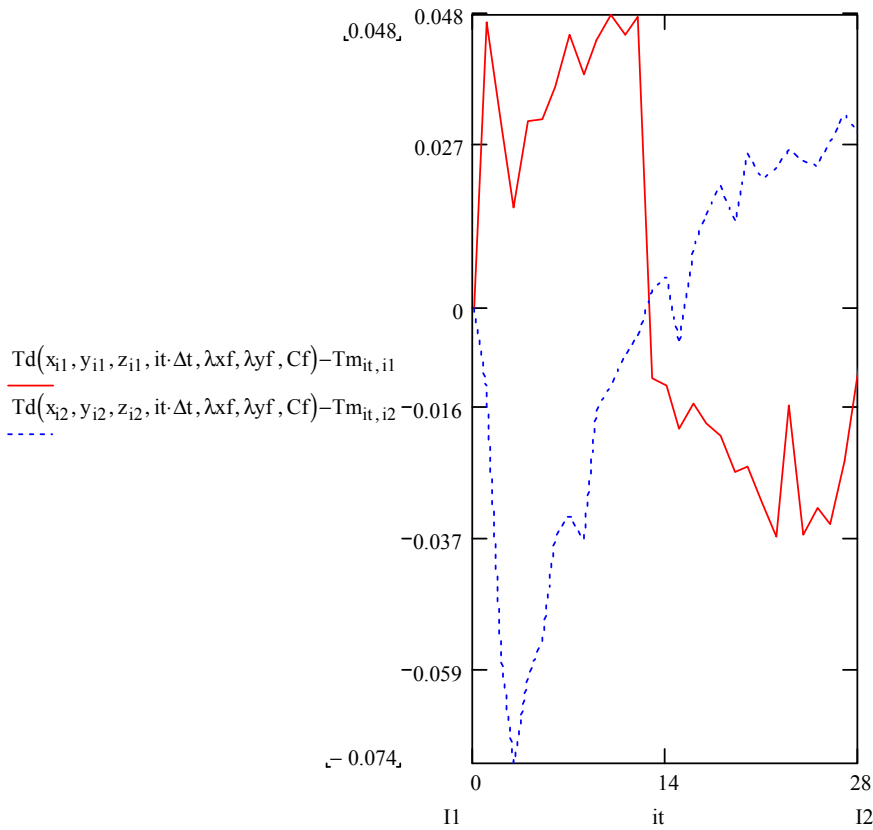
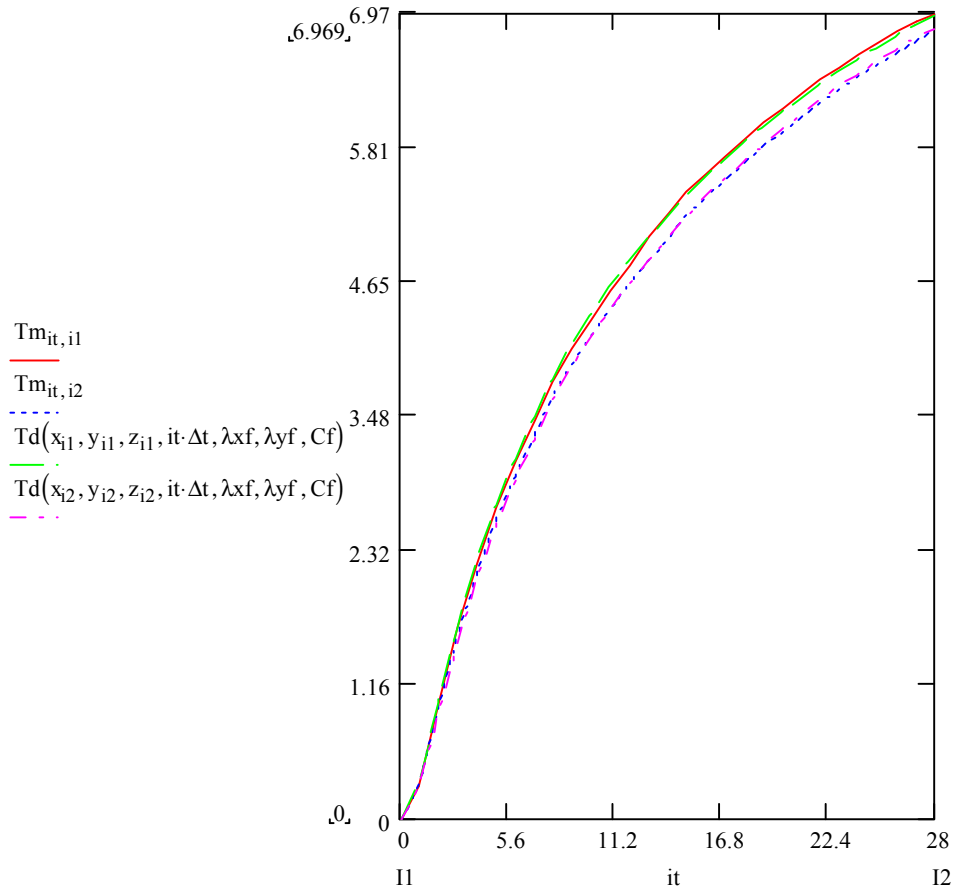
New measure, (B1)
 29-61
 E6f6



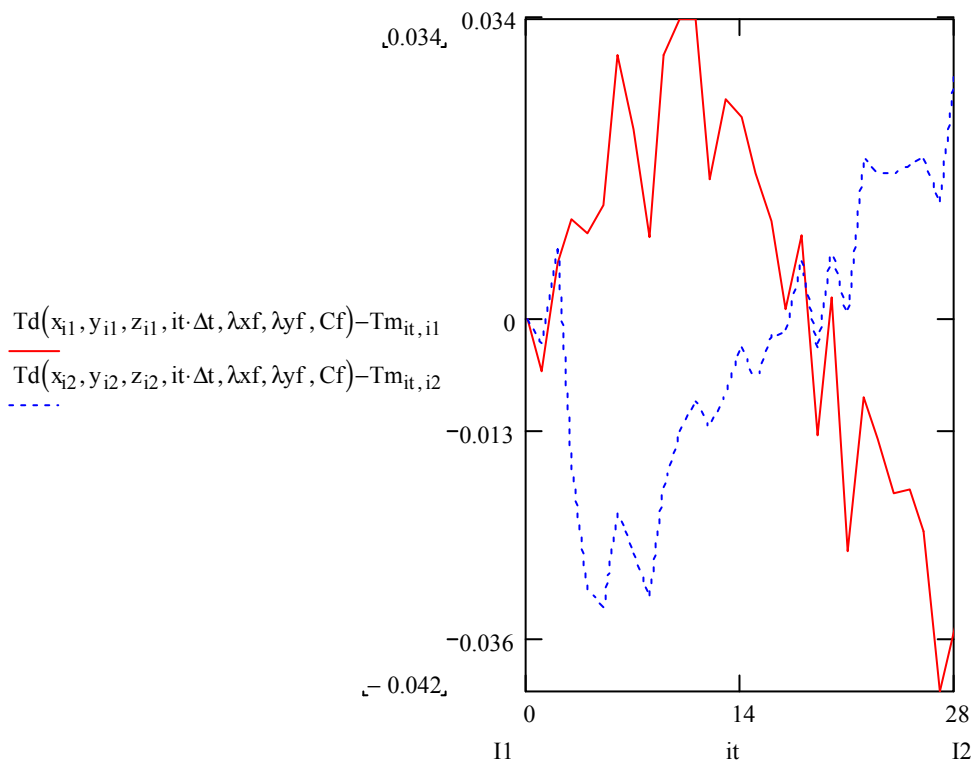
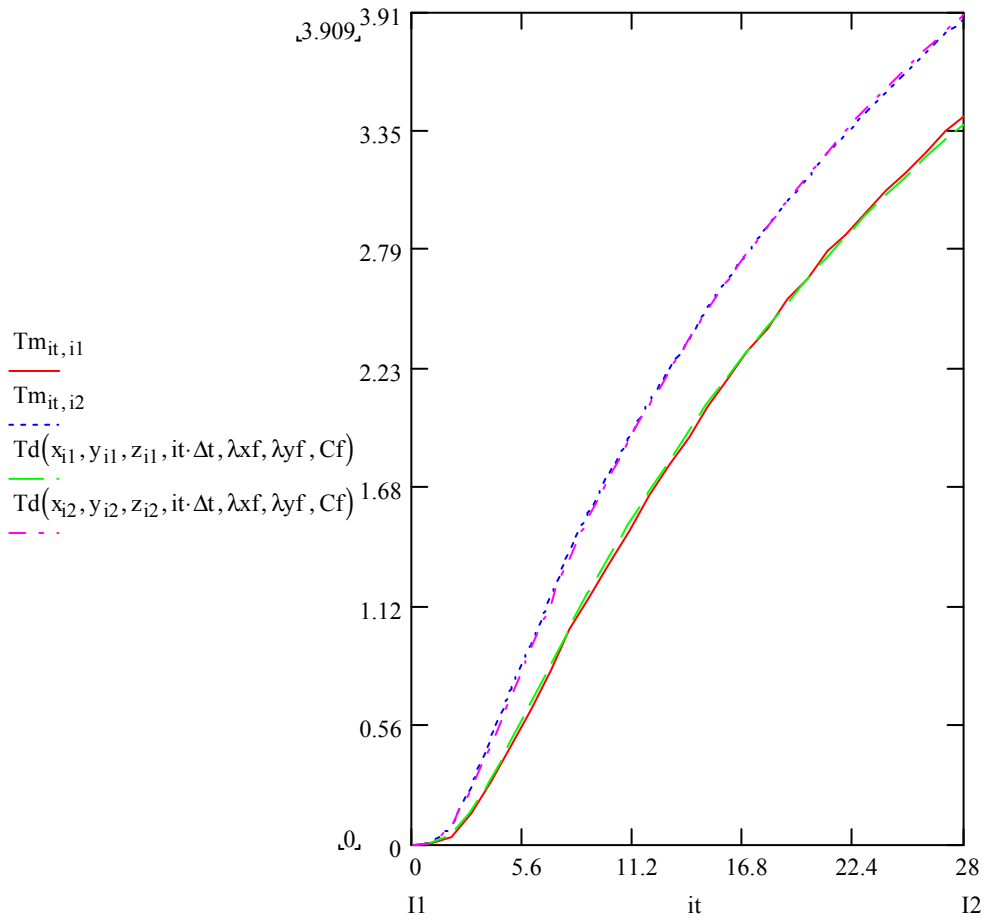
New measure, (B1)
 0-28
 C1d1



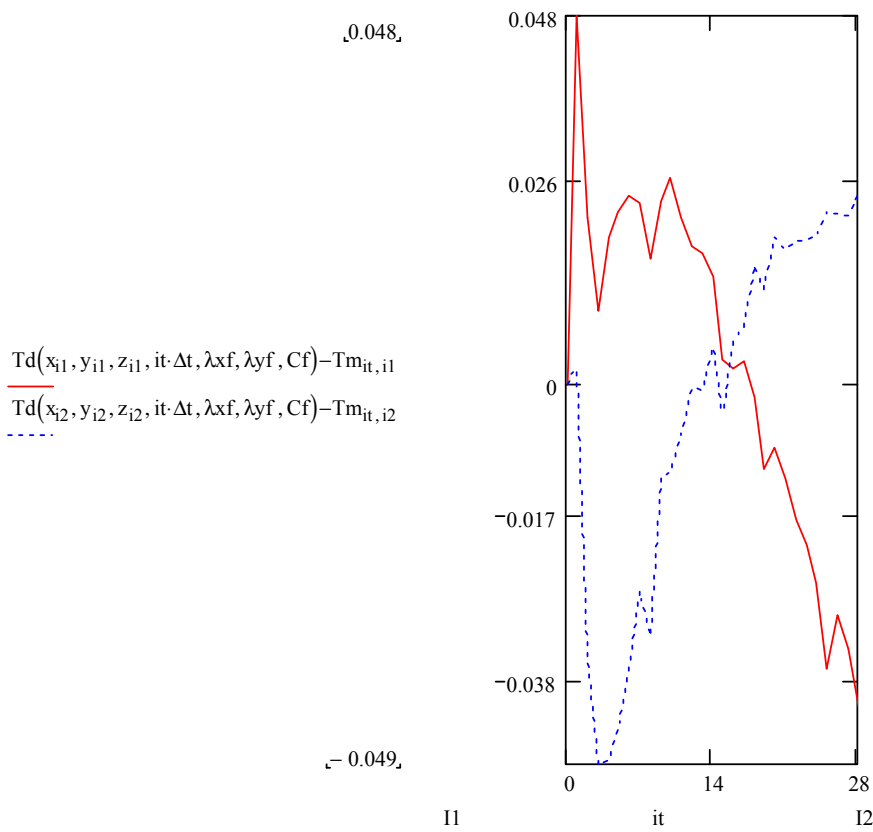
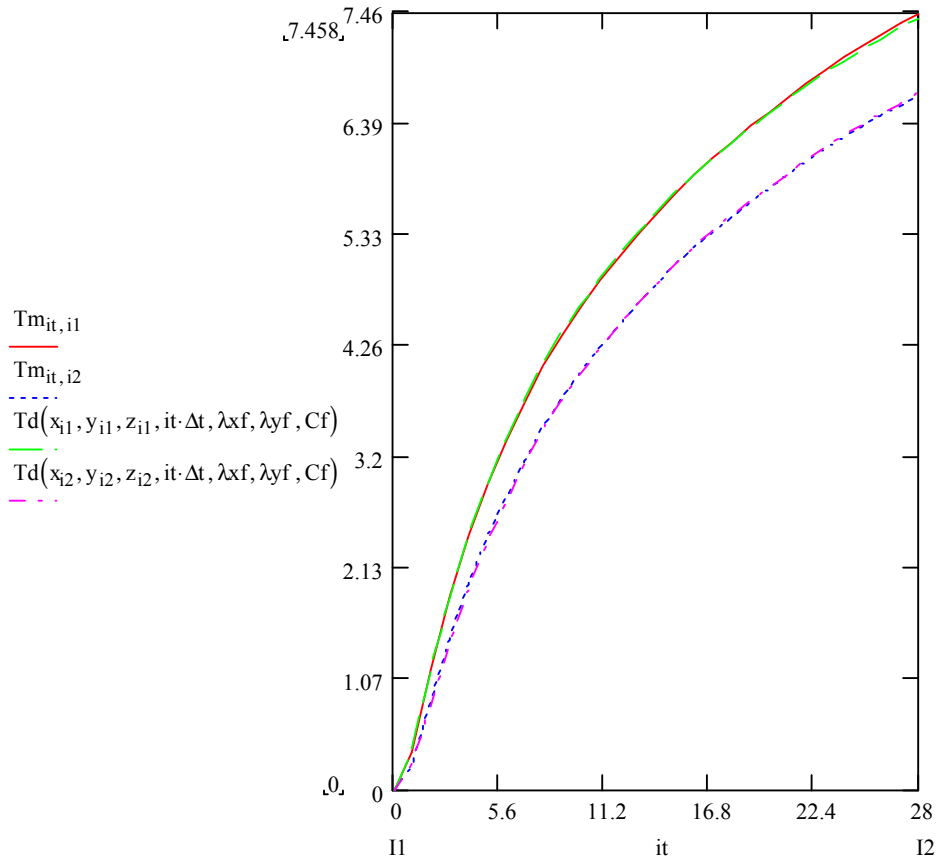
New measure, (B1)
0-28
E1f1



New measure, (B1)
 0-28
 C2d2



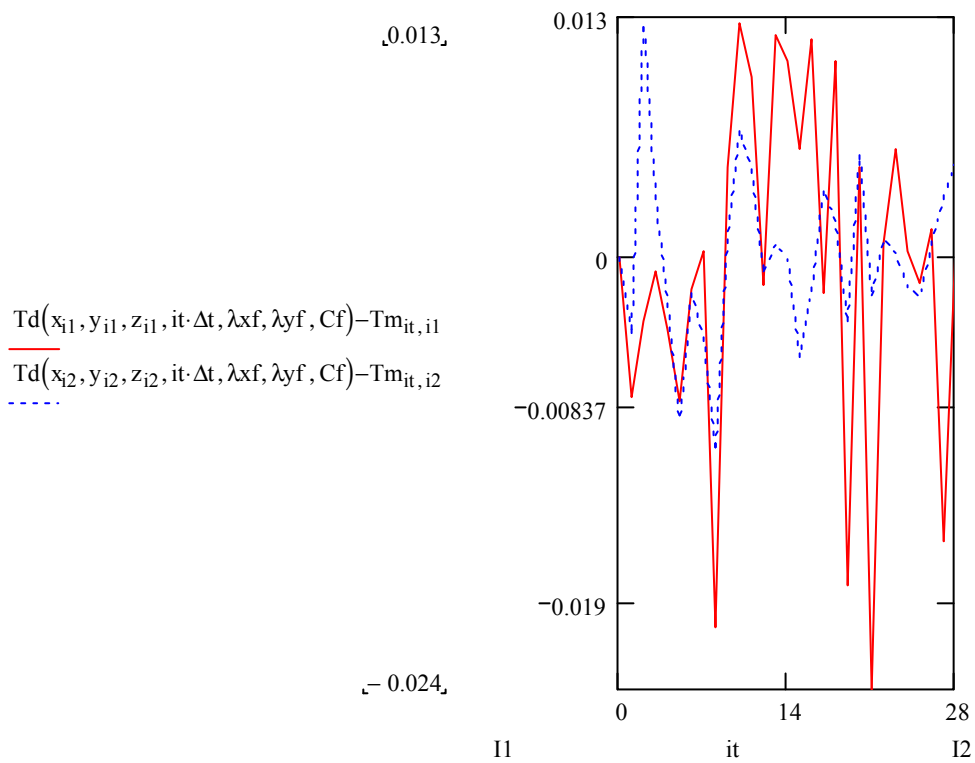
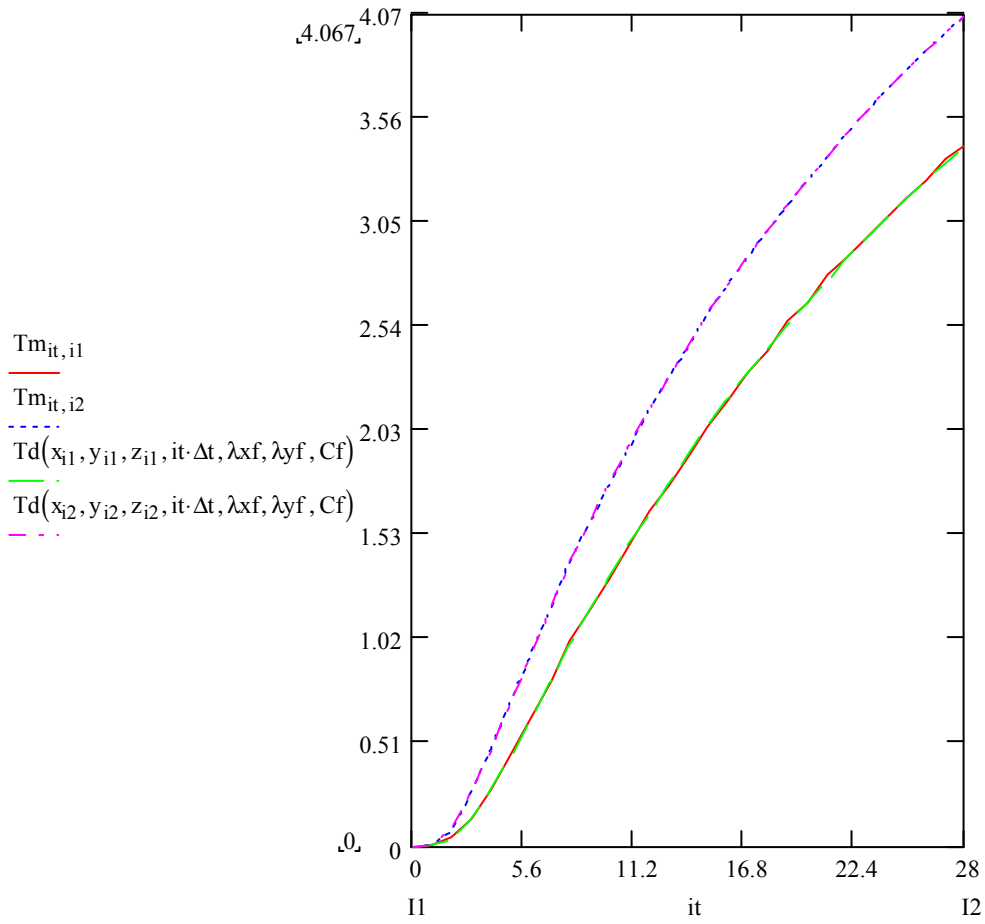
New measure, (B1)
 0-28
 E2f2



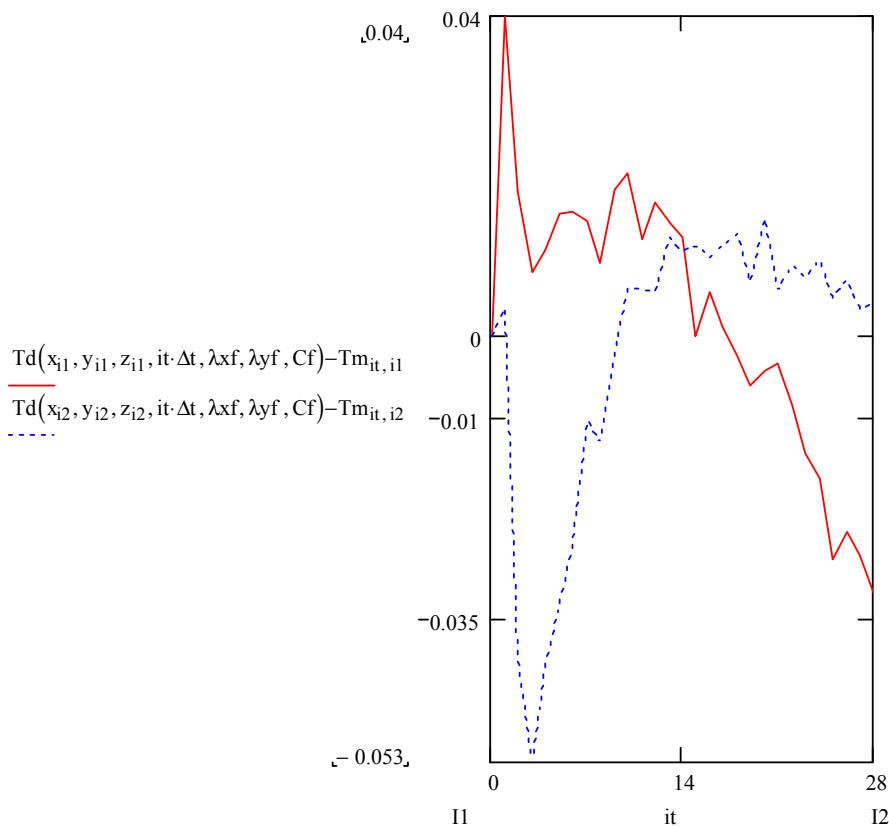
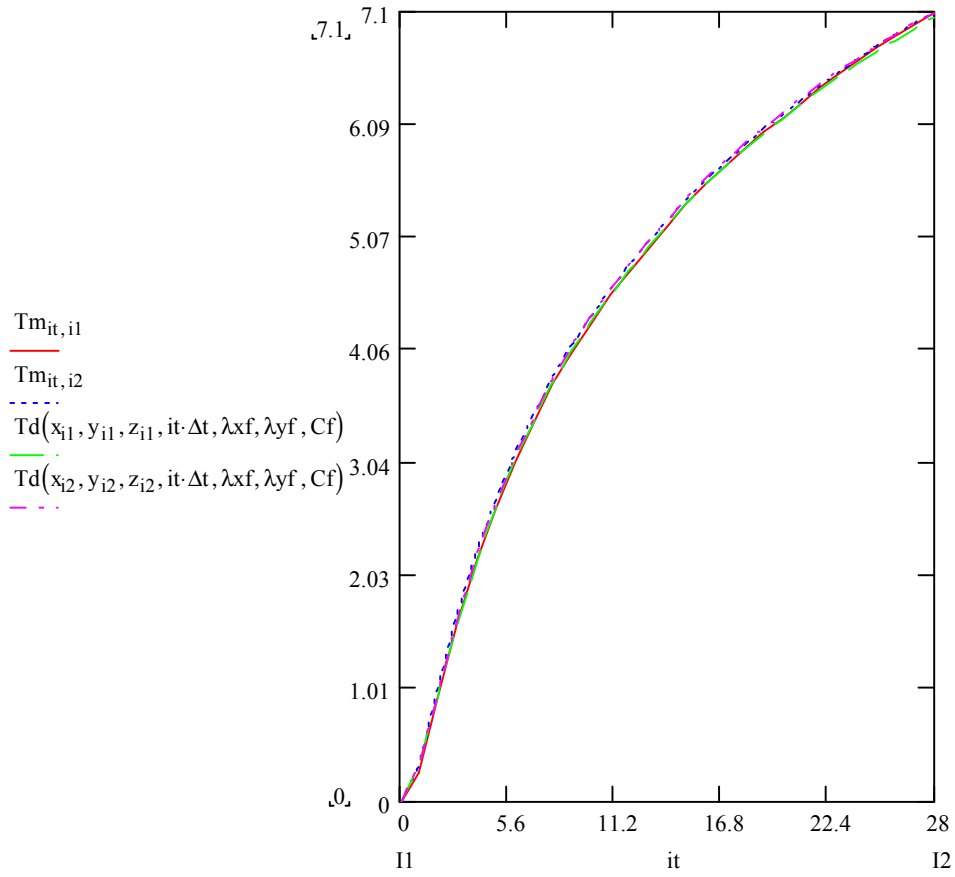
New measure, (B1)

0-28

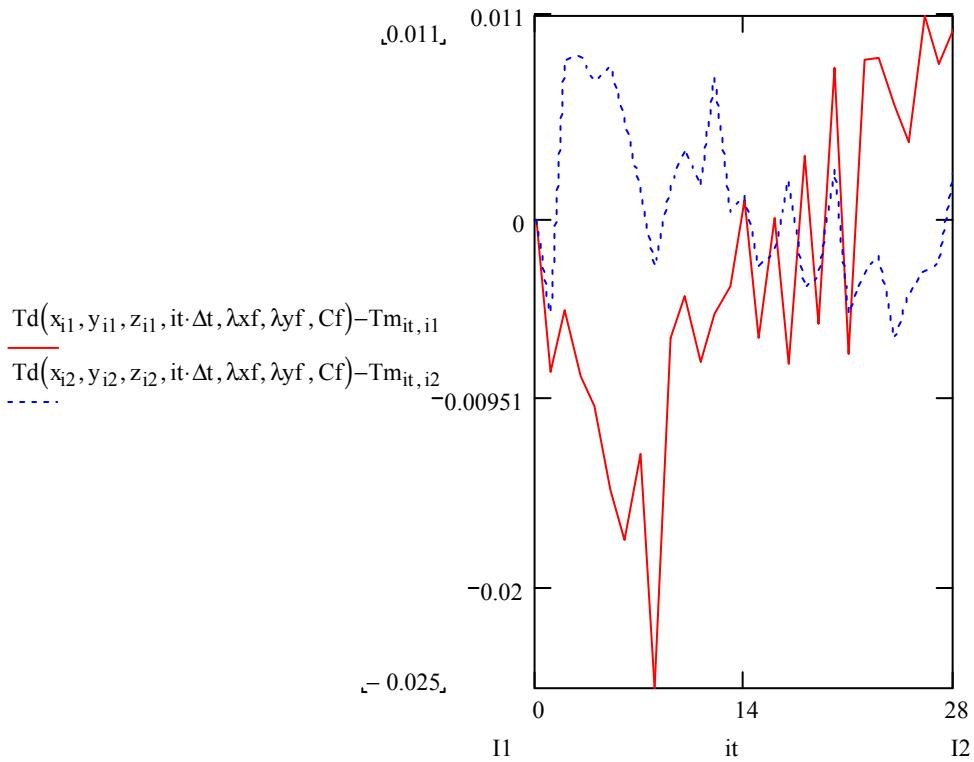
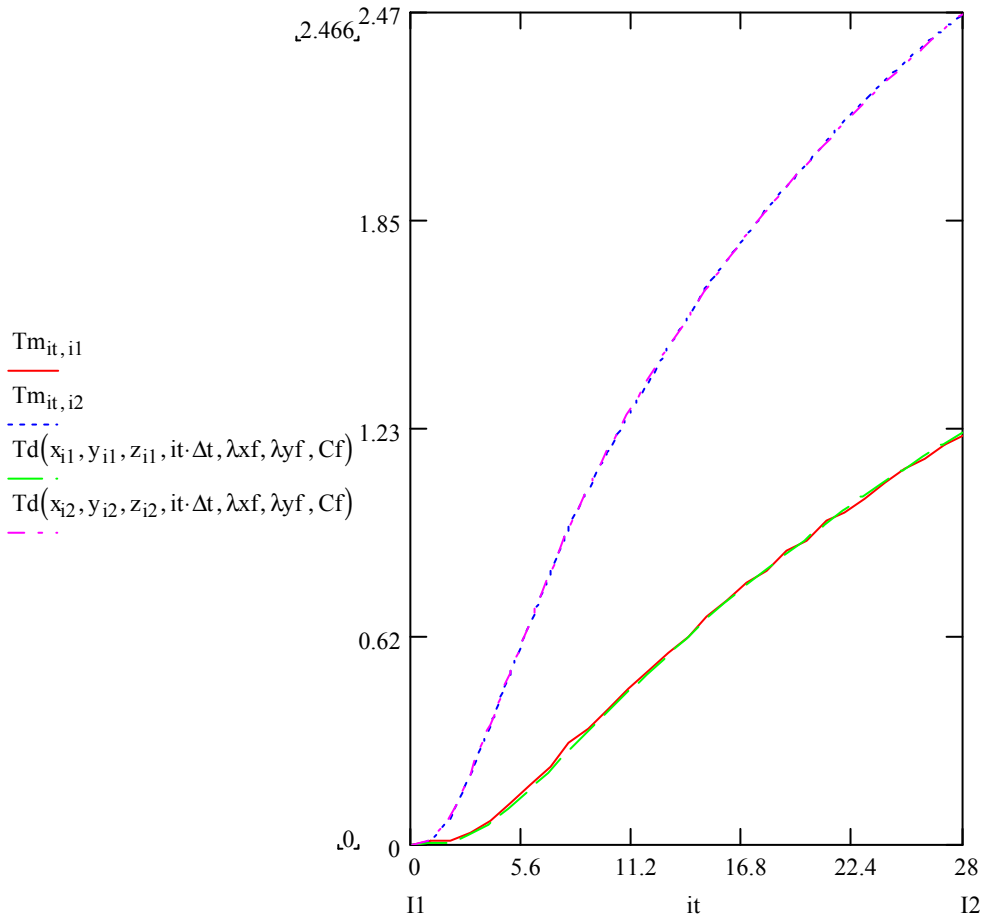
C3d3



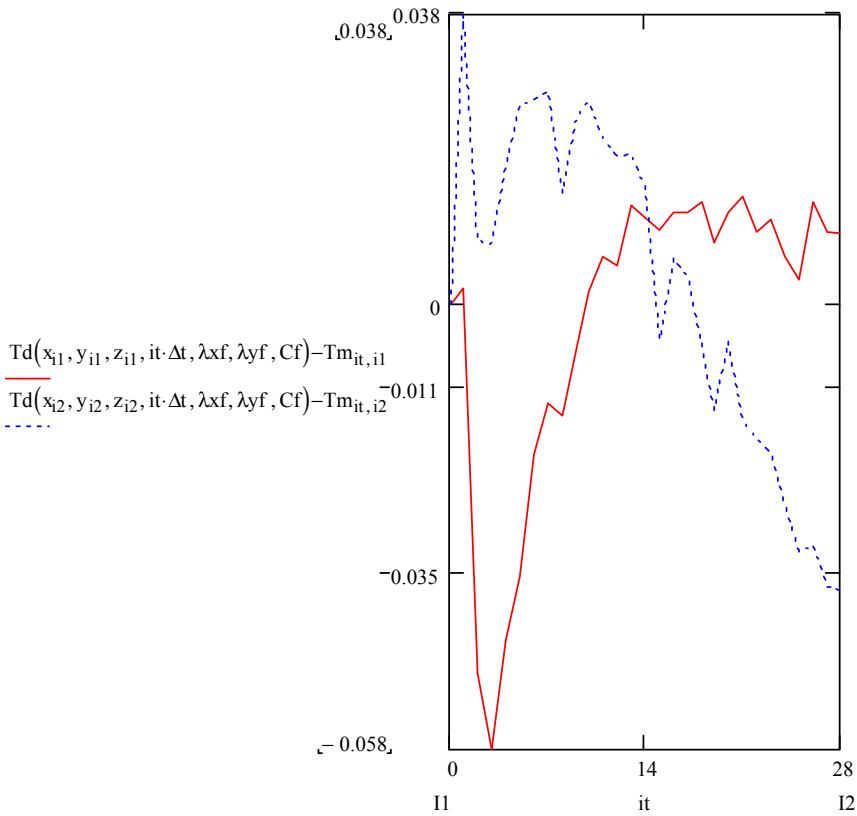
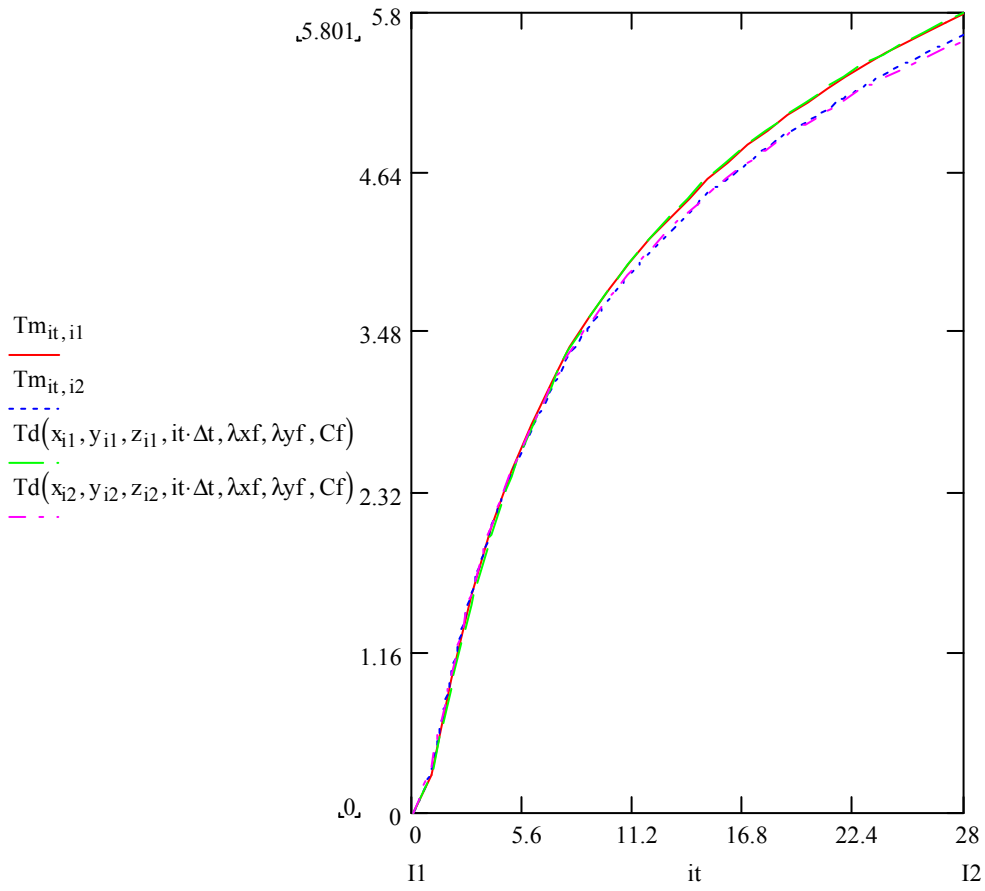
New measure, (B1)
 0-28
 E3f3



New measure, (B1)
 0-28
 C4d4



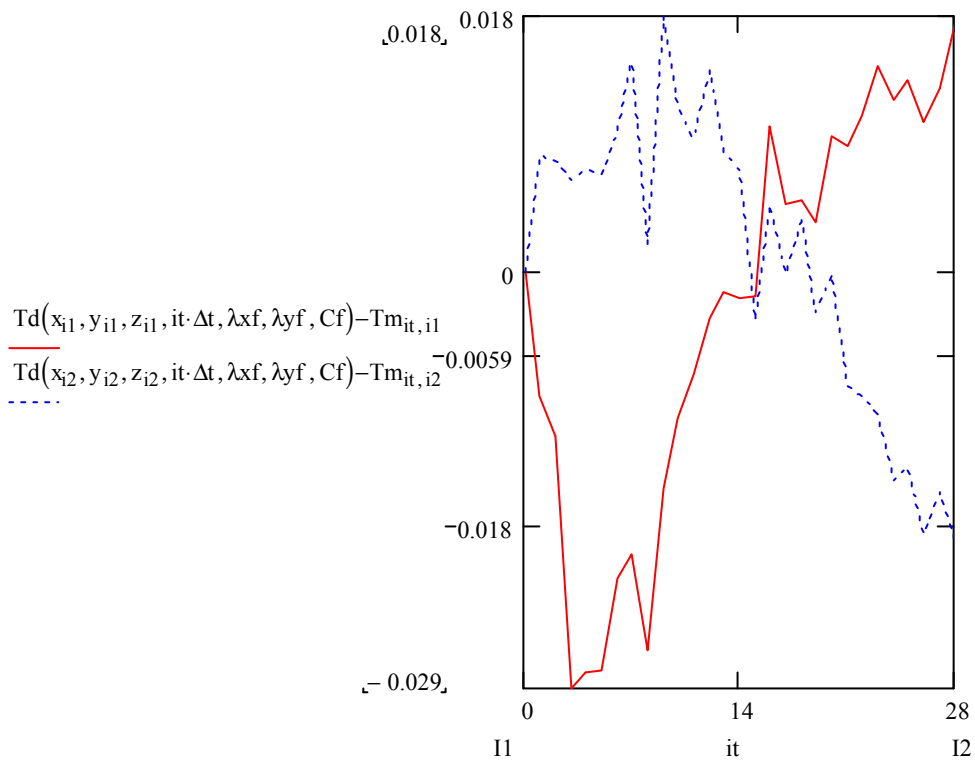
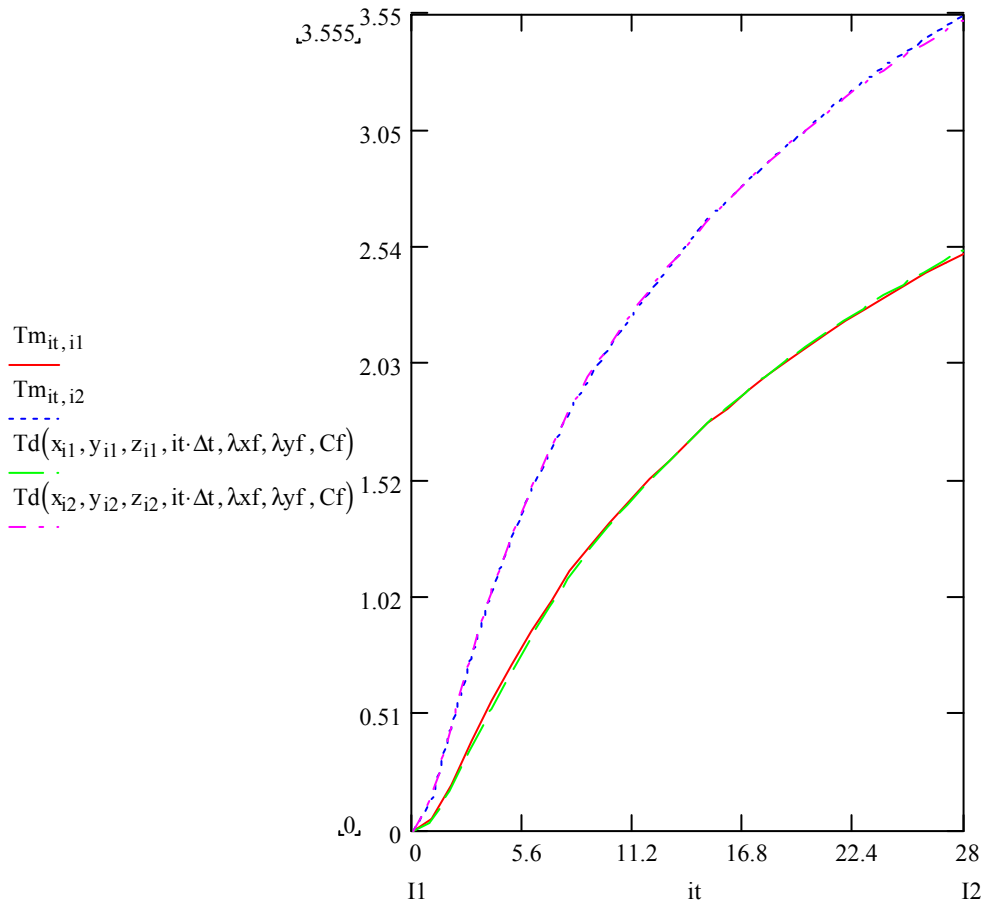
New measure, (B1)
 0-28
 E4f4



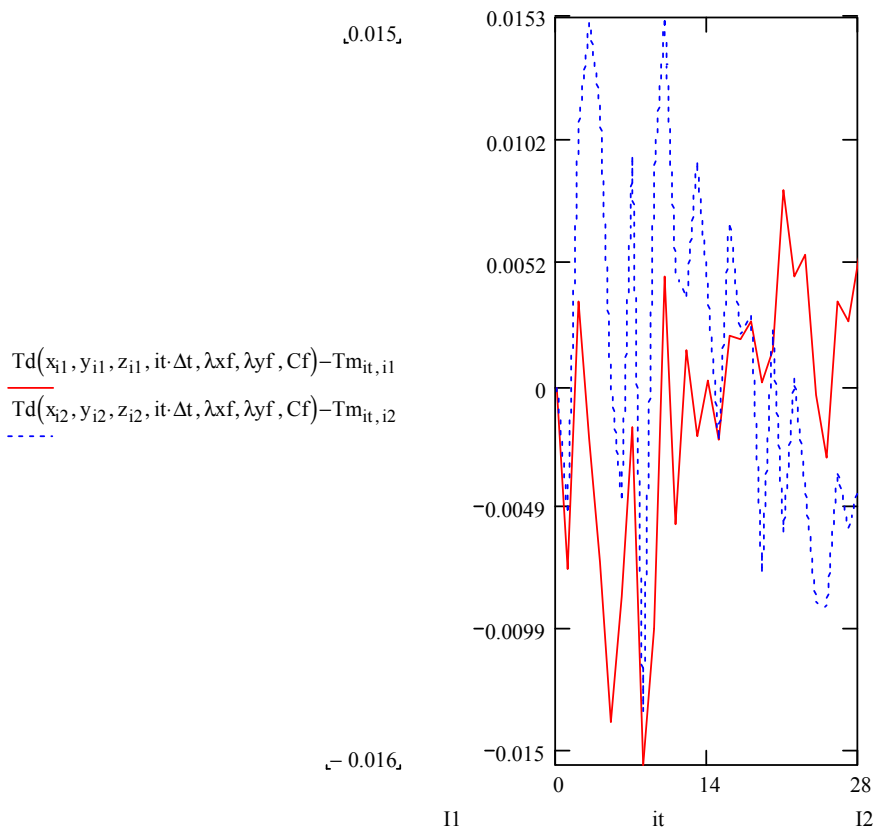
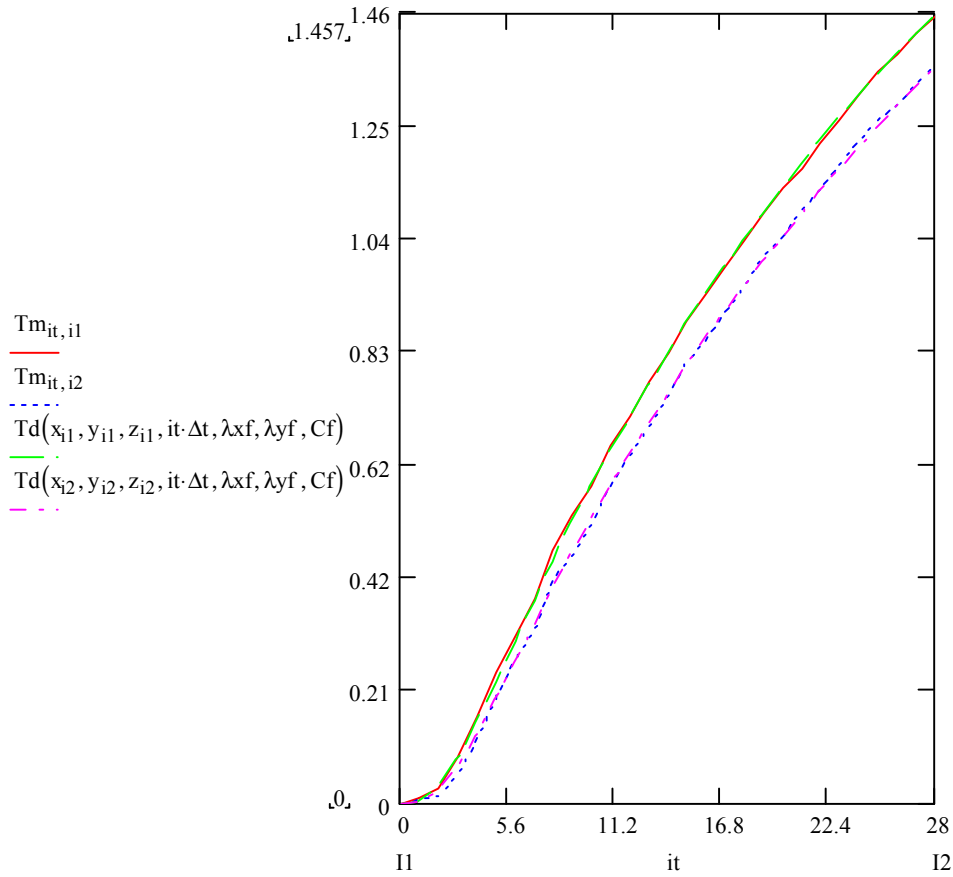
New measure, (B1)

0-28

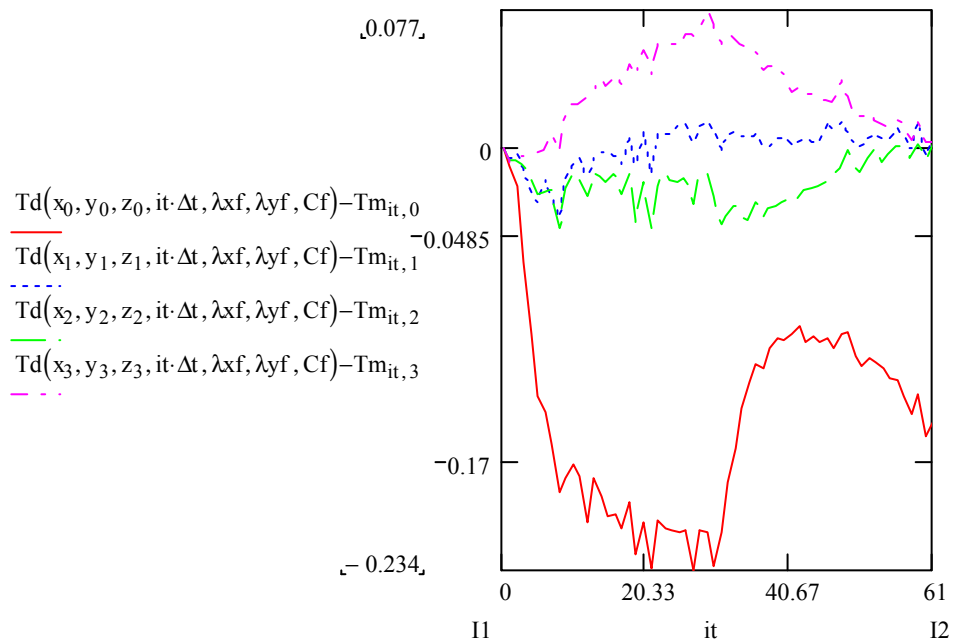
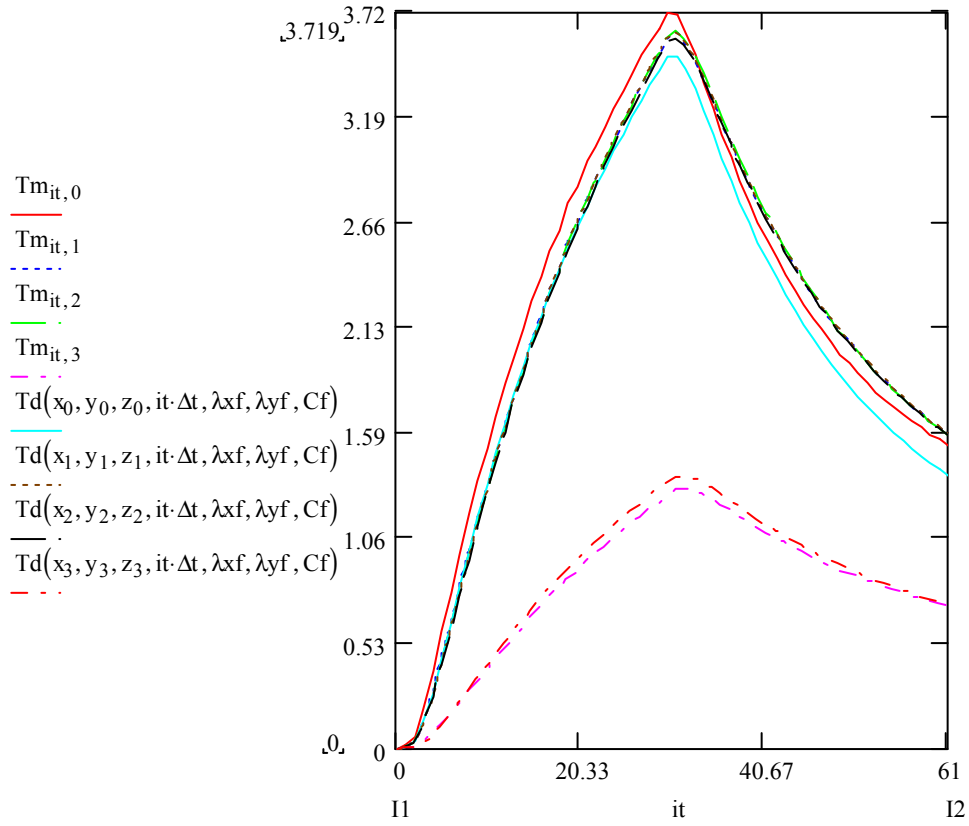
E5f5

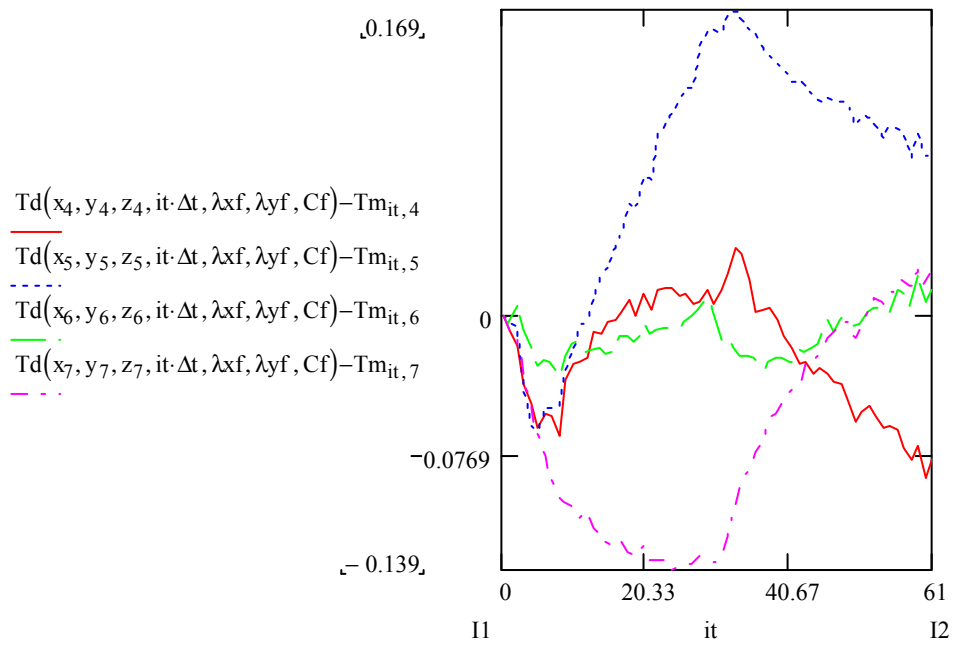
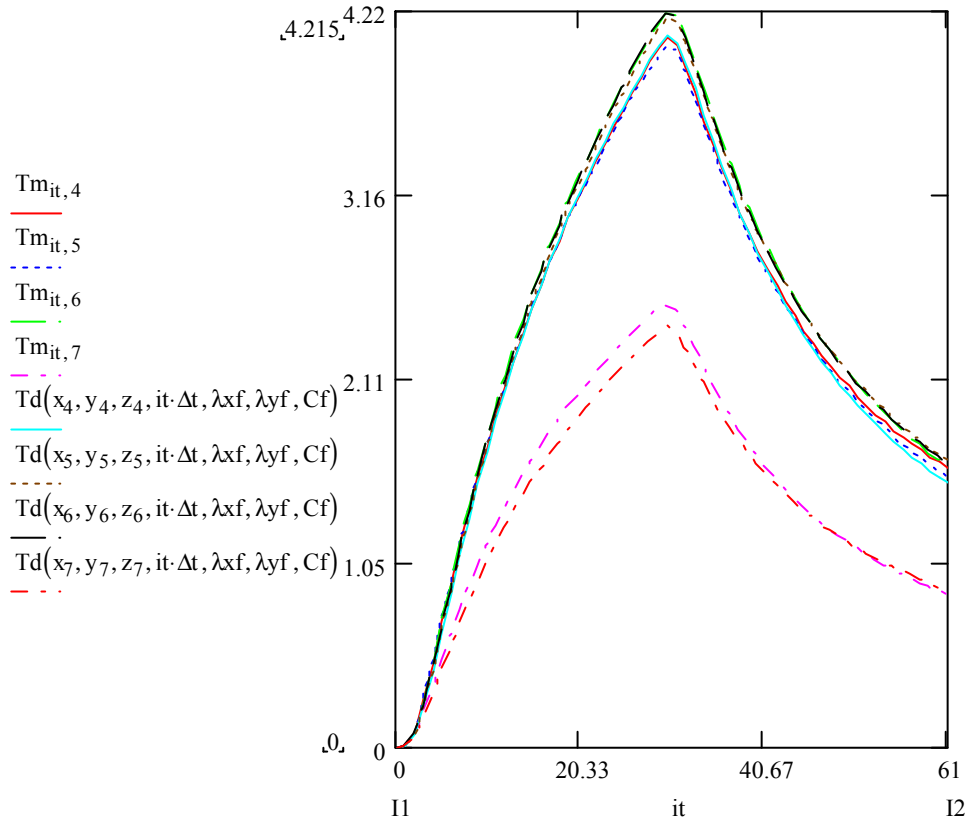


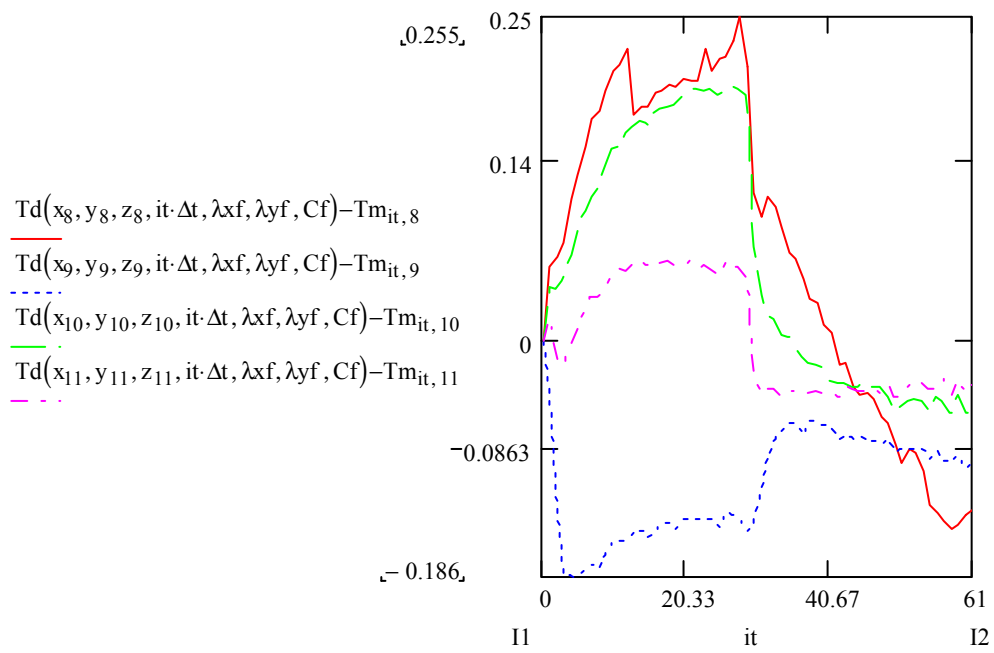
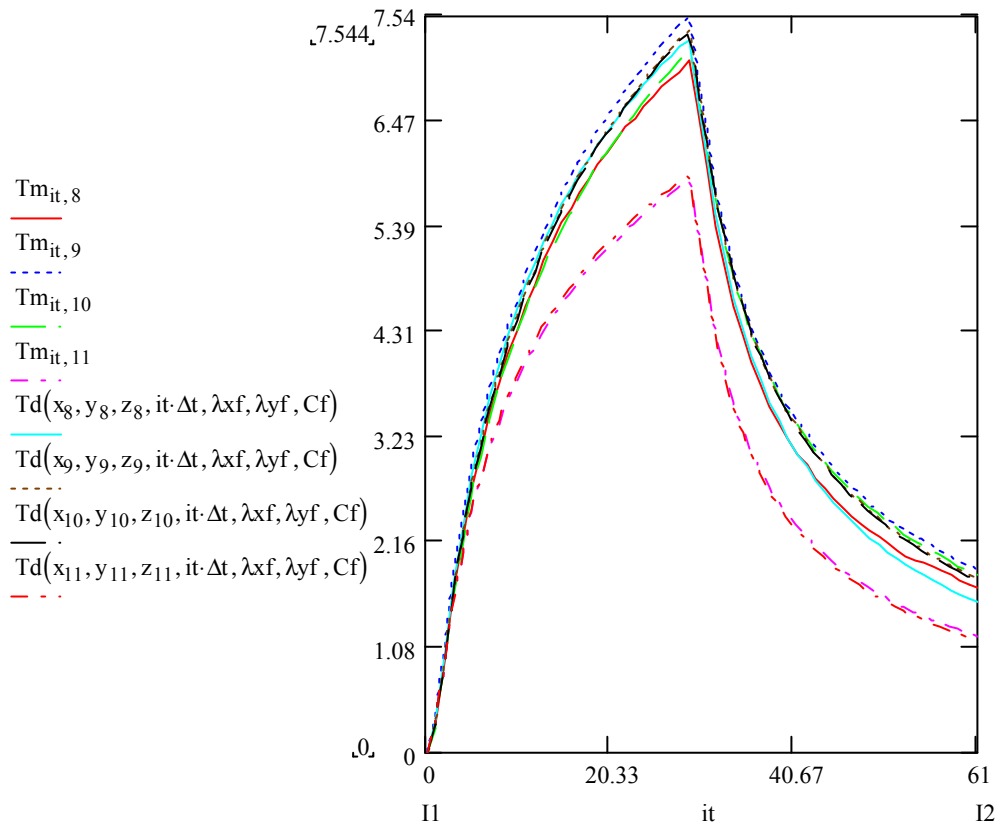
New measure, (B1)
 0-28
 E6f6

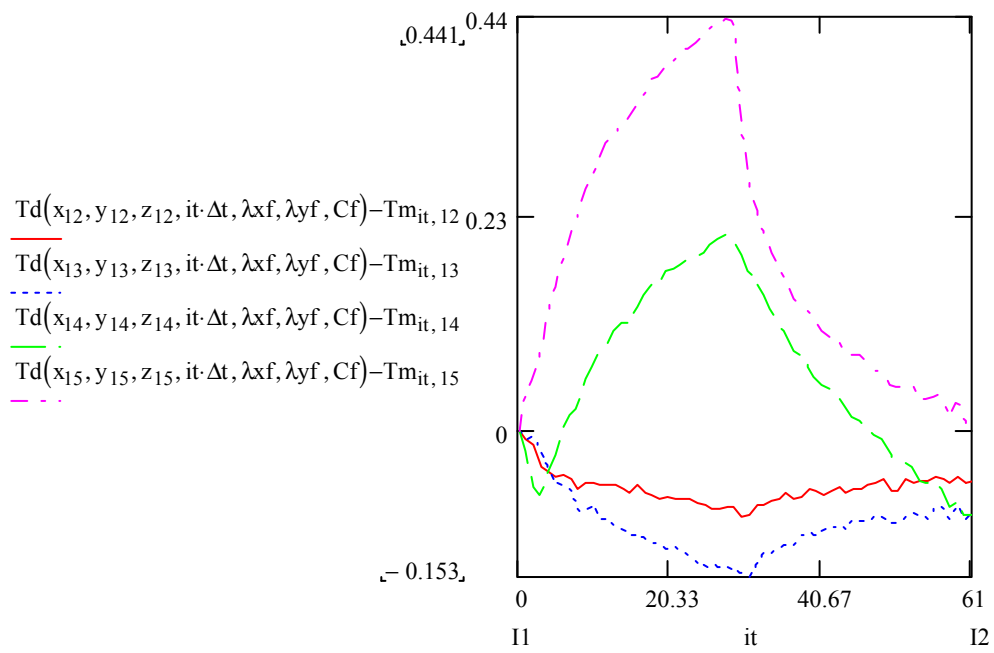
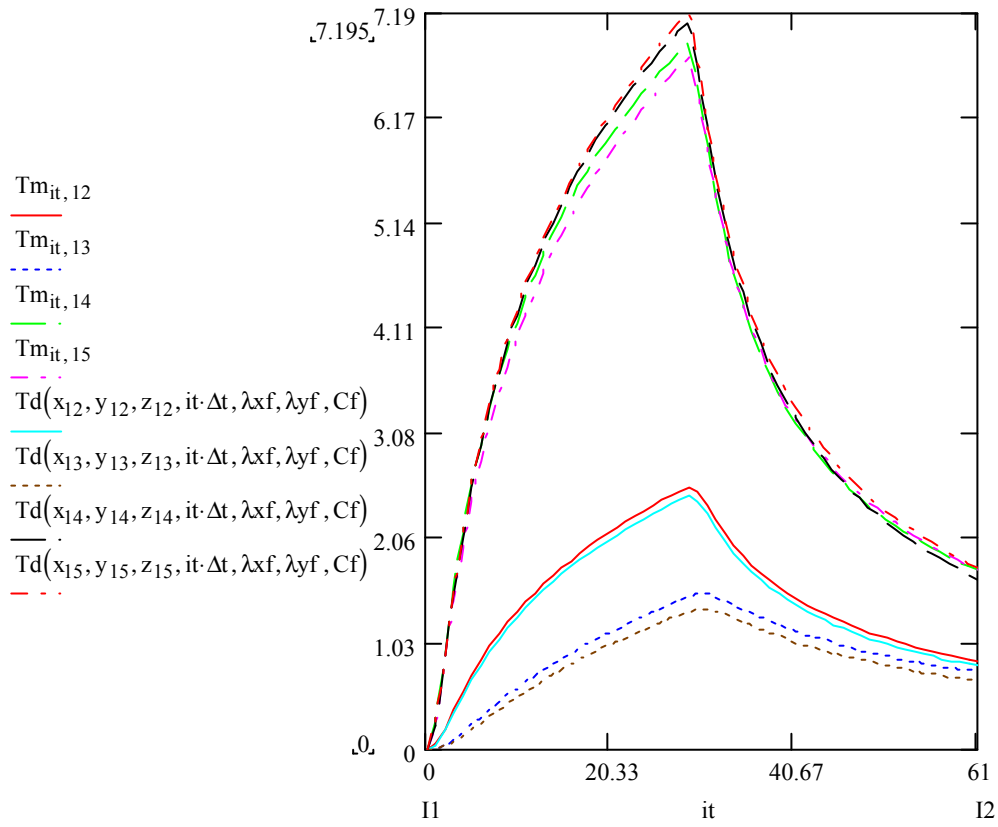


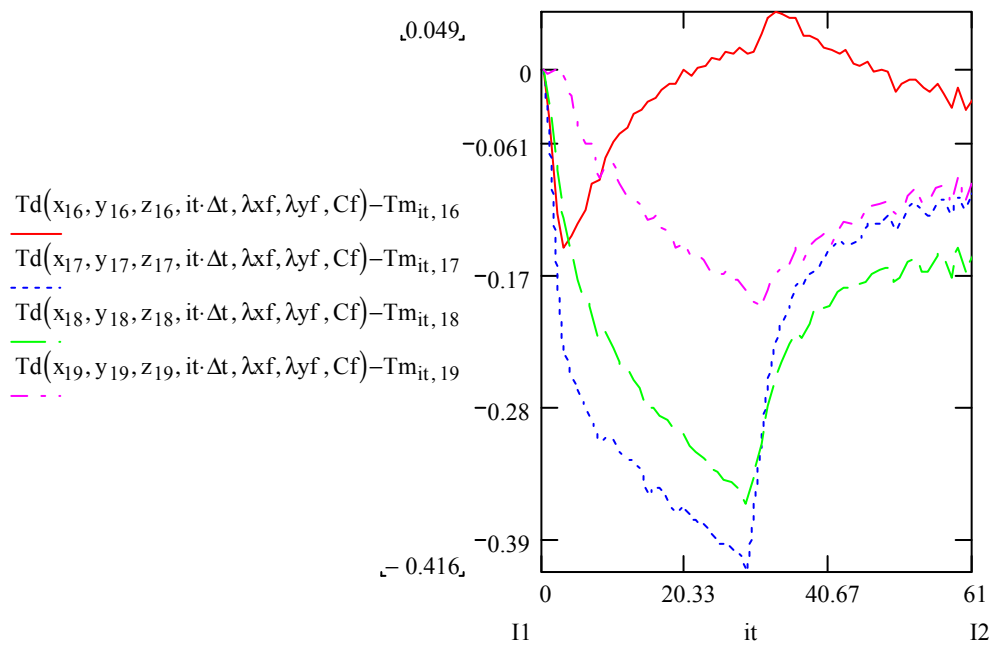
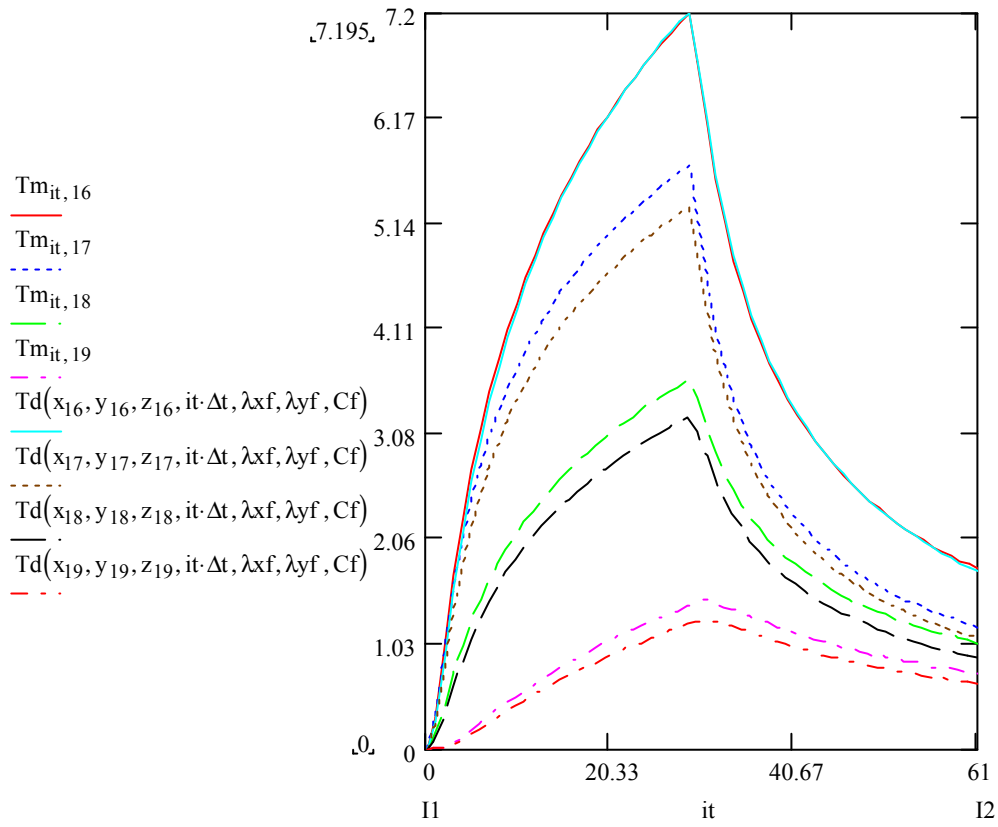
New measure, (C1)
 0-61
 Cdef123456



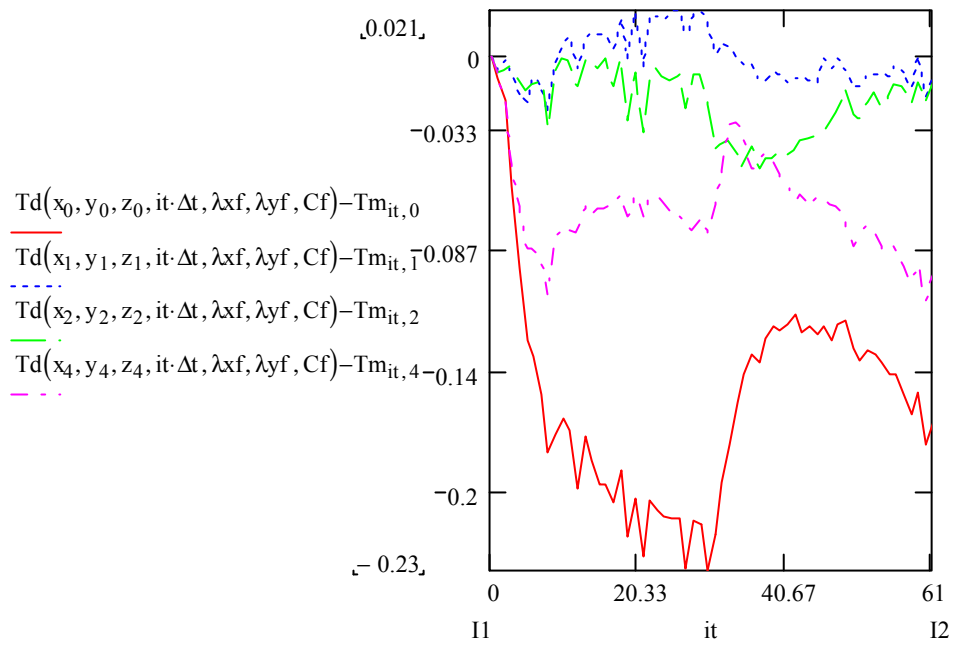
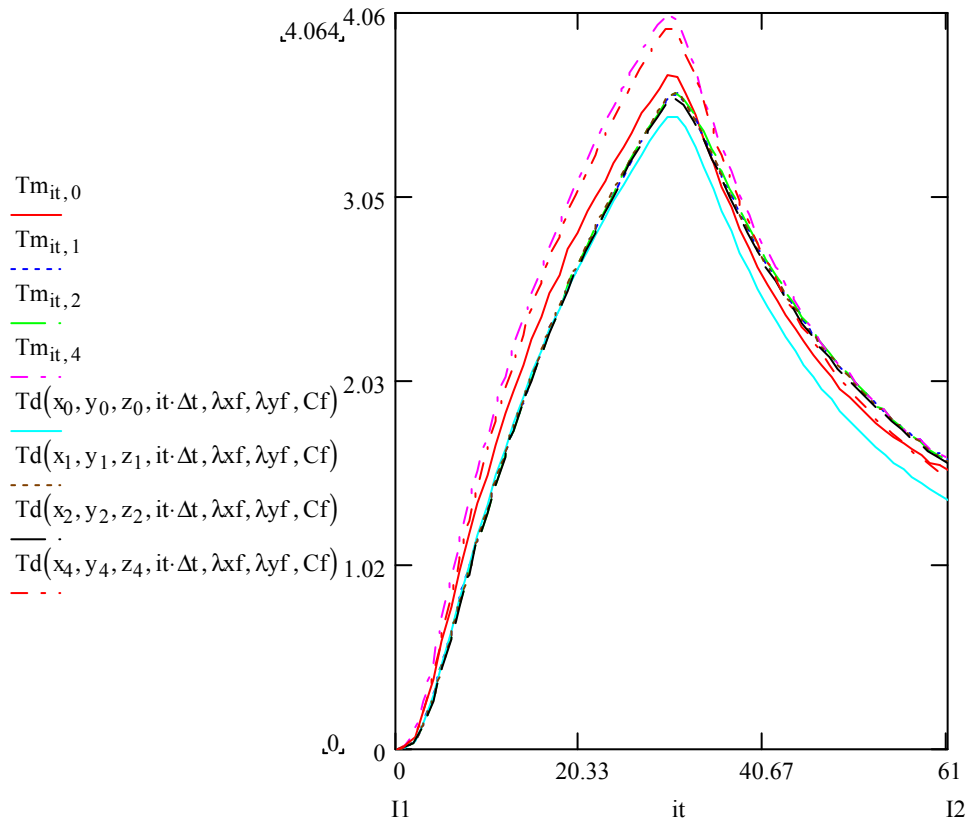


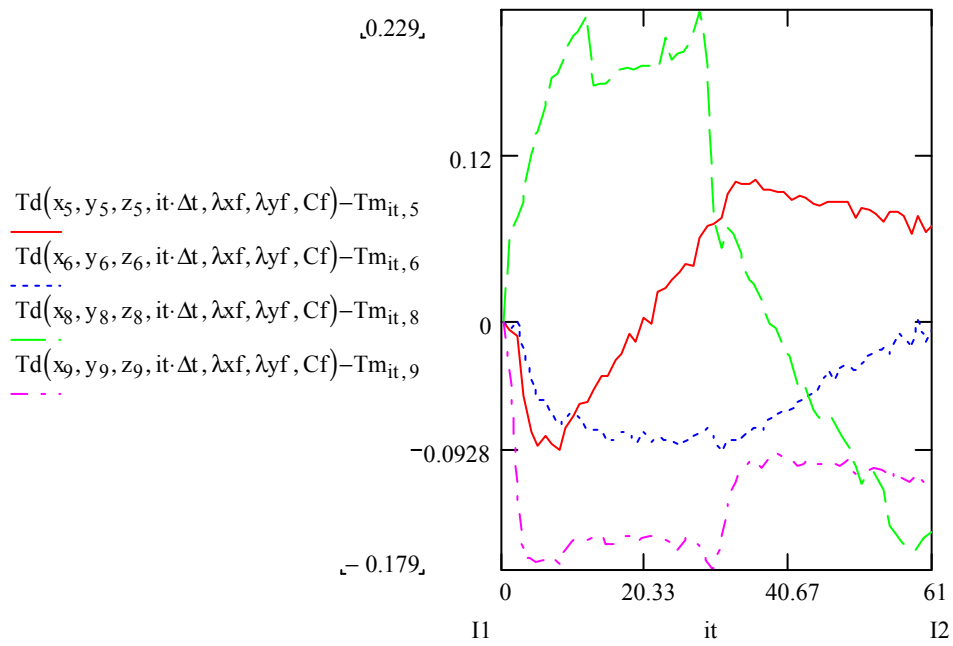
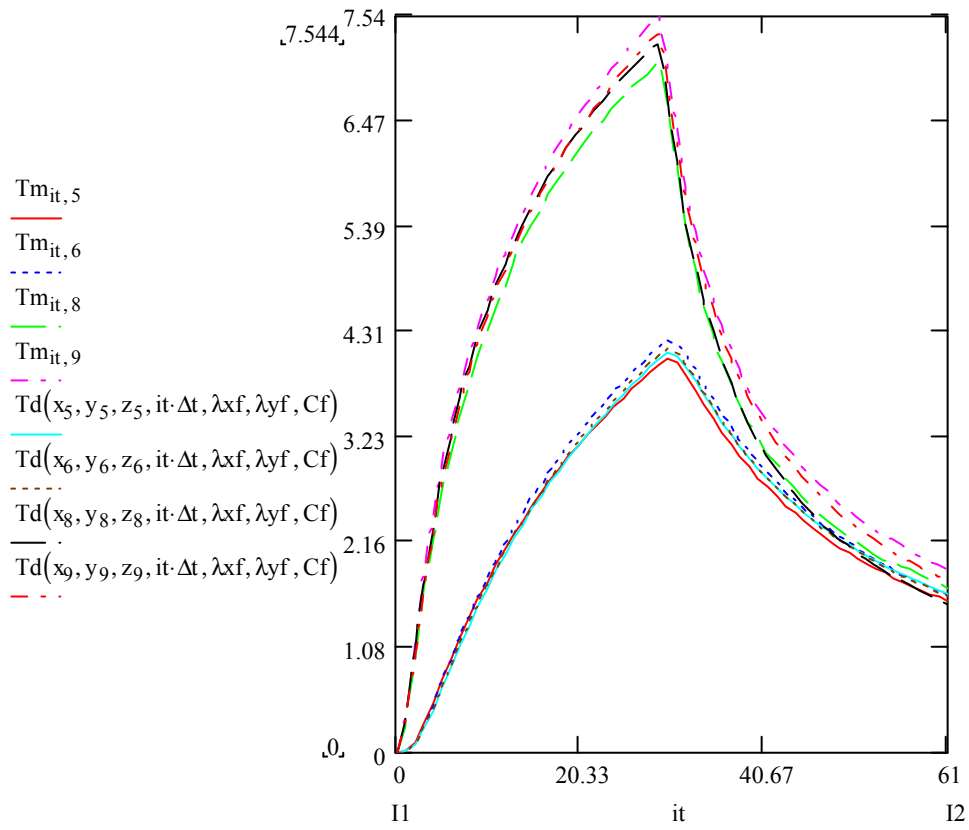


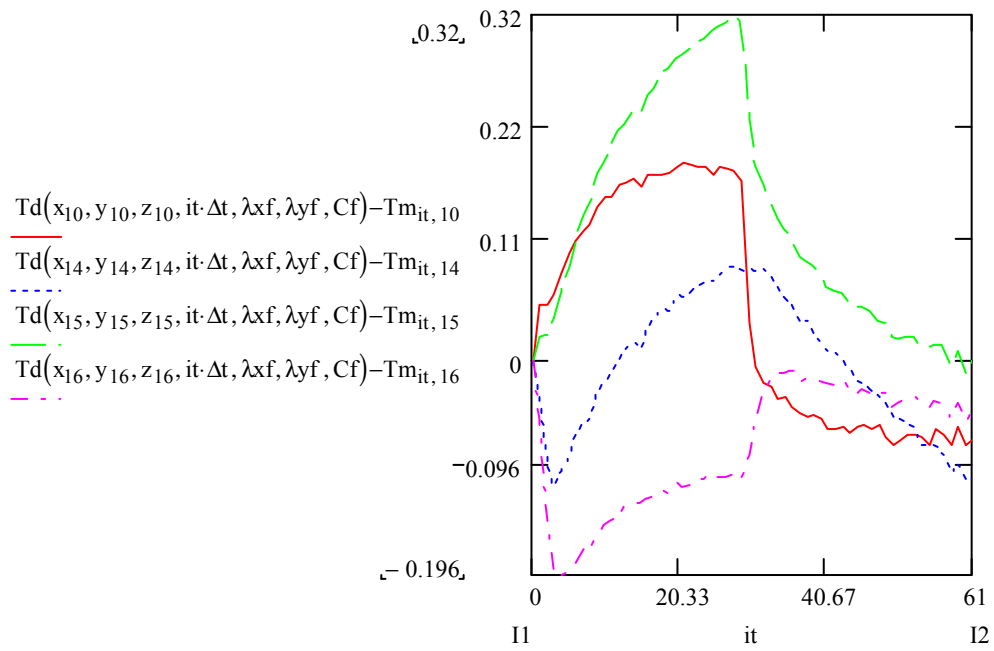
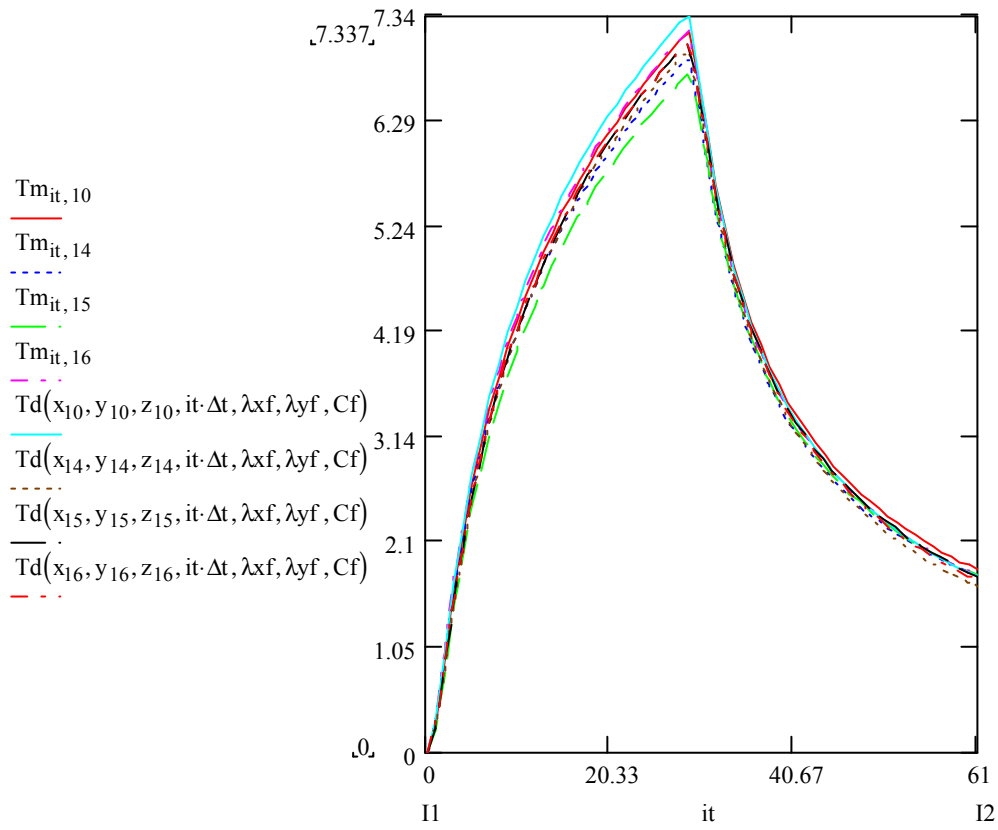




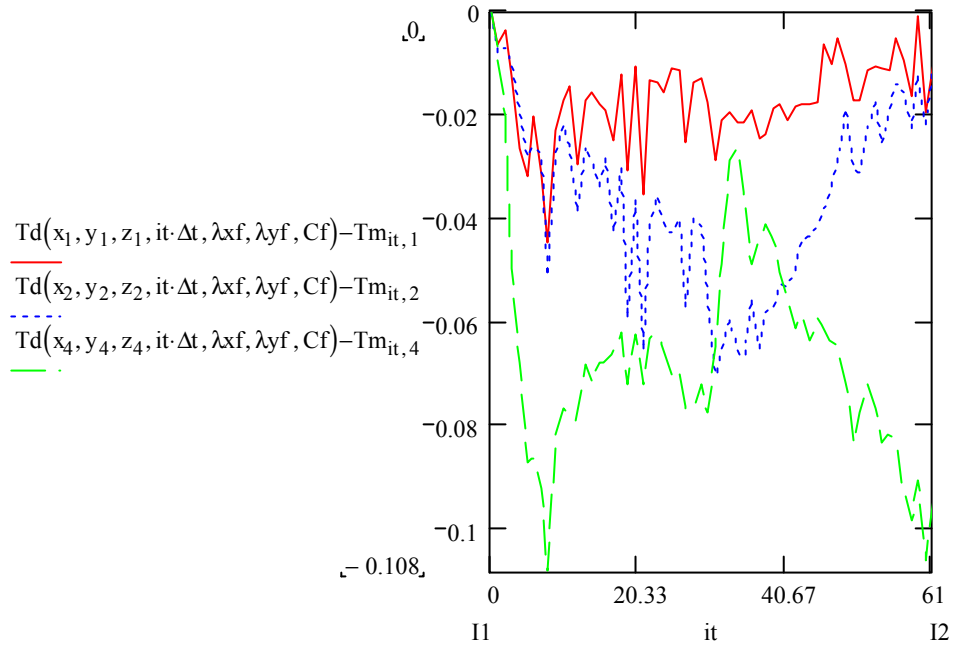
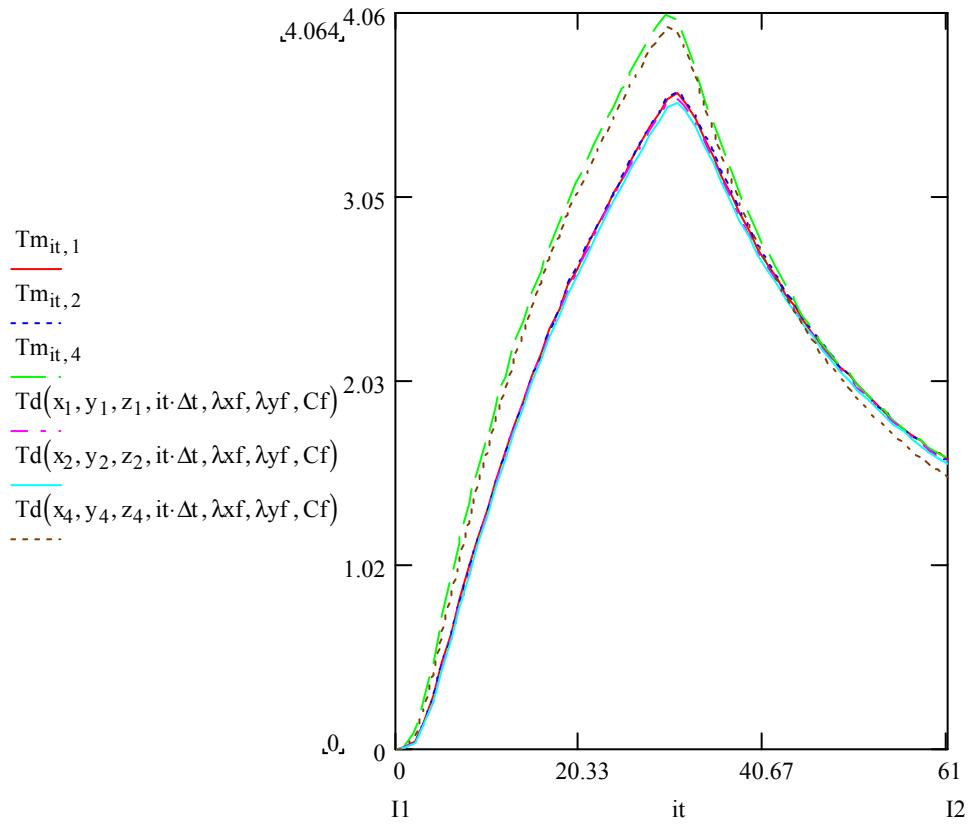
0-61 (C2)
Cdef123

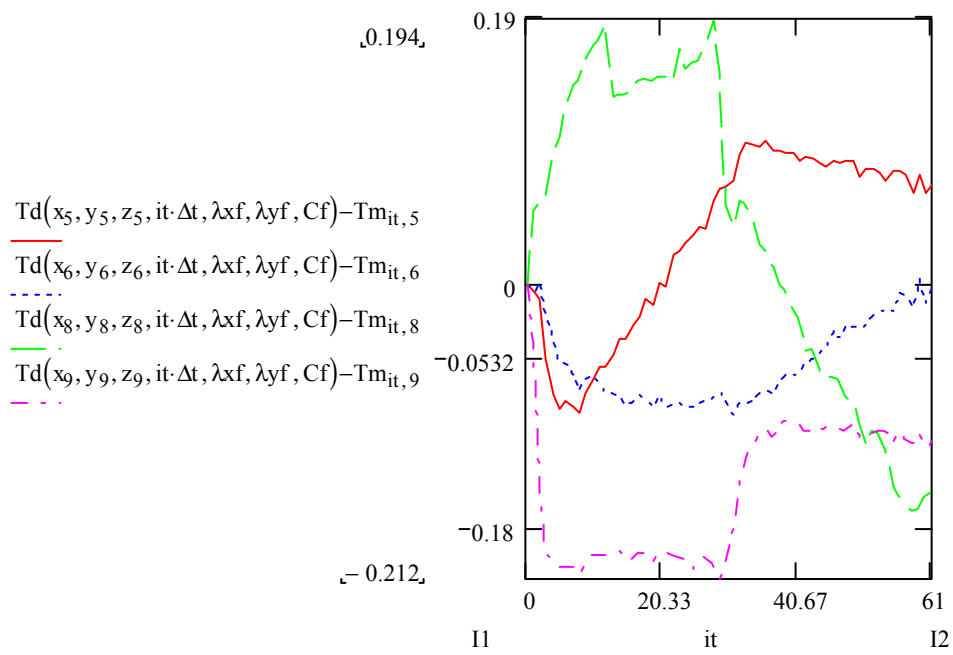
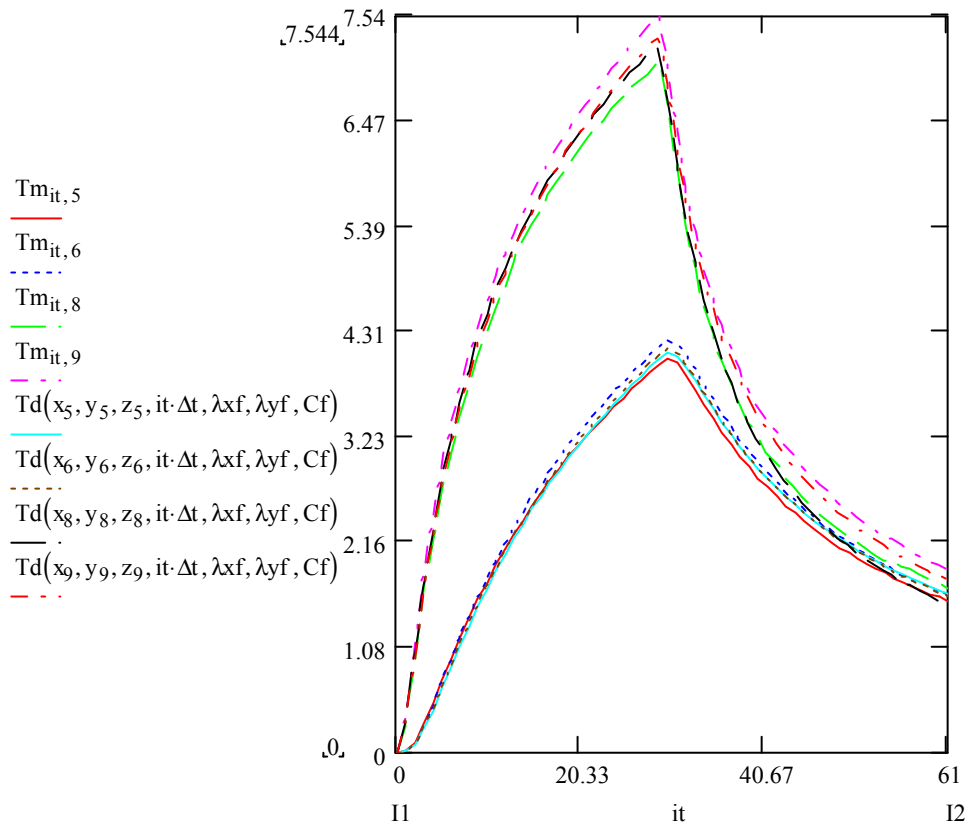


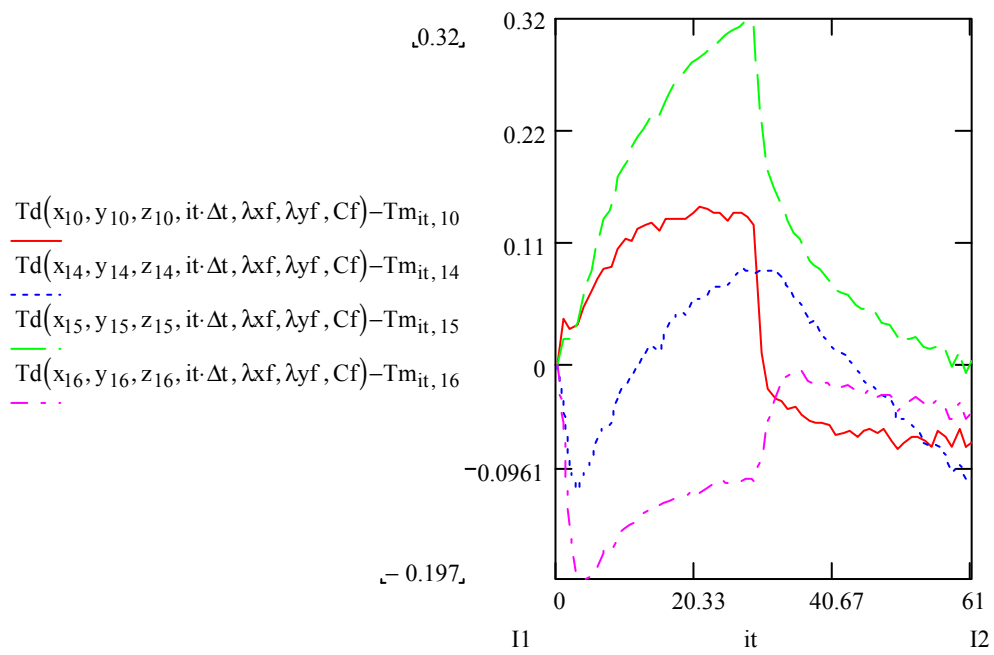
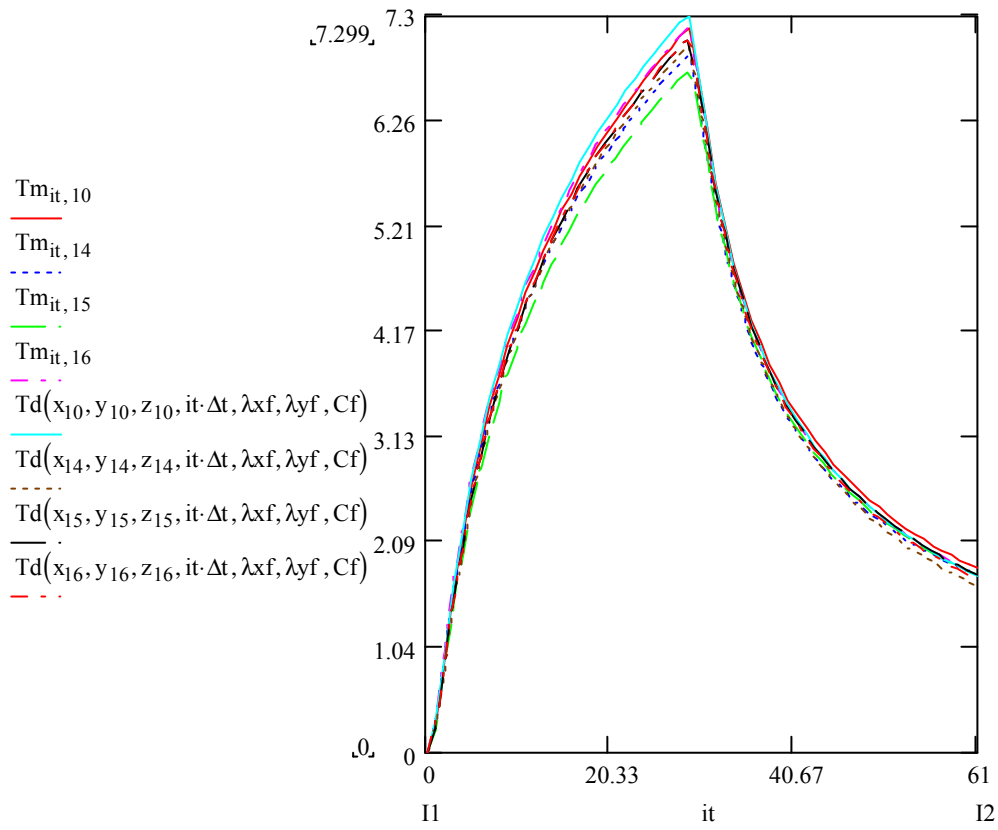




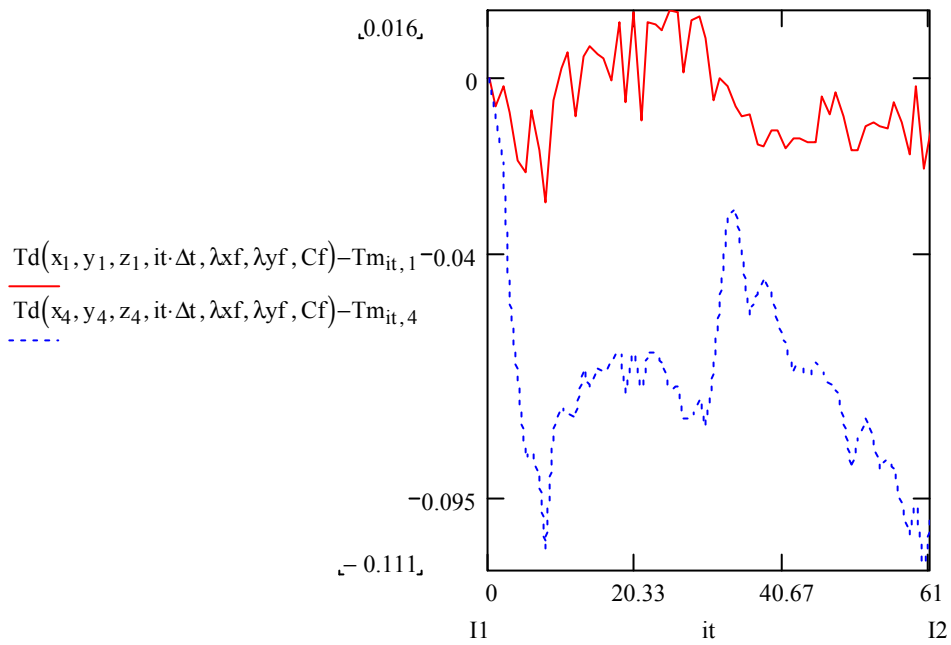
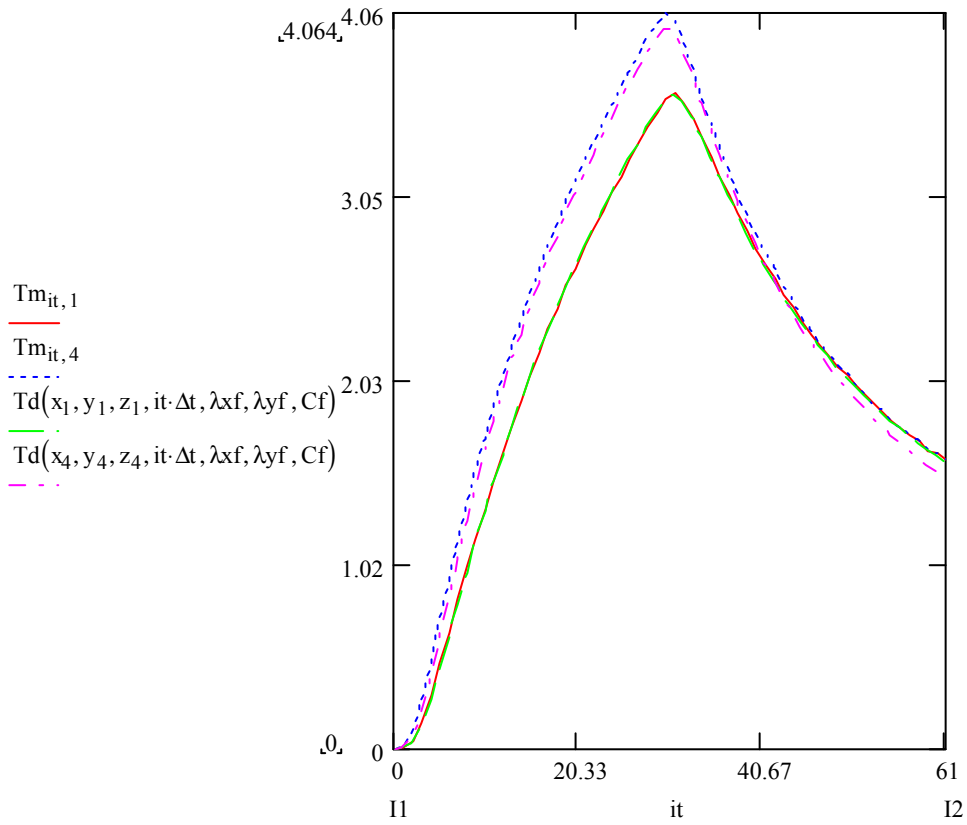
0-61 (C3)
Cdef123-c1

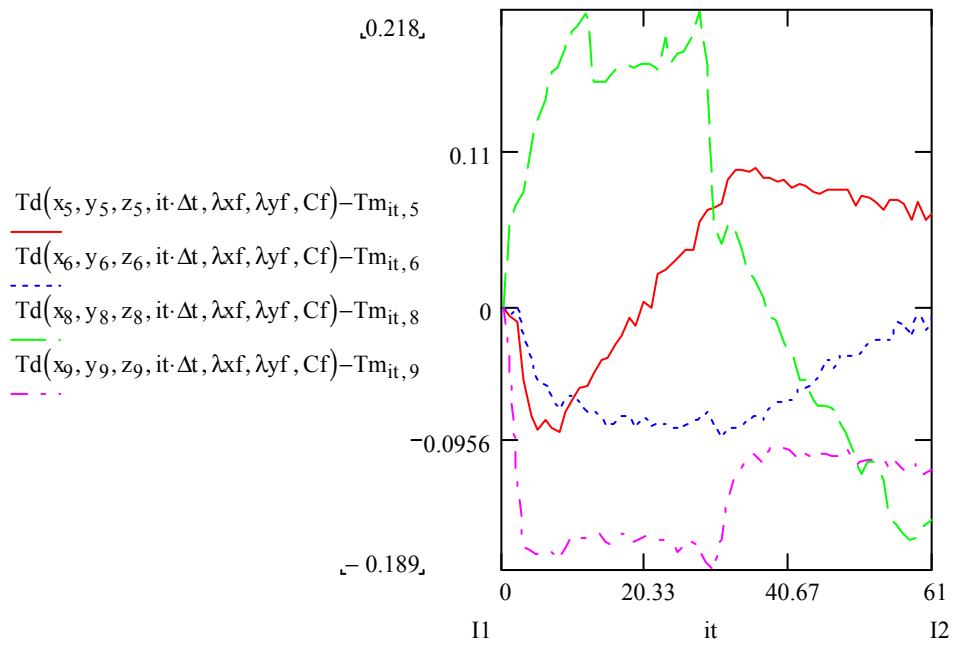
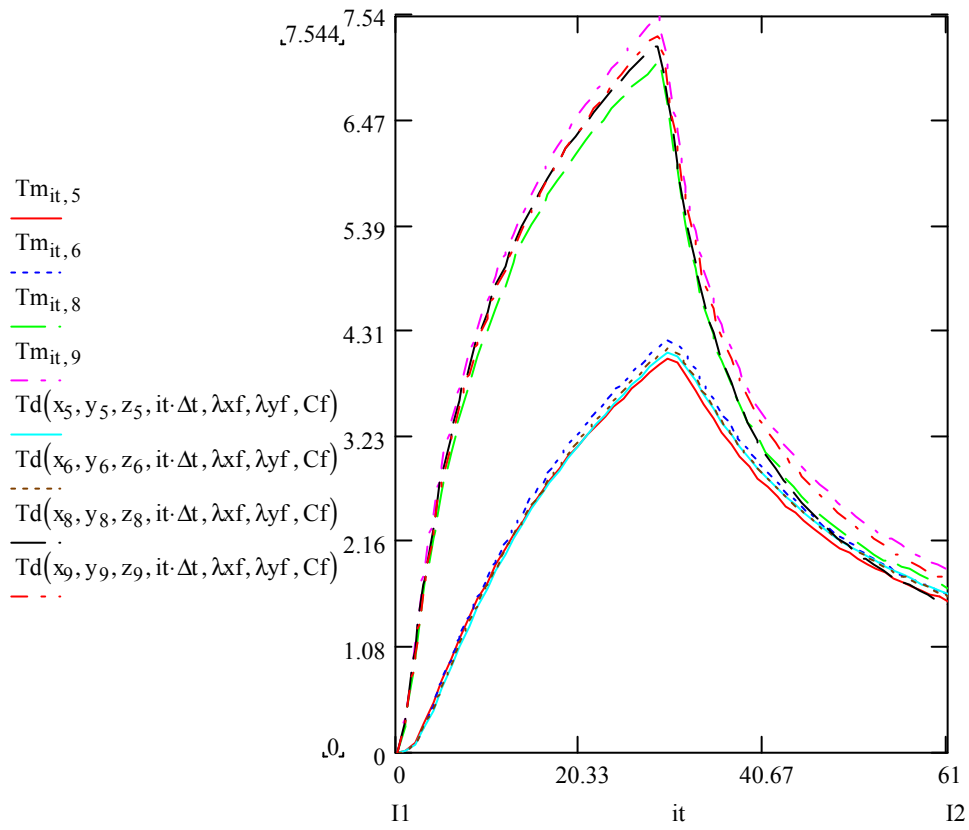


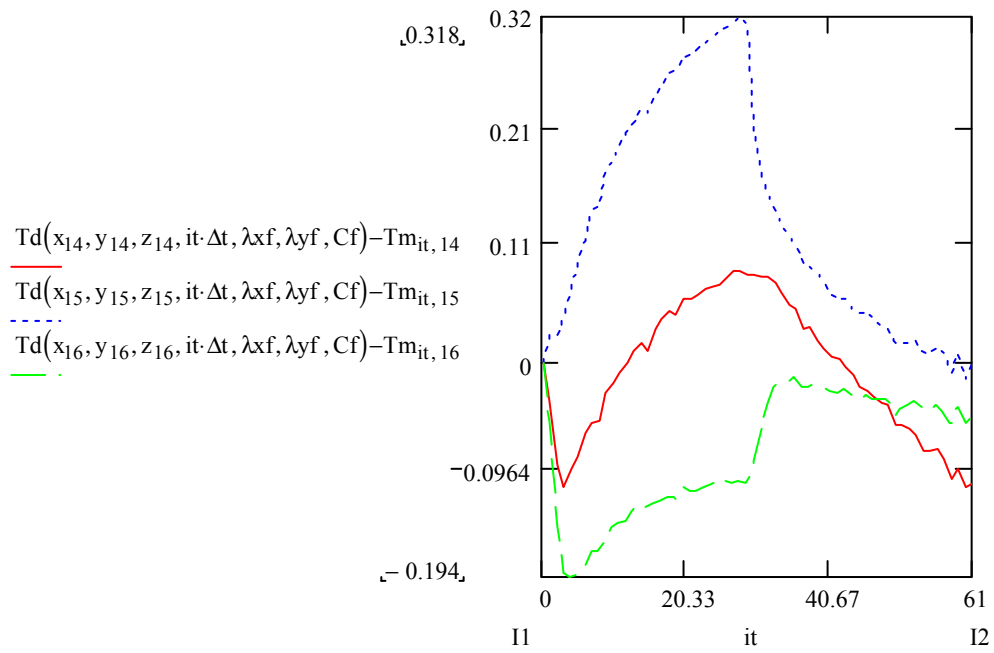
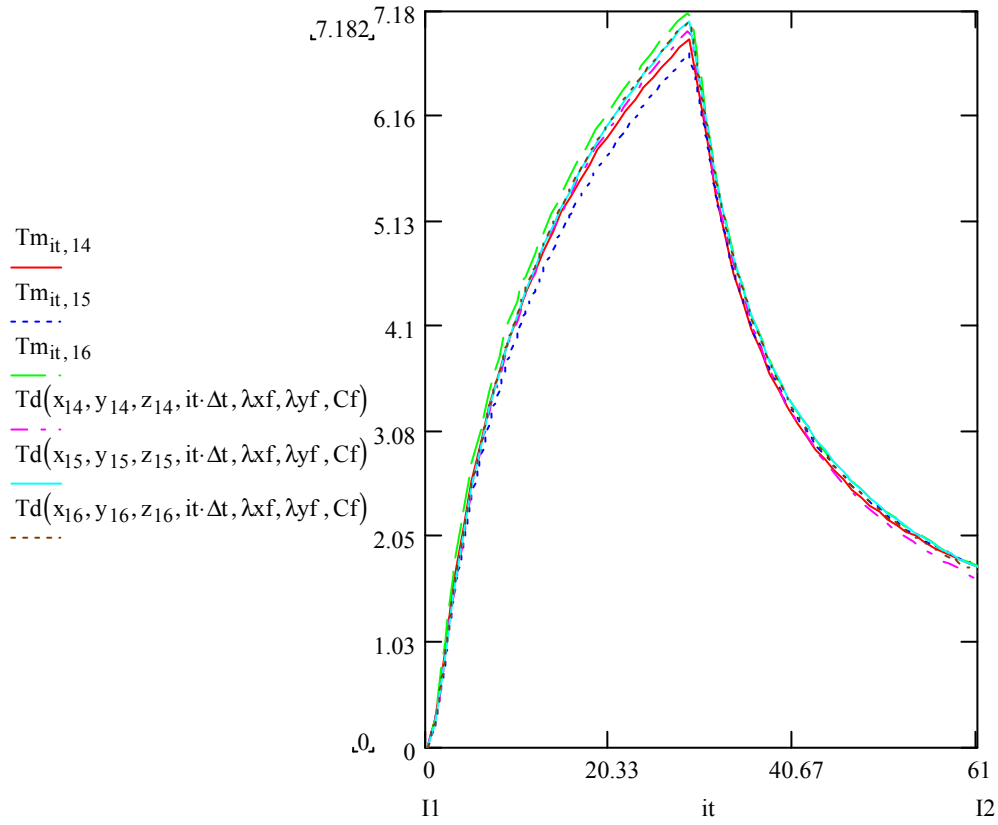




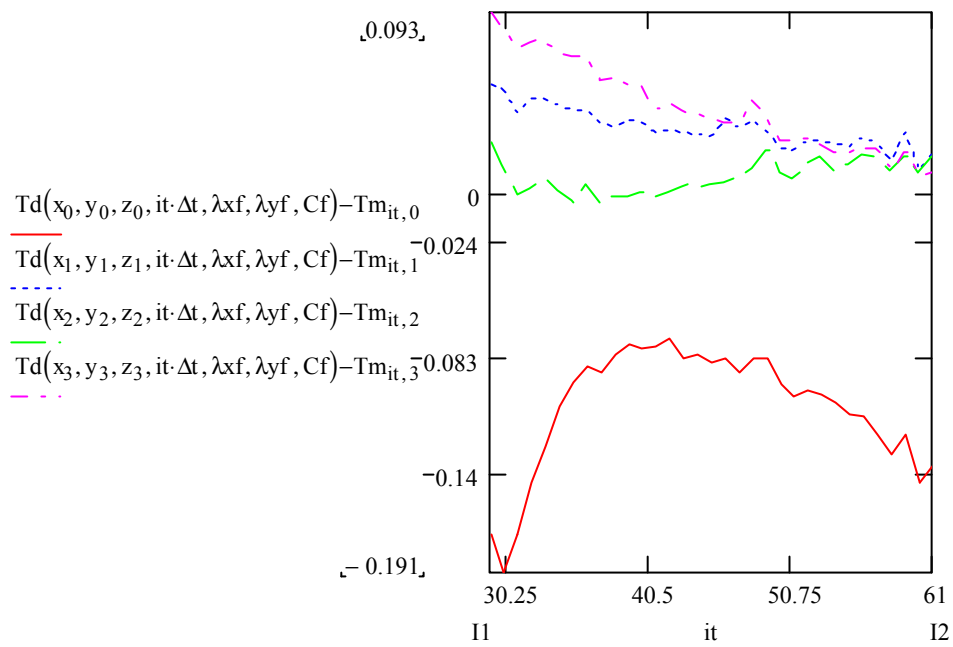
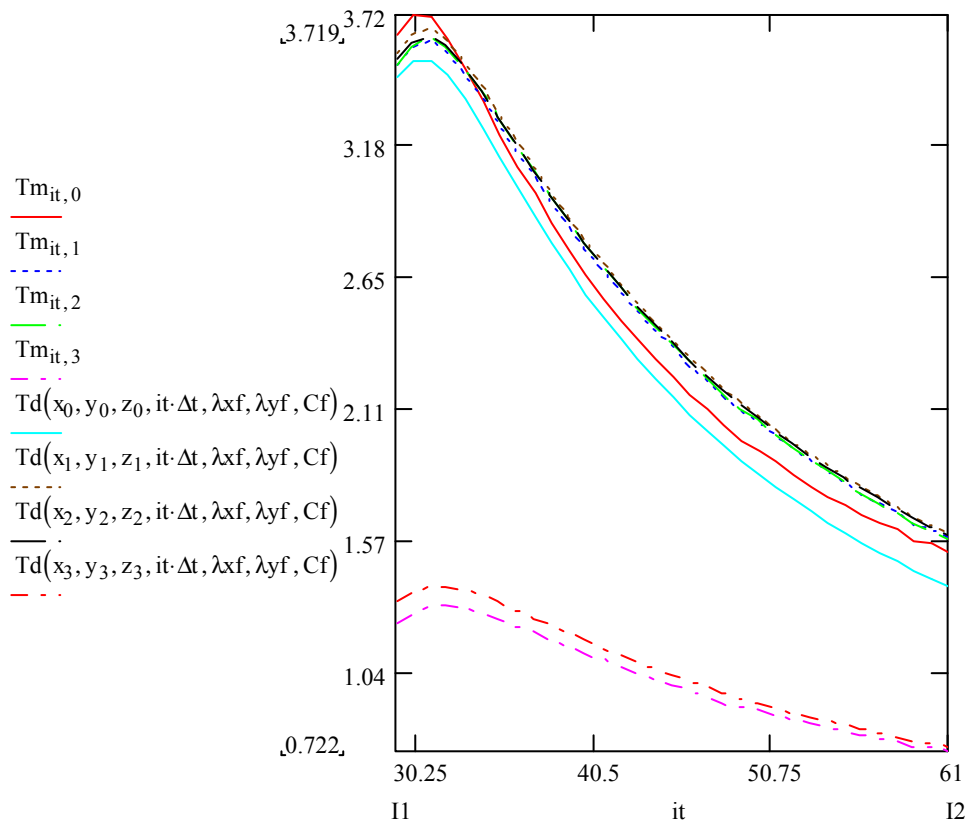
0-61 (C4)
Cdef123-c1c3e3

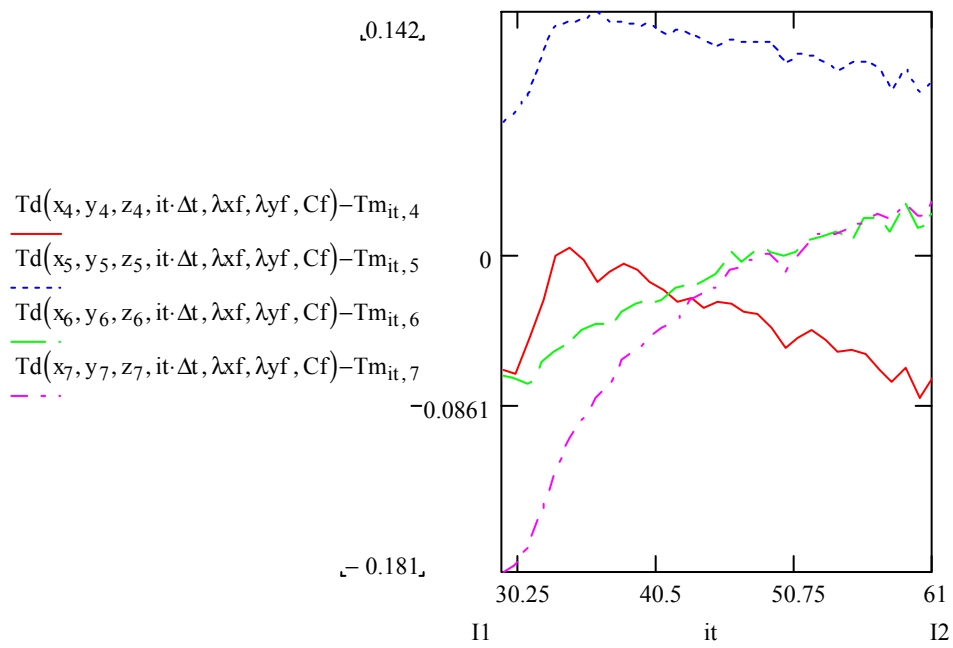
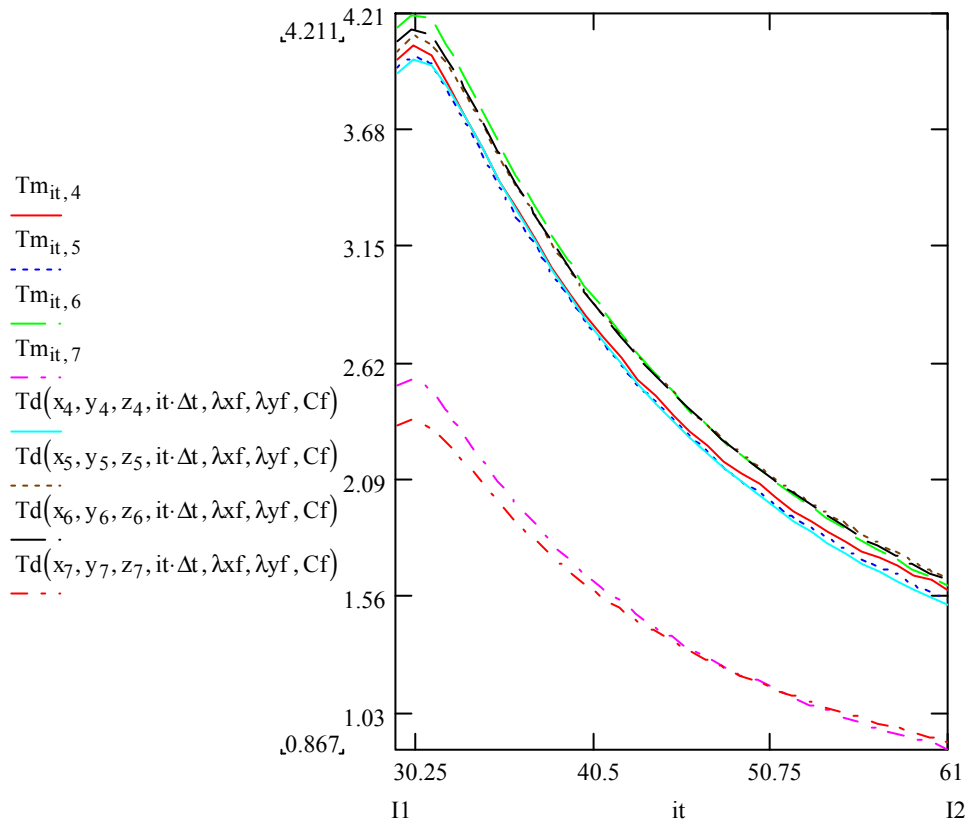


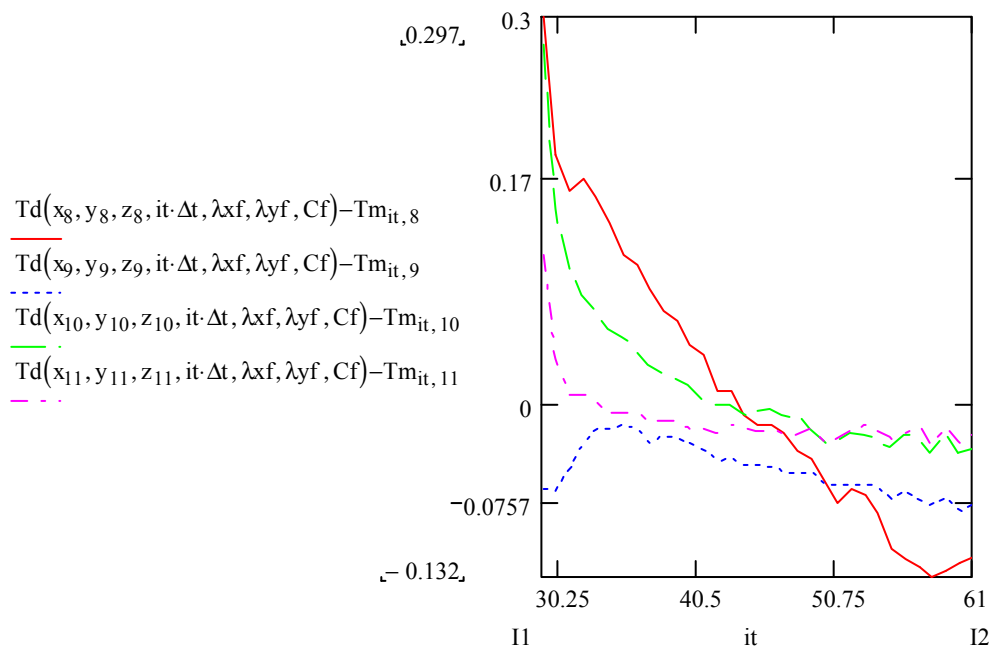
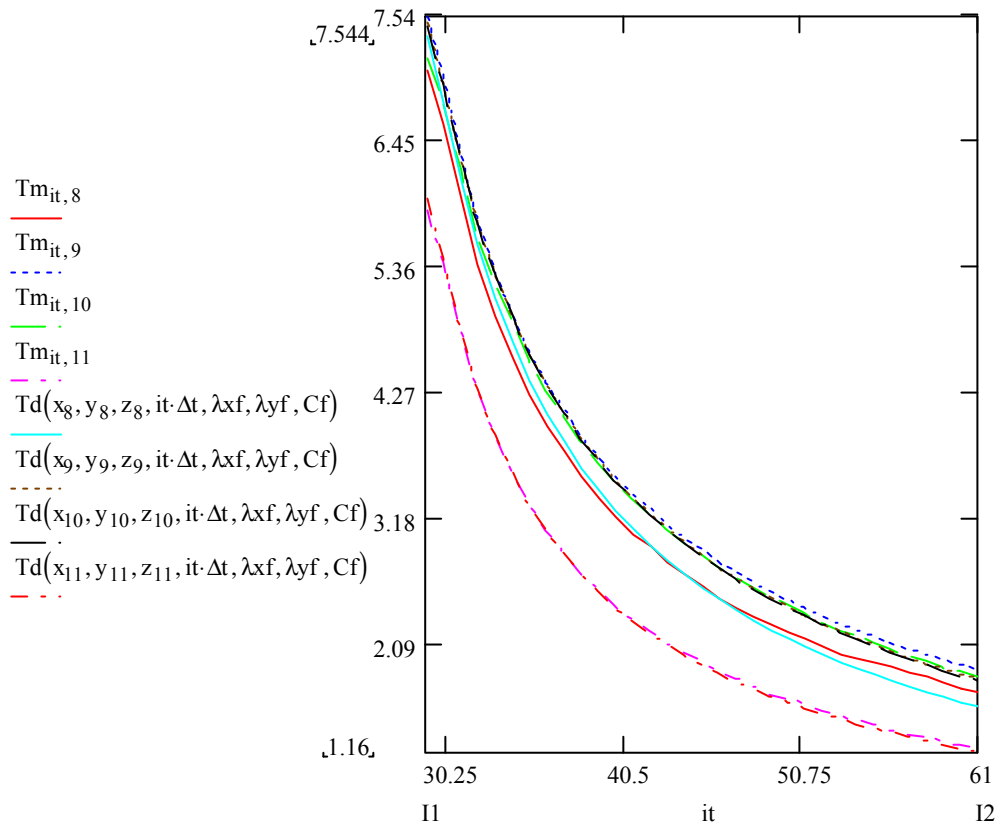


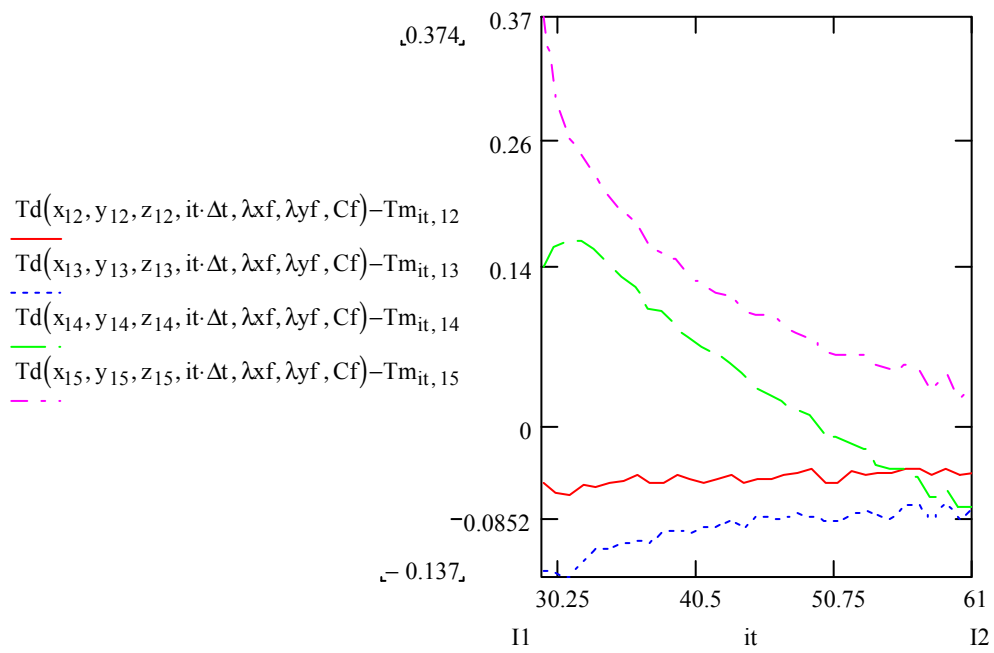
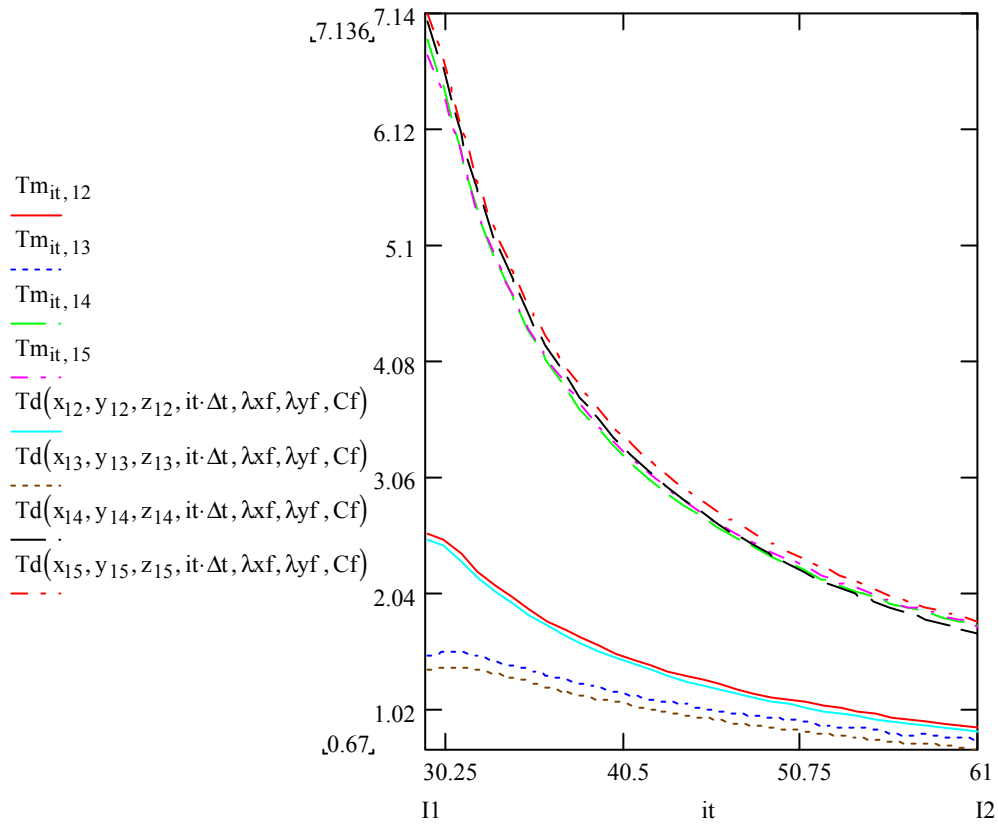


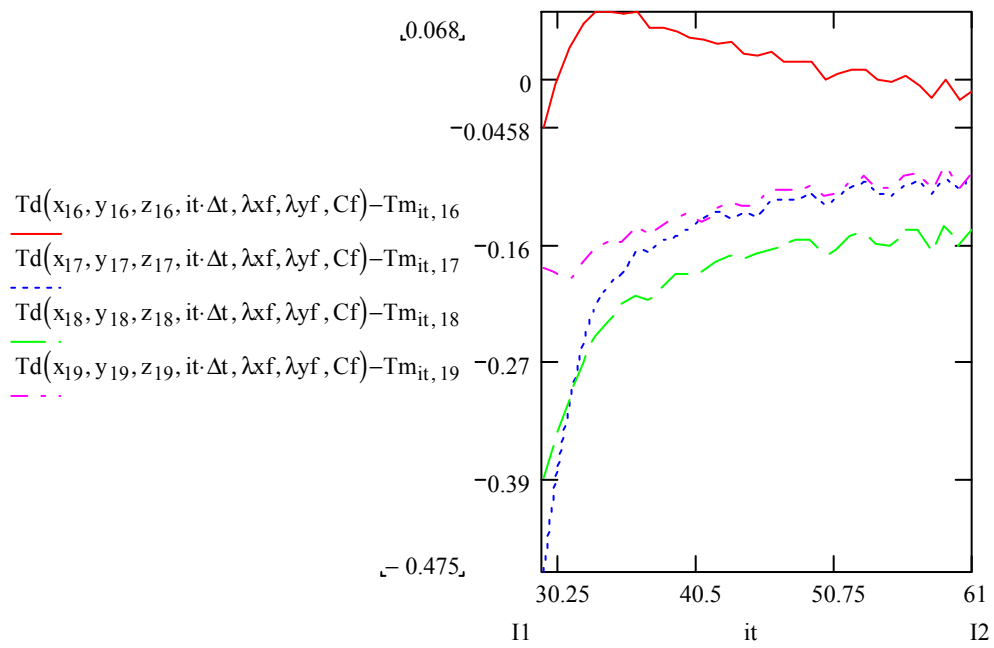
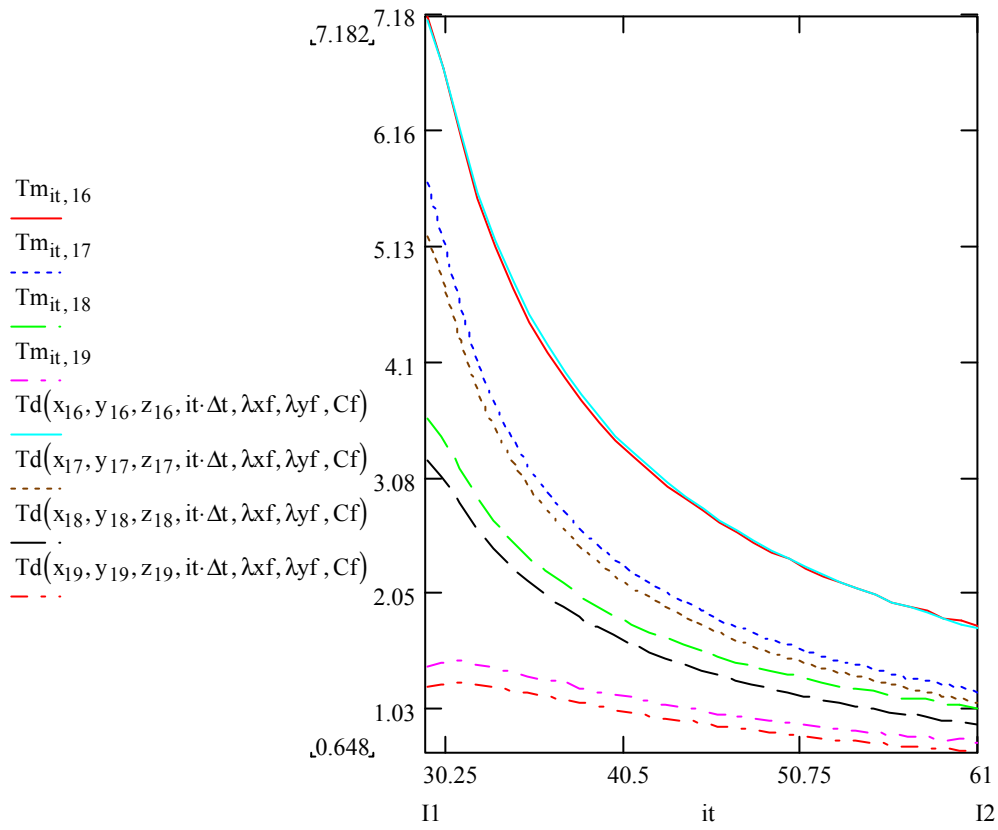
29-61 (C1)
Cdef123456



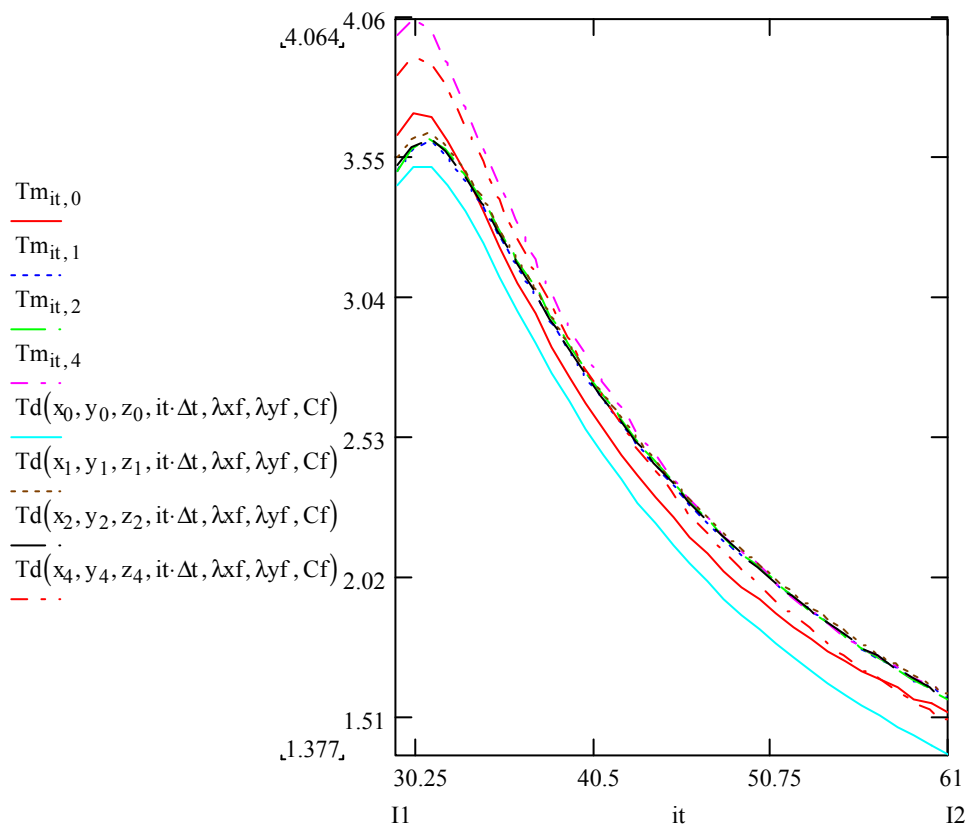
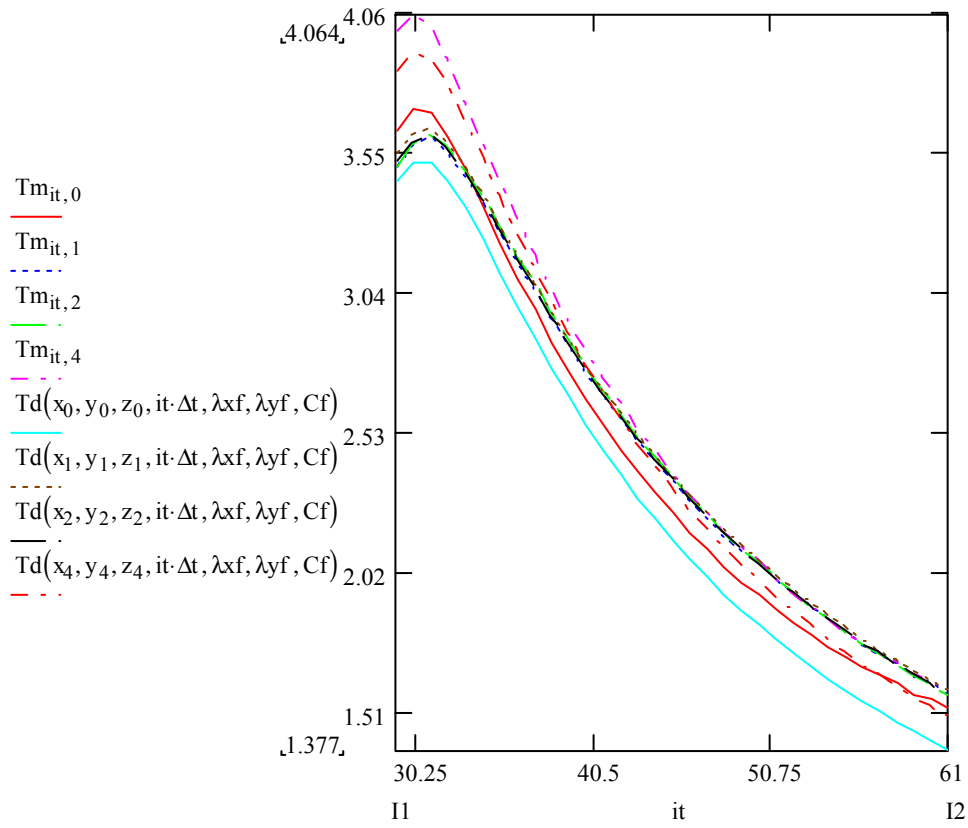


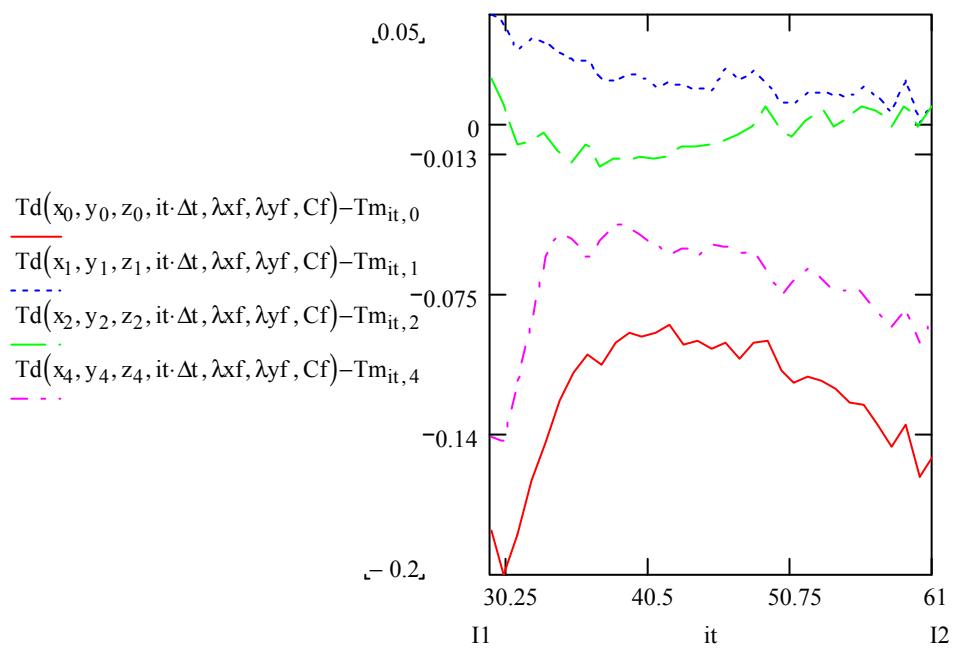
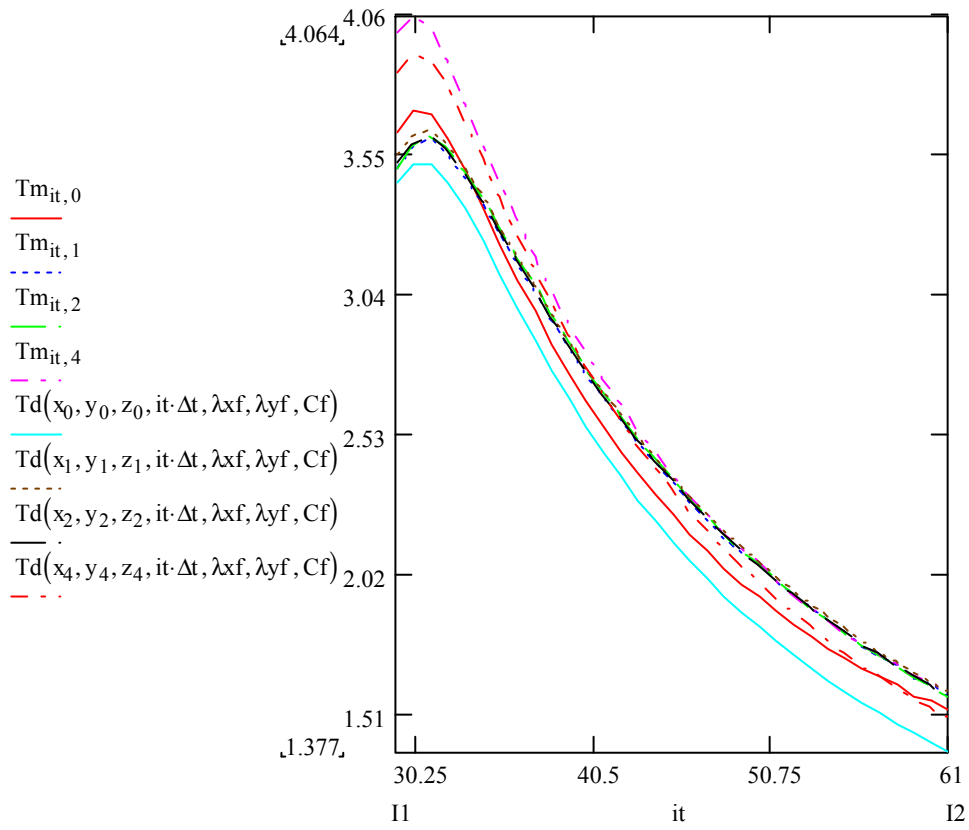


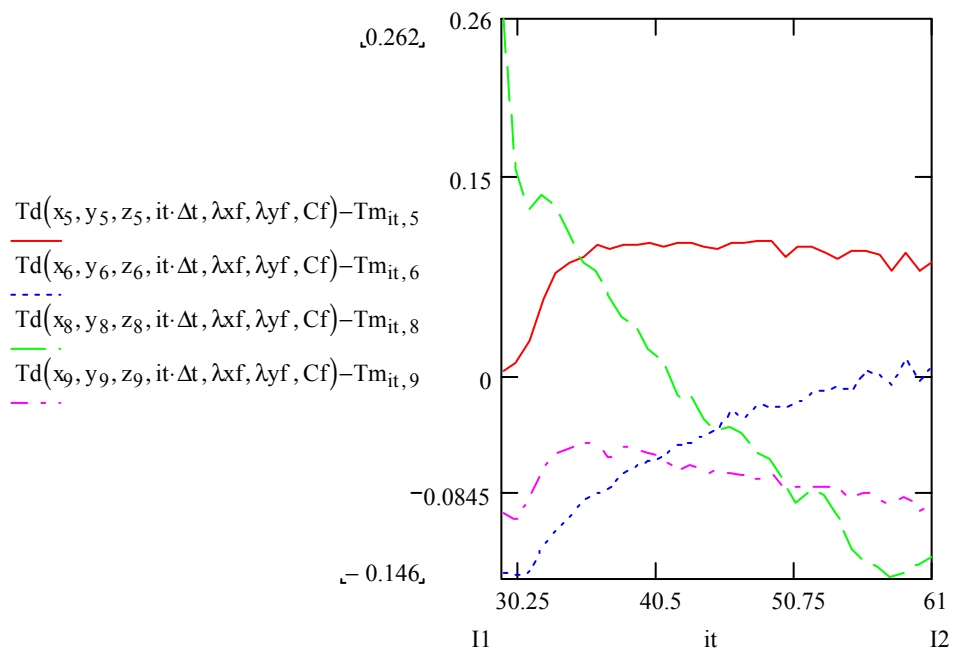
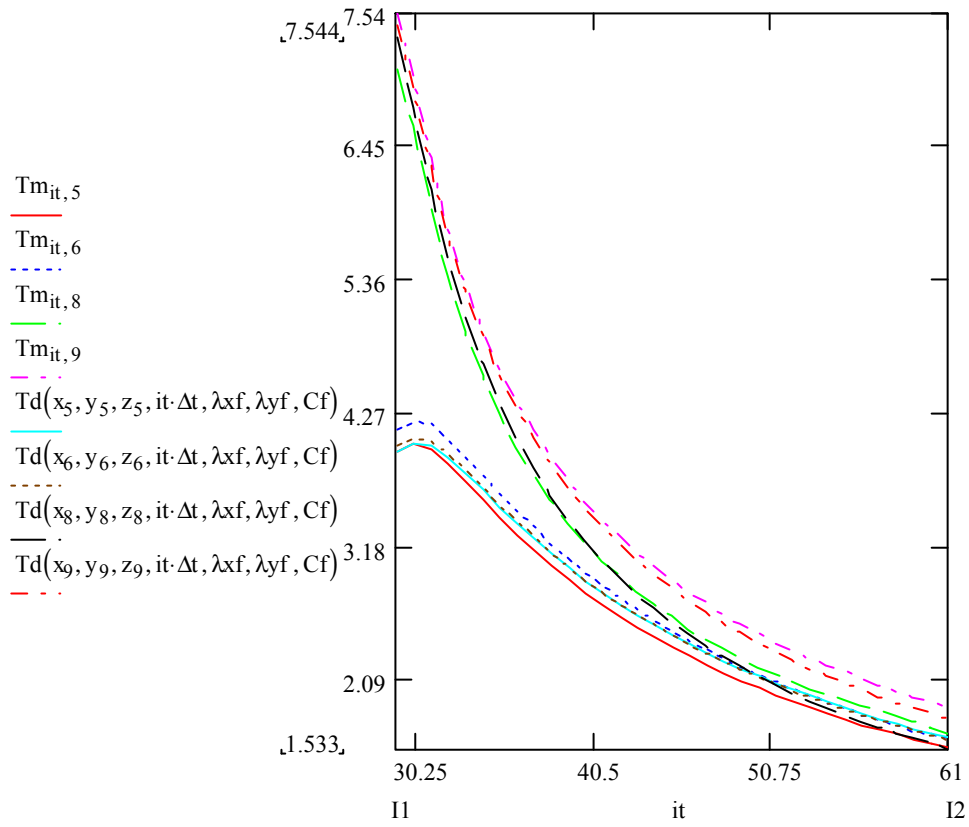


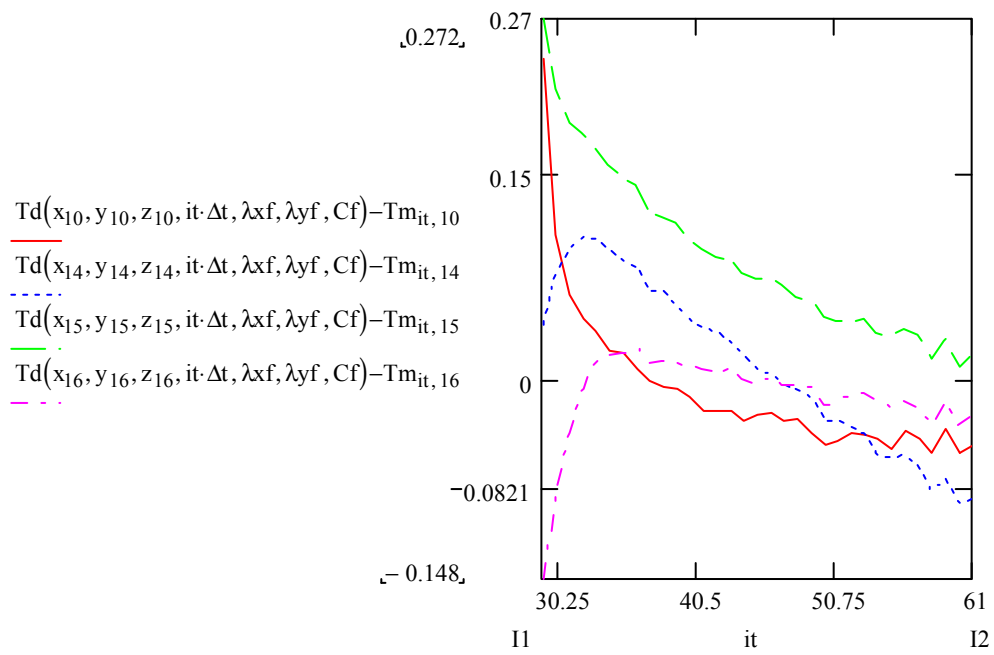
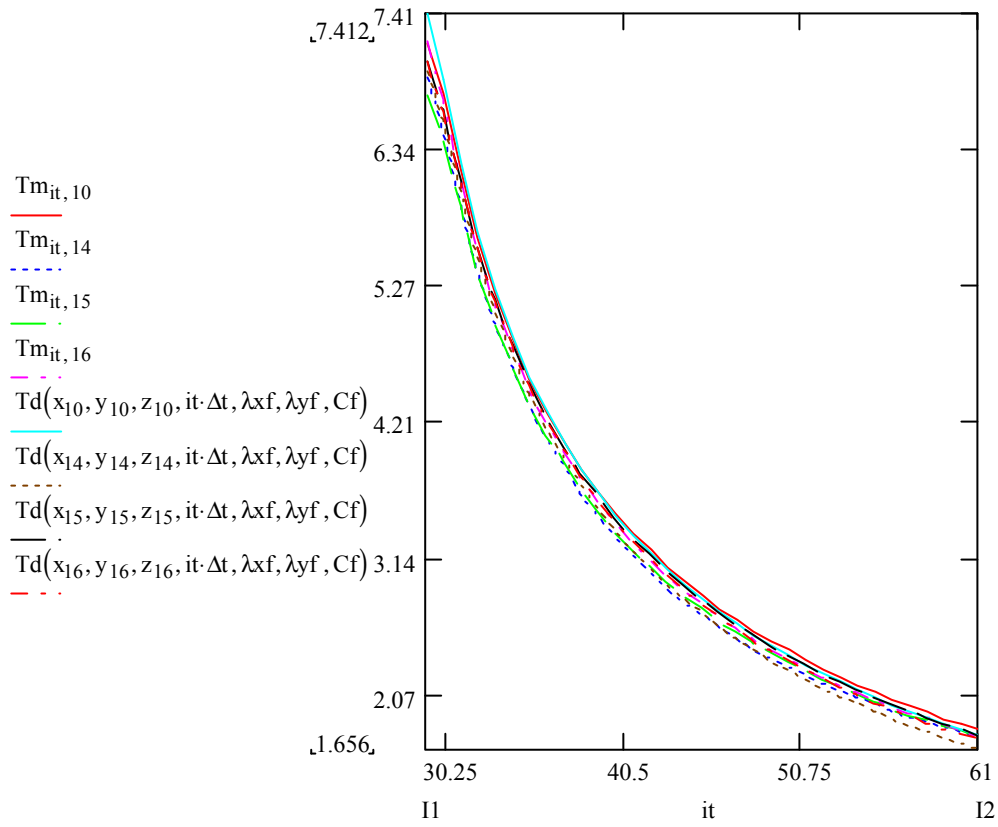


29-61 (C2)
Cdef123

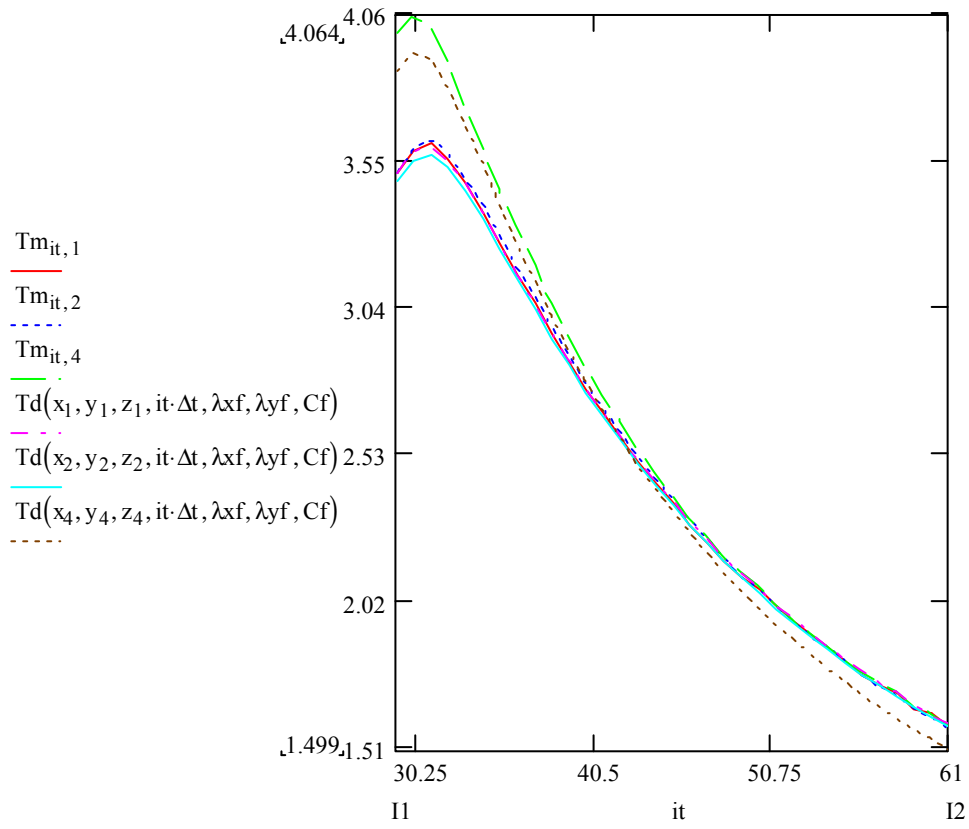


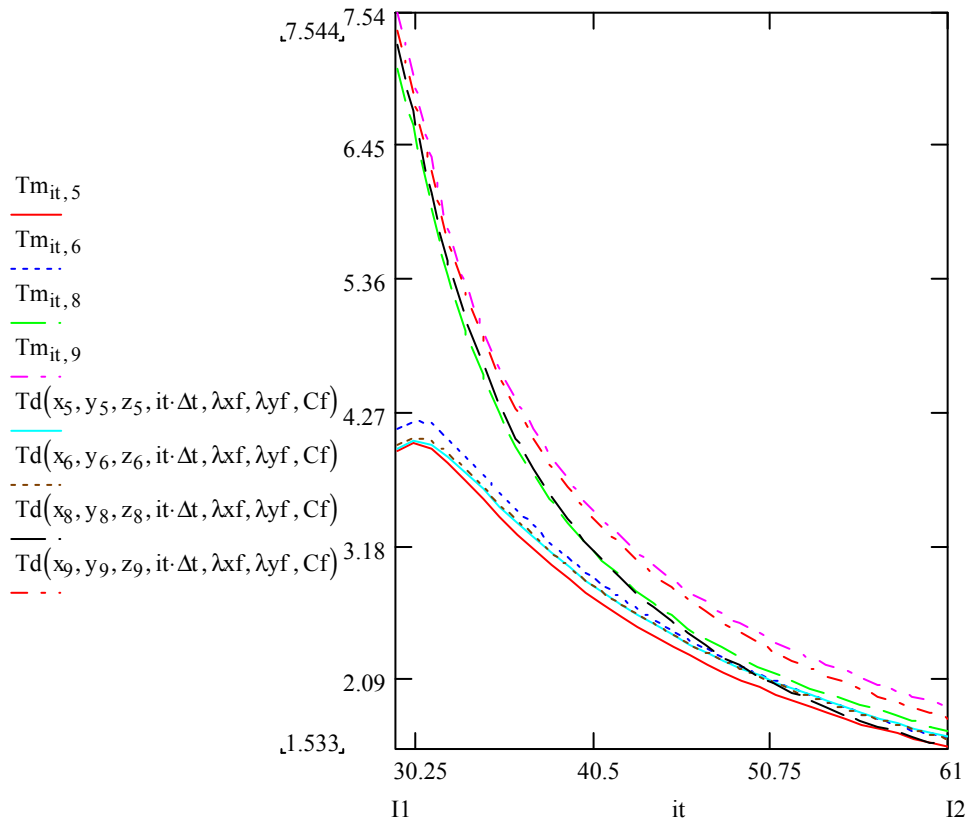
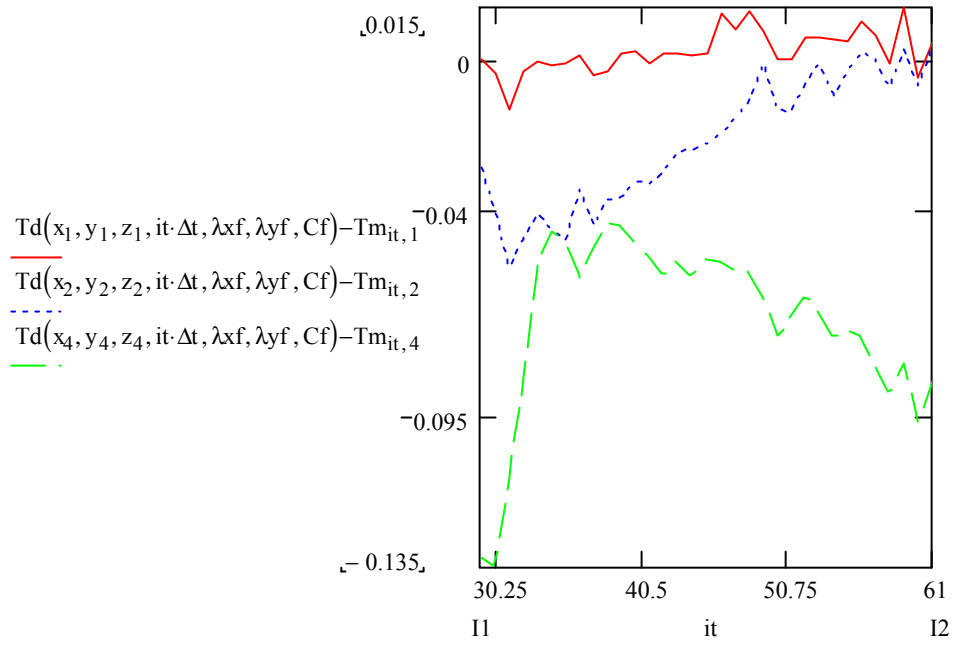


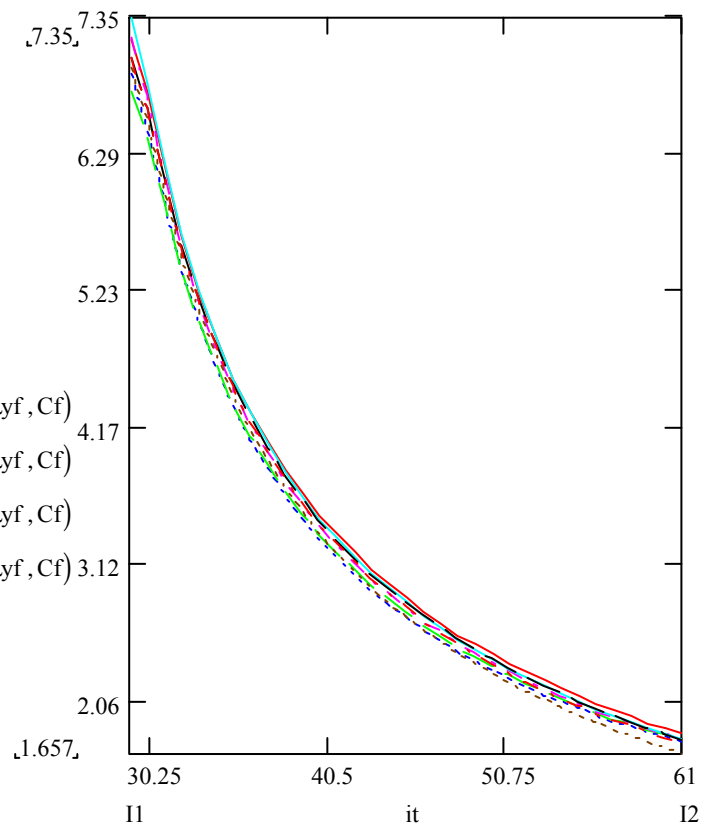
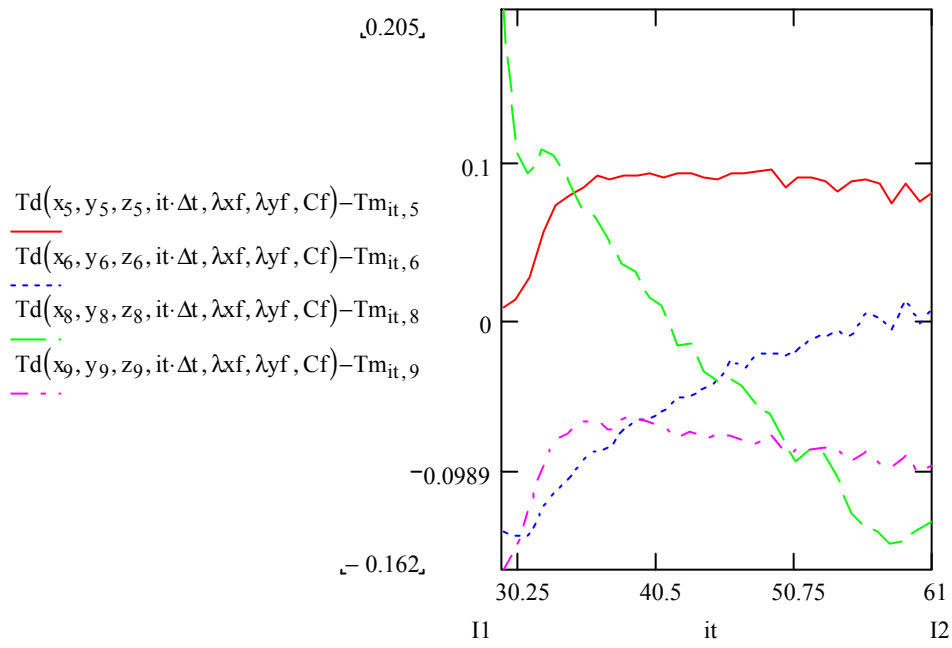


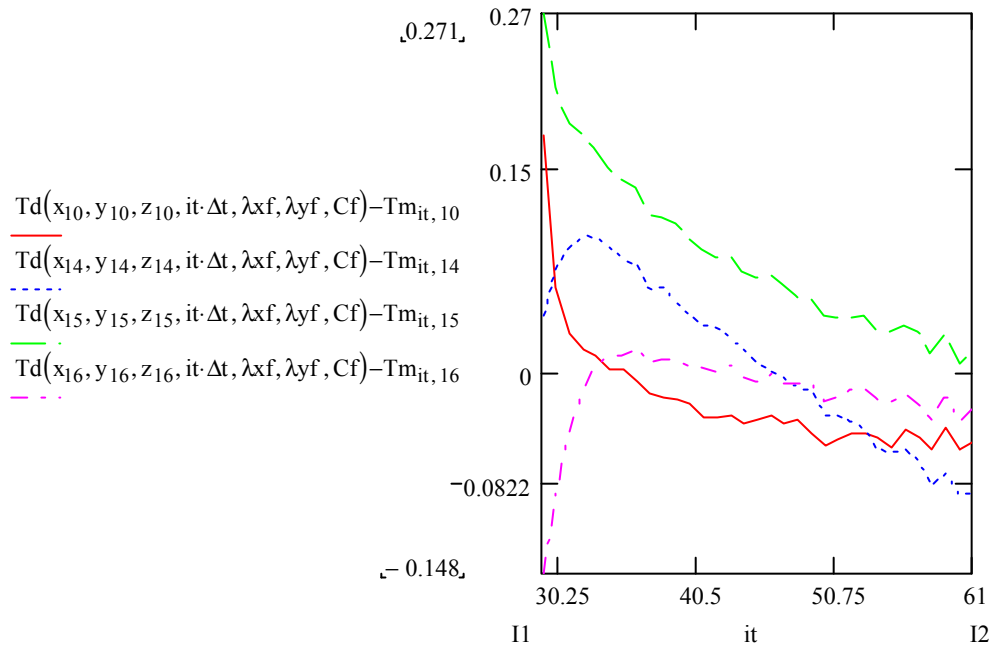


29-61 (C3)
Cdef123-c1

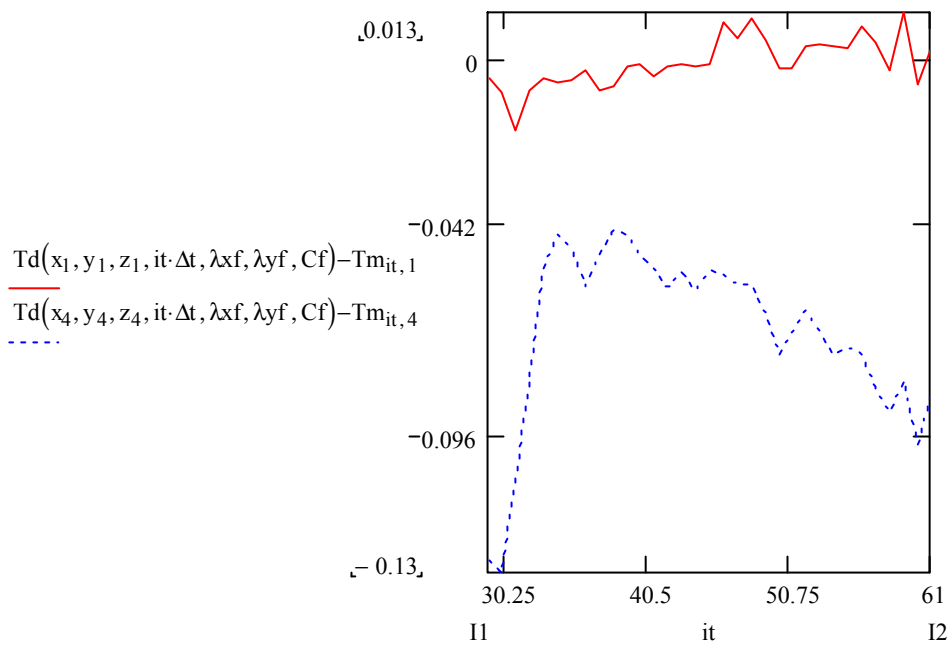
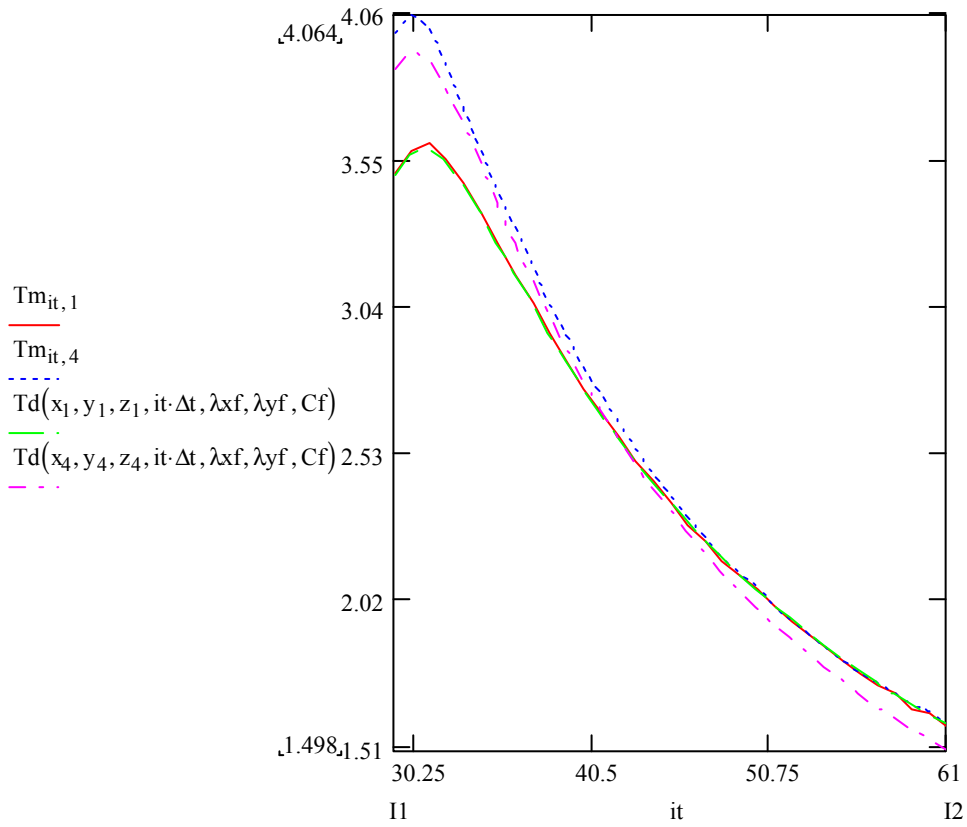


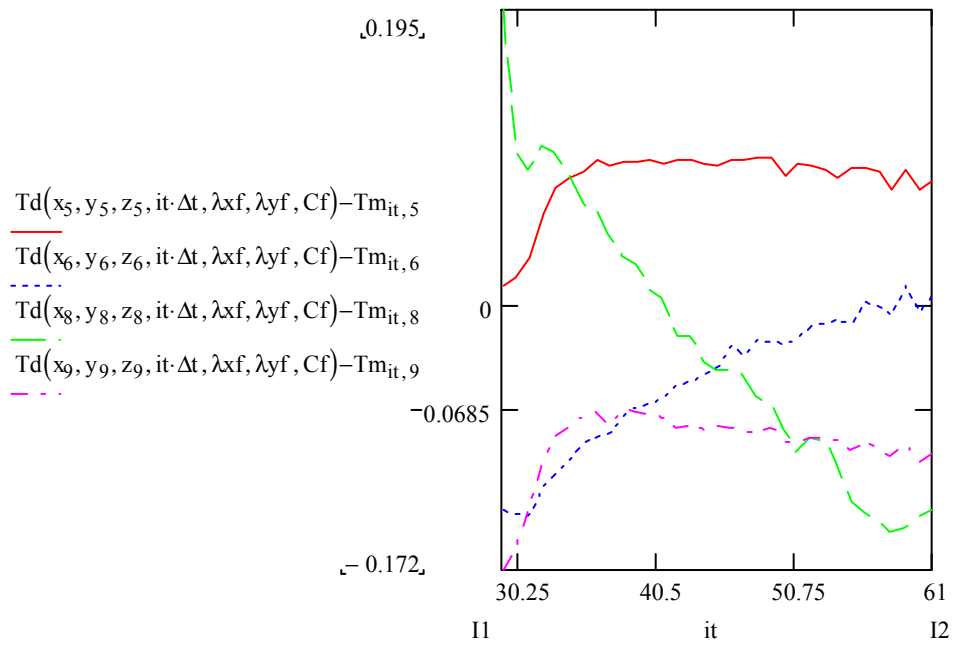
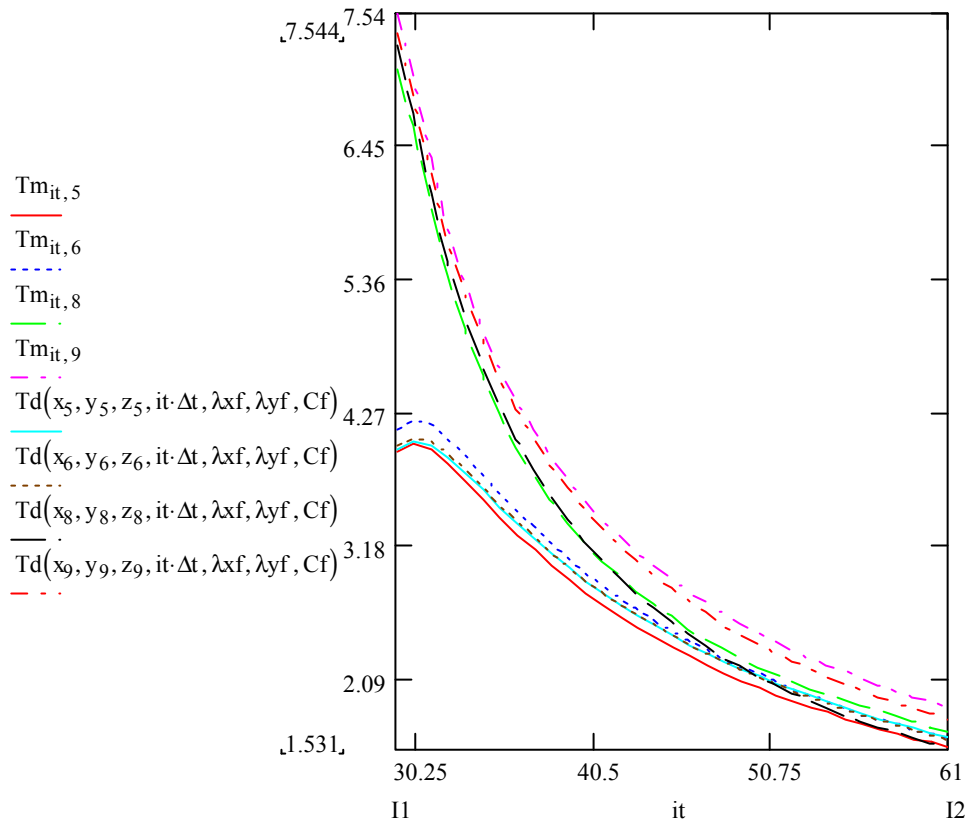


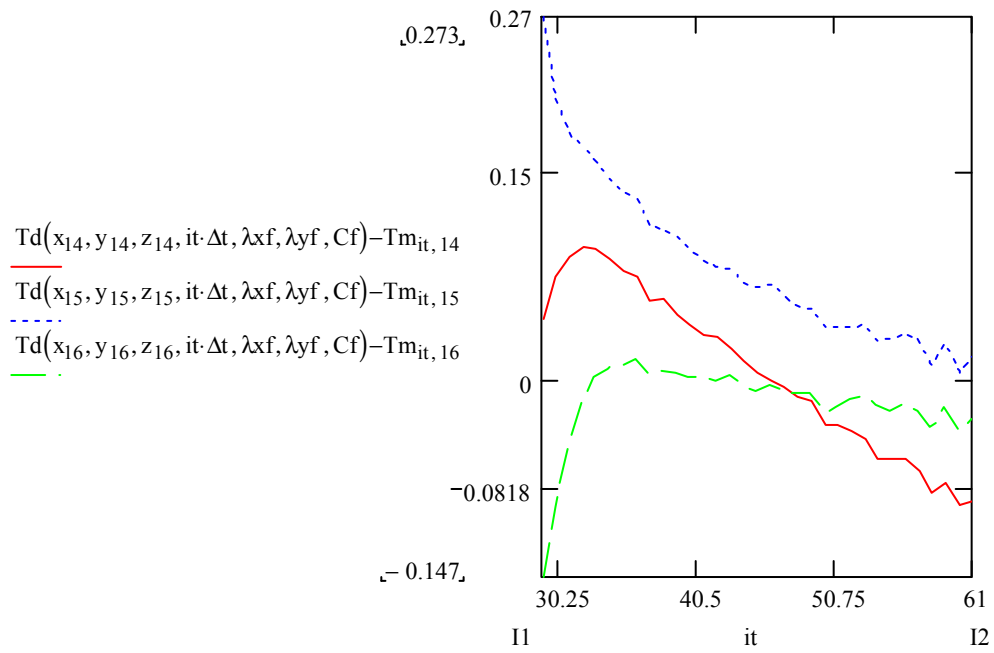
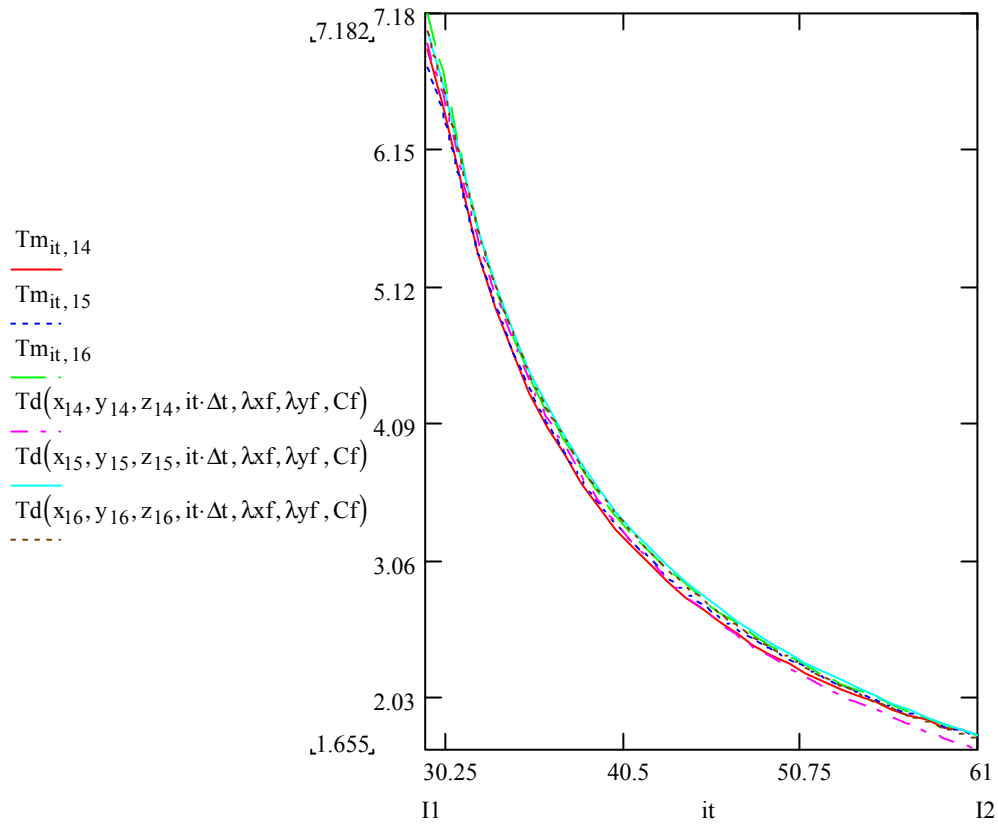




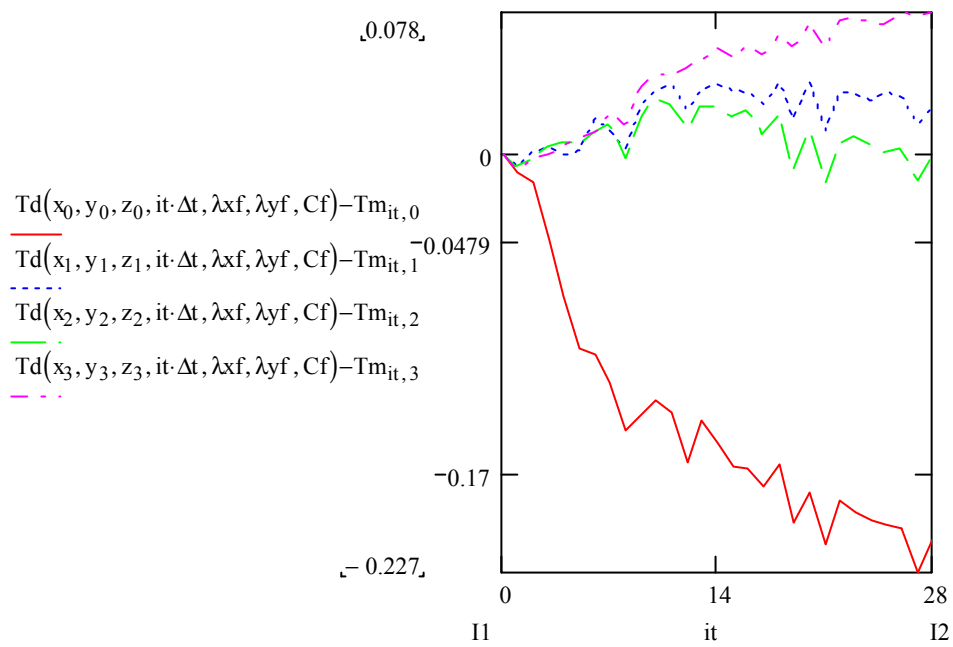
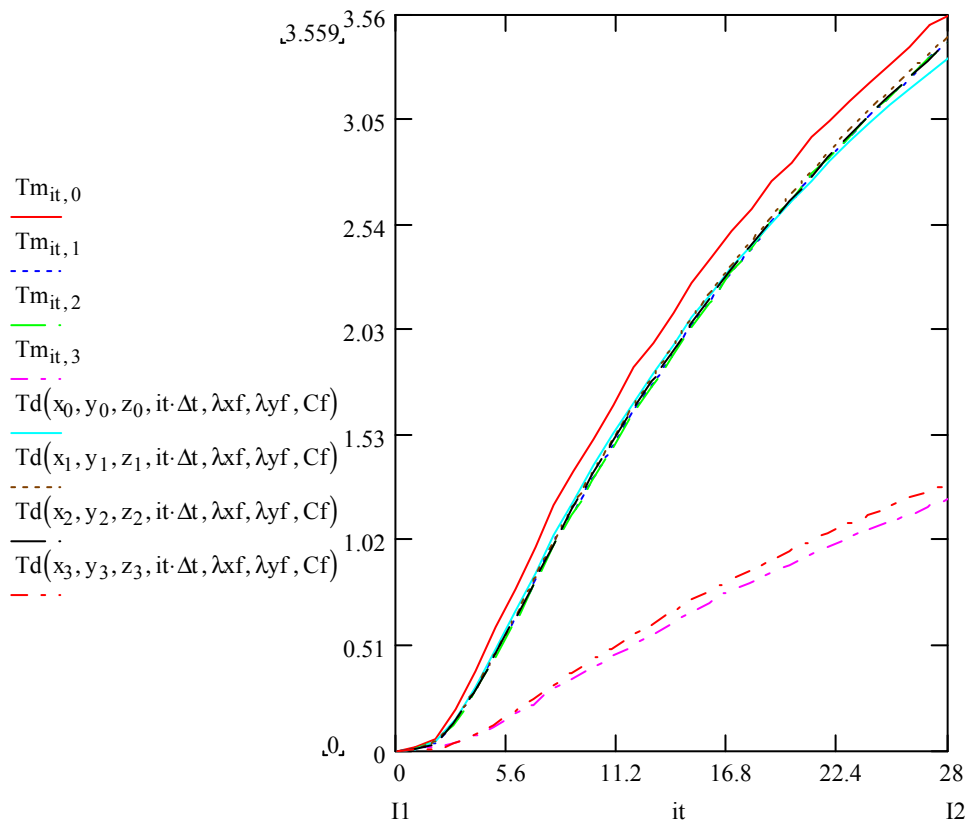
29-61 (C4)
 Cdef123-c1c3e3

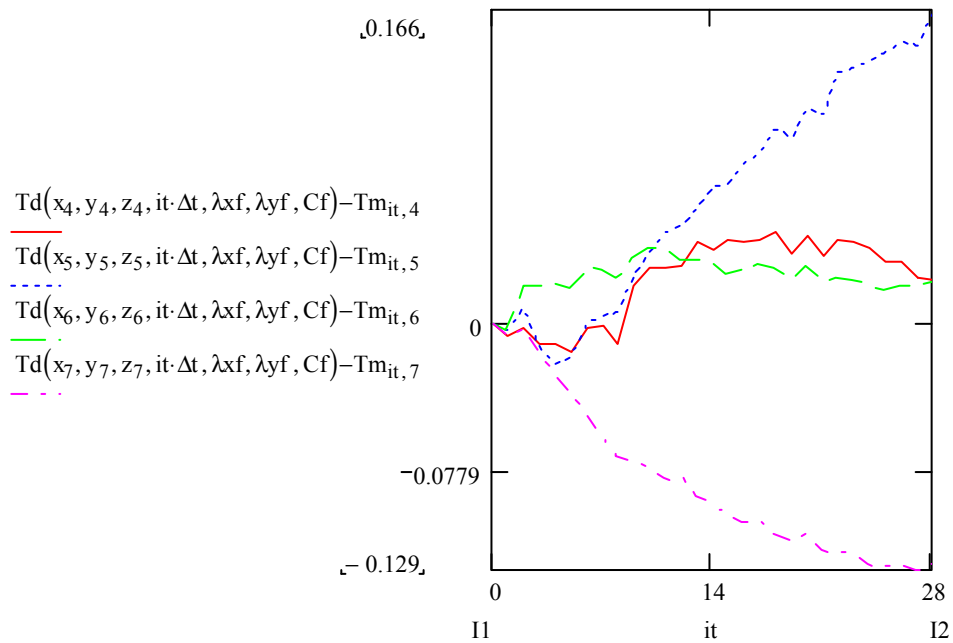
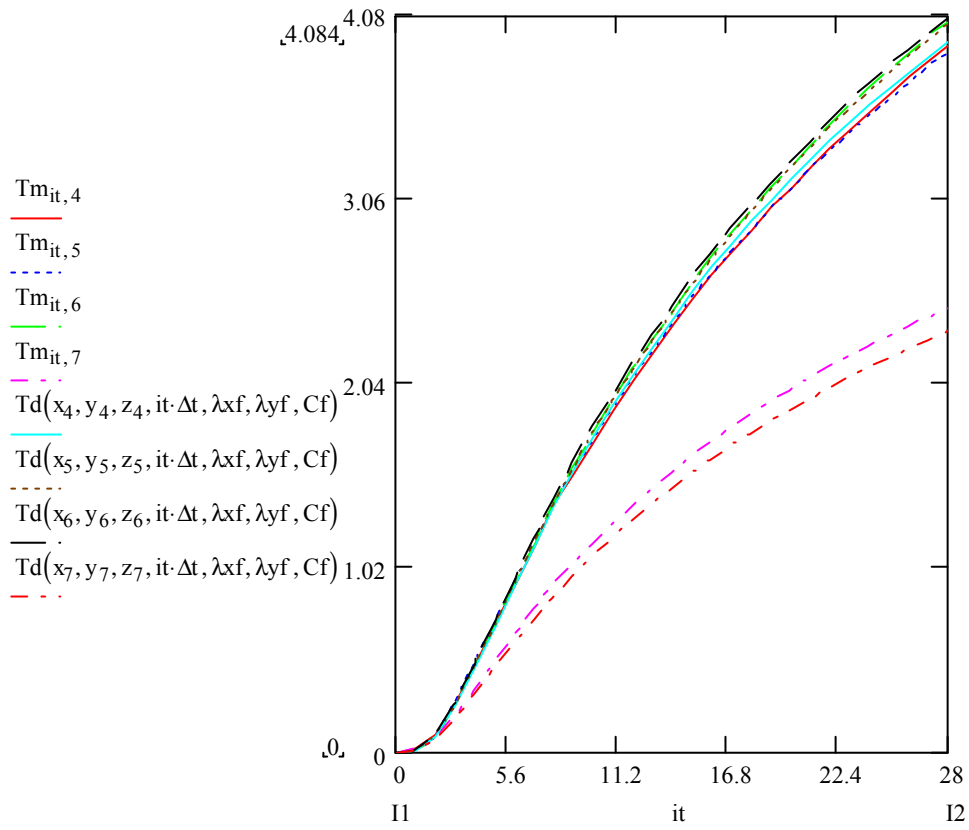


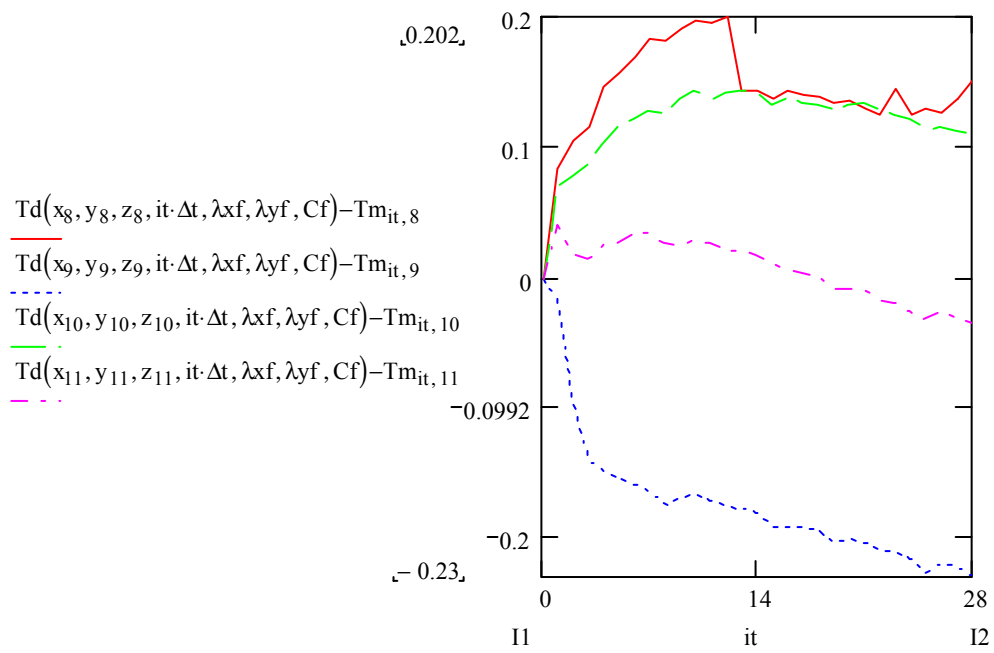
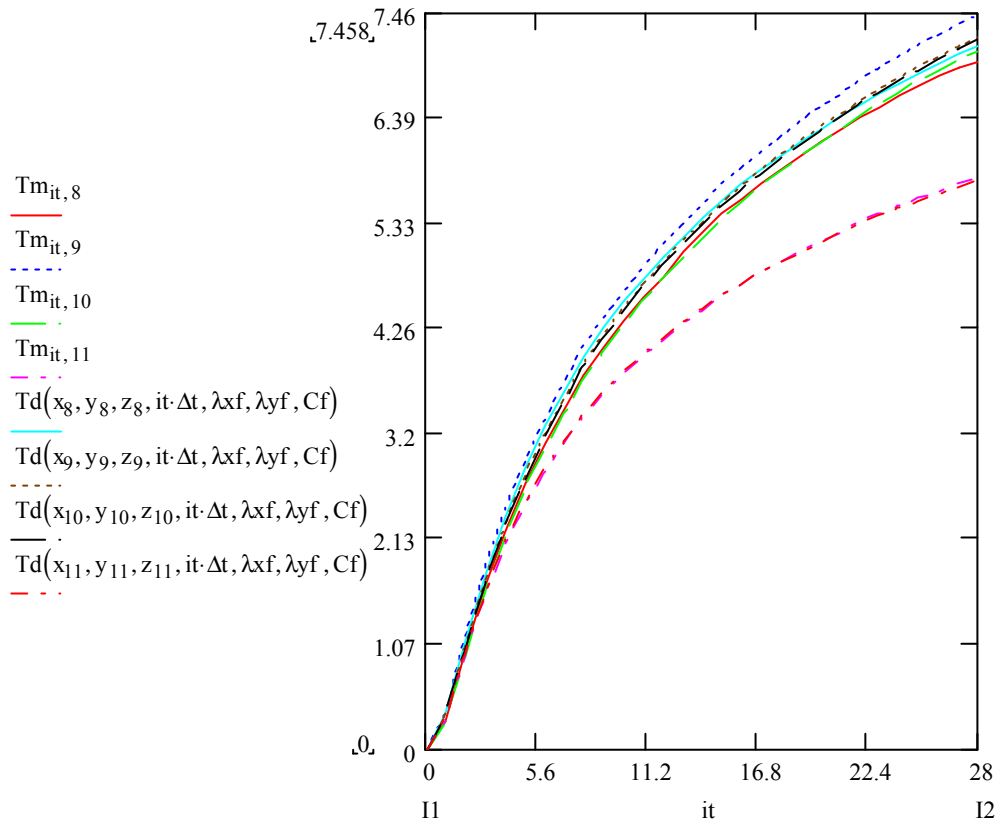


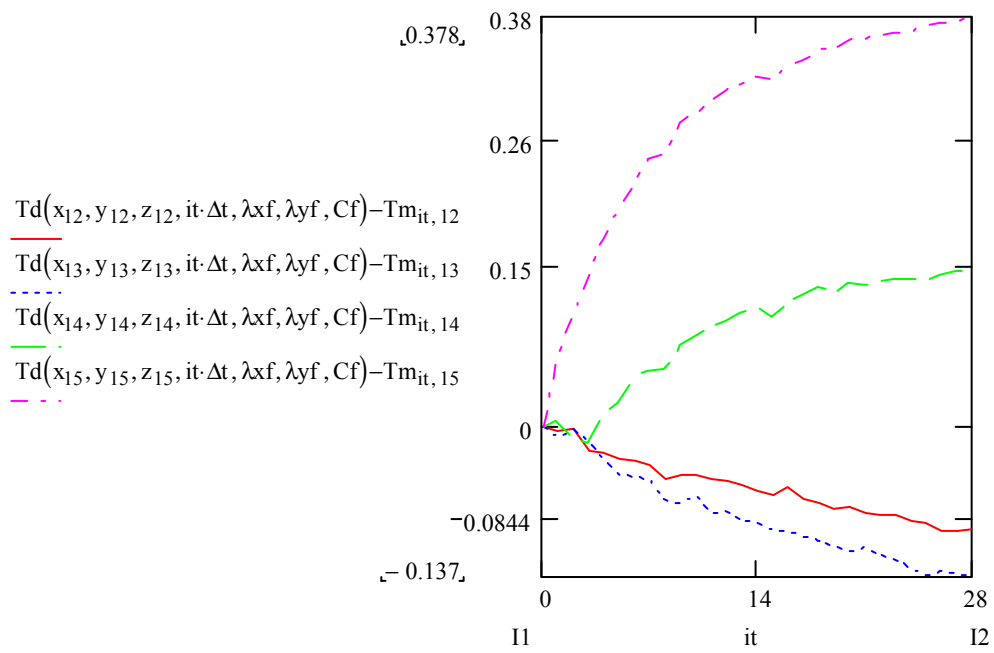
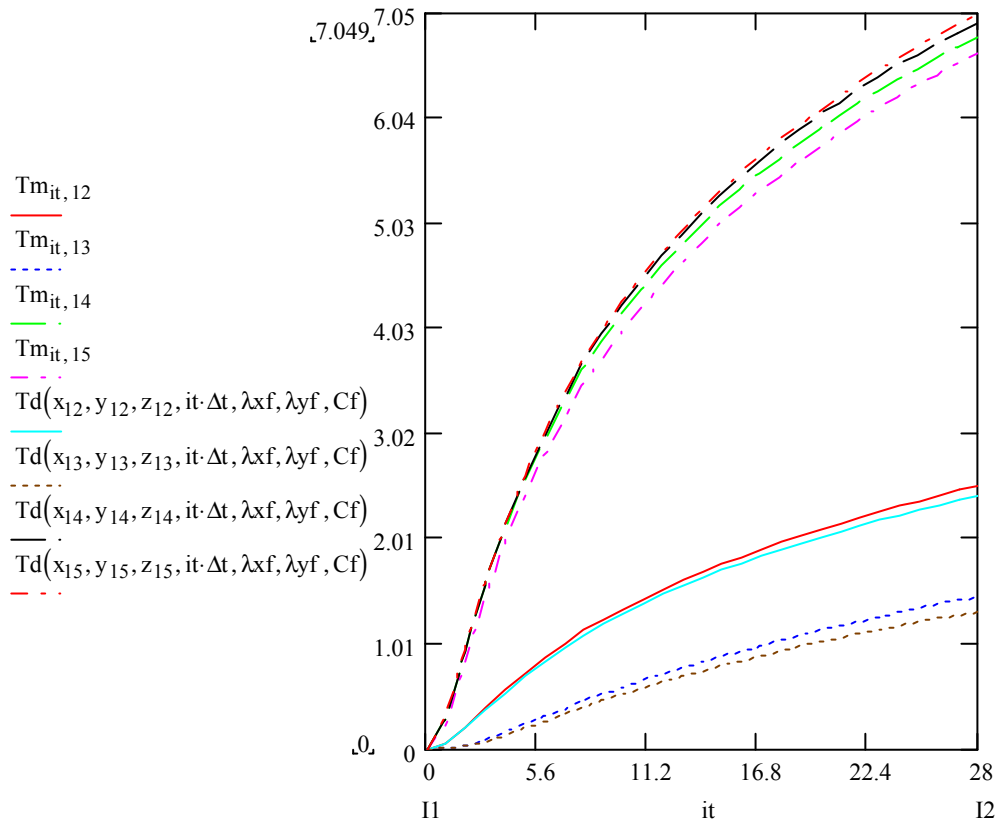


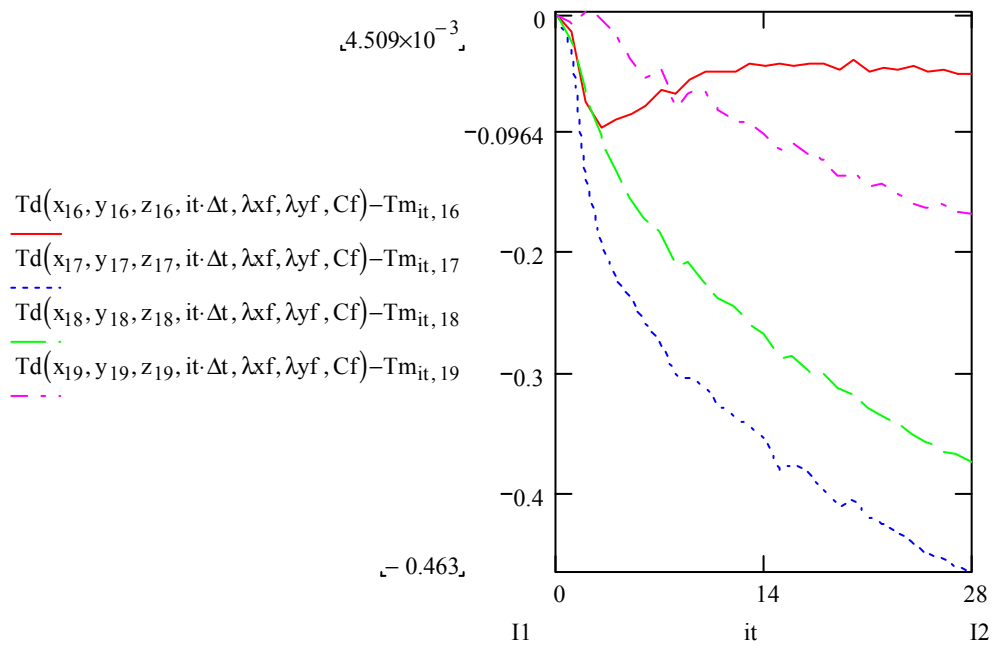
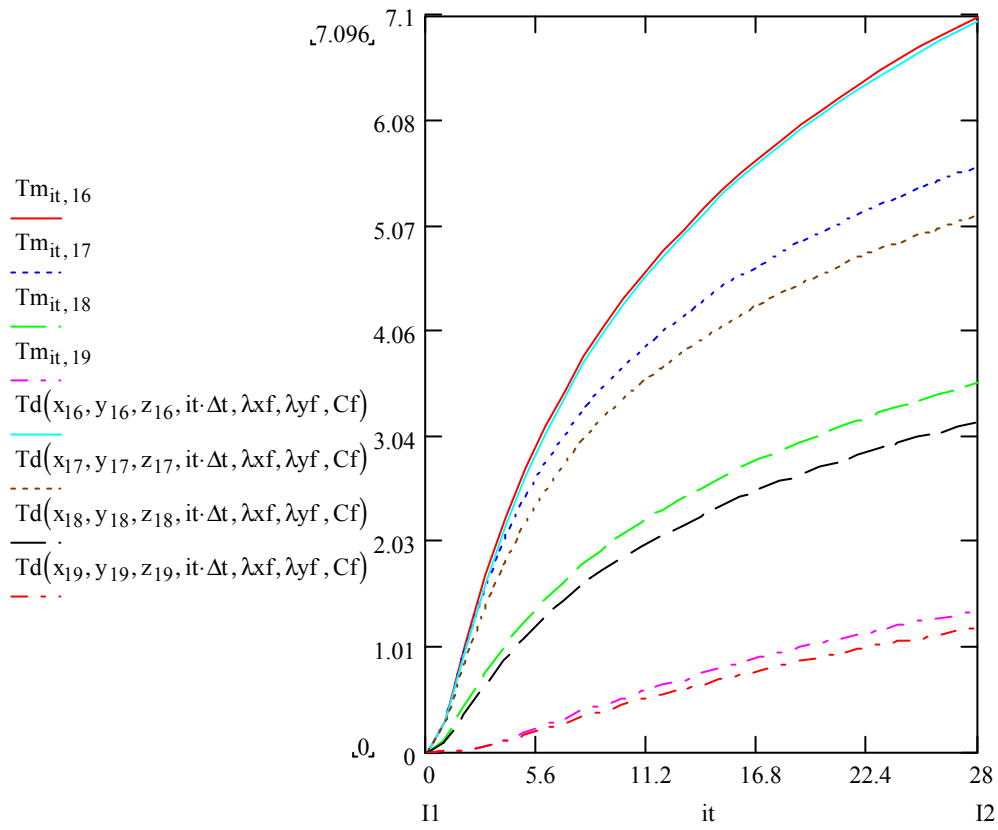
0-28 (C1)
Cdef123456



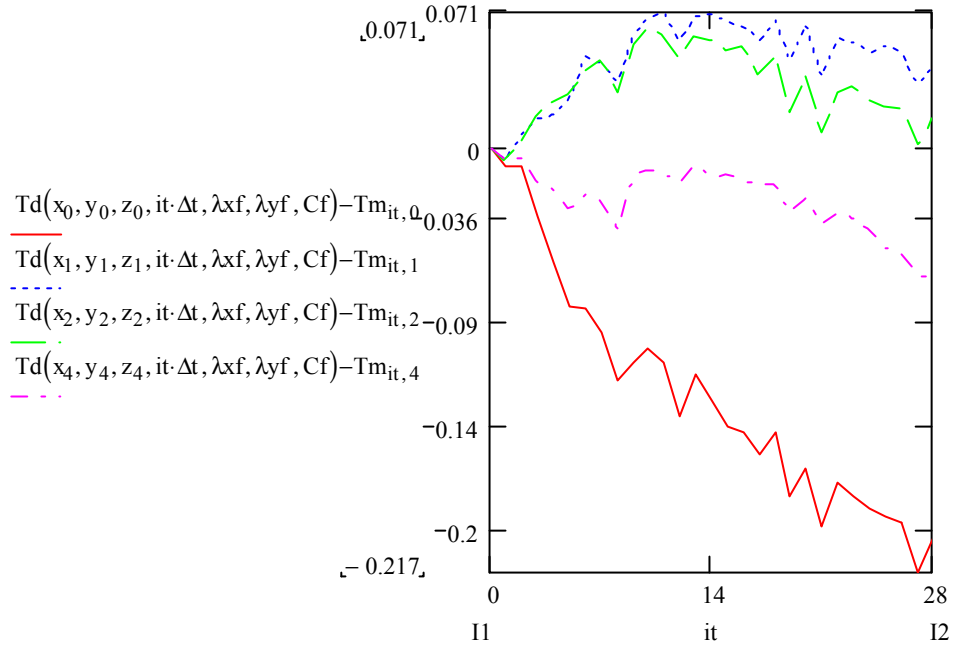
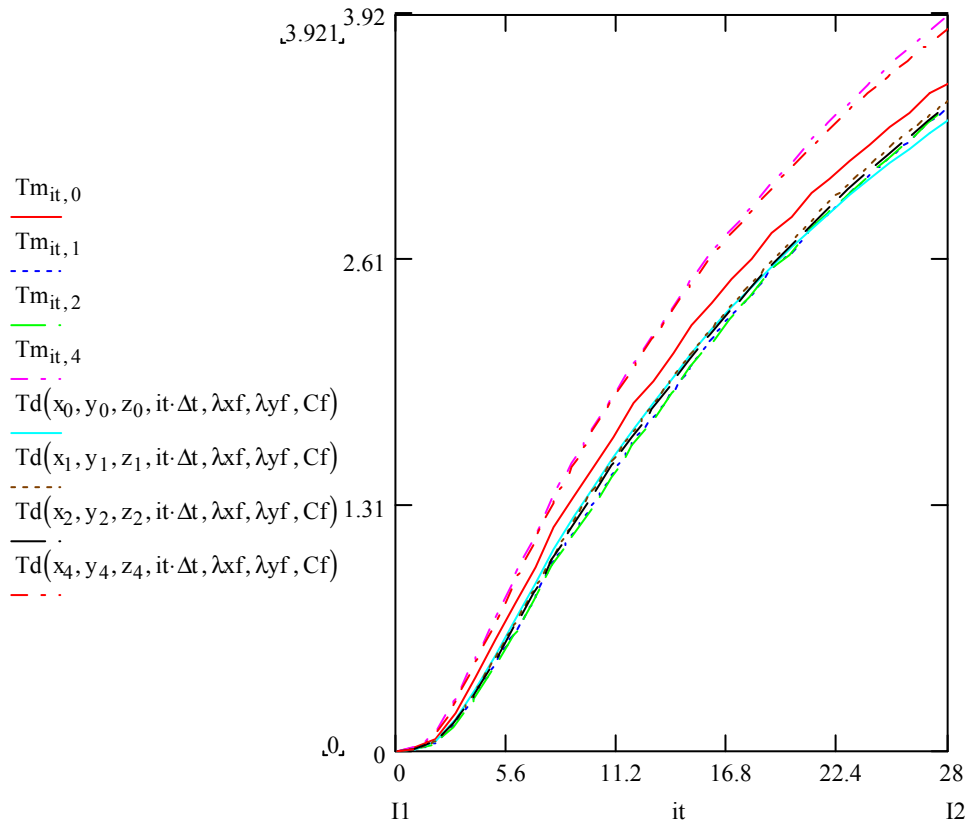


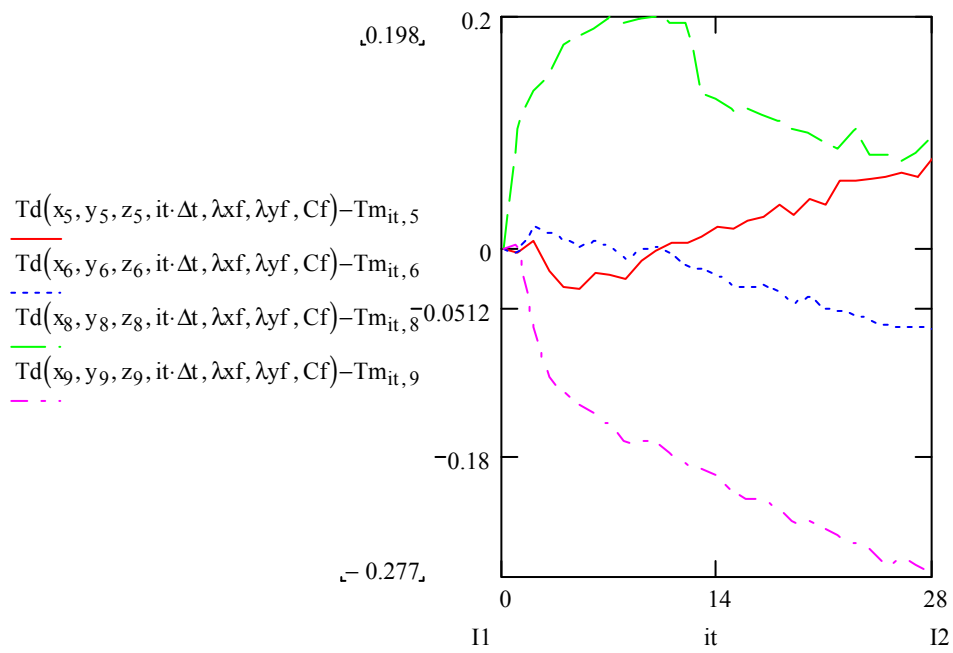
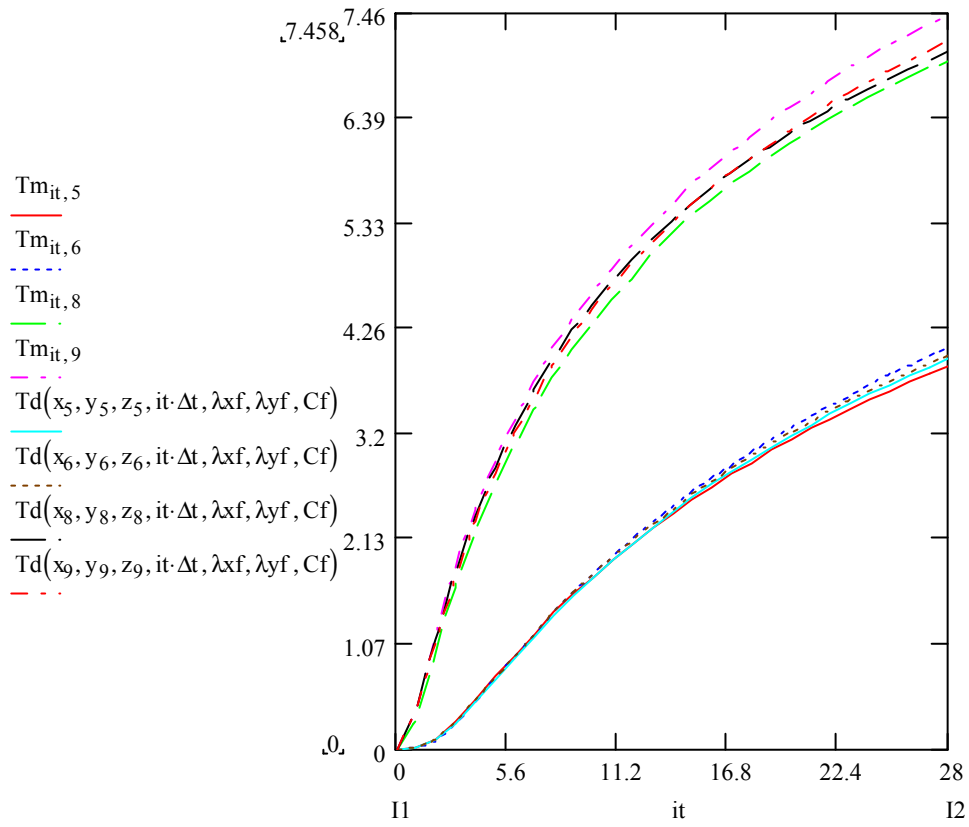


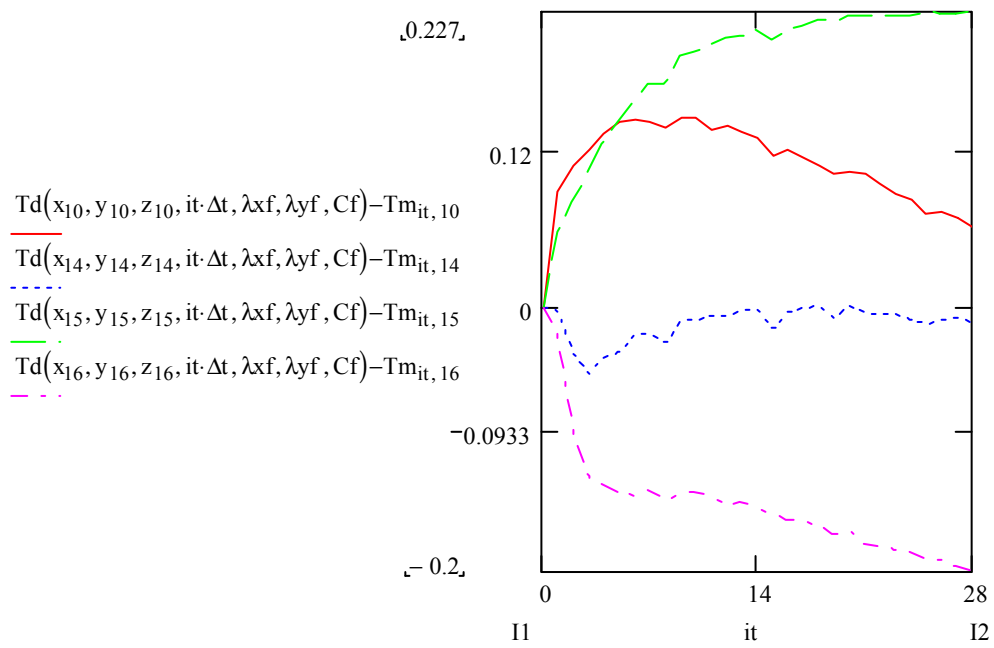
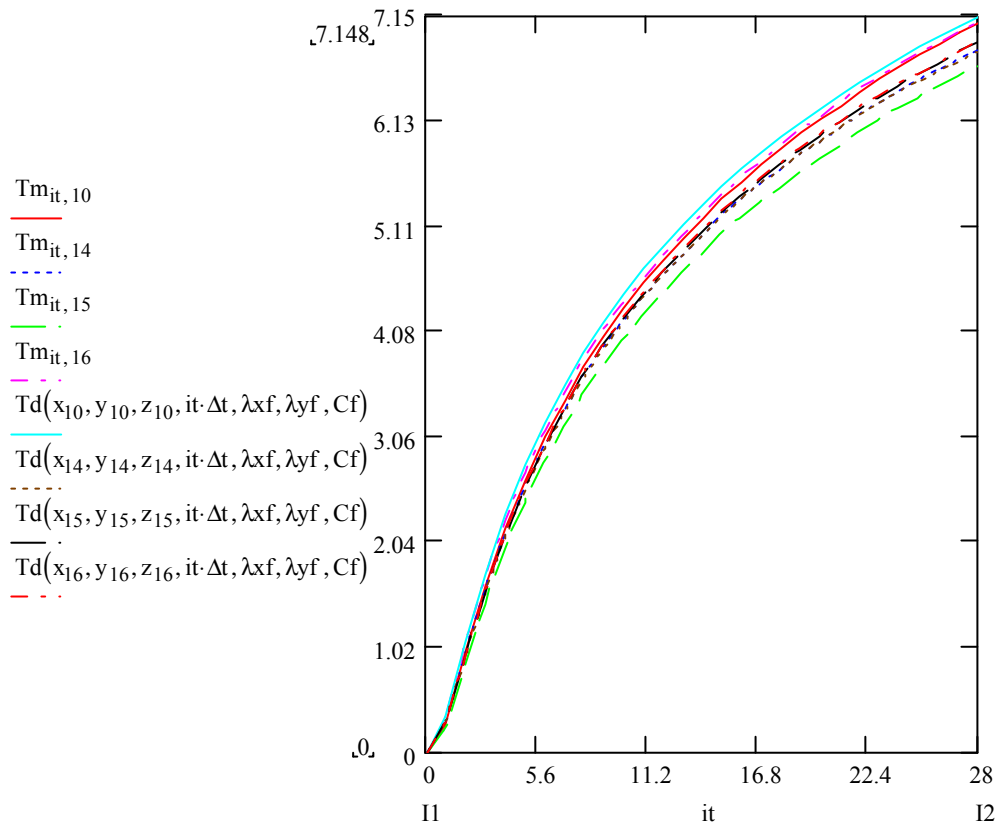




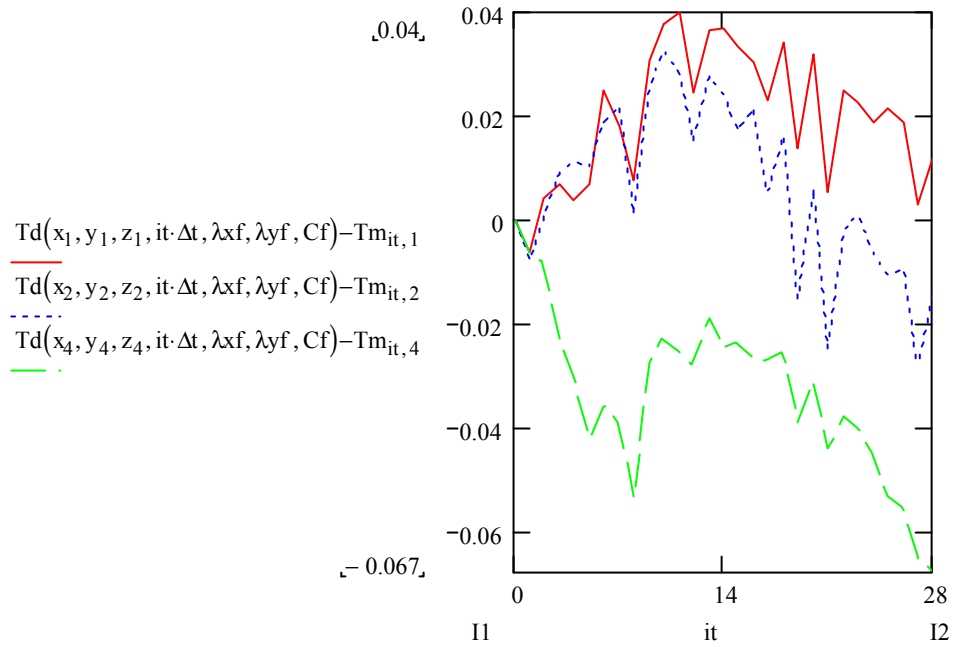
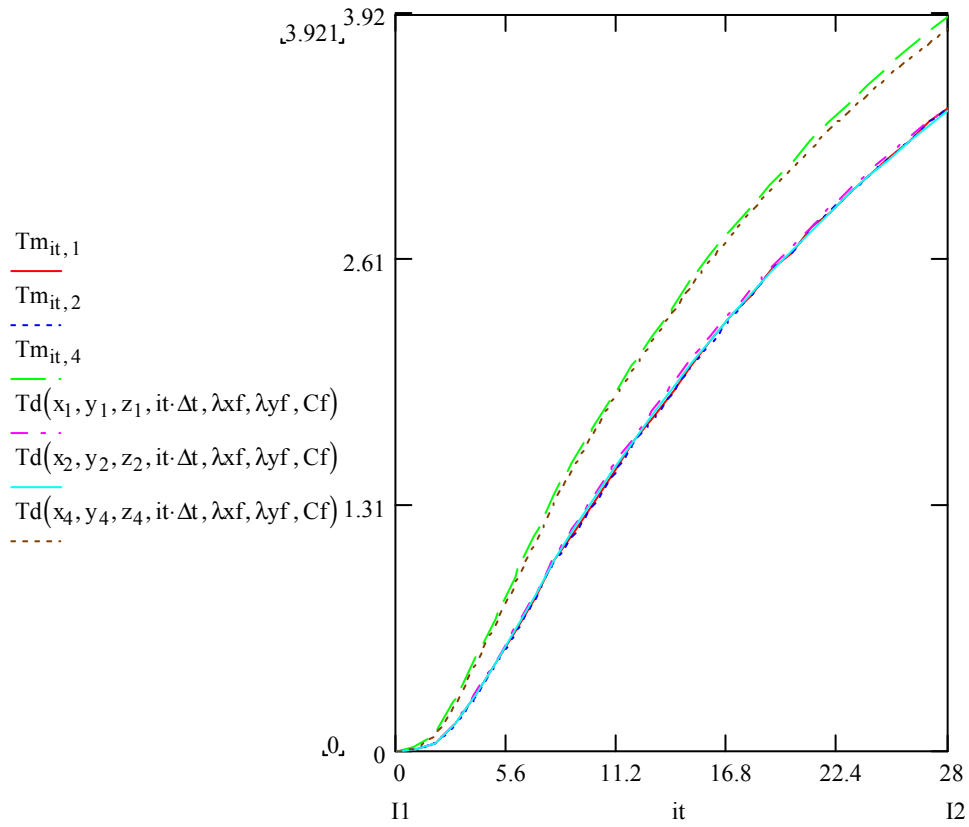
0-28 (C2)
Cdef123

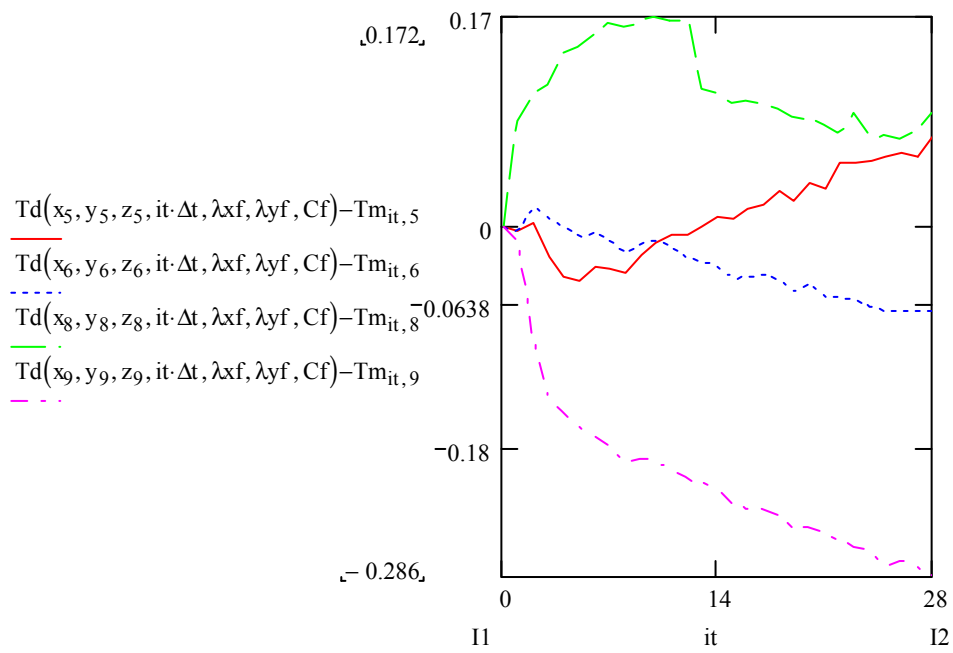
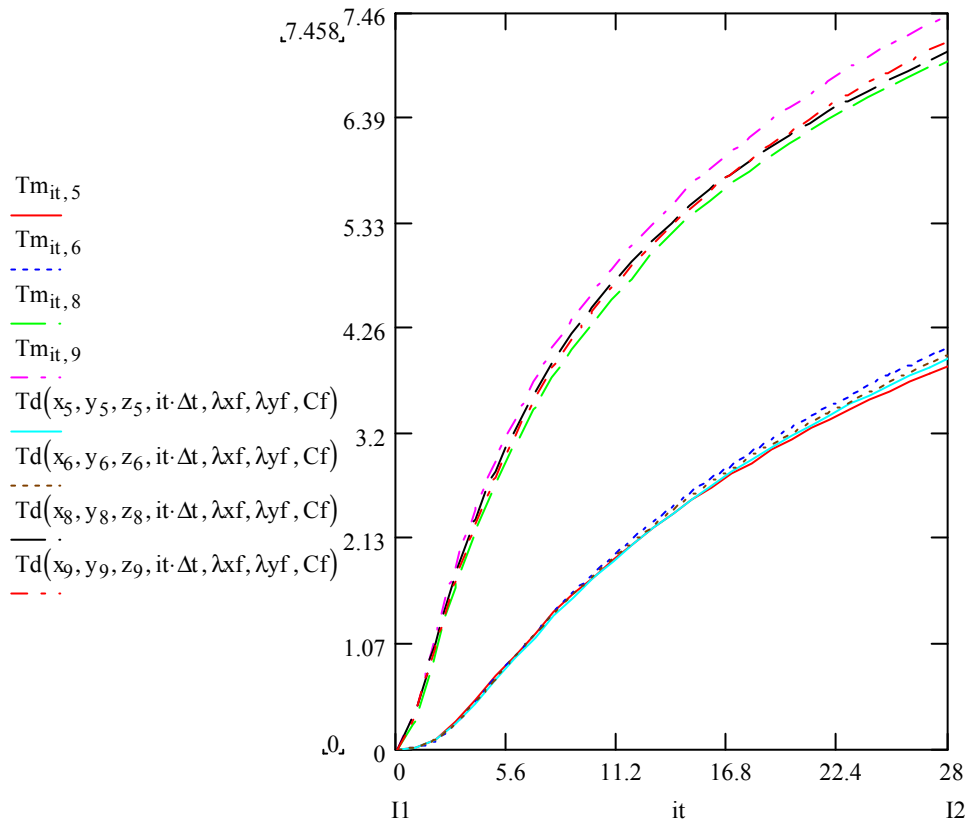


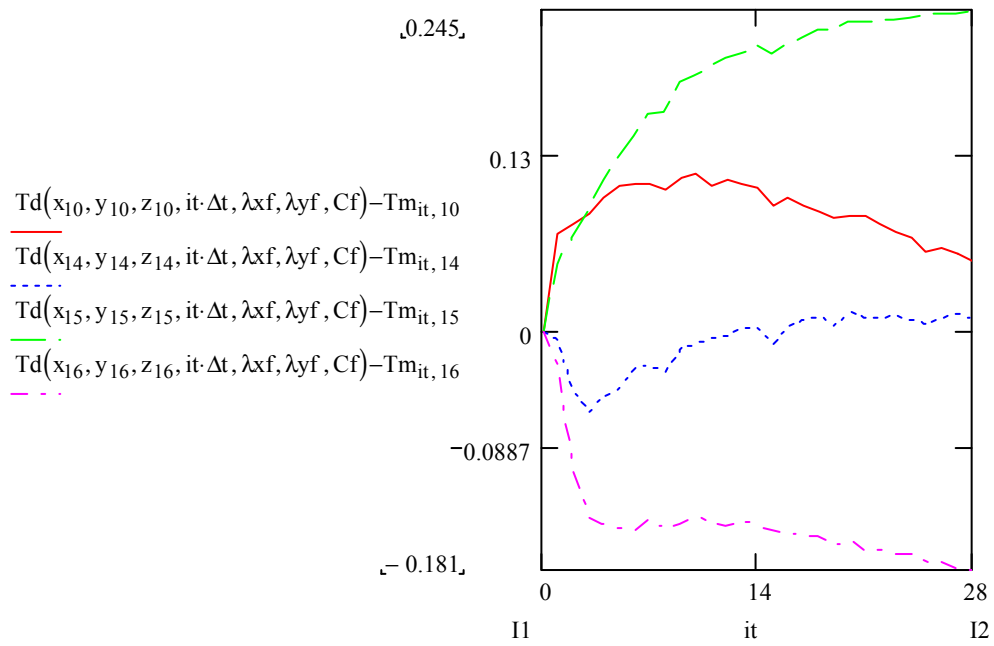
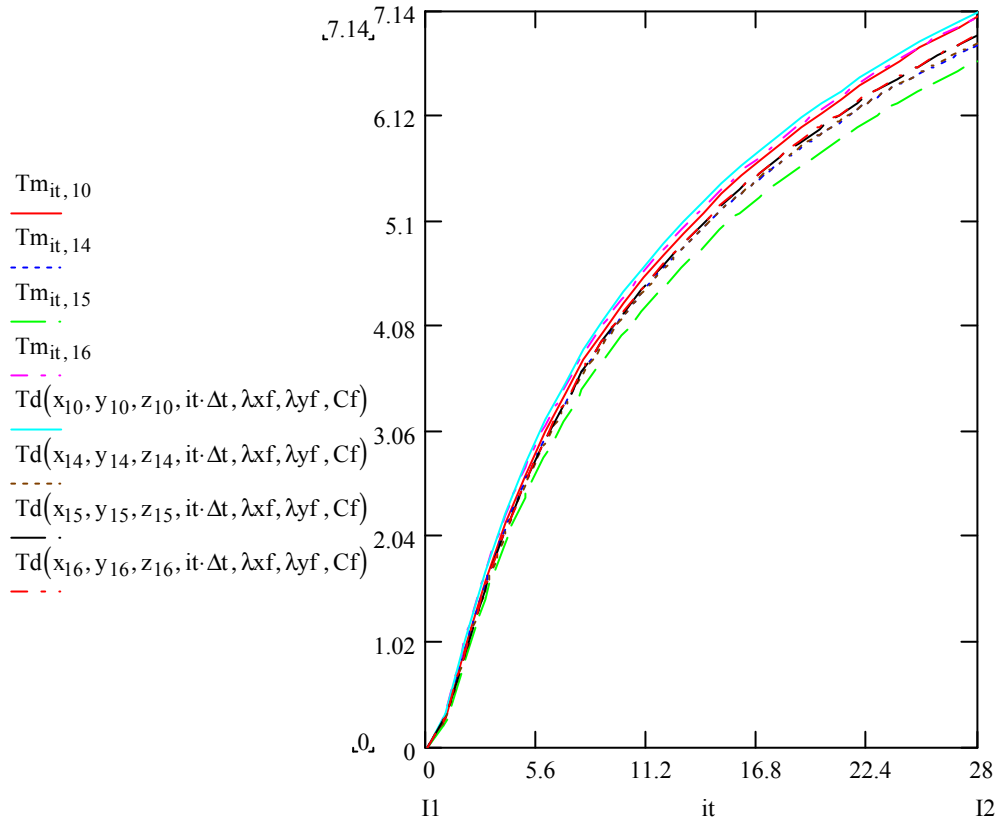




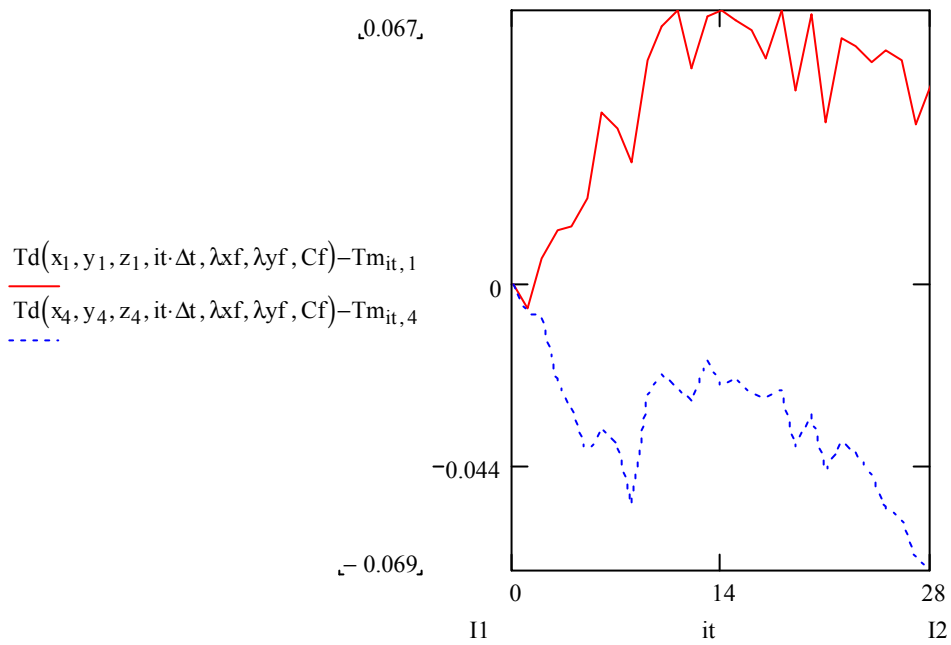
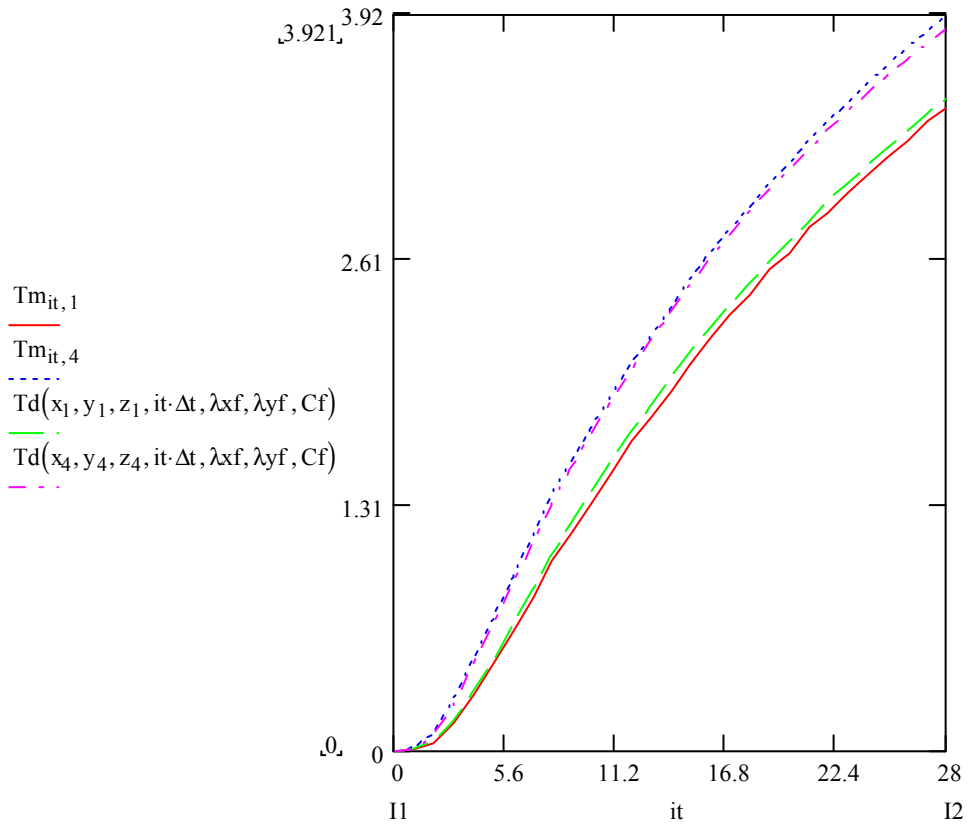
0-28 (C3)
Cdef123-c1

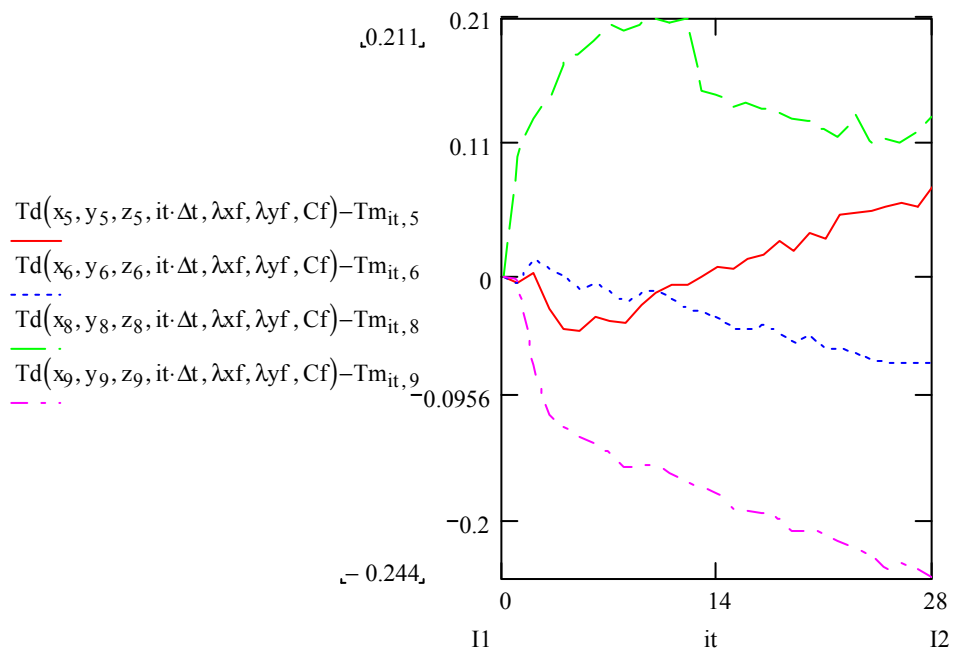
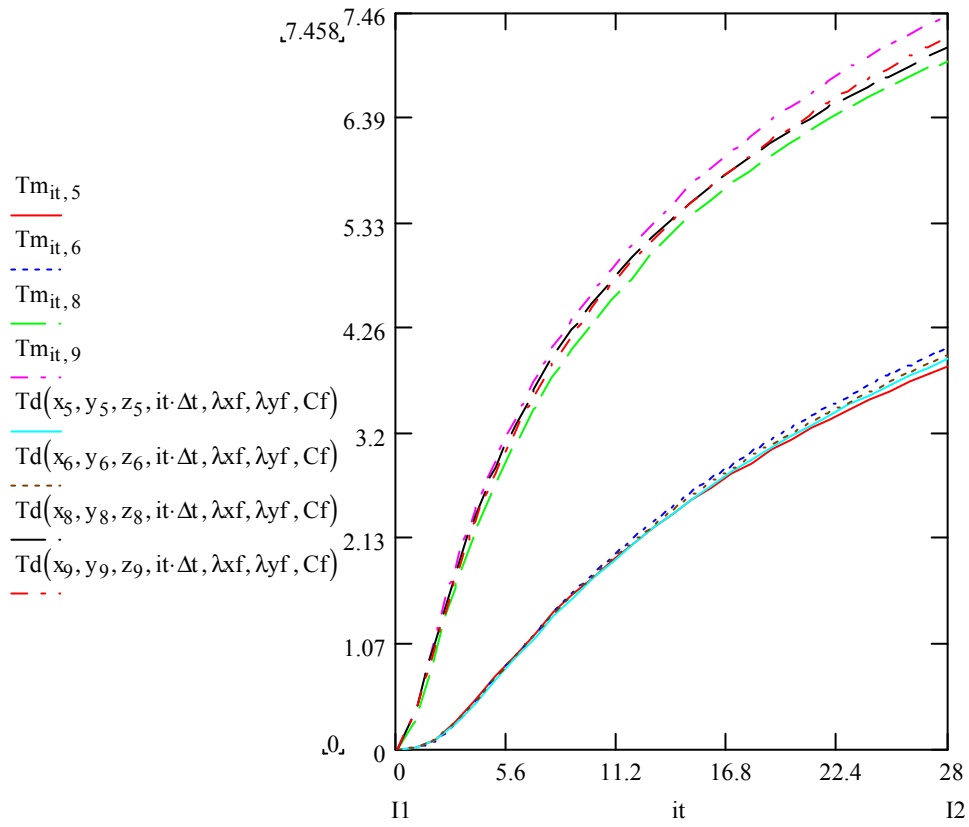


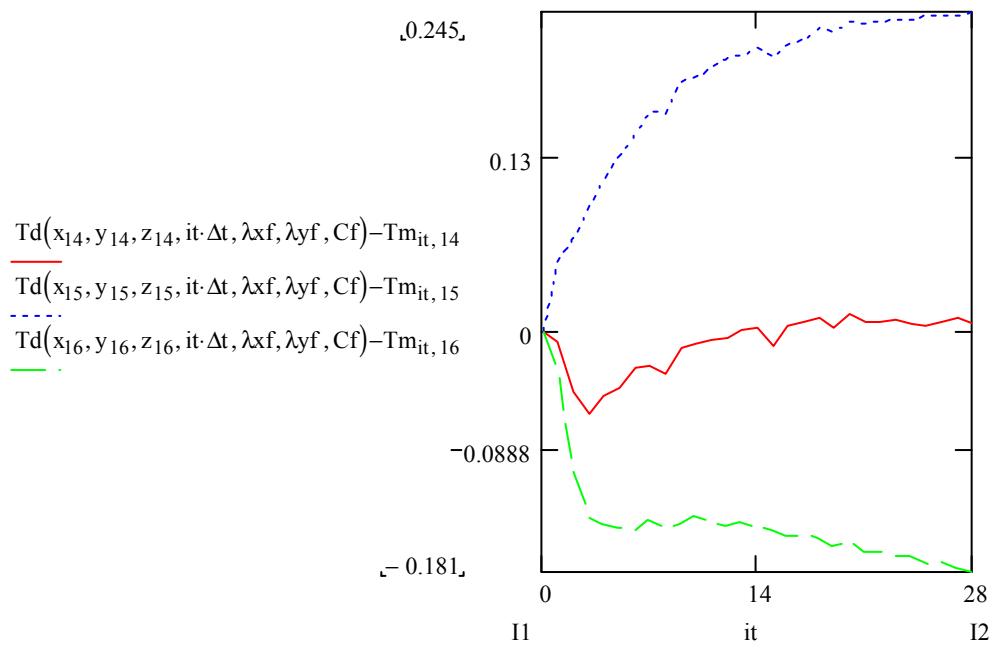
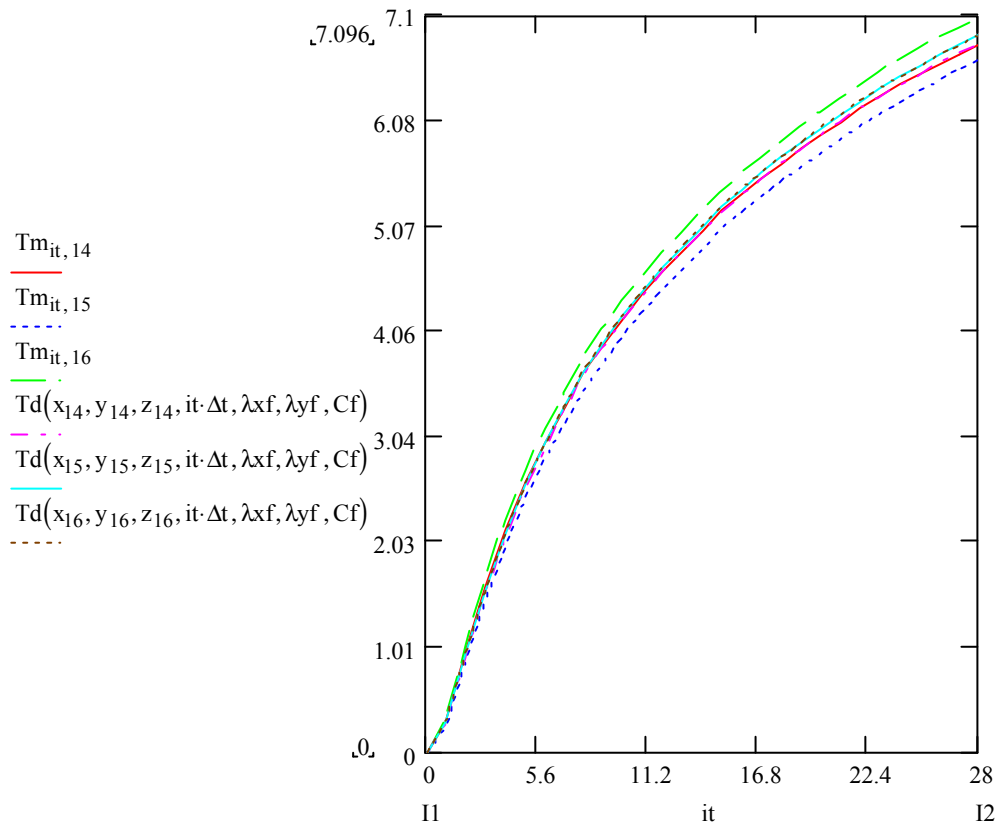




0-28 (C4)
Cdef123-c1c3e3







APPENDIX 1.7 – Uncertainty calculations regarding heater and sensor positions

Uncertainty calculation of horizontal heater position

Heater borehole radius: 38 mm

Heater stick radius: 10.5 mm

Heater cable diameter: 3.6 mm

The heater cable was folded along the stick on both sides as shown in Figure 42.

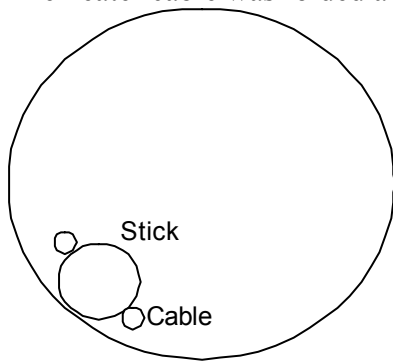


Figure 42 Stick and heater cable in borehole B. It is unknown where in the borehole that the stick is located after the insertion of bentonite. Thus, the figure shows the longest possible distance from the centre as the worst case scenario.

The picture's measures are not correct in relation to each other. However, the thickness of the stick makes it impossible for the cables on each side to both touch the borehole wall simultaneously, which is the important fact that the figure illustrates.

This means that the longest distance between the centre of the stick (considered centre of heater) and the borehole centre is:

$$38 - 10.5 = 27.5 \text{ mm.}$$

This means that the uncertainty of the horizontal heater position is ± 27.5 mm.

Uncertainty calculation of horizontal sensor position

Sensor borehole radius: 28 mm
Assumed sensor side measure: 5 mm
Sensor stick diameter: 16 mm

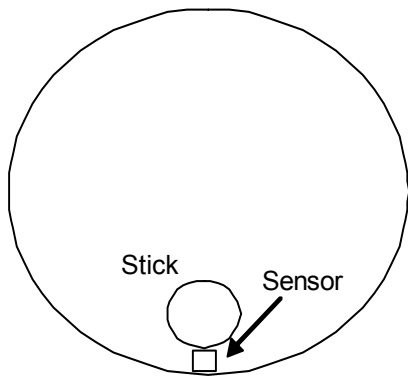


Figure 43 *Stick and sensor in sensor borehole. Maximum possible distance between sensor centre and borehole centre.*

The picture's measures are not correct in relation to each other. The picture only exists to simplify the explanation of the calculation.

The longest possible distance between the sensor centre and borehole centre is:

$$28 - (5 / 2) = 25.5 \text{ mm.}$$

This means that the uncertainty of the horizontal sensor position is 25.5 mm.

A FORMULA FOR A CONTINUOUS LINE HEAT SOURCE IN ANISOTROPIC GROUND

Johan Claesson

December 2006

1. Point heat source

Let the heat Q (J) be released at time $t = 0$ in the point $(0, 0, 0)$ in an infinite solid material with the thermal conductivity λ (W/(m,K)), the density ρ (kg/m³) and the heat capacity c (J/(kg,K)). The undisturbed temperature is zero throughout the solid. The temperature from the point heat source is according to Carslaw and Jaeger¹:

$$T_{\text{point}}(x, y, z, t) = \frac{Q}{\rho c} \cdot \frac{1}{\sqrt{4\pi at}} \cdot e^{-\frac{x^2}{4at}} \cdot \frac{1}{\sqrt{4\pi at}} \cdot e^{-\frac{y^2}{4at}} \cdot \frac{1}{\sqrt{4\pi at}} \cdot e^{-\frac{z^2}{4at}}. \quad (0.1)$$

This solution satisfies the heat equation for an isotropic material:

$$\rho c \cdot \frac{\partial T}{\partial t} = \lambda \cdot \frac{\partial^2 T}{\partial x^2} + \lambda \cdot \frac{\partial^2 T}{\partial y^2} + \lambda \cdot \frac{\partial^2 T}{\partial z^2}, \quad a = \frac{\lambda}{\rho c}. \quad (0.2)$$

Here, a (m²/s) is the thermal diffusivity.

The corresponding heat equation for an anisotropic material with different conductivities the three direction x , y and z is

$$\rho c \cdot \frac{\partial T}{\partial t} = \lambda_x \cdot \frac{\partial^2 T}{\partial x^2} + \lambda_y \cdot \frac{\partial^2 T}{\partial y^2} + \lambda_z \cdot \frac{\partial^2 T}{\partial z^2}. \quad (0.3)$$

The solution for a point heat source Q (J) released at $t = 0$ at the point $(0, 0, 0)$ is then:

$$T_{\text{point}}(x, y, z, t) = \frac{Q}{\rho c} \cdot \frac{1}{\sqrt{4\pi a_x t}} \cdot \frac{1}{\sqrt{4\pi a_y t}} \cdot \frac{1}{\sqrt{4\pi a_z t}} \cdot e^{-\frac{x^2}{4a_x t} - \frac{y^2}{4a_y t} - \frac{z^2}{4a_z t}}. \quad (0.4)$$

Here, the three exponents are multiplied together. There are different diffusivities in the three directions:

¹ Carslaw, Jaeger, Conduction of Heat in Solids, Oxford Univ. Pr. 1959. Page 256.

$$a_x = \frac{\lambda_x}{\rho c}, \quad a_y = \frac{\lambda_y}{\rho c}, \quad a_z = \frac{\lambda_z}{\rho c}. \quad (0.5)$$

This solution may be written in the following way:

$$T_{\text{point}}(x, y, z, t) = \frac{Q}{4\pi\sqrt{\lambda_x\lambda_y} \cdot t} \cdot e^{-\left(\frac{x^2 a_z + y^2 a_z}{a_x a_y}\right) \frac{1}{4a_z t}} \cdot \frac{1}{\sqrt{4\pi a_z t}} \cdot e^{-\frac{z^2}{4a_z t}}. \quad (0.6)$$

2. Line heat source

The next step is to consider a line heat source. The heat q (J/m) is released at time $t = 0$ along the z -axis in the interval $-H \leq z \leq H$. The solution for a unit heat release at $(0, 0, z) = (0, 0, z')$ is from (0.6):

$$T(x, y, z, t) = \frac{1}{4\pi\sqrt{\lambda_x\lambda_y} \cdot t} \cdot e^{-\left(\frac{x^2 \lambda_z + y^2 \lambda_z}{\lambda_x \lambda_y}\right) \frac{1}{4a_z t}} \cdot \frac{1}{\sqrt{4\pi a_z t}} \cdot e^{-\frac{(z-z')^2}{4a_z t}}. \quad (0.7)$$

Here, a_z / a_x is replaced by λ_z / λ_x . To get the solution for the line heat, we have to integrate over $-H \leq z' \leq H$. The heat source Q is replaced by the infinitesimal heat $q \cdot dz'$. We get an integral involving the last factor in z :

$$\begin{aligned} \int_{-H}^H \frac{q}{\sqrt{4\pi a_z t}} \cdot e^{-\frac{(z-z')^2}{4a_z t}} dz' &= \left[z' = z + s \cdot \sqrt{4a_z t} \right] = q \cdot \frac{1}{\sqrt{\pi}} \cdot \int_{-(H+z)/\sqrt{4a_z t}}^{(H-z)/\sqrt{4a_z t}} e^{-s^2} ds = \\ &= \frac{q}{2} \cdot \left[\operatorname{erf}\left(\frac{H-z}{\sqrt{4a_z t}}\right) - \operatorname{erf}\left(-\frac{H+z}{\sqrt{4a_z t}}\right) \right] \end{aligned} \quad (0.8)$$

Here, $\operatorname{erf}(x)$ is the error function:

$$\operatorname{erf}(x) = \frac{2}{\sqrt{\pi}} \cdot \int_0^x e^{-s^2} ds, \quad \operatorname{erf}(-x) = -\operatorname{erf}(x). \quad (0.9)$$

The solution for a line heat source is then:

$$T_{\text{line}}(x, y, z, t) = \frac{q}{4\pi\sqrt{\lambda_x\lambda_y} \cdot t} \cdot e^{-\left(\frac{x^2 \lambda_z + y^2 \lambda_z}{\lambda_x \lambda_y}\right) \frac{1}{4a_z t}} \cdot \frac{1}{2} \cdot \left[\operatorname{erf}\left(\frac{H-z}{\sqrt{4a_z t}}\right) + \operatorname{erf}\left(\frac{H+z}{\sqrt{4a_z t}}\right) \right] \quad (0.10)$$

3. Continuous line heat source

Finally, we consider a continuous line heat source. There is a steady heat release q (W/m) along $-H \leq z \leq H$ from the start $t = 0$. We have to integrate (0.10) with t replaced by $t - t'$ over $0 \leq t' \leq t$:

$$T_{\text{clhs}}(x, y, z, t) = \int_0^t \frac{q}{4\pi\sqrt{\lambda_x\lambda_y} \cdot (t-t')} \cdot e^{-\left(\frac{x^2\lambda_z + y^2\lambda_z}{\lambda_x\lambda_y}\right) \frac{1}{4a_z(t-t')}} \cdot \frac{1}{2} \cdot \left[\operatorname{erf}\left(\frac{H-z}{\sqrt{4a_z(t-t')}}\right) + \operatorname{erf}\left(\frac{H+z}{\sqrt{4a_z(t-t')}}\right) \right] dt'. \quad (0.11)$$

We make the substitution

$$s = \frac{H}{\sqrt{4a_z(t-t')}}, \quad t-t' = \frac{H^2}{4a_z s^2}, \quad dt' = \frac{2H^2}{4a_z s^3} ds. \quad (0.12)$$

Then we get:

$$T_{\text{clhs}}(x, y, z, t) = \frac{q}{4\pi\sqrt{\lambda_x\lambda_y}} \cdot \int_{H/\sqrt{4a_z t}}^{\infty} e^{-\left(\frac{x^2\lambda_z + y^2\lambda_z}{\lambda_x\lambda_y}\right) \left(\frac{s}{H}\right)^2} \cdot \frac{1}{s} \cdot F(s, z) ds. \quad (0.13)$$

Here, the function $F(s, z)$ is defined by:

$$F(s, z) = \operatorname{erf}\left[\left(1 - z/H\right) \cdot s\right] + \operatorname{erf}\left[\left(1 + z/H\right) \cdot s\right]. \quad (0.14)$$

In the particular case $\lambda_z = \lambda_x$, we get:

$$T_{\text{clhs}}(x, y, z, t) = \frac{q}{4\pi\sqrt{\lambda_x\lambda_y}} \cdot \int_{H/\sqrt{4a_x t}}^{\infty} e^{-\left(x^2 + \frac{\lambda_x}{\lambda_y} y^2\right) \left(\frac{s}{H}\right)^2} \cdot \frac{1}{s} \cdot F(s, z) ds, \quad a_x = \frac{\lambda_x}{\rho c}. \quad (0.15)$$

Small-scale field measurements using the multi probe method: Assessment of anisotropy of thermal properties in granitic rock at Forsmark

Date: 2006-01-23

Our ref.: 05030

Project leader: John Wrafter

Conducted by: Fredrik Mossmark

Auditor: Jan Sundberg

Objective

The objective of this study is to measure thermal transport properties of granitic rock (rock code 101057) at two selected locations at Forsmark. In particular, the data is evaluated with respect to anisotropic thermal transport properties primarily caused by foliation of the rock. The results from the measurements made in this study will be compared to large-scale field measurements and to laboratory measurements. This study also aims to develop evaluation methods further.

Methodology

A total of six measurements were conducted in boreholes at two different locations in the Forsmark area; see figure 1. Three vertical holes, 18 mm in diameter, were drilled parallel to one another at each measurement position. The configuration of the boreholes is illustrated in figure 3. Prior to the field experiment, geologists had mapped the locations to assess the orientation of foliation or lineation. The dominant structure at both locations is a vertical or sub-vertical foliation. The geologists also selected the location and orientation of boreholes, so that the holes are parallel, or close to parallel, with the foliation, and the directions from the heating probe to the observation holes were parallel and perpendicular to the foliation respectively. At a distance of some metres, away from the influence of the heat source, an observation hole for background temperature measurement was drilled. Figure 2 illustrates the setup for measurement at HFM95.

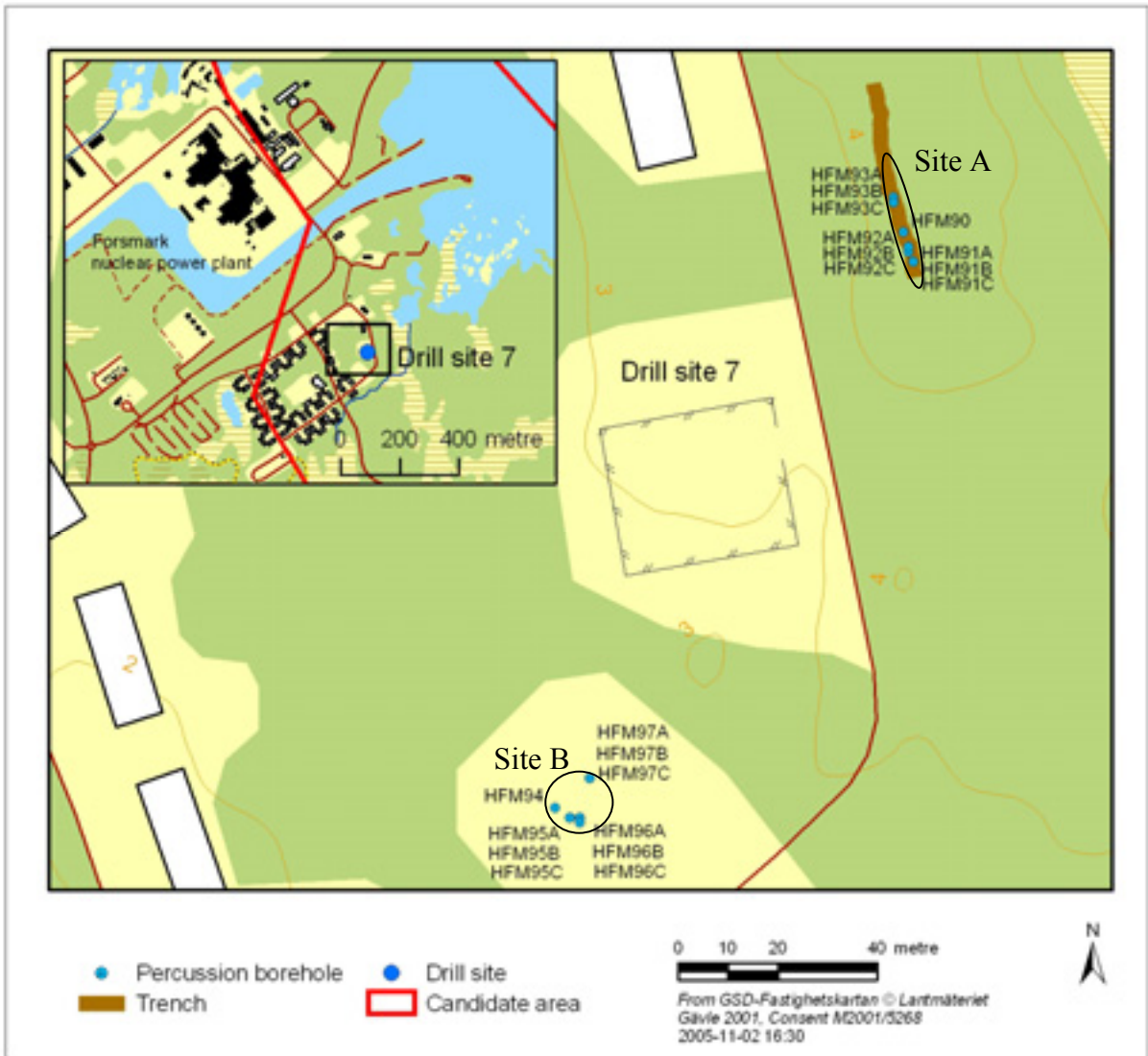


Figure 1. Map of the investigation area and its two sites. The boreholes used (HFM90-97) are indicated in the map. HFM90 and HFM94 are reference holes for measuring background temperature.



Figure 2. *Logger, thermistors, and heat probe installed at location HFM95.*

The method has previously been described in Sundberg (1988), but has been modified for application to the measurement of anisotropic thermal properties. The experiment is conducted by heating the rock with a probe installed in one borehole and monitoring changes of temperature in observation boreholes at a known distance from the probe (figure 3).

The heating probe used had a length of 1.2 m and the borehole used had been drilled to a suitable depth. The boreholes for the observation thermistors were drilled to accommodate the thermistors at half the depth of the heat probe borehole. A bentonite clay/water mixture (slurry) was filled into the boreholes to fill the space between the rock and the installed equipment. The heat probe consisted of a resistor and was designed to have an even heat output along its length. Temperature was monitored with thermistors of type YSI 44033 that have a tolerance of ± 0.1 °C. Data measurements were logged with a data logger (Datataker 500), see figure 2.

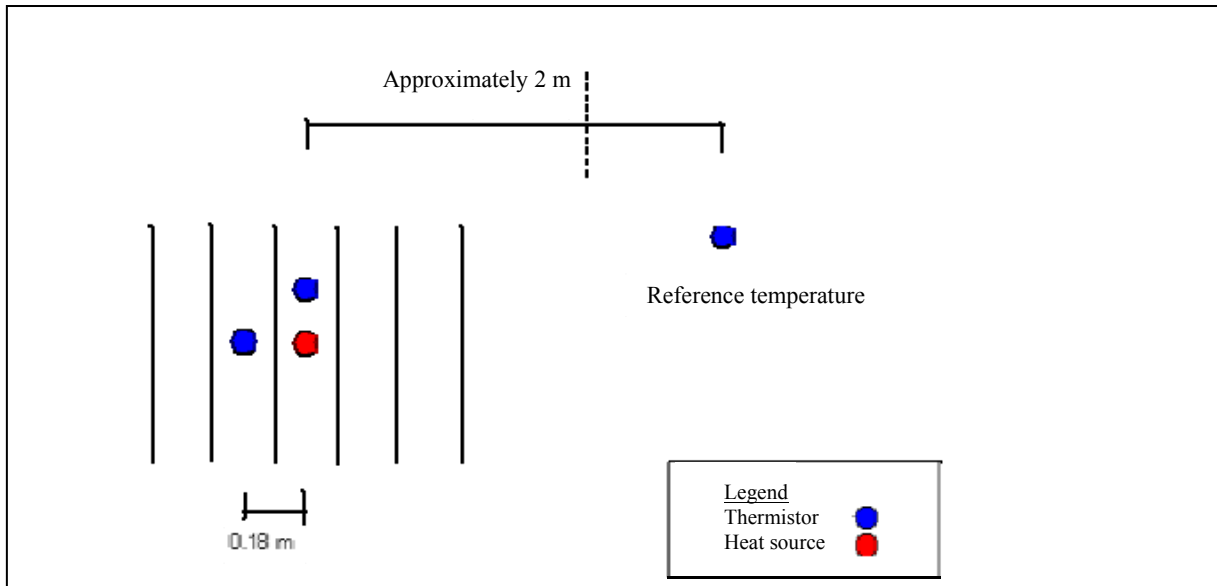


Figure 3. Schematic layout of an installation of heat probe, observation and reference thermistors for the field experiment. The lines in the figure indicate the direction of foliation.

After installation of the equipment at a location, but before the experiment commenced, stable temperature readings were required. Temperature was thus measured for a period of about 20 minutes to be certain that the thermistors had reached equal temperatures to the surrounding rock.

During the experiment, the heat was applied for approximately two hours. The heat output was held stable at approximately 100 W/m through supplying the heat probe electrically from a device with a constant electrical current and voltage output (Delta Elektronika ES030-5). The heat output was assessed by serially connecting the heat probe to a constant resistance shunt, the electrical tension over the shunt was measured and logged. Fluctuation in background temperature in the rock was monitored with a thermistor located at a distance of two or more metres from the experiment (figure 3).

Results, data processing and discussion

The results from the measurements of heat output and temperature were analyzed through fitting to analytical values. A programme developed with the Mathcad tool specifically for this experiment was primarily used. Three data sets used for fitting were derived from data processing using three different approaches:

- All measured data collected from the thermistors during an experiment was used without compensation for temperature drift.
- All data was used, but after compensation with data from temperature drift measurements from the reference thermistor.
- Only compensated data captured after 2500 seconds of heating was included.

The exclusion of data for $t < 2500$ s was made to avoid interference from noise during the initial unaffected period and from transition resistance caused by the bentonite clay surrounding the heat probe. After 2500 s the temperature increase was approximately 0.1 K.

Temperature data fitting procedure

The temperature increase during an experiment such as in this study can be calculated according to equations 1 and 2 if thermal properties are known, and have been developed by /Claesson 2005/. In the equations, variables are defined as:

T_1 : temperature increase parallel to foliation (K)

T_2 : temperature increase perpendicular to foliation (K)

H: half length of heat probe (m)

t: time (s)

λ_x : thermal conductivity parallel to foliation (W/(m·K))

λ_y : thermal conductivity perpendicular to foliation (W/(m·K))

C: heat capacity (J/(m³·K))

x_1, y_1 and x_2, y_2 : coordinates for the monitoring thermistors in relation to the heat probe (m)

Q: Heat output from probe (W)

Q_H : $Q/(4 \cdot \pi \cdot H)$ (W/m)

$$T_1(t, \lambda_x, \lambda_y, C) := Q_H \cdot \frac{L}{\sqrt{\frac{4 \cdot \lambda_x(t)}{C}}} \cdot \int_0^{\infty} \frac{e^{-x_1^2 + \frac{\lambda_x}{\lambda_y} \cdot y_1^2} \cdot \frac{s}{L} \cdot \left(\operatorname{erf} \frac{(H-z_1) \cdot s}{L} + \operatorname{erf} \frac{(H+z_1) \cdot s}{L} \right)}{2 \cdot s \cdot \sqrt{\lambda_x \cdot \lambda_y}} ds \quad (1)$$

$$T_2(t, \lambda_x, \lambda_y, C) := Q_H \cdot \frac{L}{\sqrt{\frac{4 \cdot \lambda_x \cdot t}{C}}} \cdot \int_0^{\infty} \frac{e^{-x_2^2 + \frac{\lambda_x}{\lambda_y} \cdot y_2^2} \cdot \frac{s}{L} \cdot \left(\operatorname{erf} \frac{(H-z_2) \cdot s}{L} + \operatorname{erf} \frac{(H+z_2) \cdot s}{L} \right)}{2 \cdot s \cdot \sqrt{\lambda_x \cdot \lambda_y}} ds \quad (2)$$

λ_z was assumed to be the same as λ_x and could hence be removed from the equation. Furthermore, thermal diffusivity, κ (m^2/s) is not explicitly included in the equation after simplifications but can be calculated through dividing the thermal conductivity by the heat capacity.

HFM 91

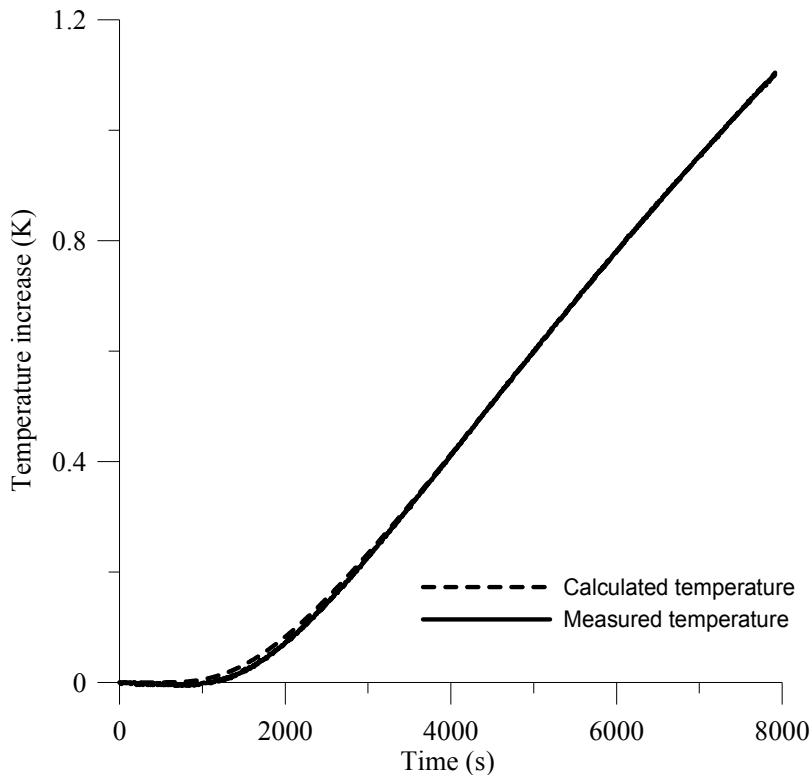


Figure 4. Measured and fitted (calculated) temperature development at HFM91.

If only the temperature increase is known, thermal properties can be assessed through iterative fitting between a calculated and a measured temperature curve. In this study, the minimizing of deviation between measured and calculated values uses a function that used the Conjugate-Gradient method. Iteration was done until results from the two most recent calculations are within 0.001. From the iterations based on temperature change (T , K) for different t (time, s), thermal conductivity (λ , $\text{W}/(\text{m}\cdot\text{K})$) and heat capacity (C , $\text{J}/(\text{m}^3, \text{K})$) were estimated. Figure 4 compares the measured temperature increase during an experiment at HFM91 with the calculated (fitted) curve.

Selection of most reliable data set for fitting

Figure 5 through 7 illustrate the deviation between the measured temperature and the temperature development calculated from equations 1 and 2, with the thermal properties assessed with the fitting procedure for the described data sets. When using the uncorrected data, the deviation is jagged (figure 5) which could be caused by errors of measurements. The errors seem to appear simultaneously at all thermistors since the jaggedness is not present for the compensated data (figure 6 and 7). This type of error could be caused by a variation in the electrical tension in the power supply to the data logger.

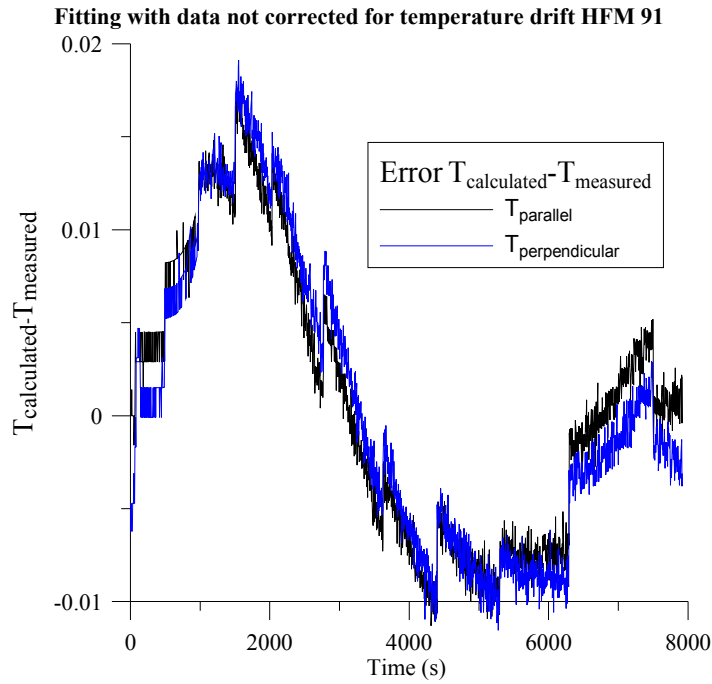


Figure 5. Deviation (error) between uncorrected measured and analytical temperature data for development of temperature at HMF91.

For all plots illustrating the deviation between the fitted and the measured data a noise is present. The noise could be caused by limits of resolution for the data logger. The plot illustrating deviation for fitting with the entire time series of data have more evenly distributed deviation compared to the fitting where the initial 2500 s has been excluded. For the latter, a larger deviation was found for the initial time period that was not used in the fitting procedure.

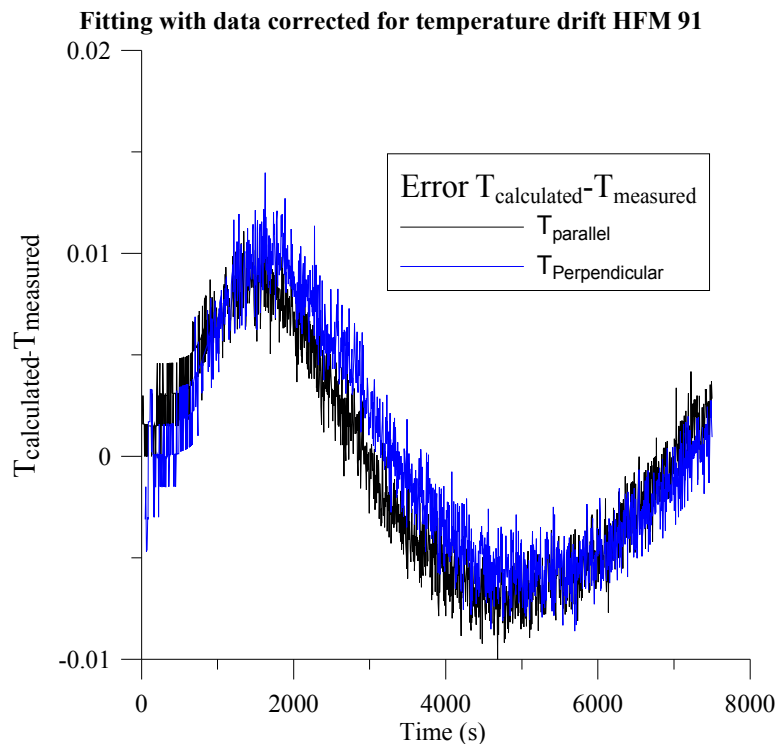


Figure 6. Deviation of measured data compensated for thermal drift from analytical data for development of temperature.

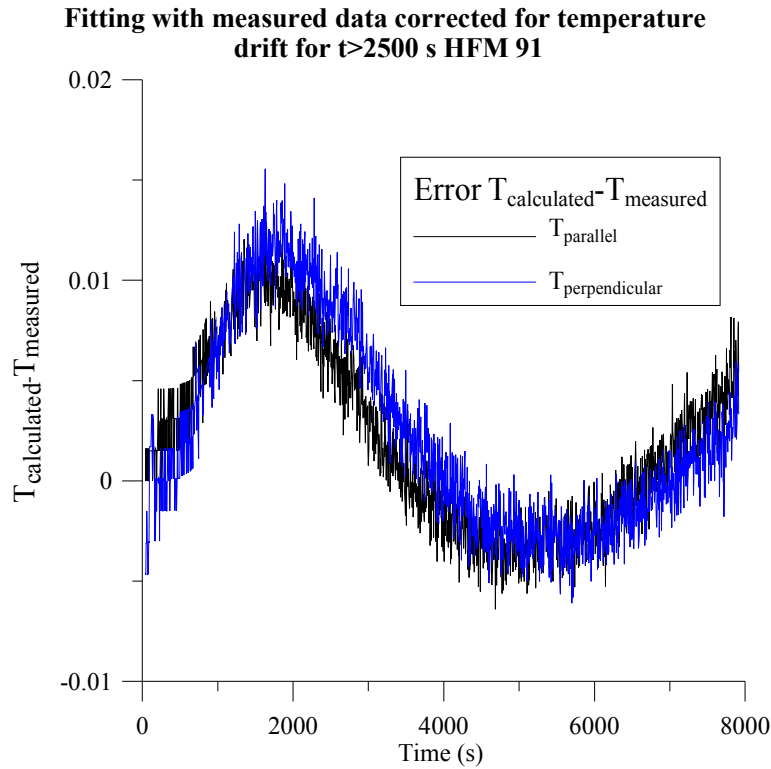


Figure 7. Deviation of measured data $t > 2500$ s compensated for thermal drift from analytical data for development of temperature.

In order to compare the results from fitting analytical data to the three different sets of measured data, the deviation data was used, as presented in figure 8. An arithmetic average of absolute values of deviation of analytical data from the measured data was calculated for each of the data sets for all locations individually. Data captured before 3000 s of heating were excluded since this initial period includes possible errors related to, for example, high noise to reading quota, and skin factor caused by the bentonite clay surrounding the heat probe.

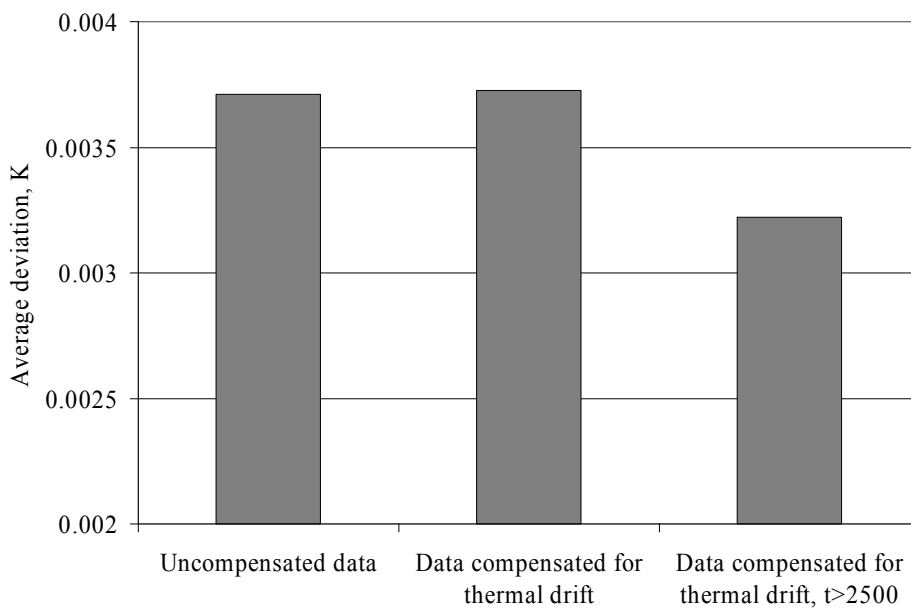


Figure 8. Average deviation in Kelvin between measured and calculated data through fitting.

For the three different types of data sets, namely uncompensated data, data compensated for thermal drift, and data for which the initial period of 2500 s has been excluded, a geometric average was calculated. The results, presented in figure 8 as deviation in K, show a smaller average deviation for fitting with data where the initial period has been excluded. The correction for thermal drift had little impact on the deviation of the fitted curve from the measured data according to this method.

For further comparison of the deviation between measured and calculated temperature increase, the correlation coefficient r^2 was also calculated. In the calculation of r^2 , data collected during the initial 4000 s of the experiments were excluded. Figure 9 shows the arithmetic average of r^2 for the different data sets. As in the calculation of deviation, the fit associated with the data that has been compensated for thermal drift during the experiment, and the data for which the initial 2500 s has been excluded were found to have the highest correlation coefficient. Contrary to the calculation of deviation, the fitting procedure where data sets that had been compensated for thermal drift and the entire time series had been used were found to have a good correlation between calculated and measured temperature values.

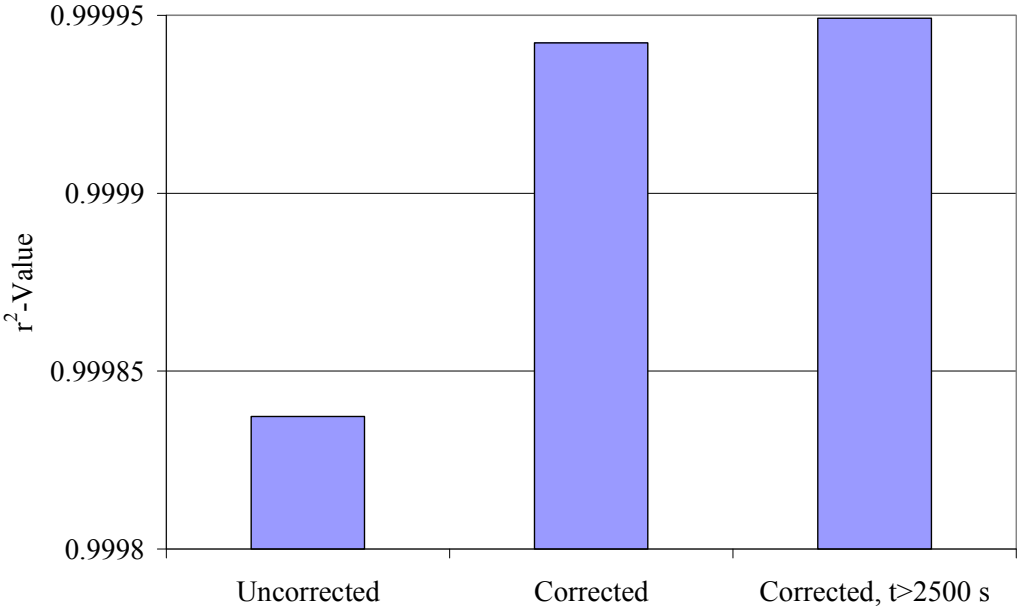


Figure 9. Average of correlation coefficient r^2 for the three different data sets.

According to figures 8 and 9, the correlation between the measured and the fitted data was higher when data $t > 2500$ s was excluded, and therefore this procedure produces the preferred results from this study. Figure 10 illustrates the correlation coefficient for this fitting procedure for each individual location.

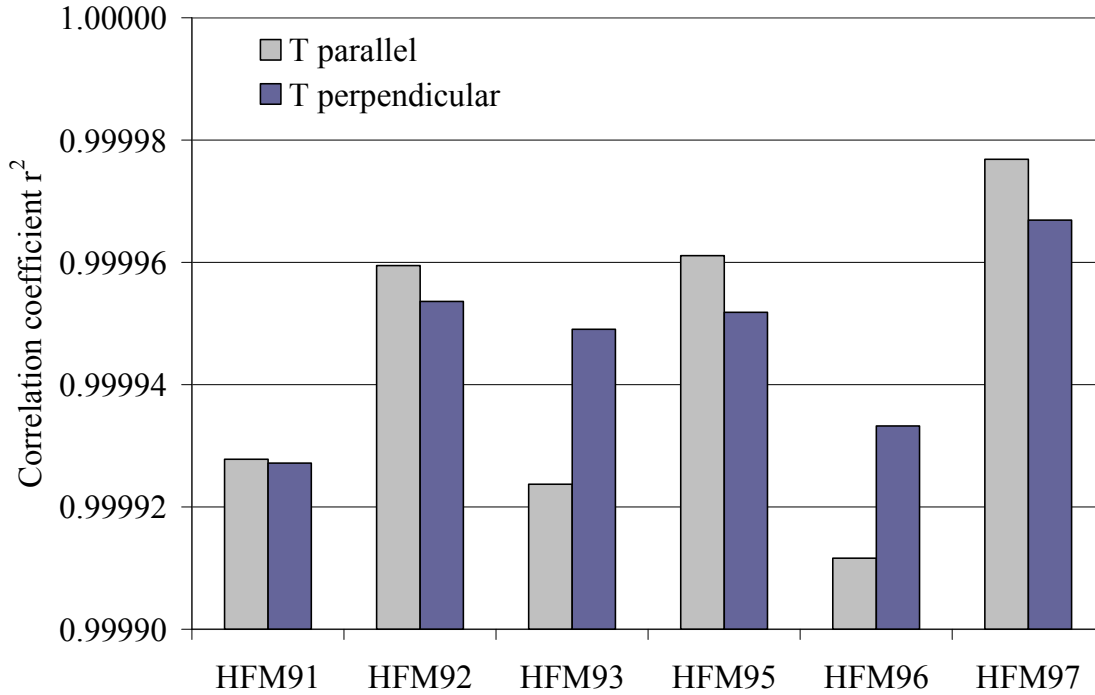


Figure 10. Correlation coefficient for fitting with data corrected for thermal drift and where data $t < 2500$ s have been excluded.

Results from data processing

In table 1, thermal property results from the fitting procedure concluded to be of highest accuracy is presented. Data for the two other data sets are presented in appendix A. Despite the different data sets, the results for thermal conductivity are similar. For heat capacity, larger differences are found for some of the locations; for example, at HFM95 a 7 % lower heat capacity was found when using data compensated for thermal drift compared to for uncompensated data.

Table 1. Fitting with data where the initial experimental period ($t < 2500$ s) has been excluded. From the previous comparison of deviation between measured data and fitted curve, the deviation was found to be smaller for this method. Site A includes HFM91-93, while site B includes HFM95-97.

Location	Thermal conductivity, λ		Thermal diffusivity, κ		Heat capacity, C ($\text{J}/(\text{m}^3 \cdot \text{K})$)
	$\lambda_{\text{parallel}}$ ($\text{W}/(\text{m} \cdot \text{K})$)	$\lambda_{\text{perpendicular}}$ ($\text{W}/(\text{m} \cdot \text{K})$)	κ_{parallel} (mm^2/s)	$\kappa_{\text{perpendicular}}$ (mm^2/s)	
HFM91	3.64	3.19	1.83	1.60	$1.99 \cdot 10^6$
HFM92	3.86	3.27	1.96	1.66	$1.97 \cdot 10^6$
HFM93	3.41	3.36	1.69	1.67	$2.02 \cdot 10^6$
HFM95	3.44	3.45	1.78	1.79	$1.93 \cdot 10^6$
HFM96	4.02	2.88	1.96	1.40	$2.05 \cdot 10^6$
HFM97	3.55	3.26	1.72	1.58	$2.07 \cdot 10^6$

As presented in table 1, the thermal conductivity parallel to the foliation ($\lambda_{\text{parallel}}$) varied between 3.41 W/(m·K) and 4.02 W/(m·K), whereas its perpendicular counterpart ($\lambda_{\text{perpendicular}}$) varied between 2.88 W/(m·K) and 3.45 W/(m·K). The heat capacity varied between 1.93 J/(m³,K) and 2.07 J/(m³,K), the thermal diffusivity varied between 1.65 mm²/s and 1.80 mm²/s. There is no noticeable difference between the two sites, site A and site B as regards thermal properties. Site A includes HFM91-93, while site B includes HFM95-97 as presented in figure 2.

Besides curve fitting using the Mathcad tool, evaluation was also made with the software Termsond, developed by the Swedish Geotechnical Institute. Like the model developed for Mathcad, Termsond also uses numerical iteration to accomplish curve fitting. However, the numerical model assumes isotropic thermal properties, and the fitting to the two sets of observation data for each experiment is done individually. Figure 11 shows a comparison of average thermal conductivity (perpendicular and parallel) for each of the locations with the two evaluation methods.

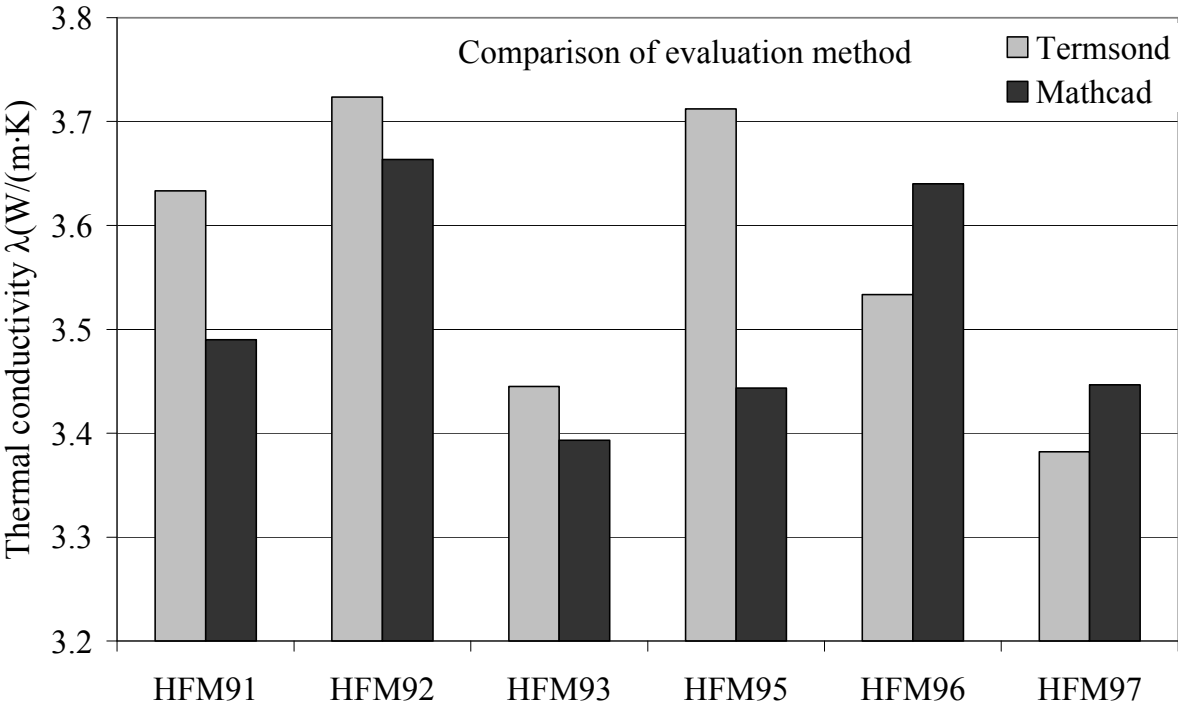


Figure 11. Average thermal conductivity for the six locations of thermal measurements evaluated using a model developed for Mathcad and with software developed by the Swedish Geotechnical Institute (SGI). Site A includes HFM91-93, while site B includes HFM95-97.

The considerable deviation for HFM95 could be caused by misinterpretation by Termsond of data related to heat output. For Termsond, the data used for fitting was selected manually and the thermal drift compensation was uncertain. The various data included in the curve fitting process using Termsond could have caused the deviation in results for the remaining locations. For four of the six locations, the deviation between the two methods was less than three percent.

Anisotropic thermal properties

By comparing thermal conductivity results for the direction parallel to the foliation to those for the perpendicular direction, the degree of anisotropy can be expressed. In figure 12, the results for compensated data are compared by dividing $\lambda_{\text{parallel}}$ with $\lambda_{\text{perpendicular}}$. For four of the locations, more than eight percent higher conductivity was found for $\lambda_{\text{parallel}}$ than for $\lambda_{\text{perpendicular}}$. The differences between the locations are significant, for HMF 96 the parallel conductivity was 40 % higher than the perpendicular conductivity while for HMF95 isotropic properties were found. The calculated ratio between $\lambda_{\text{parallel}}/ \lambda_{\text{perpendicular}}$ is similar regardless of data selection and possible correction for thermal drift as presented in table 1 and in appendix A.

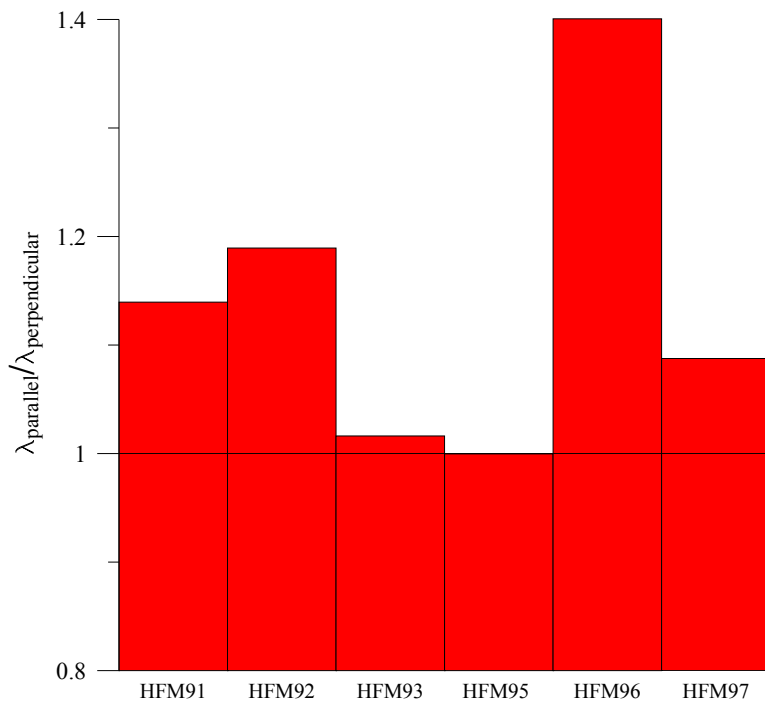


Figure 12. $\lambda_{\text{parallel}}/ \lambda_{\text{perpendicular}}$ for results of thermal conductivity from fitting procedure with compensated temperature data where the initial 2500 s of the experiment period has been excluded.

Table 2 presents the arithmetic mean of thermal properties for different sets of data. Calculations have been made of the geometric and harmonic means with similar results. All data sets for fitting and all selections of average calculations result in a 13 % higher $\lambda_{\text{parallel}}$ than $\lambda_{\text{perpendicular}}$.

Table 2. Arithmetic mean of thermal properties and $\lambda_{\text{parallel}}$ divided by $\lambda_{\text{perpendicular}}$.

Arithmetic average	Thermal conductivity (W/(m·K))			Heat capacity (J/(m ³ ,K))
	$\lambda_{\text{parallel}}$	$\lambda_{\text{perpendicular}}$	$\lambda_{\text{parallel}}/ \lambda_{\text{perpendicular}}$	
Uncorrected	3.64	3.21	1.13	$2.05 \cdot 10^6$
Corrected	3.62	3.21	1.13	$2.00 \cdot 10^6$
Corrected, t>2500 s	3.65	3.24	1.13	$2.00 \cdot 10^6$

Conclusions

A higher thermal conductivity was found for directions parallel to the foliation than for directions perpendicular in five locations out of six. The results from the sixth location, HMF95, indicated isotropic thermal properties. The variation in degree of anisotropy for thermal conductivity was large between the different locations, with the parallel conductivity varying from 0 % through 40 % higher than the perpendicular. An arithmetic average of thermal properties calculated through fitting to the most relevant set of data (corrected to thermal drift, $t > 2500$ s) indicate a 13 % higher thermal conductivity parallel to the foliation compared to perpendicular. The assessed thermal conductivity for the measured locations varied from 3.41 W/(m*K) to 4.02 W/(m*K) for the direction parallel to the foliation, and between 2.88 W/(m*K) and 3.45 W/(m*K) for the perpendicular direction (fitting for data set with $t > 2500$ s).

For each location, calculations were made by fitting to three different sets of temperature data: uncompensated, data compensated for thermal drift, and compensated data where the initial experimental period ($t < 2500$ s) had been excluded. When comparing the correlation coefficient between the fitted curve and the measured temperature data, temperature correction had a noticeable impact. A curve more closely mimicking the measured temperature data was also achieved when data from the initial experimental period was excluded. These two steps of data processing are hence recommended before commencing the fitting procedure.

References

Claesson J. 2005. Personal communication.

Sundberg J. 1988. Thermal properties of soils and rocks. Chalmers University of Technology, dissertation. ISSN 0348-2367. Sweden.

Appendix A

Table A.1. Thermal properties determined by fitting with data from the entire time series that has not been compensated for thermal drift during the experiment.

Location	Thermal conductivity		Correlation coefficient		Heat capacity, c (J/(m ³ ,K))
	$\lambda_{\text{parallel}}$ (W/(m·K))	$\lambda_{\text{perpendicular}}$ (W/(m·K))	$T_{\text{parallel}} (r^2)$	$T_{\text{perpendicular}} (r^2)$	
HFM91	3.66	3.21	0.9996335	0.999545	$2.09 \cdot 10^6$
HFM92	3.95	3.32	0.999898485	0.999573	$2.06 \cdot 10^6$
HFM93	3.40	3.34	0.999869	0.999944	$2.01 \cdot 10^6$
HFM95	3.40	3.40	0.999036	0.999802	$2.06 \cdot 10^6$
HFM96	3.94	2.81	0.999634	0.999796	$2.08 \cdot 10^6$
HFM97	3.48	3.20	0.99998	0.999978	$2.03 \cdot 10^6$

Table A.2. Thermal properties determined through fitting with data from the entire time series that has been compensated for thermal drift during the experiment.

Location	Thermal conductivity		Correlation coefficient		Heat capacity, c (J/(m ³ ,K))
	$\lambda_{\text{parallel}}$ (W/(m·K))	$\lambda_{\text{perpendicular}}$ (W/(m·K))	$T_{\text{parallel}} (r^2)$	$T_{\text{perpendicular}} (r^2)$	
HFM91	3.59	3.15	0.999852	0.999608	$1.99 \cdot 10^6$
HFM92	3.84	3.26	0.99991328	0.999706	$1.97 \cdot 10^6$
HFM93	3.39	3.33	0.99996	0.999959	$2.01 \cdot 10^6$
HFM95	3.41	3.42	0.99993	0.99991	$1.93 \cdot 10^6$
HFM96	3.97	2.84	0.99985	0.999869	$2.00 \cdot 10^6$
HFM97	3.54	3.25	0.99998	0.999975	$2.06 \cdot 10^6$

Table A.3. Position/orientation of boreholes

ID- code/djup	X	Y	Z	Rikt gra- der	Lutning gra- der
HFM94	6 700 065.811	1 630 999.650	-1.262	33.8147	-88.7213
0.1	6 700 065.813	1 630 999.651	-1.362		
0.2	6 700 065.815	1 630 999.652	-1.462		
0.3	6 700 065.817	1 630 999.654	-1.562		
0.4	6 700 065.819	1 630 999.655	-1.662		
0.5	6 700 065.821	1 630 999.656	-1.762		
0.6	6 700 065.822	1 630 999.657	-1.862		
HFM95A	6 700 064.354	1 631 002.893	-1.428	346.89915	-89.72352
0.1	6 700 064.354	1 631 002.893	-1.528		
0.2	6 700 064.355	1 631 002.892	-1.628		
0.3	6 700 064.355	1 631 002.892	-1.728		
0.4	6 700 064.356	1 631 002.892	-1.828		
0.5	6 700 064.356	1 631 002.892	-1.928		
0.6	6 700 064.357	1 631 002.892	-2.028		
0.7	6 700 064.357	1 631 002.892	-2.128		
0.8	6 700 064.358	1 631 002.892	-2.228		
0.9	6 700 064.358	1 631 002.892	-2.328		
1.0	6 700 064.359	1 631 002.892	-2.428		
1.1	6 700 064.359	1 631 002.891	-2.528		
1.175	6 700 064.359	1 631 002.891	-2.603		
HFM95B	6 700 064.418	1 631 003.063	-1.327	6.5455	89.4086
0.1	6 700 064.419	1 631 003.063	-1.427		
0.2	6 700 064.420	1 631 003.063	-1.527		
0.3	6 700 064.421	1 631 003.063	-1.627		
0.4	6 700 064.422	1 631 003.063	-1.727		
0.5	6 700 064.423	1 631 003.063	-1.827		
0.6	6 700 064.424	1 631 003.063	-1.927		
0.63	6 700 064.424	1 631 003.063	-1.957		
HFM95C	6 700 064.186	1 631 002.959	-1.326	181.5700	-89.5550
0.1	6 700 064.185	1 631 002.959	-1.426		
0.2	6 700 064.185	1 631 002.959	-1.526		
0.3	6 700 064.184	1 631 002.959	-1.626		
0.4	6 700 064.183	1 631 002.959	-1.726		
0.5	6 700 064.182	1 631 002.959	-1.826		
0.6	6 700 064.182	1 631 002.959	-1.926		
0.625	6 700 064.181	1 631 002.959	-1.951		
HFM96A	6 700 063.580	1 631 004.792	-1.341	274.4964	-89.5523
0.1	6 700 063.580	1 631 004.791	-1.441		
0.2	6 700 063.580	1 631 004.790	-1.541		
0.3	6 700 063.580	1 631 004.789	-1.641		
0.4	6 700 063.580	1 631 004.788	-1.741		
0.5	6 700 063.580	1 631 004.788	-1.841		
0.6	6 700 063.581	1 631 004.787	-1.941		
0.7	6 700 063.581	1 631 004.786	-2.041		
0.8	6 700 063.581	1 631 004.785	-2.141		
0.9	6 700 063.581	1 631 004.785	-2.241		

1.0	6 700 063.581	1 631 004.784	-2.341		
1.1	6 700 063.581	1 631 004.783	-2.441		
1.17	6 700 063.581	1 631 004.782	-2.511		
HFM96B	6 700 063.591	1 631 004.976	-1.312	92.4826	-89.7455
0.1	6 700 063.591	1 631 004.977	-1.412		
0.2	6 700 063.591	1 631 004.977	-1.512		
0.3	6 700 063.591	1 631 004.978	-1.612		
0.4	6 700 063.591	1 631 004.978	-1.712		
0.5	6 700 063.591	1 631 004.979	-1.812		
0.6	6 700 063.591	1 631 004.979	-1.912		
0.605	6 700 063.591	1 631 004.979	-1.917		
HFM96C	6 700 063.403	1 631 004.802	-1.373	68.3550	-89.0614
0.1	6 700 063.404	1 631 004.803	-1.473		
0.2	6 700 063.405	1 631 004.805	-1.573		
0.3	6 700 063.405	1 631 004.806	-1.673		
0.4	6 700 063.406	1 631 004.808	-1.773		
0.5	6 700 063.406	1 631 004.809	-1.873		
0.6	6 700 063.407	1 631 004.811	-1.973		
0.615	6 700 063.407	1 631 004.811	-1.988		
HFM97A	6 700 071.590	1 631 007.356	0.096	115.2174	-89.0903
0.1	6 700 071.590	1 631 007.357	-0.004		
0.2	6 700 071.589	1 631 007.359	-0.104		
0.3	6 700 071.588	1 631 007.360	-0.204		
0.4	6 700 071.588	1 631 007.362	-0.304		
0.5	6 700 071.587	1 631 007.363	-0.404		
0.6	6 700 071.586	1 631 007.365	-0.504		
0.7	6 700 071.586	1 631 007.366	-0.604		
0.8	6 700 071.585	1 631 007.367	-0.704		
0.9	6 700 071.584	1 631 007.369	-0.804		
1.0	6 700 071.584	1 631 007.370	-0.904		
1.1	6 700 071.583	1 631 007.372	-1.004		
1.18	6 700 071.582	1 631 007.373	-1.084		
HFM97B	6 700 071.555	1 631 007.182	0.084	64.2672	-89.3657
0.1	6 700 071.555	1 631 007.183	-0.016		
0.2	6 700 071.555	1 631 007.184	-0.116		
0.3	6 700 071.556	1 631 007.185	-0.216		
0.4	6 700 071.556	1 631 007.186	-0.316		
0.5	6 700 071.557	1 631 007.187	-0.416		
0.6	6 700 071.557	1 631 007.188	-0.516		
0.635	6 700 071.558	1 631 007.188	-0.551		
HFM97C	6 700 071.769	1 631 007.321	0.094	175.3852	88.9692
0.1	6 700 071.767	1 631 007.321	-0.006		
0.2	6 700 071.765	1 631 007.321	-0.106		
0.3	6 700 071.764	1 631 007.321	-0.206		
0.4	6 700 071.762	1 631 007.321	-0.306		
0.5	6 700 071.760	1 631 007.321	-0.406		
0.6	6 700 071.758	1 631 007.322	-0.506		
0.615	6 700 071.758	1 631 007.322	-0.521		

Forsmark site investigation

Borehole KFM90B

An anisotropic analysis of thermal properties of rocks using a calorimetric method and TPS method

Bijan Adl-Zarrabi

SP Swedish National Testing and Research Institute

September 2006

Keywords: Thermal properties, thermal conductivity, thermal diffusivity, heat capacity, Transient Plane Source method, Anisotropic analysis, AP PF 400-06-023

Abstract

Thermal properties on six specimens of drill hole KFM90B, Forsmark, Sweden, were measured at ambient temperature (20°C). The samples were taken from the rock type (101057), at the depths between 8 and 18 m. The determination of the thermal properties is based on a direct measurement method, the so called “Transient Plane Source Method” (TPS). Thermal properties are determined under assumption that the specimens are anisotropic. For anisotropic analysis with the TPS method specific heat is needed. The specific heat capacity was measured by calorimetry.

The measured specific heat capacity was ranged between 0.80 and 0.83 J/(g, K). Thermal conductivity in the foliation direction and perpendicular to the foliation direction were in the range of 3.64-4.25 and 2.78-3.51 W/(m, K) respectively. Thermal diffusivity in direction of the foliation and perpendicular to the foliation direction were 1.69-1.97 and 1.26-1.59 mm²/s respectively.

Sammanfattning

Termiska egenskaper hos sex provkroppar från borrhål KFM90B, Forsmark, bestämdes vid rumstemperatur (20°C). Proverna hade tagits från bergarten (101057), i djupet 8-18 meter. TPS metoden, ”Transient Plane Source”, användes för bestämning av de termiska egenskaperna. De termiska egenskaperna är bestämda under antagandet att provkropparna är anisotropa. För anisotropisk analys med TPS metoden behövs specifika värmekapaciteten. Specifika värmekapaciteten mättes med kalorimetri.

Specifika värmen uppgick till 0.69-0.71 J/(g, K). Den termiska konduktiviteten i foliationsriktningen och vinkelrätt mot foliationsriktningen uppgick till 3.64-4.25 respektive 2.78-3.51 W/(m, K). Den termiska diffusiviteten i foliationsriktningen och vinkelrätt mot foliationsriktningen uppgick till 1.69-1.97 respektive 1.26-1.59 mm²/s.

Table of Contents

1	Introduction	6
2	Objective and scope.....	8
3	Equipment.....	9
3.1	Calorimetric method.....	9
3.2	Transient Plane Source	10
4	Execution.....	11
4.1	Description of the samples	11
4.2	Test procedure	12
4.3	Nonconformities	14
5	Results	15
5.1	Specific heat capacity	15
5.2	Thermal conductivity and thermal diffusivity	16
6	References	24
	Appendix A	25
	Appendix B	26
	Appendix C	27

1 Introduction

SKB is planning to build a final repository for nuclear waste in bedrock. A final repository for nuclear waste demands knowledge about thermal properties of the rock. Forsmark, Sweden, is one of the areas selected for site investigations. The activity presented in this report is part of the site investigation program at Forsmark /1/.

This report presents an anisotropic analysis of the thermal properties of rock samples from borehole KFM90B at Forsmark. The analysis is performed by Transient Plane Source Method (TPS), Gustafsson, 1991 /2/. The method determines thermal conductivity and diffusivity of a material. The anisotropic analysis by TPS needs volumetric heat capacity. Thus, the specific heat capacity (J/g,K) determined by a calorimeter /3/ and the dry and wet densities, as well as porosity of the samples, were determined within the scope of parallel activities /4/.

Rock samples were selected at Forsmark based on the preliminary core logging with the strategy to investigate the thermal properties of the dominant rock type. The specimens to be tested were cut from the rock samples in the shape of circular discs. The rock samples arrived at SP in June 2006. The thermal properties were determined on water-saturated specimens. Testing was performed during August 2006.

The controlling documents for the activity are listed in Table 1-1. Activity Plan and Method Descriptions are SKB's (The Swedish Nuclear Fuel and waste Management Company) internal controlling documents as well as SP's (Swedish National Testing and Research Institute) Quality Plan (SP-QD 13.1).

Table 1-1. Controlling documents for performance of the activity.

Activity Plan	Number	Version
KFM90B. Bergmekaniska och termiska laboratoriebestämningar	AP PF 400-06-023	1.0
Method Description	Number	Version
Determining thermal conductivity and thermal capacity by the TPS method	SKB MD 191.001	2.0
Quality Plan		
SP-QD 13.1		



Figure 1-1. Location of the eight telescopic boreholes first drilled and of KFM90B at the Forsmark candidate area (marked red).

2 Objective and scope

The purpose of this activity is to determine the anisotropic behaviour concerning thermal properties of rock specimens. The obtained thermal properties will be used as input data for mechanical and thermal analysis in a site descriptive model that will be established for the candidate area selected for site investigation at Forsmark.

3 Equipment

3.1 Calorimetric method

The measurement equipment used for the calorimetric determination of the specific heat capacity is shown in Figure 3-1 and consisted of:

- Calorimeter, made of Macrolon with low heat capacity and very low heat conductivity.
- Magnetic stirrer, IKA type BigSquid.
- Temperature logger, Keithley 2000 multimeter with scanner Keithley 7700 (temperature resolution 0.01 mK, accuracy 5 mK).
- Temperature controlled bath, Heto Thermostat 13 DT-1 (resolution 0.1 °C)
- Three temperature sensors, Pt-100 Pentronic (2 for calorimeter, 1 for temperature controlled bath).
- Thermometer for Air, Pentronic CRL 206, s/n 270210 (resolution 0.01 °C)
- Balance Mettler PM 2000 (resolution 0.01 g, accuracy 0.02 g)
- Air conditioning equipment, μ AC Carel, Essén Company.
- Laptop computer Toshiba programmed on Visual Basic 6 for the temperature monitoring of three channels per three seconds.
- Pure and de-aerated water, crushed ice for fast preparation of a “steady state” condition.
- Various accessories (stand, holder, clamps, hoses, dewar, syringe, timer, etc.)

All measurement instruments are traceable via in-house calibration to national and international standards. The three temperature sensors connected to respective logger channel were calibrated immediately before the measurements. The balance was several times checked using relevant weight pieces.

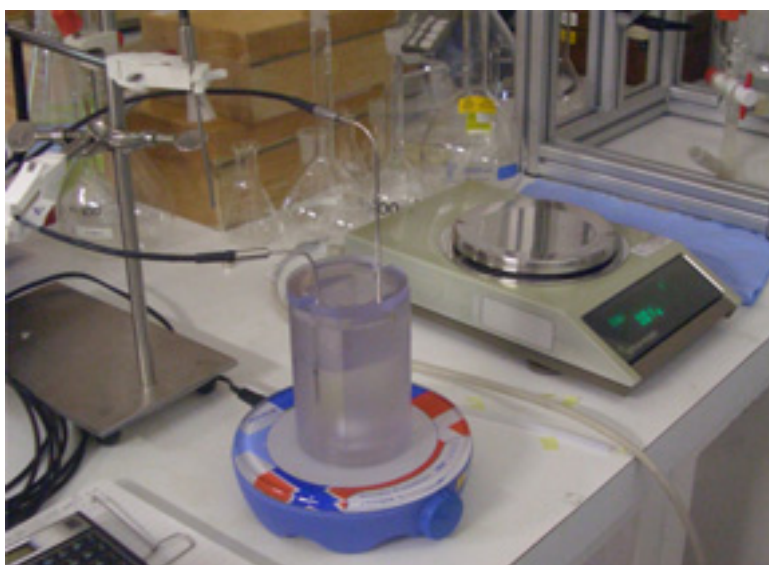


Figure 3-1. Temperature controlled bath for preparing the samples.

3.2 Transient Plane Source

Technical devices for determination of the thermal properties in question were:

- Kapton sensor 5501, with a radius of 6.403 mm, and a power output of 0.7 W. The sensor 5501 fulfils the recommended relation between sensor radius and sample geometry of the samples in /5/.
- TPS-apparatus, Source meter Keithley 2400, Multi-meter Keithley 2000 and bridge, see Figure 3-2.
- PC + Microsoft Office and Hot Disk version 5.4.
- Stainless Sample holder.

Function control of TPS instrumentation was performed according to BRk-QB-M26-02 (SP quality document), see Appendix A.

The experimental set-up is shown in Figure 3-3.



Figure 3-2. TPS-apparatus with source meter, multi-meter, bridge, and computer.



Figure 3-3. Specimens prior to mounting (left), mounted in stainless sample holder (middle), and sample holder with mounted specimens wrapped in plastic (right).

4 Execution

Specific heat capacity was determined according to /3/ at SP Measurement Technology. The procedure of temperature measurement in conjunction with the determination of specific heat was modified in this project. The modification is explained in 4.3.

Determination of thermal properties conductivity and diffusivity was made in compliance with SKB's method description SKB MD 191.001 (SKB internal controlling document) and Hot Disc Instruction Manual /5/ at SP Fire Technology.

The density determinations, which were performed in a parallel activity at SP /4/, were carried out in accordance with SKB MD 160.002 (SKB internal controlling document) and ISRM /6/ at SP Building Technology and Mechanics.

4.1 Description of the samples

Six cylindrical cores (50 mm in diameter and about 74 mm in height) were sampled from borehole KFM90B, Forsmark, Sweden. The cores were collected within the interval 8 m–18 m. Each sample was cut in the axial direction of the cylinder into two half cylinders. The samples were chosen so that the axial direction of the samples lies in the foliation plane of the rocks. Twelve specimens with a thickness of 25 mm each (see Figure 4-1) were prepared at SP.

The identification marks, rock type and sampling levels of the specimens are presented in Table 4-1. Detailed geological description of the entire core of KFM90B is given in SKB's database SICADA (Boremap data).

Table 4-1 Rock type and identification marks (Rock-type classification according to bore map)

Identification	Rock type	Sampling depth (Adj sec low)
KFM90B-294-90V	(101057)	8.26
KFM90B-295-90V	(101057)	9.00
KFM90B-296-90V	(101057)	10.22
KFM90B-297-90V	(101057)	14.75
KFM90B-298-90V	(101057)	17.51
KFM90B-299-90V	(101057)	18.06

4.2 Test procedure

The present activity was performed parallel to other activities, conducted by the department of Building Technology and Mechanics at SP, by which the wet and dry density as well as the porosity of the specimens were determined /4/ and by the department of Measurement Technology at SP, by which specific heat capacity was determined /3/.

The following logistic sequence was applied for the activities:

1. Specimens were cut and polished by SP Building Technology and Mechanics.
2. Specimens were photographed by SP Building Technology and Mechanics.
3. Specimens were water saturated and wet density was determined by SP Building Technology and Mechanics /4/.
4. Specimens were sent from SP Building Technology and Mechanics to SP Measurement Technology.
5. Specific heat was determined by SP Measurement Technology /3/.
6. Specimens were sent from SP Measurement Technology to SP Fire Technology.
7. Thermal properties were determined by SP Fire Technology.
8. Specimens were sent from SP Fire Technology to SP Building Technology and Mechanics.
9. Dry density of the specimens was determined at SP Building Technology and Mechanics.

The rock samples were water saturated and stored under this condition for 7 days. This yielded complete water saturation, whereupon the density and the thermal properties were determined. The specimens were photographed before testing.

Determinations of the thermal properties as well as density and porosity measurements were performed during August 2006.

The dry weight was measured after the specimens had been dried to constant mass according to ISMR /6/ at 105°C. The drying procedure took seven days.

Peter Lau at SP Measurement Technology conducted the specific heat capacity measurements, Patrik Nilsson and Ingrid Wetterlund at SP Fire Technology conducted the thermal property measurements and preparation of the report.

4.2.1 Principle of the calorimetric method

The calorimetric technique involves heating the samples after mass determination to a well defined temperature. The samples are therefore placed in a temperature controlled water bath long enough to stabilize.

The calorimeter is filled with prepared water (pure and de-aerated of 17 °C) to a predefined level and stirred to produce nearly steady state conditions. Thereafter it is placed on the balance and excessive water is extracted with a syringe to reach a nominal mass, chosen with respect to the sample volume.

The so prepared calorimeter is stirred and the temperature logging program is started. After 90 to 150 seconds the sample is quickly transferred (3 to 5 seconds) from the bath into the calorimeter. The temperature rise of water can be followed graphically during the equalization process, which typically takes 150 seconds and the experiment is terminated after another 300 to 600 seconds.

The calorimeter, water and sample are weighed again to determine the amount of water that unavoidably did follow with the sample into the calorimeter. This amount is typically 0.33 % of the water contained in the calorimeter. If accidentally a water splash happens during the sample insertion those droplets are absorbed with a small piece of prepared tissue that is weighed dry and wet. The corresponding mass is subtracted from the initial water mass. In extreme cases it has amounted to 0.03 % of the total water mass.

All mass values for the determination of the specific heat were manually documented in a prepared form that was a printout of the corresponding Excel calculation sheet.

With the termination of the logging program each experiment was saved as raw data in an Excel file on the SP network. The main information was the bath temperature and two calorimeter temperatures as function of time.

4.2.2 Principle of Transient Plane Source

The principle of the TPS-method is to install a sensor consisting of a thin metal double spiral, embedded in an insulation material, between two rock samples. During the measurement the sensor works both as a heat emitter and a heat receptor. The input data and results of the direct measurement are registered and analysed by the same software and electronics that govern the measurement. The method gives information on the thermal conductivity and diffusivity of a material.

The thermal properties of the water-saturated specimens were measured in ambient air (20°C). In order to remain water saturation and obtain desired temperature, the specimens and the sensor were kept in a plastic bag during the measurements, see Figure 3-2.

Each pair of specimens (A and B) was measured five times. The time lag between two repeated measurements was at least 20 minutes. The result of each measurement was evaluated separately. The average value of these five measurements was calculated.

In an anisotropic measurement by TPS, thermal conductivity and thermal diffusivity of an orthotropic sample can be obtained if the volumetric specific heat is known. In this project the TPS sensor lies on the foliation plane and thermal conductivity in this plane and perpendicular to foliation plane is determined, see figure 4-1.

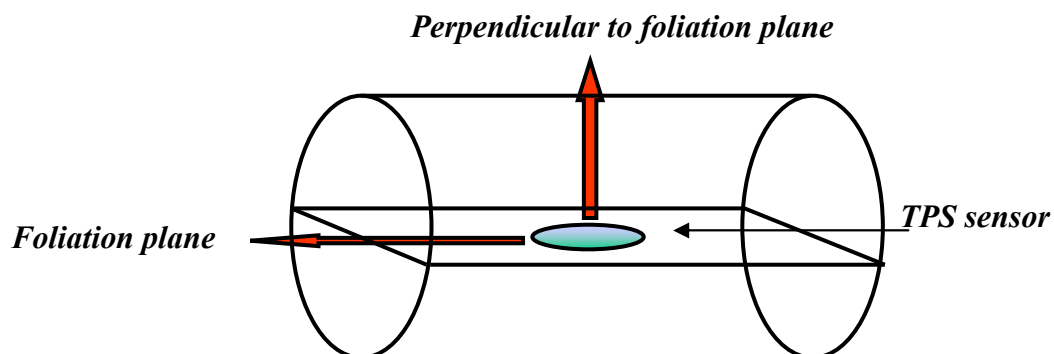


Figure 4-1. TPS sensor lies on the foliation plane of the rock sample.

Measured raw data were saved as text files and analysed data as Excel files. These files were stored on the hard disc of the measurement computer and sent to the SKB catalogue at the SP network. Further calculations of mean values and standard deviations were performed in the same catalogue.

4.3 Nonconformities

Thermal conductivity and thermal diffusivity were measured and there were no deviations to the plan.

However, the measurement of specific heat according to the suggested procedure in /3/ was modified as follows:

- The sample temperature was measured inside a drilled hole in a dummy specimen that was positioned between the prepared specimens in the preparing bath.

- Despite a relative low temperature rise ($\approx 2\text{ }^{\circ}\text{C}$) and low thermal conductivity and heat capacity of Macrolon the calorimeter is not passive in the heat exchange process. Furthermore the stirrer, which is very important for supporting the temperature equalization, generates both thermal and mechanical energy that overlays the measured heat transfer process in the calorimeter. Therefore the time and the temperature dependent influence were studied in separate experiments simulating all conditions except the existence of the sample. From these a suitable correction technique was worked out and applied to each measurement record in order to compensate for the overlaid effects.

5 Results

The results of activity are stored in SKB's database SICADA, where they are traceable by the Activity Plan number.

Measurement data concerning specific heat of samples is presented in 5.1. Mean values of measured thermal conductivity and thermal diffusivity, five repeated measurements, are reported in 5.2. Conductivity and diffusivity measurements in the foliation plane are referred to as FP, while conductivity and diffusivity measurements perpendicular to the foliation plane are referred to as PFP.

The measured thermal properties are also reported in the SICADA database at SKB. Values of each separate measurement as described in section 5.1 are reported in Appendix B. Furthermore, the total measuring time, the ratio between total measuring time and characteristic time, and the number of analysed points is presented in Appendix C. In a correct measurement the ratio between the total measuring time and the characteristic time should be between 0.4 and 1.

5.1 Specific heat capacity

The result of the measured heat capacity [J/g,K] using the calorimetric method is presented in table 5-1. These results are converted to volumetric heat capacity [MJ/m³,K] by using the measured wet density of the samples. Each sample consists of a part A and B. Only part A, always being the heavier one, was measured.

Table 5-1 Rock type, sample identification and belonging specific heat

Sample	Rock type	Heat capacity [J/(g, K)]	Heat capacity [MJ/(m ³ , K)]
KFM90B-294-90V – 1 A	101057	0.804	2.14
KFM90B-295-90V – 2 A	101057	0.828	2.20
KFM90B-296-90V – 3 A	101057	0.818	2.17
KFM90B-297-90V – 4 A	101057	0.826	2.19
KFM90B-298-90V – 5 A	101057	0.810	2.15
KFM90B-299-90V – 6 A	101057	0.805	2.13

5.2 Thermal conductivity and thermal diffusivity

5.2.1 Specimens KFM90B-294-90VA and B

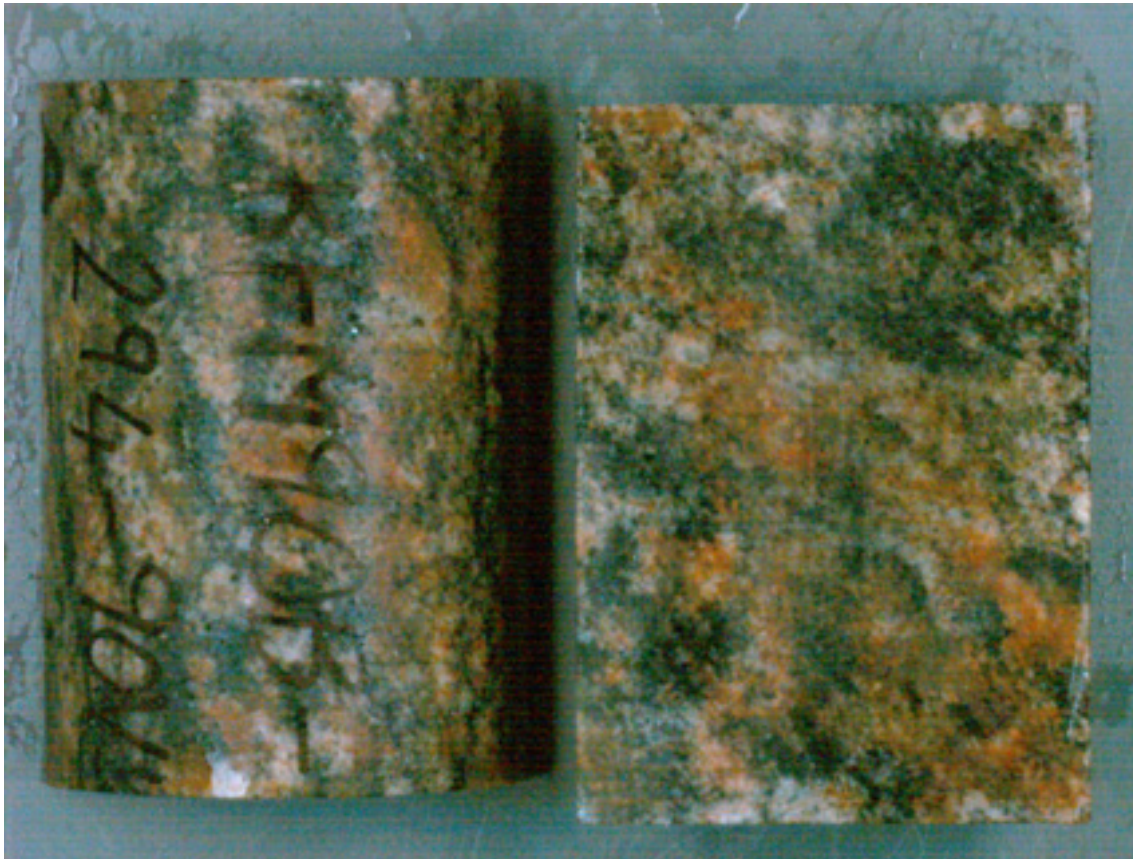


Figure 5-1. Specimens KFM90B-294-90VA and B.

Table 5-1. Porosity, wet and dry density of specimens KFM90B-294-90VA and B, average values.

Sample	Density, wet [kg/m ³]	Density, dry [kg/m ³]	Porosity [%]
KFM90B-294-90V Sec low: 8.26	2660	2650	0.5

Table 5-2. Thermal properties of specimens KFM90B-294-90VA and B in the foliation plane (FP) and perpendicular to the foliation plane (PFP), average values.

KFM90B-294-90V Sec low: 8.26	Conductivity PFP [W/(m, K)]	Diffusivity PFP [mm ² /s]	Conductivity FP [W/(m, K)]	Diffusivity FP [mm ² /s]	Heat capacity [MJ/(m ³ , K)]
Mean value	2.97	1.39	4.04	1.89	2.14
Standard deviation	0.087	0.041	0.077	0.036	-

5.2.2 Specimens KFM90B-295-90VA and B



Figure 5-2. Specimens KFM90B-295-90VA and B.

Table 5-3. Porosity, wet and dry density of specimens KFM90B-295-90VA and B, average values.

Sample	Density, wet [kg/m ³]	Density, dry [kg/m ³]	Porosity [%]
KFM90B-295-90V Sec low: 9.00	2650	2650	0.5

Table 5-4. Thermal properties of specimens KFM90B-295-90VA and B in the foliation plane (FP) and perpendicular to the foliation plane (PFP), average values.

KFM90B-295-90V Sec low: 9.00	Conductivity PFP [W/(m, K)]	Diffusivity PFP [mm ² /s]	Conductivity FP [W/(m, K)]	Diffusivity FP [mm ² /s]	Heat capacity [MJ/(m ³ , K)]
Mean value	3.51	1.59	3.72	1.69	2.20
Standard deviation	0.034	0.016	0.020	0.009	-

5.2.3 Specimens KFM90B-296-90VA and B



Figure 5-3. Specimens KFM90B-296-90VA and B.

Table 5-5. Porosity, wet and dry density of specimens KFM90B-296-90VA and B, average values.

Sample	Density, wet [kg/m ³]	Density, dry [kg/m ³]	Porosity [%]
KFM90B-296-90V Sec low: 10.22	2660	2650	0.5

Table 5-6. Thermal properties of specimens KFM90B-296-90VA and B in the foliation plane (FP) and perpendicular to the foliation plane (PFP), average values.

KFM90B-296-90V Sec low: 10.22	Conductivity PFP [W/(m, K)]	Diffusivity PFP [mm ² /s]	Conductivity FP [W/(m, K)]	Diffusivity FP [mm ² /s]	Heat capacity [MJ/(m ³ , K)]
Mean value	3.10	1.43	4.01	1.84	2.17
Standard deviation	0.020	0.009	0.009	0.004	-

5.2.4 Specimens KFM90B-297-90VA and B.

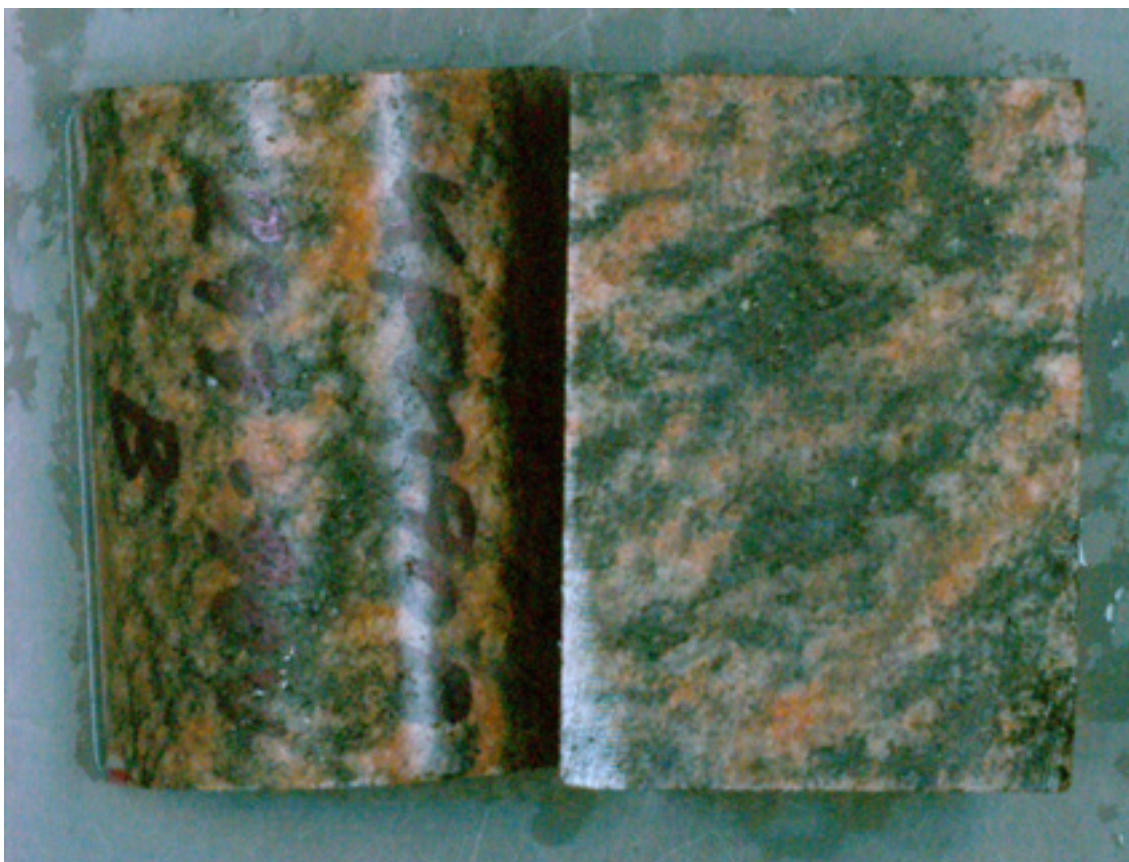


Figure 5-4. Specimens KFM90B-297-90VA and B.

Table 5-7. Porosity, wet and dry density of specimens KFM90B-297-90VA and B, average values.

Sample	Density, wet [kg/m ³]	Density, dry [kg/m ³]	Porosity [%]
KFM90B-297-90V Sec low: 14.75	2660	2650	0.4

Table 5-8. Thermal properties of specimens KFM90B-297-90VA and B in the foliation plane (FP) and perpendicular to the foliation plane (PFP), average values.

KFM90B-297-90V Sec low: 14.75	Conductivity PFP [W/(m, K)]	Diffusivity PFP [mm ² /s]	Conductivity FP [W/(m, K)]	Diffusivity FP [mm ² /s]	Heat capacity [MJ/(m ³ , K)]
Mean value	2.78	1.26	4.13	1.88	2.19
Standard deviation	0.028	0.013	0.028	0.013	-

5.2.5 Specimens KFM90B-298-90VA and B



Figure 5-5. Specimens KFM90B-298-90VA and B.

Table 5-9. Porosity, wet and dry density of specimens KFM90B-298-90VA and B, average values.

Sample	Density, wet [kg/m ³]	Density, dry [kg/m ³]	Porosity [%]
KFM90B-298-90V Sec low: 17.51	2650	2650	0.5

Table 5-10. Thermal properties of specimens KFM90B-298-90VA and B in the foliation plane (FP) and perpendicular to the foliation plane (PFP), average values.

KFM90B-298-90V Sec low: 17.51	Conductivity PFP [W/(m, K)]	Diffusivity PFP [mm ² /s]	Conductivity FP [W/(m, K)]	Diffusivity FP [mm ² /s]	Heat capacity [MJ/(m ³ , K)]
Mean value	2.85	1.32	4.25	1.97	2.15
Standard deviation	0.085	0.039	0.068	0.032	-

5.2.6 Specimens KFM90B-299-90VA and B



Figure 5-6. Specimens KFM90B-299-90VA and B.

Table 5-11. Porosity, wet and dry density of specimens KFM90B-299-90VA and B, average values.

Sample	Density, wet [kg/m ³]	Density, dry [kg/m ³]	Porosity [%]
KFM90B-299-90V Sec low: 18.06	2650	2650	0.5

Table 5-12. Thermal properties of specimens KFM90B-299-90VA and B in the foliation plane (FP) and perpendicular to the foliation plane (PFP), average values.

KFM90B-299-90V Sec low: 18.06	Conductivity PFP [W/(m, K)]	Diffusivity PFP [mm ² /s]	Conductivity FP [W/(m, K)]	Diffusivity FP [mm ² /s]	Heat capacity [MJ/(m ³ , K)]
Mean value	2.47	1.16	4.26	1.99	2.13
Standard deviation	0.031	0.015	0.035	0.016	-

5.2.7 TPS results for the entire test series

Table 5-13 displays the mean value of five repeated measurements of the thermal properties measured with the TPS method. Standard deviation is shown in Table 5-14.

The measured heat capacity was in the range 0.804-0.828 J/(g, K). Thermal conductivity in the foliation plane (FP) and perpendicular to the foliation plane (PFP) were in the range of 3.64-4.25 and 2.78-3.51 W/(m, K) respectively. Thermal diffusivity in the foliation plane and perpendicular to the foliation plane were 1.69-1.97 and 1.26-1.59 mm²/s respectively.

A graphical representation of thermal conductivity, parallel to and perpendicular to foliation, and heat capacity versus borehole length is given in Figure 5-10.

Table 5-13. Mean value of thermal properties of samples at 20 °C.

Sample identification	Conductivity PFP [W/(m, K)]	Diffusivity PFP [mm ² /s]	Conductivity FP [W/(m, K)]	Diffusivity FP [mm ² /s]
Rock type 101057				
KFM90B-294-90V	2.97	1.39	4.04	1.89
KFM90B-295-90V	3.51	1.59	3.72	1.69
KFM90B-296-90V	3.10	1.43	4.01	1.84
KFM90B-297-90V	2.78	1.26	4.13	1.88
KFM90B-298-90V	2.85	1.32	4.25	1.97
KFM90B-299-90V	2.47	1.16	4.26	1.99

Table 5-14. Standard deviation of measured values at 20 °C.

Sample identification	Conductivity PFP [W/(m, K)]	Diffusivity PFP [mm ² /s]	Conductivity FP [W/(m, K)]	Diffusivity FP [mm ² /s]
Rock type 101057				
KFM90B-294-90V	0.087	0.041	0.077	0.036
KFM90B-295-90V	0.034	0.016	0.020	0.009
KFM90B-296-90V	0.020	0.009	0.009	0.004
KFM90B-297-90V	0.028	0.013	0.028	0.013
KFM90B-298-90V	0.085	0.039	0.068	0.032
KFM90B-299-90V	0.031	0.015	0.035	0.016

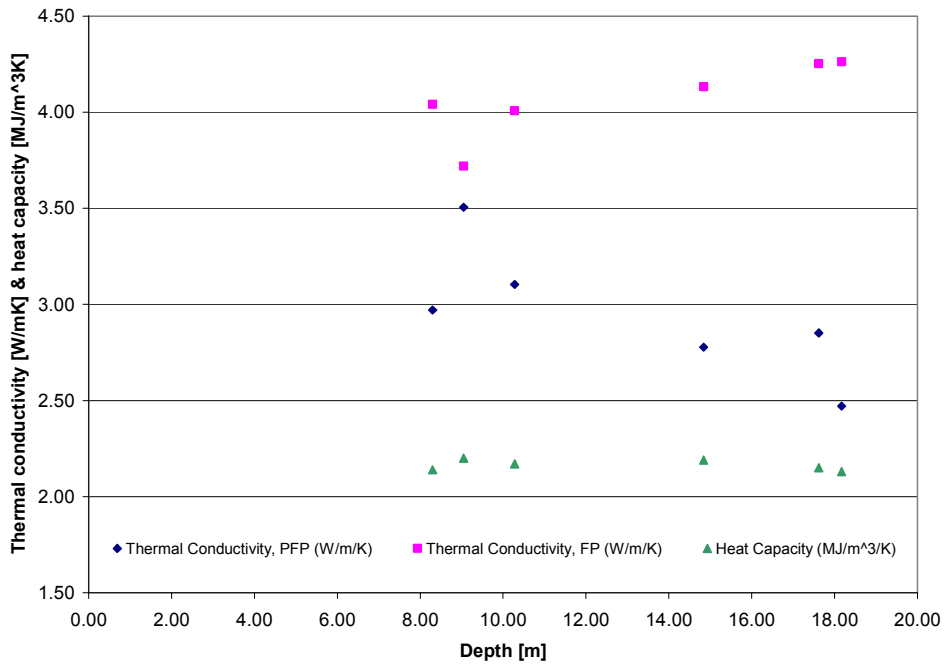


Figure 5-7. Thermal conductivity in foliation direction (FP) and perpendicular to foliation (PFP) measured with TPS method at 20 °C. Specific heat capacity measured with calorimeter. Results are displayed versus borehole depth.

6 References

- /1/ **SKB, 2001.** Site investigations. Investigation methods and general execution programme. SKB TR-01-29, Svensk Kärnbränslehantering AB.
- /2/ **Gustafsson, S E, 1991:** "Transient plane source techniques for thermal conductivity and thermal diffusivity measurements of solid materials". Rev. Sci. Instrum. 62 (3), March 1991, American Institute of Physics.
- /3/ **Lau, P, 2005.** Determination of specific heat capacity of rock samples, P502681-12, SP Swedish National Testing and Research Institute, Measurement Technology.
- /4/ **Liedberg, L, 2005.** Forsmark site investigation. Borehole KFM90B. Determination of porosity by water saturation and density by buoyancy technique. SKB P-report P-05-220. Svensk Kärnbränslehantering AB.
- /5/ Instruction Manual Hot Disc Thermal Constants Analyser Windows 95 Version 5.0, 2001.
- /6/ ISRM Commission on Testing Methods, ISRM, 1979.

Appendix A

Calibration protocol for Hot Disk Bridge System

Electronics:	Keithley 2400	Serial No. 0925167
	Keithley 2000	Serial No. 0921454
Hot Disk Bridge:		Serial No. 2003-0004
Computation Device:		Serial No. 2003-0003, ver 1.5
Computer:	Hot Disk computer	Serial No. 2003-0003
Test sample:	SIS2343. mild steel	Serial No. 3.52
Sensor for testing:	C5501	

Test measurement: 10 repeated measurements on the test sample at room temperature.

Conditions: Power 1 W. Measurement time 10 s

Results

Thermal Conductivity:	13.45 W/(m. K)	±0.06%
Thermal Diffusivity:	3.530 mm ² /s	±0.13%
Heat Capacity:	3.810 MJ/(m ³ . K)	±0.15%

This instrument has proved to behave according to specifications described in BRk-QB-M26-02.

Borås 14/08 2006

Patrik Nilsson

Appendix B

Table B-1. Thermal properties of samples at 20 °C.

Measurement number	Conductivity PFP [W/(m, K)]	Diffusivity PFP [mm ² /s]	Conductivity FP [W/(m, K)]	Diffusivity FP [mm ² /s]
KFM90B-294-90V				
1	3.10	1.45	3.92	1.84
2	3.03	1.42	4.00	1.88
3	2.92	1.37	4.08	1.91
4	2.90	1.36	4.10	1.92
5	2.90	1.36	4.10	1.92
KFM90B-295-90V				
1	3.52	1.60	3.72	1.69
2	3.49	1.58	3.73	1.69
3	3.48	1.58	3.73	1.69
4	3.56	1.62	3.69	1.67
5	3.48	1.58	3.73	1.70
KFM90B-296-90V				
1	3.14	1.44	3.99	1.84
2	3.08	1.42	4.02	1.85
3	3.10	1.43	4.01	1.84
4	3.10	1.43	4.01	1.84
5	3.10	1.43	4.01	1.84
KFM90B-297-90V				
1	2.79	1.27	4.14	1.88
2	2.81	1.28	4.10	1.86
3	2.77	1.26	4.13	1.88
4	2.73	1.24	4.18	1.90
5	2.79	1.27	4.12	1.87
KFM90B-298-90V				
1	2.92	1.36	4.19	1.95
2	2.96	1.37	4.17	1.94
3	2.81	1.31	4.29	1.99
4	2.81	1.30	4.29	1.99
5	2.76	1.28	4.32	2.01
KFM90B-299-90V				
1	2.44	1.14	4.28	2.00
2	2.51	1.17	4.22	1.97
3	2.49	1.16	4.24	1.98
4	2.44	1.14	4.31	2.02
5	2.48	1.16	4.26	2.00

Appendix C

Table C-1. Total time of measurement, ratio of total time and characteristic time, and number of analysed points at 20 °C

Measurement number	Total time(s)	Total/Char. Time	Points
KFM90B-294-90V			
1	20	0.60	79- 200
2	20	0.52	88- 200
3	20	0.50	91- 200
4	20	0.52	89- 200
5	20	0.50	91- 200
KFM90B-295-90V			
1	20	0.56	82- 200
2	20	0.50	89- 200
3	20	0.54	85- 200
4	20	0.55	83- 198
5	20	0.57	81- 200
KFM90B-296-90V			
1	20	0.84	54- 200
2	20	0.83	55- 200
3	20	0.80	58- 200
4	20	0.87	52- 200
5	20	0.83	55- 200
KFM90B-297-90V			
1	20	0.58	83- 200
2	20	0.65	75- 200
3	20	0.66	74- 200
4	20	0.62	78- 200
5	20	0.62	78- 200
KFM90B-298-90V			
1	20	0.75	62- 200
2	20	0.70	67- 200
3	20	0.69	68- 200
4	20	0.65	72- 200
5	20	0.65	72- 200
KFM90B-299-90V			
1	20	0.49	96- 200
2	20	0.52	92- 200
3	20	0.55	88- 200
4	20	0.48	98- 200
5	20	0.48	98- 200

Forsmark site investigation

Borehole KFM90B.

Determination of porosity by water saturation and density by buoyancy technique

Marjo Savukoski
Swedish National Testing and Research Institute, SP

September 2006

Keywords: Rock mechanics, Petro-physics, Density, Porosity, AP PF 400-06-023

Abstract

The density and porosity was determined on 6 specimens (each divided into two pieces) from borehole KFM90B, Forsmark, Sweden. The core samples were taken at a level of between 8 and 18 m in borehole length.. The investigated rock types are mapped granite. The results for the dry density varied around $2,650 \text{ kg/m}^3$, and for the wet density between $2,650$ and $2,660 \text{ kg/m}^3$. Finally, the porosity results varied between 0.4 and 0.5 %.

Sammanfattning

Densiteten och porositeten bestämdes på 6 provkroppar (varje provkropp delad i två delar) från borrhål KFM90B i Forsmark. Proverna togs från en nivå i borrhålet mellan 8-18 m borrhålslängd. De undersökta bergarten är karterade som granit. Resultaten för torrdensiteten varierade runt 2650 kg/m^3 och för våtdensiteten mellan 2650 och 2660 kg/m^3 . För porositeten, slutligen, varierade resultaten mellan 0,4 och 0,5 %.

Contents

Abstract.....	3
Sammanfattning.....	4
Contents.....	5
1 Introduction	6
2 Objective and scope.....	8
3 Equipment.....	9
4 Execution.....	10
4.1 Description of the specimens.....	10
4.2 Testing	11
4.3 Nonconformities	12
5 Results	13
5.1 Results grouped according to rock type of the specimens	13
5.2 Results for the entire test series	14
References	16
Appendix – Result minutes and photos	17

1 Introduction

Specimens were sampled from the drill core of borehole KFM90B at the Forsmark site investigation area, Sweden, see Figure 1-1, for determination of the water saturated density, dry density and the porosity. Borehole KFM90B is a telescopic drilled borehole inclined c. 82° from the horizontal plane and with a total length of 18.2 m. The complete borehole length is core drilled

The sampling was based on the preliminary core logging with the strategy to primarily investigate the properties of the dominant rock types. The samples, which were collected by John Wrafter, SKB, on November 15, 2005, were transported to SP (Swedish National Testing and Research institute), department of Building and Mechanics, where they arrived in June 15, 2006. Testing commenced in June 2006 and was completed in August 2006.



Figure 1-1. Location of KFM90B in relation to other telescopic boreholes drilled up to November 2005 within and close to the Forsmark candidate area.

The commission was carried out in compliance with the controlling documents presented in Table 1-1. Activity Plan and Method Descriptions are SKB's (The Swedish Nuclear Fuel and waste Management Company) internal controlling documents, whereas SP-QD 13.1 is an SP internal Quality document.

Table 1-1. Controlling documents for performance of the activity.

Activity Plan	Number	Version
KFM90B. Termiska laboratoriebestämningar	AP PF 400-06-023	1.0
Method Description	Number	Version
Determining density and porosity of intact rock	SKB MD 160.002	2.0
Quality Plan		
SP-QD 13.1		

2 Objective and scope

The purpose of determining density and porosity of intact rock cores is to use these parameters in the rock mechanics and thermal site descriptive model, which will be established for the candidate area selected for site investigations at Forsmark.

The testing comprised of 6 rock samples from borehole KFM90B collected within the borehole interval 8-18 m.

3 Equipment

The following equipment was used for the density and porosity determinations:

- Thermometer (inv no 102185) for measurement of water temperature. Calibrated 2006-01-17. Measurement accuracy ± 0.4 °C.
- Scale (inv no 102291) for weight measurement. Calibrated in 2005-03-10. Measurement accuracy ± 0.2 g.
- Heating chamber (inv no 102289) for drying the specimens. Calibrated 2006-01-17. Measurement accuracy ± 5 °C.
- A covered plastic box filled with water for water saturation of the samples.
- A desiccator for cooling samples.

Uncertainty of method as expanded uncertainty with covering factor 2 (95% confidence interval):

Density ± 4 kg/m³
Porosity ± 0.09 %
Water absorption ± 0.05 %

4 Execution

Determination of the porosity and density was made in accordance with SKB's method description SKB MD 160.002, (SKB internal controlling document). This includes determination of density in accordance to ISRM 1979 /1/ and water saturation by EN 13755 /2/ and in compliance with Activity Plan AP PF 400-06-023 (internal controlling document of SKB). The department of Building Technology and Mechanics (BM) at SP performed the test.

4.1 Description of the specimens

The specimens from borehole KFM90B were sampled at levels ranging between 8 and 18 m borehole length. Table 4-1 shows the identification mark, sampling level and rock type of each specimen.

Table 4-1. Identification mark, sampling level and rock type of each specimen (rock-type classification according to Boremap).

Identification	Sampling level (m bore-hole length, Adj seclow)	Rock type
<i>KFM90B-294-90V</i>	8.26	<i>Medium grained granite</i>
<i>KFM90B-295-90V</i>	9.00	<i>Medium grained granite</i>
<i>KFM90B-296-90V</i>	10.22	<i>Medium grained granite</i>
<i>KFM90B-297-90V</i>	14.75	<i>Medium grained granite</i>
<i>KFM90B-298-90V</i>	17.51	<i>Medium grained granite</i>
<i>KFM90B-299-90V</i>	18.06	<i>Medium grained granite</i>

4.2 Testing

The execution procedure followed the prescription in SKB MD 160.002, (SKB internal controlling document), see Table 4-2.

Table 4-2. The sequence of activities applied for execution of the commission.

Activity No	Activity
1	The specimens were cut according to the marks on the rock cores. Every specimen was cut into two pieces, marked A and B and about 25 mm thick each. The same specimens were used in a parallel activity to determine the thermal properties thermal conductivity and thermal diffusivity by applying the TPS method /3/.
2	The specimens were water saturated in normal air pressure for at least seven days..
3	The specimens were photographed in JPEG-format.
4	The specimens were weighed in tapwater. The temperature of the water was 23 °C and the density 998 kg/m ³
5	The specimens were surface dried with a towel and weighed.
6	The water saturated density was determined.
7	The samples were sent from SP Building Technology and Mechanics to SP Measurement technology for measurement of thermal properties.
8	The samples were sent from SP Measurement technology to SP Fire Technology for measurement of thermal properties /3/.
9	The samples were sent back from SP Fire Technology to SP Building Technology and Mechanics.
10	The specimens were dried in a heating chamber for six days at 105 °C.
11	The specimens were transported to a desiccator for cooling.
12	The dry density and porosity were determined.

4.3 Nonconformities

The tests were performed in accordance with the Method Description. The Activity Plan was followed without deviations.

Previously, the samples were cut perpendicular to the length of the core (and to the foliation of the rock). This time the sample was cut parallel to the length.

An exception from the method was the statement of significant numbers in Appendix 1. The precision in the method for density gives only three significant digits the fourth digit given here is thus not significant. The precision in the method for porosity gives only one significant digit the second digit given here is thus not significant. It is important that this is kept in mind when the results are used for further calculation.

5 Results

The results of the porosity and density determinations of core samples from KFM90B are stored in SKB's database SICADA, where they are traceable by the Activity Plan number.

Minutes and photos are presented in Appendix 1.

5.1 Results grouped according to rock type of the specimens

Tables 5-1 to 5-2 summarize the results of the porosity and density determinations divided according to rock type of the specimens.

Table 5-1. Summary of the results for porosity, dry density and wet density. The result for each specimen is a mean value of sub samples A and B.

Specimen	Sampling level (m borehole length), according to the marks on the drill-core boxes (Adj seclow)	Porosity (%)	Dry density (kg/m ³)	Wet density (kg/m ³)
KFM90B-294-90V	8.26	0.5	2,650	2,660
KFM90B-295-90V	9.00	0.5	2,650	2,650
KFM90B-296-90V	10.22	0.5	2,650	2,660
KFM90B-297-90V	14.75	0.4	2,650	2,660
KFM90B-298-90V	17.51	0.5	2,650	2,650
KFM90B-299-90V	18.06	0.5	2,650	2,650
Mean value		0.5	2,650	2,660
Standard deviation		0.02	2	4

5.2 Results for the entire test series

Results for the entire test series are shown in the diagrams below. They are divided into three diagrams, see Figures 5-1 to 5-3, illustrating dry density, wet density and porosity.

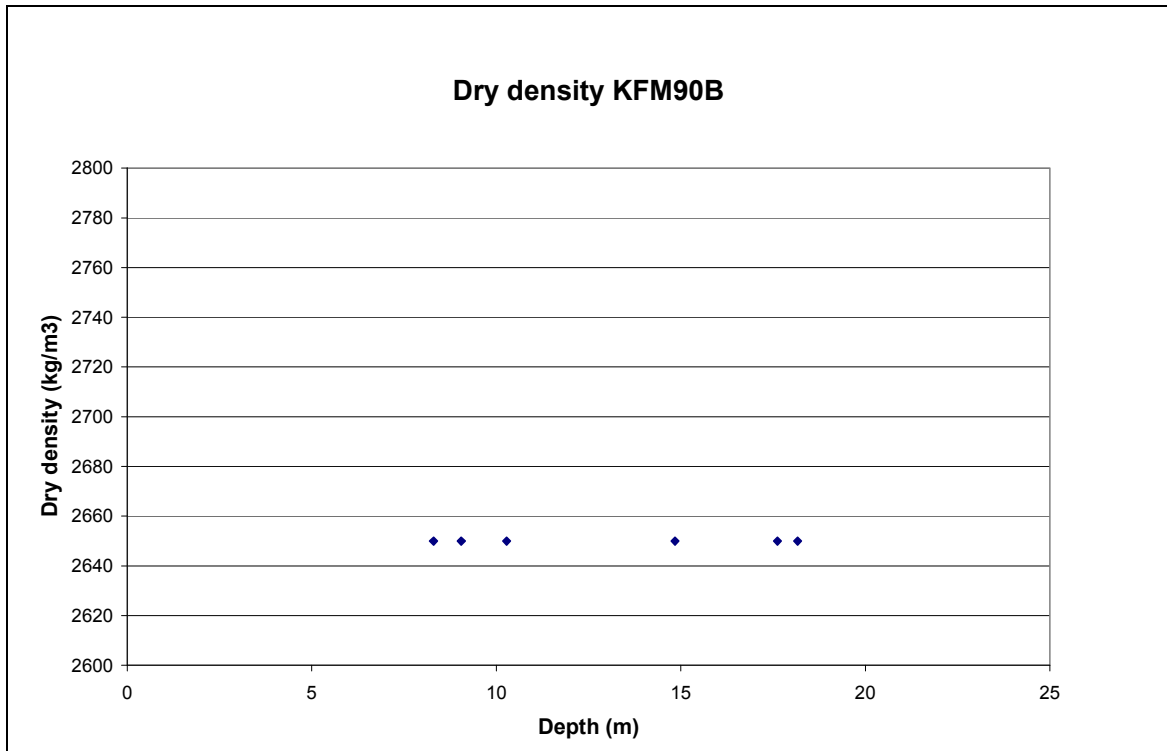


Figure 5-1. Density (dry) versus sampling level (borehole length).

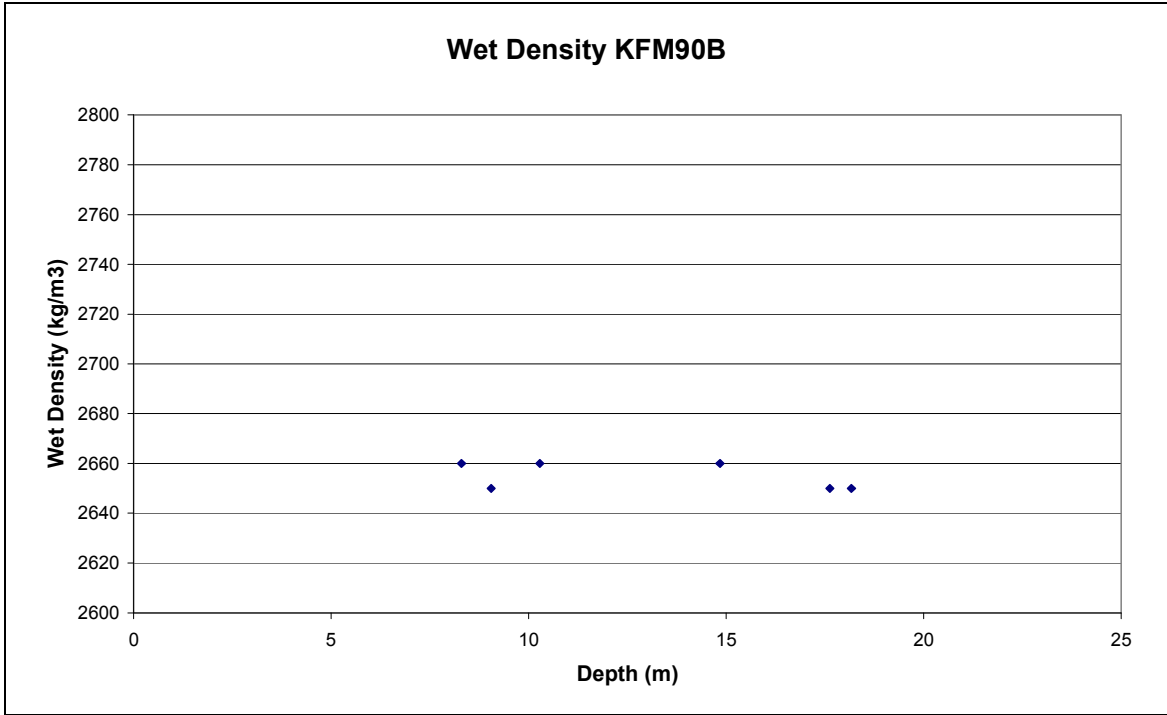


Figure 5-2. Density (wet) versus sampling level (borehole length).

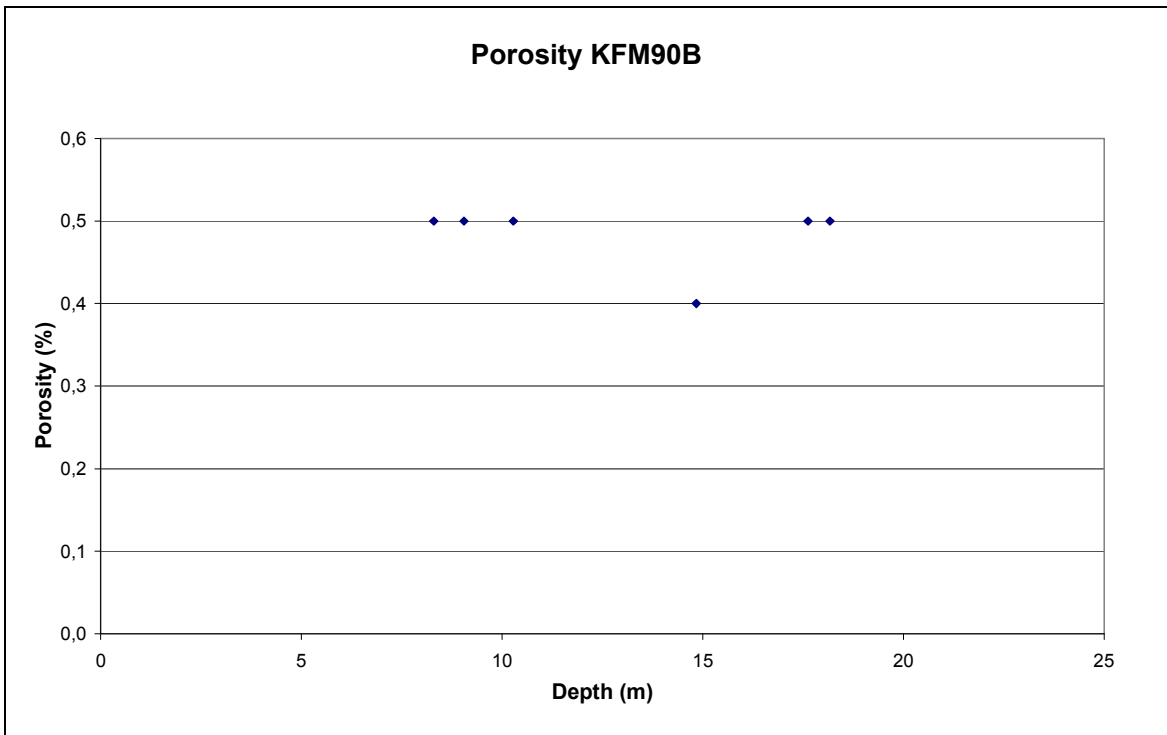


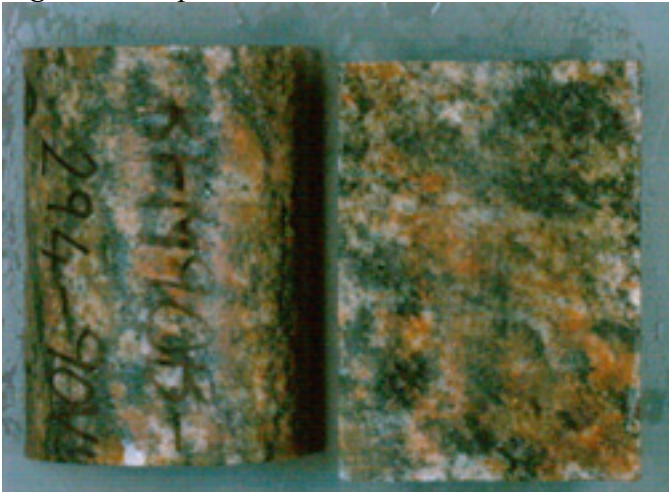
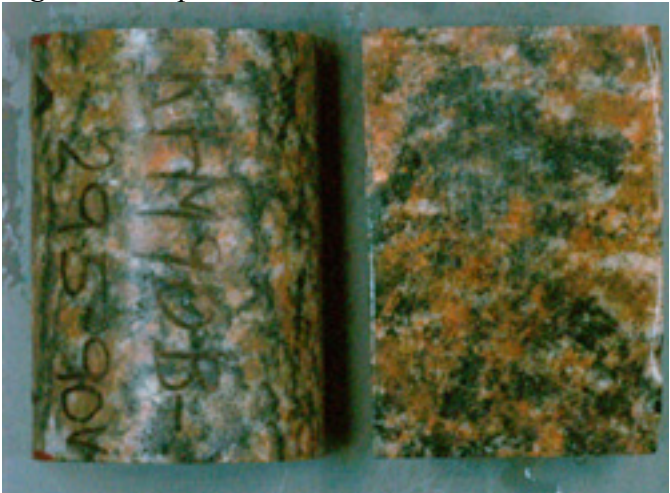
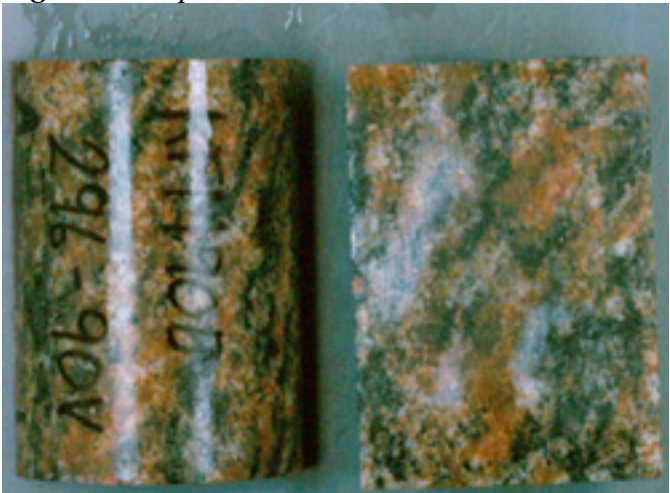
Figure 5-3. Porosity versus sampling level (borehole length).

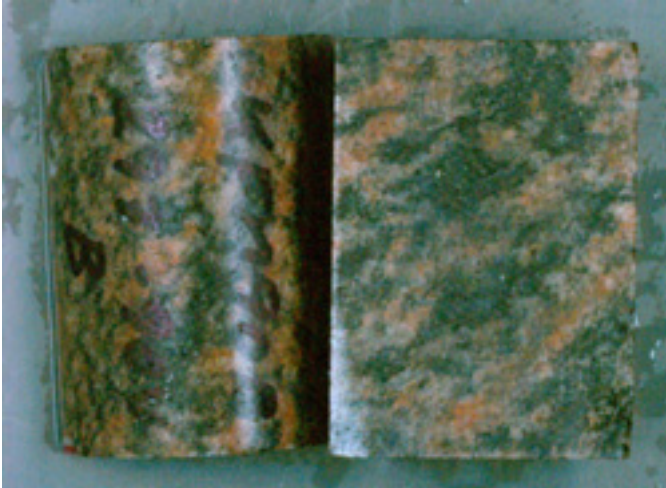


References

- /1/ ISRM 1979, Volume 16, Number 2.
- /2/ EN 13755, Natural stone test methods – Determination of water absorption at atmospheric pressure.
- /3/ **Adl-Zarrabi, B, 2005.** Borehole KFM90B. Thermal conductivity and thermal diffusivity determined using the TPS method.

Appendix – Result minutes and photos

Table A-1. KFM90B, level 8-18 m. Specimens KFM90B-294 -90V to KFM90B-299-90V.

<p>KFM90B-294 -90V (8.26 m)</p> <p>Dry density of specimen KFM90B-294-90V A 2,646 kg/m³ and porosity 0.47%.</p> <p>Dry density of specimen KFM90B-294-90V B 2,658 kg/m³ and porosity 0.49%</p>	<p><i>Figure A-1. Specimens KFM90B-294-90V A and B.</i></p> 
<p>KFM90B -90V-295 (9.00 m)</p> <p>Dry density of specimen KFM90B-295-90V A 2,650 kg/m³ and porosity 0.48%.</p> <p>Dry density of specimen KFM90B-295-90V B 2,650 kg/m³ and porosity 0.48%.</p>	<p><i>Figure A-2. Specimens KFM90B-295-90V A and B.</i></p> 
<p>KFM90B-296 -90V (10.22 m)</p> <p>Dry density of specimen KFM90B-296-90V A 2,650 kg/m³ and porosity 0.48%.</p> <p>Dry density of specimen KFM90B-296-90V B 2,654 kg/m³ and porosity 0.44%.</p>	<p><i>Figure A-3. Specimens KFM90B-296 -90VA and B.</i></p> 

<p>KFM90B-297 -90V (14.75 m)</p> <p>Dry density of specimen KFM90B-297-90V A 2,658 kg/m³ and porosity 0.41%.</p> <p>Dry density of specimen KFM90B-297-90V B 2,649 kg/m³ and porosity 0.43%.</p>	<p>Figure A- 4. Specimens KFM90B-297-90VA and B.</p> 
<p>KFM90B-298 -90V (17.51 m)</p> <p>Dry density of specimen KFM90B-298-90V A 2,650 kg/m³ and porosity 0.49%.</p> <p>Dry density of specimen KFM90B-298-90V B 2,648 kg/m³ and porosity 0.46%.</p>	<p>Figure A-5. Specimens KFM90B-298 -90VA and B.</p> 
<p>KFM90B-299-90V (18.06 m)</p> <p>Dry density of specimen KFM90B-299-90V A 2,646 kg/m³ and porosity 0.46%.</p> <p>Dry density of specimen KFM90B-299-90V B 2,649 kg/m³ and porosity 0.45%.</p>	<p>Figure A-6. Specimens KFM90B-299 -90VA and B.</p> 

Boremap mapping of KFM90B-KFM90F

Christin Döse

Eva Samuelsson

Geosigma AB

January 2006

This report concerns a study which was conducted for SKB. The conclusions and viewpoints presented in the report are those of the authors and do not necessarily coincide with those of the client.

Contents

1	Introduction	3
2	Execution	4
2.1	Description of equipment and interpretation tools	4
2.1.1	BIPS-image quality	4
2.2	Preparations	4
2.3	Execution	6
2.4	Data handling	6
2.5	Nonconformities	6
3	Results.....	8
3.1	Rock type	8
3.2	Ductile and brittle-ductile deformation	9
3.2.1	Foliation	9
3.2.2	Sealed brittle- or brittle-ductile deformation.....	10
3.3	Brittle deformation – fractures and crush	10
3.4	Alteration	10
	<u>Appendix I</u> - BIPS-images of KFM90B-F	12
	<u>Appendix II</u> - WellCad diagrams of KFM90B-F	27
	<u>Appendix III</u> - Indata: Borehole length, orientation and diameter	37

1 Introduction

KFM90A-F were drilled in order to measure the anisotropic thermal properties of the rock in large scale. The work was carried out in accordance with activity plan SKB PF 400-05-071. This PM reports the data gained from the Boremap mapping of the core drilled boreholes KFM90B, KFM90C, KFM90D, KFM90E and KFM90F. KFM90A served as a reference borehole and therefore only an overview mapping was performed for this borehole. The Boremap mapping of the boreholes were performed between the 2nd and 9th of November in 2005. The detailed documentation of the boreholes will be used in a 3D-model of the test area in order to interpret the results from the thermal measurements. In table 1-1 controlling documents for mapping boreholes with the Boremap system are listed. Both activity plan and method descriptions are SKB's internal controlling documents. Methods and assumptions not mentioned in the method descriptions can be found in a P-report by the authors /1/.

Table 1-1. Controlling documents for the performance of the activity

Activity plan	Number	Version
<i>Mätning av anisotropa termiska egenskaper i stor skala i fält</i>	AP PF 400-05-071	1.0
Method descriptions	Number	Version
<i>Metodbeskrivning för Boremapkartering</i>	SKB MD 143.006	1.0
<i>Mätsystembeskrivning för Boremap</i>	SKB MD 146.001	1.0
<i>Nomenklatur vid Boremapkartering</i>	PM, internal document	1.5
<i>Instruktion: Regler för bergarters benämningar vid platsundersökningen i Forsmark</i>	SKB MD 132.005	v.1.0

2 Execution

2.1 Description of equipment and interpretation tools

The Boremap mapping of BIPS-images and drill core was performed with the software Boremap v. 3.7.2. The Boremap software calculates actual directions (strike and dip) of planar structures penetrated by the borehole (foliations, fractures, fracture zones, rock contacts etc). Data on inclination, bearing and diameter of the boreholes are used as in-data for the calculations (Table 2-2). The BIPS-image lengths were checked and if necessary calibrated (Chapter 2.2).

Additional software used during mapping are BIPS Image Viewer and MicroSoft Access 2002. The final data presentations were made in BIPS Image Print and WellCad v. 4.0.

The following equipment was used to facilitate the core documentation: folding rule, 10 % hydrochloric acid, knife, hand lens, paint brush and a tap of water.

2.1.1 BIPS-image quality

The boreholes KFM90B-F were logged with the BIP-IV-camera with an image resolution of 720 pixels around the borehole wall and 1 pixel/mm along the borehole wall. BIP-IV images are usually somewhat darker than BIP-1500 images, and red and green colours are overexposed in the image. This colour distortion does not affect the mapping, but the following factors may do so:

- 1) blackish coatings probably related to the drilling equipment
- 2) vertical bleached bands from the clayey mixture of drill cuttings and water
- 3) light and dark bands at high angle to the drill hole related to the automatic aperture of the video camera
- 4) vertical enlargements of pixels due to stick-slip movement of the camera probe

The quality of the BIPS-image for each borehole is listed in Table 2-1. Suspensions and clay that has precipitated on the lower side of the borehole wall are the main disturbances in the BIPS-images of KFM90B-F, since the boreholes are close to surface and the water conductivity is rather high.

2.2 Preparations

The lengths registered during the BIPS-logging corresponded very well with the lengths marked in the core box. Therefore no length adjustments were made other than for borehole KFM90B, where the recorded start depth of 1.58 m corresponded well with drill core length (~1.58 m), but the end length 18.01 m needed to be adjusted to 17.90 m. This adjustment was made since it is known that the BIPS-camera cannot record the last 30 cm in the borehole, which is only 18.20 m long.

Table 2-1. BIPS Image Quality

Borehole	From	To	% visible	Comment
KFM90B	1.58	16.26	98	Good. Only white vertical streaks due to drops of water on the plexiglass
	16.26	17.90	0	Watertable. Borehole fluid is very rich in suspensions.
KFM90C	1.58	12.5	100	Good
	12.5	13.5	30-70	Precipitated suspensions on the lower side of borehole
	13.5	19.55	0-30	Precipitated suspensions on the lower side of borehole
KFM90D	1.58	19.20	100	Good, but with darker bands, due to uneven lightning.
KFM90E	1.58	15.40	100	Good, but with both darker bands and white streaks.
	15.40	18.70	40-60	Watertable. Suspensions in the borehole fluid.
	18.70	19.75	100	Acceptable. Blurred image due to suspensions in the borehole fluid.
KFM90F	1.58	12	100	Good, but with both darker bands and white streaks.
	12	16.3	100	Relatively good, but with both darker bands and white streaks.
	16.3	17.7	~50	Acceptable. Outflow with suspensions from fractures.
	17.7	19.77	100	Relatively good, but thin cover of material covers 60 % of the borehole wall.

The BIPS-images are oriented in the boreholes by a compass, and therefore some corrections had to be made. The most updated correction data in SICADA were from 2004-01-01 and these were used (Table 2-3).

Geometrical data for the boreholes are given in Table 2-2. Background data prior to the Boremap mapping included:

- Borehole diameter
- Borehole length
- Borehole bearing and inclination

Table 2-2. Borehole data for KFM90A-F

ID-code	Northing	Easting	Bearing (degrees)	Inclination (degrees)	Diameter (mm)	Borehole length (m)	BIPS-image interval (m, adjusted lengths)
KFM90A	6700073.679	1631004.140	278.3	-82.3	56	24.18	
KFM90B	6700065.591	1631008.894	261.7	-81.9	76	18.20	1.58-18.01
KFM90C	6700067.083	1631008.672	262.5	-81.8	56	19.55	1.56-19.55
KFM90D	6700065.848	1631010.387	260	-81.7	56	19.19	1.58-19.19
KFM90E	6700064.861	1631008.964	259.7	-81.8	56	19.75	1.58-19.75
KFM90F	6700065.461	1631008.075	261.4	-81.7	56	19.79	1.58-19.79

Table 2-3. Corrections for magnetic orientation

Specification	Correction
Bearing from Map North	0
Magnetic Declination	4.1
Meridian Convergence	2.1
Image Mid to Magnetic North	0

2.3 Execution

References to the methods used when mapping the boreholes are listed in Table 1.1 and completions or possible deviations are described in a P-report /2/. In the boreholes KFM90B-F, there are sections where no geological features are visible in BIPS. Since the sections were not too long the geology could be mapped with the guide-line method despite this /1, 2/, but with less accuracy for the orientations. These observations are documented as non-visible in BIPS and can be separated from the ones that are oriented in BIPS.

In cases where properties or minerals are not represented in the mineral list, the following mineral codes have been used in the mappings of KFM90B-F:

- X1 = bleached fracture walls
- X2 = interpreted grouting, which is only observed in the borehole wall and hence in the BIPS-image.
- X3 = the drill core is broken at a right angle and the broken surfaces have a polished appearance. This is caused by rotation of two core pieces along an intermediate fracture wearing away possible mineral fill. It is impossible to say whether this fracture was open or sealed in situ.

2.4 Data handling

In order to obtain the best possible data security, the mapping was performed on the SKB network, with regular back-ups on the local drive. Each day, a summary report was printed in order to find possible misprints. If misprints were observed, they were corrected before the mapping proceeded. When the mapping was completed fractures minerals were checked once more. Before exportation to SICADA, borehole lengths, mapping lengths, deviation data and length adjustments were checked after which the mapping was checked by a routine in Boremap which detects logical defects. The data are stored in SICADA.

2.5 Nonconformities

The grouting of the borehole KFM90B affects the interpretation of fracture apertures negatively. Grouting in thin fractures is probably always missed, because very thin fractures with no visible aperture usually appear white in the BIPS-image, probably due to light reflection from the edge of the fracture trace. Even though the fracture is over 1 mm wide, grouting may be missed, due to deficient communication between the mapping personnel. Therefore only large grout-filled open fractures are detected with certainty (for example the uppermost fracture in figure 5-1). The authors disclaim responsibility for correct apertures detection for fractures thinner than 3 mm in KFM90B.

Calcite is *overrepresented* relative to other minerals, since it is detected by reaction with diluted hydrochloric acid even though it is macroscopically invisible.

The well developed foliation in KFM90B-F, making it difficult to observe and measure possible lineation in the borehole, and hence no lineation was documented. The foliation was mainly parallel with the boreholes, and they were therefore difficult to measure accurately with the Boremap method. Any deviation from this parallel foliation is measured and the deviations in the SICADA database are therefore overrepresented. Therefore foliation data was complemented afterwards and this is presented in section 3.

Not all necessary in-data were available in the SICADA database when the mapping was performed. Missing technical data were obtained orally from the persons responsible for drilling and measurements.

In two boreholes (KFM90B and KFM90E), the water table can be observed in the BIPS-image at the following borehole lengths: 16.26 and 15.40 m (table 2-1). According to the activity plan, the tests should be made under the ground water table, which is not the case if these represent the natural groundwater table. An explanation for this lower water table is that the water has been pumped out before the BIPS-logging and that the water table observed in the BIPS-images hence does not reflect the natural ground water table.

3 Results

The Boremap mapping of KFM90B-F is stored in SICADA and it is only these data that shall be used for further interpretation and modelling. The interpreter should be familiar with the Boremap method.

Results from the Boremap mapping are briefly described in this chapter and the graphical presentations of the data are given in Appendix 2 (WellCad-diagrams).

3.1 Rock type

The dominant rock type in the outcrop and in the boreholes KFM90B-F is metagranite-to granodiorite (101057, 92.3%). Amphibolite (102017, 3.4%), pegmatite (101061, 3.1%) and fine grained granite (111058, 0.6%) also occur (Table 3-1 and Figure 3-1). The orientation of rock occurrences less than 1 m in width are shown in Figure 3-2.

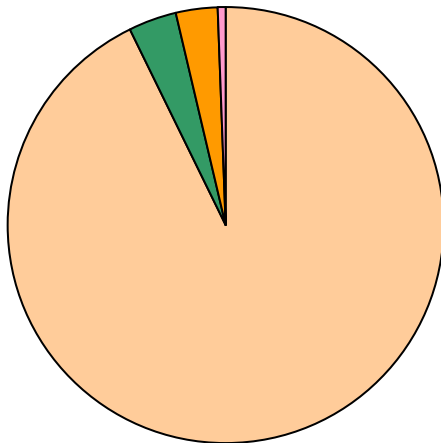


Figure 3-1: Rock distribution in KFM90B-F. ■ = metagranite-granodiorite, ■ = amphibolite, ■ = pegmatite, ■ = fine-grained granites.

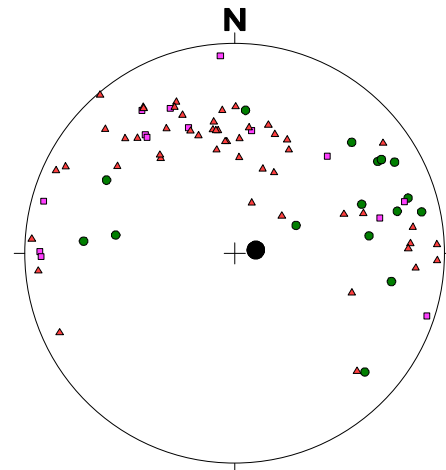


Figure 3-2: Plane to pole diagram showing upper contact of rock occurrences. ● = amphibolite, ▲ = pegmatite, ■ = fine-grained granites. ● = borehole directions.

Table 3-1. Fracture frequencies and distribution of rock types.

Borehole	Open fractures/m	Sealed fractures/m	101057 metagranite, %	102017 amphibolite, %	101061 pegmatite, %	111058 fine grained granite, %
KFM90B	2.0	4.3	91.3	3.1	3.6	2.0
KFM90C	1.5	3.6	91.4	3.8	4.6	0.2
KFM90D	2.7	2.4	89.9	6.9	2.8	0.4
KFM90E	2.0	2.5	94.7	1.8	3.3	0.2
KFM90F	1.4	2.3	96.8	1.4	1.3	0.5
TOT	1.9	3.0	92.9	3.4	3.1	0.6

3.2 Ductile and brittle-ductile deformation

3.2.1 Foliation

Knowing the foliation of the rock is very important when measuring and interpreting the thermal anisotropy of the rock. The boreholes were drilled in order to be parallel with the foliation. This has succeeded, but the foliation is not always consistent, and in places it lies at an angle of 20-30° to the drill core. It is possible that the variation in the foliation can be correlated with the occurrence of thin pegmatitic veins. Foliation parallel to the borehole axis has not always been documented, partly because parallel features cannot be confidently mapped in Boremap. Thus, the diverging foliation patterns are overrepresented in the mapping. Sections described as having foliation “presumably parallel to borehole” are sections where diverging directions have not been recorded. In Table 3-2, an attempt to compile the foliation data has been made.

No lineation was observed.

Table 3-2. Variation in foliation in KFM90A-F

Borehole	From	To	Comment	Orientation
KFM90A	0	23.30	Parallel to borehole, α -angle = 90.	
	23.3	24.18	Diverging foliation α -angle = 30.	
KFM90B	0	11.03	Parallel to borehole	~170/80
	11.03	11.28	Diverging foliation, possibly related to pegmatite.	~148/60
	11.28	18.20	Presumably parallel to borehole	
KFM90C	0	8.70	Parallel to borehole.	~180/80
	8.70	9.30	Diverging foliation, possibly related to pegmatite.	182/61
	9.30	19.99	Presumably parallel to borehole	
KFM90D	0	9.78	Parallel to borehole.	~160/80
	9.78	13.30	Undulating foliation ranging from parallel to diverging. Possibly related to pegmatite.	~160/80 - 175/60,
	13.30	15.63	Parallel to borehole.	
	15.63	15.96	Diverging foliation.	196/65
	15.96	16.89	Parallel to borehole.	
	16.89	17.39	Diverging foliation, possibly related to pegmatite.	~135/66
	17.39	19.30	Parallel to borehole.	
	19.30	20.31	Presumably parallel to borehole	
KFM90E	0	8.42	Parallel to borehole.	~185/80
	8.42	8.63	Diverging foliation. α -angle = 28.	201/55
	8.63	9.93	Parallel to borehole.	
	9.93	12.65	Parallel to borehole.	
	12.65	12.81	Diverging foliation due to pegmatite.	018/65
	12.81	18.66	Parallel to borehole.	
KFM90F	18.66	19.13	Diverging foliation.	~165/70
	19.13	20.31	Presumably parallel to borehole	
	0	17.33	Parallel to borehole.	~180/80
	17.33	18.13	Diverging foliation due to pegmatite.	145/52
	18.13	20.1	Parallel to borehole?	

3.2.2 Sealed brittle- or brittle-ductile deformation

Only a few, mostly millimetre-thin, deformation bands have been observed. They are mostly steeply dipping and do not seem to crosscut more than one borehole. Two thin breccias have been observed in KFM90E at 18.14 and 19.29 m borehole length having the orientations 023/89 and 174/77, respectively. In KFM90C two sub-horizontal (~015/14) cataclasites are observed, but despite their orientation they cannot be found in other boreholes. Two thin brittle-ductile shear zones are observed: one in KFM90B at 14.09 m striking 150/77 and one in KFM90D at 5.38-5.44 m striking 168/80.

3.3 Brittle deformation – fractures and crush

KFM90B-F are moderately fractured and have an average broken fracture frequency of 1.9 fractures/m (Table 3-1), crush excluded. The corresponding value for unbroken fractures are 3.0 fractures/m, sealed network excluded. The frequency varies somewhat from borehole to borehole.

The sub-horizontal plane observed at 5-6 m depth from ground radar investigations is probably an undulating fracture surface striking 210-265/10-25. The variation in strike from borehole to borehole is 235° in borehole KFM90B, 253° in borehole KFM90C, 210° in borehole KFM90D, 223° in borehole KFM90E and 265° in borehole KFM90F. In most boreholes it has apertures ≥ 1 mm, while in KFM90D it is indicated by its width. In KFM90B it is only interpreted from its orientation.

In addition to this sub-horizontal plane a sub-horizontal fracture zone can be observed in all boreholes between 14.3 and 17.2 m borehole lengths (Table 3-3). In KFM90F this diverges into two sections rich in fractures and two thin crushed sections are observed (striking 040/05 and 175/50). The fracture sets in Table 3-3 are very roughly estimated but indicate a dominating set of 040/10-20.

Table 3-3. Sections rich in fractures in KFM90B-F

Borehole	Interval, m	Fracture set 1	Fracture set 2
KFM90B	14.80-15.40	030/20	300/17
KFM90C	14.63-16.60	010/14	000/00
KFM90D	15.73-16.64	040/10-20	~345/30
KFM90E	15.36-16.26	040/10-20	~350/35
KFM90F	14.32-14.87 and 16.25-17.29	040/-10-20	

3.4 Alteration


The granite-granodiorite shows generally weak to moderate oxidation, which is reflected in the red staining of the rock. The red staining has a higher intensity in the densely fractured borehole sections in the lower part of the boreholes, but a higher intensity can also be observed elsewhere in the boreholes.

References

- /1/ **Döse C, Samuelsson E, 2006.** Forsmark Site Investigation. Boremap mapping of KFM07B. P-report in progress. Svensk Kärnbränslehantering AB.
- /2/ **Ehrenborg J, Dahlin P, 2005.** Oskarshamn Site Investigation. Boremap mapping of core drilled borehole KLX06. SKB P-05-185. Svensk Kärnbränslehantering AB.

BIPS-images of KFM90B

Project name: Forsmark Site Investigation

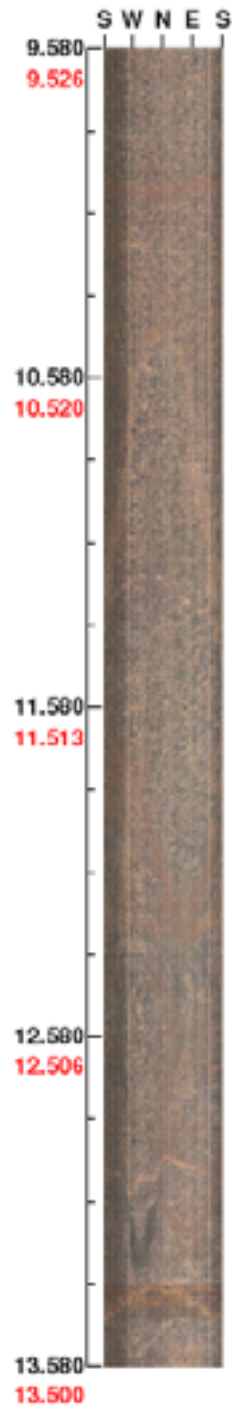
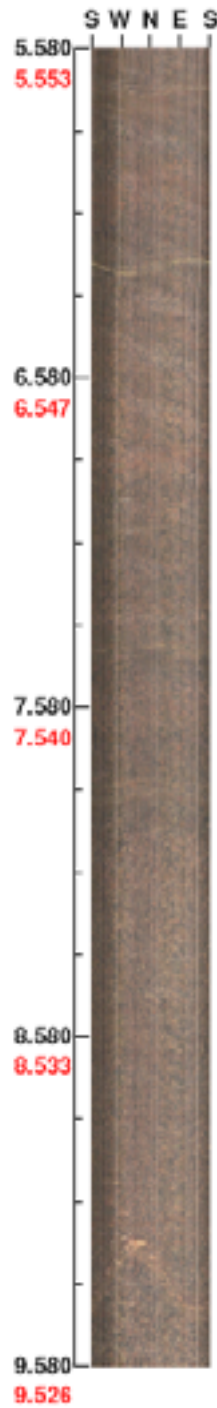
Image file : c:\bips-b~3\kfm90-~1\kfm90b.bip
BDT file : c:\bips-b~3\kfm90-~1\kfm90b.bdt
Locality : FORSMARK
Bore hole number : KFM90B
Date : 05/11/01
Time : 13:27:00
Depth range : 1.580 - 18.010 m
Azimuth : 0
Inclination : -81
Diameter : 76.0 mm
Magnetic declination : 0.0
Span : 4
Scan interval : 0.25
Scan direction : To bottom
Scale : 1/20
Aspect ratio : 150 %
Pages : 2
Color : 

Project name: Forsmark Site Investigation
Bore hole No.: KFM90B

Azimuth: 0

Inclination: -81

Depth range: 1.580 - 13.580 m



(1 / 2)

Scale: 1/20

Aspect ratio: 150 %

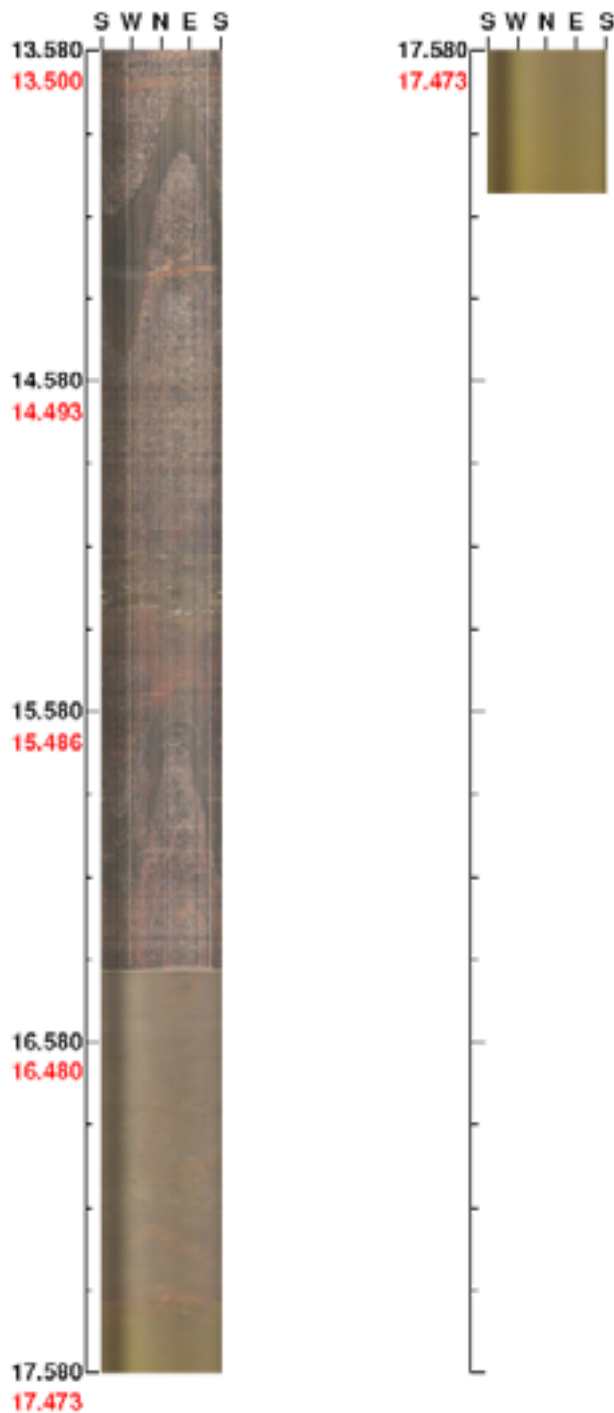
Project name: Forsmark Site Investigation

Bore hole No.: KFM90B

Azimuth: 0

Inclination: -81

Depth range: 13.580 - 18.010 m




(2 / 2)

Scale: 1/20

Aspect ratio: 150 %

BIPS-images of KFM90C

Project name: Forsmark Site Investigation

Image file : c:\bips-b~3\kfm90~1\kfm90c.bip
BDT file : c:\bips-b~3\kfm90~1\kfm90c.bdt
Locality : FORSMARK
Bore hole number : KFM90C
Date : 05/11/01
Time : 10:39:00
Depth range : 1.566 - 19.552 m
Azimuth : 0
Inclination : -81
Diameter : 56.0 mm
Magnetic declination : 0.0
Span : 4
Scan interval : 0.25
Scan direction : To bottom
Scale : 1/20
Aspect ratio : 200 %
Pages : 2
Color : 

Project name: Forsmark Site Investigation
Bore hole No.: KFM90C

Azimuth: 0

Inclination: -81

Depth range: 1.566 - 13.566 m



(1 / 2)

Scale: 1/20

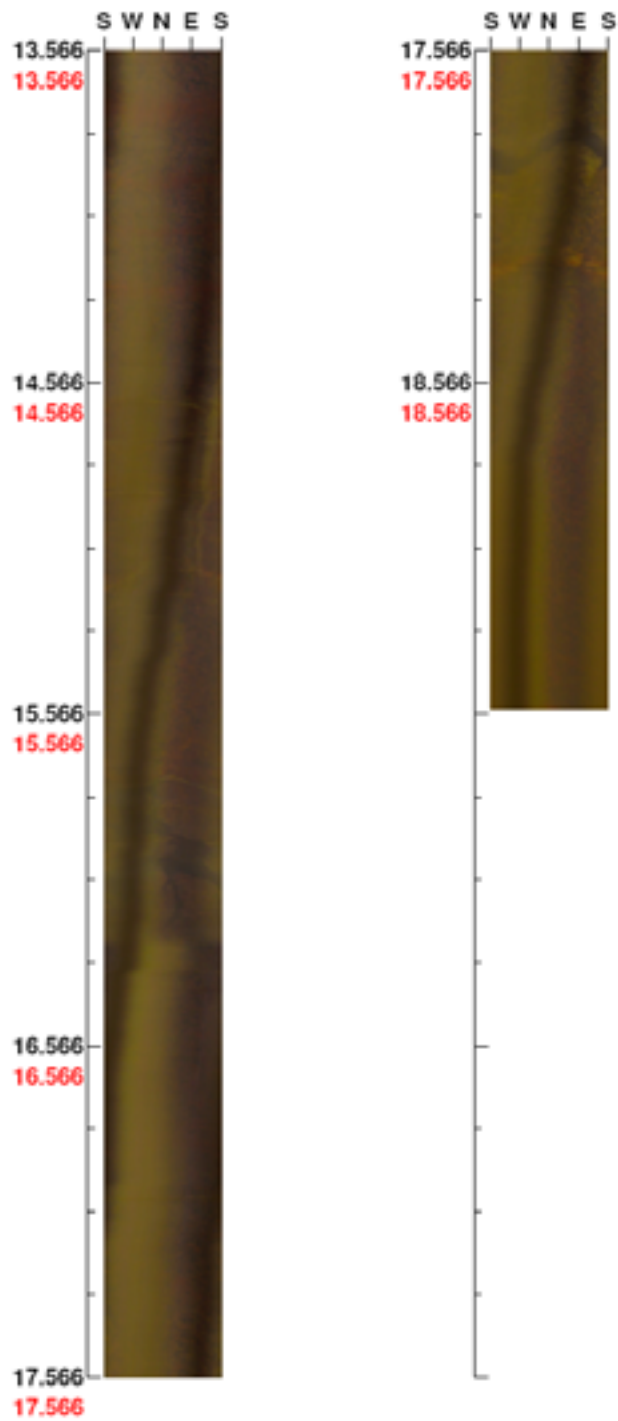
Aspect ratio: 200 %

Project name: Forsmark Site Investigation
Bore hole No.: KFM90C

Azimuth: 0

Inclination: -81

Depth range: 13.566 - 19.552 m




(2 / 2)

Scale: 1/20

Aspect ratio: 200 %

BIPS-images of KFM90D

Project name: Forsmark Site Investigation

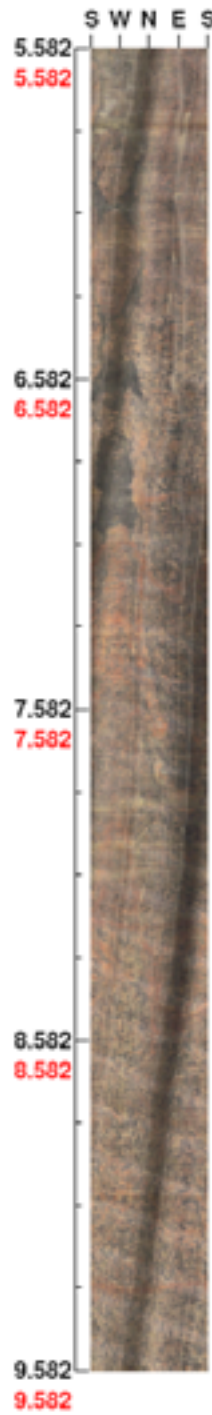
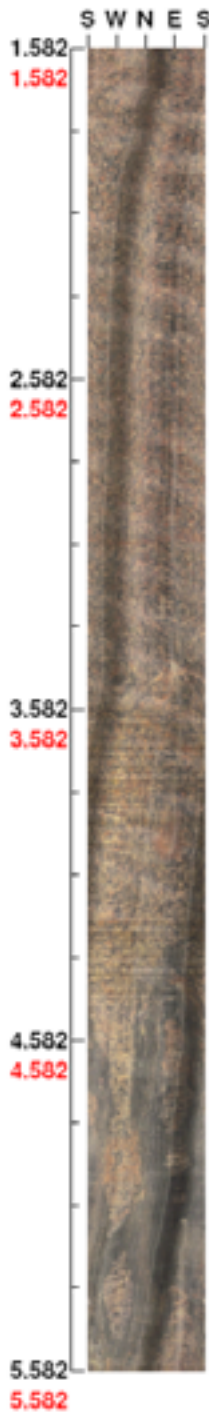
Image file : c:\bips-b~3\kfm90-~1\kfm90d.bip
BDT file : c:\bips-b~3\kfm90-~1\kfm90d.bdt
Locality : FORSMARK
Bore hole number : KFM90D
Date : 05/11/01
Time : 11:17:00
Depth range : 1.582 - 19.401 m
Azimuth : 0
Inclination : -81
Diameter : 56.0 mm
Magnetic declination : 0.0
Span : 4
Scan interval : 0.25
Scan direction : To bottom
Scale : 1/20
Aspect ratio : 200 %
Pages : 2
Color : 

Project name: Forsmark Site Investigation
Bore hole No.: KFM90D

Azimuth: 0

Inclination: -81

Depth range: 1.582 - 13.582 m



(1 / 2)

Scale: 1/20

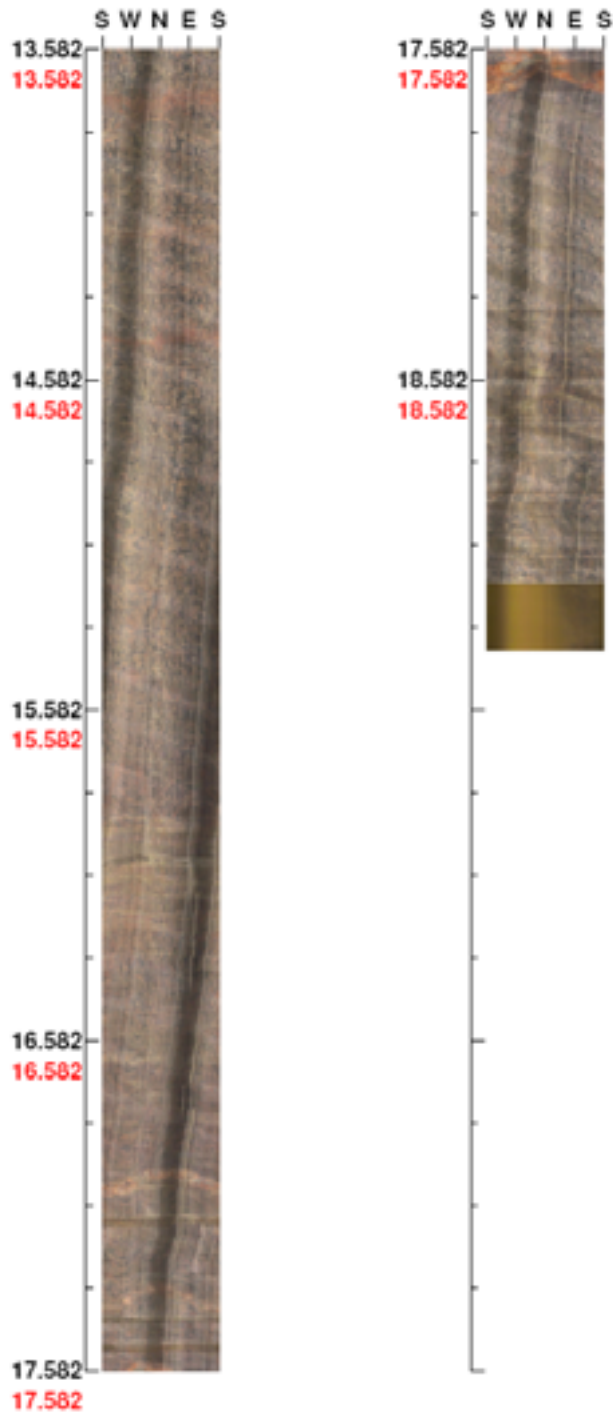
Aspect ratio: 200 %

Project name: Forsmark Site Investigation
Bore hole No.: KFM90D

Azimuth: 0

Inclination: -81

Depth range: 13.582 - 19.401 m




(2 / 2)

Scale: 1/20

Aspect ratio: 200 %

BIPS-images of KFM90E

Project name: Forsmark Site Investigation

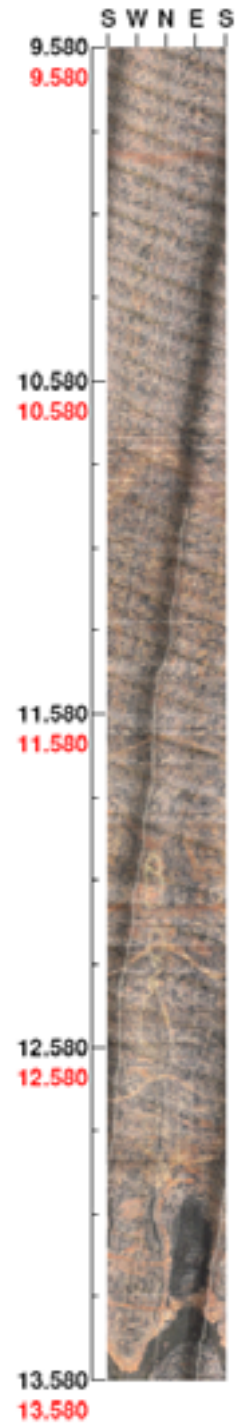
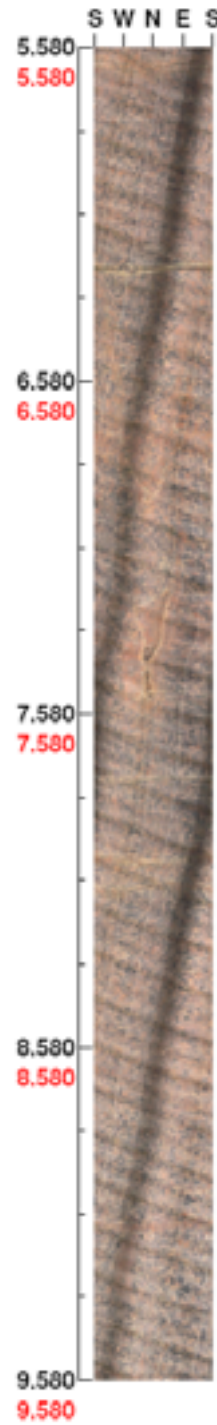
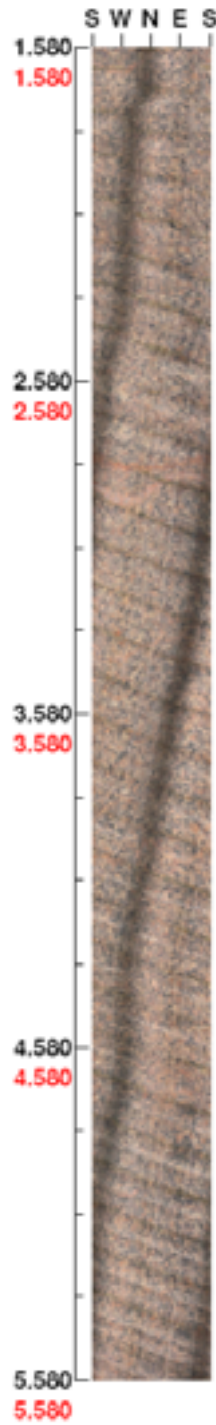
Image file : c:\bips-b~3\kfm90~1\kfm90e.bip
BDT file : c:\bips-b~3\kfm90~1\kfm90e.bdt
Locality : FORSMARK
Bore hole number : KFM90E
Date : 05/11/01
Time : 11:50:00
Depth range : 1.580 - 19.748 m
Azimuth : 0
Inclination : -81
Diameter : 56.0 mm
Magnetic declination : 0.0
Span : 4
Scan interval : 0.25
Scan direction : To bottom
Scale : 1/20
Aspect ratio : 200 %
Pages : 2
Color : 

Project name: Forsmark Site Investigation
Bore hole No.: KFM90E

Azimuth: 0

Inclination: -81

Depth range: 1.580 - 13.580 m



(1 / 2)

Scale: 1/20

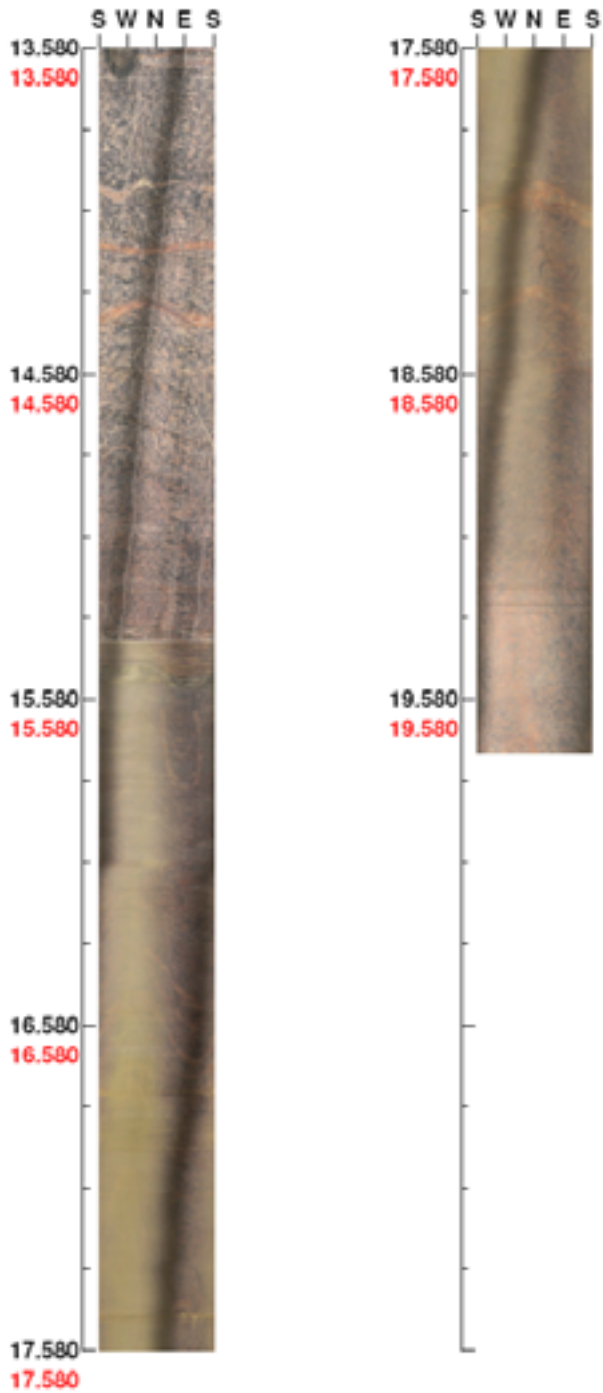
Aspect ratio: 200 %

Project name: Forsmark Site Investigation
Bore hole No.: KFM90E

Azimuth: 0

Inclination: -81

Depth range: 13.580 - 19.748 m




(2 / 2)

Scale: 1/20

Aspect ratio: 200 %

BIPS-images of KFM90F

Project name: Forsmark Site Investigation

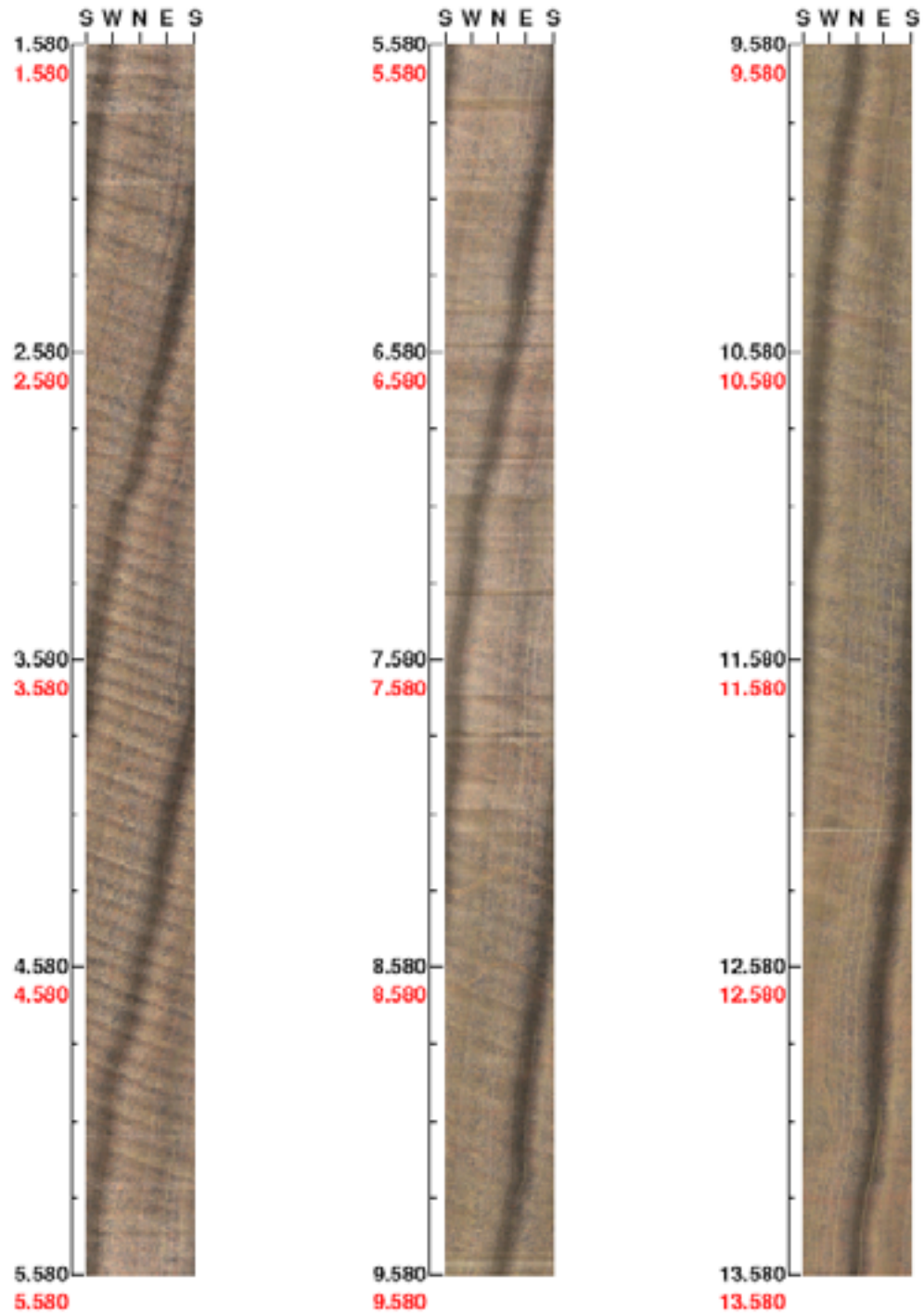
Image file : c:\bips-b~3\kfm90-~1\kfm90f.bip
BDT file : c:\bips-b~3\kfm90-~1\kfm90f.bdt
Locality : FORSMARK
Bore hole number : KFM90F
Date : 05/11/01
Time : 14:05:00
Depth range : 1.580 - 19.765 m
Azimuth : 0
Inclination : -81
Diameter : 56.0 mm
Magnetic declination : 0.0
Span : 4
Scan interval : 0.25
Scan direction : To bottom
Scale : 1/20
Aspect ratio : 200 %
Pages : 2
Color : 

Project name: Forsmark Site Investigation
Bore hole No.: KFM90F

Azimuth: 0

Inclination: -81

Depth range: 1.580 - 13.580 m



(1 / 2)

Scale: 1/20

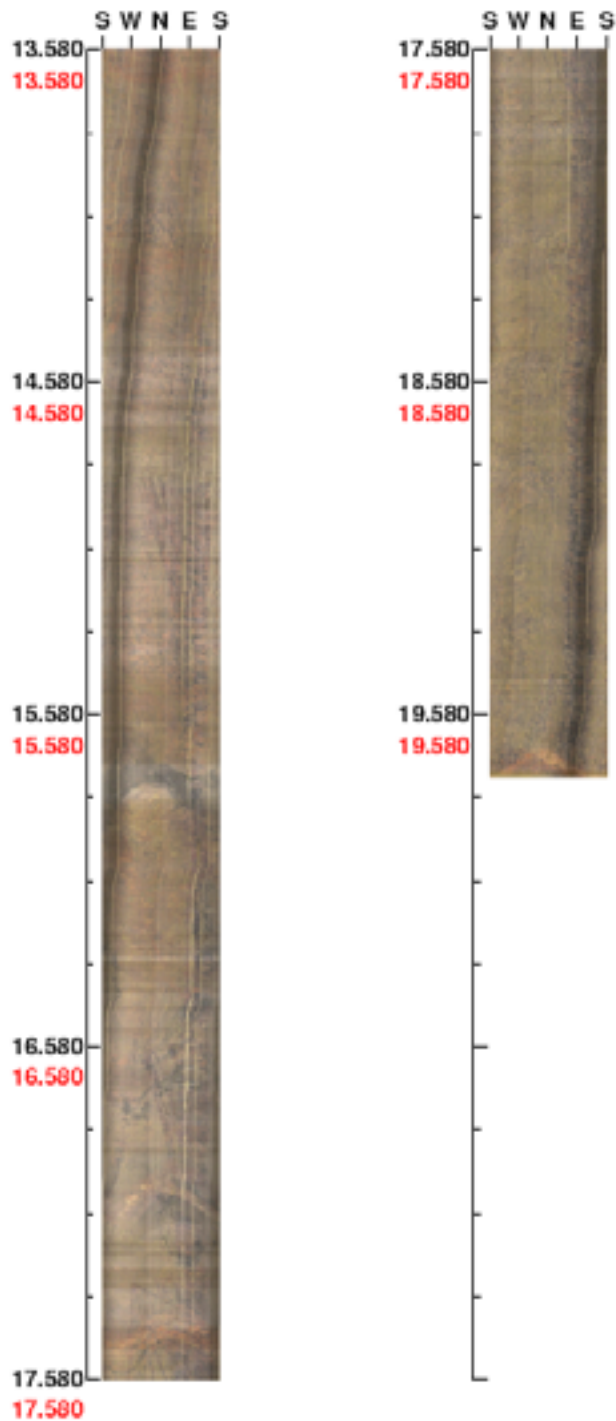
Aspect ratio: 200 %

Project name: Forsmark Site Investigation
Bore hole No.: KFM90F

Azimuth: 0

Inclination: -81

Depth range: 13.580 - 19.765 m



(2 / 2)

Scale: 1/20

Aspect ratio: 200 %

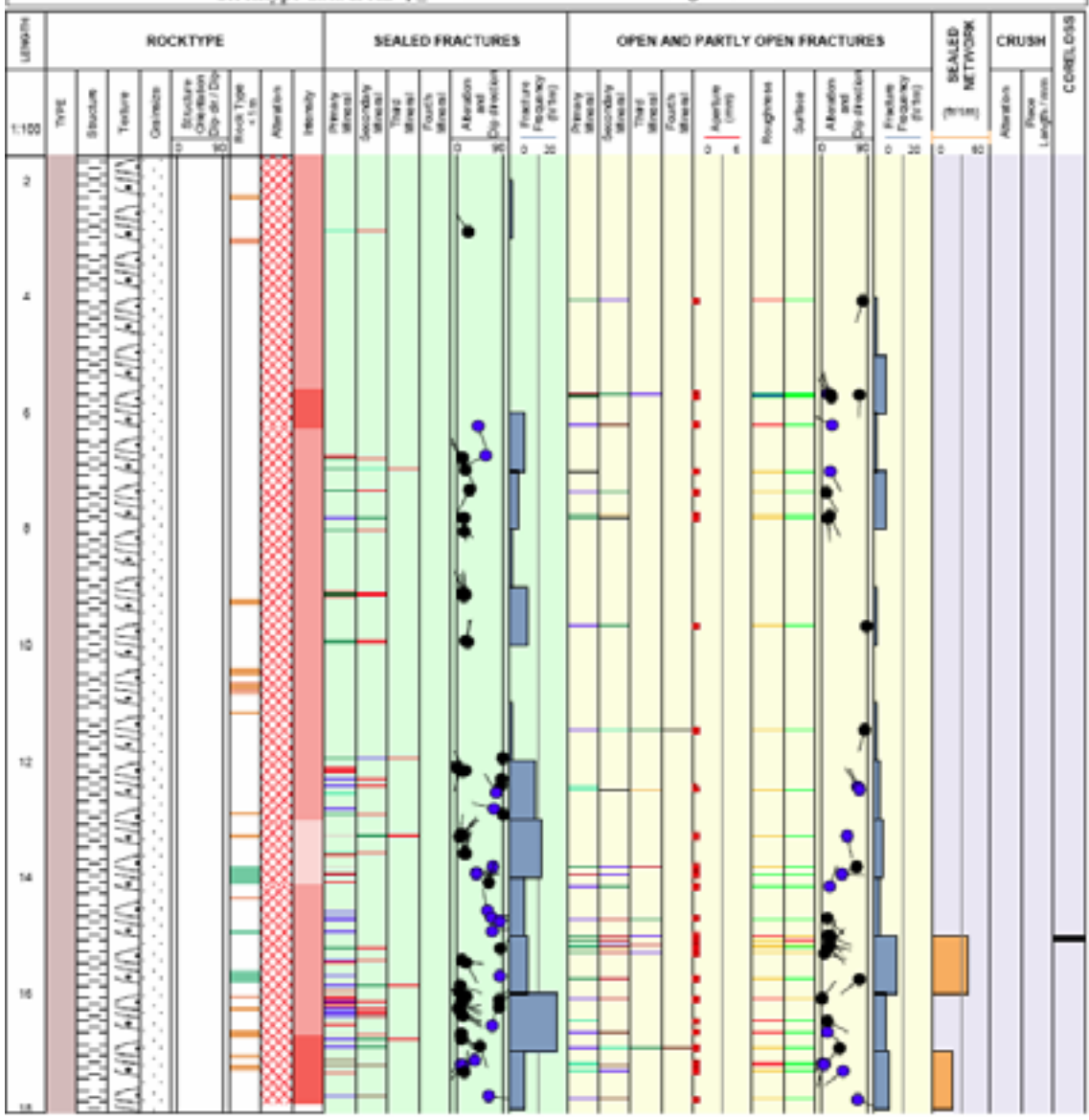
Appendix II

WellCad diagrams of KFM90B-F

Title	LEGEND FOR FORSMARK	KFM90B	Appendix IIa										
	Site FORSMARK Borehole KFM90B Plot Date 2006-05-14 21:24:33 Signed data												
	<table border="0"> <tr> <td> ROCKTYPE FORSMARK Granite, fine- to medium-grained Pegmatite, pegmatitic granite Granitoid, metamorphic Granite, granodiorite and tonalite, metamorphic, fine- to medium-grained Granite, metamorphic, aplitic Granite to granodiorite, metamorphic, medium-grained Granodiorite, metamorphic Tonalite to granodiorite, metamorphic Diorite, quartz diorite and gabbros, metamorphic Ultramafic rock, metamorphic Amphibolite Calc-silicate rock (skarn) Magnetite mineralization associated with calc-silicate rock (skarn) Sulphide mineralization Felsic to intermediate volcanic rock, metamorphic Mafic volcanic rock, metamorphic Sedimentary rock, metamorphic </td> <td> ROCK ALTERATION Oxidized Chloritized Epidotized Weathered Tectonized Sericitized Quartz dissolution Silicification Argillization Albitization Carbonatization Saponitization Steatitization Uralitization Lamproitization Fract zone alteration </td> <td> MINERAL Hematite Calcite Chlorite Unknown Prehnite </td> </tr> <tr> <td> STRUCTURE Cataclastic Schistose Gneissic Mylonitic Ductile Shear Zone Brittle-Ductile Zone Veined Banded Massive Foliated Brecciated Linedated </td> <td> STRUCTURE ORIENTATION Schistose Gneissic Bedded Cataclastic Ductile Shear Zone Brittle-Ductile Shear Zone Veined Banded Linedated Brecciated Mylonitic Foliated </td> <td> ROCK ALTERATION INTENSITY No intensity Faint Weak Medium Strong ROUGHNESS Planar Undulating Stepped Irregular SURFACE Rough Smooth Slickensided </td> <td> FRACTURE ALTERATION Slightly Altered Moderately Altered Highly Altered Completely Altered Gouge Fresh FRACURE DIRECTION STRUCTURE ORIENTATION Dip Direction 0 - 360° 0/000° 270° 90° 180° Dip 0 - 90° </td> </tr> <tr> <td> TEXTURE Hornfelsed Porphyritic Ophitic Equigranular Augen-bearing Unequigranular Metamorphic </td> <td> GRANITE Aphanitic Fine-grained Fine to medium grained Medium to coarse grained Coarse-grained Medium-grained </td> <td> CRUSH ALTERATION Slightly Altered Moderately Altered Highly Altered Completely Altered Gouge Fresh </td> <td></td> </tr> </table>			ROCKTYPE FORSMARK Granite, fine- to medium-grained Pegmatite, pegmatitic granite Granitoid, metamorphic Granite, granodiorite and tonalite, metamorphic, fine- to medium-grained Granite, metamorphic, aplitic Granite to granodiorite, metamorphic, medium-grained Granodiorite, metamorphic Tonalite to granodiorite, metamorphic Diorite, quartz diorite and gabbros, metamorphic Ultramafic rock, metamorphic Amphibolite Calc-silicate rock (skarn) Magnetite mineralization associated with calc-silicate rock (skarn) Sulphide mineralization Felsic to intermediate volcanic rock, metamorphic Mafic volcanic rock, metamorphic Sedimentary rock, metamorphic	ROCK ALTERATION Oxidized Chloritized Epidotized Weathered Tectonized Sericitized Quartz dissolution Silicification Argillization Albitization Carbonatization Saponitization Steatitization Uralitization Lamproitization Fract zone alteration	MINERAL Hematite Calcite Chlorite Unknown Prehnite	STRUCTURE Cataclastic Schistose Gneissic Mylonitic Ductile Shear Zone Brittle-Ductile Zone Veined Banded Massive Foliated Brecciated Linedated	STRUCTURE ORIENTATION Schistose Gneissic Bedded Cataclastic Ductile Shear Zone Brittle-Ductile Shear Zone Veined Banded Linedated Brecciated Mylonitic Foliated	ROCK ALTERATION INTENSITY No intensity Faint Weak Medium Strong ROUGHNESS Planar Undulating Stepped Irregular SURFACE Rough Smooth Slickensided	FRACTURE ALTERATION Slightly Altered Moderately Altered Highly Altered Completely Altered Gouge Fresh FRACURE DIRECTION STRUCTURE ORIENTATION Dip Direction 0 - 360° 0/000° 270° 90° 180° Dip 0 - 90°	TEXTURE Hornfelsed Porphyritic Ophitic Equigranular Augen-bearing Unequigranular Metamorphic	GRANITE Aphanitic Fine-grained Fine to medium grained Medium to coarse grained Coarse-grained Medium-grained	CRUSH ALTERATION Slightly Altered Moderately Altered Highly Altered Completely Altered Gouge Fresh
ROCKTYPE FORSMARK Granite, fine- to medium-grained Pegmatite, pegmatitic granite Granitoid, metamorphic Granite, granodiorite and tonalite, metamorphic, fine- to medium-grained Granite, metamorphic, aplitic Granite to granodiorite, metamorphic, medium-grained Granodiorite, metamorphic Tonalite to granodiorite, metamorphic Diorite, quartz diorite and gabbros, metamorphic Ultramafic rock, metamorphic Amphibolite Calc-silicate rock (skarn) Magnetite mineralization associated with calc-silicate rock (skarn) Sulphide mineralization Felsic to intermediate volcanic rock, metamorphic Mafic volcanic rock, metamorphic Sedimentary rock, metamorphic	ROCK ALTERATION Oxidized Chloritized Epidotized Weathered Tectonized Sericitized Quartz dissolution Silicification Argillization Albitization Carbonatization Saponitization Steatitization Uralitization Lamproitization Fract zone alteration	MINERAL Hematite Calcite Chlorite Unknown Prehnite											
STRUCTURE Cataclastic Schistose Gneissic Mylonitic Ductile Shear Zone Brittle-Ductile Zone Veined Banded Massive Foliated Brecciated Linedated	STRUCTURE ORIENTATION Schistose Gneissic Bedded Cataclastic Ductile Shear Zone Brittle-Ductile Shear Zone Veined Banded Linedated Brecciated Mylonitic Foliated	ROCK ALTERATION INTENSITY No intensity Faint Weak Medium Strong ROUGHNESS Planar Undulating Stepped Irregular SURFACE Rough Smooth Slickensided	FRACTURE ALTERATION Slightly Altered Moderately Altered Highly Altered Completely Altered Gouge Fresh FRACURE DIRECTION STRUCTURE ORIENTATION Dip Direction 0 - 360° 0/000° 270° 90° 180° Dip 0 - 90°										
TEXTURE Hornfelsed Porphyritic Ophitic Equigranular Augen-bearing Unequigranular Metamorphic	GRANITE Aphanitic Fine-grained Fine to medium grained Medium to coarse grained Coarse-grained Medium-grained	CRUSH ALTERATION Slightly Altered Moderately Altered Highly Altered Completely Altered Gouge Fresh											

Title **GEOLOGY IN KFM90B** Appendix:

SKB	Site	FORSMARK	Coordinate System	RT90-RHB70
	Borehole	KFM90B	Northing [m]	6700063.39
	Diameter [mm]	77	Easting [m]	1631008.89
	Length [m]	18.200	Elevation [m.a.s.l.]	-0.54
	Bearing [°]	261.66	Drilling Start Date	2005-10-15 09:10:00
	Inclination [°]	-81.84	Drilling Stop Date	2005-10-18 13:45:00
	Date of coremapping	2005-11-08 16:47:00	Plot Date	2006-04-09 21:14:57
	Rocktype data from	p_rock	Signed data	

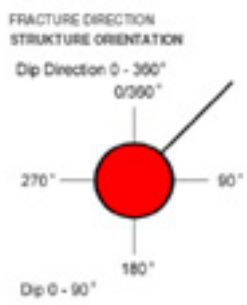


Title LEGEND FOR FORSMARK KFM90C Appendix IIb



Site FORSMARK
 Borehole KFM90C
 Plot Date 2006-05-14 21:24:33
 Signed data

ROCKTYPE FORSMARK		ROCK ALTERATION		MINERAL	
	Granite, fine- to medium-grained		Oxidized		Hematite
	Pegmatite, pegmatitic granite		Chloritized		Calcite
	Granitoid, metamorphic		Epidotized		Chlorite
	Granite, granodiorite and tonalite, metamorphic, fine- to medium-grained		Weathered		Clay Minerals
	Granite, metamorphic, aplitic		Tectorized		Prehnite
	Granite to granodiorite, metamorphic, medium-grained		Sericitized		
	Granodiorite, metamorphic		Quartz dissolution		
	Tonalite to granodiorite, metamorphic		Silicification		
	Diorite, quartz diorite and gabbro, metamorphic		Argillization		
	Ultramafic rock, metamorphic		Albitization		
	Amphibolite		Carbonatization		
	Calc-silicate rock (skarn)		Sauvignitization		
	Magnetite mineralization associated with calc-silicate rock (skarn)		Staurolitization		
	Sulphide mineralization		Uralitization		
	Felsic to intermediate volcanic rock, metamorphic		Laumontitization		
	Mafic volcanic rock, metamorphic		Fract zone alteration		
	Sedimentary rock, metamorphic				
STRUCTURE		ROCK ALTERATION INTENSITY		FRACTURE ALTERATION	
	Cataclastic		No intensity		Fresh
	Schistose		Faint		Gouge
	Gneissic		Weak		Completely Altered
	Mylonitic		Medium		Highly Altered
	Ductile Shear Zone		Strong		Moderately Altered
	Brittle-Ductile Zone				Slightly Altered
	Veined	ROUGHNESS			
	Banded		Planar		
	Massive		Undulating		
	Foliated		Stepped		
	Brecciated		Irregular		
	Lined	SURFACE			
	Porphyritic		Rough		
	Ophitic		Smooth		
	Equigranular		Slickensided		
	Augen-bearing	CRUSH ALTERATION			
	Unequigranular		Slightly Altered		
	Metamorphic		Moderately Altered		
	Aphanitic		Highly Altered		
	Fine-grained		Completely Altered		
	Fine to medium grained		Gouge		
	Medium to coarse grained		Fresh		
	Coarse-grained	FRACTURE DIRECTION			
	Medium-grained	STRUCTURE ORIENTATION			



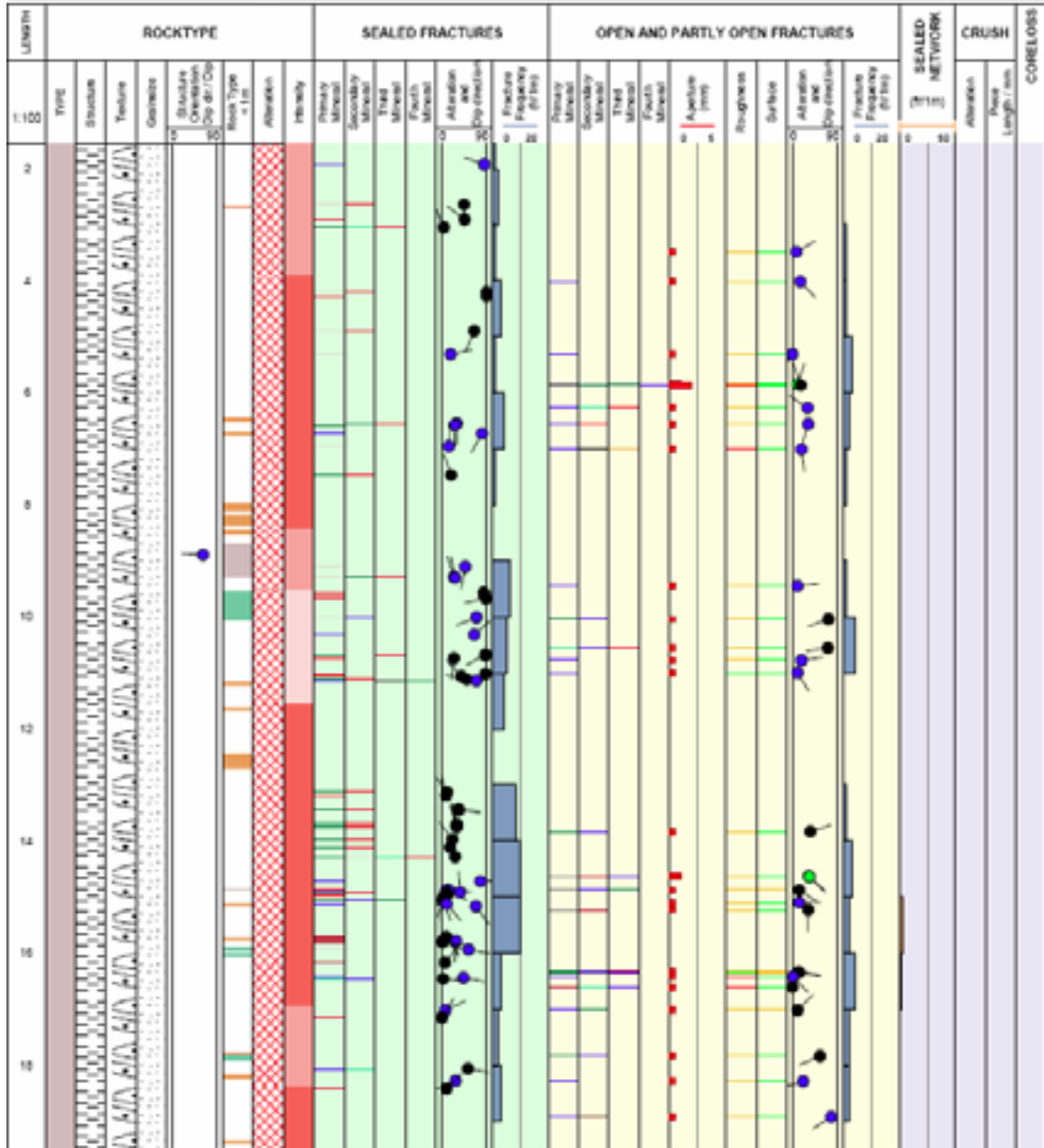
Title **GEOLOGY IN KFM90C**

Appendix:



Site **FORSMARK**
 Borehole **KFM90C**
 Diameter [mm] **56**
 Length [m] **20.000**
 Bearing [°] **262.52**
 Inclination [°] **-81.81**
 Date of coremapping **2005-11-07 17:39:00**
 Rocktype data from **p_rock**

Coordinate System **RT90-RHB70**
 Northing [m] **6700067.08**
 Easting [m] **1631008.67**
 Elevation [m.a.s.L.] **-0.77**
 Drilling Start Date **2005-10-31 14:55:00**
 Drilling Stop Date **2005-11-01 09:10:00**
 Plot Date **2006-04-09 21:14:57**
 Signed data

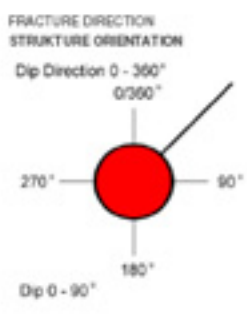


Title **LEGEND FOR FORSMARK** KFM90D Appendix IIc



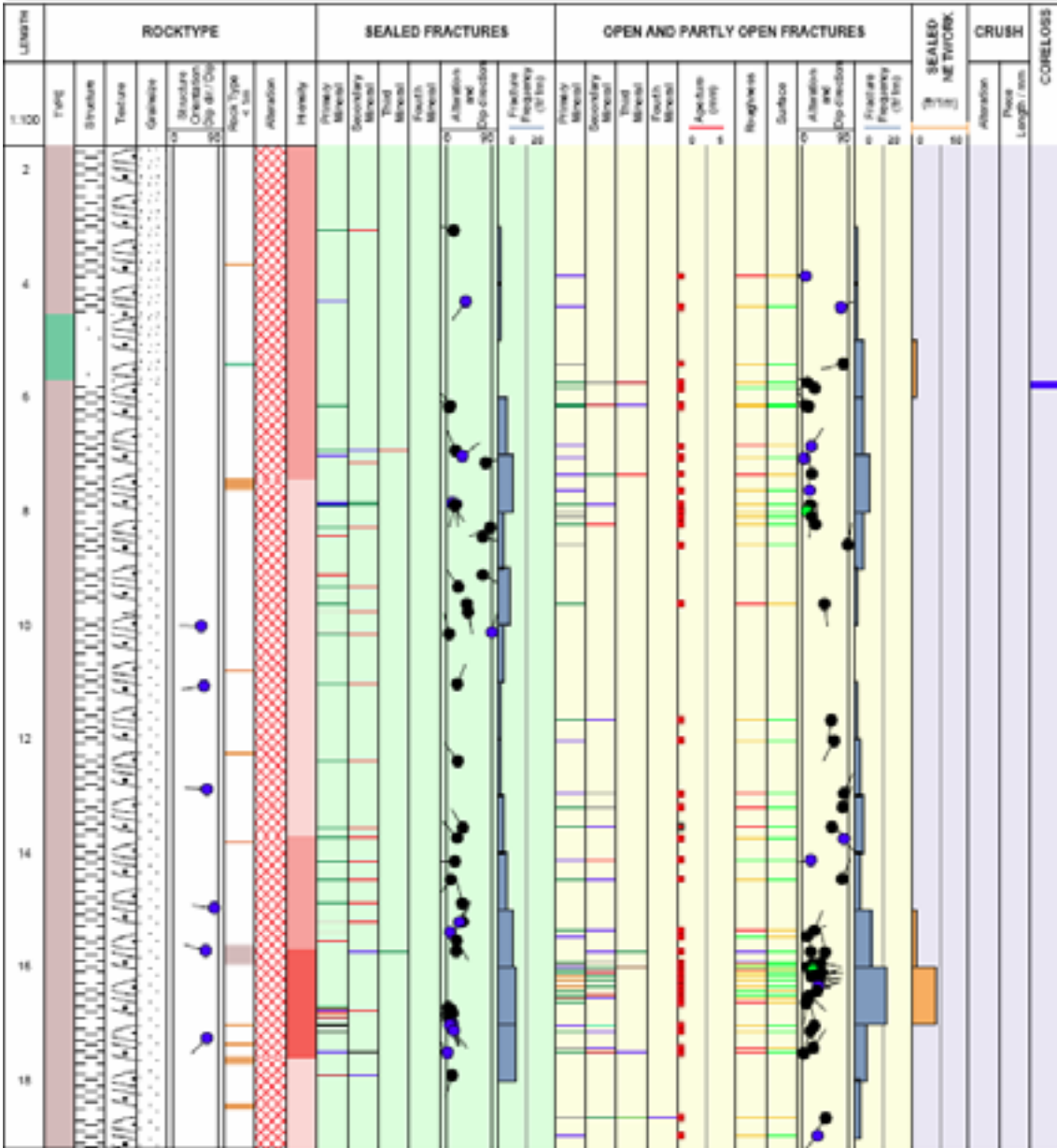
Site FORSMARK
 Borehole KFM90D
 Plot Date 2006-05-14 21:24:33
 Unsigned data

ROCKTYPE FORSMARK		ROCK ALTERATION		MINERAL	
	Granite, fine- to medium-grained		Oxidized		Hematite
	Pegmatite, pegmatitic granite		Chloritized		Calcite
	Granitoid, metamorphic		Epidotized		Chlorite
	Granite, granodiorite and tonalite, metamorphic, fine- to medium-grained		Weathered		Clay Minerals
	Granite, metamorphic, aplitic		Tectonized		Asphalt
	Granite to granodiorite, metamorphic, medium-grained		Sericitized		Iron Hydroxide
	Granodiorite, metamorphic		Quartz dissolution		Oxidized Walls
	Tonalite to granodiorite, metamorphic		Silicification		
	Diorite, quartz diorite and gabbro, metamorphic		Argillization		
	Ultramafic rock, metamorphic		Albitization		
	Amphibolite		Carbonatization		
	Calc-silicate rock (skarn)		Sauuritization		
	Magnetite mineralization associated with calc-silicate rock (skarn)		Stearitization		
	Sulphide mineralization		Uralitization		
	Felsic to intermediate volcanic rock, metamorphic		Laumontitization		
	Mafic volcanic rock, metamorphic		Fract zone alteration		
	Sedimentary rock, metamorphic				
STRUCTURE		ROCK ALTERATION INTENSITY		FRACTURE ALTERATION	
	Cataclastic		No intensity		Fresh
	Schistose		Faint		Gouge
	Gneissic		Weak		Completely Altered
	Mylonitic		Medium		Highly Altered
	Ductile Shear Zone		Strong		Moderately Altered
	Brittle-Ductile Zone				Slightly Altered
	Veined	ROUGHNESS			
	Banded		Planar		
	Massive		Undulating		
	Foliated		Stepped		
	Brecciated		Irregular		
	Lined	SURFACE			
	Horofelsed		Rough		
	Porphyritic		Smooth		
	Ophitic		Slickensided		
	Equigranular	CRUSH ALTERATION			
	Angon-Bearing		Slightly Altered		
	Unequigranular		Moderately Altered		
	Metamorphic		Highly Altered		
	Aphanitic		Completely Altered		
	Fine-grained		Gouge		
	Fine to medium grained		Fresh		
	Medium to coarse grained	FRACTURE DIRECTION			
	Coarse-grained	STRUCTURE ORIENTATION			
	Medium-grained	Dip Direction 0 - 360°			



Title **GEOLOGY IN KFM90D** Appendix:

SKB	Site	FORSMARK	Coordinate System	RT90-RHB70
	Borehole	KFM90D	Northing [m]	6700065.85
	Diameter [mm]	56	Easting [m]	1631010.39
	Length [m]	20.400	Elevation [m.a.s.l.]	-0.35
	Bearing [°]	260.02	Drilling Start Date	2005-10-20 11:05:00
	Inclination [°]	-81.73	Drilling Stop Date	2005-10-20 17:56:00
	Date of coremapping	2005-11-02 13:24:00	Plot Date	2006-04-05 21:14:48
	Rocktype data from	p_rock	Signed data	



Title **LEGEND FOR FORSMARK** KFM90E Appendix II d

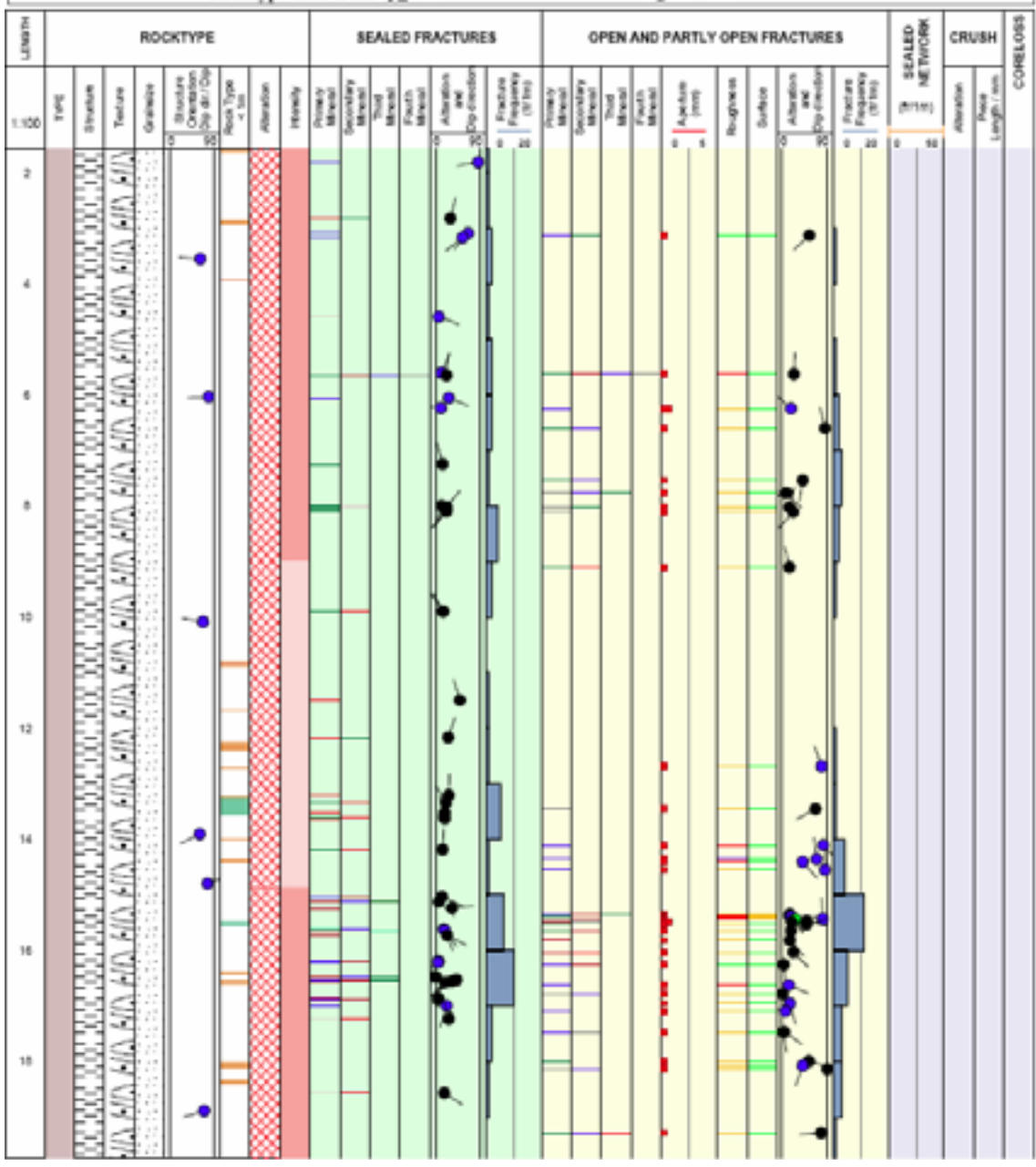


Site FORSMARK
 Borehole KFM90E
 Plot Date 2006-05-14 21:24:33
 Unsigned data

ROCKTYPE FORSMARK		ROCK ALTERATION		MINERAL	
	Granite, fine- to medium-grained		Oxidized		Hematite
	Pegmatite, pegmatitic granite		Chloritized		Calcite
	Granitoid, metamorphic		Epidotized		Chlorite
	Granite, granodiorite and tonalite, metamorphic, fine- to medium-grained		Weathered		Clay Minerals
	Granite, metamorphic, aplitic		Tectonized		
	Granite to granodiorite, metamorphic, medium-grained		Sericitized		
	Granodiorite, metamorphic		Quartz dissolution		
	Tonalite to granodiorite, metamorphic		Silicification		
	Diorite, quartz diorite and gabbro, metamorphic		Argillization		
	Ultramafic rock, metamorphic		Albitization		
	Amphibolite		Carbonatization		
	Calc-silicate rock (skarn)		Sonsworritation		
	Magnetite mineralization associated with calc-silicate rock (skarn)		Steatization		
	Sulphide mineralization		Uralitization		
	Felsic to intermediate volcanic rock, metamorphic		Lammonitization		
	Mafic volcanic rock, metamorphic		Fract zone alteration		
	Sedimentary rock, metamorphic				
STRUCTURE		ROCK ALTERATION INTENSITY		FRACTURE ALTERATION	
	Cataclastic		No intensity		Fresh
	Schistose		Faint		Gouge
	Gneissic		Weak		Completely Altered
	Mylonitic		Medium		Highly Altered
	Ductile Shear Zone		Strong		Moderately Altered
	Brittle-Ductile Zone				Slightly Altered
	Veined				
	Banded				
	Massive				
	Foliated				
	Brecciated				
	Lined				
	Horofolbed				
	Porphyritic				
	Ophitic				
	Equigranular				
	Augen-Bearing				
	Unequigranular				
	Metamorphic				
TEXTURE		ROUGHNESS		FRACTURE DIRECTION	
	Aphanitic		Planar		
	Fine-grained		Undulating		
	Fine to medium grained		Stepped		
	Medium to coarse grained		Irregular		
	Coarse-grained				
	Medium-grained				
GRAN SIZE		SURFACE			
	Aphanitic		Rough		
	Fine-grained		Smooth		
	Fine to medium grained		Slickensided		
	Medium to coarse grained				
	Coarse-grained				
	Medium-grained				
STRUCTURE ORIENTATION		CRUSH ALTERATION			
	Cataclastic		Slightly Altered		
	Bedded		Moderately Altered		
	Gneissic		Highly Altered		
	Schistose		Completely Altered		
	Brittle-Ductile Shear Zone		Gouge		
	Ductile Shear Zone		Fresh		
	Lined				
	Banded				
	Veined				
	Brecciated				
	Foliated				
	Mylonitic				

Title **GEOLOGY IN KFM90E** Appendix:

SKB	Site	FORSMARK	Coordinate System	RT90-RHB70
	Borehole	KFM90E	Northing [m]	6700064.86
	Diameter [mm]	56	Easting [m]	1631008.96
	Length [m]	20.300	Elevation [m.a.s.l.]	-0.42
	Bearing [°]	259.71	Drilling Start Date	2005-10-28 08:00:00
	Inclination [°]	-81.76	Drilling Stop Date	2005-10-28 15:28:00
	Date of coremapping	2005-11-03 13:52:00	Plot Date	2006-04-05 21:14:48
	Rocktype data from	p_rock	Signed data	



Title **LEGEND FOR FORSMARK** KFM90F Appendix IIe

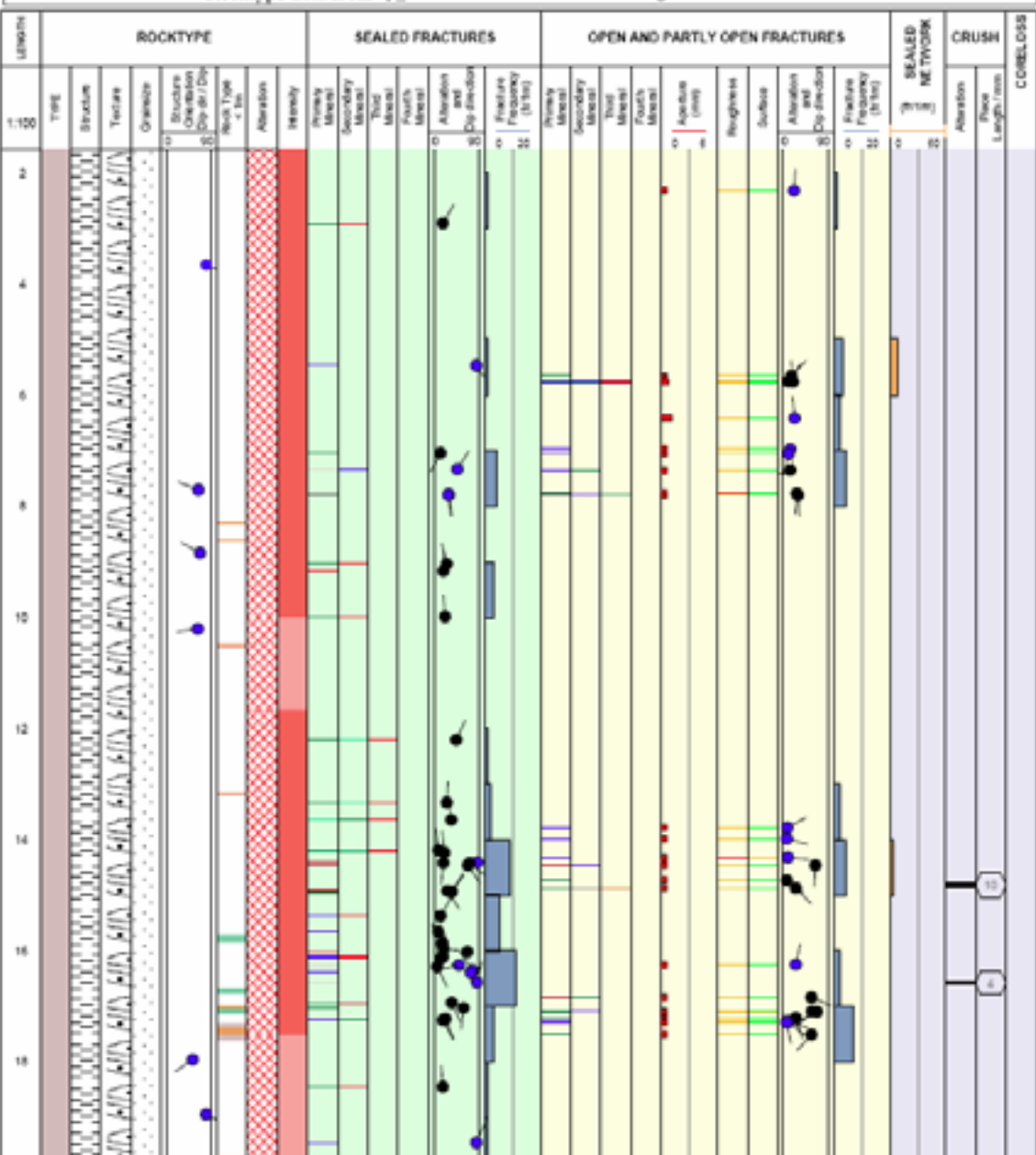


Site FORSMARK
 Borehole KFM90F
 Plot Date 2006-05-14 21:24:33
 Unsigned data

ROCKTYPE FORSMARK		ROCK ALTERATION		MINERAL	
	Granite, fine- to medium-grained		Oxidized		Fluorite
	Pegmatite, pegmatitic granite		Chloritized		Hematite
	Granitoid, metamorphic		Epidotized		Calcite
	Granite, granodiorite and tonalite, metamorphic, fine- to medium-grained		Weathered		Chlorite
	Granite, metamorphic, aplitic		Tectonized		
	Granite to granodiorite, metamorphic, medium-grained		Sericitized		
	Granodiorite, metamorphic		Quartz dissolution		
	Tonalite to granodiorite, metamorphic		Silicification		
	Diorite, quartz diorite and gabbro, metamorphic		Argillization		
	Ultramafic rock, metamorphic		Albitization		
	Amphibolite		Carbonatization		
	Calc-silicate rock (skarn)		Sonswurization		
	Magnetite mineralization associated with calc-silicate rock (skarn)		Steatization		
	Sulphide mineralization		Uralitization		
	Felsic to intermediate volcanic rock, metamorphic		Lammonitization		
	Mafic volcanic rock, metamorphic		Fract zone alteration		
	Sedimentary rock, metamorphic				
STRUCTURE		ROCK ALTERATION INTENSITY		FRACTURE ALTERATION	
	Cataclastic		No intensity		Fresh
	Schistose		Faint		Gouge
	Gneissic		Weak		Completely Altered
	Mylonitic		Medium		Highly Altered
	Ductile Shear Zone		Strong		Moderately Altered
	Brittle-Ductile Zone				Slightly Altered
	Veined	ROUGHNESS			
	Banded		Planar		
	Massive		Undulating		
	Foliated		Stepped		
	Brecciated		Irregular		
	Lineated				
	Textured	SURFACE			
	Horofolbed		Rough		
	Porphyritic		Smooth		
	Ophitic		Slickensided		
	Equigranular	CRUSH ALTERATION			
	Augen-bearing		Slightly Altered		
	Unequigranular		Moderately Altered		
	Metamorphic		Highly Altered		
	Granite		Completely Altered		
	Aphanitic		Gouge		
	Fine-grained		Fresh		
	Fine to medium grained	FRACTURE DIRECTION			
	Medium to coarse grained	STRUCTURE ORIENTATION			
	Coarse-grained	Dip Direction 0 - 360°			
	Medium-grained	Dip 0 - 90°			

Title **GEOLOGY IN KFM90F** Appendix:

SKB	Site	FORSMARK	Coordinate System	RT90.RHB70
	Borehole	KFM90F	Northing [m]	6700065.46
	Diameter [mm]	56	Easting [m]	1631008.08
	Length [m]	20.100	Elevation [m.a.s.l.]	-0.61
	Bearing [°]	261.42	Drilling Start Date	2005-10-25 14:08:00
	Inclination [°]	-81.72	Drilling Stop Date	2005-10-25 18:25:00
	Date of coremapping	2005-11-07 11:06:00	Plot Date	2006-04-05 21:14:48
	Rocktype data from	p_rock	Signed data	



Appendix III

Indata: Borehole length, orientation and diameter

Borehole Direction T - Surveying: Borehole direction

KFM90B, 2005-10-25 09:00:00

Length (m)	Bearing (degrees)	Inclination (degrees)	Bearing Err (degrees)	Inclination Err (degrees)	Magnetic Bearing (degrees)	In Use Flag	Coord System
0.00	261.6626	-81.8535	0.2000	0.2000		*	RT90-RHB70

Printout from SICADA 2005-12-20 09:16:01.

Hole Diam T - Drilling: Borehole diameter

KFM90B, 2005-10-15 09:10:00 - 2005-10-18 13:45:00 (0.000 - 18.200 m)

Sub Secup (m)	Sub Seclow (m)	Hole Diam (m)	Comment
0.000	18.200	0.0770	

Printout from SICADA 2006-05-15 14:31:08.

Borehole Direction T - Surveying: Borehole direction

KFM90C, 2005-11-07 14:25:00

Length (m)	Bearing (degrees)	Inclination (degrees)	Bearing Err (degrees)	Inclination Err (degrees)	Magnetic Bearing (degrees)	In Use Flag	Coord System
0.00	262.5203	-81.8152	0.2000	0.2000		*	RT90-RHB70

Printout from SICADA 2005-12-20 09:16:48.

Hole Diam T - Drilling: Borehole diameter

KFM90C, 2005-10-31 14:55:00 - 2005-11-01 09:10:00 (0.000 - 20.000 m)

Sub Secup (m)	Sub Seclow (m)	Hole Diam (m)	Comment
0.000	20.000	0.0560	

Printout from SICADA 2006-05-15 14:32:37.

Borehole Direction T - Surveying: Borehole direction

KFM90D, 2005-10-25 09:30:00

Length (m)	Bearing (degrees)	Inclination (degrees)	Bearing Err (degrees)	Inclination Err (degrees)	Magnetic Bearing (degrees)	In Use Flag	Coord System
0.00	260.0223	-81.7359	0.2000	0.2000		*	RT90-RHB70

Printout from SICADA 2005-12-20 09:17:53.

Hole Diam T - Drilling: Borehole diameter

KFM90D, 2005-10-20 11:05:00 - 2005-10-20 17:56:00 (0.000 - 20.400 m)

Sub Secup (m)	Sub Seclow (m)	Hole Diam (m)	Comment
0.000	20.400	0.0560	

Printout from SICADA 2006-05-15 14:33:46.

Borehole Direction T - Surveying: Borehole direction

KFM90E, 2005-11-07 14:45:00

Length (m)	Bearing (degrees)	Inclination (degrees)	Bearing Err (degrees)	Inclination Err (degrees)	Magnetic Bearing (degrees)	In Use Flag	Coord System
0.00	259.7087	-81.7712	0.2000	0.2000		*	RT90-RHB70

Printout from SICADA 2005-12-20 09:18:30.

Hole Diam T - Drilling: Borehole diameter

KFM90E, 2005-10-28 08:00:00 - 2005-10-28 15:28:00 (0.000 - 20.300 m)

Sub Secup (m)	Sub Seclow (m)	Hole Diam (m)	Comment
0.000	20.300	0.0560	

Printout from SICADA 2006-05-15 14:35:06.

Borehole Direction T - Surveying: Borehole direction

KFM90F, 2005-10-27 16:50:00

Length (m)	Bearing (degrees)	Inclination (degrees)	Bearing Err (degrees)	Inclination Err (degrees)	Magnetic Bearing (degrees)	In Use Flag	Coord System
0.00	261.4190	-81.7335	0.2000	0.2000		*	RT90-RHB70

Printout from SICADA 2005-12-20 09:19:10.

Hole Diam T - Drilling: Borehole diameter

KFM90F, 2005-10-25 14:08:00 - 2005-10-25 18:25:00 (0.000 - 20.100 m)

Sub Secup (m)	Sub Seclow (m)	Hole Diam (m)	Comment
0.000	20.100	0.0560	

Printout from SICADA 2006-05-15 14:36:14.

Appendix 6

RVS modelling of outcrop AFM001264

Forsmark

Flavio Lanaro

Ulrika Lindberg

Berg Bygg Konsult AB

September 2007

Abstract

This appendix contains the explanation of the steps taken for the construction of the RVS model of outcrop AFM001264 at Forsmark.

The modeling resulted in the identification of several amphibolite veins. Moreover, five borehole sections with increased fracture frequency could be identified. Four of those are gently dipping and one sub-vertical. The report also contains considerations about the fracture sets in the modeling volume, rock foliation and some correlation between the fractures observed in the outcrop and those logged in the boreholes.

Sammanfattning

Rapporten innehåller förklaringen för modelleringsstegen och besluten som ledde till RVS-modellen av häll AFM001264 i Forsmark.

Modelleringen identifierade några amfibolitkroppar i form av ådringar. Dessutom modellerades fem borrhålssektioner med högre sprickfrekvens, av vilka fyra svagt sluttande zoner och en brant stående zon. Rapporten innehåller också tolkningar av sprickset, foliation och några korrelationer mellan sprickor på hällen och i borrhålen.

Contents

1	Introduction	6
1.1	Outcrop AFM001264	7
1.2	Position of the boreholes	7
2	Input data	10
2.1	Lithological map.....	11
2.2	Outcrop fracture mapping.....	12
2.3	Boremap data.....	14
3	Understanding of the outcrop	15
3.1	Possible kinematics	15
3.2	Rock types	19
3.3	Foliation.....	22
3.4	Core loss and crushed rock.....	26
4	RVS visualization and modelling of fractures.....	28
4.1	Fracture sets.....	28
4.1.1	Visualization of fractures on the outcrop	30
4.1.2	Visualization of fractures in the boreholes.....	31
4.2	Modelling of borehole sections with increased fracture frequency in KFM90B-F and correlation with KFM90A	35
5	Conclusions	44
6	References	45

1 Introduction

A thermal experiment was conducted at the location of the outcrop AFM001264 at Forsmark. The experiment required the drilling of six approximately 20 m long sub-vertical boreholes (KFM90A, B, C, D, E and F). A heater was installed in KFM90B, while in all the other boreholes temperature gauges were installed. The heater was set up for about one month during which the temperature variations were measured.

The purpose of the thermal experiment was to evaluate the anisotropy of the rock mass thermal properties (e.g. thermal conductivity). It is believed that any anisotropy of these properties is due to the existence of a pronounced foliation.

The Rock Visualization System (RVS) modeling in this report aims to provide a geological model of the rock volume relevant for the experiment. This model will be used as a basis for interpretation of the thermal anisotropy results. The modeling steps carried out in this report are as follows:

- 1) Determination of the rock occurrences, structure, alteration and foliation along the boreholes;
- 2) Determination of the fracture sets based on the borehole and outcrop mappings;
- 3) Simultaneous visualization of the rock occurrences along the boreholes and of the lithological map of the outcrop;
- 4) Visualizations of the fracture planes intercepting the boreholes and the outcrop, and of foliation according to borehole and core loggings;
- 5) Model fractures that potentially appear simultaneously in several boreholes and/or on the outcrop;
- 6) Model borehole sections with increased fracture frequency.

Additionally, some comments will be made about:

- 7) Correlation between certain rock types and fracture orientation
- 8) Possible correlation between the modeled borehole sections with increased fracture frequency in KFM90B-F and fractures in KFM90A
- 9) Possible kinematical processes of interest for the outcrop.

1.1 Outcrop AFM001264

Figure 1-1 shows a panoramic view of the outcrop for the thermal experiment. The location of borehole KFM90B is approximately at the same position as the shovel in the picture.



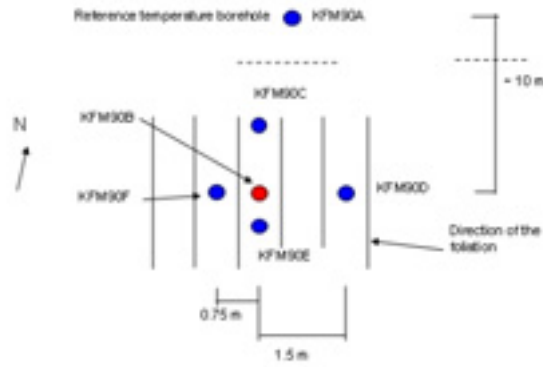
Figure 1-1. Overview of the outcrop AFM001264 at Forsmark as seen from East.

1.2 Position of the boreholes

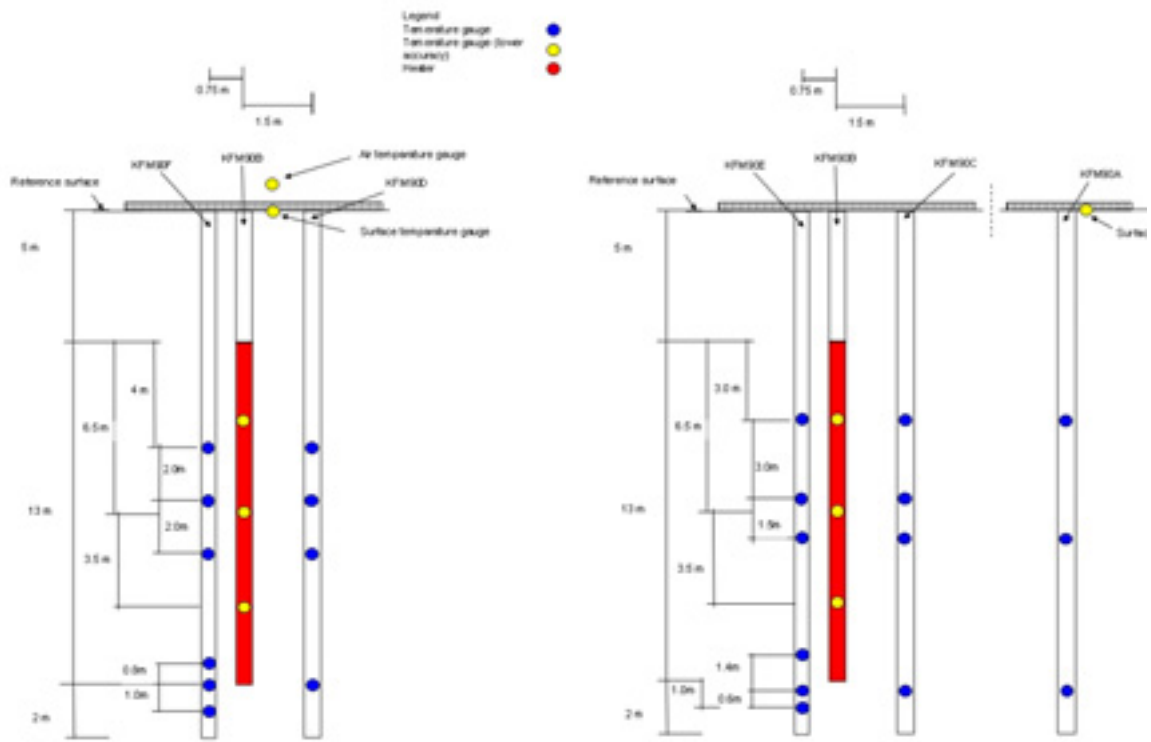
The relative location of the boreholes drilled on the outcrop AFM001264 with the positions of the heater and the temperature gauges are presented in Figure 1-2 and Figure 1-3. The orientations of the boreholes present are listed in Table 1-1.

Table 1-1. Orientation of the boreholes drilled at outcrop AFM001264 at Forsmark

Borehole	Azimuth [°]	Inclination [°]	Diameter [mm]	Length [m]
KFM90A	276	82	56	24.18
KFM90B	262	82	76	18.2
KFM90C	263	82	56	19.6
KFM90D	260	82	56	19.2
KFM90E	260	82	56	19.8
KFM90F	261	82	56	19.8



a)



b)

c)

Figure 1-2. Schematic views from top (a), south (b) and east (c) of the set-up of the thermal experiment (GeoInnova 2006, personal communication).

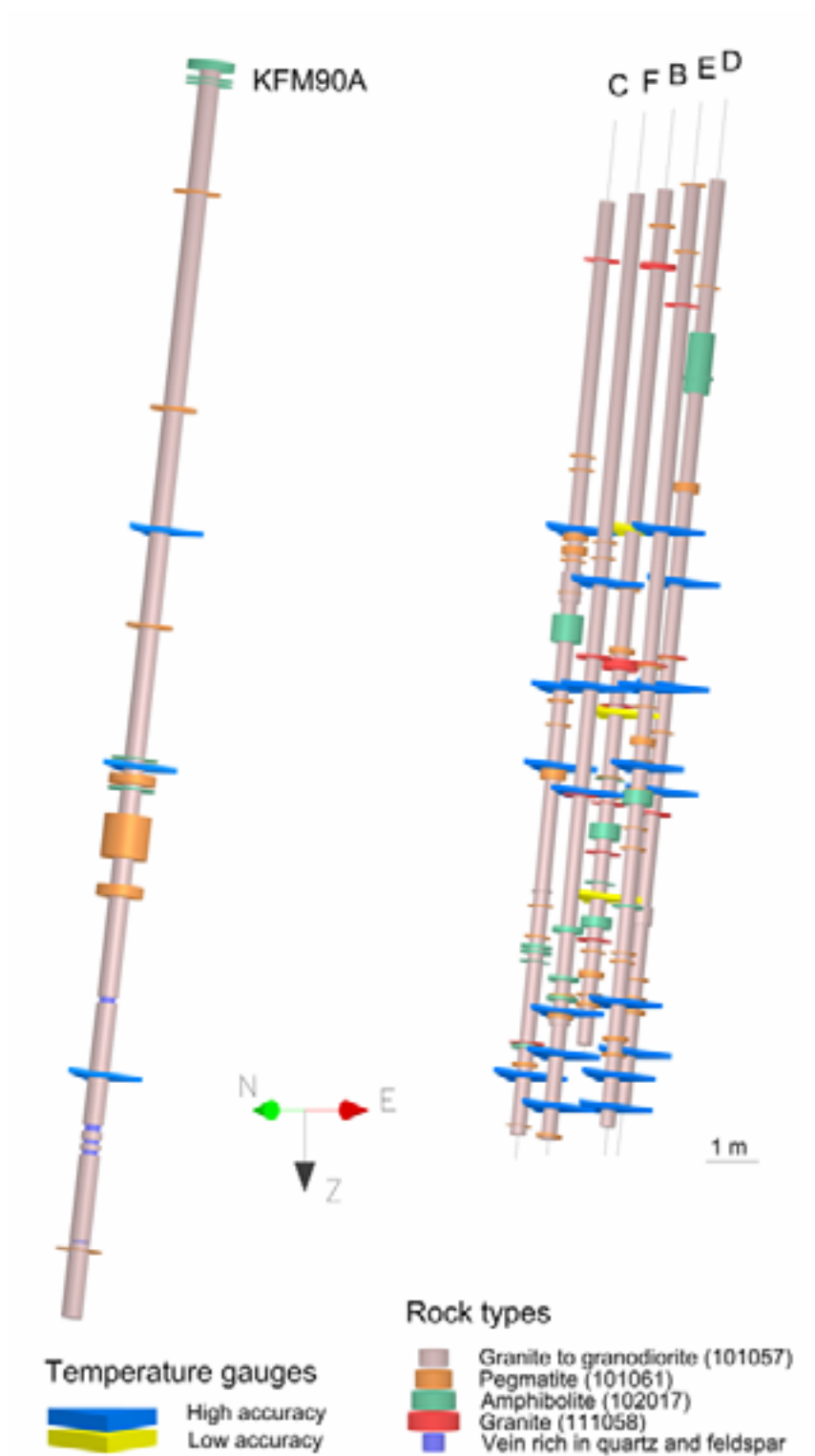


Figure 1-3. RVS visualization of temperature gauges in relation to rock types along KFM90A-F

2 Input data

The geological data available consists of outcrop mapping of the rock types and fractures, borehole core mapping analyzed together with the BIPS pictures of the borehole walls and an overview mapping on KFM90A. For details, see Table 2.1.

Table 2-1. Available data and their usage in this report.

Available data	Reference	Usage
Boremap mapping data from boreholes KFM90B-F object_location.xls p_fract_core.xls p_fract_crush.xls p_fract_sealed_nw.xls p_rock.xls p_rock_alter.xls p_rock_occur.xls p_rock_struct_feat.xls p_rqd.xls p_freq_1m.xls; also 3, 4, 5, 10, 30 m	Data delivery 2006-04-06 Sicada_06_069	Evaluation of rock- and fracture features DIPS determination of fracture sets RVS visualizations
Mapping data from KFM90A KFM90A.xls Snabbkartering av geotermiborrhål, 2005-10-31	Delivered via John Wrafter 2006-05-11 Christin Döse, GEOSIGMA	Evaluation of possible correlation with features in KFM90B-F Estimation of RQD and fracture frequency RVS visualization of rock types, fractures, fracture frequency and RQD
Measuring levels from the thermal experiment beräkningar av mätnivåer060403.xls borrhålsskiss med mätnivåer_060403.xls	Delivered via John Wrafter 2006-04-03	RVS visualization of measuring points Figure in report
Detailed fract_map AFM001264_Fractures.dgn AFM001264_outcrop_mapped.dgn AFM001264_Scanlines.dgn AFM001264_Topography.dgn AFM001264_Fractures.xls AFM001264_Suscept.xls	Delivered via Assen Simeonov 2006-05-04	DIPS determination of fracture sets and RVS visualizations
Bedrock map AFM001264_Bedrock.jpg AFM001264_BEDROCK.dwg	Delivered via Assen Simeonov 2006-05-09 and 2006-05-12	Estimation of orientations of foliation, rock contact, shear- and deformation zone for RVS visualization Figure in report
Outcrop mapping tables EG165_AFM001264_Area_surveying.xls EG170_Line_surveying_LFM000909_LFM000910.xls GE075_Detailed_fracture_mapping_line_LFM000909_LFM000910.xls GE076_Detailed_fracture_mapping_surface_AFM001264.xls	Delivered via Assen Simeonov 2006-05-09 AFM001264_SICADA.zip (Preliminary data at the time of delivery)	DIPS determination of fracture sets and RVS visualization

2.1 Lithological map

The following rock types were identified during the mapping of outcrop AFM001264:

- 1) Granite to granodiorite (code 101057)
- 2) Aplitic granite (code 101058)
- 3) Pegmatite (code 101061)
- 4) Amphibolite (code 102017).

These rock types are shown in the lithological map in



Figure 2-1. Besides the occurring rock types, the direction of the foliation and the position of a deformation zone cutting the outcrop along an approximately North-South direction as well as shear zones were observed.



Figure 2-1. Lithological map of the outcrop AFM001264 /Sicada 2006/.

2.2 Outcrop fracture mapping

Fracture traces and orientation were logged on outcrop AFM001264. Data were provided as tables and design files making it possible to relocate each fracture on the outcrop /preliminary data from Sicada 2006/. Figure 2-2 shows the traces of the measured fractures. Three-dimensional visualizations of the fractures are presented in Section 4.1.1.

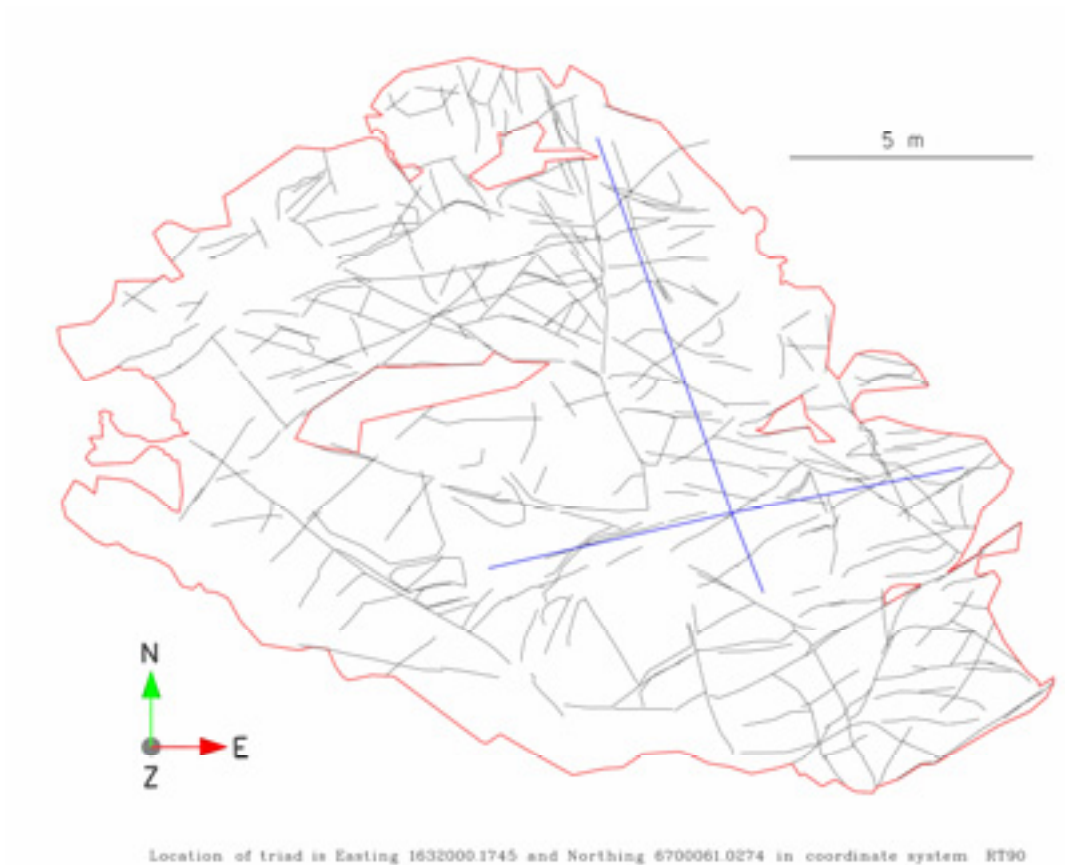


Figure 2-2. Fracture traces (black) mapped on outcrop AFM001264 (truncation length 50 cm) and along two scan lines (truncation length 20 cm).

2.3 Boremap data

Borehole KFM90B-F were mapped by examining the cores and the BIPS pictures taken on their walls /Döse & Samuelsson, 2006a/. The geological parameters described are stored in SKB's database SICADA. Rock types, rock alteration and structural features were studied for all boreholes, by means of both core logging and BIPS pictures. The overview mapping of KFM90A /Döse, 2006/ is not stored in SKB database SICADA. This mapping is used here to study the correlation with the features in boreholes KFM90B-F.

Each fracture observed along the borehole was classified either as “broken” or “unbroken”. The “broken” fractures include all naturally open fractures and those originally sealed that were broken during drilling process. The fractures in the group “broken” were classified into the groups “open” or “sealed” based on the geological evaluation of the core. The visualizations in this appendix are based on the properties of the “open” fractures. The following geological features of the fractures were observed:

- Depth of occurrence
- Mineralization or infilling
- Roughness and surface features
- Alteration conditions
- Orientation (strike and dip)
- Width and aperture

For the analysis of the fracture orientation and sets, the following parameters were also determined:

- Bias correction of the orientation and spacing by Terzaghi's weighting
- Assignment of each fracture to fracture sets.

3 Understanding of the outcrop

3.1 Possible kinematics

The picture in Figure 1-1 seems to indicate that the south-western part of the outcrop presents higher fracture intensity. Moreover, the blocks isolated by the fractures on this side of the outcrop appear to be somehow dislocated and disturbed from their possible initial position. Traces of the possible disturbance can also be noticed from the lithological map that not casually is cut into two parts. In fact, by shifting the blocky part of the outcrop towards west, a better agreement between the rock types North and South of the East-West border can be achieved (

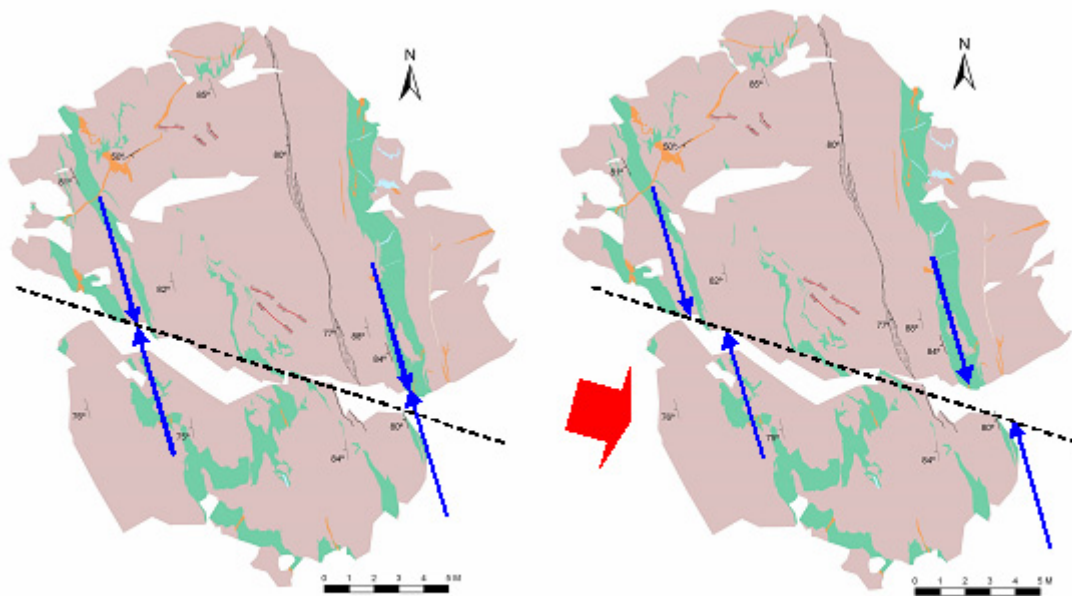


Figure 3-1).

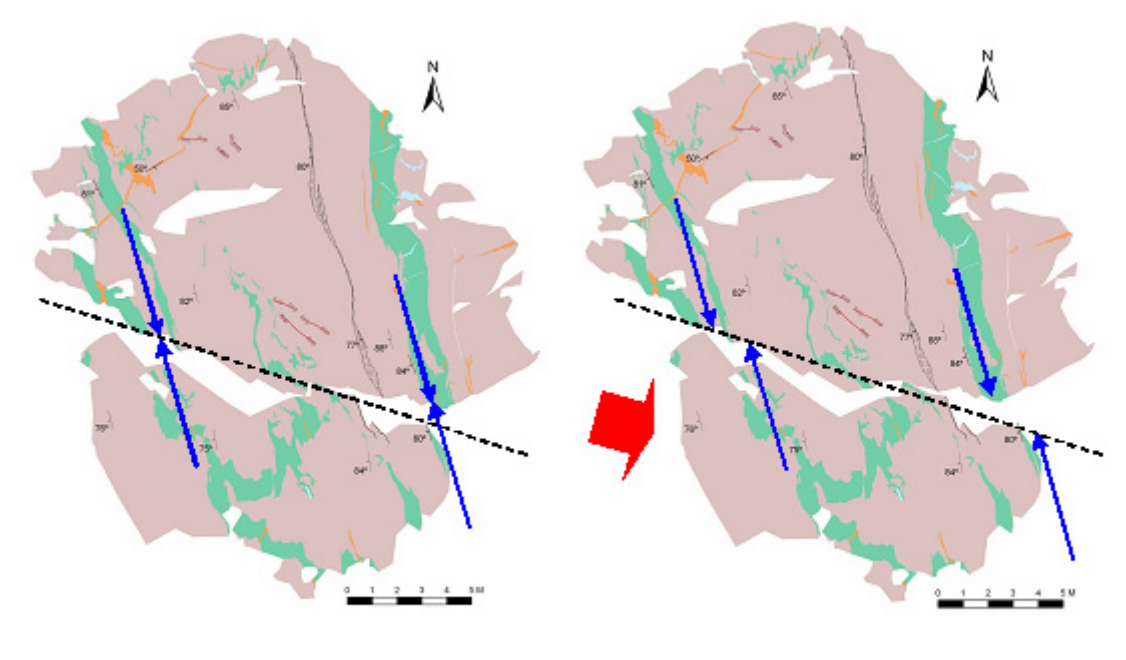


Figure 3-1. Outcrop AFM001264 layout before and after a possible dislocation phenomenon (present appearance on the right).

The dislocation shown in

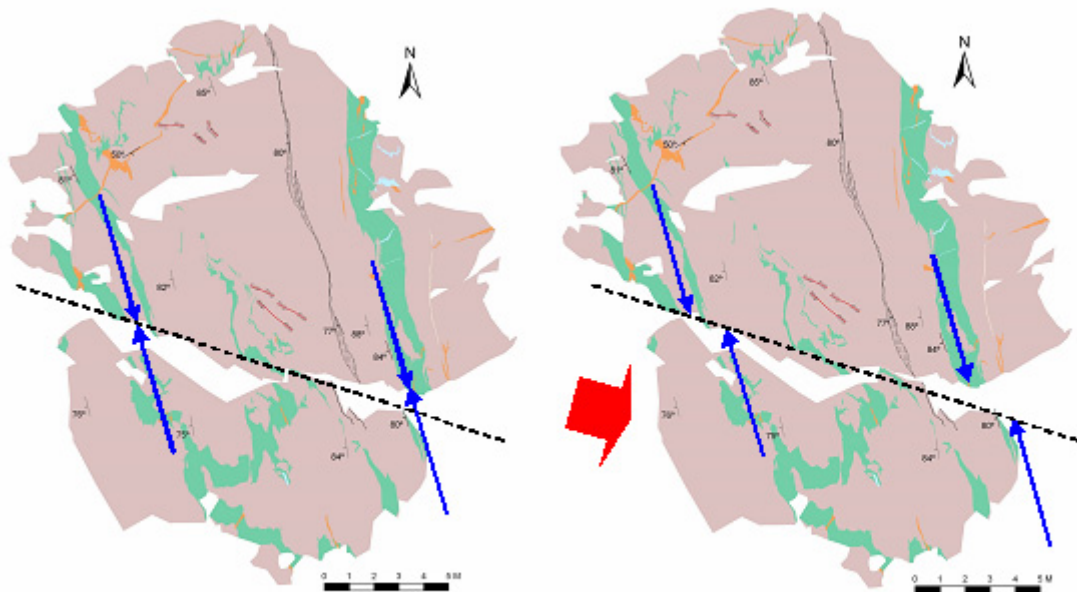


Figure 3-1 could be tentatively explained in two ways:

- 1) Dislocation of blocks due to glacial erosion. The blocks located between the bedrock surface and a sub-horizontal fracture might have been removed to leave the fracture plane exposed (Figure 3-2 b). This hypothesis explains the dislocation observed in

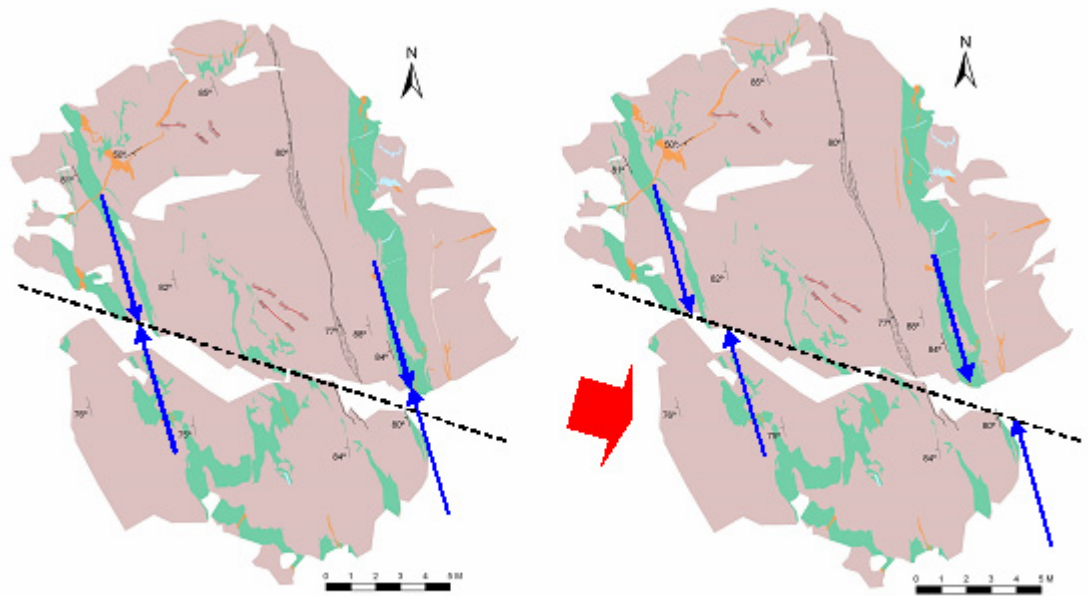


Figure 3-1 as a disturbance of the original positions of the blocks that are dragged and dislocated;

- 2) Dislocation of the outcrop due to faulting. The sharp edge of the hanging wall of the fault might have been removed by glacial erosion (Figure 3-2 c). This hypothesis explains the dislocation observed in

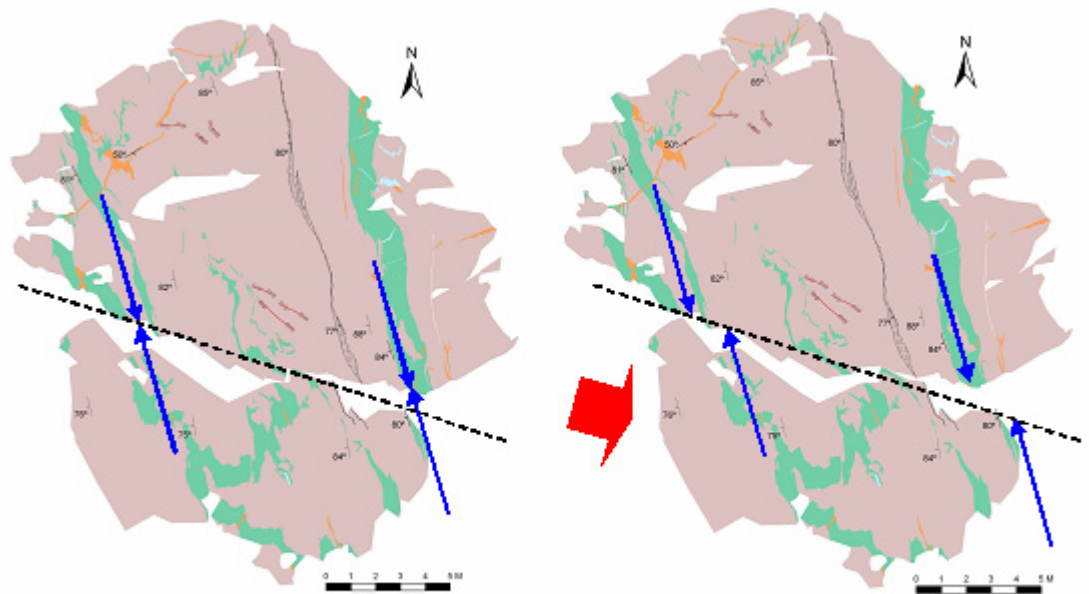


Figure 3-1 as a cinematic process of slip along a plane in East-West direction along a possible gently dipping plane.

The hypothesis 1) might be more plausible because the fracture plane exposed on the outcrop might not be a fault.

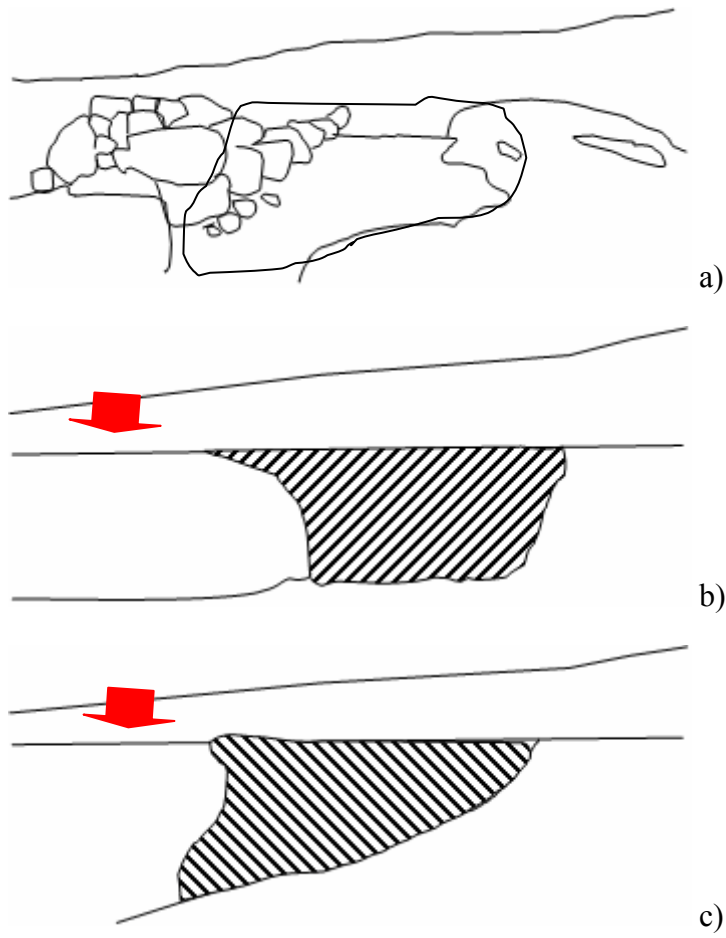


Figure 3-2. Possible explanations of the dislocation phenomenon observed at outcrop AFM001264 in

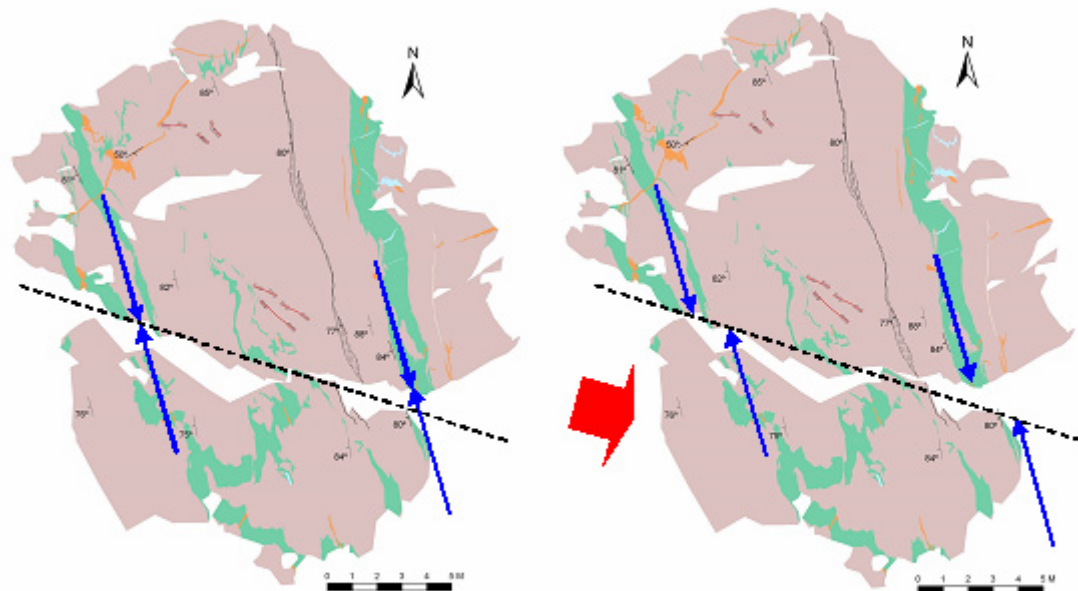


Figure 3-1: a) actual shape of the outcrop; b) glacial removal of blocks above a sub-horizontal fracture and; c) faulting and removal of blocks.

3.2 Rock types

The dominating rock type in KFM90B-F is granite to granodiorite, metamorphic, medium-grained (101057, 92.3% in volume). The structure of this rock type is dominated by foliation. A few brecciated and cataclastic parts were found in KFM90E and KFM90C, respectively. Based on grain size, colour and structure intensity /p_rock properties/, KFM90C, KFM90E and the upper part of KFM90D belong to a more fine-grained, reddish grey/grayish red granite with weaker intensity in foliation.

The dominating upper contact orientation of the amphibolites (102017, 3.4% in volume) strikes ca 160°, and dips ca 70°. The upper amphibolite in KFM90D has a massive structure and includes a section with a brittle-ductile shear zone, possibly connected to the shear zone with similar orientation found in KFM90B. This might also be connected to the shear zones or the deformation zone found on the outcrop map (see section 2.1). The orientation of this deformation zone fits well with the shear zones in the boreholes, whereas the shear zones on the surface mapping strikes more ENE/WNW (the dip is not available). This possible shear zone is modeled in Section 4.2.

Pegmatites (101061, 3.1% in volume) occur in two cases as foliated, in all other cases as massive. Most of the occurrences strike approx. East-West and dip approx. 45° South, but many other orientations are also present.

Granite, fine- to medium grained (111058, 0.6%) occurs as thin bands, all massive except one in KFM90F which is lineated.

Granite, metamorphic, aplitic (101058) and quartz (not specified) identified on the outcrop mapping is not recorded in boreholes KFM90B-F.

The alteration type in KFM90B-F is oxidization varying in intensity: faint, weak and medium.

To get a visual idea of how the amphibolites might appear between the boreholes, the contact orientation of the upper contacts of amphibolites smaller than 1 m was visualised as discs given a colour according to the type of structure (see

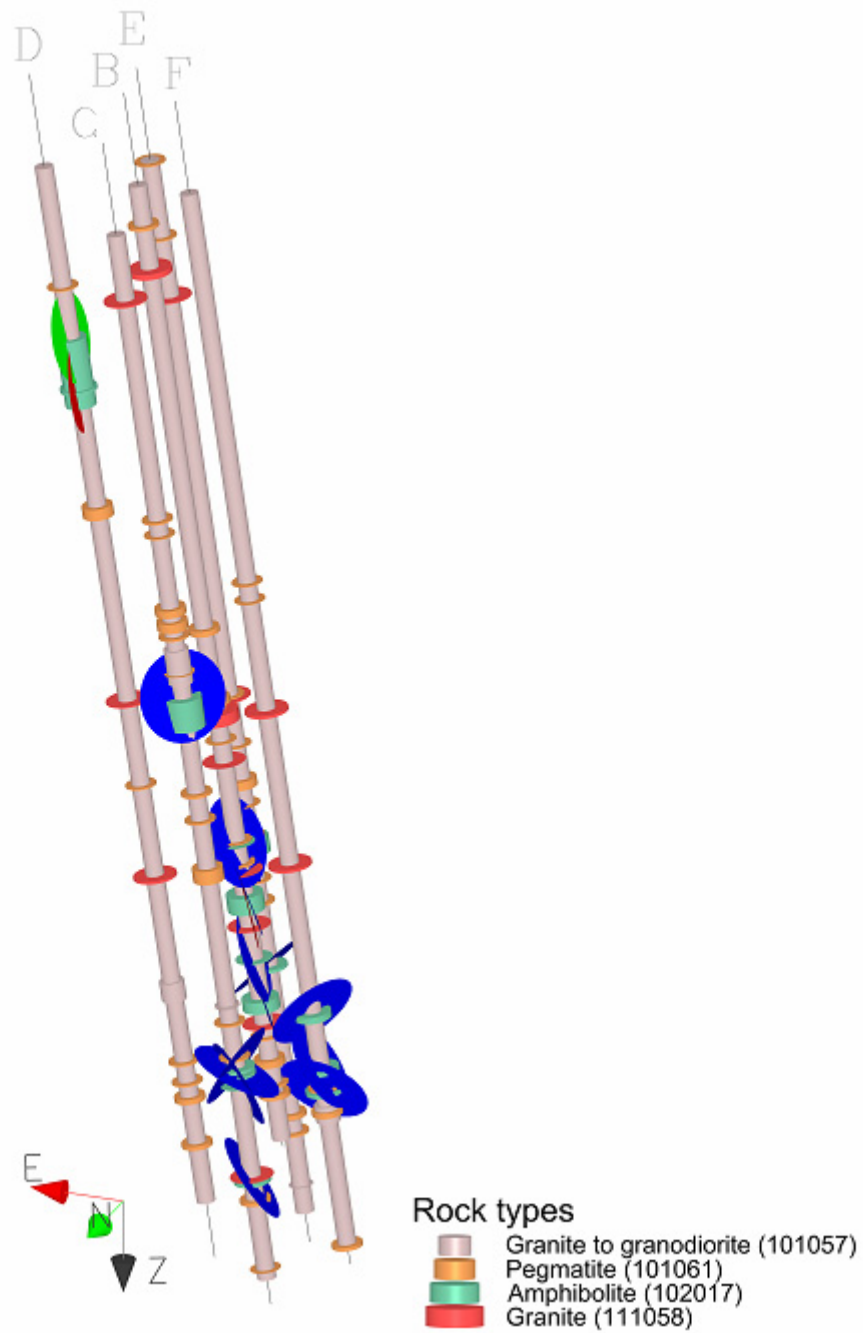


Figure 3-3). The figure illustrates the undulating morphology of amphibolites. Based on the presented parameters, a detailed modelling of the rock volume would be limited to pure guessing in many cases.

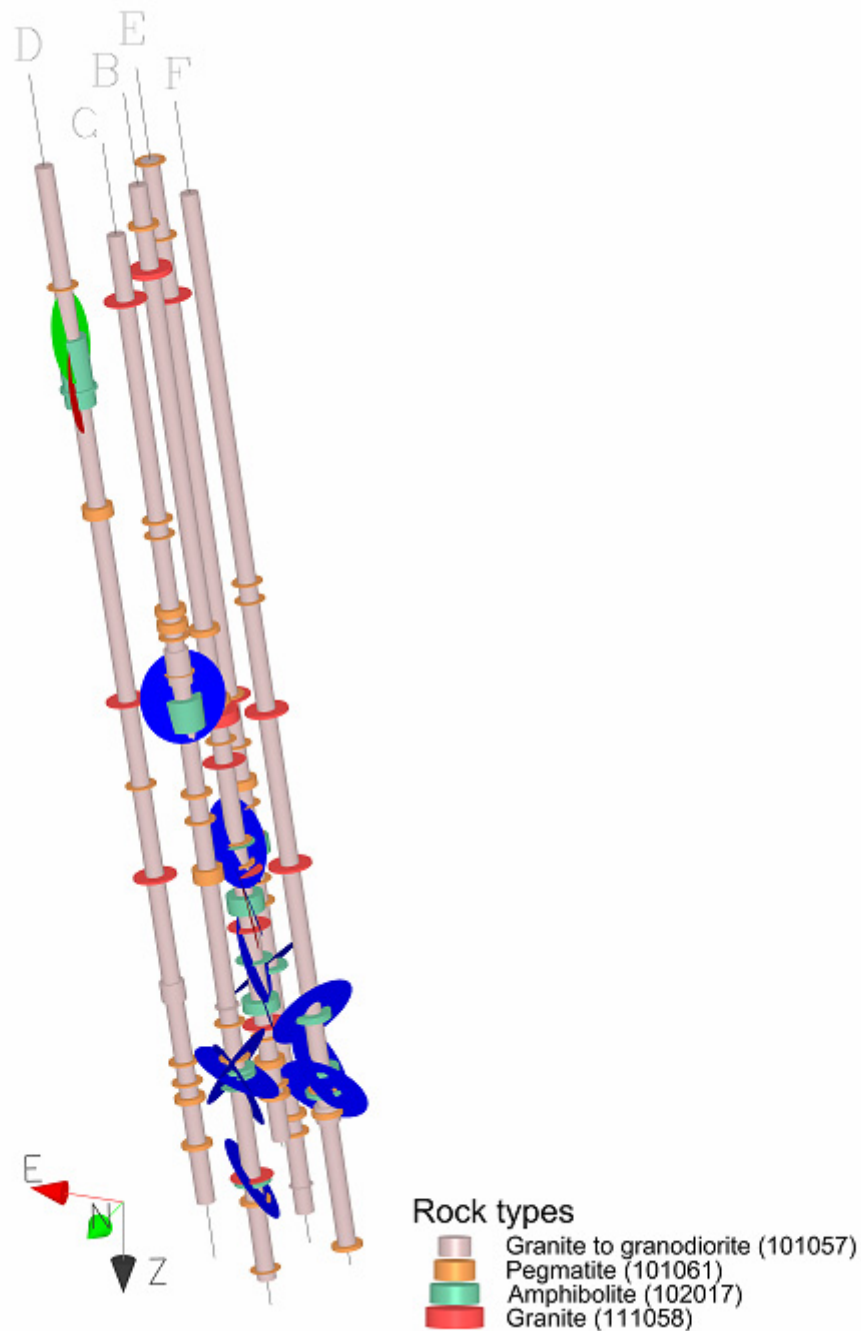


Figure 3-3. Orientation of the upper amphibolite contacts classified based on their structure: foliated (blue), shear zone (red) and massive (green).

In KFM90A, the dominating rock type is granite (91%). 1% of the borehole consists of amphibolites, all biotite-altered, whereof one heavily oxidized. Pegmatites (6%) and quartz-rich veins (2%) are also found. The rock types in KFM90A are presented in Table 3-1.

Table 3-1. Rock types in KFM90A

Rock type	Length of borehole [%]	Occurrences, core length (from – to) [m]	Description
Granite	91	0,17 – 24,18	
Pegmatite	6	2,51 – 2,545 6,66 – 6,72 10,85-10,905 13,73 – 13,915 14,52 – 15,34 15,86 – 16,08 22,89 – 22,9	Undulating contact Undulating contact
Veins rich in quartz and feldspar	2	18,005 – 18,12 20,475 – 20,615 20.765 – 20.845 20.96 – 21.05 22.705 – 22.720 22.730 – 22.75	Fine- to mediumgrained Fine- to mediumgrained Fine- to mediumgrained Fine- to mediumgrained, irregular No feldspar
Amphibolite	1	0,0 – 0,17 0,335 – 0,355 0,43 – 0,45 13,42 – 13,44 13,99 – 14,02	Fine- to mediumgrained Biotite-altered, undulating Biotite-altered, does not crosscut core axis Biotite-altered, schlieren Biotite-altered, heavily oxidized. Lengths insecure. Fractured. Core loss Biotite-altered. Lengths insecure. Heavily fractured

3.3 Foliation

The boreholes were drilled with the intention of being parallel to the foliation (bearing/inclination 260-263°/82°). Therefore, it was difficult to measure the orientation of the foliation with accuracy in Boremap. The orientation information for KFM90B-F as reported to SICADA consists of the foliation diverging from parallel to the boreholes, reported as point-observations. The BOREMAP mapping report /Döse and Samuelsson, 2006/ provide the diverging foliation related to borehole intervals. Visualizations of the different data sets are presented in Figure 3-5.

The foliation in KFM90A is parallel to the borehole (bearing/inclination ~270/82) from 0 – 23.3 m and seems to deviate ca 30 degrees from the borehole axis between 23.3 and 24.18 m.

The dominating orientation of the foliation on the outcrop was estimated from the map



Figure 2-1) to a strike of 167° and a dip of 82° . Orientations from boreholes KFM90B-F and the outcrop are presented in stereogram (Figure 3-4).

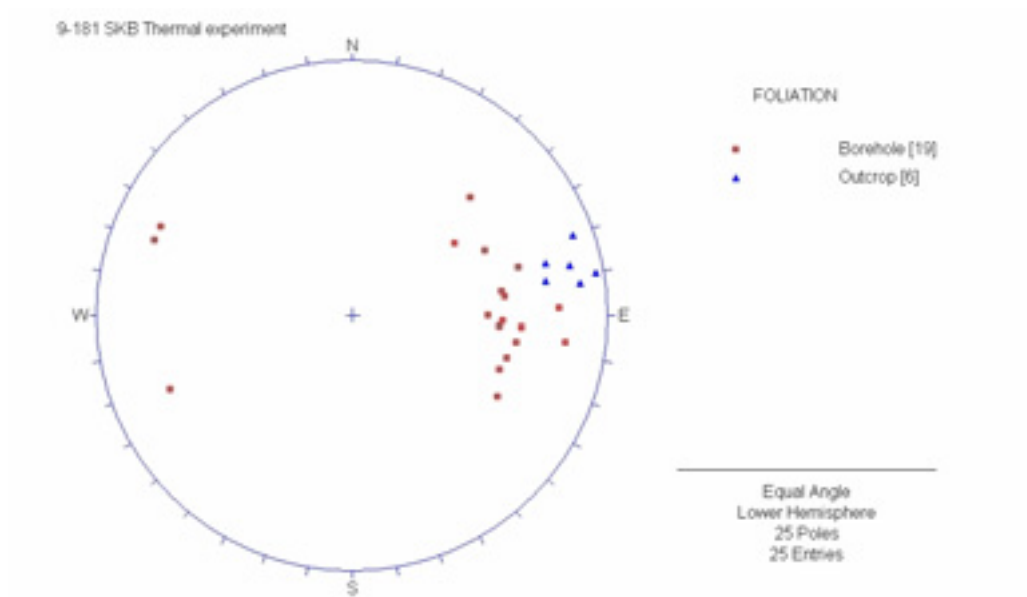
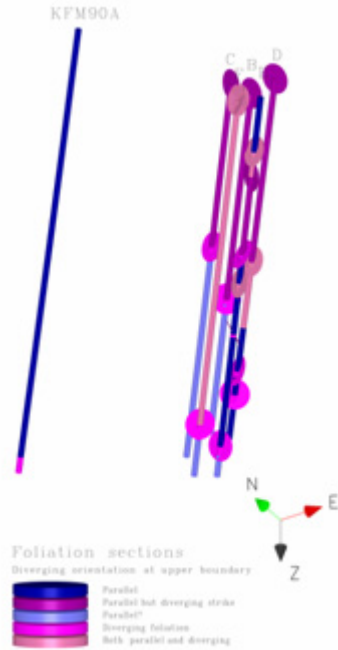
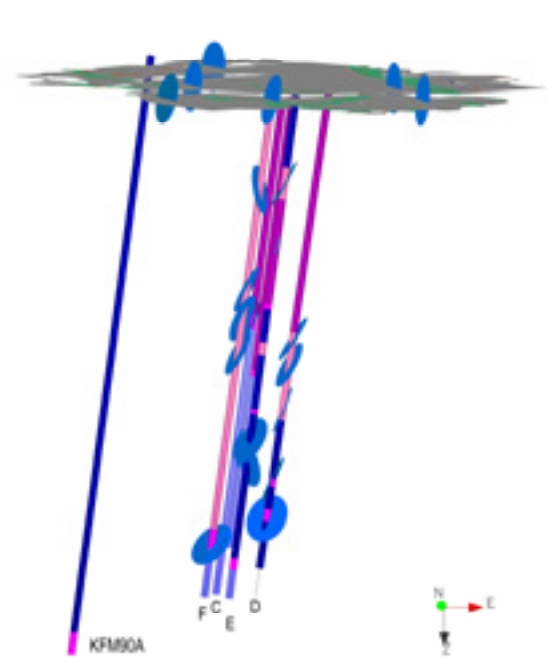


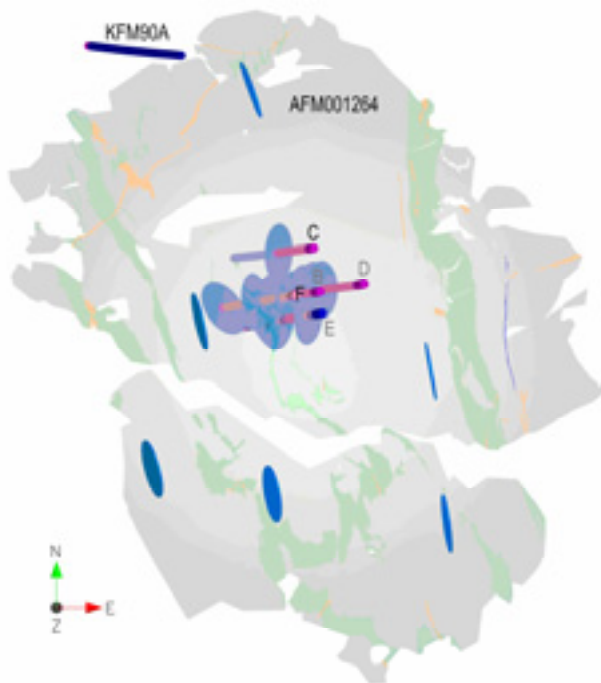
Figure 3-4 Stereoplot of the foliation observed on the outcrop (blue triangles) and in the boreholes KFM90B-F (red squares). The orientations from the boreholes relate to directions of the foliation that diverge from the prominent foliation which is parallel to the borehole axes. Only the diverging foliation is available in SICADA.



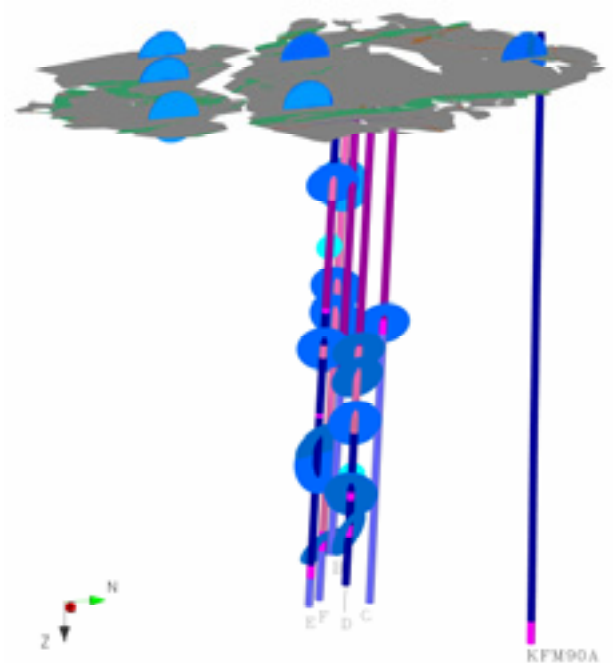
a) Foliation data for borehole KFM90B-F from Boremap mapping report /Döse and Samuelsson, 2006/: intervals of varying degrees of deviation of foliation orientation shown as cylinders. The discs represent the orientations of the same intervals shown at the upper limit of the interval. In KFM90A, the foliation data from /Döse, 2006/.



b) Here, the deviation cylinders from fig a) are shown with the foliation data reported to Sicada as blue discs along borehole KFM90B-F, seen from North. The smaller turquoise discs represent weak intensity as all the other ones are reported as medium. On top, foliation data from the outcrop map shown as blue discs representing orientation.



c) Top view of the same data as in fig. b).



d) The same data as in Fig. b) and c) as seen from East.

Figure 3-5. Visualizations of foliation on outcrop AFM001264 and borehole KFM90A-F according to four different data sets: *p_rock_struct_feat.xls* and *AFM001264_bedrock.jpg* /Sicada, 2006/, /Döse and Samuelsson, 2006/ and /Döse, 2006/.

3.4 Core loss and crushed rock

Boreholes KFM90B-F have an average frequency of “broken” fractures of about 2 fractures/m, which is rather low. However, the fracture frequency is not constant but varies with depth. Two high frequency intervals can be observed between 5 and 8 m and between 14 and 17 m from the surface (Figure 3-6). At these locations, core loss, crush rock and low RQD (percentage of total length of core with rock pieces longer than 100 mm) were also observed (Table 3-2 and Figure 3-6). This indicates the presence of two structural features that will be studied in Section 4.2.

Table 3-2. Core loss, crush rock and low RQD along borehole KFM90A-F.

Borehole	Core loss SECUP ¹⁾ [m]	Crush rock SECUP- SELOW ¹⁾ [m]	Crush piece length [mm]	RQD < 40 LENGTH ¹⁾ [m]
KFM90A ²⁾	~7.2 m ~13.4 m			13 – 15 m
KFM90B	~15 m			
KFM90C				
KFM90D	~5.7 m			16-17 m
KFM90E				
KFM90F		14.78-14.85 m 16.55-16.61 m	10 mm 4 mm	

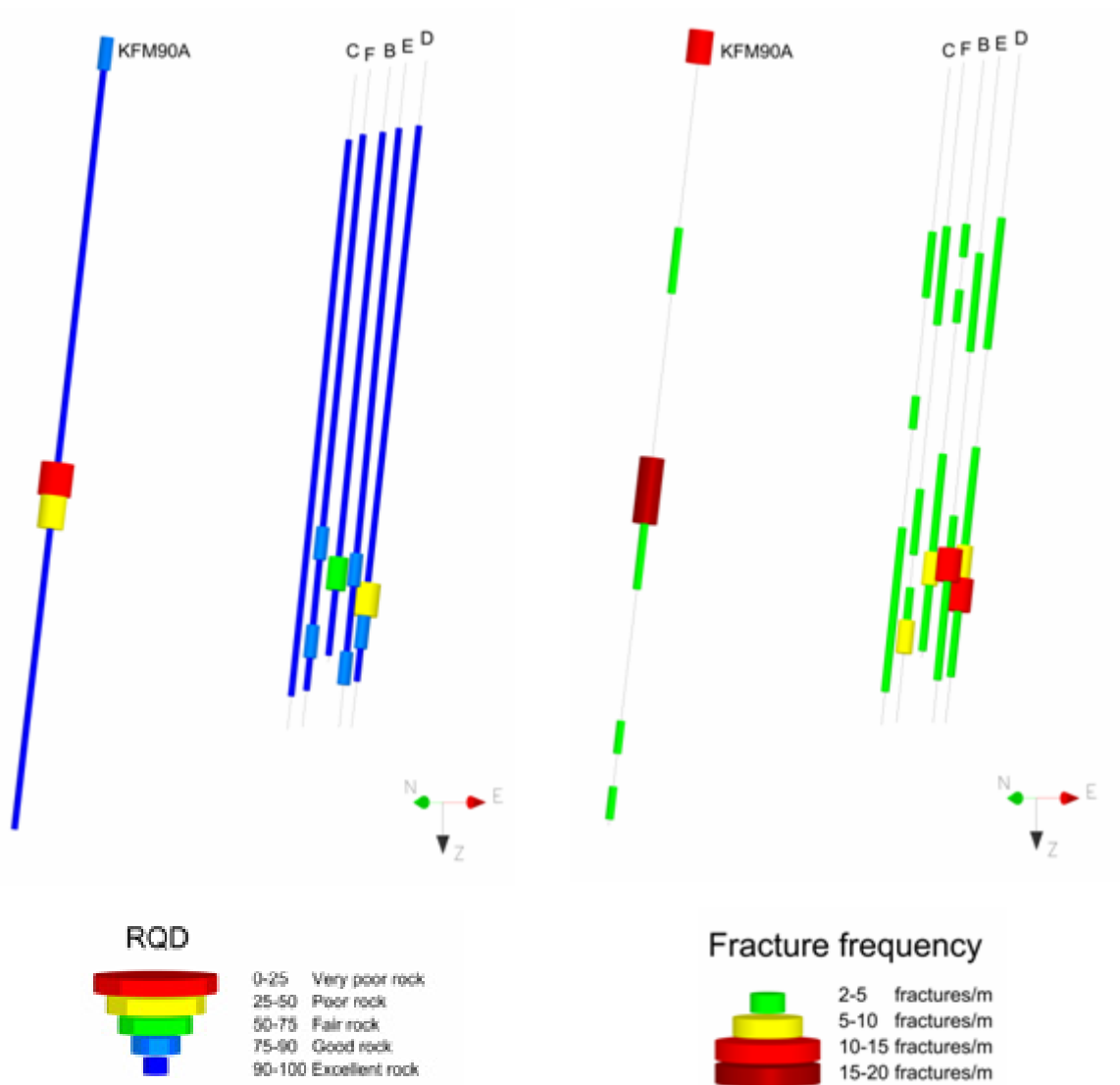
¹⁾ Adjusted SECUP and SELOW in KFM90B-F, borehole length in KFM90A.

²⁾ Estimated from overview mapping.

Fractures along KFM90A were logged with respect to orientation of the core axis, roughness and if they may be artificial. Observations of core loss were made at 7.225-7.235 m and 13.42-13.44m.

Section 0.12-0.23 m is noted as fractured. Section 13.41-14.485 m is heavily fractured, with fractures approximately every 5 cm. This section consists of at least three fracture sets and includes two amphibolites, both heavily fractured.

For visualization and evaluation purposes, the fractures in the fractured sections in KFM90A were extrapolated, as the location of individual fractures in these sections were not logged. Estimations of fracture frequency and RQD are based on the total amount of fractures per 1 meter sections (Figure 3-6).



a) RQD (Rock Quality Designation) values from Sicada for borehole KFM90B-F; estimated RQD values from overview mapping /Döse, 2006/ for borehole KFM90A.

b) Frequency of open fractures from Sicada for borehole KFM90B-F. In KFM90A the fracture frequency was estimated from the overview mapping /Döse, 2006/ and reflects the total amount of fractures.

Figure 3-6. RQD and fracture frequency for borehole sections of 1 m.

4 RVS visualization and modelling of fractures

The RVS visualizations were carried out in order to gain an understanding of fracture patterns and lithologies in the rock volume defined by outcrop AFM001264 and borehole KFM90A-F. Based on fracture properties, some borehole sections with increased fracture frequency could be identified. However, the lithology as well as the foliation could not be modeled with confidence due to the irregularity of the rock occurrences and foliation (see sections 3.2 and 3.3).

The modeling area is 25 m². The RT90-RHB70 coordinates of the modeling box are Easting 1630995 and Northing 6700052 in the lower left corner. The height of the box is 30 m, whereof 25 m is below sea level.

4.1 Fracture sets

Three data sets were available on fractures for the analysis of the site: two from outcrop mapping and one from Boremap logging of the cores (GE041). For the outcrop, data consists of both outcrop mapping (GE076), resulting in 321 identified fractures, and mapping along two scanlines (GE075), resulting in 39 identified fractures from 40 observations. 27 of those observations are identified by 'Area frac nr' as the same fractures in the outcrop mapping. The total actual amount of fractures on the outcrop is 333 (4 fractures did not fit into the fracture sets described below). For 12 of the 27 common fractures, strike and dip do not match between the two mappings. In those cases the orientation from the outcrop mapping is used in the fracture analysis. For borehole KFM90B-F, the 169 broken/open fractures from 'p_fract_core.xls' were selected for analysis: 164 of those was divided into fracture sets. The five fractures that did not fit into the sets were not further considered.

Stereoplots of the DIPS analyses on fractures from outcrop AFM001264 and borehole KFM90B-F are shown in

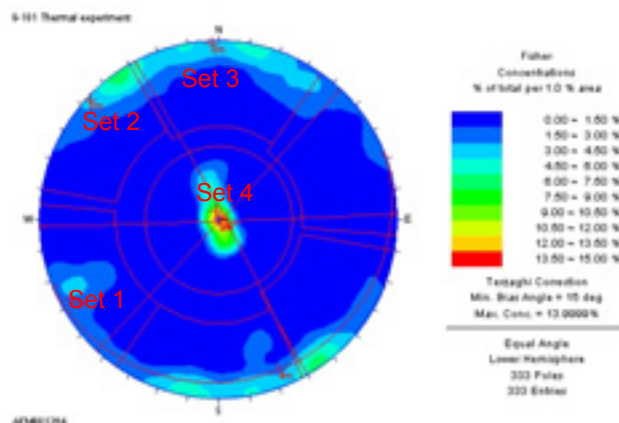


Figure 4-1
and

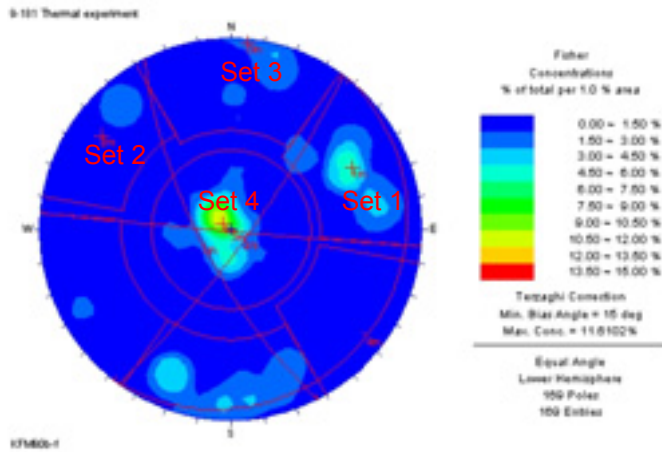


Figure 4-2 , respectively. Terzaghi correction of the orientation data was applied to take into account the sampling bias. Four fracture sets were identified by the fracture analysis (see **Fel! Hittar inte referenskälla.**). Three of them (Set 1, 2 and 3) are sub-vertical while one (Set 4) is sub-horizontal. Sub-vertical Set 1 has an orientation very similar to the orientation of the amphibolite veins and of the fractured borehole section (see Section 3.2). A closer analysis also shows that most of these fractures are located inside the amphibolite veins.

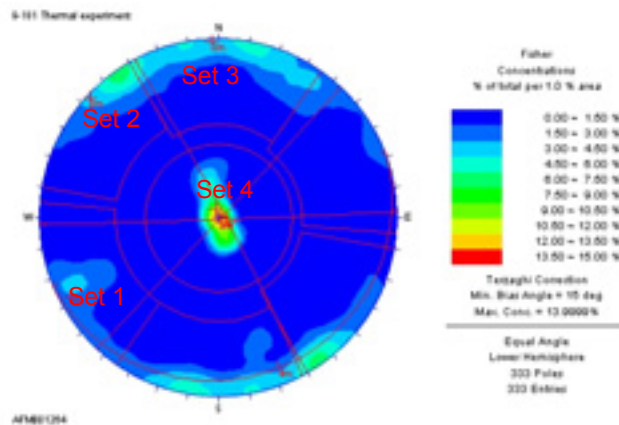


Figure 4-1. Stereonet of the fracture orientation from mapping of outcrop AFM001264 (truncation length 50 cm) and scanlines LFM000909 and LFM000910 (truncation length 20 cm).

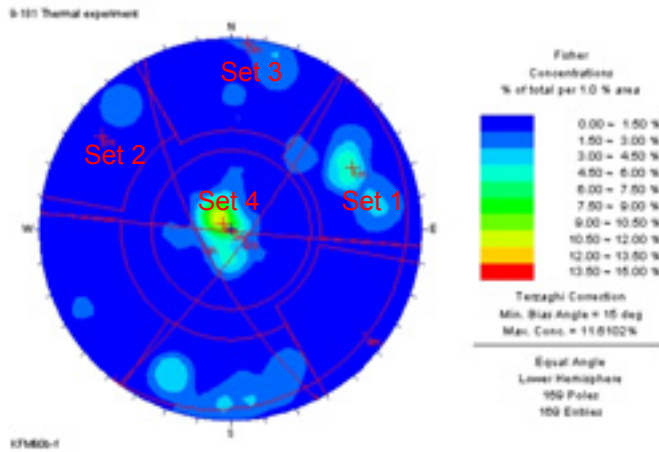


Figure 4-2. Stereoplot of the fracture orientations from Boremap logging of borehole KFM90B-F.

Table 4-1. Fracture sets identified by the fracture analysis of outcrop AFM001264 and borehole KFM90B-F.

Fracture set	Strike [°]	Dip [°]
1	154 ¹⁾ 332 ²⁾ (~152°)	72 ¹⁾ 85 ²⁾ (~90°)
2	043 ¹⁾ 037 ²⁾	89 ¹⁾ 82 ²⁾
3	274 ¹⁾ (~094°) 088 ²⁾	89 ¹⁾ (~90°) 89 ²⁾
4	066 ¹⁾ 046 ²⁾	03 ¹⁾ 06 ²⁾

¹⁾ Weighted mean from outcrop mapping

²⁾ Weighted mean from borehole logging.

4.1.1 Visualization of fractures on the outcrop

The fractures on the outcrop were visualized using the RVS tool “Fracture observations” which allows the user to input one fracture at the time. The observations were given the SKB standard LUT colors of the rock type in which they occur, according to ‘GE076_Detailed_fracture_mapping_surface_AFM001276.xls’. Fractures on the scanlines had no information on rock type available, so they were visualized in blue. Thickness and size of the circle represent the aperture and trace length of the fractures, respectively. The mean position of the fracture was calculated as mean value from the coordinates in “AFM001264_Fractures.xls” originating from the detailed fracture mapping.

The fractures were named according to the fracture set number and mapped fracture number. The rock type was noted in the description column, making it possible to sort the observations either by set number or rock type.

When visualizing the outcrop fractures as discs, the centre position of the disc had to be evaluated based on the few points measured on the fracture traces. This kind of visualization shows that some of the fracture orientations mapped on the outcrop provided visualizations that did not fit well with some of the measured fracture traces.

4.1.2 Visualization of fractures in the boreholes

For KFM90B-F, fracture set information from DIPS analysis was put together with strike, dip and rock type/occurrence (bestrock_code). The dominating fracture mineral (min1_code) was also visualized. Those were imported into RVS as ascii-files set by set; making it possible to visualize the different fracture sets one at the time or together.

The fractures in KFM90A were not mapped using the BOREMAP method. The available data, a traditional mapping of the core, was used to estimate the fractures along this borehole with the purpose to possibly correlate the modeled fracture planes in borehole KFM90B-F along sections with increased fracture frequency in borehole KFM90A. As these fractures were mapped only with consideration to orientation relative to core axis (α -angle), they were visualized perpendicular to the borehole direction as thin cylinders, given the color of the rock type they occur in. As mentioned in Section 3.4, the fractures in the fractured sections were extrapolated (every 2 cm in core section 0.12-0.23 m and every 5 cm in core section 13.41 – 14.485 m).

Fracture set 1

Fracture Set 1 is sub-vertical and striking roughly in north-south direction. Fractures in this set seem to occur uniformly on the outcrop and along the boreholes (Figure 4-3), even considering the sampling bias applied by the boreholes on sub-vertical fractures.

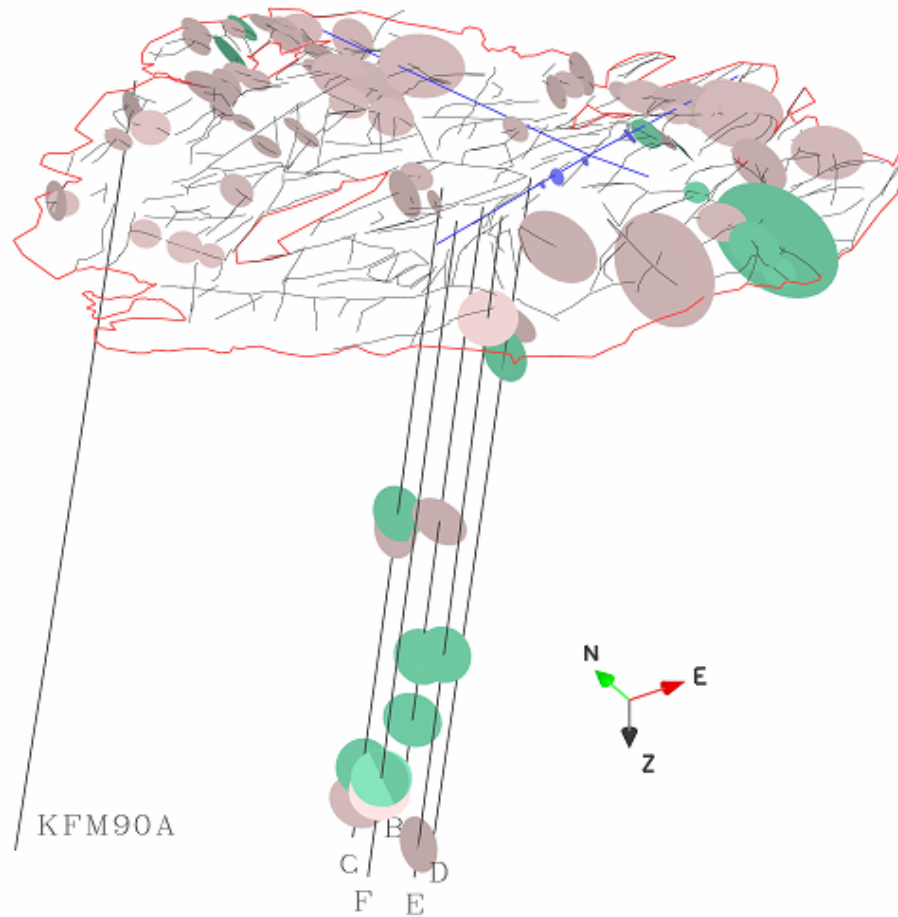


Figure 4-3. Visualization of the fracture planes of Set 1 from outcrop mapping and borehole logging. Outcrop outline (red line), scan lines (blue) and fracture traces (black)

Fracture set 2

Fracture Set 2 appears mainly on the outcrop (Figure 4-4). The fractures in this set are sub-vertical and strike about 45° east.

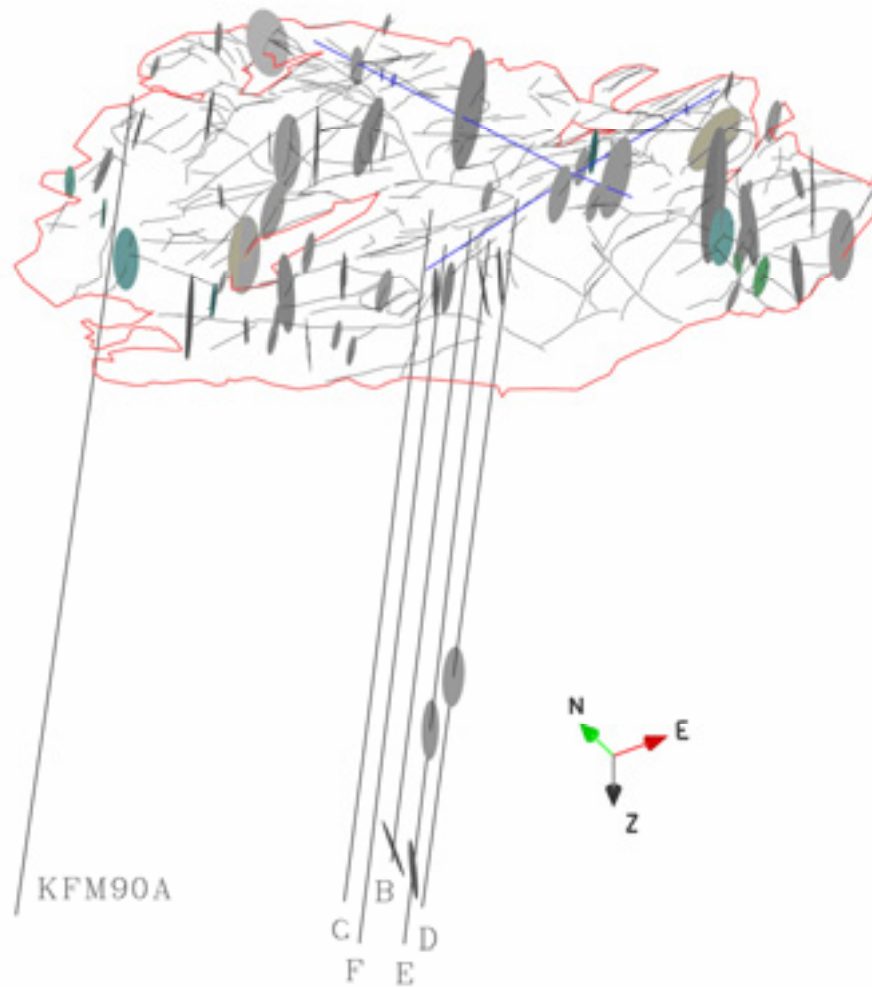


Figure 4-4. Visualization of the fracture planes of Set 2 from outcrop mapping and borehole logging.

Fracture set 3

Fracture set 3 is sub-vertical and strikes east-west. This fracture set occurs rather uniformly on the outcrop but most of the fractures in the boreholes are located around 11-14 m (Figure 4-5).

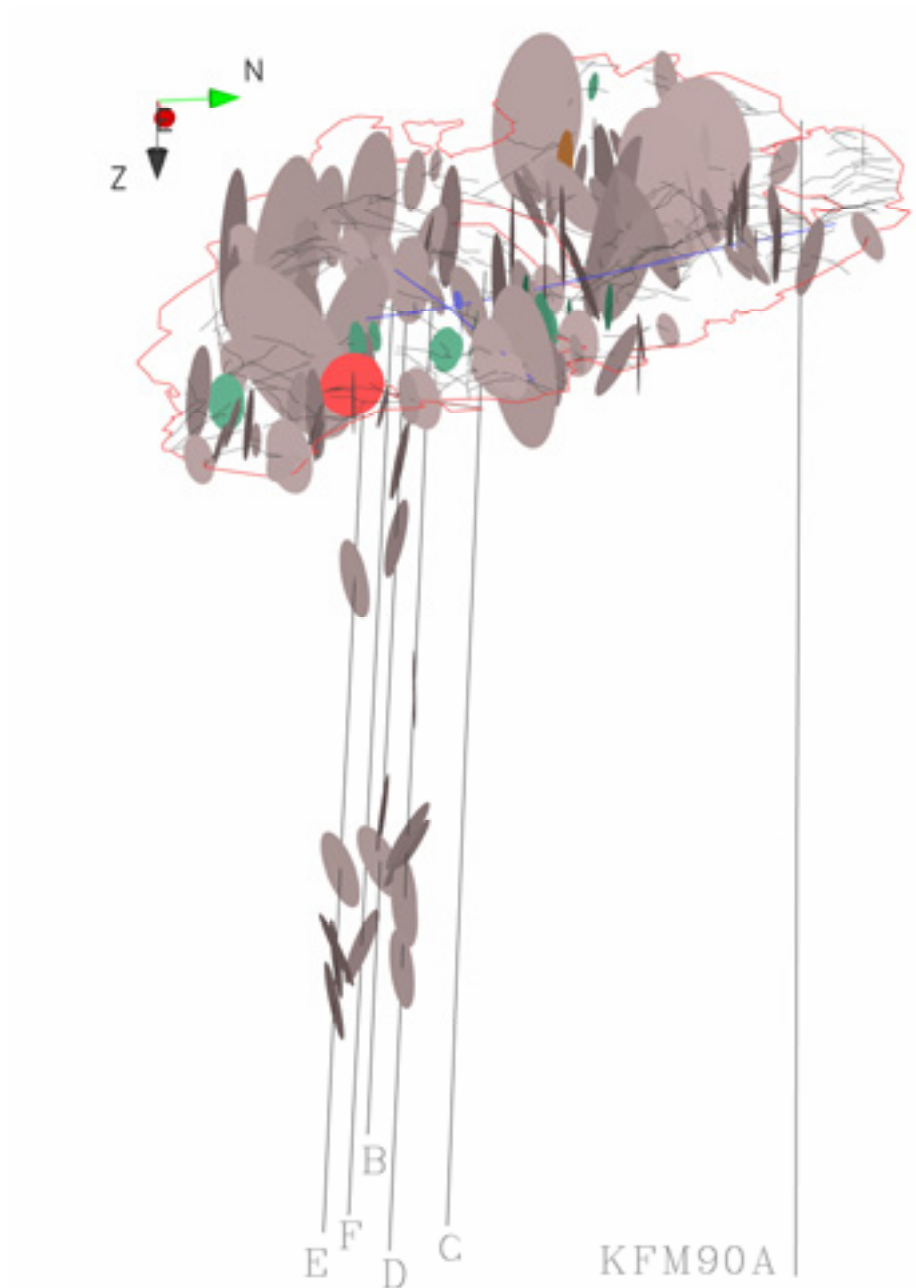


Figure 4-5. Visualization of fracture Set 3 from outcrop mapping and borehole logging.

Fracture Set 4

Sub-horizontal fractures are assigned to fracture Set 4. These fractures are concentrated in three positions:

- 1) The outcrop surface
- 2) At depth between 5 and 8 m
- 3) At depth about 14 and 17 m.

Subset 1 supports the hypothesis of a sub-horizontal fracture zone ending in proximity of the outcrop that might have being eroded and dislocated (see Section 3.1). The

fractures in subset 2 were also detected at a depth of about 5 m by ground radar loggings according to /Döse & Samuelsson, 2006/. The fractures in subsets 2 and 3 constitute the basis for the modeling of gently dipping zones in section 4.2.

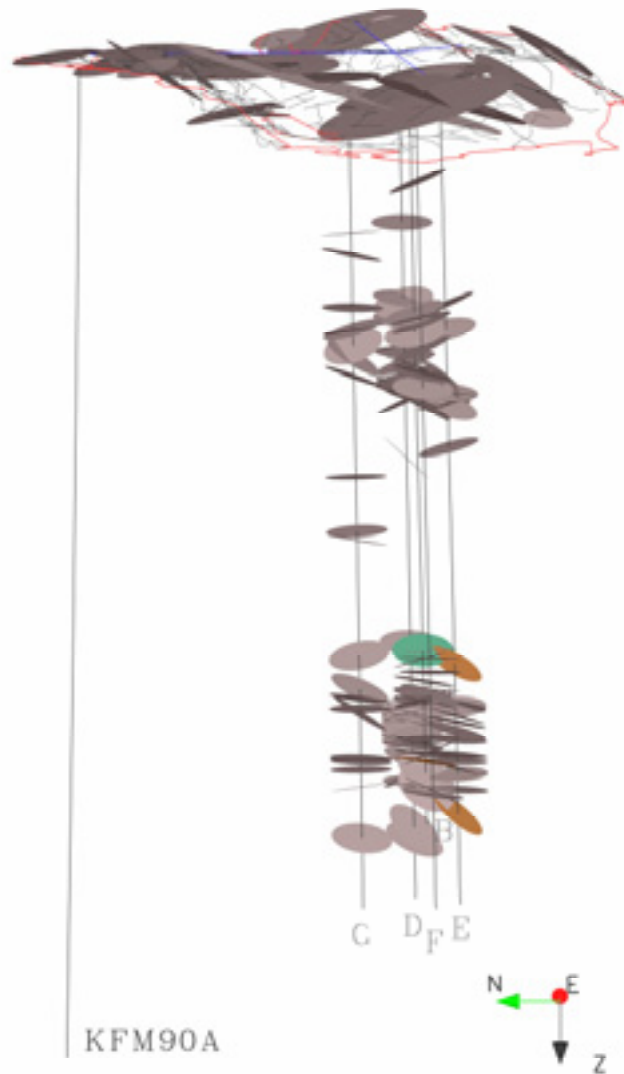


Figure 4-6. Visualization of the fracture planes of Set 4 from outcrop mapping and borehole logging.

4.2 Modelling of borehole sections with increased fracture frequency in KFM90B-F and correlation with KFM90A

Five fractured sections could be identified based on the fracture frequency and orientations along the boreholes: one sub vertical and four gently dipping (see Table 4-2).

As observed in section 4.1.1, two levels along borehole KFM90B-F have higher fracture frequencies, at about 5 to 8 m and 14 to 17 m, respectively. In KFM90A, the fractures are concentrated at three levels: 0-7 m, 13-16 m and 21-24 m.

Two sections might be identified at the upper level of KFM90B-F: between 5 and 8 m depth. Two rather distinct swarms of fractures with preferential orientations can be observed in Figure 4-7. Another fracture cluster is observed between the depth of 14 and 17 m. This section was first modeled as horizontal (see Figure 4-10). Correlation with KFM90A shows that with slight modifications the modeled sections would fit the fractured sections at 0-7 and 13-16 m in KFM90A (Figure 4-8, Figure 4-9, and Figure 4-11).

In chapter 3.1, it was suggested that the northern part of outcrop AFM001264 could be the remnant of a gently dipping fracture section, section 4, which cuts the rock mass below the blocky volume on the southern part. Based on a rough interpolation of the outcrop topography, this zone was modeled as planar with strike 95° and dip 10° (Figure 4-12). This orientation fits satisfactorily with the orientation of many of the fractures in set 4 mapped on the outcrop. It might also correspond to the fractured section at the uppermost part in KFM90A.

A deformation zone with strike $\sim 158^\circ$ and dip angle between 77° and 80° , was mapped on the eastern part of the outcrop AFM001264



Figure 2-1). It was suggested in section 3.2 that the structure of two amphibolite contacts mapped as brittle-ductile shear zones in the boreholes might be connected to the deformation zone or the shear zones on the outcrop. Based on this, a generalized

plane was modeled through the amphibolite shear contact at secup 5.38 m in KFM90D. This plane is shown together with the fractures in set 1 (Figure 4-13 and Figure 4-14).

Table 4-2. Orientations of modelled fractured sections in KFM90B-F before and after correlation with KFM90A

	Before correlation [Strike/dip]	Figure nr	After correlation [Strike/dip]	Figure nr
Fractured section 1	230/20	Figure 4-7	230/35	Figure 4-8
Fractured section 2	140/25	Figure 4-7	100/30	Figure 4-9
Fractured section 3	000/00	Figure 4-10	060/10	Figure 4-11
Fractured section 4	095/10	Figure 4-12	-	-
Fractured section 5	165/78	Figure 4-14	165/70	Figure 4-15

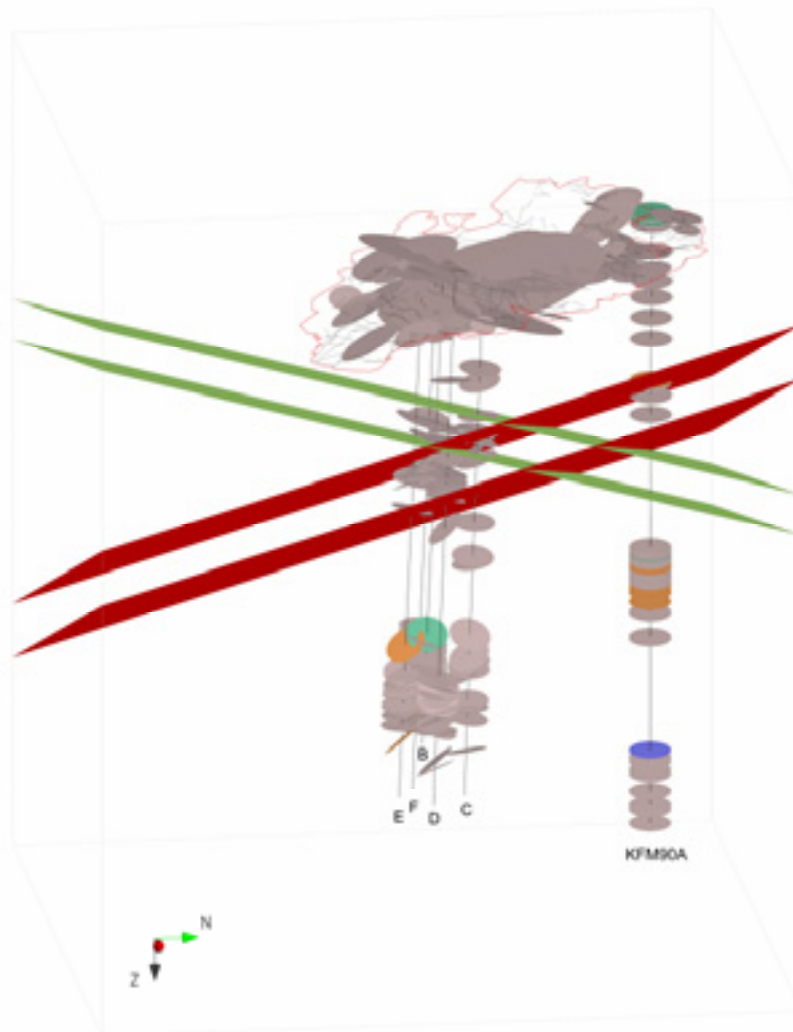


Figure 4-7. Modelling of the fractured sections at depth between 5 and 8 m: section 1 (in green) and section 2 (in red), shown with the fractures from set 4 visualized as discs representing the orientation and with the color of the rock in which they occur. In borehole KFM90A, the fractures do not represent an orientation.

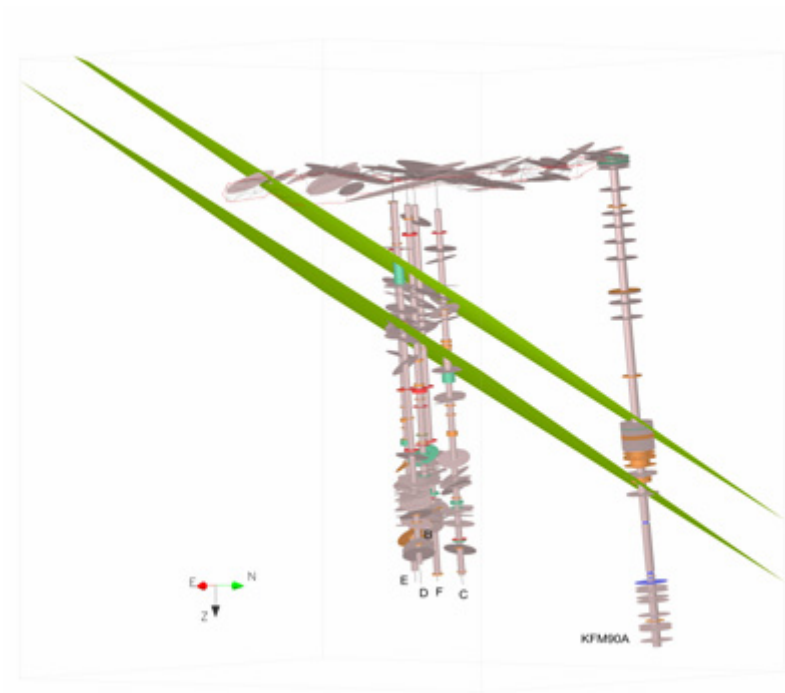


Figure 4-8 Fractured section 1 remodelled after correlation with KFM90A.

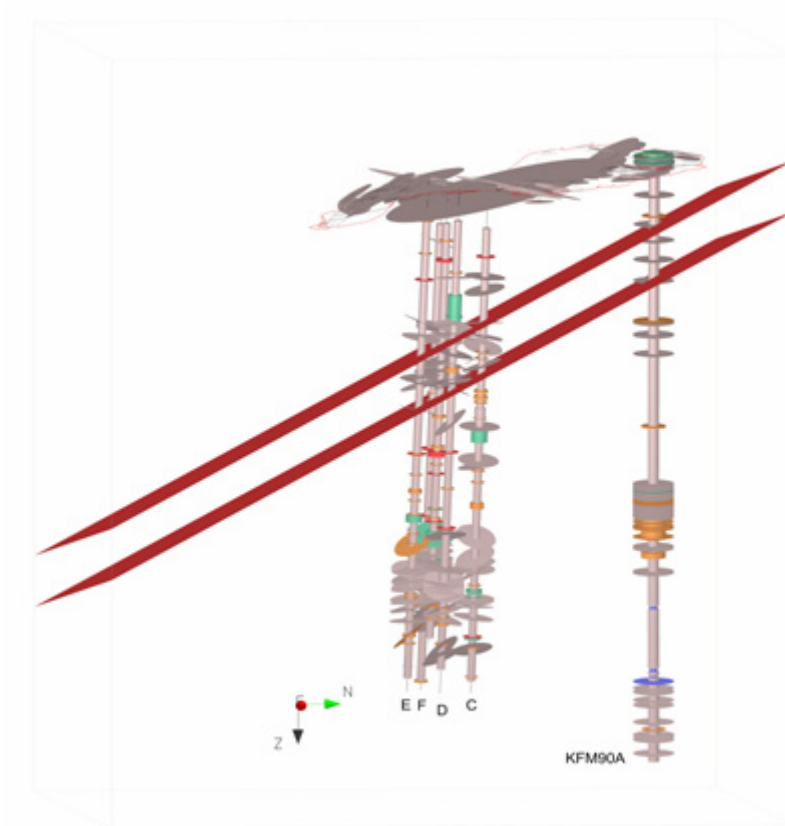


Figure 4-9 Fractured section 2 remodelled after correlation with KFM90A.

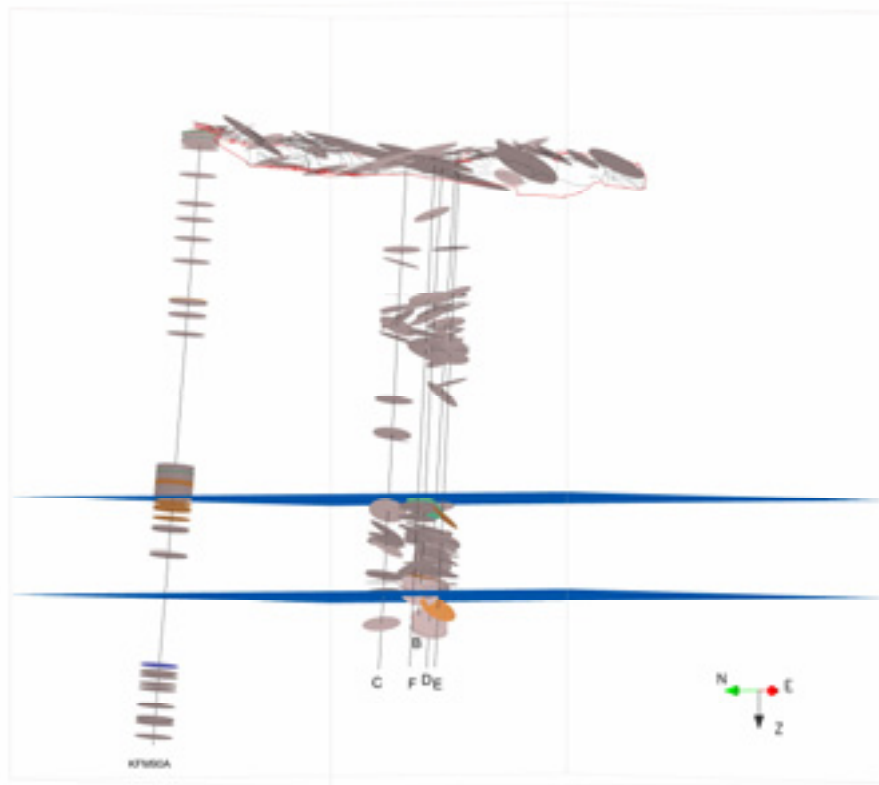


Figure 4-10. Modelling of the fractured section at depth between 14 and 17 m: section 3.

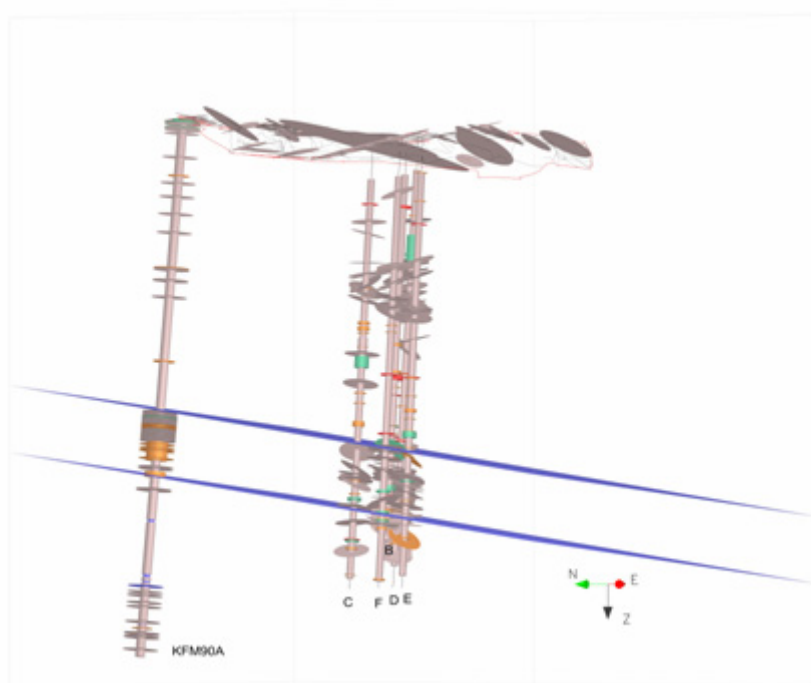


Figure 4-11 Fractured section 3 remodelled after correlation with KFM90A.

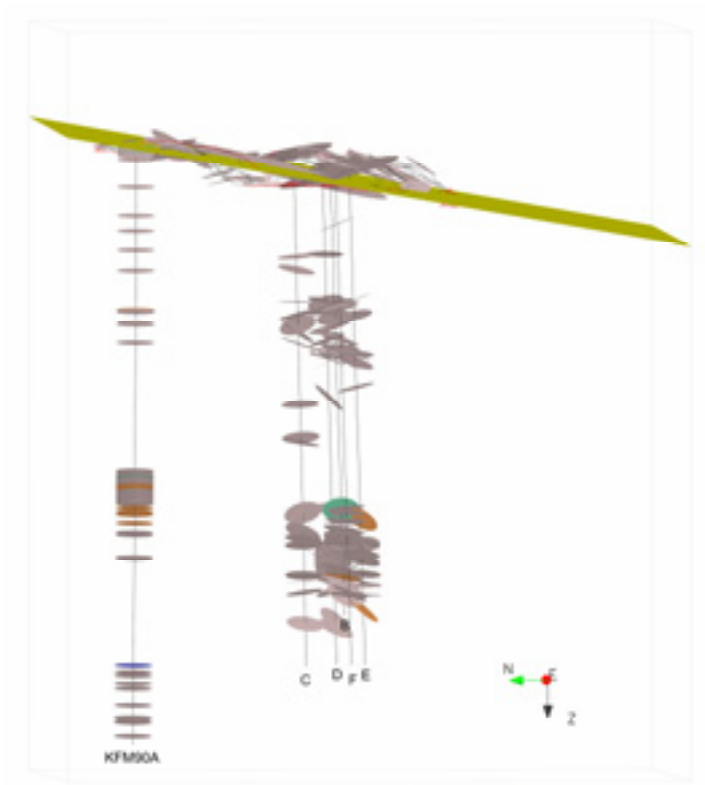


Figure 4-12. Modelling that fits the topography of the northern part of outcrop AFM001264: section 4.

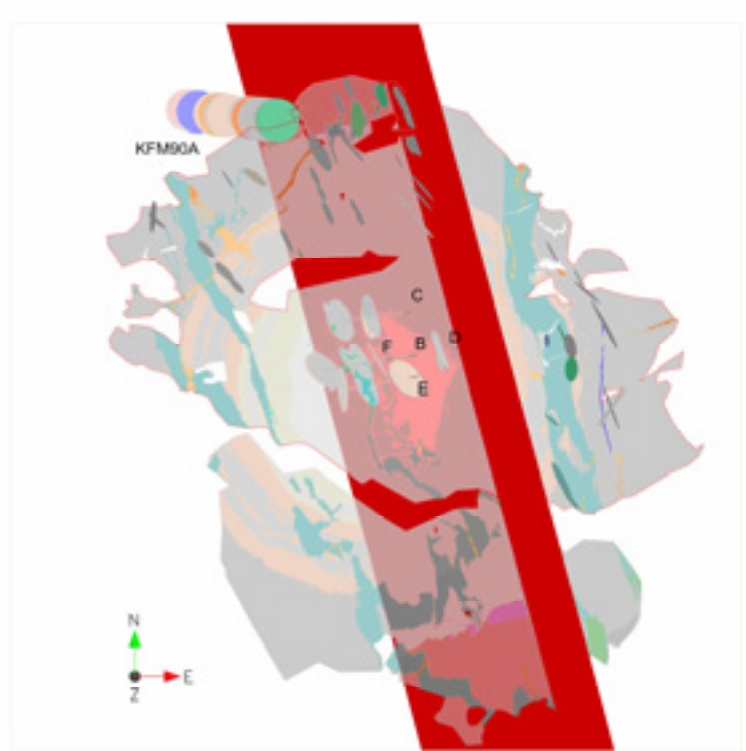


Figure 4-13. Sub-vertical fractured section 5 in top view, shown with fractures in Set 1 in borehole KFM90B-F and outcrop AFM001264. The discs representing fractures in KFM90A are visualized perpendicular to the borehole, hence they do not show fracture orientation.

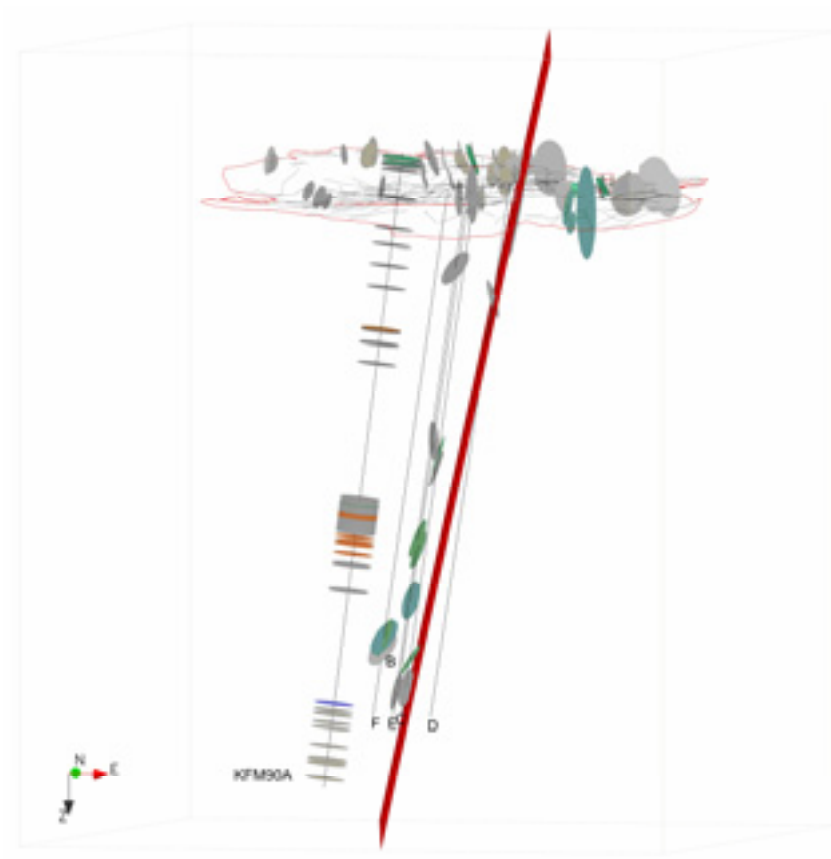


Figure 4-14. Sub-vertical fractured section viewed from south together with fracture set 1 on outcrop and in borehole KFM90B-F. In KFM90A, the orientation of the fractures does not represent an orientation.

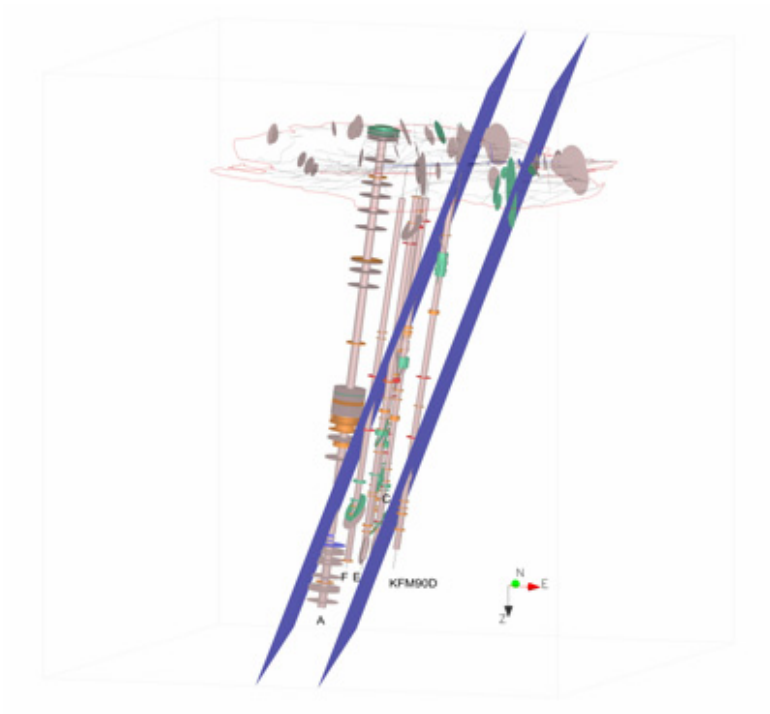


Figure 4-15 Fractured section 5 remodelled after correlation with KFM90A.

5 Conclusions

The lithology of the site is complex to investigate at a small scale. The most prominent amphibolite dykes on the outcrop do not intersect the boreholes. On the other hand, according to the mapped information on the surface, the amphibolite in the central area of the outcrop has a rather irregular morphology. For this reason, it is tricky to determine a relation both between the lithology in the boreholes and between the surface and the boreholes.

The fracture visualization of KFM90B-F allows the recognition of possibly the same fracture on the outcrop and in the boreholes in several cases. Furthermore, several sections with increased fracture frequency could be identified and an estimation of their orientation and position provided after correlation with KFM90A. Particularly, indication of the sub-vertical zone mapped on the outcrop could be found even at depth in the boreholes.

6 References

Döse C, Samuelsson E, 2006. Boremap mapping of KFM90B-KFM90F, report in preparation, Svensk Kärnbränslehantering AB.

Döse C, 2006. Traditional mapping of KFM90A, personal communication.



DOKUMENT-ID Fel!	VER Fel!	TILLHÖR Fel! Okänt namn på	SIDA 1 (3)
ÄRENDENR Fel! Okänt namn	GÄLLER FR O M Fel! Okänt	GÄLLER T O M Fel! Okänt	
FÖRFATTARE Anders Eng	DATUM 2006-03-17		
GRANSKAD Thomas Karlsson	DATUM Fel! Okänt namn på dokumentegenskap.2006-03-20		
GODKÄND John Wrafter	DATUM Fel! Okänt		

Installation av givare och värmare för mätning av anisotropiska termiska egenskaper i stor skala i fält.

1 Inledning

Fältförsök i Forsmark pågår för att undersöka anisotropiska termiska egenskaper i berg. En berghäll i anslutning till borrhålsplats 7 har frilagts för ändamålet. I berghällen kommer ett antal hål att borrar i vilka utrustning ska installeras. Utrustningen består av värmare samt temperaturgivare. Under försöket skall värmarna aktiveras och temperaturspridningen i berget övervakas. I detta dokument beskrivs i korthet hur givarna samt värmarutrustningen installerats.

Vad ska mätas

Värmarnas aktuella effekt samt temperaturen i ett antal punkter i berget kommer att mätas och loggas. Både hög absolut och relativ noggrannhet i mätningarna är viktigt under mätningarna. Önskemålet om noggrannhet på de absoluta mätningarna ligger under 0,1 grader.

Hur ska det mätas

Givarna är kopplade till ett loggersystem som omvandlar de analoga givarsignalerna till en digital motsvarighet. Loggerenheten är i sin tur kopplad till en dator där en mjukvara övervakar förloppet och lagrar de uppmätta värdena för senare analys. Detta dokument redovisar enbart vilken mätkanal på loggerutrustningen som används för respektive givare.

2 Temperaturgivare

Innan monteringen kalibrerades samtliga givare. Kalibreringen gjordes i vattenbad vid 12 grader och i ett nollgradigt isbad. För att kalibreringen skulle vara korrekt kopplades samtliga givare in på sina rätta mätkanaler i loggersystemet innan kalibreringen och har därefter inte rörts förrän försöket avslutades. Kalibreringen skedde med temperatur kalibrator tempmaster 100.

Installationen av givare i hålen skedde på följande sätt. Borrhålen mättes noggrant in med avseende på djup och lutning. Aktivitetsledaren meddelade de aktuella djup som givarna skulle installeras på. Dessa djup markerades på stavar (el-rör, 16 mm diameter) som var anpassade till borrhålens djup. Vid varje givarposition monterades en givare (med eltejp och stripes). Varje givare märktes både vid givarelementet och vid kabeländen med beteckningen på den position som givaren monterades vid. Givarpositionen fördes också in i en tabell med



PM

DISTRIBUTION

DOKUMENT-ID Fel!	VER Fel!	TILLHÖR Fel! Okänt namn på	SIDA 2 (3)
ÄRENDENR Fel! Okänt namn	GÄLLER FR O M Fel! Okänt	GÄLLER T O M Fel! Okänt	
FÖRFATTARE Anders Eng			DATUM 2006-03-17
GRANSKAD Thomas Karlsson			DATUM Fel! Okänt namn på dokumenteg enskap.2006 -03-20
GODKÄND John Wrafter			DATUM Fel! Okänt

givarnas serienummer så att full spårbarhet finns mellan givarens ID nummer och mätposition. I värmarhålet är givarna av typen termoelement (typ K), samtliga övriga givare är PT100 givare (klass 1/10).

När samtliga givare för ett borrhål var monterade på sina rätta positioner fördes hela paketet ner i hålet. Givarpaketet står således på hålbotten. Vid slutförd givarinstallation återfylldes hålen med bentonitslurry.

På grund av svårigheter att föra ner paketen i hålen tillsammans med slang för återfylldnad kunde inte utrustning för att positionera paketet i sidled monteras. Detta innebär att noggrannheten i givarnas position i horisontalled i borrhålet inte kan anges exakt. Bedömningen som gjordes var det viktigaste var erhålla en homogen återfylldnad av borrhålet.

Tabellen nedan anger relevanta parametrar för installationen.



PM

DISTRIBUTION

DOKUMENT-ID Fel!	VER Fel!	TILLHÖR Fel! Okänt namn på	SIDA 3 (3)
ÄRENDE NR Fel! Okänt namn		GÄLLER FR O M Fel! Okänt	GÄLLER T O M Fel! Okänt
FÖRFATTARE Anders Eng			DATUM 2006-03-17
GRANSKAD Thomas Karlsson			DATUM Fel! Okänt namn på dokumentegenskap.2006-03-20
GODKÄND John Wrafter			DATUM Fel! Okänt

Nivåerna för tempgivaren i borrhål för termiska mätningar (051109)

Borrhål	pos kod	z rel. KFM90B [m]	mät djup rel KFM90B [m]	mät djup [m]	dip (vid ytan) [°]	sin dip	sträcka till givare från markytan [m]	GivarID
KFM90A	A1	0,90	8,00	8,90	82,34	0,991	8,98	379968
	A2	0,90	12,50	13,40	82,34	0,991	13,52	379949
	A3	0,90	18,40	19,30	82,34	0,991	19,47	379944
KFM90B	B1	0,00	8,00	8,00	81,85	0,990	8,08	217456
	B2	0,00	11,50	11,50	81,85	0,990	11,62	217393
	B3	0,00	15,00	15,00	81,85	0,990	15,15	217397
KFM90C	C1	-0,23	8,00	7,77	81,82	0,990	7,85	379962
	C2	-0,23	11,00	10,77	81,82	0,990	10,88	379961
	C3	-0,23	12,50	12,27	81,82	0,990	12,40	379960
	C4	-0,23	18,40	18,17	81,82	0,990	18,36	379945
KFM90D	D1	0,19	9,00	9,19	81,74	0,990	9,29	379967
	D2	0,19	11,00	11,19	81,74	0,990	11,31	379965
	D3	0,19	13,00	13,19	81,74	0,990	13,33	379966
	D4	0,19	18,00	18,19	81,74	0,990	18,38	379946
KFM90E	E1	0,13	8,00	8,13	81,77	0,990	8,21	379971
	E2	0,13	11,00	11,13	81,77	0,990	11,25	379972
	E3	0,13	12,50	12,63	81,77	0,990	12,76	379958
	E4	0,13	17,00	17,13	81,77	0,990	17,31	379950
	E5	0,13	18,40	18,53	81,77	0,990	18,72	379941
	E6	0,13	19,00	19,13	81,77	0,990	19,33	379942
KFM90F	F1	-0,07	9,00	8,93	81,73	0,990	9,02	379969
	F2	-0,07	11,00	10,93	81,73	0,990	11,04	379970
	F3	-0,07	13,00	12,93	81,73	0,990	13,07	379963
	F4	-0,07	17,20	17,13	81,73	0,990	17,31	379948
	F5	-0,07	18,00	17,93	81,73	0,990	18,12	379947
	F6	-0,07	19,00	18,93	81,73	0,990	19,13	379943
Yta, vid värmarhälet (KFM90B)								379964
Lufttemperatur								379959

3 Värmare

På grund av problem med de värmare som installerades till en början har istället en värmekabel installerats (se avvikelserapport 6_2006 Forsmark). Kabeln var en HSQ 1M1600 3846W/400V, 26m värme + 2x12m kallkabel. Kabelns diameter är 3,6 mm.



PM

DISTRIBUTION

DOKUMENT-ID Fel!	VER Fel!	TILLHÖR Fel! Okänt namn på	SIDA 4 (3)
ÄRENDENR Fel! Okänt namn	GÄLLER FR O M Fel! Okänt	GÄLLER T O M Fel! Okänt	
FÖRFATTARE Anders Eng	DATUM 2006-03-17		
GRANSKAD Thomas Karlsson	DATUM Fel! Okänt namn på dokumenteg enskap.2006 -03-20		
GODKÄND John Wrafter	DATUM Fel! Okänt		

Värmekabeln installerades genom att fästas längs en trästav, diameter 21mm, som stoppades ner i värmehålet. Kabeln löpte ner till botten och upp igen, dvs. var ”dubbelvikt” längs hela sträckan. Då kabeln är indelad i sektioner begränsas uppvärmningen till de tretton nedersta metrarna i hålet, i sträckan ovanför är kabeln kall.

När värmarkabeln var installerad återfylldes även värmehålet med bentonitslurry. Att uppnå en bra värmespridning genom en homogen återfyllnad var högsta prioritet, av denna anledning kunde inte utrustning för att styra värmarkabelns position i horisontalld i borrhålen användas. Således kan inte den exakta horisontella positionen för värmekällan i borrhålet anges.

Värmarkabeln kopplades till en tyristor med vilken effektstyrning var möjlig. Effekten reglerades till 150 W/m.

4 Mätssystem

Mätssystemet installerades i en container i försöksgruppen. Containern var uppvärmd för att undvika stora temperaturskillnader under mätperioden.

Mät datorn var uppställd i ytterligare en container på borrhållsplats 7. Mät datorn var uppkopplad på SKBs nätverk och fjärrstyrdes genom Pc-Duo.